

POLITECNICO DI MILANO

SCUOLA DI INGEGNERIA INDUSTRIALE E DELL'INFORMAZIONE

DIPARTIMENTO DI CHIMICA, MATERIALI E INGEGNERIA CHIMICA "G. NATTA"



Theoretical and kinetic modeling of the combustion of aromatic hydrocarbons

DOCTORAL DISSERTATION FOR DEGREE OF DOCTOR OF PHILOSOPHY IN INDUSTRIAL
CHEMISTRY AND CHEMICAL ENGINEERING

Author:

Luna PRATALI MAFFEI
922263

Supervisor:

Prof. Tiziano FARAVELLI

Tutor:

Prof. Valentina BUSINI

Head of the Doctoral Program:

Prof. Alessio FRASSOLDATI

Cycle XXXIV 2018-2022

To my family

Acknowledgements

First, I want to thank my supervisor Prof. Tiziano Faravelli for the helpful discussions and continuous support, even when our opinions were not "perfectly" aligned, and for his inspiring motivation and passion for research. I am very grateful to Prof. Carlo Cavallotti, for guiding me since my master thesis in the field of theoretical kinetics, for caring and believing in me, and saying things honestly, but nicely. I want to express my gratitude to Dr. Stephen Klippenstein, who supervised me both remotely and in person at Argonne, for giving me this American-dream-like opportunity, for his continuous availability, and for being such a precious guide and an amazingly pressure-free advisor. I also wish to thank Prof. Henry Curran for his availability as part of my defense committee and for his careful reading of this work.

The whole CRECK modeling group in Politecnico deserves a special mention. In particular, I am grateful to Prof. Eliseo Ranzi for the discussions during my first year of PhD. I am deeply thankful to Prof. Alberto Cuoci, for being silently inspiring, always supportive and always present. I wish to acknowledge Dr. Matteo Pelucchi, for all the valuable insights and advice, for pushing me, and for being a role model researcher, and Dr. Alessandro Stagni, for his support and fascination for the realm of theoretical kinetics. I need to mention Kik, my first precious office mate, with whom I often worked until late hours, for the enthusiastic collaboration for the development of the model. I am also grateful to Andrea Nobili, for his valuable scientific insights, his inspirational hard work, and for always saying what he thinks without filters. Thanks should also go to Sangi, for the experienced-PhD guidance and the weekend runs. I also want to thank Andrea Bertolino, for both the fruitful collaboration and the friendship we built in these years. Finally, I am grateful to all the colleagues at Argonne National Lab, for the productive and enjoyable time spent together.

A special mention goes to my longtime friends Davide, Matteo, Federica, Elena, who supported me through these years. To Leonardo and Zhibek, for sharing KAUST memories and building new ones. To Shiva, for being a great friend and flatmate and for sharing the emotional load that goes together with a PhD. And to Marisa, Lucia, Daria, and Sara, my new Chicago friends who made the months spent there special.

I feel deeply grateful to Vins, not only for some proofreading and his appreciation of all the "MAH" in this thesis, but for his unconditional support, for his openness, honesty, care.

Most of all, I wish to thank my family, and especially my sister Dalia, my parents Amina and Sergio, and my uncle Sandro, without whom this experience would not have been possible, and who have helped and help me to shape my present and future every day.

Publications

- **L. Pratali Maffei**, C. Cavallotti, A. Caracciolo, N. Balucani, P. Casavecchia, "Rate rules for the reactions of oxygen atoms with terminal alkenes", *Fuel* 263 (2020) 116536
- A. Caracciolo, G. Vanuzzo, N. Balucani, D. Stranges, P. Casavecchia, **L. Pratali Maffei**, C. Cavallotti, "Combined Experimental and Theoretical Studies of the $O(^3P) + 1$ -Butene Reaction Dynamics: Primary Products, Branching Fractions, and Role of Intersystem Crossing", *The Journal of Physical Chemistry A* 123 (2019), 9934–9956
- S. Namysl, M. Pelucchi, **L. Pratali Maffei**, O. Herbinet, A. Stagni, T. Faravelli, F. Battin-Leclerc, Experimental and modeling study of benzaldehyde oxidation, *Combustion and Flame* 211 (2020), 124–132
- **L. Pratali Maffei**, M. Pelucchi, T. Faravelli, C. Cavallotti, "Theoretical study of sensitive reactions in phenol decomposition", *Reaction Chemistry and Engineering* 5 (2020) 452–472 (Cover page article for March 2020)
- **L. Pratali Maffei**, T. Faravelli, C. Cavallotti, M. Pelucchi, "Electronic structure-based rate rules for $\cdot H$ ipso addition-elimination reactions on mono-aromatic hydrocarbons with single and double OH/CH₃/OCH₃/CHO/C₂H₅ substituents: a systematic theoretical investigation", *Physical Chemistry Chemical Physics* 22 (2020), 20368–20387 (Hot Article PCCP 2020)
- C. Cavallotti, C. De Falco, **L. Pratali Maffei**, A. Caracciolo, G. Vanuzzo, N. Balucani, P. Casavecchia, "A Theoretical Study of the Extent of Intersystem Crossing in the $O(^3P) + C_6H_6$ Reaction with Experimental Validation", *Journal of Physical Chemistry Letters* 11 (2020) 9621-9628
- **L. Pratali Maffei**, M. Pelucchi, C. Cavallotti, A. Bertolino, T. Faravelli, "Master equation-based lumping approach for multi-well potential energy surfaces: a bridge between ab initio calculations and large kinetic mechanisms", *Chemical Engineering Journal* 422 (2021), 129954
- A. Nobili, **L. Pratali Maffei**, A. Baggioli, M. Pelucchi, A. Cuoci, C. Cavallotti, T. Faravelli, "On the radical behavior of large polycyclic aromatic hydrocarbons in soot formation and oxidation", *Combustion and Flame* 235 (2021), 111692
- **L. Pratali Maffei**, A. Nobili, M. Pelucchi, T. Faravelli, Q. Mao, H. Pitsch, "Polycyclic Aromatic Hydrocarbons Evolution and Interactions with Soot Particles During Fuel Surrogate Combustion: A Rate Rule-Based Kinetic Model", *SAE Technical Paper* 2021-24-0086 (2021)
- S. Dong, S. W. Wagnon, **L. Pratali Maffei**, G. Kukkadapu, A. Nobili, Q. Mao, M. Pelucchi, L. Cai, K. Zhang, M. Raju, T. Chatterjee, W. J. Pitz, T. Faravelli, H. Pitsch, P. K. Senecal, H. J. Curran, "A new detailed kinetic model for surrogate fuels: C3MechV3.3", *Applications in Energy and Combustion Science* 9 (2022), 100043

- A. Stagni, **L. Pratali Maffei**, S. Arunthanayothin, O. Herbinet, F. Battin-Leclerc, T. Faravelli, "An experimental, theoretical and kinetic-modeling study of hydrogen sulphide pyrolysis and oxidation", *Chemical Engineering Journal* (2022), 136723
- **L. Pratali Maffei**, M. Pelucchi, T. Faravelli, C. Cavallotti, "Theoretical Kinetics of $\text{HO}_2 + \text{C}_5\text{H}_5$: a Missing Piece in Cyclopentadienyl Radical Oxidation Reactions", *Proceedings of the Combustion Institute* (2022), in press, <https://doi.org/10.1016/j.proci.2022.08.020>
- A. Nobili, **L. Pratali Maffei**, M. Pelucchi, M. Mehl, A. Frassoldati, A. Comandini, N. Chaumeix, "Experimental and kinetic modeling study of α -Methylnaphthalene laminar flame speeds", *Proceedings of the Combustion Institute* (2022), in press, <https://doi.org/10.1016/j.proci.2022.08.017>
- B. Chen, P. Liu, M. Pelucchi, C. Guidici, **L. Pratali Maffei**, S. Faller, Q. Xu, J. Huang, F. Zhang, C. Huang, K. Leonherd, Z. Wang, M. Mehl, W. Roberts, T. Faravelli, H. Pitsch, "New insights into the oxidation chemistry of the N-containing biomass tar component pyrrole", *Proceedings of the Combustion Institute* (2022), in press, <https://doi.org/10.1016/j.proci.2022.07.019>
- **L. Pratali Maffei**, M. Pelucchi, R.D. Bütting, K.A. Heufer, T. Faravelli, C. Cavallotti, "Rate constants for the H-abstraction reactions from mono-aromatic hydrocarbons by H, CH_3 , OH and $^3\text{O}_2$: a systematic theoretical investigation", *Combustion and Flame* (2022), in press, <https://doi.org/10.1016/j.combustflame.2022.112421>
- **L. Pratali Maffei**, K. B. Moore III, Y. Georgievskii, C. R. Mulvihill, S. N. Elliott, J. Cho, R. Sivaramakrishnan, T. Faravelli, S. J. Klippenstein, "Automated identification and calculation of prompt effects in kinetic mechanisms using statistical models", *Combustion and Flame* (2022), in press, <https://doi.org/10.1016/j.combustflame.2022.112422>
- B. Hanamirian, A. Della Libera, **L. Pratali Maffei**, C. Cavallotti, "Investigation of methylcyclopentadiene reactivity: abstraction reactions and methylcyclopentadienyl radical unimolecular decomposition", *Journal of Physical Chemistry A* (2023), submitted

Contributions to conferences and workshops

- *1st International conference on Smart Energy Carriers*, Centro Congressi Università Federico II, Napoli, 20th - 23rd January 2019. Organized by the COST action. **Poster presentation:** "Theoretical and kinetic modelling study of phenol and phenoxy radical decomposition to CO and C₅H₆/C₅H₅ in pyrolysis conditions" by L. Pratali Maffei, M. Pelucchi, T. Faravelli and C. Cavallotti
- *Future of Fuels*, King Abdullah University of Science and Technology, Thuwal (Jeddah), Saudi Arabia, 3rd - 8th March 2019. **Oral presentation:** "Ab initio calculations of relevant reaction pathways in phenol pyrolysis and combustion" by L. Pratali Maffei, M. Pelucchi, T. Faravelli and C. Cavallotti.
- *International conference of chemical kinetics*, College of Science and technologies of Orleans University, 23rd - 27th June 2019. **Oral presentation:** "A Theoretical and Kinetic Analysis of Phenol Pyrolysis" by L. Pratali Maffei, M. Pelucchi, T. Faravelli and C. Cavallotti
- *Italian Celebration for the 50 years of CECAM*, Bologna, 9th July 2019. **Poster presentation:** "Theoretical calculation of rate constants of phenol pyrolysis", by L. Pratali Maffei, M. Pelucchi, T. Faravelli and C. Cavallotti.
- *4^{2nd} Meeting of the Italian Section of the Combustion Institute*, Camera di Commercio di Ravenna, 9 - 11th September 2019. **Oral presentation:** "Theoretical and Kinetic Modeling of the Oxidation of Oxygenated Aromatic Hydrocarbons: Reaction Classes and Rate Rules" by S. Caruso, G. Cislighi, L. Pratali Maffei, W. Pejpichestakul, M. Pelucchi, C. Cavallotti, A. Frassoldati, and T. Faravelli
- *5th International (and 1st Virtual) Flame Chemistry Workshop 2020*, 30th November – 4th December 2020 (online). **Oral presentation:** "Kinetics of the formation of first and second aromatic ring in premixed and counterflow flames: a comparative analysis", by L. Pratali Maffei, A. Nobili, M. Pelucchi, C. Cavallotti, T. Faravelli, Q. Mao, L. Cai, H. Pitsch.
- *10th European Combustion Meeting*, 14-15th April 2021 (online). **Poster presentation:** "Lumping of the low temperature oxidation of n-pentane: application of MEL", by L. Pratali Maffei, M. Pelucchi, T. Faravelli.
- *2022 Spring Technical Meeting of The Central States Section of the Combustion Institute*, 15-17th May 2022 (not attended). "Automated Construction of Fully Representative Stereochemical Reaction Mechanisms", by K. B. Moore III, S. N. Elliott, A. V. Copan, C. R. Mulvihill, L. Pratali Maffei, S. J. Klippenstein.
- *39th International Symposium on Combustion*, Vancouver Convention Center, 23-29th July 2022. **Oral presentation:** "Theoretical Kinetics of HO₂+C₅H₅: a Missing Piece

in Cyclopentadienyl Radical Oxidation Reactions", by L. Pratali Maffei, M. Pelucchi, T. Faravelli, C. Cavallotti.

- *6th International (and 2nd Virtual) Flame Chemistry Workshop*, 15-19th August 2022 (online). **Oral presentation:** "Automated calculation of prompt effects in kinetic mechanisms using statistical models: the case of butene flame chemistry", by L. Pratali Maffei, K. B. Moore III, Y. Georgievskii, C. R. Mulvihill, S. N. Elliott, J. Cho, R. Sivaramakrishnan, T. Faravelli, S. J. Klippenstein.

Abstract

The increase in the world energy demand and the unstable geopolitical scenario call for short and medium-term sustainable alternatives for energy production, including high energy density fuels for transportation. This motivates the research on biomass-derived biofuels, which satisfy net zero-CO₂ balance. However, the large amounts of particulate matter (soot) emissions produced due to their high content of aromatic hydrocarbons raise both environmental and health concerns and therefore stand in the way of their widespread use. At the same time, large amounts of aromatic species in fuel mixtures may be exploited for different purposes, such as the formulation of anti-knocking additives, the upgrade to high-value chemicals, or the synthesis of carbon nano-materials for sensors and energy storage.

Kinetic models are being used to evaluate the combustion properties of a fuel mixture in terms of compatibility with existing engine infrastructure, emission control, and new potential applications. In particular, kinetic modeling of the reactivity of reference model compounds for complex fuels (i.e., surrogate mixtures) has driven fuel formulation, design and development for the past decades. In the last 30 years, *ab initio* theoretical calculations have proven to be a very useful tool to predict thermochemical properties and rate constants. More recently, the generation and use of theory-informed kinetic mechanisms has become the standard and recommended practice, thanks to automated codes for electronic structure (ES) calculations and theoretical kinetics, to the availability of higher computational power, and to the increasing accuracy of theoretical methodologies.

In this thesis, state-of-the-art *ab initio* theoretical methodologies are exploited to build a more consistent and theory-based kinetic model for the combustion of monocyclic and polycyclic aromatic hydrocarbons (MAHs, PAHs). This thesis streamlines an effective approach that combines accurate theoretical calculations, systematic theoretical investigations of potential energy surfaces, and a new lumping technique, in a consistent reaction class-based framework. Model compounds here addressed with theoretical calculations are: C5 unsaturated rings, and in particular cyclopentadiene, a key species in both MAH/PAH decomposition and growth; benzene, the simplest MAH and a key building block in PAH growth; substituted oxygenated MAHs (OAHs) such as phenol, catechol, and anisole, used as fuel surrogate components for biomass-derived biofuels.

Despite the interest in the combustion kinetics of MAHs/OAHs, several aspects of their decomposition, oxidation and growth chemistry are still unclear. Therefore, reaction classes and rate rule approaches for model organization, widely spread for reference components of conventional fuels (e.g., alkanes), have not been developed for aromatic systems. Secondly, while advanced computational capacity provides a remarkable opportunity of untangling the complex chemistry of aromatic hydrocarbons, theoretical calculations are challenging (i) due to the large species size, (ii) due to the poor assessment of the accuracy of ES methodologies for these compounds, and (iii) due to the scarce knowledge of relevant reaction channels. Finally, the complex multi-step reactivity of aromatic hydrocarbons is characterized by a large number of intermediate species, that are difficult to integrate in global combustion kinetic mechanisms, thus often discouraging the use of theoretical kinetics for detailed or

semi-detailed kinetic model development. In fact, too large a mechanism size might prevent its use for practical applications (e.g., model reduction for fluid dynamics simulations of real reactors).

This thesis addresses some of the challenges listed above. For the first time, the subset of C5 and aromatic species reactivity of the CRECK kinetic mechanism is organized systematically and hierarchically according to the reaction classes formulated in this work. Similar kinetic parameters are adopted for compounds with the same chemical functionality. Rate rules developed from the theoretical results of this work provide more accurate scaling relations for some reaction classes.

State-of-the-art theoretical calculations for relevant reactions of C5, benzene, and substituted MAHs are carefully performed. The appropriateness of the theoretical methodologies adopted is assessed by comparison with microkinetic experimental data and a critical evaluation of the sensitivity of the rate constants to different theoretical treatments, leading to reasonable uncertainty estimates. The present results also highlight that while many reaction types are successfully automated, human intervention is still required in many cases to avoid large errors in the predictions. This aspect opens up more philosophical discussions on the role of scientists and on the risks of fully-automated streamlines.

Theoretical calculations for a large number of H-atom abstraction and ipso addition-elimination reactions for benzene and substituted MAHs/OAHs reveal systematic trends and guide rate rule development for aromatic systems. For instance, the behavior of the aromatic ring sites is found to be very similar, while more complex functional relations are derived to account for the effect of lateral substituents. Preliminary tests on 2-ring PAHs suggest that the presence of additional aromatic rings might significantly affect the entropy and therefore the rate constants of bimolecular reactions with respect to MAHs.

The chemistry of relevant aromatic species in the CRECK kinetic mechanism is updated with theoretical calculations from both this thesis and from the literature, upon careful revision, focusing mostly on oxidation kinetics. Complex multi-step reactions are simplified with a lumping approach specifically developed in this work for the integration of theoretically-derived rate constants into kinetic mechanisms, called master equation-based lumping (MEL). The ability of MEL to significantly reduce the system size while simultaneously retaining the macroscopic reactive behavior is proved with several examples. Applications of MEL are clearly not limited to aromatic systems, thus providing a useful and general tool for the simplification of kinetic mechanisms based on first principles.

The final updated kinetic mechanism is tested against a wide range of experimental reactor data for C5, MAHs, and OAHs pyrolysis and oxidation. A class-based heat map flux analysis, implemented in this work, provides a general overview of relevant reaction classes at different operating conditions, highlights similarities and differences among MAHs, and helps to identify the reasons for model shortcomings. The kinetic model thus obtained shows overall reasonable performances. The discrepancies with experimental observations are in some cases attributed to the semi-detailed theoretical description of MAH reactivity attempted in this work, which generates "imbalances" in the radical pool with respect to the former simplified subset of MAH/PAH reactivity of the CRECK mechanism.

This work sets the grounds for future consistent, simple and physically meaningful kinetic model development for MAHs and PAHs combustion. Methodological aspects related to theoretical calculations, uncertainty estimates, master equation-based lumping, and reaction class organization will contribute to future integrated and automated workflows for systematic kinetic mechanism development.

Sommario

Con l'aumentare del fabbisogno energetico e dell'instabilità dello scenario geopolitico mondiali, è divenuto necessario ricercare fonti di energia sostenibile a breve e medio termine, tra cui figurano i combustibili ad alta densità energetica per il settore dei trasporti. Ciò è promotore della ricerca condotta sui biocombustibili derivati da biomasse, poiché caratterizzati da neutralità carbonica. Tuttavia, la grossa quantità di particolato che generano durante l'ossidazione a causa del loro elevato contenuto di idrocarburi aromatici, è dannosa per la salute e per l'ambiente e quindi ne potrebbe prevenire uso e diffusione. Allo stesso tempo, l'elevato contenuto di idrocarburi aromatici presenti nelle miscele di combustibili può essere impiegato per svariati fini, ad esempio nella produzione di additivi antidetonati, di altri prodotti dell'industria chimica, o nella sintesi di nanomateriali in carbonio, utilizzati per esempio per sensori e per lo stoccaggio di energia.

Attraverso la modellazione cinetica, si possono valutare le proprietà di combustione delle miscele di combustibili in termini di compatibilità con le infrastrutture esistenti, conformità alle limitazioni sulle emissioni e potenziale per nuovi utilizzi. Infatti, negli ultimi decenni è stata proprio la modellazione cinetica della reattività dei composti di riferimento per i combustibili complessi (miscele surrogate) a fungere da base per l'ottimizzazione e lo sviluppo di combustibili. Negli ultimi trent'anni, si sono inoltre rivelati di estrema utilità calcoli teorici *ab initio* che permettono di derivare con accuratezza proprietà termodinamiche e costanti cinetiche. Più di recente, il loro impiego nello sviluppo di meccanismi cinetici è diventato prassi grazie anche all'automatizzazione dei calcoli di struttura elettronica, a una maggiore disponibilità di risorse computazionali, e alla crescente accuratezza dei metodi teorici.

In questo lavoro di tesi ci si è avvalsi di calcoli teorici *ab initio* utilizzando metodologie allo stato dell'arte per costruire un modello cinetico più coerente e fisicamente accurato con cui descrivere la combustione di idrocarburi aromatici monociclici e policiclici (MAH, PAH). Seguendo un approccio sistematico che si basa su classi di reazione, si è delineato un metodo di lavoro efficace che combina accurati calcoli teorici e sistematici su superfici di energia potenziale a una nuova metodologia di lumping. I composti presi in esame nell'elaborato sono: anelli a 5 insaturi, in particolare il ciclopentadiene, specie determinante sia nella decomposizione sia nella crescita di MAH e PAH; il benzene, l'MAH più semplice nonché struttura di base per la crescita dei PAH; MAH ossigenati sostituiti (OAH) come fenolo, catecolo e anisolo, che vengono utilizzati come componenti rappresentativi dei combustibili ottenuti da biomasse.

Nonostante l'interesse per la cinetica di combustione di MAH e OAH, rimangono poco chiari numerosi aspetti in merito alle loro reazioni di decomposizione, ossidazione e crescita. Di conseguenza, non esiste ancora per i composti aromatici un'organizzazione sistematica secondo classi di reazione e regole per l'estensione di costanti cinetiche, diffuse invece per le molecole rappresentative di combustibili più convenzionali, come gli alcani. Inoltre, nonostante le avanzate capacità computazionali, i calcoli teorici *ab initio* rimangono di difficile applicazione a sistemi aromatici a causa della grandezza delle molecole in questione, della scarsa valutazione della precisione dei metodi di struttura elettronica, e di una limitata

conoscenza dei cammini di reazione rilevanti per la loro combustione. Infine, le complesse reazioni degli idrocarburi aromatici si caratterizzano per un cospicuo numero di specie intermedie, difficili da integrare nei meccanismi cinetici globali di combustione. Ciò scoraggia quindi l'uso della cinetica teorica per lo sviluppo di modelli dettagliati o semidettagliati. Una grandezza esagerata del meccanismo rischierebbe infatti di impedirne un'applicazione pratica (ad esempio, la riduzione per simulazioni di fluidodinamica in motori reali).

In questa tesi sono state affrontate alcune delle problematiche sopraelencate. La reattività di anelli a 5 insaturi e di anelli aromatici del meccanismo cinetico sviluppato dal gruppo CRECK è stata per la prima volta organizzata in modo gerarchico e sistematico secondo classi di reazione formulate in questo lavoro. Sono stati adottati parametri cinetici analoghi per composti con la stessa funzionalità chimica, mentre regole derivate dai risultati teorici hanno fornito relazioni più accurate per l'estensione dei parametri cinetici per alcune classi di reazione.

Inoltre, sono stati effettuati calcoli teorici *ab initio* con metodologie allo stato dell'arte per studiare reazioni chiave nella combustione di anelli insaturi a 5, benzene e MAH sostituiti. La validità dei metodi teorici adottati è stata esaminata tramite il confronto con dati sperimentali e la valutazione dell'impatto di diverse scelte metodologiche sulle costanti cinetiche ottenute, derivando così ragionevoli stime dell'incertezza dei risultati. I risultati evidenziano anche come, nonostante l'efficace automatizzazione del calcolo delle costanti, in molti casi sia ancora necessario l'intervento umano per evitare errori grossolani. Questo aspetto solleva dunque questioni più filosofiche sul ruolo degli scienziati nei processi interamente automatizzati.

Attraverso il calcolo teorico di numerose reazioni di estrazione di atomi di idrogeno e di reazioni di ipso addizione-eliminazione su benzene e MAH/OAH sostituiti si è riusciti a sviluppare regole di riferimento per l'assegnazione di parametri cinetici dei sistemi aromatici. Ad esempio, si è osservato che il comportamento dei siti degli anelli aromatici è molto simile, mentre sono state derivate relazioni funzionali più complesse per spiegare gli effetti dei gruppi laterali. Da prove preliminari si è evidenziato come, per quanto concerne gli MAH, la presenza di ulteriori anelli aromatici potrebbe portare a importanti variazioni entropiche e dunque a deviazioni delle costanti cinetiche di reazioni bimolecolari.

La reattività delle specie aromatiche in esame descritta nel meccanismo cinetico del gruppo CRECK è stata dunque attentamente revisionata e aggiornata secondo i calcoli teorici sia di questa tesi sia di lavori di letteratura, ponendo particolare attenzione alla cinetica di ossidazione. Cinetiche complesse caratterizzate da più step elementari sono state semplificate con un approccio denominato master equation-based lumping (MEL), ideato appositamente in questa tesi per l'integrazione di costanti derivate con metodi *ab initio* nei meccanismi cinetici. Attraverso numerosi esempi si è dimostrato come l'approccio MEL sia in grado di ridurre significativamente il numero di reazioni del sistema, mantenendone tuttavia intatto il comportamento macroscopico. L'utilizzo del MEL non si limita chiaramente a sistemi aromatici e rappresenta dunque uno strumento utile alla semplificazione dei meccanismi cinetici basati su conti teorici.

Il meccanismo cinetico ottenuto è stato infine testato con simulazioni di esperimenti in

reattori per la pirolisi e l'ossidazione di anelli a 5, MAH e OAH. Un nuovo approccio implementato in questa tesi per l'analisi dei flussi basato sulle classi di reazione individuate chiarisce la loro rilevanza a seconda delle diverse condizioni operative, evidenziando anche affinità e differenze tra gli MAH e facilitando la comprensione degli aspetti manchevoli del modello. Il modello riproduce ragionevolmente i dati sperimentali. Alcune delle discrepanze tra le simulazioni e i dati sono probabilmente dovute a diversi livelli di dettaglio nella descrizione della reattività degli MAH, che genera "squilibri" tra i radicali rispetto alla precedente rappresentazione semplificata del meccanismo CRECK.

La presente tesi getta le basi per uno sviluppo di modelli cinetici per la combustione di MAH e PAH che sia coerente, semplice e fisicamente accurato. Gli aspetti metodologici legati a calcoli teorici, stime di incertezza, all'approccio MEL e all'organizzazione in classi di reazione contribuiranno a flussi di lavoro futuri integrati e automatizzati volti allo sviluppo sistematico di meccanismi cinetici.

Contents

Acknowledgements	iv
Publications	v
Contributions to conferences and workshops	vii
Abstract	ix
Sommario	xii
List of Figures	xix
List of Tables	xxv
List of Abbreviations	xxix
List of Symbols	xxxii
1 Introduction and background	1
1.1 The role of aromatic hydrocarbons in the energy transition	1
1.1.1 Biomass-derived biofuels	3
1.1.2 Particulate matter emissions	4
1.1.3 The role of monocyclic aromatic hydrocarbons and unsaturated 5- membered rings	6
1.2 Kinetic modeling of combustion processes	9
1.3 <i>Ab initio</i> theoretical kinetics for kinetic modeling	15
1.4 Kinetic modeling of aromatic hydrocarbons	19
1.5 Objectives and structure of this thesis	22
2 Fundamentals of kinetic modeling	25
2.1 Reactions and kinetic parameters	25
2.1.1 Elementary reactions and rate laws	25
2.1.2 Equilibrium reactions	27
2.1.3 Temperature dependence	27
2.1.4 Pressure dependence	28
2.2 Thermochemistry	30
2.3 Transport properties	32
2.4 What controls macroscopic combustion properties?	33

2.5	CRECK mechanism: a hierarchical kinetic scheme	35
2.6	Reaction classes and rate rules for mechanism development	36
2.6.1	Reaction classes	36
2.6.2	Analogy and rate rules	40
2.7	Kinetic simulations	43
3	Computational chemistry	49
3.1	Electronic structure calculations	50
3.1.1	Self-consistent field and Hartree-Fock theory	51
3.1.2	Basis set approximation	52
3.1.3	Electron correlation methods	54
3.1.4	Density functional theory	58
3.2	Statistical thermodynamics	60
3.2.1	Partition functions	60
3.2.2	The rigid rotor harmonic oscillator approximation and the treatment of anharmonicities	60
3.2.3	Thermochemical parameters	62
3.3	Theoretical kinetics	64
3.3.1	Potential energy surface	64
3.3.2	Transition state theories	65
3.3.3	Tunneling corrections for reactions with barriers	73
3.3.4	Dealing with pressure dependence	73
3.4	Semi-automated calculation of rate constants	79
3.4.1	EStokTP	79
3.4.2	Auto-Mech	82
3.5	Application of computational chemistry to MAH reactive systems	84
3.5.1	Computational cost	84
3.5.2	Uncertainty estimate for rate constants	85
3.5.3	Contributions of this work	92
4	Bridging computational chemistry and kinetic modeling	95
4.1	Motivation	95
4.2	Conventional lumping techniques	96
4.3	A new approach: master equation-based lumping	97
4.3.1	Methodology	97
4.3.2	Implementation	101
4.3.3	Species selection	104
4.4	Application of MEL	105
4.4.1	CH ₃ COOH	105
4.4.2	C ₅ H ₅ +OH	106
4.4.3	C ₅ H ₅ +C ₅ H ₅	110
4.5	Summary and future perspectives	113

5	Cyclopentadiene pyrolysis and oxidation	117
5.1	Background and literature review	117
5.2	Reaction classes and kinetic model updates by class	122
5.2.1	Decomposition and oxidation	122
5.2.2	Growth	129
5.3	Theoretical calculations	134
5.3.1	H-atom abstraction reactions by H and OH from C ₅ H ₆ and extension to C ₉ H ₈ and C ₅ H ₅ OH	134
5.3.2	C ₅ H ₅ + HO ₂	138
5.3.3	Reactivity of C ₅ H ₅ O	152
5.4	Model performance and analysis	157
5.4.1	Pyrolysis	157
5.4.2	Oxidation	163
5.4.3	Summary	171
6	MAHs pyrolysis and oxidation	173
6.1	Background and literature review	173
6.1.1	Benzene	173
6.1.2	Oxygenated MAHs	177
6.2	Reaction classes and kinetic model updates by class	183
6.2.1	Decomposition and oxidation	183
6.2.2	Growth	193
6.3	Theoretical calculations	198
6.3.1	C ₆ H ₆ +O(³ P)	198
6.3.2	C ₆ H ₅ OH and C ₆ H ₅ O decomposition	205
6.3.3	C ₆ H ₅ +O ₂ and C ₆ H ₅ O+O(³ P)	214
6.4	Theoretical calculations by reaction class: H-atom abstraction reactions from mono-substituted MAHs	238
6.4.1	Motivation	238
6.4.2	Theoretical methodology	238
6.4.3	Rate constant calculations	240
6.4.4	Systematic trends	256
6.4.5	Exploration of rate extension to two ring PAHs	259
6.4.6	Summary	262
6.5	Theoretical calculations by reaction class: ipso addition-elimination reactions on mono and di-substituted MAHs	263
6.5.1	Motivation and background	263
6.5.2	Rate constant calculation	265
6.5.3	Determination of rate rules	271
6.5.4	Summary	284
6.6	Model performance and analysis	287
6.6.1	Benzene	288

6.6.2	Oxygenated aromatics	303
6.6.3	Summary	320
7	Conclusions and outlooks	325
7.1	Theoretical calculations and integration into global kinetic mechanisms	326
7.2	Reaction classes and rate rules for the reactivity of MAHs and PAHs	328
7.3	First principles-based kinetic modeling: general comments and outlooks . . .	329
A	Species table	333
	Bibliography	337

List of Figures

1.1	BP energy consumption and production (2021 review)	1
1.2	Contribution to GHG emissions by sector in the US in 2019 according to EPA	2
1.3	Schematic potential routes from biomass to biofuels through gasification or fast pyrolysis.	4
1.4	Particulate Matter generation by sector	5
1.5	Shares of different tyPES for hydrocarbons in the composition of conventional and biomass-derived fuels.	6
1.6	Relevant MAHs in different tyPES for fuels	7
1.7	Qualitative representation of the evolution from gas-phase aromatics to soot in a premixed flame. Adapted from Bockhorn, 1994.	8
1.8	The role of kinetic modeling in assessing the viability of fuels from the molecular level to the device level.	10
1.9	Iterative steps for kinetic model development, update and testing.	11
1.10	Increase in theory-informed chemical kinetic works at the Combustion symposia from 2000 on. Adapted from [88].	15
1.11	Examples of (automated) workflows for first-principle calculations of thermochemical parameters and rate constants.	16
1.12	Examples of aromatic radicals derived from bond-fission or H-atom abstraction reactions from benzene, toluene, phenol and anisole.	20
1.13	Schemes of molecular decomposition reactions of phenol (top) and catechol (bottom).	20
1.14	Example of growth from phenyl radical to naphthalene through HACA pathway.	21
1.15	Example of complex PES investigated in this work ($C_6H_5 + O_2$ reaction). . .	22
1.16	Structure of this thesis.	23
2.1	Example of bimolecular and unimolecular pressure-dependent rate constants calculated in this work	30
2.2	Reactions written in CHEMKIN format in CRECK model according to the Troe and PLOG formalisms	31
2.3	Example of NASA polynomials for C_5H_5 calculated in this work.	32
2.4	Schematic representation of the CRECK mechanism modular structure	36
2.5	Example of hierarchical organization of the MAH kinetics according to reaction classes (highlighted in bold).	39
2.6	Schematic representation of rate extension via analogy and rate rules from benzene to phenol, naphthol and catechol	44

2.7	Schematic workflow of OpenSMOKE++ kinetic simulation procedure.	45
3.1	Correlation methods and basis set size	53
3.2	Example of PES and MEP	64
3.3	Sketch of variational TST	67
3.4	Pivot points in VRC-TST	69
3.5	MECP and hopping probability	72
3.6	Energy transfer and reaction in multi-well ME	74
3.7	Schematic representation of the steps automatically performed by EStokTP .	80
3.8	Schematic representation of the steps automatically performed by EStokTP for barrierless reactions	81
4.1	Typical number of reactions and species of detailed, lumped and reduced global kinetic mechanisms	96
4.2	Qualitative representation of MEL approach	98
4.3	Qualitative PES for the reaction $a + a_2 = w = s = b + b_2$	100
4.4	Flowchart of the algorithm used for the implementation of MEL	103
4.5	Diagram of the procedure of selection of accumulating species and merged pseudospecies composition	104
4.6	The PES for CH ₃ COOH decomposition	105
4.7	Lumped simulation profiles for CH ₃ COOH	106
4.8	Simplified C ₅ H ₅ OH PES	107
4.9	Comparison between the lumped and elementary rate constants of C ₅ H ₅ OH isomers	108
4.10	Elementary, well-extended, lumped rate constants for C ₅ H ₅ OH isomers	109
4.11	Well-extended and lumped branching fractions for C ₅ H ₅ OH isomers	109
4.12	Scheme of the main reaction channels of the C ₁₀ H ₁₀ and C ₁₀ H ₉ PESs	110
4.13	Detailed and lumped mechanism performances for C ₁₀ H ₁₀ PES	111
4.14	Detailed and lumped mechanism performances for C ₁₀ H ₉ PES	112
4.15	Kinetic simulations for the pyrolysis of C ₅ H ₆ in a PFR	113
5.1	PES and rate constants for H-atom abstraction by H and OH from cyclopentadiene and indene	136
5.2	Rate constants for the H-atom abstraction by H from the CH ₂ and OH groups of 1,3-C ₅ H ₅ OH and 1,4-C ₅ H ₅ OH	138
5.3	Sensitivity coefficients of CO ₂ and C ₁₀ H ₈ in cyclopentadiene and benzene oxidation	138
5.4	Potential energy surface of HO ₂ +C ₅ H ₅ reaction	144
5.5	Minimum energy path for HO ₂ recombination with C ₅ H ₅ and resulting rate constant	145
5.6	Minimum energy path of OH recombination with 2,4-C ₅ H ₅ O and resulting rate constant	146

5.7	Minimum energy path and rate constants for the recombination of hydroxyl radical on the oxygen atom of 1,3-C ₅ H ₅ O	147
5.8	Pressure-dependent product branching fractions of HO ₂ +C ₅ H ₅ and OH+2,4C ₅ H ₅ O reactions	148
5.9	Investigation of possibly relevant reaction channels on the 1,3-C ₅ H ₅ O + OH PES	149
5.10	Minimum energy paths and rate constant for the recombination of hydroxyl radical on the ortho carbon atom of 1,3-C ₅ H ₅ O	149
5.11	Possible H-transfer and ring opening pathways deriving from the OH recombination on the meta site of 1,3-C ₅ H ₅ O	150
5.12	Experimental and simulated mole fraction profiles of significant species for C ₅ H ₆ oxidation in the JSR of Wang et al. [338] and in the PFR of Butler et al. [336]	152
5.13	Experimental and simulated mole fraction profiles of relevant species in the oxidation of benzene in the Princeton PFR [334] and in the Yale JSR [368] . .	153
5.14	Rate constants of the radical H-atom abstractions by H, OH, and ³ O ₂ from C ₅ H ₅ O	154
5.15	Speculated reaction pathways deriving from the recombination of ³ O ₂ on the ortho and meta carbon sites of 1,3-C ₅ H ₅ O.	156
5.16	Experimental and simulated species profiles for cyclopentadiene pyrolysis in the PFR of Djokic et al. [297]	158
5.17	Experimental and simulated species profiles for cyclopentadiene pyrolysis doped with ethylene in the PFR of Vervust et al. [298]	159
5.18	Global flux analysis for cyclopentadiene pyrolysis at 1000 K and ~50% conversion	159
5.19	Flux analysis for cyclopentadiene pyrolysis organized by class type	160
5.20	Flux analysis for growth reactions in cyclopentadiene pyrolysis organized by addition type	161
5.21	Kinetic simulations of indene pyrolysis in the ST of Laskin et al. [348]	161
5.22	Kinetic simulations of indene pyrolysis in the PFR of Jin et al. [337]	162
5.23	Flux analysis for indene pyrolysis	163
5.24	Kinetic simulations of cyclopentadiene oxidation in the JSR of Wang et al. [338]	164
5.25	Flux analysis for low T cyclopentadiene oxidation	165
5.26	Kinetic simulations for cyclopentadiene oxidation in the PFR of Butler et al. [336]	167
5.27	Flux analysis for cyclopentadiene oxidation at 1150 K in a PFR	168
5.28	Kinetic simulations, flux and sensitivity analysis for IDT/LFS of C ₅ H ₆	170
6.1	Schematic overview of relevant reaction pathways identified in the pyrolysis and oxidation of benzene in the literature	174
6.2	Relevant literature reaction pathways in OAH combustion	178
6.3	Potential energy surface for the O(³ P) + C ₆ H ₆ reaction	201

6.4	Total rate constant for the reaction of O(³ P) addition to C ₆ H ₆	201
6.5	Triplet-singlet MECP geometries and corresponding SOCs, and branching fractions of O(³ P) + C ₆ H ₆	202
6.6	PES for phenol decomposition	208
6.7	Global rate constants for the decomposition of phenol and comparison with available literature data	211
6.8	PES for phenoxy decomposition and corresponding global rate constant . . .	211
6.9	Scheme of the main channels on C ₆ H ₅ +O ₂ and C ₆ H ₅ O+O PESs identified in the literature	215
6.10	Channels of C ₆ H ₅ OO PES accessed from C ₆ H ₅ + O ₂	224
6.11	Channels of C ₆ H ₅ OO PES accessed from C ₆ H ₅ O + O(³ P) recombination on the ortho position	224
6.12	Channels of C ₆ H ₅ OO PES accessed from C ₆ H ₅ O + O(³ P) recombination on the para position	225
6.13	MEP and high-pressure limit rate constant for C ₆ H ₅ + O ₂	226
6.14	MEPs of the recombination of O(³ P) on the different sites of C ₆ H ₅ O	227
6.15	MEPs and rate constants for the recombination of O(³ P) on the different sites of C ₆ H ₅ O	227
6.16	Geometry parameters for the TS of the O insertion in the aromatic ring . . .	229
6.17	15e,13o AS selected for the oxygen insertion in the aromatic ring	229
6.18	MEP and different electronic states for the oxygen ring insertion at the CASPT2 level	231
6.19	Experimental O and H profiles from microkinetic experiments of C ₆ H ₅ + O ₂ at different levels of theory and corresponding product branching fractions from C ₆ H ₅ + O ₂	233
6.20	Main production and consumption pathways of O and H atoms in the microkinetic ST experiments of Michael and Frank	234
6.21	Lumped rate constants for C ₆ H ₅ + O ₂ and C ₆ H ₅ O + O	235
6.22	Calculated rate constants for different abstracting radicals H, CH ₃ , OH and ³ O ₂ on the functional groups and on the aromatic ring of the investigated MAHs	241
6.23	Rate constants of the H-atom abstraction reaction by H from benzene	243
6.24	Rate constants of the reaction C ₆ H ₆ + CH ₃ = C ₆ H ₅ + CH ₄	244
6.25	Calculated rate constant for OH + C ₆ H ₆ = H ₂ O + C ₆ H ₅	246
6.26	Total rate constant for the H-atom abstraction by H from phenol and from the toluene methyl group	247
6.27	Rate constants for the H-atom abstraction by H, CH ₃ , OH from the anisole methoxy group	249
6.28	TS structure and rate constant of H-atom abstraction by CH ₃ from the phenol hydroxy group and toluene methyl group	250
6.29	Total rate constant for H-atom abstraction by OH from toluene	251
6.30	Rate constant of H-atom abstraction by OH from the hydroxy group of phenol	253
6.31	Potential energy surface for the ³ O ₂ + C ₆ H ₅ OH reaction	254

6.32	Relation between the energy barriers and 0 K reaction enthalpy for H-atom abstractions by H, OH, CH ₃ , and ³ O ₂ from the functional groups of anisole (-OCH ₃), phenol (-OH), toluene (-CH ₃), and benzene (-H)	257
6.33	Rate constants for H-atom abstraction reaction by H, CH ₃ , ³ O ₂ , and OH from different sites of α -naphthol and α -methylnaphthalene in comparison with the MAHs counterparts	261
6.34	Qualitative PES for the H ipso substitution on the generic doubly-substituted aromatic R'C ₆ H ₄ R + H to form well A and the products C ₆ H ₅ R + R'	264
6.35	PES for H ipso substitution on phenol and toluene	267
6.36	Computed global rate constants for H ipso substitution reactions on phenol and toluene	267
6.37	PES for the H-atom addition reactions to o-OHC ₆ H ₄ R and to o-CH ₃ C ₆ H ₄ R and β -scission of the adduct A to C ₆ H ₅ + OH and o C ₆ H ₅ + CH ₃ , respectively	268
6.38	Forward global rate constants $k_{\vec{g}}$ for H ipso substitutions on o-R'C ₆ H ₄ R + H, m-R'C ₆ H ₄ R + H and p-R'C ₆ H ₄ R + H	269
6.39	Branching fraction for H ipso substitution channel with respect to the total rate of H ipso substitution and H-atom abstractions by H on all available sites (ring substituents and aromatic H-atoms)	271
6.40	Effect of the R side group (CH ₃ in blue, OH in red) in the ortho, meta, and para positions on the relative increase of the apparent activation energies ΔE_A of the H-atom addition channel R'C ₆ H ₄ R + H with respect to the mono-substituted molecule (R = H).	272
6.41	Apparent activation energies E_A of the H-atom addition channel in replacement of CH ₃ by H $E_{A,R}^{CH_3}$ as a function of that in the replacement of OH by H $E_{A,R}^{OH}$	272
6.42	Energy differences ΔE_{HL-L1} between 0 K energies at the CCSD(T)/CBS and ω B97X-D/6-311+G(d,p) levels of theory for all 14 PESs computed in this work	273
6.43	PESs for the R'C ₆ H ₅ + H = C ₆ H ₆ + R' reactions with R' = OCH ₃ /CHO/C ₂ H ₅ and b) corresponding global rate constants $k_{\vec{g}}$	275
6.44	Parity plots of the rate constants of H-atom addition to R'C ₆ H ₄ R predicted by the rate rules derived in this work versus the calculated rate constants	282
6.45	Experimental and simulated species profiles for benzene pyrolysis in the ST of Laskin et al. [382] and Sun et al. [130]	289
6.46	Experimental and simulated species profiles for benzene oxidation in the JSR of Ristori	290
6.47	Flux analysis for intermediate T benzene oxidation	291
6.48	Experimental and simulated species profiles for benzene oxidation in the JSR of Chai	292
6.49	Sensitivity analysis for phenol and cyclopentadiene in the JSR of Chai and Ristori	293
6.50	Experimental and simulated species profiles for benzene oxidation in the JSR of Marchal.	294

6.51	Experimental and simulated species profiles for benzene oxidation in the JSR of Da Costa	295
6.52	Experimental and simulated species profiles for benzene oxidation in the PFR of Lovell	296
6.53	Experimental and simulated species profiles for benzene oxidation in the flame of Tregrossi	298
6.54	Experimental and simulated species profiles for benzene oxidation in the flame of Bittner	299
6.55	Experimental and simulated species profiles for benzene oxidation in the flame of Detilleux	299
6.56	Experimental and simulated species profiles of benzene IDT	301
6.57	Experimental and simulated benzene LFS	302
6.58	Experimental and simulated species profiles of phenol pyrolysis in a PFR . . .	304
6.59	Experimental and simulated species profiles of CO, H from phenol pyrolysis in a ST	304
6.60	Experimental and simulated species profiles of phenol hydrogenolysis in a PFR	306
6.61	Experimental and simulated species profiles of phenol oxidation in a PFR . .	306
6.62	Flux analysis of phenol oxidation in a PFR	307
6.63	Sensitivity analysis for phenol oxidation in a PFR	308
6.64	Experimental and simulated phenol IDT in a RCM	309
6.65	Experimental and simulated species profiles for catechol pyrolysis in a PFR .	310
6.66	Experimental and simulated species profiles for catechol pyrolysis and oxidation in a PFR	311
6.67	Experimental and simulated species profiles for anisole pyrolysis in a PFR . .	312
6.68	Flux analysis of anisole consumption in a JSR at 900 K	312
6.69	Experimental and simulated species profiles for anisole pyrolysis and oxidation in a JSR	314
6.70	Experimental and simulated species profiles for anisole oxidation in a JSR . .	315
6.71	Experimental and simulated IDTs for anisole oxidation in ST and RCM experiments	317
6.72	Experimental and simulated LFS of anisole	318
6.73	Experimental and simulated species profiles of guaiacol pyrolysis and oxidation	319
7.1	Ideal world of first principle-based kinetic modeling	331

List of Tables

2.1	OpenSMOKE++ reactor solvers used in this work	45
3.1	Recommended methodologies for ES and kinetic calculations by reaction type	86
3.2	List of the main rate constants calculated in this work	93
4.1	Nomenclature and notations for MEL methodology.	98
5.1	Some theoretical and experimental works on cyclopentadiene and indene since the 1990s	120
5.2	Reaction classes for decomposition and oxidation of C5,X-M species types . .	124
5.3	Reaction classes for decomposition and oxidation of C5,X-RSR species types .	127
5.4	Reaction classes for growth of CY,X-M species types forming C5 species or involving C5 species	131
5.5	Reaction classes for growth of CY,X-R/RSR species types forming C5 species or involving C5 species	132
5.6	Theoretical results for the enthalpy (H) and entropy (S) variation of cyclopentadienyl radical	143
5.7	Lumped set of rate constants for the calculated portion of the C ₅ H ₅ + HO ₂ PES for the CRECK model	151
5.8	Energies of the entrance well, transition state and products of the radical H-atom abstraction reactions from C ₅ H ₅ O	154
5.9	Simulation database of flow reactors included for the testing of the sub-mechanism of cyclopentadiene and indene	157
6.1	Some experimental and kinetic modeling works on oxygenated aromatics . . .	178
6.2	Reaction classes for decomposition and oxidation of species types A1-M and A1,X-M with X = H groups	186
6.3	Reaction classes for decomposition and oxidation of species types A1,X-M with X = alkyl group	187
6.4	Reaction classes for decomposition and oxidation of species types A1,X-M, with X = oxygenated group	188
6.5	Reaction classes for decomposition and oxidation of A1,X-R	190
6.6	Reaction classes for decomposition and oxidation of A1CH ₂ -RSR, A1CH ₂ ,OH-RSR	191
6.7	Reaction classes for decomposition and oxidation of A1O,X-RSR (X = CH ₃ , OH), A1CO-RSR	192

6.8	Reaction classes for growth of CY,X-M species types forming A1 species or involving A1,X-M species	194
6.9	Reaction classes for growth of CY,X-R/RSR species types forming A1 species or involving A1,X-R/RSR species	195
6.10	History of the branching fractions of the $O(^3P) + C_6H_6$ reaction and present experimental and theoretical estimates.	204
6.11	Fits of the modified Arrhenius expressions for the rate constants of $O(^3P)$ addition to benzene	204
6.12	Multireference diagnostics and recommended values for the decarbonylation channel on phenol PES	209
6.13	Energy barriers for the decarbonylation channel at the DFT geometry	210
6.14	Energy barriers for the decarbonylation channel at the CASPT2 geometry . .	210
6.15	Arrhenius fits for the rate constants of phenol and phenoxy decomposition . .	213
6.16	Literature experimental studies on $C_6H_5+O_2$ recombination channel	215
6.17	Literature CMB experiments for the $C_6H_5+O_2$ reaction	215
6.18	Literature flow reactor "microkinetic" experiments for $C_6H_5 + O_2$ reaction . .	216
6.19	Literature PES theoretical studies for $C_6H_5+O_2$ reaction	217
6.20	Literature theoretical studies of the $C_6H_5+O_2$ recombination channel	219
6.21	Literature theoretical studies of the C_6H_5O+O recombination channel	219
6.22	Effect of the level of theory (basis set, active space) on the energy barriers for the oxygen insertion in the aromatic ring on saddle points found at the DFT level	230
6.23	Energy barrier for the oxygen ring insertion TS at the CASPT2 maximum found along the IRC path	232
6.24	Lumped set of rate constants for C_6H_5OO PES	235
6.25	Arrhenius fits in the 500–2000 K temperature range of the calculated rate constants for H-atom abstraction reactions by H, CH_3 , OH, and 3O_2 on benzene, phenol, anisole, and toluene	242
6.26	Seven lowest vibrational frequencies at the saddle point of the PES for $C_6H_5OCH_3 + CH_3 = C_6H_5OCH_2 + CH_4$ reaction obtained using different DFTs and basis sets	249
6.27	Impact on the rate constants computed in this work of the use of variational transition state theory and of variational transition state theory with internal coordinate treatment with respect to conventional TST	255
6.28	Difference between the energy barriers at PNO-LCCSD(T)-F12/CBS (PNO) and M06-2X/6-311+G(d,p) (DFT) levels and the benchmark values at the CCSD(T)/CBS level of theory (HL).	257
6.29	Difference between the 0 K enthalpy of reactions at the PNO-LCCSD(T)-F12/CBS (PNO) and M06-2X/6-311+G(d,p) (DFT) levels and the benchmark values at the CCSD(T)/CBS level of theory (HL).	258

6.30	Differences in energy barriers (ΔH^\ddagger) and 0 K reaction enthalpies (ΔH_r) between the CCSD(T)/CBS and M06-2X/6-311+G(d,p) levels of theory for all the reactions investigated in this work	258
6.31	Approximate corrections to the pre-exponential factors and activation energies of the Arrhenius fits for $C_6H_5Y + R = C_6H_4Y + RH$ reactions with differences of a factor >2 with respect to the reference abstraction reaction from benzene	259
6.32	Arrhenius fits in the 300–2500 K range of the calculated forward and backward global rate constants for H ipso substitution on C_6H_5OH , $C_6H_5CH_3$, o-,m-,p- $C_6H_4(CH_3)_2$, o-,m-,p- $CH_3C_6H_4OH$, o-,m-,p- $C_6H_4(OH)_2$	270
6.33	Arrhenius fits in the 300–2500 K range of the calculated global rate constants for H ipso substitution on $C_6H_5OCH_3$, C_6H_5CHO , and $C_6H_5C_2H_5$	275
6.34	Corrections $\Delta E_{A,R-H}^{R'}$ to the energy barriers (kcal/mol) for the H-atom addition reaction to $R'C_6H_4R$ with respect to the reference $R'C_6H_5$ obtained with the rate rules derived in this work	277
6.35	Schematic representation of the rate constant calculations for the reactions o-,m-,p- $R'C_6H_4R + H \rightarrow C_6H_5R + R'$ performed in this work	280
6.36	Arrhenius expressions for the rate constants k_{rule} of H addition to o-,m-,p- $R'C_6H_4R$, ($R, R' = OH/CH_3/OCH_3/CHO/C_2H_5$) in the 300–2000 K range obtained with the rate rules derived in this work	280
6.37	Arrhenius expressions for the rate constants k_{rule} of H-atom addition to vanillin in the 300–2000 K range obtained with the rate rules derived in this work	284
6.38	Simulation database of flow reactor results included for the testing of the sub-mechanism of benzene	287
6.39	Simulation database of measurements in laminar flames included for the testing of the sub-mechanism of benzene	287
6.40	Simulation database for the testing of the sub-mechanism of OAHs	287

List of Abbreviations

AI-TST-ME	Ab Initio Transition State Theory-based Master Equation
AO	Atomic Orbital
AS	Active Space
ATcT	Active Thermochemical Tables
BP	British Petroleum
BDE	Bond Dissociation Energy
BEV	Battery Electric Vehicle
BF	Branching Fractions
CASSCF	Complete Active Space Self Consistent Field
CBH	Connectivity Based Hierarchy
CBS	Ccomplete Basis Set limit
CF	Counterflow Flame
CFD	Computational Fluid Dynamics
CI	Configuration Interaction
CMB	Crossed Molecular Beam
CN	Cetane Number
COM	Center Of Mass
CSE	Chemically Significant Eigenvalues
DFT	Density Functional Theory
DOF	Degree Of Freedom
DOS	Density Of States
EP	Evans Polanyi
ES	Electronic Structure
GA	Group Additivity
GHG	Greenhouse Gases
GTO	Gaussian Type Orbital
HACA	Hydrogen Abstraction Carbon Addition
HAVA	Hydrogen Abstraction Vinylacetylene Addition
HEV	Hybrid Electric Vehicle
HF	Hartree Fock
HL	High Level
HP	High Pressure
HR	Hindered Rotor
IERE	Internal Energy Relaxation Eigenvalues
IRC	Intrinsic Reaction Coordinate
ISC	InterSystem Crossing
JSR	Jet Stirred Reactor
KMC	Kinetic Monte Carlo
LCAO	Linear Combination of Atomic Orbitals
LFER	Linear Free Energy Relationship
LFS	Laminar Flame Speed
LJ	Lennard-Jones

MAH	Monocyclic Aromatic Hydrocarbons
MC	Monte Carlo
MCSCF	MultiConfiguration Self Consistent Field
MDS	Multifaceted Dividing Surface
ME	Master Equation
MECP	Minimum Energy Crossing Point
MEL	Master Equation based Lumping
MEP	Minimum Energy Path
MO	Molecular Orbital
MON	Motor Octane Number
MP	Moller-Plesset
MSX	Minimum Seam of Crossing
MW	Molecular Weight
NA	Non Adiabatic
NTC	Negative Temperature Coefficient
OAH	Oxygenated monoAromatic Hydrocarbons
ODE	Ordinary Differential Equation
OME	OxyMethyl Ethers
PAH	Polycyclic Aromatic Hydrocarbons
PES	Potential Energy Surface
PF	Partition Function
PF1	Premixed Flame
PFR	Plug Flow Reactor
PM	Particulate Matter
PSSA	Pseudo Steady-State Approximation
PST	Phase Space Theory
QCT	Quasi Classical Trajectory
QCT-SH	Quasi Classical Trajectory-Surface Hopping
RCM	Rapid Compression Machine
ROPA	Rate Of Production Analysis
RON	Research Octane Number
RRHO	Rigid Rotor Harmonic Oscillator
RRKM	Rice Ramsperger Kassel Marcus
RS	Rayleigh-Schrödinger
SA	Sensitivity Analysis
SAR	Structure Activity Relationship
SCF	Self Consistent Field
SD	Slater Determinant
SH	Surface Hopping
SM	Supplementary Material
SOC	Spin-Orbit Coupling
SPE	Single Point Energy
ST	Shock Tube
STO	Slater Type Orbital
TOF	Time of Flight
TS	Transition State
TST	Transition State Theory
VTST	Variational Transition State Theory
VRC	Variable Reaction Coordinate
ZPE	Zero Point Energy
1/2DHR	one/two-Dimensional Hindered Rotor

List of Symbols

LATIN	SYMBOLS	
C_I	concentration of species I	mol cm^{-3}
C_P	heat capacity	$\text{cal mol}^{-1} \text{K}^{-1}$
e, n	(as subscript) electrons, nuclei	
E	energy	E_h or cal mol^{-1}
G	molar Gibbs free energy	cal mol^{-1}
\mathbf{H}	hamiltonian operator	
H	molar enthalpy	cal mol^{-1}
F_{Ij}	normalized flux of species I in reaction j	
k_{IJ}	rate constant of reaction $I \rightarrow J$	s^{-1} (unimol.) $\text{cm}^3 \text{mol}^{-1} \text{s}^{-1}$ (bimol.)
k'_{IJ}	rate constant of pseudo unimolecular reaction (for bimol. reactions $I + I_2$, $k'_{IJ} = k_{IJ}c_{I_2}$)	s^{-1} s^{-1}
r_j	rate of reaction j	mol s^{-1}
m	mass	kg
n_i	Population of the system in the quantum state i (in the master equation context)	
p_{ij}	Probability of transition from state i to j (in the master equation context)	s^{-1}
p	pressure	Pa
T	temperature	K
Q	partition function	
R, P	Generic reactant, product	
S	molar entropy	$\text{cal mol}^{-1} \text{K}^{-1}$
X	mole fraction	
GREEK	SYMBOLS	
$\Delta H_f^0(T)$	formation enthalpy	cal mol^{-1}
λ	reaction coordinate	\AA (bond distances) $^\circ$ (angles)
ν	vibrational frequency	cm^{-1}
ν_{Ij}	stoichiometric coefficient of species I in reaction j	
μ	reduced mass	kg
Φ	equivalence ratio	
Ψ	wavefunction	
OTHER	SYMBOLS	
\sim	accent for lumped quantities	

Chapter 1

Introduction and background

1.1 The role of aromatic hydrocarbons in the energy transition

The increase in the world energy demand requires feasible short and medium term solutions for energy production with the smallest possible environmental impact. Despite the efforts of the past decades towards decarbonization and electrification, combustion processes of conventional fuels still account for above 75% of primary world energy consumption (Figure 1.1a) [1], and for about 50% of electricity production, notwithstanding the exponential increase in the share of renewable energy sources (Figure 1.1b). According to the 2021 British Petroleum energy outlook [2], if government policies, technology and society continue to evolve as in the recent past, the share of fossil fuels in the primary energy consumption will decrease only slightly. On the other hand, in a "Rapid Transition Scenario" or "Net Zero Scenario", the increase in hydrocarbon-based fuel prices, and a shift in societal attitudes and government policies would lead to a 50–70% decrease in the use of fossil fuels for energy production. It is noted that the compensation of the energy demand by renewable energy sources includes a significant share of biofuels and biomass, which still involve combustion processes.

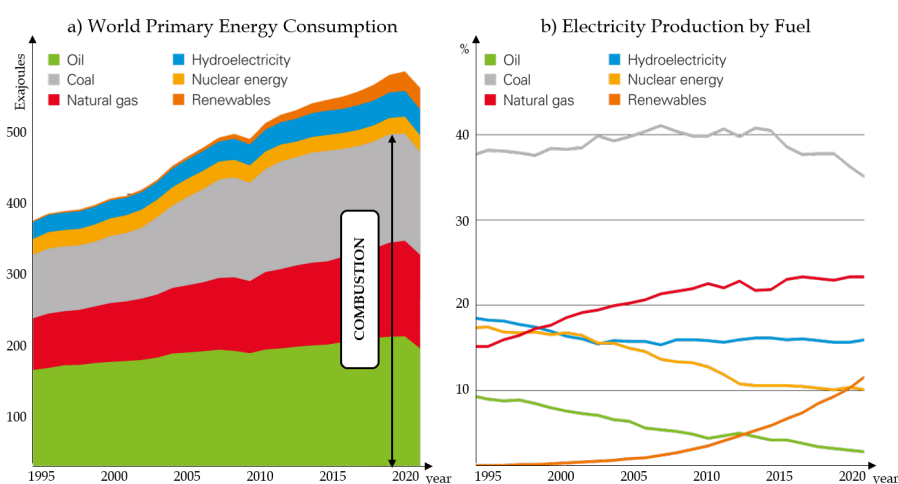


FIGURE 1.1: a) Primary world energy consumption by fuel and b) Electricity production by fuel according to the British Petroleum statistical review of world energy 2021 [1]. Adapted from [1].

The past 20 years have proven that an immediate shift to a fully decarbonized economy is impractical. This is particularly true for the transportation sector. In fact, renewable

energy sources such as nuclear, solar, and wind are only suitable for stationary applications for power generation. On the other hand, fuels for transportation need to be of high energy density, which is easily achieved by liquid hydrocarbon fuels, especially for heavy-duty, marine and aviation vehicles. Additionally, short and medium term solutions for low-carbon fuels must rely on the existing infrastructure. Low-density fuels such as hydrogen are not expected to take the lead in decarbonizing the transportation sector very soon, also due to their incompatibility with conventional gasoline and diesel engines, especially in terms of injection characteristics [3], [4]. Infrastructural difficulties also hinder the rapid spread of battery electric vehicles (BEVs). Additional challenges for BEVs are the limited availability of battery materials - hence their high price - and exhausted battery disposal. Furthermore, BEVs are not as carbon-free as the media may suggest. In fact, the advantage of BEVs compared to internal combustion engine vehicles (ICEVs) mainly relates to the use phase. However, cradle-to-gate emissions of a BEV (i.e., emissions in the production phase) are about 50% higher than those of ICEVs [5]. Considering the full life cycle assessment (LCA) of ICEVs and BEVs, the environmental impact of BEVs may be even higher than conventional ICEVs in regions of the world such as China and Australia [6]. Overall, optimal solutions for transportation depend on both the application and the location. "Electrified" vehicles including both BEVs and hybrid electric vehicles (HEVs), still partially relying on ICEs, seem a more realistic scenario [7]. In conclusion, diversified solutions for energy production ought to continue to be explored and optimized for emissions reduction.

The main concern associated with the combustion of hydrocarbon-based fuels is their environmental impact. The increase of global CO₂ emissions attributed to anthropogenic activities is mainly due to the combustion of hydrocarbon-based fuels and ultimately causes air deterioration and climate change. For instance, the US environmental protection agency (EPA) identified the industrial and transportation sectors as those contributing the most to GHG emissions (Figure 1.2).

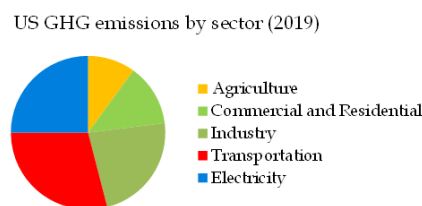


FIGURE 1.2: Contribution to GHG emissions by sector in the US in 2019 according to EPA [8].

Consequently, international agreements such as the Kyoto Protocol (1998) and the Paris Agreement (2016) have set global targets for emission reduction and temperature increase, as well as providing financial resources and guidelines to limit climate change. New emission regulations and local government bans are pushing towards a limited use of fossil fuels and foreshadow a partial ban of fossil fuel cars by 2035–2050 [7]. In any case, hydrocarbon-based fuels, both conventional and renewable, will still contribute significantly to energy production in the next 20–30 years, suggesting the value of a continued search for alternative biofuels as a short term action to mitigate the environmental impact of hydrocarbon-based fuels. Besides

environmental reasons, novel biofuels would also reduce our dependence of fossil fuels, which are an intrinsically finite resource, as well as that of foreign countries and, therefore, of the delicate geopolitical equilibria that determine fossil fuel prices and availability.

1.1.1 Biomass-derived biofuels

Biofuels are hydrocarbon-based fuels. However, they are considered renewable energy sources because of their comparable depletion and generation timescale. Biofuels are derived from biomass, namely crops, as well as forest and crop residues; therefore, they are renewable by nature. Solid biomass is currently the primary renewable energy source for stationary power generation, and its relevance is expected to rise, especially for heat generation in domestic applications and for combined heat and power [9]. In particular, biomass burning for combined heat and power achieves 80% efficiency and reduces carbon emissions by 30% compared to conventional heat and power generation. However, using solid biomass worsens air quality in terms of particulate matter (PM) and NO_x emissions [9]. Additionally, solid biomass is currently inapplicable to road transportation due to the high volume, weight, and to the incompatibility with the current engines and infrastructure. Hence, biomass is converted to liquid fuels with high energy density through thermochemical conversion.

So-called "first generation biofuels" include fuels derived mostly from crops. In particular, bioethanol derives from the fermentation of corn or sugar cane. On the other hand, biodiesel is produced from the transesterification of vegetable oils. The main advantage of these biofuels is that they can be blended to some extent with gasoline and diesel fuels without requiring the modification of existing ICEs. Nevertheless, the major concern of first generation biofuels is their competition with food crops leading to higher food prices. "Second generation" biofuels derived from low-cost lignocellulosic biomass are considered a more valuable route for the production of renewable fuels.

The explored routes for biomass conversion to liquid fuels are mostly two, as schematically represented in Figure 1.3. The former consists of biomass gasification to syngas (mostly CO and H₂) and successive conversion to liquid fuels. The latter step is generally performed with Fischer-Tropsch (FTS) synthesis, however in the past 15 years catalytic microbial fermentation has also become a feasible alternative [10], [11]. In both cases, producing the final liquid fuel involves a complex multi-step process. A recent widely explored alternative is biofuel production via the fast pyrolysis of biomass, which is becoming economically feasible at an industrial scale, with liquid fuel yields up to 75% in weight [12], [13]. The potential integration of such processes into existing biorefineries would allow the simultaneous CO₂ reduction from the use of lignin and the production of either biofuels or high-value chemicals [12]. Challenges associated with the pyrolytic conversion process mainly relate to the optimization of heat and mass transfer, catalyst morphology and regeneration, and the characterization of the pyrolysis products [14].

The bio-oil derived from the fast pyrolysis of biomass has about 5–20 times higher energy density than the original biomass, and about half of the energy density of petroleum-derived oils. However, biomass-derived bio-oils are characterized by high acidity (Ph 2–3), limited volatility, and immiscibility with commercial hydrocarbon fuels [15]. Hence, they require

catalytic upgrading through dehydroxygenation, hydrogenation, and alkylation processes to be converted to biofuels such as green jet fuels [15]–[17]. More recently, integrated catalytic pyrolysis processes were developed, allowing promising single-step conversions based on zeolite catalysts [18], [19].

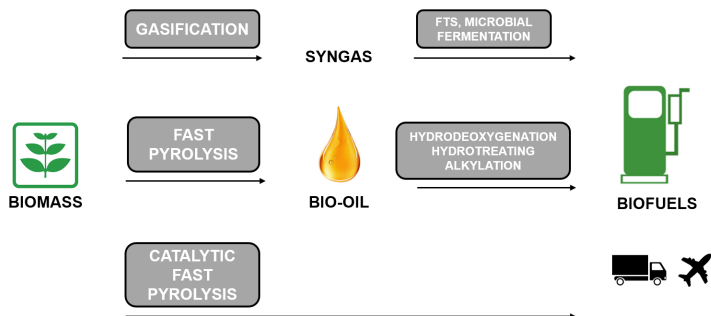


FIGURE 1.3: Schematic potential routes from biomass to biofuels through gasification or fast pyrolysis.

Finally, the products of biomass fast pyrolysis may be upgraded to high-value chemicals, and in particular to aromatic species [20]. For instance, lignin contains a large amount of phenolic-based monomers, which may be catalytically converted to phenol, one of the most important chemicals in industry and precursor of nylon, bisphenol-A, and other pharmaceuticals [21]. The valorization of biomass for the production of p-xylene and, therefore, of polyethylene terephthalate (PET) from sustainable sources also seems to be a near-future possibility [22].

The use of bio-oils for biofuels and high-value chemical production strongly depends on the characterization of their physico-chemical and combustion properties. However, the composition of bio-oils is significantly different from that of fossil fuels, particularly because of the presence of oxygenated compounds (about 60% by weight). Bio-oil composition strongly varies with the raw biomass and with the thermal degradation process used [23], [24]. Hence, the identification of simple model compounds representative of the pyrolysis and combustion behavior of bio-oils and biofuels derived from their upgrading is essential to aid in the exploration of their applications. Model compounds also allow a better selection of appropriate biofuel candidates from the knowledge of the desired combustion properties, necessary also for the design and optimization of biofuel production processes [25].

1.1.2 Particulate matter emissions

CO₂ emissions are not the only environmental concern of hydrocarbon-based fuels. Primary pollutants derived from the combustion of both conventional and renewable fuels also include polycyclic aromatic hydrocarbons (PAHs) and particulate matter (PM), hazardous for both the environment and human health [26]–[28]. PAHs and PM (also called soot) result from incomplete combustion, generally in fuel-rich conditions and at high temperatures. In Europe and the US, combustion in the transportation and industrial sectors contributes to about 50% of the total PM emissions (Figure 1.4).

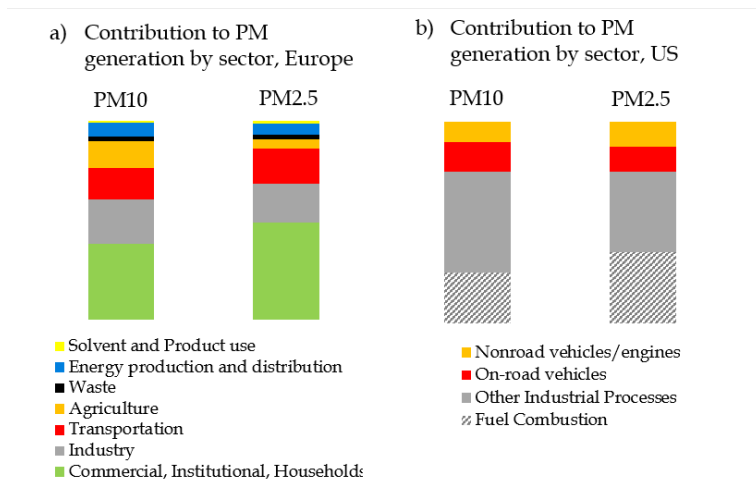


FIGURE 1.4: Particulate Matter generation by sector in Europe in 2012 according to the EEA a) and in the US in 2014 according to the EPA [29].

PAHs are particularly harmful because of their toxic effects on the environment and human health. Additionally, some PAHs are carcinogenic [30]. PAHs are the main precursors of PM/soot, namely carbonaceous nanoparticles. These are classified according to particle diameter. PM10 includes particles with diameter below $10\ \mu\text{m}$, which can be inhaled. The most hazardous ones are however PM2.5 particles ($d < 2.5\ \mu\text{m}$), as they can penetrate into the lungs and the cardiovascular system causing lung cancer [31]. As a result, regulations about PAHs and PM emissions are becoming more restrictive. Even in the case of stationary applications, the efficiency of abatement techniques such as electrostatic precipitators decreases significantly for small particles (PM10 and below). Finally, soot formation also affects the efficiency of combustion devices, reducing heat exchange and requiring maintenance in case of soot accumulation in the system.

The formation of PAHs and soot is a kinetically controlled process and mostly derives from incomplete combustion of the fuel. Reduction of soot emissions can therefore be achieved by optimizing the combustion process or by the after-treatment of exhausted gases. Fuel composition plays a major role in PAHs and soot formation. The presence of aromatic compounds in the fuel boosts the formation of polycyclic aromatic compounds and therefore of soot. Unfortunately, many low-carbon and biomass-derived biofuels are subject to high PM emissions due to their high aromatic content. For instance, biomass gasification and combustion produce large amounts of tar. Oxygenated compounds may increase or decrease soot formation depending on their nature. For example, dimethylethers and oxymethylethers are also emerging as promising alternatives to fossil fuels thanks to their low PM emissions [32], while dimethylfuran (DMF) shows high soot propensity [33], [34].

Current research on carbonaceous nanoparticles is not only exploring their behavior in terms of emission control but also as an opportunity for material synthesis. In fact, graphene and other high-performance carbonaceous nanomaterials may be produced from black carbon for various applications such as photocatalysis, sensors, and energy storage [35]. In particular, carbonaceous nanoparticle synthesis in flames is becoming both a technically

and economically viable route [36]. In such processes, the optimal control of flame conditions and deep knowledge of how operating conditions affect carbon nanoparticle formation, coagulation, oxidation, and morphology are key to the success of the synthesis process.

Overall, both emission control and the exploitation of soot for nanomaterials would benefit from a detailed understanding of the mechanism of combustion and growth of their gas phase precursors, namely mono- and polycyclic aromatic hydrocarbons (MAHs and PAHs). A knowledge of the gas phase combustion of aromatic hydrocarbons would also help assess the extent of pollutant formation in potential biomass-derived biofuels, particularly those rich in aromatic and oxygenated aromatic compounds.

1.1.3 The role of monocyclic aromatic hydrocarbons and unsaturated 5-membered rings

Figure 1.5 depicts the approximate composition of conventional gasoline, diesel and jet fuels and of biomass-derived biofuels, highlighting the large amount of aromatic species, also depicting representative structures of the classes of compounds of these fuels. Despite the complexity and variety in fuel composition, it is generally possible to reproduce macroscopic properties of interest to the combustion behavior simulating the reactivity of a limited number of reference species. The resulting species mixture is called a surrogate mixture. Gasoline fuel surrogate mixtures generally include the primary reference fuels (PRFs), namely *n*-heptane and iso-octane; toluene was recently added as a representative of the aromatic compounds in the mixture (TPRF mixtures). Other substituted and di-substituted aromatic compounds, such as xylene and ethylbenzene, have also been included in gasoline surrogate models. Alkylated aromatic hydrocarbons are also used as surrogate components for jet fuels [37], as depicted in Figure 1.6.

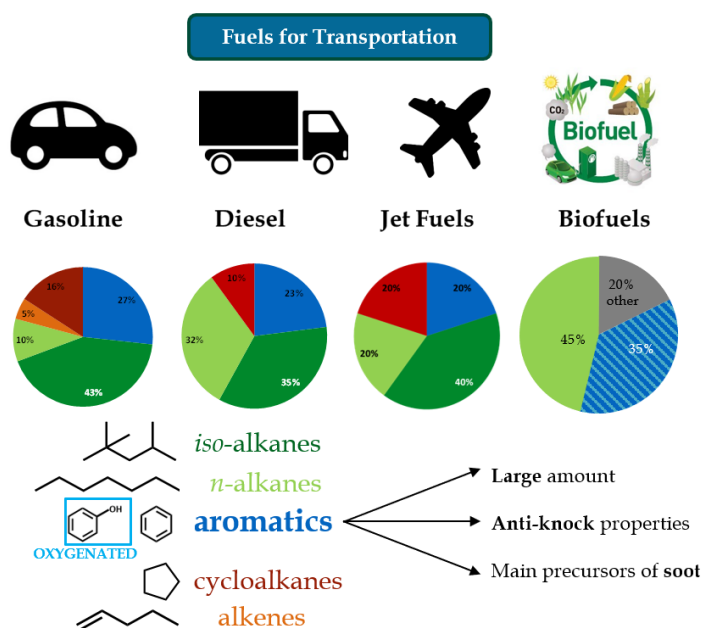


FIGURE 1.5: Shares of different types of hydrocarbons in the composition of conventional and biomass-derived fuels.

The large amounts of oxygenated aromatic hydrocarbons in biomass-derived bio-oils and biofuels are not represented in conventional fuel surrogate mixtures. For instance, 30% of biomass derived bio-oil is constituted of phenolic species [38], [39], namely aromatic rings with hydroxyl substituents. In fact, phenol is one of the most important components in lignin [40]–[43]. Therefore, recently formulated surrogate mixtures of biomass-derived bio-oils and biofuels include phenol, catechol, guaiacol, and vanillin [44]–[46] (Figure 1.6). Additional components of interest derived from biomass fast pyrolysis include anisole, aldehydes, and cresols [15], [21], [47], [48]. In particular, anisole is used as the simplest surrogate for primary tar from lignin pyrolysis to model the formation of PAHs in biomass pyrolysis and combustion [49]. Additionally, anisole is the reference model compound for the more complex investigation of the kinetics of some di- and tri-substituted MAHs, namely guaiacol, cresol, and vanillin [50], [51].

Finally, oxygenated MAHs (OAHs) were also highlighted as potential gasoline anti-knocking additives [52], [53]. In fact, their peculiar pyrolysis and oxidation reactivity associated with the stability of the aromatic ring slows down their ignition, as confirmed experimentally in the case of phenol and anisole [54], [55].

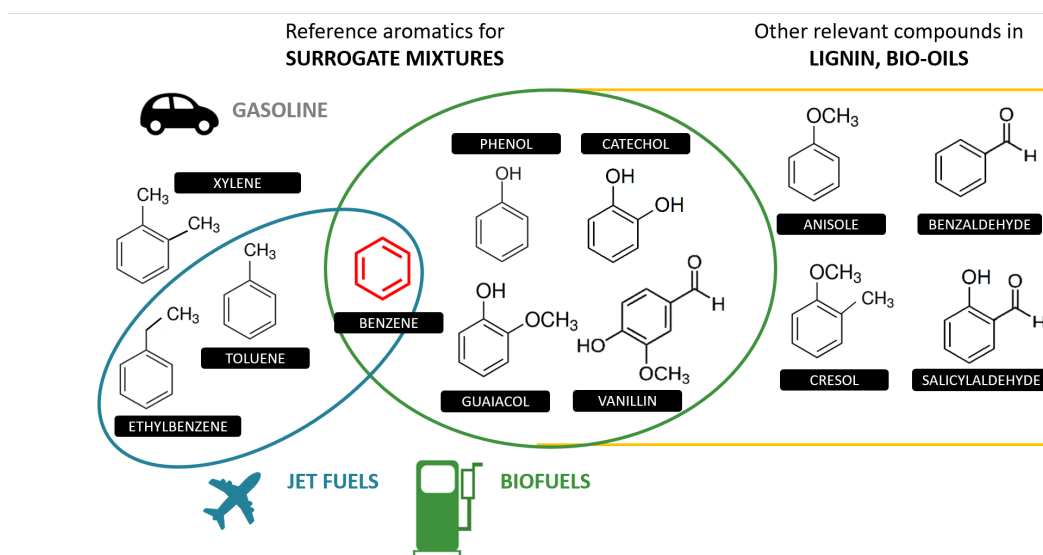


FIGURE 1.6: Monocyclic aromatic hydrocarbons used as surrogate components for different fuel types and other relevant oxygenated MAHs representative of lignin and bio-oil components.

Figure 1.6 shows benzene at the intersection of all reference components used in fuel surrogate mixtures. A detailed knowledge of benzene reactivity is key to understanding the kinetic behavior of all substituted MAHs modeled in fuel surrogate mixtures. Additionally, benzene may be formed from the incomplete combustion of linear and branched hydrocarbons (n-alkenes and iso-alkenes) such as acetylene, ethylene, propyne, and butenes. As a fuel or a combustion product, benzene is key in combustion processes because it is one of the main constituents of PAHs and therefore of soot [56]. Figure 1.7 represents the qualitative formation of PAHs and soot in a premixed flame. As the reaction proceeds, incomplete combustion products (C_2 – C_4 unsaturated species) may grow to form 5- or 6-membered rings. These may thereafter grow to PAHs such as indene (C_9H_8), naphthalene ($C_{10}H_8$),

acenaphthylene ($C_{12}H_8$), fluorene ($C_{13}H_{10}$), phenanthrene ($C_{14}H_{10}$), pyrene ($C_{16}H_{10}$), and coronene ($C_{24}H_{16}$), identified as important soot precursors and all depicted in Figure 1.7.

In addition to C_6 aromatic rings, C_5 unsaturated rings such as cyclopentadiene (C_5H_6 , highlighted in red in Figure 1.7) also play a relevant role in MAHs combustion and PAHs growth. C_5H_6 is an important intermediate in the pyrolysis and oxidation of benzene and other M/OAHs, determining the competition between decomposition processes (via C_5 ring opening reactions) and growth to PAHs. Additionally, the resonance-stabilized cyclopentadienyl radical C_5H_5 is representative of stable structures recently detected in long-lived PAHs [57], as also confirmed by theoretical findings [58]. Hence, C_5 unsaturated species are model compounds for studying the formation and oxidation of large PAHs and soot [59], [60]. Finally, these structures may also explain possible mechanisms for soot nucleation [61], one of the most debated issues in the combustion and material science communities.

Overall, understanding the kinetics of PAHs and soot formation in combustion conditions is beneficial to both controlling PM emissions and exploiting carbonaceous nanoparticles for nanomaterials engineering. Still, their combustion kinetics is far from being understood [61], [62]. Although the gas-phase kinetics of monocyclic aromatic hydrocarbons has been widely explored, a detailed understanding of the pyrolysis and combustion of MAHs and OAHs is still lacking. Advancements in experimental, theoretical and kinetic modeling techniques are slowly allowing a deeper knowledge of such processes.

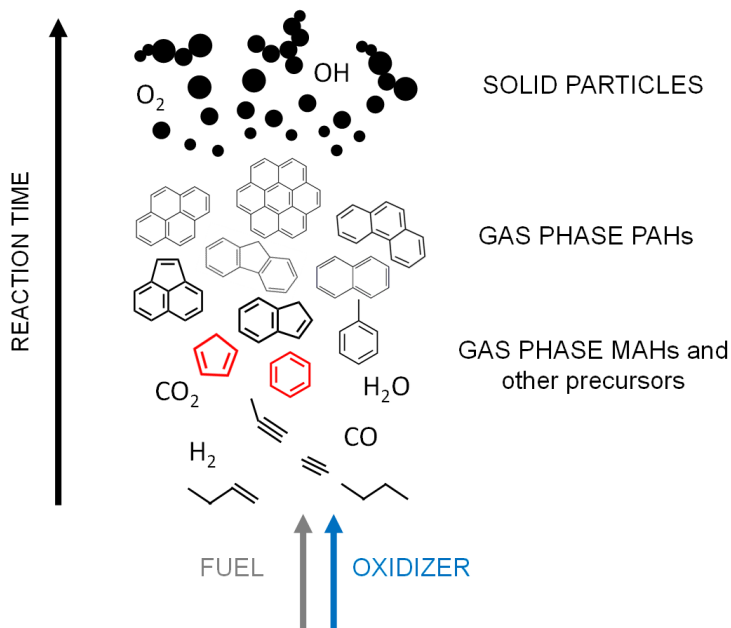


FIGURE 1.7: Qualitative representation of the evolution from gas-phase aromatics to soot in a premixed flame. Adapted from Bockhorn, 1994.

1.2 Kinetic modeling of combustion processes

Kinetic modeling of combustion processes greatly facilitates the development of novel fuels. In fact, it allows the testing of new fuel concepts and the assessment of their combustion properties. While the kinetic model must be validated with experimental data, in principle no experimental measurements are needed if the model is predictive.

The typical procedure to assess the viability of a new fuel candidate from the molecular to the device level is depicted in Figure 1.8. As anticipated above, a few representative components reproducing the physico-chemical and combustion properties of the fuel are identified.

The second step is the development of a kinetic mechanism describing the behavior of the selected component in pyrolysis and oxidation conditions, both in low and high-temperature environments, and possibly including a wide range of pressures (typically 1–100 atm). The combustion properties of the fuel are assessed with kinetic simulations of ideal reactor experiments providing relevant insight into the ignition properties and the formation of products and pollutants. Ideally, the kinetic mechanism obtained should reproduce the experimental data within the (often undeclared) experimental uncertainty.

The kinetic mechanism for the description of the combustion of PRFs, renewable fuel components (e.g., ethanol) or aromatic compounds is extremely complex and includes a large number of species ($10^2 - 10^4$) and reactions ($10^3 - 10^5$). The number of intermediate species required for the description of pyrolysis and oxidation pathways increases exponentially with molecular weight. This constitutes a major challenge for both the development of kinetic models for heavy aromatic species and the computational cost of kinetic simulations (especially for flames), which scale with the number of species by a power of 2–3. As a result, most computational fluid dynamics (CFD) simulations cannot be performed with detailed kinetic mechanisms as they are too computationally expensive. Lumping and reduction techniques allow for a reduction in the number of species and reactions, while retaining chemical accuracy [63]–[66].

CFD simulations with reduced schemes are mostly used to reproduce the results of autoignition experiments such as the research octane number (RON) and motor octane number (MON) for gasoline spark ignition engines and the cetane number (CN) for compression ignition engines. These tests are performed in research or real engines and aim at quantifying the knocking propensity of a fuel, which limits the operating pressure of the engine. Even at the engine level, the results of CFD simulations are strongly affected by the chemical kinetics described in the reduced kinetic scheme, hence its predictive capability largely depends on the accuracy and reliability of the starting detailed mechanism. The fuel ignition propensity together with information on combustion products and pollutant emissions, physico-chemical fuel properties and the sustainability of the fuel production process eventually assess the viability of a new fuel candidate.

This work focuses on the detailed gas-phase kinetic mechanism development of MAHs and PAHs. The approach to model development and testing is a multiscale iterative procedure, as summarized in Figure 1.9 and explained in detail in Chapter 2 and 3.

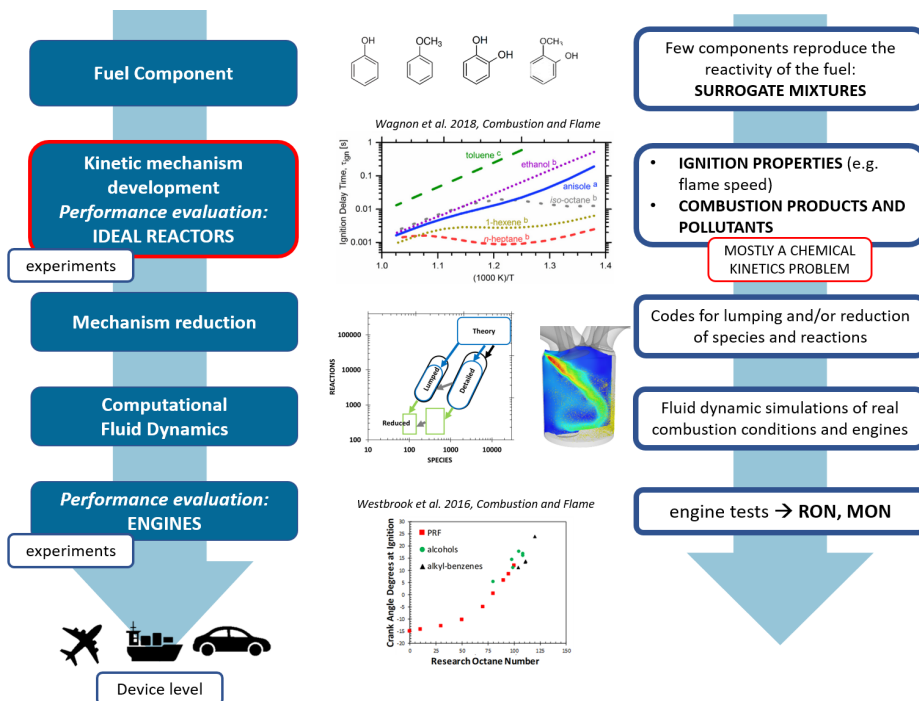


FIGURE 1.8: The role of kinetic modeling in assessing the viability of fuels from the molecular level to the device level.

This work mostly refers to the CRECK kinetic mechanism, developed in a hierarchical and modular way in the last ~ 40 years in the CRECK modeling group (<http://creckmodeling.chem.polimi.it>). A more detailed description of the structure of the CRECK model is provided in Section 2.5. During the course of this work, a portion of the CRECK mechanism was also adapted to build a joint global kinetic scheme among different research groups within the context of the C3 project (<https://fuelmech.org/>), leading to the development of C3MechV3.3 [67]. Most of the theoretical results of this work and the kinetic mechanism organization and alignment were also implemented in C3MechV3.3.

The first step in the construction of a kinetic mechanism is the definition of the main reaction pathways involved in the fuel decomposition and oxidation. Manual construction is time consuming and highly prone to errors, especially for non-experts. Over the last 30 years, a lot of effort was invested in the automation of such generation procedures according to various approaches. For instance, the MAMOX code by Ranzi and coworkers [68] generates the reactions describing the primary fuel decomposition steps for alkanes. With the advent of cheminformatics and automatic procedures for structure identification, recent codes such as RMG and Genesys [69], [70] can identify the possible reaction pathways for a given chemical species among a set of user-defined reaction families. The main challenges of current mechanism generation approaches are the proper definition of the reaction families to consider, and the selection of relevant (and physical) reaction pathways so as to avoid the unmanageable explosion of the number of species and reactions in the final kinetic mechanism. Such species explosion issues are particularly problematic for low temperature where

the important chain branching pathways have much lower flux than the propagation pathways. Difficulties also arise for larger species and for mixtures of species (e.g., fuel surrogate mixtures).

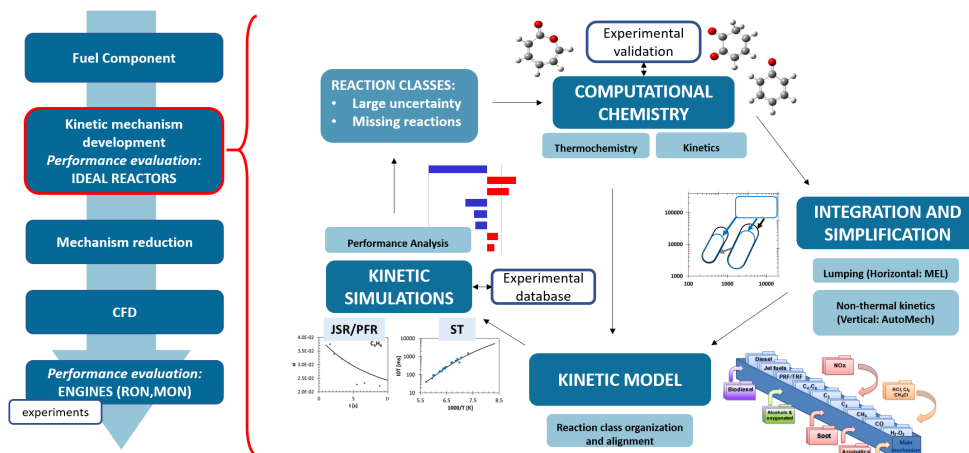


FIGURE 1.9: Iterative steps for kinetic model development, update and testing.

After identifying the main reaction pathways, the corresponding reference kinetic parameters, i.e., the rate constants, and the thermodynamic and transport properties of the species are assessed. All of these steps have historically relied on experimental measurements, together with rate rules for the extension of reference kinetic parameters to analogous reactions [71]. Nevertheless, experiments are generally unable to cover the full range of operating conditions of temperature and pressure of interest to combustion. Furthermore, the huge number of kinetic parameters and the increasing complexity of kinetic schemes are incompatible with the practical and economic limitations of experimental facilities. In the last 30 years, the technological progress of high-performance computers and the implementation of theoretical chemistry into commercial software packages [72], [73] has permitted the theoretical calculation of large numbers of kinetic parameters often reaching experimental accuracy [74]. Today, automated tools for theoretical kinetics are used on a daily basis for the derivation of accurate kinetic parameters. The comparison between theoretical results and experimental data is still necessary for the validation of the theoretical methodologies adopted. However, there may be a time when well-validated theoretical approaches will not need any experimental comparison.

Introducing computational chemistry in the iterative flow of kinetic mechanism development adds further complexity to an already complex problem. In fact, the high level of detail of theoretical calculations may lead to a consistent increase in the size of the kinetic scheme. Additionally, introducing relatively accurate kinetic parameters derived theoretically into an existing kinetic mechanism based on lumped reactions such as the CRECK kinetic mechanism generally disrupts the internal consistency and equilibrium of the model often based on error cancellation. Hence, bridging the level of detail of computational chemistry and existing kinetic mechanism of reasonable size poses a significant challenge still today. In this thesis, this problem is specifically tackled in Chapter 4.

The theoretical determination of rate constants for specific reaction pathways can also be exploited to derive approximate rate constants for analogue reactions. The pioneering work of Benson et al. [75], [76] on analogy rules is based on the idea that the reactivity of a portion of a molecule is only affected by short-range interactions, hence the thermochemistry and reactivity of the same moiety in different molecules are similar. Reactions involving the same reactive moieties may be grouped together as belonging to the same reaction class, consequently having the same (or similar) kinetic parameters. The approach of defining reaction classes and reference kinetic parameters was successfully applied within the CRECK kinetic mechanism for the description of a variety of pyrolysis and combustion processes and lies at the basis of the model internal consistency [71], [77]. More recently, the coupling of theoretically derived reaction parameters with the reaction classes and rate rule approach proved as a powerful tool for the systematic development and update of the complex low temperature oxidation kinetics of alkanes [78], [79]. This approach was also adopted in this work to organize the submechanism for the combustion of aromatic hydrocarbons, as described in Section 2.6.

The kinetic mechanism is tested with kinetic simulations performed with commercial softwares such as CHEMKIN [80], CANTERA [81] or open-source softwares such as OpenSMOKE++ [82]. The detailed mechanism is tested with kinetic simulations of ideal reactors such as plug flow reactors (PFRs), jet stirred reactors (JSRs), shock tubes (STs), rapid compression machines (RCMs), premixed and counterflow flame burners. In particular, speciation measurements in flow reactors (PFRs, JSRs, STs) focus on product formation. Instead, ignition delay time (IDT) experiments in shock tubes and rapid compression machines and laminar flame speed (LFS) experiments in burners mostly characterize the ignition propensity. IDT and LFS experiments are performed at experimental conditions closer to engine applications and directly impact the design of real devices.

The performance of the kinetic model is evaluated by comparing kinetic simulations with available reactor experimental data. This comparison may be performed by simply plotting the results or with more general and automated tools such as Curve Matching [83]. Proper model validation should take into consideration the uncertainties of both the kinetic parameters of the model and those of the experimental data. Reasonable uncertainty quantification remains at present one of the biggest challenges in the combustion community [84]. As for experiments, some sources of errors such as flaws in mass and heat transfer, poor mixing, and human errors in the measurements, are difficult to quantify. The uncertainty of reaction parameters depends entirely on how the rate constant is derived and on the accuracy of the underlying assumptions. A discussion of the uncertainty in the theoretical reaction parameters derived in this work is presented in Section 3.5. In recent years, Burke et al. [85], [86] put considerable effort into the development of an integrated framework for kinetic model improvement, which considers the uncertainty from different sources. Their multiscale informatics approach has already proven effective in explaining anomalous kinetic behavior and is a promising tool for the interpretation and optimization of complex kinetic mechanisms.

An extensive validation of the kinetic mechanism at different operating conditions should also ensure model predictive capability at relevant engine conditions, which are not tested in ideal reactor experiments. Experimental data should be ideally stored in an organized, effective and reliable way to facilitate kinetic mechanism validation. This issue was tackled by a number of kinetic databases, such as PrIME (<https://www.primekinetics.org>), Cloud-Flame (<https://cloudflame.kaust.edu.sa/>), or ReSpecTh (<http://respecth.hu>). More recently, SciExpeM (<https://sciexpem.polimi.it/>), developed at Politecnico di Milano, made another step forward in data and simulation management, bringing together kinetic mechanisms, kinetic simulation results, and performance evaluation procedures. Despite the effort at converging towards common nomenclature and formatting, common rules for data storage and management have not yet been established. Nevertheless, conventions in species name and structure is becoming common practice thanks to InChI species identification. Finally, even these well-established conventions may fail in more complex and less explored tasks such as the description of stereochemistry and resonance-stabilized species.

In the common event of poor model performance, analysis tools help identify deficiencies and guide the iterative improvement of a kinetic mechanism. In particular, sensitivity analysis highlights reactions that most strongly affect the simulated profiles of selected output properties (temperature, mole fraction, etc.). On the other hand, rate of production analyses (ROPA) identify the main reaction pathways contributing to the destruction or formation of a species in specific experimental conditions. The uncertainty of the reaction parameters of the relevant reactions identified should then guide model update. Generally, well-studied and validated literature kinetic parameters are not tuned or modified based on simulation results. On the other hand, reaction pathways scarcely studied in the literature or with no available experimental or theoretical literature estimates may be either tuned to best match macroscopic reactor data or further investigated, either experimentally or theoretically. Finally, one of the hardest steps in model improvement is the identification of missing reaction pathways. These may be added by chemical intuition in an attempt to explain the macroscopic experimental evidence not captured by the tested kinetic mechanism. These new reaction pathways may then be confirmed by new theoretical or experimental evidence. Alternatively, literature theoretical studies independent of the specific kinetic model may unravel new kinetic reaction pathways that cannot be observed experimentally but may have a significant impact on model performance.

Overall, the development of a fully predictive kinetic model with modern automated tools seems currently possible but still requires overcoming multiple challenges. The multitude of automated tools developed in the past years partially face the increasing complexity of kinetic model development and testing. Increasing automation is also risky, as kinetic models are progressively becoming black boxes whose physics is harder and harder to unravel. The main critical challenges include big data storage and management, uncertainty quantification, increase in the accuracy of theoretical calculations and appropriate integration into kinetic mechanisms, model size management, automated performance evaluation and optimization. Finally, despite the fact that some tools to address specific problems are available, complete

integration of all of them would allow consistent automation of the entire workflow depicted in Figure 1.9.

1.3 *Ab initio* theoretical kinetics for kinetic modeling

In the past 30 years, the increase in computational power and the advancements in theoretical methodologies allowed to reach high accuracy in *ab initio* calculations for the prediction of thermochemical properties and rate constants [87]. First-principle theoretical kinetics has become an essential tool to build combustion kinetic models. As an example, Figure 1.10 shows that in the last 20 years the contribution of theory-informed works for chemical kinetics at the combustion symposia increased from 15% to almost 40%.

As anticipated in Section 1.2, theoretical kinetics for combustion modeling brings several advantages. In fact, performing experiments to derive the huge number of kinetic parameters of a global kinetic mechanism is unfeasible and it does not allow us to explore the full range of operating conditions of combustion processes. Theoretical kinetics allows the exploration of a wide range of temperatures and pressures and, if used wisely, it allows for the quantification of kinetic parameters with an accuracy comparable to that of experiments. Additionally, unexpected reaction pathways can be found. The physical soundness of first-principle methodologies allows fundamental understanding of reactive processes, and therefore more physical and predictive kinetic mechanisms. Finally, theoretical kinetics helps us to face several unsolved challenges in the kinetic modeling of combustion processes, such as the investigation of biofuel combustion and the kinetics of soot formation.

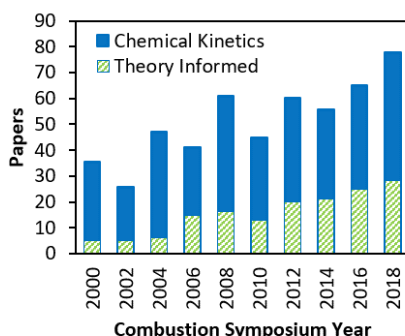


FIGURE 1.10: Increase in theory-informed chemical kinetic works at the Combustion symposia from 2000 on. Adapted from [88].

Figure 1.11 represents schematically the main steps required to derive thermochemistry and rate constants from first principles, highlighting some of the available literature codes to automate the workflow.

Both thermochemistry and rate constants are derived theoretically from information about molecular partition functions. Quantum chemistry allows to compute relevant quantities contained in the partition functions, mostly energy and vibrations. The accuracy in the description of partition functions is key in obtaining accuracy in the resulting thermochemical and kinetic properties.

The main steps for the derivation of thermochemistry from first principles are illustrated in the top part of Figure 1.11 (green flow). First, a molecule of interest is identified. The structure identification may be obtained from a guess for its geometry. Recently, the advent of cheminformatics has introduced unambiguous species identifiers such

as the International Chemical Identifier (InChI, <https://www.inchi-trust.org/>), a character string generated by a computer algorithm. Unique identifiers can be converted to geometry inputs for electronic structure (ES) calculations with open-source codes such as RDKit (<https://www.rdkit.org>) and Open Babel (http://openbabel.org/wiki/Main_Page, [89]).

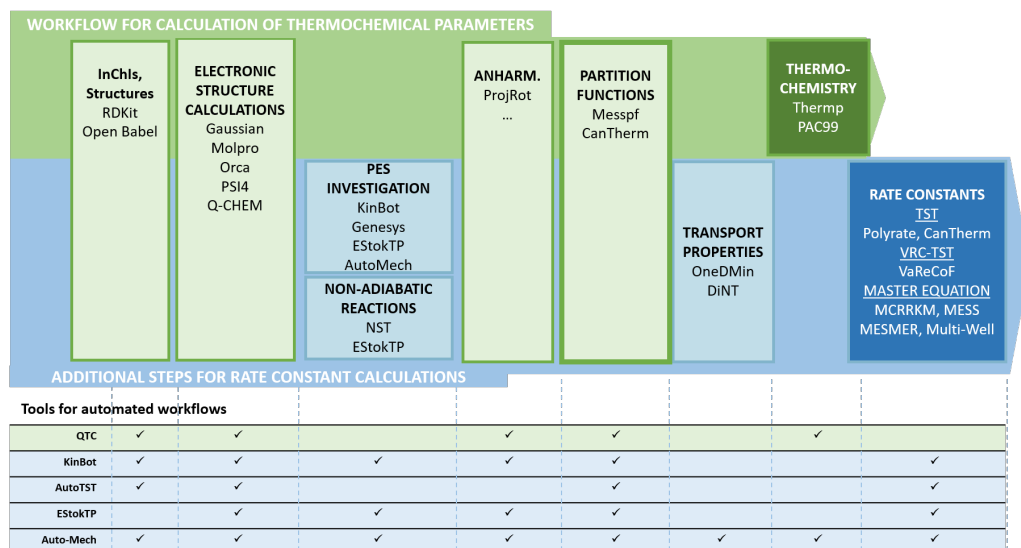


FIGURE 1.11: Examples of (automated) workflows for first-principle calculations of thermochemical parameters and rate constants.

Then, electronic structure calculations permit the optimization of the geometry of the guess structure, the calculation of the corresponding vibrational frequencies, and permit us obtain the electronic energy. ES calculations are performed by using several codes available in the literature, such as Gaussian and Molpro [72], [73], or open-source ES packages such as ORCA, PSI4 and Q-CHEM [90]–[93].

Partition functions are then derived from electronic energies, vibrational frequencies and other molecular properties (see Section 3.2.1). Additional complexity arises from the anharmonic behavior of molecular vibrational motions and their coupling. In many cases, accounting for anharmonicities is necessary for a proper derivation of the final partition functions. From a theoretical standpoint, many challenges have not been addressed yet and automated codes only include basic features to consider the coupling of vibrational motions. Section 3.2.2 presents the treatment of anharmonic vibrations in this work.

Finally, thermochemical properties such as heat capacity (C_P), enthalpy (H) and entropy (S) are calculated from partition functions and their first and second derivatives. These quantities are then fitted to a specific formatting so that they can be processed in global kinetic mechanisms (see Section 2.2, 3.2.3).

The calculation of kinetic parameters from first principles requires additional steps, as shown in the blue flowchart of Figure 1.11. Theoretical rate constants for reactions that are independent of pressure are generally derived with transition state theory (TST), via the identification of the molecular configuration along the reaction coordinate that minimizes the reactive flux (Section 3.3.2). The transition state (TS) search has been automated

in various codes using different protocols. For instance, KinBot and Genesys [70], [94], [95] search for the TS configuration on the basis of known reactants and products. Other software like EStokTP and Auto-Mech [96]–[98] search for the TS according to the reaction types. TS search may be extremely complex for some reaction types. For instance, non-adiabatic reactions occur across potential energy surfaces (PESs) with different spin states, and therefore require specific algorithms to search for the minimum seam of crossing (which, strictly speaking, is not a TS) and the application of different theories, as implemented in NST ([99]) and EStokTP (see Section 3.3.2.6). TST provides pressure-independent rate constants, as implemented in codes such as Polyrate and CanTherm [100], [101]. Reactions with barriers generally require an energy-dependent correction of the rate constant due to quantum tunneling effects [102].

Barrierless reactions without a well-defined TS configuration are treated differently. The rate constant is determined based on the energy, rovibrational properties, and transitional degrees of freedom of multiple molecular configurations identified for a given reaction pathway (see Section 3.3.2.4). At present, the most advanced theories for the treatment of barrierless reactions were only implemented in VaReCoF [103], [104] and POLYRATE [100], [105].

In some cases, such as for barrierless recombination reactions, or when molecular configurations with the same stoichiometry are all connected by identified TSs, the pressure dependence of the rate constants should also be considered. Quantification of pressure dependence is necessary to properly represent fuel combustion behavior at engine relevant conditions. Pressure dependence is controlled by the competition between energy transfer processes through collisions between molecules and reactive phenomena. A correct representation of this competition requires a microcanonical treatment of the time dependence of the microcanonical population distributions through a population balance, i.e., the master equation (ME), whose solution can be related to phenomenological rate coefficients implemented in kinetic mechanisms (Section 3.3.4). Figure 1.11 lists some of the available ME solvers, such as MESS [106], MCRKRM [107] (both used in this work), MESMER [108] and Multi-Well [109]. The theoretical results of pressure-dependent rate constant calculations are strongly influenced by the energy transfer properties of the molecules involved. In particular, collision parameters (e.g., Lennard-Jones) determine the number of effective collisions between the molecules and the bath gas, while collision efficiency parameters determine the amount of energy transferred. The theoretical determination of collision properties can be performed by coupling of *ab initio* calculations with classical trajectory calculations [110]–[112], as implemented in a few codes [113], [114]. More recently, these data were used to derive trajectory-based rules for the prediction of such parameters [115].

The complexity and the multitude of tasks for the theoretical derivation of rate constants led research efforts to automating the whole theoretical workflow. Some examples are reported in the bottom part of Figure 1.11. For instance, QTC by Keceli et al. [116] determines thermochemical properties of well-defined structures. KinBot by Zador, Van de Vijver et al. [94], [95] mostly focuses on PES exploration. AutoTST by Bhoorasingh et al. [96] implements different versions of TST for the calculation of rate constants belonging to specific reaction families and automatically generated by other codes (RMG). EStokTP by

Cavallotti et al. [97] investigates elementary reaction channels based on TS search protocols by reaction type and eventually derives temperature and pressure-dependent rate constants. Finally, Auto-Mech by Elliott et al. [98], based on EStokTP, is the only code at present able to automate the entire workflow from species and reaction identification to transport and thermochemical properties and rate constants.

Several automation challenges still need to be tackled. For instance, the large amount of data generated by automated theoretical calculations require a solid file and database management system. Ruscic et al. [117] put considerable effort into generating a combined experimental and theoretical thermochemistry database. However, conventional formatting and theoretical calculation storage has not yet been dealt with. Additionally, sharing such a large amount of theoretical data with the combustion and theoretical kinetics community presumes unique identification of both species and reactions. Species identification is generally performed with InChIs, however this practice is still not widespread and the treatment of lumped species in kinetic mechanisms (identified by multiple -sometimes several- structures) is an additional unsolved issue. The problem is even more challenging for reaction identification. Finally, from an implementation standpoint, the coupling of different codes and automatic correction of errors are still important challenges to smooth automation.

Nevertheless, recent automation efforts have proven extremely successful, allowing the calculation of a number of rate constants that was unimaginable only 10 years ago. Systematic theoretical efforts focusing on specific classes of reactions also led to *ab initio* based reaction rate rules, which then guide kinetic mechanism development and further reduce computational efforts. In particular, ES based rate rules were particularly successful in building predictive low-temperature alkane combustion mechanisms [118]–[121].

Current efforts of automated theoretical kinetics aim at the *ab initio* derivation of entire kinetic mechanisms. For instance, RMG by Gao et al. [69] generates reactions (and possibly estimates of the associated kinetic parameters) iteratively on the basis of reaction families. The application of RMG was partially successful and highlights numerous future challenges, involving accurate and physical reaction pathway generation and thermochemistry prediction, and most importantly the need of tools to avoid the explosion of the number of kinetic parameters to be computed. Bridging *ab initio* theoretical kinetics and global kinetic modeling still poses significant issues.

Overall, theoretical kinetics is proving to be an extremely powerful tool to aid the development of accurate kinetic mechanisms. As kinetic theories advance, more accuracy but also more complexity are added to an already complex problem. Recent automation efforts generated large amounts of data that need storage and management. Hence, the future of theoretical kinetics will face multi-disciplinary challenges. The incredible progress of the past 30 years on all research fronts suggests that full integration and automation are possible with the support of a solid theoretical knowledge and the collaboration of the whole chemical kinetics community.

1.4 Kinetic modeling of aromatic hydrocarbons

Because of the relatively recent interest of the combustion community in aromatic compounds, their combustion kinetics is less known than that of aliphatic hydrocarbons. Systematic investigations of the latter led to the development of detailed sound kinetic models arranged according to reaction classes with well-determined and consistent kinetic parameters [79], [120], [122]–[124]. On the other hand, no systematic investigations of the reactivity of MAHs and PAHs were performed. Moreover, fewer experimental data are available because many aromatics are solids at room temperature, some are toxic and corrosive, and they accumulate on the reactor walls causing fouling, faulty measurements, and high uncertainty in the measurements [125], [126]. As a result, literature kinetic models for benzene oxidation were developed on the basis of only a limited set of experimental data [127], [128]. Toluene was studied more extensively due to its relevance as a reference fuel for surrogate mixtures [129]. In the case of oxygenated aromatics, more recent experimental data for the pyrolysis and oxidation of phenol, anisole, catechol, guaiacol and vanillin provided guidelines for the development of the first kinetic models for OAHs [45], [46], [50].

The kinetics of the pyrolysis and oxidation of MAHs can only be partially derived from the knowledge of aliphatic hydrocarbons because of the peculiar behavior of the stable aromatic ring. For instance, the decomposition of the benzene ring via ring-opening reactions occurs only at very high temperatures [130]. Therefore, the ignition of MAHs is strongly delayed compared to aliphatic hydrocarbons. Additionally, there is no net distinction between low and high temperature kinetics. In fact, the chain branching pathways typical of the low temperature oxidation of aliphatic hydrocarbons, which undergo consecutive oxygen additions leading to the production of reactive OH radicals, do not occur in the oxidation of MAHs and OAHs.

On the other hand, the electrophilic character of the aromatic ring favors radical additions at low temperatures. At higher temperatures, H-atom abstraction and also bond-fission reactions contribute to radical generation. Figure 1.12 shows the radicals resulting from H-atom abstraction or bond-fission reactions in benzene, toluene, phenol and anisole. The relevance of these reaction pathways is related to the bond dissociation energy (BDE) of the bond being broken. BDEs for lateral substituents are generally lower than BDEs for C–C and C–H cleavage in the aromatic ring. Therefore, the lateral substituent strongly affects the kinetics of the substituted MAH [46]. For instance, in toluene H-atom abstraction reactions from the methyl group generate resonance-stabilized benzyl radicals which are key in both oxidation (via additions) and growth (mostly via self-recombination) [129]. On the other hand, in anisole the cleavage of the C–O bond in the methoxy group is generally favored with respect to H-atom abstraction reactions from the methyl site, resulting in large amounts of stable phenoxy radicals [131]. Finally, the presence of multiple lateral substituents, extremely common in model compounds for biomass-derived biofuels (e.g., catechol, guaiacol, cresol, vanillin), adds further complexity due to the interaction between the different substituents.

Another challenge to the fundamental understanding of substituted MAHs reactivity are

their peculiar unimolecular decomposition reactions rarely studied both theoretically and experimentally. These involve complex multi-step processes, such as H-transfer reactions followed by ring opening, and elimination reactions, as for the molecular decomposition of phenol [132], [133] (top scheme of Figure 1.13). Another example are H-transfer reactions concerted with molecular decomposition, such as in catechol [134] (bottom scheme of Figure 1.13).

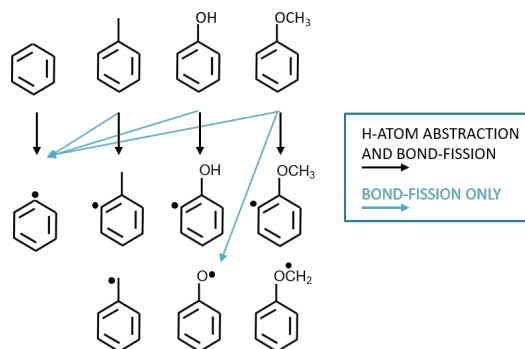


FIGURE 1.12: Examples of aromatic radicals derived from bond-fission or H-atom abstraction reactions from benzene, toluene, phenol and anisole.

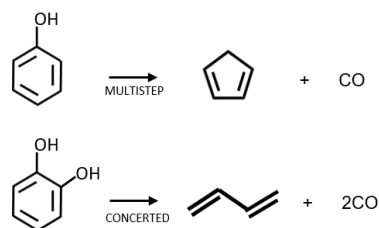


FIGURE 1.13: Schemes of molecular decomposition reactions of phenol (top) and catechol (bottom).

Finally, several experimental observations of the products of MAHs and OAHs pyrolysis and oxidation are still unexplained. For instance, some OAHs seem to produce CO_2 abundantly even in pyrolytic conditions [135], [136] or at the earliest stages of oxidation [125].

Other kinetic modeling challenges involve the rationalization of the growth of MAHs and OAHs to larger PAHs. For instance, Figure 1.14 shows the well known hydrogen abstraction carbon addition (HACA) pathway for the formation of the second aromatic ring from benzene [137]–[139]. However, numerous theoretical investigations of the past 20 years revealed that PAHs grow through a number of different processes [140], [141]. Additionally, recent findings highlighted that large PAHs behave differently than their smaller counterparts and should probably be modelled as resonance-stabilized π radicals or diradicals [58], [61], [142]. The size-dependent nature of PAHs reactivity further complicates the generation of rate rules. Finally, despite the fact that recent research efforts mostly focused on PAHs growth, oxidation pathways also need to be clarified to quantitatively assess their competition with growth reactions, which is key to quantitative predictions of soot volume fractions.

In the past 20 years, most of the kinetic investigations of MAHs and PAHs formation and growth included detailed theoretical studies. However, performing accurate theoretical

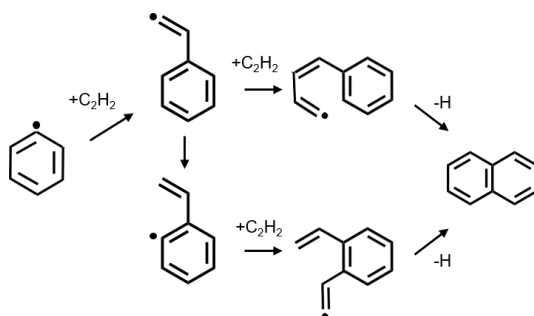


FIGURE 1.14: Example of growth from phenyl radical to naphthalene through HACA pathway.

calculations or at least accurate enough to be of any use for kinetic modeling is not trivial. Firstly, the recent exponential increase in the number of theoretical calculations of aromatics was not coupled with any extensive validation of the theoretical methodologies adopted. Secondly, the high number of heavy atoms (at least 7 for mono-substituted MAHs) makes state-of-the-art theoretical treatments prohibitive. The CPU time for less accurate DFT methodologies (see Section 3.1.4) scale as $O(N^3)$ or $O(N)$ in some cases [143], where N is the number of atoms in the system. However, other methodologies such as CASPT2 or coupled cluster (see Section 3.1.3) may scale as $O(N^5) - O(N^7)$, where N is the number of correlated electrons considered in the system. Despite continuous efforts to reduce computational time [144]–[147], in most cases only methodologies based on local correlations and orbitals achieve high accuracy. None of these methodologies has been extensively tested on aromatics, however they might be unsuitable to describe the significant electron delocalization of aromatics. Additionally, delocalization effects might not be well captured even by state-of-the-art ES methodologies such as coupled cluster.

As far as PES investigation is concerned, the level of complexity rapidly increases even for simple MAHs. For instance, Figure 1.15 shows part of the PES for the $C_6H_5 + O_2$ system investigated in this work. Theoretical challenges include not only the optimization of several stationary points and TSs, but also the treatment of barrierless channels and peculiar TSs such as ring insertion.

Overall, there is still a lot of theoretical and kinetic modeling work to do on the combustion of aromatic systems. Indeed, systematic theoretical investigations on relevant reaction classes in MAHs pyrolysis and oxidation would set a useful basis for future consistent model development. Additionally, clarifications of the actually relevant reaction classes to these systems would also guide future theoretical work. Finally, the integration of theoretically-based rate constants with large number of species and reactions into global combustion kinetic mechanisms still poses a major challenge.

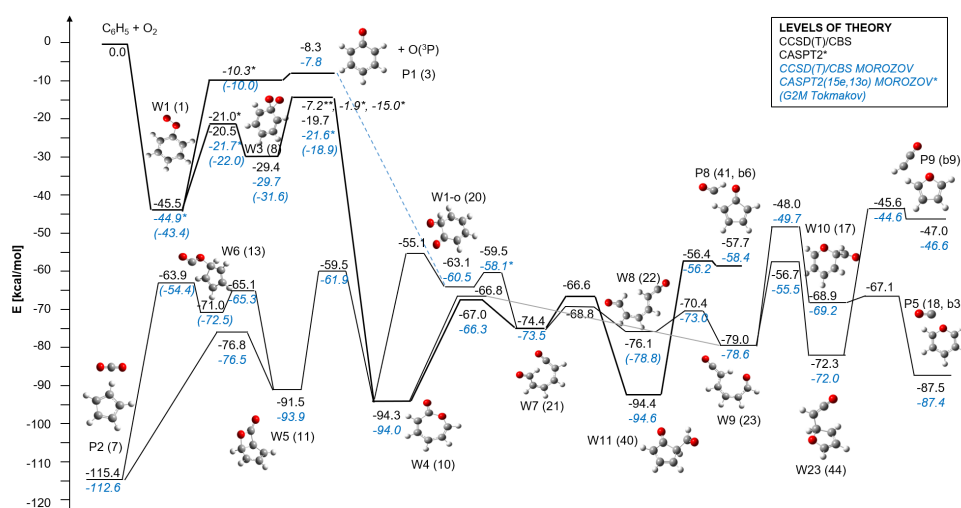


FIGURE 1.15: Example of complex PES investigated in this work ($C_6H_5 + O_2$ reaction).

1.5 Objectives and structure of this thesis

In the complex context of the kinetic modeling of the combustion of aromatic hydrocarbons described in this Chapter, the main goal of this thesis is the theoretically-based systematic revision of the kinetic mechanism of MAHs combustion, with a focus on cyclopentadiene, benzene and phenol. In particular, a solid workflow for theoretically-based kinetic mechanism development for MAHs combustion is built, also through an improved understanding of both appropriate theoretical methodologies and relevant reaction classes.

Specific objectives of this work include:

- Identification of the main reaction classes and organization of models according to reaction classes and rate rules (Section 2.6, 5.2, 6.2).
- State of the art theoretical calculations and critical assessment of the accuracy of the methodologies adopted for uncertainty quantification (Section 3.5, Section 5.3, 6.3).
- Building a framework to connect *ab initio* calculations and global kinetic modeling (Chapter 4).
- Kinetic model update with new theoretical findings and critical model performance assessment (Section 2.7, 5.4, 6.6).

Figure 1.16 shows the organization of this thesis.

Chapter 2 presents an overview of the general structure of kinetic mechanisms and of the hierarchical organization of the CRECK kinetic mechanism. It also describes the rationale behind the reaction class and rate rule approaches. The tools used for kinetic simulations and the analysis of model performance are presented.

Chapter 3 describes the theoretical methodologies adopted in this work. It provides the background of both *ab initio* calculations and kinetic theories and describes how these

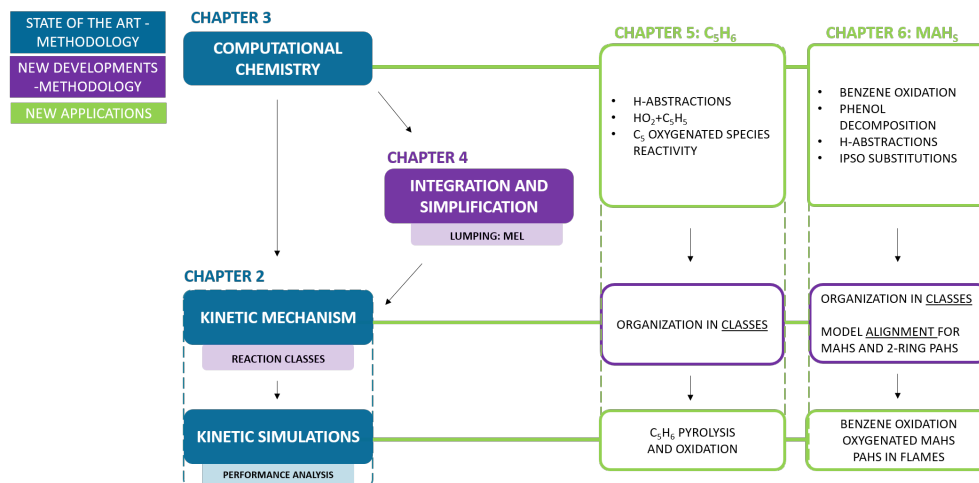


FIGURE 1.16: Structure of this thesis.

methods are applied to derive thermochemistry and rate constants. Sources of uncertainty in the present theoretical calculations are commented on.

Chapter 4 presents a novel methodology developed in this work for the integration of theoretically-derived rate constants into kinetic mechanisms.

Chapters 5 and 6 contain the main results of the theoretical calculations and kinetic modeling of the sub-mechanisms of cyclopentadiene and MAHs oxidation. The former sets the basis for the development of MAHs combustion mechanisms. Both chapters present the systematic model organization and alignment according to reaction classes and the theoretical calculations performed based on relevant reactions identified. Finally, the results of kinetic simulations are discussed.

Chapter 7 draws the conclusions of this work and suggests future perspectives and directions for the systematic kinetic modeling of MAHs and PAHs.

Chapter 2

Fundamentals of kinetic modeling

Chapter 1.2 illustrated the general workflow of kinetic modeling construction and use in kinetic simulations. This chapter discusses in more detail the three main blocks of the kinetic mechanism, i.e., the kinetic parameters (Section 2.1) and the thermochemical and transport properties (Section 2.2, 2.3). The organization of the CRECK mechanism, i.e., the kinetic mechanism used and updated in this work, is illustrated in Section 2.5. Section 2.6 presents the approach for reaction classification and rate assignment according to analogy and rate rules. Finally, Section 2.7 briefly summarizes the methodology used for kinetic simulations.

This work adopts the most common format for kinetic schemes in the combustion community, namely the CHEMKIN format [80]. The portions of text files reproduced in this work all refer to the CHEMKIN format.

2.1 Reactions and kinetic parameters

The core of the kinetic mechanism is the set of kinetic parameters. A CHEMKIN format kinetic file is organized in three main sections, namely the list of elements, the list of species, and the list of reactions with the corresponding kinetic parameters. Chemical kinetics studies the rates at which chemical processes occur. Combustion processes are largely controlled by the complex interplay of fluid dynamics and chemical kinetics, hence it is essential to provide an accurate and physically meaningful description of the combustion kinetics to obtain a predictive model.

2.1.1 Elementary reactions and rate laws

The core of a kinetic mechanism is a list of reactions and their kinetic parameters. Combustion mechanisms generally consider only homogeneous gas-phase reactions (with the exception of soot formation, which is not considered in depth in this work), hence the discussion of this section excludes heterogeneous phenomena.

The reaction rate describes the rate of evolution of a chemical species I due to a chemical reaction. For instance, the molar concentration of a species C_I evolves in time due to a set of reactions NR according to

$$\frac{dC_I}{dt} = \sum_{j=1}^{NR} r_{Ij}(T, p, C_J) \quad (2.1)$$

where r_{Ij} is the reaction rate of species I in reaction j and NR is the total number of reactions. In general, the reaction rate has a complex dependence on temperature, pressure and concentration. However, combustion mechanisms assume that all reactions are elementary, i.e., single step reactions where the molecularity coincides with the stoichiometry (ν_{Jj}). Therefore

- the reaction rate r_{Ij} can be expressed as the product of the reaction rate r_j and the stoichiometric coefficient of species I in the reaction:

$$r_{Ij} = \nu_{Ij} r_j$$

- r_j is proportional to the concentration of its reactants to the power of their stoichiometric coefficients according to a rate constant k_j which is only a function of temperature and pressure:

$$r_j = k_j(T, p) \cdot \prod_{J=1}^{N_{reac}} C_J^{|\nu_{Jj}|}$$

The general dependence of r_j on the concentration of chemical species is called a power law and the power exponent associated to each species J defines the reaction order of reaction j with respect to species J (i.e., the absolute value of the stoichiometric coefficient $|\nu_{Jj}|$ defined above).

Combustion mechanisms generally include unimolecular ($I \rightarrow P$) and bimolecular ($I_1 + I_2 \rightarrow P$) reactions, namely reactions with a global first or second order of reaction. Termolecular reactions such as $I_1 + I_2 + M \rightarrow P$ instead normally do not define a simultaneous collision between three species, but rather a bimolecular collision generating a hot complex, which is then thermally stabilized by a third collision with an abundant third body M - the bath gas. These phenomena are related to the pressure dependence of rate constants, as discussed in Section 2.1.4 and 3.3.4.

Finally, it must be noted that even though the reaction order corresponds to the reaction stoichiometry for all reactions in the kinetic mechanism, not all of them occur in a single elementary step. In particular, global reactions involving multiple steps include

1. well-skipping channels (see Section 3.3.4): multi-step processes where a rovibrationally excited (high-energy) species dissociates directly to bimolecular products, or isomerizes to a well through multiple steps, skipping the stabilization of intermediate wells. Most of the processes investigated in this work involve such rate constants. For instance, ipso addition-elimination reactions occur in two steps $IR + H = IRH = IH + R$. The high-pressure limit rate constants are associated to the single steps, however at lower pressures the global well-skipping process $IR + H = IH + R$ also occurs and generally prevails over IRH stabilization. An example of unimolecular well-skipping process is the isomerization of para hydroxyphenyl p-C₆H₄OH to phenoxy radical C₆H₅O through the following steps: p-C₆H₄OH = m-C₆H₄OH = o-C₆H₄OH = C₆H₅O, which may occur globally as p-C₆H₄OH = C₆H₅O (see Section 6.3.2).

2. horizontally-lumped reactions: when multi-step processes occur through a set of intermediate wells, relatively unstable intermediates may be "skipped" and similar intermediates may be "lumped" so as to simplify the phenomenological description of the reactivity. This concept is another form of well-skipping reaction channels and is discussed in detail in Chapter 4.
3. vertically-lumped reactions: global reactions that assume a fast decomposition of a given product. These reactions are written as irreversible and may include more than 2 products. Theoretically, this behavior is justified in terms of prompt dissociation chemistry [88], [148], [149]. These particular cases will not be discussed in detail in the present work.

2.1.2 Equilibrium reactions

The reactions in the mechanism may be written as irreversible ($A \rightarrow B$) or reversible ($A = B$). In this work, irreversible reactions generally refer to "horizontally" lumped rate constants, as the thermochemistry of a lumped pseudospecies may result in incorrect or inaccurate values of the backward rate constants (see Section 4.3). Also "vertically lumped" or "prompt" reactions with more than 2 decomposition products are generally written only in the forward direction, e.g., $A \rightarrow B+C+D$. In these cases, the backward reaction would be at least termolecular, which is an extremely unlikely process. Exceptions to this rule may be high-energy non-Boltzmann chemically termolecular reactions [150], explored in recent years but mostly excluded from kinetic mechanisms because of the complex rate constant dependence on species concentration.

As for reversible reactions, the rate constant of the backward reaction k_{bw} is derived from that of the forward reaction k_{fw} through thermodynamic consistency, here reported under the ideal gas assumption:

$$K_{eq} = \prod_{I=1}^N a_I^{\nu_I} = \left(\frac{p}{p_{ref}}\right)^{\Delta\nu} \cdot \prod_{I=1}^N X_{I,eq}^{\nu_I} = \exp\left(-\frac{\Delta G_r^0}{RT}\right) \quad (2.2)$$

$$\frac{k_{bw}}{k_{fw}} = \left(\frac{p}{RT}\right)^{-\Delta\nu} \cdot \prod_{I=1}^N X_{I,eq}^{-\nu_I} = \left(\frac{p_{ref}}{RT}\right)^{-\Delta\nu} \cdot \exp\left(\frac{\Delta G_r^0}{RT}\right)$$

where a_I , ν_I and X_I are the activity coefficients, stoichiometric coefficients, and mole fractions of species I , respectively, and $\Delta\nu = \sum_I \nu_I$. p_{ref} is the reference pressure (generally 1 atm), eq indicates equilibrium conditions, and ΔG_r^0 is the molar Gibbs free energy of the reaction.

2.1.3 Temperature dependence

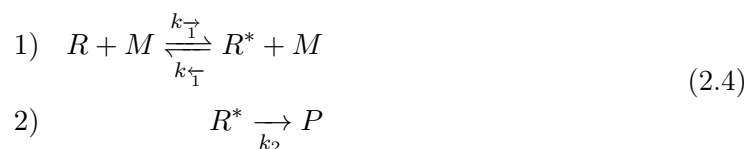
The most common expression to describe the temperature dependence of a rate constant is the modified Arrhenius expression:

$$k = k_0 \cdot T^\alpha \cdot \exp\left(-\frac{E_A}{RT}\right) \quad (2.3)$$

where k_0 is the pre-exponential factor, and E_A is the activation energy. The units generally used in CHEMKIN mechanisms (and in this work) are mol, cal, s, cm³. The rate constant of a pressure-independent reaction is fully characterized by these three kinetic parameters. A sum of multiple Arrhenius expressions is sometimes required for an accurate description of temperature dependence. CHEMKIN allows multiple Arrhenius expressions as long as the keyword `DUPLICATE` or `DUP` is specified. In PLOG formalism (see below), multiple Arrhenius expressions at each pressure may also be specified consecutively (i.e., without repeating the reaction name or specifying `DUP`).

2.1.4 Pressure dependence

Pressure dependence arises from the competition between chemical processes such as dissociation and isomerization, and energy transfer processes mostly occurring through collisions between the reacting species and the bath gas. These aspects were first theorized by Lindemann [151]. Despite the fact that the Lindemann mechanism proved to be too simplistic and was not in complete agreement with experiments, it set the basis for important kinetic theories for pressure-dependent reactions, as illustrated in Section 3.3.4. Essentially, Lindemann theorized that the elementary unimolecular reaction $R \rightarrow P$, where R is a unimolecular reactant and P may be either an isomerization or a dissociation product, actually occurs through a multi-step process: first, reactant R gains the necessary energy for transformation into P by an activating intermolecular collision with the bath gas M . The translational energy of the colliding body M is transferred to R in the form of rovibrational energy. Then, the rovibrationally excited R^* may be either thermally re-equilibrated through another collision or form products:



Assuming that the rovibrationally excited complex R^* is at steady state ($dC_{R^*}/dt = 0$), the rate of product formation can be written as

$$r = \frac{k_2 k_{\bar{1}} C_R C_M}{k_{\bar{1}} C_M + k_2} \tag{2.5}$$

where C_M is the concentration of the bath gas and therefore contains the dependence on pressure. The high and low-pressure limit expressions for r allow one to derive the corresponding rate constants for $R \rightarrow P$:

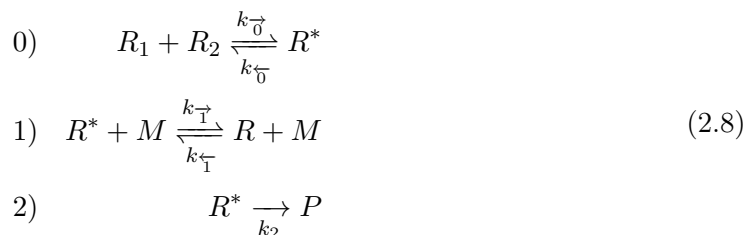
$$r_{\infty} = \left(\frac{k_2 k_{\bar{1}}}{k_{\bar{1}}} \right) C_R = k_{\infty} C_R \tag{2.6}$$

$$r_{low} = (k_{\bar{1}} C_M) C_R = k_{low} C_R \tag{2.7}$$

The global rate constant for $R \rightarrow P$ depends linearly on the concentration of M at very low pressures (k_{low}), where collisional deactivation is significantly slower than product formation ($k_{-1} \ll k_2$) so that every excited R^* forms P , while it is independent of M at

high pressures (k_∞). Rate constants at intermediate pressures describe the so-called fall-off regime. It is noted that different colliders M transfer different amounts of energy through collisions, mostly (but not only) according to their collisional cross sections. Namely, each collider has a different "efficiency". Therefore, the fall-off behavior of a chemical reaction largely depends on the collider considered. Energy transfer greatly affects the fall-off regime of reactions involving small species.

Similar considerations apply to bimolecular reactants R_1+R_2 . However, in these cases the collision between R_1 and R_2 forms the activated complex R^* . Then, the collision of R^* with the bath gas results in thermalization, namely the stabilization of complex R , originating a new product channel. Hence, the global process can be described as



where steps 1 and 2 are identical to those of Equation (2.4). Global reaction $R_1 + R_2 = R$ (0+1) describes the formation of adduct R , while $R_1 + R_2 = P$ (0+2) describes the formation of a product (either a well or bimolecular product). Pressure dependence of these two processes derives from the competition of steps 1, 2. The latter is generally referred to as a well-skipping reaction (Section 3.3.4). It is noted that in some cases no adduct is formed, such as in some H-atom abstraction reactions which proceed directly to products. In these cases, no pressure dependence is expected.

Figure 2.1 shows the pressure-dependent rate constants of two reactions calculated in this work. Part a) shows the recombination of H atom on phenoxy radical to form C_6H_6O adducts (steps 0+1 of Eqn. (2.8)) as well as the direct decomposition to bimolecular products (0+ a series of steps like 2 of Eqn. (2.8)), while part b) shows the rate constant of the O–H bond-fission in C_6H_5OH . It is evident that pressure effects may be significant, showing an increase in the rate constants of about one order of magnitude at 2500 K as the pressure increases from 0.1 to 100 atm. At high temperatures, pressure effects are stronger because product formation is faster, as shown in Figure 2.1a. In fact, at low pressures the depletion of the pool of chemically active R^* is faster than its re-population due to the low number of collisions (low bath gas concentration).

In a CHEMKIN format kinetic file, pressure dependence of chemical reactions may be represented through different expressions, such as the Troe, PLOG, Chebyshev, Lindemann formats. This section briefly summarizes the common PLOG and Troe formats. The former was used for all the pressure-dependent reactions calculated in this work and consists in a simple set of modified Arrhenius expressions parametrically dependent on pressure. The bottom of Figure 2.2 illustrates a simple example of a PLOG expression calculated in this work (corresponding to the rate constant of Figure 2.1b). Arrhenius parameters fit the temperature-dependent values at each pressure. Values at intermediate pressures are derived by kinetic simulators such as OpenSMOKE++ [82] (Section 2.7) as a linear interpolation

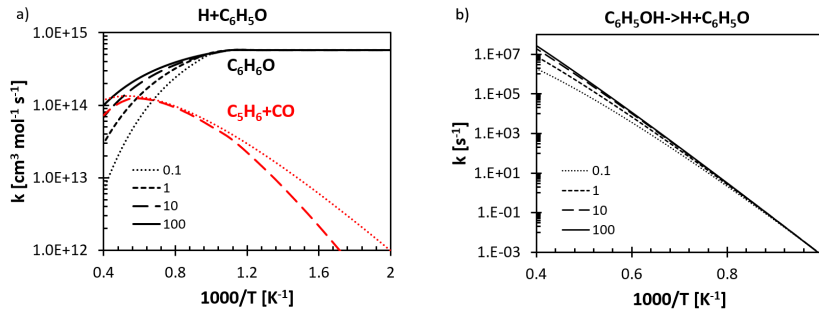


FIGURE 2.1: Example of bimolecular a) and unimolecular b) pressure-dependent rate constants calculated in this work (Section 6.3.2) at different pressures (0.1–100 atm).

of the logarithms of the rate constants at consecutive pressures. The main drawback of the PLOG formalism is that the rate constant is independent of the bath gas composition. However, it is possible to include different PLOG expressions for specific colliders.

On the other hand, the Troe formalism [152]–[154] describes the pressure dependence as a function of k_{low} and k_{∞} including linear dependence on the collision efficiencies of different colliders:

$$\begin{aligned}
 k &= k_{\infty} \cdot \frac{p_{red}}{1 + p_{red}} \cdot f(p_{red}, F) \\
 p_{red} &= \frac{k_{low}}{k_{\infty}} \cdot M_{eff} \\
 F &= (1 - \alpha) \exp -\frac{T}{T^{***}} + \alpha \exp -\frac{T}{T^*} + \exp -\frac{T^{**}}{T} \\
 M_{eff} &= \sum_{M=1}^{N_{coll}} eff_M C_M
 \end{aligned} \tag{2.9}$$

where α , T^* , T^{**} , T^{***} are the coefficients describing the pressure dependence (details are found in [153]) and eff_M are the collider efficiencies, which scale the corresponding collider concentrations C_M . The top of Figure 2.2 shows the Troe formalism for the recombination of H on hydroxyphenyl (C_6H_4OH) radical. (+M) indicates a generic collider. The first and second lines in the expression list the Arrhenius parameters of k_{∞} and k_{low} , respectively. The four TROE parameters are listed in the order described above. Finally, the collider efficiencies eff_M for specific molecules are included at the bottom, while $eff_M = 1$ for any other collider.

2.2 Thermochemistry

Thermochemical properties are essential to determine the chemical equilibrium in the system as well as energy transfer. In particular, the heat capacity C_P and enthalpy H are required to solve the energy balances in kinetic simulations so as to describe temperature evolution. In the energy balance, each reaction contributes to the temperature change accordingly to its enthalpy, calculated as $\Delta H_j = \sum_I^N \nu_{Ij} \Delta H_I$, where ΔH_I is the heat of formation of each species. Prior to any kinetic information, the reaction enthalpy already provides the

```

! [REACTIONCLASS] [A1-R] [REC_H_WELL]
H+C6H4OH(+M)=C6H5OH(+M) +8.33E+13 0.00 0.
LOW / +5.50E+75 -10.63 7000. /
TROE / 1. 0.1 584.9 6113. /
H2 / 2.000 / H2O / 6.000 / CH4 / 2.000 / CO / 1.500 / CO2 / 2.000 /
! [ENDREACTIONCLASS] [A1-R] [REC_H_WELL]

! [REACTIONCLASS] [A1,OH-M] [BONDFISSION_OH]
C6H5OH=>C6H5O+H 8.29E+48 -9.92 102202
PLOG/ 0.1 8.29E+48 -9.92 102202 /
PLOG/ 1 6.58E+38 -6.88 97737 /
PLOG/ 10 1.32E+32 -4.88 94606 /
PLOG/ 100 1.14E+29 -3.97 93140 /
PLOG/ 1000 2.47E+28 -3.77 92839 /
! [ENDREACTIONCLASS] [A1,OH-M] [BONDFISSION_OH]

```

FIGURE 2.2: Example of reactions written in CHEMKIN format in CRECK model according to the Troe and PLOG formalisms. Reaction classes are specified according to the methodology described in Section 2.6.

indication of its endothermicity or exothermicity. Also, important combustion properties of oxidizer-fuel mixtures such as the adiabatic flame temperature are entirely derived from thermodynamic properties [155]. Finally, in many cases it was proven in the literature that it is possible to link the activation energy of the reaction, i.e., kinetic properties, to the reaction enthalpy (e.g., Evans Polanyi relations, Section 2.6.2). Combined information on enthalpy H and entropy S allows one to derive the Gibbs free energy of the reaction and therefore the equilibrium constant (Equation (2.2)).

Thermodynamic properties for the species in a kinetic mechanism may be determined in several ways. Group additivity methods assume that thermodynamic properties depend linearly on those of the fragments constituting the species [75], [76]. More accurate values may be obtained by combining experimental and theoretical information. At present, the Active Thermochemical Tables (ATcT) by Ruscic et al. [117] are considered the most reliable reference database to determine thermodynamic properties. Theoretical calculations are generally able to achieve high accuracy by estimating thermodynamic properties from partition functions, as explained in Section 3.2.3. In this work, the thermodynamic properties of several new species introduced in the kinetic mechanisms were determined theoretically using Auto-Mech routines (Section 3.4.2).

The thermochemistry of species in CHEMKIN format is described according to NASA polynomials. NASA polynomials consist of two sets of 7 coefficients describing the temperature dependence of heat capacity, enthalpy and entropy:

$$\begin{aligned}
 \frac{C_P}{R} &= a_1 + a_2 \cdot T + a_3 \cdot T^2 + a_4 \cdot T^3 + a_5 \cdot T^4 \\
 \frac{H}{RT} &= a_1 + \frac{a_2}{2} \cdot T + \frac{a_3}{3} \cdot T^2 + \frac{a_4}{4} \cdot T^3 + \frac{a_5}{5} \cdot T^4 + \frac{a_6}{T} \\
 \frac{S}{R} &= a_1 \cdot \ln T + a_2 \cdot T + \frac{a_3}{2} \cdot T^2 + \frac{a_4}{3} \cdot T^3 + \frac{a_5}{4} \cdot T^4 + a_7
 \end{aligned}
 \tag{2.10}$$

where R is the universal gas constant. The two sets of coefficients a_i define these properties over two adjacent temperature intervals. Kinetic simulators such as OpenSMOKE++ (Section 2.7) allow one to remove small discontinuities ($<0.1\%$) at the intersection of the two

intervals. Figure 2.3 exemplifies the CHEMKIN format of the NASA polynomials of C_5H_5 as derived in this work. The first line lists the species name, its stoichiometry, and the minimum, maximum, and intermediate temperatures (200, 3000, 1000 K) defining the intervals of the two sets of NASA polynomials. The next three lines contain the 14 a_i coefficients, where the set of 7 coefficients fitting the properties for the high-temperature interval are listed first.

```

C5H5          H 5 C 5 O 0 N 0 G   200.0   3000.0  1000.0   1
6.30017275E+00 2.42118246E-02-1.20379379E-05 2.90851454E-09-2.76593571E-13 2
2.79955524E+04-1.21471026E+01-2.38445528E-02 2.58701887E-02 3.44942795E-05 3
-7.31677705E-08 3.39331273E-11 3.01567756E+04 2.34195200E+01 4

```

FIGURE 2.3: Example of NASA polynomials for C_5H_5 calculated in this work.

2.3 Transport properties

Transport properties are essential for the simulation of experimental conditions where transport phenomena (e.g., diffusion) have a comparable timescale to the kinetics. For instance, flames involve a strong interplay between mass and energy transfer and chemical kinetics. In these cases, diffusion coefficients, thermal conductivity and diffusivity, and viscosity have to be estimated. High accuracy is required for small C_0 – C_3 species, which largely control the transport behavior in flames.

In a CHEMKIN format mechanism, the listed transport properties include:

- index: indicates whether the species is atomic (0), linear (1), or non-linear (2).
- ϵ/k_B [K]: Lennard-Jones well depth.
- σ [Å]: hard-sphere collision parameter.
- μ [D]: dipole moment.
- α [Å³]: polarizability.
- Z_{rot} : rotational relaxation collision number at 298 K.

ϵ/k_B (K) and σ are used to determine the interaction energy between two species according to the well-known Lennard-Jones potential [156]. This potential is corrected for non-binary mixtures in the case of non-zero dipole moments, obtaining the Stockmayer potential [157].

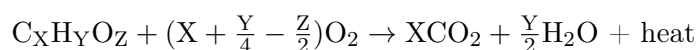
Despite the fact that the combustion community has mostly focused on the determination of thermochemical and kinetic parameters [158], in some cases kinetic simulations are substantially affected by transport phenomena. In particular, in fuel/air flames in both premixed and counterflow configurations backward diffusion of small radicals (H atom in particular) substantially affects the composition of the mixture and therefore the global reactivity of the system and product distribution.

It is worth mentioning that in certain reactor configurations major diffusion phenomena (such as backward diffusion) may result in discrepancies between experimental measurements

and kinetic simulations. These discrepancies are generally fixed by fictitiously "shifting" the results of the kinetic simulations according to the behavior of the experimental apparatus. However, this generally implies a detailed knowledge of the simulated reactor.

2.4 What controls macroscopic combustion properties?

Global combustion processes can be represented as fuel + air forming products and releasing heat. The stoichiometric oxidation of an hydrocarbon fuel (potentially containing oxygen) eventually produces CO_2 and H_2O according to the reaction



This global reaction occurs in a series of complex and interconnected elementary steps. The detailed kinetic representation of these steps through the kinetic mechanism allows one to investigate effects of temperature, pressure, equivalence ratio, and pollutant formation.

The macroscopic behavior of the fuel, e.g., its ignition properties, is governed by the competition between different types of reactions, namely chain initiation, propagation, and branching. The detailed oxidation mechanism for hydrogen, which is the basis for the combustion mechanism of any fuel, can be simply described by 8 species and about 20 reactions [159]. The reactivity starts with chain initiation reactions such as O_2 abstracting hydrogen from H_2 ($\text{H}_2 + \text{O}_2 = \text{H} + \text{HO}_2$) or bond-fission, e.g., $\text{H}_2 = 2\text{H}$. The radicals produced may either be converted to other radicals through chain propagation or produce additional radicals through chain branching reactions. For example, the branching reaction $\text{H} + \text{O}_2 = \text{O} + \text{OH}$ is the most sensitive high temperature reactions in flame propagation for H_2 and also for hydrocarbon fuels. Propagation reactions generally produce significant amounts of heat. For instance, $\text{H}_2 + \text{OH} = \text{H}_2\text{O} + \text{H}$ is a relevant reaction in determining the equilibrium between H atoms and OH radicals as well as heat release; in the combustion of hydrocarbons, the radical propagation reaction $\text{CO} + \text{OH} = \text{CO}_2 + \text{H}$ is also an essential exothermic reaction for the conversion of CO into CO_2 . Finally, chain termination reactions (often the reverse of chain initiation reactions) inhibit the reactivity. For instance, the recombination of methyl radicals to ethane $2\text{CH}_3 = \text{C}_2\text{H}_6$ is the main reason for the low ignition propensity of methane [160].

The complex interplay among chain propagation, branching and termination determines the global combustion behavior and strongly depends on temperature and pressure. For instance, in the intermediate and low pressure range increasing pressure accelerates chain branching reactions, thus accelerating the reactivity. At high pressures, chain termination reactions also become more relevant, inhibiting the reactivity.

The consumption and production of H atoms and OH radicals, respectively, via chain branching reactions is also key in controlling the ignition behavior of hydrocarbon fuels. In particular, at high temperatures reactions of the "core chemistry", such as those listed above, always appear in sensitivity analyses for fuel ignition. The next paragraph briefly summarizes the well-known important factors in the ignition of alkanes and then highlights the differences in the ignition of aromatic hydrocarbons.

The first step in the high temperature combustion of alkanes is fuel decomposition via H-atom abstraction (preferentially from secondary carbon sites) and bond-fission reactions. The alkyl radicals and H atoms produced lead to propagation/termination and branching, respectively. H atoms and OH radicals preferentially react with the hydrocarbon fuel; once the fuel is decomposed, H and OH react with small hydrocarbon products as well as via the propagation and branching reactions mentioned above.

The high temperature ignition properties of alkanes are all similar because the kinetics is mostly controlled by the reactions of the core chemistry occurring after the decomposition of the fuel. At engine relevant conditions (1–50 atm), the reactivity of alkanes increases with increasing temperature, i.e., the ignition delay time decreases.

Despite the similar high temperature behavior, octane numbers of alkanes strongly vary with their degree of branching. This is related to their complex intermediate and low temperature (< 1000 K) kinetics. At low temperatures, fuel decomposition is slower. Therefore, additions of alkyl radicals to O_2 become relevant. The fate of the RO_2 alkylperoxy radicals formed determine the intermediate and low temperature reactivity. At intermediate temperatures (800–950 K), RO_2 back-dissociates or isomerizes to hydroperoxyalkyl radicals QOOH, which mostly dissociate to olefins, ethers, or other β -scission products, resulting in a smaller heat release. On the other hand, at $T < 800$ K, additional pathways activate: QOOH radicals stabilize and a second O_2 addition and further isomerizations and β -scission reactions eventually produce OH and alkoxy radicals, thus leading to chain branching pathways. The lower heat release at intermediate temperatures results in a negative temperature coefficient (NTC) behavior (such as that shown for the n-heptane IDT curves in Scheme 1.8). Low temperature behavior of alkanes is favored by long linear chains (many secondary carbon sites, higher fractions of stabilized RO_2 and QOOH radicals, fast isomerization reactions) such as those of n-heptane, while the low temperature branching pathways are inhibited in heavily branched alkanes such as iso-octane.

The discussion on alkanes anticipates the intrinsic difference in the reactivity of aromatic hydrocarbons, introduced in Section 1.4. The resonance stabilization of the aromatic ring and the planar structure prevent the low temperature chain branching pathways or the NTC behavior observed in alkanes (e.g., see toluene and anisole IDTs in Scheme 1.8). Hence, the kinetics of the low and high temperature reactivity is similar, with H-atom abstraction reactions controlling fuel consumption, and decomposition reactions occurring generally at very high temperatures. The ignition reactivity of aromatics is therefore slower than alkanes, even at high temperatures. Another important consequence of the slower decomposition of aromatics is the increased relevance of growth pathways with respect to oxidation and decomposition, as extensively discussed in this thesis.

Because of the slow decomposition of the aromatic ring, the reactivity of substituted aromatics is largely controlled by that of the lateral substituents. For instance, in toluene ($C_6H_5CH_3$) the lateral methyl group rapidly loses an H atom to form the resonance-stabilized benzyl radical [129]. Benzyl then determines the competition between growth (via self-recombination) and oxidation (mostly via O_2 addition) pathways. In alkylated aromatics such as ethylbenzene, butylbenzene and hexylbenzene, the most reactive alkyl site is that

adjacent to the aromatic ring [161]. However, the low temperature reactivity is shifted towards $R + O_2$ due to the stability of benzyl-like structures. Low temperature branching pathways are therefore observed only for MAHs substituted with long alkyl chains (i.e., from pentyl and hexyl- substituted MAHs). When toluene is mixed with more reactive species such as n-heptane, its inhibiting effect is related to both its intrinsically slow reactivity and its role as a radical scavenger [162].

As far as oxygenated aromatics are concerned, different lateral groups may result in very different behaviors. For instance, MAHs substituted with methoxy (OCH_3) groups are more reactive than OH-substituted MAHs due to the low bond dissociation energy of $O-CH_3$, which rapidly produces phenoxy radicals [50]. In all oxygenated MAHs, the role of phenoxy and consequently of cyclopentadienyl radicals are crucial in the determination of the overall combustion behavior.

2.5 CRECK mechanism: a hierarchical kinetic scheme

The CRECK kinetic mechanism has been developed by the CRECK modeling group at Politecnico di Milano over the last ~ 40 years [46], [65], [77], [163]. The CRECK mechanism (available at <http://creckmodeling.chem.polimi.it>) is able to describe the oxidation and pyrolysis of a wide variety of fuels from hydrogen and syngas to heavy biodiesels, including oxygenated species such as alcohols, aldehydes and ethers. More recent developments also include nitrogen-based fuels. The kinetics of formation of NOx and SOx pollutants is also described.

The CRECK mechanism has a modular and hierarchical structure. It is of relatively small size compared to other literature mechanisms thanks to both its structure and the massive use of lumping methodologies. Figure 2.4 depicts the hierarchical modular structure of the CRECK mechanism. A kinetic mechanism of a specific fuel is developed on top of a "core" mechanism, which describes the combustion kinetics of the building blocks of small molecules and radicals. The core mechanism plays a key role in controlling the macroscopic combustion behavior (e.g., ignition, flame speed). In particular, the H_2-O_2 subset represented in Fig. 2.4 is necessary to represent the reactivity of any fuel. Then, the C_1 portion (CH_4 , CO) is always considered together with the C_2 , C_3 subsets, as C_2 species are easily formed from additions of C_1 species and a similar reasoning applies to the C_3 subset. The current C_0-C_4 subset of the CRECK mechanism (highlighted in red in Figure 2.4) was adapted from AramcoMech2.0 [164]. Larger aliphatic hydrocarbons such as hexane, primary reference fuels, jet and diesel fuels are all included hierarchically (lowest molecular weight or chain length is included first) on top of the lower-level modules, as illustrated in Figure 2.4. Hence, when the combustion kinetics of a larger fuel is newly introduced in the mechanism, only the first fuel decomposition and oxidation steps have to be defined, while the combustion of all its fragments is automatically accounted for by the underlying modules.

As far as aromatic hydrocarbons are concerned, the main aromatic species included in the main mechanism are benzene (C_6H_6), toluene (C_7H_8), and phenol (C_6H_5OH). Benzene is massively produced in C_2-C_3 flames, while toluene is the reference aromatic fuel in TPRF

surrogate mixtures. Phenol is instead included because of its central role in the oxidation of benzene. These species are necessary to represent correctly the ignition behavior of TPRFs. The combustion of aromatic hydrocarbons is also especially interesting due to their role in pollutants formation, namely the growth of PAHs and the formation of soot. PAH and soot formation are described in additional modules, as shown on the upper side of the "main mechanism" of Figure 2.4. Finally, the combustion behavior of OAHs such as anisole and vanillin may be included through the "phenolics and vanillin" subset depicted in Figure 2.4.

The kinetic subsets used and partially modified in this work are highlighted with dashed boxes in the scheme. The total kinetic mechanism used includes about 500 species and 18500 reactions. For kinetic simulations of high-temperature processes such as flame speciation and laminar flame speed, a smaller subset (excluding low-temperature oxidation of small species) consisting of about 300 species and 6000–11000 reactions (depending on the simulated system) was used.

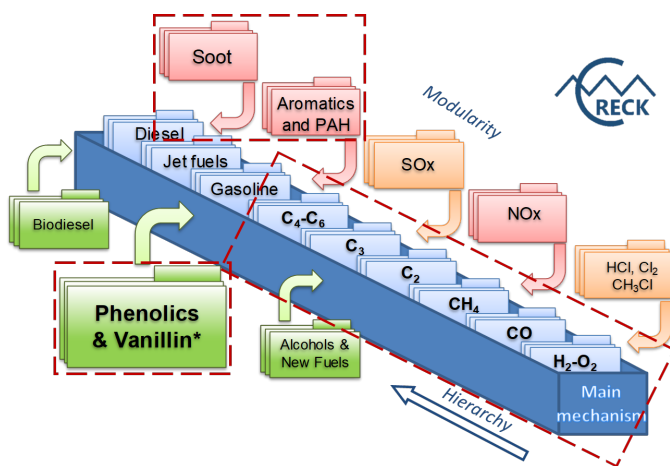


FIGURE 2.4: Schematic representation of the CRECK mechanism modular structure. Green modules refer to "unconventional" fuels while pink and orange modules describe pollutant formation. Dashed boxes highlight the modules considered and partially updated in this work.

2.6 Reaction classes and rate rules for mechanism development

2.6.1 Reaction classes

Reaction classes and rate rules have a long history in chemical kinetics [75], [165], [166]. In fact, identifying the main reaction classes and their reference kinetic parameters in the combustion mechanism of a fuel is essential for 1) complete mechanism development and 2) potential extension of the reaction subset and kinetic parameters to molecules with similar structures. Molecules "with similar structures" are species having the same reactive moieties and functional groups involved in the reaction. For instance, 1-butene and 1-pentene may both undergo C–C bond-fission ejecting C_2H_3 radical. The extension of a set of reactions to "similar" species can be performed systematically and consistently using rate rules, namely

reference kinetic parameters assigned to a reaction type and correction factors accounting for structural, energetic, and entropic effects (Section 2.6.2).

The reaction classes and rate rules approach was extensively and successfully applied to the development, refinement and optimization of the combustion mechanisms of alkanes [63], [64], [120], [122], [167], [168]. Depending on the work, about 15–30 reaction classes were identified for the description of the high and low temperature oxidation of the fuel and its primary decomposition products (i.e., fuel alkyl radical and corresponding alkene, RO_2 , QOOH and O_2QOOH radicals, cyclic ethers). Two main aspects of the reaction classification performed in these works are clarified:

1. Each **reaction class** is generally identified by the **type of species** and the **class type** corresponding to an elementary reaction. In some cases, reaction classes are also called reaction families [69]. Examples are: fuel bond-fission reactions, H-atom abstraction reactions from the fuel, H transfer reactions in alkyl radicals. Each reaction class shares a similar type of TS structure. Because of the similarity in the TS structures, it should be possible to associate each elementary reaction to a given TS search protocol in electronic structure codes [97].
2. Within each reaction class, different **reaction types** identify specific reactions associated to reference kinetic parameters which may be extended via analogy or rate rules. For instance, in the classification of Cai et al. [120] the reaction class "fuel decomposition" has three reaction types, namely bond-fission of C–H, C– CH_3 , and QC–CQ', where Q represents a generic alkyl substituent. Another illustrative example applies to the reaction class of "H-atom abstraction reactions" by a given radical according to Ranzi et al. [63]. In this case, reaction types are distinguished on the basis of the abstraction site, namely primary, secondary or tertiary.

In the literature, no such classification is available for aromatic hydrocarbons. This is due to both the lack of massive experimental and theoretical data for elementary reactions of aromatic hydrocarbons and to intrinsic differences with respect to reaction classes for linear aliphatic species, which regard:

1. The type of species: reaction classes for aliphatic hydrocarbons are generally the same for a set of hydrocarbons with different chain length and degree of branching. On the other hand, the most studied MAHs have one aromatic ring with a certain degree of substitution. The reactivity depends both on the aromatic ring(s) and on the type of substituent. Additionally, it is still unclear to which extent the reaction classes for MAHs may be applied to PAHs.
2. The complexity in the reactivity: reaction classes for the oxidation of aliphatic hydrocarbons are generally well represented by elementary reaction types, such as bond-fission, isomerization, etc. In few cases, reaction classes may incorporate multiple lumped elementary steps, such as the decomposition of OOQOOH to form keto-hydroperoxides which consists of H-transfer + O–O β -scission [63], [64]. However,

in these cases the number of lumped elementary steps is generally 2 and the extension of the reactivity of these classes is relatively simple. On the other hand, the reactivity of MAHs and PAHs is often characterized by complex multi step processes involving several intermediates. Hence, phenomenological reactions included in kinetic mechanisms are often well-skipping processes or heavily lumped rate constants, which are harder to associate to "elementary" reaction classes.

In light of these considerations, this work proposes the first hierarchical classification of the combustion reactivity for cyclopentadiene-like rings, MAHs and 2-ring PAHs. The rationale for the definition of reaction classes mostly follows that used for aliphatic hydrocarbons, with intrinsic differences related to the type of species and reactions considered. Each class is characterized by both the species type and the class type:

1. The **species type** corresponds to the reactivity of a specific **functional group** rather than multiple sites on the same species (e.g., in aliphatic hydrocarbons the reactivity of primary, secondary, and tertiary carbon sites is all classified within the same class). The notation used for species naming A-B reflects the nature of the functional group reacting (A) and the radical character of the species (-B). Values for suffix -B may be -M, -R, and -RSR indicating a molecule, a radical, and a resonantly-stabilized radical, respectively. For instance, **[A1-M]** indicates the reactivity of the sites of the benzene aromatic ring, may it be substituted or not, while **[A1,X-M]** indicates the reactivity of the X substituent in a MAH, e.g., OH in phenol, catechol, guaiacol. The comma in A1,OH reflects the fact that the reactivity of A1 (unsubstituted ring sites) is already accounted for in a class at a "lower" level. Instead, A1-R and A1O-RSR indicate the reactivity of a phenyl-like and a phenoxy-like radical, respectively. In this case, A1O is not written as A1,O because its reactivity is intrinsically different from that of A1-R, including that of the aromatic ring.
2. Each **class type** mostly defines a **global reaction pathway**, possibly including different reaction channels. The reaction class is therefore defined as [species type][class type]. Within each reaction class, the **reaction type** identifies a single reaction pathway, which may be an elementary step or a lumped pathway, with given reference kinetic parameters. For cases such as for bond-fission and H-atom abstraction reactions the reaction types are similar to those defined for aliphatic hydrocarbons. However, the classification of most of the decomposition and oxidation reactivity differs substantially. For instance, the reaction class [A1-M][ADD_O] includes the reaction channels accessed from the addition of atomic oxygen to an unsubstituted site of the aromatic ring. Within this class, reaction types are intersystem crossing, and intersystem crossing + molecular decomposition, which both include multiple elementary steps (e.g., addition, intersystem crossing, ring opening, H transfer, CO elimination).

Figure 2.5 presents a simplified example of the reaction class organization performed for benzene, phenol, and catechol. In benzene, the species type is always A1-M. Reaction types exemplifying a few of the reactions are identified and are thoroughly listed in Section 6.2.

The same reaction classes are also present in phenol and catechol - and are named in the same way. The rate constants of these classes in phenol and catechol will be rescaled based on analogy or rate rules (see Section 2.6.2), e.g., the reference rate constant of benzene is multiplied by 5/6 in phenol to account for the different number of aromatic ring sites.

Reaction classes for [A1,OH-M] instead describe the reactivity of OH functional group on an aromatic ring such as in phenol. Therefore, in this case the [A1,OH-M][BONDFISSION] class only includes bond-fission reactions of the C–O and O–H bonds. The [A1,OH-M][DECO] class includes for instance the molecular decomposition, only possible in the presence of an OH substituent (Section 6.3.2). Instead, the [A1,OH-M][HABS] class contains the H-atom abstraction reactions from the hydroxy substituent. Finally, the [A1,OH-M][IPSO] reaction class includes ipso addition-elimination reactions where the OH group is replaced by a given radical. Also in this case, all the reference rate constants for each reaction type are extended to catechol.

The reactivity of catechol is almost completely described by the reaction classes of [A1-M] and [A1,OH-M] species types. Hence, the only additional reactivity in this case will be specific to the simultaneous presence of 2 adjacent OH substituents, such as the concerted molecular decomposition involving H-transfer from each of the OH groups [A1,OH,OH-M][DECO] [134].

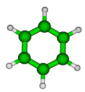
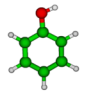
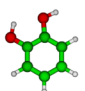
SPECIES	[A1-M][CLASS TYPE][REACTION TYPE]	[A1,OH-M][CLASS TYPE][REACTION TYPE]	[A1,OH,OH-M][CLASS TYPE][REACTION TYPE]
	[A1-M][BONDFISSION][BONDFISS_CH] [A1-M][HABS][HABS_H],[HABS_OH]... [A1-M][ADD_O][ISC,ISC_DECO] [A1-M][ADD_O2][ADD_O2_ROPEN]		
	Same as above	[A1,OH-M][BONDFISSION][BONDFISS_CO/OH] [A1,OH-M][DECO][MOLEC_DECO],[EL_H2O] [A1,OH-M][HABS][HABS_H],[HABS_OH] [A1,OH-M][IPSO][IPSO_H],[IPSO_O]	
	Same as above	Same as above	[A1,OH,OH-M][DECO][MOLEC_DECO],[EL_H2O]

FIGURE 2.5: Example of hierarchical organization of the MAH kinetics according to reaction classes (highlighted in bold).

Finally, the relation between elementary steps studied theoretically, reaction types and class types is clarified. In this work, computational chemistry methodologies are employed for the determination of rate constants of elementary steps which may be interconnected on complex multi-well potential energy surfaces (PESs, see Section 3.3.1). Each elementary step may be studied with different theoretical methodologies according to the elementary reaction type, such as H-atom abstraction, H transfer, addition or β -scission, recombination or bond-fission, ring opening, concerted elimination, and to the type of species. The (global) reaction types described in this work may include multiple elementary steps. The names of reaction types provide general information on both the steps of the reaction and the reactants and/or products. For instance, IPSO_H indicates the addition-elimination reaction with H atom, which occurs via two consecutive β -scission steps. On the other hand, class types are broader and generally include multiple reaction types. For instance, [ADD_O] refers

to additions or recombinations with atomic oxygen, and provides no information on the formation of products. [ADD_O] includes several reaction types, such as [ADD_O_ISC] and [ADD_O_ISC_DECO], which describe the reaction pathways for intersystem crossing and the following molecular decomposition (theoretical calculations in Section 6.3.1). In few cases, the class type does correspond to the elementary reaction type, such as for bond-fission or H-atom abstraction reactions.

A complete list of reaction classes identified in this work is presented in Section 5.2 for the sub-mechanism of C5-ring species and in Section 6.2 for MAHs.

2.6.2 Analogy and rate rules

Reaction classification allows one to adopt the reference rate constants of a class for analogous reactions of similar compounds within the same class. Similar compounds in the case of aromatic hydrocarbons may be aromatics with the same functional groups but a larger number of rings, or multi-substituted MAHs. Rate rules define reference kinetic parameters of a class and rules to apply them to similar compounds. For instance, the Evans Polanyi (EP) relationship [169] allows one to derive energy barriers of H-atom abstraction reactions by different radicals from a given abstraction site (i.e., the species type identified in this work) from the reaction enthalpy. Hence, this rule applies to the rate constants of class [SPECIES TYPE][HABS] (see Figure 2.5).

The reference rate constant of a given reaction class/type may be extended according to different approaches, as summarized in recent reviews [165], [166], [170]. While the first rate rules for combustion kinetics were based on empirical observations or group additivity [76], [169], the recent increase in systematic theoretical investigations led to electronic structure (ES) based rate rules [171]. It is highlighted that the performance of rate rules strongly depends on the reaction class and on the level of detail of the classification, hence considerations on a specific class cannot generally be applied to other reaction classes. The performance of rate rule approaches is considered good when the derived rate constants are within a factor of 2 from e.g., a theoretical estimate at the same level of theory used for the rate rule derivation. In many cases, such as for H-atom abstraction reactions, discrepancies can be smaller (e.g., factor of 1.5 [171]).

Since the modified Arrhenius expression (Eqn. (2.3)) is the most common fitting type found in kinetic mechanisms, rate rules are generally developed in terms of corrections to the pre-exponential factor k_0 or the activation energy E_A . The temperature dependence described by T^n in the modified Arrhenius expression is instead generally taken as the average of a reference set and kept fixed for each class [165].

Several relations are available for the derivation of the energy barriers. For instance, the Evans Polanyi (EP) relationship [169] or the linear free energy relationship (LFER) [172], [173] relate the change in the energy barrier to the enthalpy of the reaction and to that of the transition state, respectively. Correction factors for both k_0 and E_A may instead be derived from structural considerations. For instance, Wang and Dean [166] carefully listed the main reaction classes and ES based rate rules for the combustion of linear alkanes and alkenes. Strain effects on the TS structures are key to determine reference parameters for

each class. For instance, rate rules for H-migrations are based on the size of the ring-like TS structure. In this work, ring-strain effects are not considered because only small substituents are treated, such as OH, CH₃, OCH₃.

A more detailed ES-based procedure is the reaction class approach RC-TST/SAR (Reaction Class-TST/Structure Activity Relationship) developed by Truong et al. [170], [174]. RC-TST/SAR proposes detailed corrections both for k_0 and E_A based on partition function contributions. Despite the generally good performances, this approach requires a significant amount of theoretical calculations and its accuracy is strongly dependent on reliable estimates for the energy barriers [170]. RC-TST is very effective for H-atom abstraction reactions, however the error increases significantly for β -scission reactions [170] and O addition reactions to PAHs [175]. Another common methodology is the extension of Benson's group additivity (GA) approach [76] to determine the properties of transition states [176]–[178]. GA is based on the assumption that molecules consist of independent functional groups able to fully characterize their chemical properties. GA approaches mostly fail for the extension of rate constants to similar compounds with multiple substituents (e.g., from phenol to catechol) because they generally consider independent functional groups or only nearest-neighbor interactions. This may result in large errors also in the case of significant steric effects [179]. The only GA work for MAHs including non-nearest neighbor interactions aimed only at deriving thermodynamic properties [180]–[182].

Most rate rule approaches were successfully applied to H-atom abstraction reactions [71], [165], [175]–[178], [183]–[186]. The most successful example of ES-based rate rules is probably the work of Carstensen and Dean [165], who developed rate rules for H-atom abstractions by H from primary, secondary and tertiary C-H groups in linear and branched alkanes, and from allylic groups in alkenes. In this case, averaging the Arrhenius parameters resulted in a satisfactory performance of the rules obtained, however this approach was not applied to any other reaction classes.

Only a few studies have focused on the rate constants for β -scissions and carbon-centered radical addition reactions [187]–[190]. In these cases, the application of neither RC-TST nor GA was as successful as for H-atom abstraction reactions. Finally, the only set of rate rules for H-addition to unsaturated hydrocarbons was determined with GA by Sabbe et al. [179]. The results of the truncated GA method were satisfactory, in spite of discrepancies up to a factor of 3.5 in the presence of large steric effects.

As for pressure dependence, only recent works started focusing on the development of ES-based pressure-dependent rate rules. For instance, Yao et al. [191], [192] and Sun et al. [193] considered pressure-dependent rate rules for H-migration reactions in peroxy radicals (i.e., hydroperoxyalkylperoxy [191], normal-alkyl cyclohexylperoxy [192], and alkenyl peroxy [193] radicals), which show significant pressure dependence. However, also in this case, similar to what is generally done in the case of high-pressure limit rate constants, rate rules were built simply by averaging the kinetic parameters for a set of reference reactions in each class, but parametrically, at different pressures. Despite the observations of Yao et al. [191], who noticed that pressure dependence decreases with increasing molecular size, this piece of information was not included in the derivation of rate rules.

In this work, reference kinetic parameters for some of the relevant reaction classes identified were determined with high-level theoretical calculations, as extensively described in Sections 5.3 and 6.3. For other reaction classes, estimates from the current version of the CRECK mechanism or other literature values were adopted. A full list of the kinetic mechanism updates and the corresponding sources are provided in Sections 5.2 and 6.2.

The extension of the reference kinetic parameters calculated in this work for reference reactions were extended to similar compounds by analogy and rate rules, as explained below. Model alignment for other relevant reaction classes was also attempted, sometimes with heavier approximations (e.g., the same rate constants were adopted for all species with similar chemical functionality).

The extension of reference kinetic parameters to similar compounds can be performed according to the following methods:

- **Analogy rules:** analogy rules refer to the simplest extension of reference kinetic parameters by structural considerations which share similar assumptions to common GA approaches. In particular, reference kinetic parameters of a reaction class are adopted for all the compounds sharing the same reactive functional groups. The reference kinetic parameters are simply scaled according to symmetry and structural considerations. For instance, Figure 2.6 represents the extension of the rate constant for the H-atom abstraction by H from the benzene ring [A1-M][HABS] to the phenol, naphthol, and catechol rings via analogy rules. The reference rate constant for benzene is rescaled by the number of abstraction sites (i.e., the H atoms bonded to the aromatic ring). This scaling can also be explained by considerations on the symmetry number of the TSs and reactants for the abstractions from each site.
- **ES-based rate rules:** systematic theoretical investigations were performed for H-atom abstraction reactions from both the aromatic ring and some lateral substituents such as OH, CH₃, OCH₃ (Section 6.4). The large number of theoretical calculations resulted in the derivation of ES-based rate rules and the formulation of Evans-Polanyi relations (Section 6.4.4), which allowed for the verification of the consistency of rate constants within each class. Additionally, systematic calculations for H ipso addition-elimination reactions on MAHs established reference rate constants for a large set of reaction classes ([A1,X-M][IPSO], with X = OH, CH₃, OCH₃, HCO, C₂H₅, Section 6.5). In this case, corrections for both pre-exponential factors and activation energies were derived to account for the presence of multiple substituents on the aromatic ring, showing that in some cases correction factors for the energy barriers may also be extended to different reaction classes (Section 6.5.2.4). Figure 2.6 exemplifies rate-rule derivation of the kinetic parameters of the H-atom abstraction reactions from the hydroxy group [A1,OH-M][HABS] in phenol to that of naphthol and catechol. For both naphthol and catechol, an EP relationship may be used (Sections 6.4.4 and 6.4.5). In catechol, it is also possible to extend the systematic trends observed in the reaction class of ipso addition-elimination reactions to derive the energy correction. The bottom of

Figure 2.6 shows the ES-based rate rule derived for the reaction class [A1,OH-M][IPSO] to account for the presence of the second hydroxy substituent (Section 6.5.3).

- **TS energy corrections** for specific reaction types within a class: electronic energies obtained with theoretical calculations at a relatively low level of theory are corrected according to scaling factors derived for analogue TSs (generally for the same reaction computed on smaller species) treated at a higher level of theory. For instance, in this work a few H-atom abstraction reactions or H ipso addition-elimination reactions for 2-ring PAHs or multi-substituted MAHs were calculated. In many cases, calculating high-level energies was too computationally demanding. Hence, the energy barriers were determined at a lower level of theory and corrected according to $\Delta E_{\text{HL}} - \Delta E_{\text{L1}}$ of the corresponding 1-ring MAH, where HL and L1 refer to the higher and lower levels of theory, respectively. For instance, Figure 2.6 shows the derivation of the energy barrier of the H-atom abstraction reactions from naphthol hydroxy group from that of phenol. Clearly, this correction requires low-level theoretical calculations for the system of interest and both high-level and low-level theoretical calculations for the reference system. Hence, while more computationally expensive, the resulting rate constant are expected to have much higher accuracy than those derived via analogy or rate rules (see Sections 6.5.3.1, 6.5.3.2, and 6.5.3.3).

For some reactions in this work, other approximations were employed, e.g., see Section 5.3.3.2.

Finally, it is noted that this work provides insights into rate rule extensions from MAHs to PAHs. In the CRECK kinetic mechanism, the same rate constants are applied to all gas-phase PAHs, especially for growth reactions. However, preliminary investigations of this work assessed that such extension might be inaccurate even for 2-ring PAHs (Section 6.4.5). Additional uncertainty is related to the increasing radical character of PAH molecules with increasing ring size [58].

It should be mentioned that when scaling rate constants to larger PAHs, also pressure dependence may change. The investigation of this aspect is indeed interesting but premature, considering for instance that most of the growth reactions involving PAHs are lumped and pressure-independent in several kinetic mechanisms, including the CRECK mechanism considered in this work.

2.7 Kinetic simulations

Kinetic mechanisms are tested by simulating the chemical evolution (as a function of time, reactor length, temperature ...) of a system at given operating conditions, monitoring its physico-chemical properties such as temperature, pressure, density, velocity, and species concentrations.

Kinetic simulations require the solution of coupled mass, energy, and momentum balances. The initial mixture generally consists of fuel or surrogate molecules at pyrolysis or

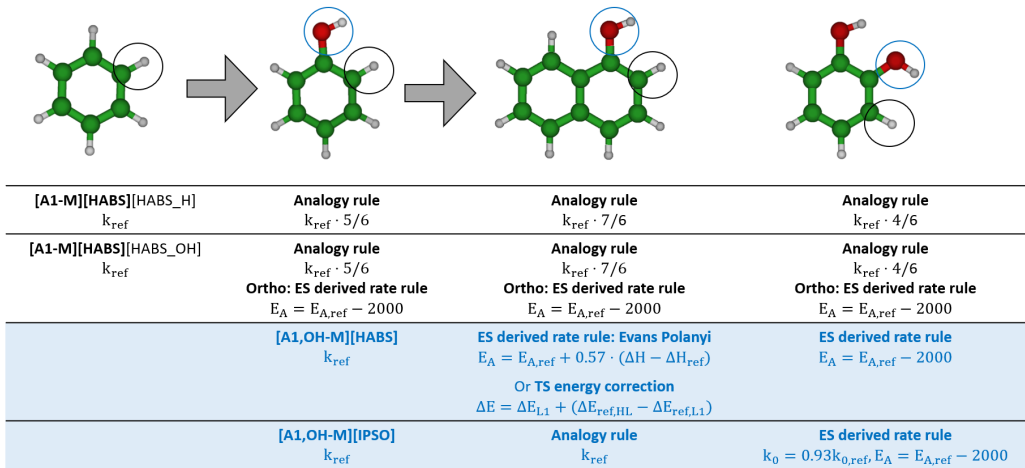


FIGURE 2.6: Schematic representation of rate extension via analogy and rate rules from benzene to phenol, naphthol and catechol. See the text for details.

combustion-relevant conditions, which typically vary with the fuel. For instance, the pyrolysis of benzene and phenol is active starting from about 1000-1200 K at atmospheric pressure, while the decomposition of other MAHs such as anisole and guaiacol already occurs around 800 K. The combustion chemistry of a fuel is ideally analyzed in a wide range of temperature T , pressure p , and equivalence ratio Φ , i.e., the fuel/oxygen ratio with respect to that at stoichiometric conditions. physico-chemical properties are monitored in ideal or real reactors such as jet stirred reactors (JSR) or plug flow reactors (PFR) and compared to experimental data obtained at the same operating conditions conditions. The performance of the kinetic mechanism is evaluated on the basis of such comparisons.

In this work, kinetic simulations were performed with the open-source software OpenSMOKE++ [82]. OpenSMOKE++ Suite (written in C++) is specifically built to perform numerical simulations of combustion processes in various reactor types using large kinetic mechanisms. Figure 2.7 illustrates the main steps of the kinetic simulations procedure. First, the different portions of the CRECK modular kinetic scheme are joined together through TailorSMOKE obtaining a single kinetic file in CHEMKIN format [80]. Then, the kinetic mechanism is compiled by processing the information of the kinetic, thermochemistry, and transport property files obtaining a single XML file used by reactor solvers. The compiled kinetic mechanism is read together with the input of a kinetic simulation which specifies the reactor type, fuel, and operating conditions. Then, OpenSMOKE++ solves complex ODE and DAE systems and provides simulation results in both ASCII and XML formats. The latter may be post-processed with the graphical OpenSMOKE++ post-processor to plot output profiles or read the results of performance analysis.

Table 2.1 lists the available OpenSMOKE++ reactor types used for the kinetic simulations of this work, together with the macroscopic quantities of interest of the corresponding outputs. All OpenSMOKE++ solvers rely on the same set of libraries but are called independently. Depending on the type of simulation, the user may need additional input

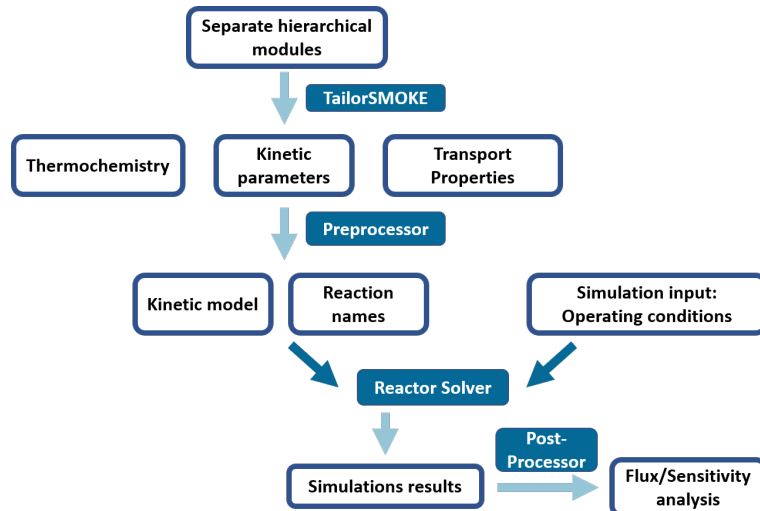


FIGURE 2.7: Schematic workflow of OpenSMOKE++ kinetic simulation procedure.

to reproduce correctly some experimental conditions of interest. For instance, when simulating rapid compression machine (RCM) experiments, the experimental volume or pressure traces are required, while in premixed flame simulations the input must list the experimental temperature profile. The full list of options is provided in the user guide at <https://github.com/acuoci/OpenSMOKEppTutorials>, while the numerical details of the solvers are reported in the corresponding publication [82].

TABLE 2.1: List of available OpenSMOKE++ reactor solvers and modes used in this work and corresponding macroscopic quantities of interests.

Reactor Type in OpenSMOKE	Mode	Macroscopic quantity
Batch	Isothermal, Non-isothermal/Adiabatic	Species concentration
	Non-Isothermal, ConstantVolume	ignition delay time (ST)
	Non-Isothermal, User-defined Volume	ignition delay time (RCM)
Plug Flow	Isothermal, Non-isothermal, T Profile	Species concentration
Jet Stirred	Isothermal, Non-isothermal	Species concentration
Laminar flame	Premixed laminar flame	Species concentration
	Flame speed	Laminar flame speed
Counterflow flame	Counterflow diffusion flame	Species concentration

OpenSMOKE++ also provides useful tools for kinetic analysis. In particular, flux or rate of production analysis (ROPA) and sensitivity analysis (SA) highlight relevant reaction pathways to the production and consumption of a species of interest and therefore guide rate constant calculations for potential model improvement.

ROPA is used to determine the contribution of a reaction to the production or consumption of a species. Normalized production F_{Ij}^p and consumption F_{Ij}^c terms for a species I participating in reaction j according to the net stoichiometric coefficient $\nu_{Ij} = \nu_{Ij}^{fw} - \nu_{Ij}^{bw}$ (where fw and bw stand for forward and backward directions) are derived as

$$F_{Ij}^p = \frac{\max(\nu_{Ij}, 0) \cdot r_j}{\sum_{k=1}^{NR} (\max(\nu_{Ik}, 0) \cdot r_k)} \quad F_{Ij}^c = \frac{\min(\nu_{Ij}, 0) \cdot r_j}{\sum_{k=1}^{NR} (\min(\nu_{Ik}, 0) \cdot r_k)} \quad (2.11)$$

where NR is the total number of reactions and r_j indicates the local reaction rate of reaction

j. In this work, most of the ROPA are performed globally, namely they are integrated over the main reactor coordinate, e.g., reactor length or time.

A flux analysis provides information about the direct effect of a given reaction on the selected species. However, the kinetic mechanism constitutes a complex reaction network where all reactions and species are interdependent. As a consequence, flux analysis might not be enough to gain insight into the main reactions affecting mechanism performance. For instance, the reactivity of C₀–C₃ species (described in the core mechanism, see Section 2.5) dramatically affects the high temperature reactivity of large species, including aromatic fuels. In fact, high-temperature combustion mostly occurs via pyrolysis followed by oxidation of smaller fragments. Sensitivity analysis (SA) is able to quantitatively assess the impact of any reaction in the model on the production and consumption of a species. This requires one to consider the full system of differential equations. Defining \mathbf{y} as the dependent variables, ξ as the integration variable and α as the set of kinetic parameters, the ODE system is described as

$$\frac{d\mathbf{y}}{d\xi} = \mathbf{f}(\mathbf{y}, \xi; \alpha) \quad (2.12)$$

and the first-order local sensitivity coefficients are

$$s_{I,j} = \frac{\partial y_I}{\partial \alpha_j} \quad (2.13)$$

where y_I is the parameter (e.g., concentration of species I) and α_j is the variable considered (e.g., pre-exponential factor k_0 of a reaction). The raw sensitivity coefficients are normalized in the form of logarithmic derivatives for direct use in model performance analysis and may also be integrated to obtain global sensitivity coefficients.

Equation (2.13) highlights the potentially high computational cost of sensitivity analysis: for instance, performing local SA for three species in a kinetic mechanism of 30000 reactions would add $3 \times 3 \times 30000 = 270000$ equations to the system, assuming that each reaction only includes the three parameters of a single modified Arrhenius expression. OpenSMOKE++ simplifies this problem by first solving the model equations and then using the solution in a set of independent sensitivity equations equal to the number of α parameters of the kinetic model, as described in detail in [82].

Finally, the reactions identified through either flux or sensitivity analysis may be further grouped together to highlight trends in the reactivity. Following the definition of the main reaction classes for MAHs according to the criteria described in Section 2.6, the reactions may be grouped according to species type, class type, reaction type, or multiple criteria identified hierarchically. A simple Python post-processor was written to generate heat maps highlighting the main reaction classes contributing to the production and consumption of species. For each identified species, the flux analysis was normalized with respect to the largest flux in absolute value. The comparison of such heat maps at different conditions and for different species provides a global synoptic view of reactivity trends. This simplifies the identification of important reaction classes and potentially missing classes for certain species.

The post-processor is available at https://github.com/lpratalimaffei/OpenSmoke_RXN_CLASS.

Chapter 3

Computational chemistry

This chapter provides an overview of the computational methodologies adopted in this work for the theoretical calculation of kinetic parameters.

Section 3.1 focuses on electronic structure calculations, used to determine molecular structures, vibrational frequencies, and electronic energies. Basic concepts of Hartree-Fock (HF) and self consistent field (SCF) theories and the basis set approximation are illustrated in Section 3.1.1 and 3.1.2. Then, electron correlation methodologies used for accurate estimates of electronic energies are summarized in Section 3.1.3. Finally, density functional theory (DFT, used for most structure optimizations of this work) is described in Section 3.1.4.

The quantities derived with ES methodologies are used to determine partition functions (PFs). Molecular partition functions are described in Section 3.2.1. The treatment of intramolecular motions according to the harmonic oscillator approximation and other theories is discussed in Section 3.2.2. Finally, the derivation of thermochemical properties from partition functions is presented in Section 3.2.3.

Partition functions are also at the core of theoretical kinetics, discussed in Section 3.3. First, the concept of the potential energy surface (PES) is introduced (Section 3.3.1). Transition state theories for the calculation of pressure-independent rate constants are described in Section 3.3.2, including both canonical and microcanonical theories, while the treatment of pressure-dependent rate constants with master equation (ME) simulations is discussed in Section 3.3.4. This last section also clarifies the connection between the results of theoretical kinetics and phenomenological rate constants used in kinetic models (Section 3.3.4.3).

Theoretical calculations of this work were performed with semi-automated codes, namely EStokTP and Auto-Mech, whose workflows are briefly described in Section 3.4.

The application of the theoretical methodologies presented in this chapter is discussed in Section 3.5, focusing on computational cost (Section 3.5.1) and on the sources of uncertainty in the present theoretical calculations (Section 3.5.2). Section 3.5.3 summarizes the selected methodologies for the theoretical calculations of this work, discussed more extensively in Section 5.3, 6.3, 6.4, and 6.5.

3.1 Electronic structure calculations

Ab initio electronic structure (ES) calculations allow one to describe the electronic structure of a system *a priori*, namely without the aid of experimental data. The "system" is composed of N_e identical charged particles (the electrons) identified by electronic spatial coordinates and spin $\mathbf{x} = (\mathbf{r}, \boldsymbol{\omega})$ in a field of N_n fixed classical charges (the nuclei) identified by spatial nuclear coordinates \mathbf{R} . The electronic structure of the system is described through the Schrödinger equation, here considered in its time independent (stationary) form:

$$\mathbf{H}\Psi = E\Psi \quad (3.1)$$

where E is the total energy, \mathbf{H} is the Hamiltonian operator and Ψ is the wavefunction. The first postulate of quantum mechanics states that the physical state of a system is completely described by its wavefunction. Ψ^2 (at least for a real wavefunction) relates to the probability to find a particle in the phase space where the wavefunction is defined.

The Hamiltonian operator contains the contribution from the kinetic energy \mathbf{T} of the electrons and nuclei and the potential energy \mathbf{V} associated with the interaction between the particles:

$$\mathbf{H} = \mathbf{T}_n(\mathbf{R}) + \mathbf{T}_e(\mathbf{r}) + \mathbf{V}_{ne}(\mathbf{r}, \mathbf{R}) + \mathbf{V}_{ee}(\mathbf{r}) + \mathbf{V}_{nn}(\mathbf{R}) \quad (3.2)$$

The expansion of each term of the Hamiltonian leads to the following:

$$\begin{aligned} \mathbf{H} = & \sum_{I=1}^{N_n} -\frac{\hbar^2}{2M_I} \nabla_I^2 + \sum_{i=1}^{N_e} -\frac{\hbar^2}{2m} \nabla_i^2 + \sum_{i,I=1}^{N_e, N_n} -\frac{e^2 Z_I}{4\pi\epsilon_0 |\mathbf{R}_I - \mathbf{r}_i|} \\ & + \sum_{i<j}^{N_e} \frac{e^2}{4\pi\epsilon_0 |\mathbf{r}_i - \mathbf{r}_j|} + \sum_{I<J}^{N_n} \frac{e^2 Z_I Z_J}{4\pi\epsilon_0 |\mathbf{R}_I - \mathbf{R}_J|} \end{aligned} \quad (3.3)$$

where m , M are the mass of the electrons and nuclei, respectively; Z_I is the nuclear atomic mass number; indices i, j and I, J run over the electrons and nuclei, respectively.

The solution of the stationary Schrödinger equation is usually restricted to a single electronic surface according to the adiabatic approximation. Within the adiabatic approximation, the Born-Oppenheimer approximation allows one to decouple nuclear and electronic wavefunctions. In fact, nuclei are heavier than electrons (about 4 orders of magnitude), hence they move slowly. As a result, the electronic wavefunction is invariant with \mathbf{T}_n , and \mathbf{V}_{nn} may be considered constant.

The decoupled electronic and nuclear Schrödinger equations are:

$$\mathbf{H}_e \Psi_e(\mathbf{x}; \mathbf{R}) = (\mathbf{T}_e + \mathbf{V}_{ne} + \mathbf{V}_{ee}) \Psi_e = E_e \Psi_e(\mathbf{x}; \mathbf{R}) \quad (3.4)$$

$$\mathbf{H}_n \Psi_n(\mathbf{R}) = (\mathbf{T}_n + \mathbf{V}_{nn} + E_e) \Psi_n = E \Psi_n(\mathbf{R}) \quad (3.5)$$

In this picture, the electrons move in a field of fixed nuclei, while the nuclei move in a potential $\mathbf{V}_{nn} + E_e$, where E_e is calculated from the solution to the electronic Schrödinger equation (3.4). Finally, the total energy E in Eqn. (3.5) includes the electronic, vibrational, rotational, and translational energy.

Electronic structure calculations deal with the solution of Eqn. (3.4). The exact solution is only possible for one electron systems, while the theories discussed here propose approximate solutions to systems with many electrons. On the other hand, the solution of Eqn. (3.5) allows one to determine the energy levels for vibrations and rotations and therefore to determine molecular partition functions (see Section 3.2).

3.1.1 Self-consistent field and Hartree-Fock theory

Hartree-Fock theory was one of the first methodologies proposed to approximate the solution of the electronic Schrödinger equation. In some of the theoretical calculations of this work, HF is employed to generate a reasonable guess wavefunction for more accurate methodologies such as coupled cluster (CC) (see Sections 3.1.3.2 and 3.1.3.3).

Hartree-Fock theory relies on the mean field approximation, which describes each electron in a potential (mean) field generated by all the other electrons. The two-electron operator \mathbf{V}_{ee} in Eqn. (3.4) is therefore assumed constant, allowing to consider independent (and easier to solve) N_e one-electron wavefunctions. The total electronic wavefunction Ψ_e is written as a combination of N spin-orbitals $\chi_i(\mathbf{x}_i)$. The form of this combination is constrained by the condition that upon switching two electrons, Ψ_e must 1) yield the same probability density (because electrons are indistinguishable), and 2) be anti-symmetric (Pauli exclusion principle). Ψ_e thus takes the form of a Slater determinant (SD):

$$\Psi_e = \frac{1}{\sqrt{N!}} \begin{vmatrix} \chi_1(\mathbf{x}_1) & \chi_2(\mathbf{x}_1) & \cdots & \chi_N(\mathbf{x}_1) \\ \chi_1(\mathbf{x}_2) & \chi_2(\mathbf{x}_2) & \cdots & \chi_N(\mathbf{x}_2) \\ \vdots & \vdots & \ddots & \vdots \\ \chi_1(\mathbf{x}_{N_e}) & \chi_2(\mathbf{x}_{N_e}) & \cdots & \chi_N(\mathbf{x}_{N_e}) \end{vmatrix} \quad (3.6)$$

The Hartree-Fock equations are derived from this formulation using the variational principle, which states that the ground-state configuration of the system minimizes its energy. Hence, any trial wavefunction approximating the exact solution will yield a higher energy. E_e of Eqn. (3.4) is therefore minimized with respect to each spin-orbital $\chi_i(\mathbf{x}_i)$. The minimization can be performed with the Lagrange multipliers method: the energy variation δE_e with respect to $\delta \chi_i$ is constrained with the orthonormality of the varied spin-orbital ($\chi + \delta \chi_i$). N_e Fock equations are thus derived:

$$f(i)\chi_a(\mathbf{x}_i) = \left[h_0(i) + \sum_{b=1}^N (J_b(i) - K_b(i)) \right] \chi_a(\mathbf{x}_i) = \epsilon_a \chi_a(\mathbf{x}_i) \quad (3.7)$$

The Fock operator $f(i)$ includes the one-body term $h_0(i)$ (motion of electron i in the mean field) and two-body terms: $J_b(i)$ is the coulomb operator accounting for electrostatic interactions; $K_b(i)$ is the exchange operator accounting for the effect of switching electrons in a quantum system. a, b indicate spin-orbital indexes and are defined to highlight the distinction with electron indexes i .

HF equations constitute a strongly coupled non-linear eigenvalue problem: all the equations are coupled through $J_b(i), K_b(i)$; additionally, the Fock operator is described through

the orbitals themselves, which however can only be found by solving the eigenvalue problem. The solution procedure is therefore iterative, and it is called “self consistent field” (SCF) because the spin-orbitals obtained are consistent with the electric field they produce.

The resulting spin-orbitals χ_a are constituted by a spatial ψ_a and a spin ω_i part. ψ_a physically corresponds to the molecular orbitals where electrons are allocated. “Unrestricted” HF procedures determine N_e spatial orbitals. Instead, “Restricted” HF procedures assume that all orbitals are doubly occupied, and therefore determine only $N_e/2$ spatial orbitals. Since HF equations derive from a single Slater determinant, they only describe a single electronic state, i.e., the ground state.

3.1.2 Basis set approximation

The molecular orbitals ψ_a are conveniently expressed in terms of known functions which are 1) physically meaningful (i.e., the probability to find an electron should asymptotically go to zero at large distances from a nuclei) and 2) easily integrated. Therefore, ψ_a are expanded as a linear combination of atomic orbitals (LCAO):

$$\psi_a(\mathbf{r}_i) = \sum_{\lambda=1}^{N_\lambda} (c_{\lambda a} \phi_\lambda(\mathbf{r}_i)) \quad (3.8)$$

where ϕ_λ are the atomic orbitals and $c_{\lambda a}$ are the coefficients of the combination. Substituting Eqn. (3.8) into (3.7) and integrating over ϕ_λ results in N_λ “Roothan-Hall” equations:

$$\sum_{\lambda=1}^{N_\lambda} (F_{\nu\lambda} c_{\lambda j}) = \epsilon_j \sum_{\mu=1}^{N_\mu} (S_{\sigma\mu} c_{\mu j}) \quad (3.9)$$

where $F_{\nu\lambda}$ is the Fock matrix $\int d\mathbf{r}_i \phi_\nu^*(\mathbf{r}_i) f(i) \phi_\lambda(\mathbf{r}_i)$, and $S_{\sigma\mu}$ is the overlap matrix $\int d\mathbf{r}_i \phi_\sigma^*(\mathbf{r}_i) \phi_\mu(\mathbf{r}_i)$, unitary if the AOs are orthonormal, and the indexes $\lambda\nu\mu\sigma$ refer to AOs. The N_e molecular orbitals with the lowest energy are occupied (those appearing in the SD of Eqn. (3.6)), while the remaining $N_\lambda - N_e$ MOs are virtual.

The LCAO expansion of MOs can be seen as a change of basis from spatial coordinates of electrons to atomic orbitals, which can therefore be regarded as basis functions. Every AO is represented by one or more functions, and the complete set of functions is called a basis set. The accuracy of the basis set is essential to produce accurate MOs. In principle, an infinite number of AOs yields exact MOs and is thus called the *complete basis set limit* (CBS). The number of AOs is clearly limited by computational cost, which scales with N_λ^4 for HF methods.

Gaussian-type orbitals (GTOs) are commonly used for their computational efficiency and easy integration. Each AO is described as a contraction of N_G Gaussian functions:

$$\phi_\lambda = \sum_{i=1}^{N_G} d_{\lambda i} g_{\lambda i}(u_{\lambda i}) \quad (3.10)$$

where $d_{\lambda i}$ are the coefficients of the contraction and $g_{\lambda i}$ are Gaussian functions with exponents $u_{\lambda i}$. Contraction coefficients and exponents are fitted semi-empirically to selected properties

(e.g., the energy). Core orbitals require a larger number of Gaussian functions to describe the region in the vicinity of the nucleus, while valence orbitals often require representation of long-range interactions as they participate in chemical reactions. Hence, the number and type of basis functions is often split according to the distance from the nucleus. Such basis sets are called “split valence”. For instance, a double zeta (DZ) basis set doubles the number of valence orbitals. Improvements in the description of bonds may be achieved by adding polarization and diffuse functions. The former add to an AO functions of different orbitals characterized by a higher angular momentum to generate a polar component in the electron density: for instance, p functions can be added to s orbitals. The latter are slowly-decaying functions generally relevant in the description of chemical reactions. The resulting basis sets are often called “augmented”. Finally, the description of core electrons and their interaction with valence electrons can be improved with tight functions (large exponents), generally indicated with a C.

While using an infinite basis set is computationally impossible, several extrapolation procedures combining different basis sets and levels of theory allow one to approach the CBS limit. These procedures exploit the systematic improvement of the predicted energies with increasing basis set, which is particularly effective in correlation consistent basis sets, as well as the fixing of different sources of errors in HF theory (see Section 3.1.3).

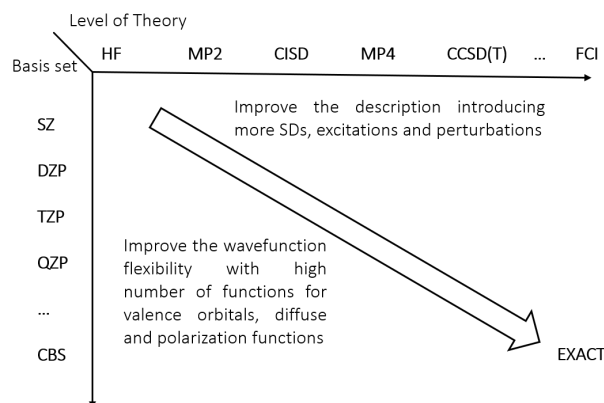


FIGURE 3.1: Qualitative representation of the systematic convergence to the exact multi-electron wavefunction improving the basis set size and the level of theory.

In this work, two main types of basis sets were used, i.e., correlation consistent basis sets and Pople style basis sets. Correlation-consistent (cc) basis sets introduce at the same stage different functions contributing to the correlation energy (see Section 3.1.3) and are considered particularly suitable to describe chemical reactions. cc basis sets used in this work include cc-pVDZ, cc-pVTZ, cc-pVQZ, cc-pCVTZ, cc-pCVQZ, aug-cc-pVTZ. In these acronyms, p indicates polarization functions, C indicates augmented core functions, aug the diffuse function augmentations for valence electrons, and VXZ the type of valence splitting. A basis set extrapolation scheme commonly used in this work combines coupled cluster and MP2 methods (Section 3.1.3) with VTZ and VQZ basis sets:

$$\begin{aligned}
& \text{CCSD(T)/aug-cc-pVTZ} \\
& + (\text{MP2/aug-cc-pVQZ} - \text{MP2/aug-cc-pVTZ}) \\
& + (\text{CCSD(T),core/cc-pCVTZ} - \text{CCSD(T)/cc-pCVTZ})
\end{aligned} \tag{3.11}$$

where the first correction term aims at converging to CBS while the latter enhances the description of core electrons. cc basis sets were also used for all multireference (MR) calculations of this work (Section 3.1.3.3). In particular, CASPT2/aug-cc-pVTZ was often used to determine MR energies, while in some cases the lower level CASPT2/cc-pVDZ or CASPT2/cc-pVTZ were adopted for the geometry optimization and frequency calculations for stationary points. In some cases, cc type basis sets were also used for DFT calculations (see Section 3.1.4), however Pople Style basis sets were generally preferred for the computationally efficient addition of diffuse functions.

Pople style basis sets are split-valence basis sets whose computational efficiency is increased by fixing exponents for s and p orbital functions in the valence, at the cost of basis set flexibility. The basis set mostly used in this work is 6-311+G(d,p): core orbitals result from contraction of 6 Gaussian functions, while the valence orbitals are represented by three sets contracting 3, 1, 1 Gaussian functions, respectively. + indicates s diffuse functions while (d,p) indicate polarization functions.

3.1.3 Electron correlation methods

The main approximations introduced in the Hartree-Fock theory are the mean field approximation and the representation of the wavefunction as a single ground-state SD. The use of one-electron wavefunctions results in the underestimation of the electronic repulsion related to the correlated motion of the electrons: for instance, in HF theory two electrons may occupy the same position in space, whereas in reality a coulomb hole prevents this. Such instantaneous repulsion effects are referred to as dynamic correlation. On the other hand, the solution of a single electronic state produces incorrect orbitals when multiple electronic configurations that are close in energy contribute to the wavefunction. This missing energetic contribution is called static correlation.

By definition, the difference between the Hartree-Fock energy and the lowest possible energy in the selected basis set is called “correlation energy”. Although it only corresponds to 1% of the total energy - at least with good basis sets-, it is essential for the description of chemical phenomena and bond formation. Considerable past and current research efforts focus on the development of theoretical methodologies to recover the electron correlation energy. Electron correlation methods used in this work are briefly described in this section.

3.1.3.1 Configuration interaction

Configuration interaction (CI) builds the wavefunction from the ground-state HF wavefunction Φ_{HF} including additional Slater determinants corresponding to a specific number of excited electrons:

$$\Psi_{CI} = a_0\Phi_{HF} + \sum_i a_i\Phi_i \quad (3.12)$$

where i indicates the number of excitation considered. For instance, S , D , T indicate all the possible single, double, and triple excitations within the space of MOs. The excited Φ_i is built using the MOs obtained for the ground state Φ_{HF} , such that virtual MOs of Φ_{HF} may thus be occupied in the excited determinants.

The converged Ψ_{CI} minimizes the total energy with respect to the coefficients a_i . Exact wavefunctions are obtained with a full CI expansion, which is however prohibitive except for extremely small systems, and is therefore usually truncated to CISD (including single and double excitations). Such truncation causes problems of size consistency, i.e., the energy of two atoms at a large distance differs if the two atoms are treated together or as separate entities, and therefore in some cases other methods such as MCSCF (Section 3.1.3.3) are preferred.

3.1.3.2 Coupled cluster theory

The idea behind coupled cluster (CC) theory is similar to CI, however the wavefunction is expressed as $\Psi_{CC} = \exp(\mathbf{T})\Phi_0$, where Φ_0 is the reference wavefunction and $\exp(\mathbf{T})$ is an operator which results in excitations of different order. $\mathbf{T}_i\Phi_0$ has the same form as the CI excitations of (3.12), therefore a set of expansion coefficients has to be determined, similarly to CI. $\exp(\mathbf{T})$ can be expanded as:

$$\begin{aligned} \exp(\mathbf{T}) &= 1 + \mathbf{T}_1 + \left(\mathbf{T}_2 + \frac{1}{2}\mathbf{T}_1^2 \right) + \left(\mathbf{T}_3 + \mathbf{T}_2\mathbf{T}_1 + \frac{1}{6}\mathbf{T}_1^3 \right) \\ &+ \left(\mathbf{T}_4 + \mathbf{T}_3\mathbf{T}_1 + \frac{1}{2}\mathbf{T}_2^2 + \frac{1}{2}\mathbf{T}_2\mathbf{T}_1^2 + \frac{1}{24}\mathbf{T}_1^4 \right) + \dots \\ &= \sum_{k=0}^{\infty} \frac{1}{k!} \mathbf{T}^k \end{aligned} \quad (3.13)$$

where states of the same order are grouped together. Contrary to CI, the expansion of the wavefunction is not linear. Each order of excitation contains additional terms of "disconnected" excited states such as $\mathbf{T}_2\mathbf{T}_1$ for triple excitations, which partially solves the problem of size consistency.

As in CI expansion, truncation is needed. Usually, CCSD with $\mathbf{T} = 1 + \mathbf{T}_1 + \mathbf{T}_2$ is used. This means that Eqn. (3.13) includes terms of any order resulting from \mathbf{T}_1 and \mathbf{T}_2 , e.g., triple excitations as $\mathbf{T}_1 + \mathbf{T}_2 + \frac{1}{6}\mathbf{T}_1^3$. Connected triples \mathbf{T}_3 may be partially recovered by adding terms from perturbations computed with MP4 and MP5 (see Section 3.1.3.4), resulting in CCSD(T) [194]. In the complete basis set limit (e.g., Eqn. (3.11) using MP2/cc-pVnZ with n=Q,5 [87]), CCSD(T) generally reaches 1 kcal/mol accuracy in determining reaction energy and energy barriers and is therefore often considered the "gold standard" for energy calculation. A faster convergence to the CBS limit may be obtained using CCSD(T)-F12/cc-pVnZ-F12 [195], which improves the treatment of small electron-electron distances.

For instance, CCSD(T)-F12 with MP2/cc-pVnZ-F12 extrapolation at $n=T,Q$ has only double the computational cost of the corresponding CCSD(T) method but produces similar accuracy to CCSD(T) with MP2/cc-pVnZ with $n=Q,5$. CCSD(T) calculations are generally the most computationally expensive step in the determination of accurate electronic energies, scaling approximately with N^7 .

CCSD(T)/CBS is often used in this work for the calculation of both reaction energies and energy barriers. Failures of CCSD(T) may be due to significant multireference character of the system, such that triple excitations are insufficient to properly describe the electronic interactions. The most common way to identify such behavior is the T1 diagnostic [196]:

$$T1 = \frac{\|\mathbf{t}_1\|}{\sqrt{N_e}} \quad (3.14)$$

where $\|\mathbf{t}_1\|$ is the amplitude vector of the singly excited SDs in the CCSD wavefunction. Large excitations suggest strong multireference character. It was found that the value of T1 is related to the $1-a_0$ value of the CI method (Eqn. (3.12)), i.e., a small T1 indicates that the reference wavefunction is close to the full CI expansion. $T1 > 0.02$ for closed-shell systems and > 0.04 for open-shell systems indicate a potential strong multireference character. In some cases, such diagnostics fails to reveal the MR character of the wavefunction (e.g., see Section 6.3.2).

3.1.3.3 Multiconfiguration self-consistent field method

The main drawback of CI and CC methods is the use of a HF Φ_0 as the reference wavefunction, such that the shape of occupied orbitals in excited states is that of the virtual orbitals of Φ_0 . Multiconfiguration self-consistent field method (MCSCF) instead considers a CI expansion (Eqn. (3.12)) where also the $c_{\lambda j}$ of Eqn. (3.8) describing the MOs of every SD are optimized:

$$\Psi_{MCSCF} = \sum_i a_i \Phi_i(c_{\lambda j}) \quad (3.15)$$

Because of the extremely high computational cost of this methodology, the number of excitations considered is reduced as much as possible: the complete active space self consistent field (CASSCF) approach includes the complete set of excitations within a selected set of MOs, i.e., the active space (AS). MOs have to be manually selected, such that automated implementation of CASSCF-based methods is extremely hard.

Generally, the AS is built by adding pairs of bonding and anti-bonding orbitals, lone pairs, and radical orbitals. The AS is described in terms of the number of electrons and molecular orbitals included: for instance, a (10e,10o) AS includes 10 electrons and 10 orbitals. A proper AS representing the electronic configuration in a reaction must include the orbitals of the bonds participating in the reaction. The energy barrier is computed using the same AS for both the reactants and the transition state (TS, see Section 3.3 and 3.3.2). For simple bond-fission reactions, a (2e,2o) AS including the σ and σ^* orbitals of the breaking bond may suffice. Complications arise in the presence of π orbitals, especially when delocalized as

in MAHs/PAHs. In such cases, the full space of π and π^* orbitals should be included. For instance, the smallest AS to compute the energy barrier for an H-atom abstraction reaction by H from C_6H_6 includes (7e,7o), i.e., the 6 electrons of the π, π^* orbitals of the aromatic ring, and the radical of the H abstractor. Higher accuracy should be obtained if also the 2 electrons of the σ, σ^* C-H breaking bond are included. The presence of oxygen further complicates the AS. AS for additions of $O(^3P)$, OH and 3O_2 generally should include oxygen lone pairs, i.e., (4e,3o), (3e,2o), and (6e,4o), respectively [197], [198]. Additionally, both $O(^3P)$ and OH have multiple quasi-degenerate states. In this work, when multiple states contributed significantly to the electronic configuration, the reference CASSCF wavefunction was optimized as an average of multiple states (SA-CASSCF).

CASSCF alone rarely results in quantitatively accurate predictions. One of the main problems is that the simultaneous optimization of c_{λ_j} and a_i does not guarantee that the set of MOs actually minimizes the electronic energy. Hence, CASSCF is generally coupled with perturbation theory (Section 3.1.3.4) and is called CASPT2 [199]. With an appropriate AS and relatively small basis sets (e.g., cc-pVTZ), CASPT2 may reach 1–2 kcal/mol accuracy in the estimation of energy barriers, as in most of the cases tested in this work, while even higher accuracy (10%) may be obtained for bond-fission MEPs determined with respect to the products at large separations [200] (see Section 3.3.2.4). However, errors in CASPT2 barriers are very case-dependent and are often larger than 2 kcal/mol. Recently, it was shown that accurate TS energy for strongly multireference systems may be obtained with a spin-splitting approach [201], where CCSD(T)/CBS energy for the high-spin (HS) state is corrected according to the CASPT2 difference between the high-spin and the low-spin (LS) states:

$$E_{TS,HL} = CCSD(T)/CBS_{HS} + (CASPT2_{LS} - CASPT2_{HS}) \quad (3.16)$$

The computational cost of CASPT2 methods depends on the size of both the AS and the basis set chosen. The largest AS considered in this work, at the limit of the computational resources employed, was a (15e,13o) AS using a aug-cc-pVTZ basis set. The most computationally intensive step of the CASPT2 calculation is the MP2 correction, which scales as N^5 .

3.1.3.4 Many-body perturbation theory

Perturbation theories are post-HF methods which perturb by $\lambda \mathbf{H}'$ the reference Hamiltonian \mathbf{H}_0 such that in principle the exact solution of the Schrödinger equation is obtained:

$$\mathbf{H}\Psi = (\mathbf{H}_0 + \lambda \mathbf{H}')\Psi = W\Psi \quad (3.17)$$

W and Ψ are written as an expansion of the perturbation coefficients λ^i of order i :

$$W = \sum_i \lambda^i W_i \quad \Psi = \sum_i \lambda^i \Psi_i \quad (3.18)$$

Replacing Eqn. (3.18) in Eqn. (3.17) and isolating perturbation terms of the same order yields the generic n^{th} order perturbation equation:

$$\mathbf{H}_0\Psi_n + \mathbf{H}'\Psi_{n-1} = \sum_{i=0}^n W_i\Psi_{n-i} \quad (3.19)$$

For each n^{th} order, Ψ_n and W_n are obtained from the lower order perturbations according to different theories. The widely used Rayleigh-Schrödinger (RS) perturbation theory generates first-order perturbed wavefunctions as an expansion of the molecular orbitals obtained from the unperturbed wavefunction. Instead, Moller-Plesset theory (MP) describes H' as $\mathbf{H}' = \mathbf{V}_{ee} - 2 \langle \mathbf{V}_{ee} \rangle$, computed from the unperturbed wavefunction and MOs. A drawback of MP is the oscillatory convergence behavior with the perturbation order: MP with even order decrease the energy, while odd orders increase it.

A considerable advantage of perturbation methods is that the unperturbed WF may already include correlation, such as CI and CASSCF, such that RS/MP mostly recover the dynamic part of correlation energy. In this work, MP2 was applied to both HF (see Eqn. (3.11)) and CASSCF (as in [199]) reference wavefunctions through algorithms implemented in the ES codes used. In this work, the second-order RS2 perturbation of CASSCF wavefunction was used to obtain CASPT2 energies (as mentioned in Section 3.1.3.3). To reduce the computational cost, the RS2C protocol was adopted, i.e., a heavier contraction scheme for inactive electrons [202].

It is noted that CASPT2 may result in singularities when the energies of the unperturbed and perturbed wavefunctions are close. The corresponding perturbed states are called “intruder states”. This situation is common for instance when oxygen lone pairs participate in the reactivity. In these cases, the reference CASSCF wavefunction is often state-averaged. To avoid singularities, level shift corrections to the perturbed energy may be applied, as proposed by Roos [203]. More recent level shift corrections suggest a shift parameter based on the difference between the ionization potential and the electron affinity of the molecule, called IPEA shift [204], widely used in this work and especially recommended for chemical reactions involving oxygen [200].

3.1.4 Density functional theory

HF and post-HF methods propose approximate solutions to the Schrödinger equation by minimizing the energy with respect to the MOs. Instead, density functional theory (DFT) proposes to minimize the energy of the system as a functional of the electron density $E_e[\rho_e]$. In fact, the Hohenberg-Kohn theorem states that the ground state is a unique functional of $\rho_e(\mathbf{r})$ [205]. Since the electron density is only a function of three spatial coordinates, the computational cost is significantly reduced. The resulting poor representation of the kinetic energy is fixed by Kohn-Sham theory, which expresses the kinetic energy T_S according to a set of fictitious independent non-interacting MOs Φ_i which by definition produce the same electron density of the real system:

$$\rho(\mathbf{r})_e = \sum_{i=1}^{N_e} |\Psi_i| \quad (3.20)$$

The total energy can be written as a sum of different contributions:

$$E_{DFT}[\rho_e] = T_S[\rho_e] + E_{ne}[\rho_e] + J[\rho_e] + E_{XC}[\rho_e] \quad (3.21)$$

where E_{ne} derives from the external potential and accounts for nuclei-electron interactions and J accounts for the coulomb interactions. E_{XC} is the exchange-correlation functional contributing to $E_{DFT}[\rho_e]$ by the missing part of the fictitious kinetic energy and non-classical electron-electron interactions:

$$E_{XC}[\rho_e] = (T[\rho_e] - T_S[\rho_e]) + (E_{ee}[\rho_e] - J[\rho_e]) \quad (3.22)$$

If the expression of E_{XC} is exact, the solution is in principle exact. Research efforts over the past 90 years have focused on the accurate determination of E_{XC} , and in particular of $T[\rho_e]$, which is the largest unknown term [206].

The main drawback of DFT is that density functionals cannot be systematically improved. However, classifications such as Jacob’s Ladder [207] suggest that adding dependencies beyond the local density such as the gradient of densities (generalized gradient approximation, GGA) or orbitals does lead to improvements. Most of the expressions for E_{XC} are semi-empirical, i.e., they have functional forms such as a power series, and their coefficients are fitted to reference values of molecular properties, such as high-level CCSD(T)/CBS energies or other experimental data.

This work employs (for geometry optimizations and frequency calculations) hybrid and double-hybrid meta-GGA E_{XC} , whose functional dependencies include the gradient of the electron density (GGA) as well as the kinetic energy density (meta-); additionally, they combine exact exchange and density functionals (hybrid). In particular, the functionals used are:

- M06-2X by Zhao and Truhlar [208] (hybrid meta-GGA): heavily parametrized to reproduce properties of stable molecules and radicals. It includes a qualitative treatment of dispersion including some non-bonding interactions.
- ω B97X-D by Chai and Head-Gordon (hybrid GGA) [209]: this functional is less heavily parametrized than M06-2X and was developed by also considering long-range interactions.
- B2PLYPD3 (double-hybrid) by Grimme et al. [210]: it includes MP2-like treatment of the correlation energy as well as dispersion corrections (D3), particularly useful in the description of bonds. This functional has higher computational cost due to the MP2 component.

3.2 Statistical thermodynamics

3.2.1 Partition functions

Molecular partition functions Q describe the energy partition of a molecule according to the thermally accessible energy states E_i at a given temperature. Q allows direct derivation of macroscopic molecular properties such as heat capacity and entropy, as well as rate constants (Section 3.3.2). At thermal equilibrium, the energy partition takes the form of a Boltzmann distribution, where the probability of state i with energy E_i is

$$p_i = \frac{\exp\left(-\frac{E_i}{k_B T}\right)}{Q} \quad (3.23)$$

The normalization factor Q is the partition function

$$Q = \sum_{i=1}^{\infty} \exp\left(-\frac{E_i}{k_B T}\right) \quad (3.24)$$

For an isolated molecule of ideal gas, the total energy can be regarded as the sum of independent translational, rotational, vibrational, and electronic contributions, therefore the total partition function Q is derived as the product of each independent component. The corresponding energy states can be computed from the solution of the Schrödinger equation for a single particle in a box (Q^{tr}), a quantum rigid harmonic oscillator (Q^{vib} , approximating the energy states of intramolecular vibrations), a rotating molecule (Q^{rot}), and the electronic Schrödinger equation (Q^e):

$$Q^{tr} = \left(\frac{2\pi m k_B T}{h^2}\right)^{\frac{3}{2}} \quad (3.25)$$

$$Q^{rot} = \frac{8\pi^2 (2\pi k_B T)^{\frac{3}{2}} \sqrt{I_x I_y I_z}}{\sigma h^3} \quad (3.26)$$

$$Q^{vib} = \exp\left(-\frac{\text{ZPE}}{k_B T}\right) \prod_{i=1}^{N_{vib}} \frac{1}{1 - \exp\left(-\frac{h\nu_i}{k_B T}\right)} \quad (3.27)$$

$$Q^e = g^e \exp\left(-\frac{E_{e,tot}}{k_B T}\right) \quad (3.28)$$

where I_x, I_y, I_z are the principal moments of inertia, σ is the rotational symmetry number, g_e is the electronic degeneracy, and ZPE is the zero point energy ($\text{ZPE} = 0.5h \sum \nu_i$). The ZPE is the energy of the harmonic oscillators at 0 K: it is the lowest possible energy of a quantum mechanical oscillator and has no classical correspondence.

3.2.2 The rigid rotor harmonic oscillator approximation and the treatment of anharmonicities

The rigid rotor harmonic oscillator (RRHO) approximation treats the $3N-5/6$ internal degrees of freedom (DOF) of the molecule as uncoupled harmonic oscillators. For each DOF, a

displacement dr with respect to the "equilibrium" geometry causes a variation in energy by $E(dr) = 0.5 k dr^2$, where k is the force constant corresponding to a vibrational frequency of $\nu = (2\pi)^{-1}(k/\mu)^{0.5}$, with μ being the reduced mass.

The RRHO approximation fails when the potential describing the displacement from the equilibrium geometry strongly deviates from harmonic even for small dr . Hence, the RRHO treatment may result in errors of factors > 2 in the resulting partition functions (and therefore rate constants, see Section 3.3.2). The most common example of RRHO failure is the description of periodic potentials with small barriers (e.g., < 10 kcal/mol), such as those of internal torsional motions. Therefore, internal torsions are commonly treated according to the one-dimensional hindered rotor (1DHR) model. The energy levels for the calculation of Q^{1DHR} (taking the general form of Eqn. (3.24)) are derived solving the one-dimensional Schrödinger equation for internal rotations:

$$-\frac{\hbar^2}{2I_{red}} \frac{\partial^2 \Psi}{\partial \theta^2} + V(\theta)\Psi = E\Psi \quad (3.29)$$

where I_{red} is the reduced moment of inertia calculated according to the approach proposed by East and Radom [211], θ is the dihedral angle and $V(\theta)$ is the torsional potential.

The partition function obtained contributes to the product of the other uncoupled terms in (3.27), where the RRHO contribution of the corresponding vibrational frequency is removed. In this work, the frequency projection subroutine of EStokTP [97] was adopted: the final set of vibrational frequencies was obtained after projecting out from the Hessian torsional, rotational, and reaction coordinate (for TSs) motions [212].

The 1DHR model reproduces well the density of states of internal uncoupled torsions. However, when torsional motions involve groups closely interacting, multi-dimensional hindered rotor models are more appropriate [106], as they consider a multi-dimensional PES for the potential of all coupled rotations. For example, Pelucchi et al. [129] showed that considering 2 coupled torsions in the H-atom abstraction reaction by OH from toluene methyl group impacts the resulting rate constant by up to a factor of 2 with respect to a 1DHR treatment. Coupled torsional motions can also be treated with the multi-structural approach proposed by Zhang and Truhlar [213]. This work employs mostly the 1DHR model, while the 2DHR implementation of Georgievskii et al. [106] is used in a few cases.

Deviations from RRHO approximations may also be relevant for stretching and bending modes. For instance, the stretching potential is represented correctly by a Morse function $E(dr) = D(1 - \exp(-\alpha dr))^2$, which is usually well approximated by a second order potential (the one of RRHO) for small displacements (i.e., high frequencies). Anharmonic effects may be accounted for by considering higher order (third and fourth) derivatives, fitted to reproduce a Morse potential function. For bending modes, the second or third order derivatives are generally enough. The calculation of higher order derivatives of the energy is extremely expensive. A useful implementation in commercial codes is the second order perturbative approach [214], where third order derivatives and semi-diagonal fourth order derivatives are computed numerically on the analytical hessian matrices with perturbation theory then used to derive quadratic expansions of the energy levels in terms of the quantum numbers.

Anharmonic corrections are often necessary to reproduce vibrational spectra obtained experimentally [215] and therefore for the derivation of absolute thermochemistry. Instead, anharmonic corrections are generally unnecessary for the calculation of rate constants, because anharmonic contributions to the partition functions of the TS and reactants mostly cancel out. Recent work revealed that this is not always the case [216], [217]. In this work, an anharmonic treatment was considered for some of the H-atom abstractions from MAHs (Section 6.4) to investigate discrepancies with experimental data. In some cases, anharmonic corrections to the ZPE were significant (up to 0.79 kcal/mol).

3.2.3 Thermochemical parameters

Partition functions allow one to relate fundamental molecular properties to thermochemistry. In particular, considering the standard pressure of 1 bar (⁰ symbol), the standard molar enthalpy, heat capacity, and entropy of a species can be derived from the molecular partition functions:

$$H^0(T) - H^0(0) = RT^2 \left(\frac{\partial}{\partial T} \ln Q^0(T) \right) \quad (3.30)$$

$$C_p^0(T) = RT^2 \left(\frac{\partial^2}{\partial T^2} \ln Q^0(T) \right) + 2RT \left(\frac{\partial}{\partial T} \ln Q^0(T) \right) \quad (3.31)$$

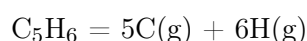
$$S^0(T) = RT \left(\frac{\partial}{\partial T} \ln Q^0(T) \right) + R \ln Q^0(T) \quad (3.32)$$

where it is noted that $C_p^0(T) = \frac{\partial}{\partial T}(H^0(T) - H^0(0))$. Generally, accurate reproduction of spectroscopy data requires scaling of theoretically derived vibrational frequencies, according to values that are very much method dependent, and are around 0.9–0.99.

Partition functions only allow one to describe the variation of enthalpy (Equation (3.30)). $H^0(0)$ are generally derived as 0 K formation enthalpies $\Delta H_f^0(0)$. $\Delta H_f^0(T)$ is the enthalpy of the reaction forming a given species from its constitutive elements in their reference state. As the amount of calorimetric experimental data for formation enthalpies is extremely limited, one generally has to rely on "species-interrelated" data.

Theoretical protocols developed in the last 50 years led to the determination of formation enthalpies with even greater reliability than "chemical accuracy" (95% confidence interval of ± 1 kcal/mol) [218]. Some widely used highly accurate protocols are Weizmann-n [219], HEAT [220], and ANL-n [221], which derive $\Delta H_f^0(T)$ from atomization energies, elements or diatomic (or selected gas phase) species, and molecules such as CH₄, respectively. Other mid-level methods (not as accurate) include for instance Gn methods, such as G4(MP2). These protocols are in principle independent of experimental data with exceptions such as spin-orbit corrections. Indeed, all methodologies are benchmarked with external databases [117], [221].

The derivation of formation enthalpy from atomization energies considers reactions of the form:



where $\Delta H_f^0 = \sum_{at} \Delta H_{f,at}^0 - TAE^0$. The TAE^0 is the total atomization energy derived theoretically, while $\Delta H_{f,at}^0$ are the formation enthalpies of the atoms (from the respective elements). Because of the simultaneous bond-breaking of all chemical bonds in atomization reactions, theoretical inaccuracies are generally amplified. Instead, deriving formation enthalpies from chemical reactions such as in the ANL-n protocols result in better cancellation of errors. The simplest scheme derives formation enthalpies from isogyric reactions, i.e., reactions where the number of unpaired electrons is preserved [222]:



in this case, reaction enthalpies $\Delta H_R^0 = \sum_i \nu_i E_i^0$ are used instead of atomization energies. More complex reaction schemes allow one to also preserve some properties of the chemical bonds. For instance, isodesmic reactions preserve the number of chemical bonds broken and formed in the reaction, while homodesmotic reactions also preserve the degree of hybridization. For instance, Sengupta et al. [223] showed the high accuracy (with relatively low level theoretical calculations) of "higher order" schemes which preserve not only the bond type but also the surrounding environment, such as the bond order across multiple centres in the molecule. These schemes are known as "connectivity based hierarchy" (CBH) schemes.

Automated implementation of all CBH schemes is available in Auto-Mech routines (Section 3.4.2). However, these schemes were not validated for aromatic species and therefore in this work the simple CBH-0 isogyric scheme based on experimental formation enthalpies of simple molecules was adopted. Thermochemical parameters were derived only for new species introduced in the CRECK kinetic mechanism. Formation enthalpies for reference species such as CH_4 were taken from the Active Thermochemical Tables (ATcT) [117]. ATcT is considered the best validated thermochemical database for gas phase species, with more than 1500 tabulated species. Thermochemical data are derived solving a thermochemical network which contains the most accurate experimental and theoretical data. The network enforces a set of constraints simultaneously satisfied by all species. Statistical analysis accounts for interspecies correlation, revising the declared uncertainty of the data to ensure self-consistency. The tables are "active" as any update in the knowledge base propagates through all affected species, thus ensuring robustness and reliability.

3.3 Theoretical kinetics

3.3.1 Potential energy surface

Elementary reactions occur through the rearrangement of atoms from the configuration of the reactants to that of the products, which can be described as the evolution of the relative position of the atoms in the system i.e., distances, angles and dihedral angles. The potential energy surface (PES) describes the energy of the system (the electronic energy + ZPE) as a function of the internal coordinates ($3N-5/6$ parameters, where N is the number of atoms of the system). At least qualitatively, a reaction follows the path from reactants to products that minimizes the energy of the system, namely the minimum energy path (MEP). The projection of this path onto the space of (internal) coordinates is the reaction coordinate λ .

The simplest case of PES/MEP is the bond-fission of a diatomic molecule such as H_2 . The only DOF (H–H distance) obviously corresponds to the reaction coordinate. The PES/MEP describes the change in energy as a function of the H–H distance. A slightly more complex case is a generic abstraction reaction of atom A_2 from the diatomic molecule A_2A_3 by atom A_1 . Figure 3.2a shows qualitatively the PES for this reaction. Assuming that the abstraction is co-linear, the energy only changes as a function of the A_1-A_2 and A_2-A_3 distances (r_1 and r_2 in Figure 3.2a). The system evolves along the MEP from a large r_1 and small r_2 to a large r_2 and small r_1 . The reaction coordinate λ describes the simultaneous change of r_1 , r_2 along the MEP. The qualitative shape of the corresponding MEP (valid also for a generic exothermic reaction) is represented in Figure 3.2b. The maximum along λ is a relative minimum with respect to all the other coordinates, and is therefore a saddle point. The saddle point is generally a good approximation to the minimum energy point on the transition state (TS) dividing surface, which best separates reactants and products in the sense that it has the smallest dynamical recrossing (see Section 3.3.2). In the transition state theory (TST) framework, the properties of the saddle point approximating the TS are essential to the determination of the rate constant of a reaction.

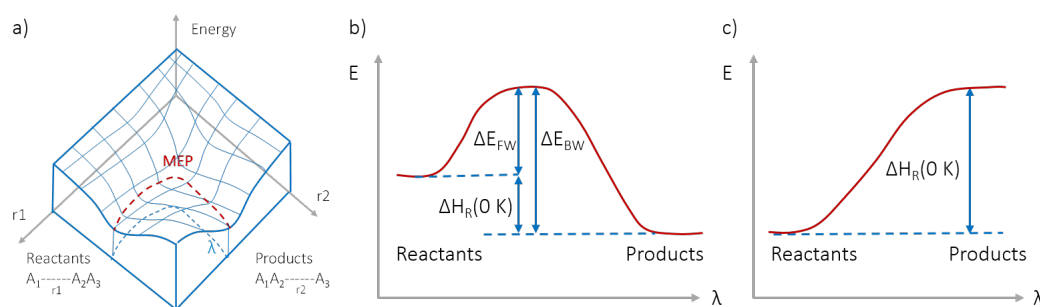


FIGURE 3.2: a) Example of the PES for an abstraction reaction of atom A_2 from the molecule A_2A_3 by A_1 to form molecule A_1A_2 , and of MEPs for reactions with well-defined barriers b) or barrierless c).

Figure 3.2b exemplifies the MEP for reactions occurring through well-defined barriers (ΔE_{FW} and ΔE_{BW} for the forward and backward reactions, respectively). This reaction type includes isomerizations, β -scissions, abstractions, eliminations. Instead, reactions with submerged barriers or without well-defined barriers are called "barrierless" and are generally

radical-radical reactions, such as bond-fissions or radical abstractions. A qualitative MEP for a bond-fission reaction is depicted in Figure 3.2c. The theoretical treatment of this type of reactions is more complex than reactions with barriers and is explained in Section 3.3.2.4, 3.3.2.5.

While the mathematical definition of PES, MEP and λ is complex, graphic representations are much simpler. In the literature, as well as in this work, a PES diagram only shows the energies of the stationary points (both wells/bimolecular fragments and saddle points) relevant to the description of the reactivity. When multiple wells are present, the PES is called multi-well and it depicts connected reaction channels described by different reaction coordinates. The MEPs shown in this work are one-dimensional. The reaction coordinate λ is identified as the arc length along the (minimum energy) reaction path, i.e., an abstract one-dimensional coordinate that represents how the reaction progresses along the reaction pathway. λ can also be thought of as a collective variable of geometric parameters that change as the reaction progresses.

3.3.2 Transition state theories

Transition state theory (TST) was first theorized in 1935 by Evans, Eyring and Polanyi [169], [224] and it became the most widely used approach for the calculation of pressure-independent rate constants for elementary reactions with barriers. Later extensions of conventional TST (Section 3.3.2.1) allowed also the treatment of barrierless reactions with variational TST (VTST, Section 3.3.2.2) and variable reaction coordinate TST (VRC-TST, Section 3.3.2.4), as well as of reactions with intersystem crossing (NA-TST, Section 3.3.2.6).

The main assumptions of transition state theories are (I) the validity of the Born-Oppenheimer approximation, and (II) species equilibration (either canonical or microcanonical). Hence, the Maxwell-Boltzmann distribution is adopted for the velocity of the particles, while the molecular rovibrational energy is treated according to the Boltzmann distribution.

TST theorizes that the reaction rate of an elementary reaction is controlled by a "dividing surface" that separates the region of the reactants from that of the products, is orthogonal to the MEP, and minimizes the dynamical recrossing (back to the reactants). Crossing the dividing surface is thus assumed to be an irreversible process resulting in the thermalization of the products (no-recrossing assumption) [225]. Hence, the dividing surface corresponds to the bottleneck of the reactive flux. TSTs treated in this section mostly differ for the identification of the dividing surface.

3.3.2.1 Conventional TST

Conventional TST identifies the configuration determining the bottleneck of the reactive flux with that of the saddle point along the MEP (maximizing the energy with respect to λ), therefore called transition state (TS).

The non-recrossing assumption allows one to express the reaction rate as the frequency ν at which the TS is crossed and the concentration of molecules at the TS configuration:

$r = \nu C_{\text{TS}}$. In the vicinity of the saddle point, this frequency is treated as a one-dimensional translation. In a small region δ , the potential is considered flat: molecules cross the surface at a frequency of $\nu/2\delta$, where ν is the velocity of the molecules.

Finally, the assumption of equilibration allows one to express C_{TS} as a function of the concentration of the reactants C_R and the respective partition functions:

$$r = \left(\frac{\nu}{2\delta} \frac{Q_{\text{TS}}}{Q_R} \right) C_R \quad (3.33)$$

where $\left(\frac{\nu}{2\delta} \frac{Q_{\text{TS}}}{Q_R} \right)$ can be identified as the rate constant; ν is the average velocity of a Maxwell-Boltzmann distribution $(2k_B T \pi^{-1} m^{-1})^{0.5}$; Q_{TS} , Q_R are expressed according to Eqn. (3.25)-(3.28). Q_{TS}^{vib*} excludes the vibrational frequency of the reaction coordinate, which is imaginary at the saddle point (due to the negative elastic constant of the corresponding harmonic oscillator). Instead, the expression for the partition function of λ is that of a 1D translation $\delta(2\pi m k_B T h^{-2})^{0.5}$. The final expression for the rate constant is:

$$k_{CTST} = \frac{k_B T}{h} \frac{Q_{\text{TS}}^{tr} Q_{\text{TS}}^{rot} Q_{\text{TS}}^{vib_0^*} g_{\text{TS}}^e}{Q_R^{tr} Q_R^{rot} Q_R^{vib_0} g_R^e} \exp\left(-\frac{\Delta E_{\text{TS}}}{k_B T}\right) \quad (3.34)$$

where Q^{vib_0} highlights that the ZPE exponential appearing in (3.27) is not excluded, as it contributes to ΔE_{TS} :

$$\Delta E_{\text{TS}} = (E_e + \text{ZPE})_{\text{TS}} - (E_e + \text{ZPE})_R \quad (3.35)$$

3.3.2.2 Variational TST

Conventional TST works when the saddle point reasonably approximates the dividing surface minimizing the reactive flux. This is generally the case for reactions with "tight" TSs, identified by narrow barriers in the vicinity of the TS (large absolute values of the imaginary frequency at the saddle point). For instance, absolute values of imaginary frequencies for H-atom abstractions by H or for H-transfer reactions between two adjacent sites are typically above 1000 cm^{-1} . Tight TSs commonly have high forward and backward energy barriers.

On the other hand, a wider shape of the MEP in the vicinity of the saddle point is typical of reactions with "loose" TSs, identified by small absolute values of imaginary frequencies. For instance, isomerization reactions occurring via ring-like TSs with more than 5 atoms have imaginary frequencies around $200\text{-}400 \text{ cm}^{-1}$. In such cases, the non-recrossing assumption breaks down at the TS [226], and k_{CTST} (Eqn. (3.34)) only provides an upper limit for the actual k . In fact, "flatter" barriers are more sensitive to entropy changes in the vicinity of the saddle point, such that the effective energy barrier is larger than that at the TS. As a result, the dividing surface minimizing the flux according to Eqn. (3.34) varies with temperature along the MEP, due to the competition of energetic and entropic effects. Hence, in variational transition state theory (VTST) the minimum of the flux is computed along the MEP, as sketched qualitatively in Figure 3.3. ES codes include reaction path following approaches [227] which follow the maximum gradient to reconstruct structures and vibrational frequencies along the MEP. This "intrinsic reaction coordinate" (IRC) scan also

allows one to verify that the TS found actually connects the identified reactants and products. However, IRC scans may be sensitive to both the choice of coordinates and the level of theory adopted, as discussed for H-atom abstraction reactions in Section 6.4.3.10.

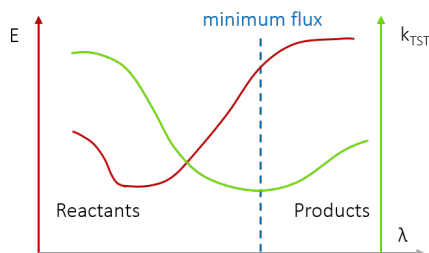


FIGURE 3.3: Sketch of the determination of the rate constant as the minimum flux in VTST.

VTST can also be applied to derive rate constants for barrierless reactions. However, recent semi-automated implementations of VRC-TST in some kinetic codes such as EStokTP allowed an easier application of the more appropriate kinetic theory for barrierless reactions (Section 3.3.2.4).

In this work, VTST was extensively applied to addition, β -scission, H-atom abstraction and isomerization reactions.

3.3.2.3 RRKM theory

Rice-Ramsperger-Kassel-Marcus (RRKM) theory [228], [229] was originally developed for the derivation of pressure-dependent rate constants, briefly introduced in Section 2.1.4 and treated in greater detail in Section 3.3.4. However, RRKM theory can also be simply considered as the microcanonical version of TST, as it relies on the same equilibrium assumption of TST [230]–[232].

As in CTST, the DOF corresponding to the reaction coordinate λ is treated as a 1D translation. Considering a total energy E (which, for simplicity, does not include external rotational DOFs in the present derivation) distributed among the internal DOFs at the TS, the reaction can only occur only at $E > E_{\text{TS}}$ and is proportional to the velocity of the 1D translation (see Eqn. (3.34)):

$$k(E) = \int_{E_{\text{TS}}}^E \frac{v(E^*)}{2\delta} P(E^*) dE^* \quad (3.36)$$

$P(E^*)$ is the probability that $E^* < E$ is deposited into the translation corresponding to the reaction coordinate while $E - E^*$ is distributed among the other degrees of freedom:

$$P(E^*) = \frac{\rho_{\text{TS}}^{\text{vib}^*}(E - E^*) \rho_{\text{TS}}^{\text{tr}}(E^*)}{\rho_R(E)} \quad (3.37)$$

where $\rho_R(E)$ is the rovibrational density of states (DOS) of the reactant. Combining (3.36) and (3.37) and expressing ρ^{tr} as the DOS of a particle in a box ($m/(2E^*)/h$), and $v(E^*)$ as the kinetic energy $(2E^*/m)^{0.5}$, the following expression is obtained:

$$k(E) = \frac{\int_{E_{\text{TS}}}^E \rho^{\text{vib}}(E - E^*) d(E^*)}{h\rho_R(E)} \quad (3.38)$$

The microcanonical rate constant obtained has no practical application for the derivation of phenomenological rate constants without the knowledge of the population of energy states. Hence, in this work RRKM theory is used within the master equation (ME), which allows one to derive the population at each energy level $n(E)$ and the calculation of $k(T, P)$. These steps are described in Section 3.3.4.1.

3.3.2.4 Variable reaction coordinate TST

Determining accurate rate constants for radical-radical reactions is key to combustion kinetics because such processes determine the competition between chain termination and chain branching reactions. However, VTST often provides poor quantitative estimates of the kinetics of barrierless processes or processes with submerged barriers, such as recombination, roaming, and radical abstraction reactions [200]. In these cases, the dividing surface minimizing the flux varies dramatically with temperature, generally shifting from 2-3 Å at combustion temperatures to larger separations at lower temperatures. Even at 2-3 Å, transitional DOFs (for barrierless reactions, vibrational normal modes in the well that become intermolecular free motions in the products) are poorly described by RRHO and 1DHR/2DHR models and are strongly coupled. Additionally, an accurate derivation of the MEP requires the inclusion of multireference effects.

In such cases, the appropriate theoretical calculation of the rate constant requires computationally expensive ab-initio trajectory simulations. Instead, variable reaction coordinate (VRC) transition state theory is a fairly cheap and physically meaningful theoretical methodology able to obtain rate constants within 15% of the results of trajectory simulations [233]–[236] and that outperforms CTST and VTST.

In VRC-TST, the variable nature of the reaction coordinate is captured by varying not only the value, but the *definition* of the reaction coordinate itself. In particular, λ is defined in terms of the center of mass (COM) of the fragments at large separations (e.g., > 4 Å) and in terms of the distance between reactive atoms at shorter separations.

Because of the different nature of transitional DOFs with respect to the conserved DOFs ("preserved" as internal normal modes), the basic idea of VRC-TST is to separate the theoretical treatment of the two groups of modes, assumed decoupled [237]–[239]. The DOS for conserved modes is derived with direct state counting using quantum chemistry. On the other hand, transitional modes are counted with Monte Carlo (MC) evaluation of the classical phase space integral, where the reacting fragments are considered as rigid bodies. Classical treatment of the transitional modes also simplifies accounting for anharmonicities and coupling between modes.

The microcanonical reaction flux as a function of the total energy E and the angular momentum J is derived as (see [235]):

$$k(E, J) = \frac{\int_0^E \rho^c(E - E') \cdot N^t(E', J) dE'}{h\rho_R(E, J)} \quad (3.39)$$

where $N^t(E', J)$ is the state count for the transitional modes and $\rho^c(E - E')$ is the density of states in the conserved modes. The numerator of $k(E, J)$ can be interpreted as the number of available states with energy less than E for the motion on the dividing surface, hence its minimization allows to evaluate the bottleneck of the reactive flux.

Calculating $N^t(E', J)$ requires the evaluation of the system Hamiltonian, and therefore of the interaction potential between the fragments. On-the-fly MC sampling on multiple dividing surfaces of the interaction potential using multireference methods allows minimizing $N^t(E', J)$. In the VRC-TST implementation of Klippenstein [233], [240], also adopted in this work, the dividing surfaces are defined with the relative distance of "pivot points" placed on the reactive atoms/fragments. Figure 3.4 exemplifies the placement of pivot points for $C_5H_5 + HO_2$ reaction (Section 5.3.2). At large separations (Figure 3.4a), pivot points are placed at the center of mass of the fragments, and each spherical dividing surface is simply defined by the fixed distance d between the pivot points. At shorter separations instead (Figure 3.4b), pivot points are more appropriately placed along the breaking bond (or corresponding MOs) [233], [240]. Hence, each dividing surface is defined by both the distance d between the pivot points and their relative position with respect to the corresponding fragment, thus allowing for a 7 dimensional optimization of the reaction coordinate. For instance, the positions of pivot points $p1$ and $p2$ in Figure 3.4b may vary in terms of both distance and angle with respect to the reference C and O atoms, respectively.

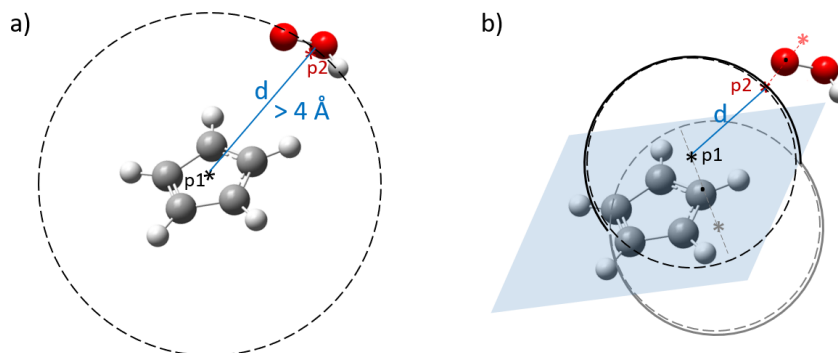


FIGURE 3.4: Schematic representation of the placement of pivot points on the two reactive fragments in VRC-TST on a) the center of masses and b) the reacting atoms to construct multifaceted dividing surfaces for the $C_5H_5 + HO_2$ reaction. In b), solid lines highlight the portion of the surfaces exposed to the flux.

Figure 3.4b also exemplifies an additional complication for short range calculations: in most cases, the dividing surface is not spherical. In the depicted case, the black dashed surface defined by $p1$, $p2$ and d contributes to the reactive flux only on its "upper" side (above the blue plane, i.e., the plane of the ring). In fact, the attack of HO_2 on the lower side of the ring at d is described by a different surface, identified by the grey dashed line. Hence, the final surface corresponding to distance d is actually a composite surface, obtained

by considering only MC sampling on the sphere lying on the same side as the pivot point [234], [235]. For practical applications, the flux on symmetrical surfaces is obtained through the sampling of a single side and appropriate rescaling with the corresponding symmetry. These composite surfaces are described by Georgievskii et al. as multifaceted dividing surfaces (MDS) [234], [235]. Multiple pivot point placements with the MDS approach also allows to consider multiple recombination sites, or on the contrary to distinguish recombination reactions on different sites, such as the N and O sites for $\text{NO}_2 + \text{CH}_3$, by setting repulsive potentials on pivot points placed on "undesired" recombination sites. This feature is essential to treat recombinations on resonance-stabilized radicals and aromatic systems in general.

In this work, the calculation of $N^t(E', J)$ was performed with VaReCoF [104], which implements the theoretical approach described here. Automated input construction and pivot point placement was produced using EStokTP [97] (Section 3.4.1).

The flux based on transitional DOFs $N^t(E', J)$ largely depends on the interaction potential between the fragments calculated on-the-fly. This potential should be calculated with multireference methods, such as CASPT2 (Section 3.1.3.3). In many cases such as the aromatic systems explored in this work, the available computational resources do not allow to reach sufficient accuracy for on-the-fly determination of the interaction potentials. The smaller accuracy of MR calculations performed during MC samplings can be compensated by imposing a distance-dependent correction potential (e.g., Section 5.3.2.2), which, if computed appropriately, allows to achieve excellent accuracy in the resulting rate constant [241], [242].

A final comment should be made on dynamical corrections for recrossing. Since in barrierless processes the basic TST assumption of non-recrossing breaks down, dynamical corrections for recrossing can be computed from direct dynamics simulations of small systems [103], [243]. This work adopts the generally accepted correction value for the rate constant of 0.85-0.9.

3.3.2.5 Phase space theory

Phase space theory (PST) is a simplified theory for the calculation of approximate rate constants for barrierless association reactions [244]–[246].

Similarly to VRC-TST, PST assumes the separation between conserved and transitional modes. Conserved modes are assumed equal to those of the separate fragments, hence their contributions cancel out with those of the reactants in Eqn. (3.39). The calculation of the flux associated with transitional modes $N^t(E', J)$ reduces to evaluating the centrifugal and rotational energies for the fragments and the interaction potential. Contrary to VRC-TST, PST simply assumes an isotropic interaction between fragments, i.e., a potential only dependent on the COM distance R , such that no phase space sampling is necessary. The effective centrifugal potential is calculated as (see [247]):

$$V_{eff}(R) = V(R) + \frac{\hbar^2 L^2}{2\mu R^2} \quad (3.40)$$

where L is the orbital angular momentum ($l(l+1)$ in its quantum version).

The interaction potential between fragments $V(R)$ is considered purely attractive (always valid for the maximum attractiveness of non-bonded interactions at large separations) and takes the general form:

$$V(R) = -\frac{C_n}{R^n} \quad (3.41)$$

where C_n and n are often used as fitting parameters. $n = 6$ is a common approximation for radical-radical interactions [248]. Since centrifugal and rotational energies of the fragments are assumed independent of R , the minimum of the flux corresponds to the maximum of the effective potential $V_{eff}(R)$.

Because of the assumption of an isotropic potential, PST only provides reasonable approximations of VRC-TST/trajectory simulations for association reactions dominated by long range interactions, i.e., at intermediate and low temperatures. PST is also inaccurate at low T (below 300 K) due to the relevance of quantum effects. Overall, PST provides estimates within one order of magnitude for radical-radical association reactions, while better accuracy is expected when it is applied to the formation of van der Waals pre-reaction complexes in radical-molecule associations, which are dominated by long-range attractive-only weaker interactions.

In this work, PST was adopted to determine rate constants for the formation of van der Waals wells which precede and follow TSs of H-atom abstraction reactions. C_n and n of Eqn. (3.41) were normally taken to be 10 au and 6, respectively.

3.3.2.6 Non-adiabatic TST

The adiabatic approximation restricts the solution of the Schrödinger equation to a single electronic surface. Therefore, the spin-orbit coupling terms of the hamiltonian H_{SO} are neglected, and the PES is constrained on a single spin state. However, some relevant kinetic phenomena occur through a change in the spin state of the system, i.e., an intersystem crossing (ISC), and are therefore called spin-forbidden reactions. A well-known example of a spin-forbidden reaction class relevant in the combustion kinetics of alkenes and aromatics is $O(^3P)$ addition [249]–[254], also treated in this work (Section 6.3.1).

A relatively simple and effective treatment for the kinetics of spin-forbidden reactions is non-adiabatic TST (NA-TST). NA-TST identifies an analogue of a saddle point at the crossing (in energy) between the two PESs with different spin states. This structure is commonly referred to as minimum energy crossing point (MECP) or minimum on the seam of crossing (MSX). The latter name highlights that in reality the hopping between the two surfaces occurs in a region (a seam) of the potential rather than at a single point. A qualitative representation of the MECP is shown in Figure 3.5a.

The determination of the microcanonical reaction flux for ISC depends on the properties of the identified MECP. The MECP can be found by minimizing the energy on a PES in a given spin state under the constraint that the energies of both PESs are equal. In this work, the MECP for the $O(^3P) + C_6H_6$ reaction was searched with a sequential least-squares

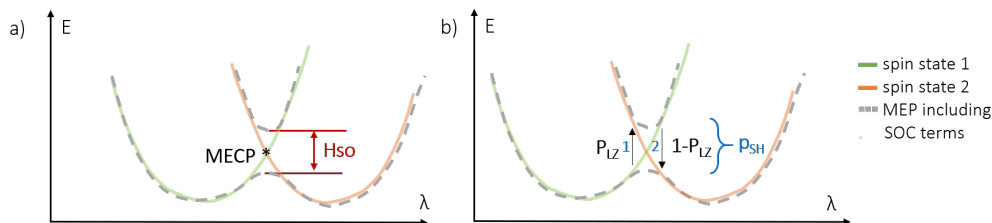


FIGURE 3.5: Schematic representation of a) the MECP and b) of the hopping probability p_{sh} between surfaces with different spin states considering double passage.

quadratic programming algorithm, imposing equality constraint through the augmented Lagrangian method, as recently implemented in EStokTP [255]. The general approach is that described by Harvey [256], [257] and was also successfully applied to several other studies of $O(^3P)$ addition to alkenes and alkynes [250], [254], [258], [259].

The microcanonical reaction flux for ISC depends on the extent of coupling between the two PESs. This is quantified by the spin orbit coupling term H_{SO} , deriving from the neglected term of the adiabatic Hamiltonian. In this work, H_{SO} was determined at the CI level of theory as the average of the off-diagonal $H_{SO,i}$ matrix elements of the Breit-Pauli operator [260]. Generally, the MECP also maximizes H_{SO} [250], [258] (with some exceptions such as in [254]).

H_{SO} is used to determine the probability of hopping between the two surfaces p_{sh} . In this work, p_{sh} was computed according to the double-passage Landau-Zener statistical theory [257], [261], as schematically represented in Figure 3.5b. P_{LZ} is the probability of single-passage hopping from the lower to the higher energy surface, i.e., surfaces derived considering SOC terms in the Schrödinger equation (grey dashed lines in the plot):

$$P_{LZ}(E) = 1 - \exp\left(-\frac{2\pi H_{SO}^2}{\hbar|\Delta F|} \sqrt{\frac{\mu}{2(E - E_0 - E^I)}}\right) = 1 - \exp\left(-\frac{C_{LZ}}{\sqrt{E - E_0 - E^I}}\right) \quad (3.42)$$

where E is the total rovibrational energy, E_0 is the energy of the MECP barrier, and E^I is the energy in the internal DOFs at the MECP. Finally, $|\Delta F|$ is the norm of the difference between the gradients of the 2 PESs F_1 and F_2 at the MECP: $|\Delta F| = (\partial E_1/\partial q - \partial E_2/\partial q)$ [262], where q is the space of coordinates.

According to the Landau-Zener representation, the hopping to the second spin state considering single-spin state surfaces (solid lines in Fig. 3.5) requires two transitions between the lower and higher energy surfaces (dashed lines in Fig. 3.5), namely a first hopping with probability P_{LZ} when the energy of spin state 2 is higher than that of spin state 1, and a second hopping with probability $1 - P_{LZ}$ to hop back once spin state 2 has lower energy:

$$p_{sh}(E) = P_{LZ} + P_{LZ}(1 - P_{LZ}) \quad (3.43)$$

This theoretical determination of p_{sh} is accurate in the absence of strong dynamical effects, generally relevant in small systems such as $O(^3P) + C_2H_4$ [259].

The hopping probability is finally used to evaluate the microcanonical rate constant of ISC:

$$k_{ISC}(E) = \frac{\int_{E_0}^E \rho_{TS}(E^I) p_{sh}(E - E_0 - E^I) dE^I}{h\rho_R(E)} \quad (3.44)$$

where ρ_{TS} excludes contributions of the reaction coordinate, counted in p_{sh} . For a given total energy E , the rate constant is obtained by convoluting the hopping probability at energy $E - E_0 - E^I$ with the DOS of the remaining DOFs with energy E^I . The state densities also include convolutions over the rotational state densities. Finally, $k_{ISC}(E)$ is included into the ME simulations to derive phenomenological rate constants.

3.3.3 Tunneling corrections for reactions with barriers

Rate constants calculated according to TST do not include quantum tunneling effects, i.e., the probability of an electron to penetrate through a region of space where the potential energy is higher than its energy. As a result, TST underestimates the rate constants of reactions with barriers (Figure 3.2b), especially at lower temperatures. Tunneling effects may be accounted for by solving the Schrödinger equation for the 1D motion of a particle along the reaction coordinate considering a potential barrier of the form $V(\lambda) = -A\xi(1 - \xi)^{-1} - B\xi(1 - \xi)^2$, where $\xi = -\exp(2\pi\lambda/l)$, and A, B, l are constants. While several complex models are available for the calculation of tunneling effects, in the temperature range of interest to combustion conditions this simple Eckart model [263] estimates tunneling corrections with reasonable accuracy. The Eckart model predicts relevant tunneling effects for reactions with high and narrow energy barriers, i.e., high absolute values of the imaginary frequency at the saddle point. The Eckart model is implemented in MESS [106] and requires the forward and backward energy barrier as well as the imaginary frequency at the TS.

Tunneling effects at 500 K may be as high as a factor of 1.5–2 for reactions such as H-atom abstractions from MAHs (Section 6.4), while above 1000 K tunneling corrections are generally below 30%.

3.3.4 Dealing with pressure dependence

The TST assumption of equilibrated species according to a Boltzmann distribution breaks down when chemical and energy transfer processes compete (see Section 2.1.4): at lower pressures, higher energy states are depleted by reactions, while collisions are not sufficient to repopulate them. This results in pressure dependence of the rate constants.

Lindemann theory [151] (Section 2.1.4) provides an estimate of pressure dependence of the rate constant, however it does not account for the effect of only partial energy redistribution upon collision.

A physically correct treatment of the competition between chemical reactions and energy transfer can be obtained only with a microcanonical representation of the system. The master equation (ME), presented in Section 3.3.4.1, is a population balance that describes explicitly the time-dependent energy distribution of rovibrationally excited species and therefore the

microcanonical reactive behavior of the system. This work adopts the RRKM-ME approach, where the expression for the microcanonical rate constant $k(E)$ derives from RRKM theory (Section 3.3.2.3). The quantification of the collisional energy transfer is briefly described in Section 3.3.4.2. Finally, the integration of the ME to derive phenomenological rate constants is treated in Section 3.3.4.3.

3.3.4.1 The master equation

The time-dependent multi-well ME is written in its primitive form as [264]:

$$\frac{dn_s}{dt} = \sum_u (p_{us}n_u - p_{su}n_s) \quad (3.45)$$

where n_s represents the population of the system in quantum state s , characterized by energy E and angular momentum J ; p_{su}, p_{us} are the probabilities per unit time of a transition between states s and u through collisions with the bath gas or chemical reactions.

A schematic representation of the competition between collisional energy transfer and chemical reactions in a multi-well PES is depicted in Figure 3.6 and guides the reading of this section.

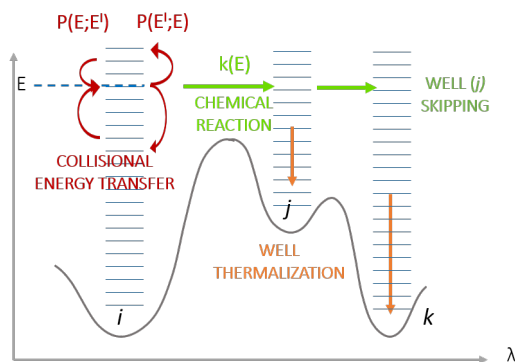


FIGURE 3.6: Scheme of the competition between energy transfer and reactive processes in a generic 3-well ME, highlighting global thermalization and well skipping processes.

Because of the large number of individual states, the ME is generally written in a coarse-grained form, i.e., it refers to the population of states with energy between E and $E + dE$. Additionally, pseudo-first order conditions are assumed also for bimolecular reactions. For a given molecular configuration i , the multi-well ME takes the form [106], [265]:

$$\begin{aligned} \frac{dn_i(E, J)}{dt} = & Z \left(\sum_{J'} \sum_{E'=0}^{E_{max}} P(E, J; E', J') n_i(E', J') - P(E', J'; E, J) n_i(E, J) \right) \\ & + \sum_{j \neq i} (k_{ji}(E, J) n_j(E, J) - k_{ij}(E, J) n_i(E, J)) \\ & - \sum_{Pr} k_{iPr}(E, J) n_i(E, J) + k_{iR}(E, J) K_{eq, iR} n_{i, eq}(E, J) n_{R_1} n_{R_2} \end{aligned} \quad (3.46)$$

where Z is the collision rate with the bath gas, i.e., the source of pressure dependence; $n_i(E, J)$ is the population of species i with energy between E and $E + dE$ and angular momentum J ; $P(E, J; E', J')$ is the probability that i turns from state (E', J') to state (E, J) upon collision, hence $Z \cdot P(E, J; E', J') n_i(E', J')$ can be regarded as a production term of $n_i(E, J)$; $k_{ij}(E, J)$ and $k_{ji}(E, J)$ are RRKM isomerization rate constants; $k_{iPr}(E, J)$ are unimolecular dissociation rate constants to bimolecular products Pr , including the reactants R ; $K_{eq,iR}$ is the equilibrium constant for the $i = R$ reaction, where R is $R_1 + R_2$; $n_{i,eq}(E, J)$ is the equilibrium population of i at the selected temperature (i.e., Boltzmann distribution); $n_{R_1} n_{R_2}$ are the population of the non-abundant fragment R_1 and of the abundant bimolecular reactant R_2 . It is noted that this form of the ME is not conservative as it does not include the formation of i from the association of products according to the "infinite sink" approximation, such that products never return to wells.

In this work, besides bimolecular association reactions treated with VRC-TST (Section 3.3.2.4), the ME is assumed independent of the angular momentum J , therefore Eqn. (3.46) can be re-written in its simpler one-dimensional form:

$$\begin{aligned} \frac{dn_i(E)}{dt} = & Z \left(\sum_{E'=0}^{E_{max}} P(E; E') n_i(E') - P(E'; E) n_i(E) \right) \\ & + \sum_{j \neq i} (k_{ji}(E) n_j(E) - k_{ij}(E) n_i(E)) \\ & - \sum_{Pr} k_{iPr}(E) n_i(E) + k_{iR}(E) K_{eq,iR} n_{i,eq}(E) n_{R_1} n_{R_2} \end{aligned} \quad (3.47)$$

The solution of the problem requires also the population of R_1 :

$$\frac{dn_{R_1}}{dt} = \sum_j \left(\sum_{E'=0}^{E_{max}} k_{jR} n_j(E) \right) - n_{R_1} n_{R_2} \sum_j \left(K_{eq,jR} \sum_{E'=0}^{E_{max}} k_{jR}(E) n_{j,eq}(E) \right) \quad (3.48)$$

3.3.4.2 Modeling energy transfer

The terms Z and $P(E, E')$ in Eqn. (3.46), (3.47), (3.48) describe the energy transfer through collisions and are therefore essential to determine the competition with chemical reactions. Because higher pressures favor well stabilization over bimolecular well-skipping channels (Figure 3.6, Section 3.3.4.3), the modeling of the energy transfer can also affect dramatically the product distribution.

In the ME solvers used in this work, Z is expressed as the Lennard-Jones (LJ) collision rate Z_{LJ} (e.g., [107]), considered satisfactory to describe collisions of polyatomic molecules with weak colliders such as diatomic molecules (N_2) or rare gases (Ar). Lennard-Jones parameters are the well depth ϵ and the hard-sphere collision parameter σ (Section 2.3), related to the chemical functionality and three-dimensional structure of the species. In many cases, LJ parameters are available in physical chemistry or chemical engineering books [266], [267]. Alternatively, they can be estimated from molecules with similar steric hindrance and functional groups or predicted with trajectory-based rules, as in [115].

The energy transfer function $P(E, E')$ (written in its 1D form for simplicity) is commonly described according to the single exponential-down model

$$P(E; E') = \frac{1}{C(E')} \exp\left(-\frac{E' - E}{\langle \Delta E_{down} \rangle}\right), E \leq E' \quad (3.49)$$

where $C(E')$ is the normalization constant and $\langle \Delta E_{down} \rangle$ is the average energy transferred in a deactivating collision. Trajectory simulations proved that $\langle \Delta E_{down} \rangle$ is dependent on temperature and may be described as a function of 2 parameters: $\langle \Delta E_{down} \rangle = \Delta E_{down}^0 \left(\frac{T}{298K}\right)^n$. While some of the assumption of the single exponential-down model are unphysical (such as the modeling of a single exponential or the independence of $\langle \Delta E_{down} \rangle$ from energy) [200], [247], the description of Eqn. (3.49) works well in practical applications if the two parameters are determined appropriately. Experimental data with different colliders are available for only a few cases, therefore ΔE_{down}^0 and n are commonly used as adjustable parameters in theoretical calculations, however the resulting model might not be predictive at different conditions. Recently, Jasper and coworkers [99], [111], [112], [268] showed the power of classical trajectory simulations combined with 2D ME simulations for an accurate description of the energy transfer, obtaining $< 25\%$ deviation from experimental data. This massive work also highlighted trends in $\langle \Delta E_{down} \rangle$ with system size, functional groups, and bath gases. As a result, Jasper [115] recently developed simple trajectory-based rules for the derivation of LJ and exponential-down model parameters, which are based on only structural information of the molecule.

In this work, the parameters for the exponential-down model were adopted from the literature (where available), from structural analogues, or from the rules of Jasper.

3.3.4.3 From ME to phenomenological rate constants

Understanding the connection between the ME and phenomenological rate constants is essential to the proper use of theoretical kinetics for macroscopic kinetic modeling. The development of a robust procedure to determine the phenomenological rate constants from the ME solution has required significant effort, with key advancements obtained thanks to the seminal works of Bartis and Widom [264], [269] and of Miller and Klippenstein [265], [270], [271].

A common solution procedure for the ME is the formulation of Eqn. (3.45)-(3.47) as an eigenvalue problem. Depending on the energy grid adopted, a huge number of eigenvalues λ_l can be obtained. However, only the least negative $N_{chem} = N - 1$ (where N is the number of species) are relevant to describe the chemical evolution of the system in time (i.e., macroscopic change in species concentration). These are called "chemically significant eigenvalues" (CSEs) and are directly related to phenomenological rate coefficients. All the other eigenvalues describe the much faster relaxation in the internal degrees of freedom of the species, and are thus called "internal-energy relaxation eigenvalues" (IEREs). Because of the large number of IEREs as well as the narrow spacing between them, the set of IEREs is sometimes referred to as a "quasi-continuum" of IEREs. Details of different solution

approaches for the eigenvalue problem are reported extensively in the literature published in the past decades [265], [270], [272], [273] and only a few concepts are recalled here.

The time evolution of the population of $n_i(E)$ can be obtained from the CSEs of Eqn. (3.47). Integration over the energy of $n_i(E, t)$ allows one to derive the time evolution in the macroscopic population of chemical species I : $X_I(t) = \sum_{E=0}^{E_{max}} n_i(E, t)$. The X_I time-dependent profiles are then post-processed to determine rate coefficients that satisfy the phenomenological law:

$$\frac{dX_I}{dt} = \left(- \sum_{J \neq I}^N k_{IJ} \right) X_I + \sum_{J \neq I}^N k_{JI} X_J \quad (3.50)$$

written in compact form as $\frac{dX}{dt} = \mathbf{K}X$. For a set of N species, k_{IJ} constitute a unique set of phenomenological rate coefficients, which can be expressed as a linear combination of the exponential functions of the CSEs, considering that $X_I(t) = \sum_{l=0}^{N_{chem}} a_{Il} e^{\lambda_l t}$, where $-a_{Il}$ is the change in the population of I associated to eigenmode l for the selected initial conditions [265], [270], [273]. For single-well PESs, the relation between the single CSE obtained and the phenomenological rate coefficient is straightforward, while for large multi-well PESs the relation between λ_j and k_{IJ} becomes complex. In these cases, well-defined k_{IJ} can generally be obtained when the timescales of IEREs and CSEs are sufficiently separated, such that N_{chem} are easily recognized [265], [269], [274].

ME simulations not only result in pressure dependence of the phenomenological rate constants obtained, but also produce new reaction channels with respect to a pressure-independent network. At the high-pressure limit, i.e., if pressure dependence was not considered, wells are fully thermalized. Therefore, the number of rate constants obtained for reversible reactions is equal to the number of TSs on the PES. On the other hand, at lower pressures it is possible for wells to convert directly into other isomers or decompose to bimolecular products through "well-skipping" processes, i.e., prior to collisional stabilization of the visited intermediate wells (see Figure 3.6). Hence, the total number of reversible reaction channels and corresponding phenomenological rate constants in the fall-off regime becomes $N(N - 1)/2$. This complicates the reaction network, especially considering that it is usually difficult to identify the key reaction steps without a kinetic simulation.

The extreme case of the scenario described above is that at higher temperatures and lower pressures (faster chemical reactivity and fewer collisions) a well is never thermalized through collisions, such that it does not "exist" from a phenomenological standpoint as it does not attain even a partial thermal energy distribution. This occurs when the lifetime of the well is comparable to the rovibrational relaxation timescale, i.e., CSEs and IEREs merge. As a result, the number of both phenomenological rate constants and species obtained from the ME becomes temperature and pressure dependent. Thermal stabilization of wells in a limited range of operating conditions represents an important challenge in the integration of ME-derived rate constants into kinetic mechanisms and is discussed in Chapter 4.

In this work, ME simulations were mostly performed using MESS [106] (available at <https://github.com/Auto-Mech/MESS>), which solves the ME based on the CSE method.

Stochastic methods such as kinetic Monte Carlo (KMC) can also be used to derive phenomenological rate constants from the ME, with the advantage of avoiding direct integration. For instance, Barbato et al. [107], [275] implemented a MC-RRKM approach, where the reactivity is started by a collisional event of a selected reactant. Then, the system evolves through random events according to the respective probabilities, associated to collision frequencies and RRKM rate constants. The species populations obtained from a large number (e.g., 10000 considered in this work) of reactive events accurately represent the average reactivity and are directly related to the product branching fractions. In this work, the MC-RRKM approach was used only for multi-well PESs involving ISC (Section 3.3.2.6), i.e., for the $O(^3P) + C_6H_6$ PES described in Section 6.3.1.

3.4 Semi-automated calculation of rate constants

The theoretical methodologies described in Sections 3.1, 3.2, and 3.3 were implemented in several codes available in the literature. In this work, most of the ES calculations were performed in the automated EStokTP framework [97], described in Section 3.4.1. The derivation of the thermochemical parameters starting from the output of ES calculations was performed with Auto-Mech, briefly presented in Section 3.4.2. While these codes largely automate most of the theoretical calculations described, this section is labelled "semi-automated" because of the consistent user effort required for both input preparation and careful checks of the generated output.

3.4.1 EStokTP

EStokTP (Electronic Structure to $k(T, p)$) [97] (available at <https://github.com/EStokTP/EStokTP>) is an open-source automated framework for electronic structure calculations for chemical kinetics. EStokTP relies on external codes such as Gaussian G09, G16 [72] and Molpro [202] for electronic structure calculations and on MESS for master equation simulations [106] (Section 3.3.4.3).

EStokTP treats elementary reaction types connecting a set of specified reactants and products. Therefore, the construction of all the possible channels on a multi-well PES was performed step by step, while an external bash script was used to build the final input for multi-well ME simulations for MESS. Supported reaction types are: bond breaking (β -scission, bond-fission), addition (which also includes backward β -scission processes), isomerization (i.e., atom/group migrations, ring opening/closure), abstraction, ISC. Each of these types correspond to a different TS search protocol as well as slightly different input structure. These protocols generally include more than one of the elementary reaction types listed in Section 2.6. For instance, the TS of an elimination reaction such as H₂O elimination (e.g., Section 5.3.2) can be found from the H-migration protocol and treated as an isomerization with two products. Finally, while no specific protocol for concerted reactions is available, it is possible to perform a TS search using 2-dimensional grids (i.e., a reaction coordinate combining two internal DOFs). Among all of the reaction channels investigated in this work, only a few required manual TS guesses, such as ring insertion or isomerization through torsions on the C₆H₅ + O₂ PES (Section 6.3.3), and the MECP on the C₆H₆ + O(³P) PES (Section 6.3.1).

Figure 3.7 presents a schematic overview of the steps performed within EStokTP for the derivation of rate constants for a single reaction channel. This structure applies to all reaction types with the exception of barrierless reactions, treated later in this section. The purple boxes in Figure 3.7 indicate user inputs. For each reaction, a guess for the geometry of the reactants (and optionally of products) and for the symmetry number is required. The geometry is provided in the form of a z-matrix, i.e., in internal coordinates specifying the 3N-5/6 internal DOFs. The reaction type must be specified, together with a grid to be used by the TS search protocol (e.g., scan along the reaction coordinate for a β -scission reaction from 1.3 to 2.0 Å with a step of 0.2 Å). If present, internal coordinates corresponding to

hindered rotations should also be indicated. The user also specifies the level of theory for the ES calculations performed. Level 0, Level 1 and high level (HL) in Fig. 3.7 refer to the levels of theory for initial structure optimization, final structure optimization and frequency calculation, and single point energies (SPEs) of the stationary points at the most accurate level adopted, respectively. The levels of theory for the derivation of hindered rotor potential, symmetry analysis, and IRC scan can in principle all be different, however in this work they were generally set equal to Level 1.

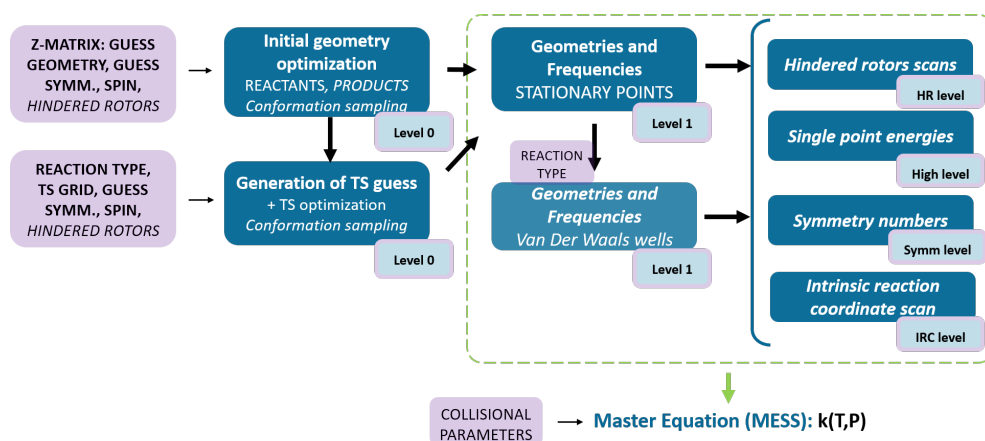


FIGURE 3.7: Schematic representation of the steps automatically performed by EStokTP. The purple boxes/contours indicate user inputs, while italics refers to optional steps.

The first step in Figure 3.7 is the optimization of the geometries of reactants (and products) at Level 0, which provides reasonable guesses for geometry optimization at a higher levels. This step was always performed with DFT methods using Gaussian G09, G16 [72], where geometry optimization is based on a quasi-Newton algorithm. The total energy (Eqn. (3.5)) is minimized with respect to the set of nuclear coordinates (\mathbf{R}) updated according to a Newton-Raphson scheme $\mathbf{R}' = \mathbf{R} - \mathbf{H}^{-1}\mathbf{g}$, where \mathbf{g} is the gradient and \mathbf{H} is the Hessian. Convergence criteria are based on the maximum and root mean square force and displacement. Level 0-optimized geometries for reactants are employed to generate a TS z -matrix and guess geometry according to the reaction type. The maximum identified with the grid scan along the specified reaction coordinate(s) is used to perform the Level 0 TS optimization. For all stationary points, random sampling of selected dihedral angles can be performed to find the minimum Level 0-energy conformer.

Level 0-optimized geometries for reactants, products and TS are guesses for Level 1 geometry optimization and frequency calculation. The results are used to determine ZPEs and the other quantities to derive DOS or partition functions for the final rate constant calculation. For addition and abstraction reaction types, the Level 1 TS structure can be used as a guess for the optimization of van der Waals entrance and exit complexes. This optimization is performed upon displacement of the reacting fragments along the reaction coordinate in the direction of the reactants or the products, using redundant coordinates.

Level 1 optimization is in principle sufficient to derive the rate constant for the elementary reaction channel. The theoretical treatment should however be improved with the steps illustrated on the right side of Figure 3.7:

- Hindered rotor scans corresponding to torsional motions with low barriers (i.e., misrepresented with RRHO, see Section 3.2.2).
- Calculation of symmetry numbers: external symmetry is identified based on external axes of symmetry; optical isomers are detected; configurations at local minima of HR potentials are further optimized to verify redundancy.
- Single point energies at a high level: the electronic energies at the stationary points are refined. This step is crucial as the energy barrier is generally the largest source of uncertainty for the rate constants obtained (see Section 3.5.2). In this work, this step was performed at the CCSD(T)/CBS level of theory or with MR methods (Section 3.1.3).
- Intrinsic reaction coordinate scan: IRC scan (Section 3.3.2.2) verifies that the optimized TS connects the desired reactants and products and allows implementing VTST.

This set of information is then used to automatically generate input files for MESS simulations. MESS output contains temperature and pressure dependent phenomenological rate constants.

Figure 3.8 depicts the steps performed within EStokTP for the calculation of reaction fluxes for barrierless reactions. In fact, additional calculations must be performed for the automated generation of the input for VaReCoF, used to compute the flux associated to transitional modes $N^t(E', J)$ (see Section 3.3.2.4).

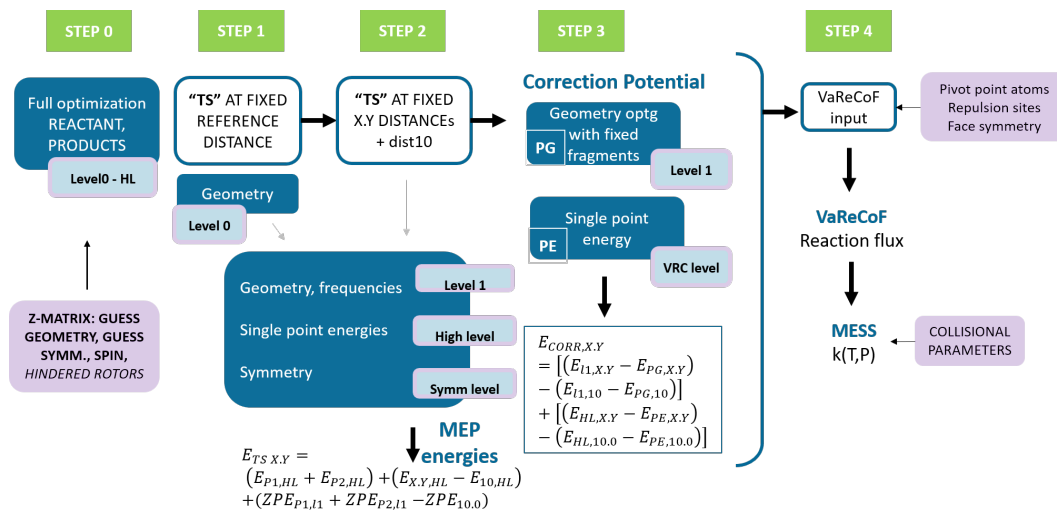


FIGURE 3.8: Schematic representation of the steps implemented in EStokTP for barrierless reactions. The purple boxes/contours indicate user inputs. Filled blue boxes indicate steps where calculations are performed.

EStokTP generates the MEP for the barrierless reaction in STEP 0–2 of Figure 3.8. This MEP may be readily used for VTST calculations. STEP 3 instead derives a distance-dependent correction potential according to the level of theory chosen for the conformational sampling in VRC-TST (see Section 3.3.2.4). This potential is then provided as an additional input for the derivation of $N^t(E', J)$ flux in STEP 4. The main tasks performed in each step of Figure 3.8 are:

0. Geometry optimization, frequency calculation, and SPE refinement for both the well (the reactant) and the fragments (the products), corresponding to the full workflow of Figure 3.7 for reactants and products.
1. Constrained geometry optimization at Level 0/1 is performed at a reference value for the reaction coordinate, i.e., a fixed distance X.Y for the breaking bond. High level SPE and symmetry number are also calculated. No TS search is performed because of the barrierless nature of the process considered.
2. The output of STEP 1 is used as a guess (for both geometry and AS selection in the case of MR calculations) for Level 1 constrained optimization of all user-specified X.Y distances along the MEP. A default distance of 10 Å provides the energy for the fragments at the same level of theory. For all X.Y distances, HL energy and symmetry number are also calculated. MEP energies are finally computed at each distance ($E_{TSX,Y}$ at the bottom of Figure 3.8) relative to the 10 Å distance.
3. The correction potential E_{CORR} is derived at each X.Y separation to scale the energies of the configurations sampled in VaReCoF to pseudo-HL energies. VaReCoF considers fixed fragment geometry and a lower level of theory (VRC level). Therefore, E_{CORR} accounts for both geometry relaxation (PG) and energy difference between high and VRC levels (PE) at each X.Y distance, as reported in Figure 3.8.
4. The correction potential, together with user-defined information on pivot point placement (i.e., reacting atoms and additional sites for repulsion potentials) as well as on the symmetry of the dividing surfaces considered for the sampling (see Section 3.3.2.4) are used to generate the input for flux calculations in VaReCoF. The flux obtained from VaReCoF is read by MESS for the calculation of $k(T, p)$.

3.4.2 Auto-Mech

Auto-Mech [98] is a recently built open-source programming package (available at <https://tcg.cse.anl.gov/papr/codes/automech.html>, <https://github.com/Auto-Mech/>) for the calculation of high-accuracy thermochemistry and rate constants via automated workflows. Auto-Mech workflow is conceived to treat full CHEMKIN mechanisms. It works with species identifiers such as InChIs and it is able to compute rate constants for a selected reaction in a kinetic mechanism without the need of further specifications. In principle, it is able to identify automatically the reaction type, the presence of hindered rotors, as well as guess geometries and symmetry numbers (all user-defined inputs in EStokTP, see Figure 3.7). Most importantly, Auto-Mech includes libraries for the calculation of accurate thermochemistry according to multiple CBH schemes (see Section 3.2.3). On the other hand, Auto-Mech is still unable to perform automated VTST and VRC-TST calculations, which is a unique feature of EStokTP.

In this work, Auto-Mech was used only to post-process the results of ES calculations performed with EStokTP to derive thermochemical parameters in the form of NASA polynomials.

A simple Auto-Mech script was used to read geometry, frequencies, symmetry and hindered rotor potentials of a selected optimized species. Auto-Mech then calls MESS to derive the corresponding partition functions. This information was then combined with the formation enthalpy computed according to the simple isogyric scheme (Section 3.2.3) to derive thermochemical properties (Eqns. (3.30), (3.31), and (3.32)). Finally, Auto-Mech libraries perform the fitting to NASA polynomials, such that the results are readily included in CHEMKIN format kinetic mechanisms.

3.5 Application of computational chemistry to MAH reactive systems

This section expands on some relevant aspects treated in the rest of this chapter to provide guidelines for theoretical calculations for MAH reactive systems as well as reasonable uncertainty estimates for the theoretical rate constants presented in this work.

3.5.1 Computational cost

The large number of heavy atoms of MAHs and PAHs does not allow one to apply as accurate ES methods as for small systems. For instance, coupled cluster can certainly be used for geometry optimization, however it is currently inapplicable to systems with more than 4-5 heavy atoms using the cc-pVTZ basis set.

The main cluster used for the theoretical calculations of this work had 16 nodes with 2.7 TB shared disk memory and 16 processors for a total 64 GB of ram in each node. Computational limits listed in this section refer to this server.

As anticipated in Section 3.1.3, the calculation of high level single point energies is generally the most expensive step in ES calculations, where coupled cluster (CC) calculations scale as N^7 , (N is the number of heavy atoms in the system). In this work, CCSD(T)/aug-cc-pVTZ calculations were performed on systems up to 9 heavy atoms (e.g., H ipso-substitution on $\text{HOC}_6\text{H}_4\text{OCH}_3$, H-atom abstraction from C_9H_8), taking up to 2-3 days. The computational cost of CCSD(T)/cc-pVTZ is only slightly lower.

CASPT2/aug-cc-pVTZ energies (see Section 3.1.3.3, 3.1.3.4) were computed for a large number of reactions in this work. With the available computational resources, the largest active space at this level of theory consisted of 15 electrons and 13 orbitals. An AS of (17e,15o) was prohibitive even with a small basis set. For the largest ASs, a SPE calculation took no longer than 1.5 days.

CASPT2 structure optimization can be performed only with smaller basis sets and active spaces, because of the high computational cost for the calculation of the hessian matrix. In this work, cc-pVDZ and cc-pVTZ were adopted using an AS up to (11e,9o) for systems with up to 8 heavy atoms. The most computationally expensive geometry optimization was performed for the H-atom abstraction by OH from phenol at CASPT2(13e,11o)/jun-cc-pVTZ level (Section 6.4), which required several weeks of calculations running in parallel on 16 different nodes.

CCSD(T) and CASPT2 calculations just described are unfeasible for PAHs. In this work, only DFT methods were used for PAHs. DFT methods (Section 3.1.4) were also employed for the geometry optimization and frequency calculation of almost all reactions investigated in this work. The employed density functionals M06-2X, ω B97X-D, and B2PLYPD3 have comparable computational cost and were never the bottleneck in terms of computational time. However, the computational cost for the frequency calculations using jun-cc-pVTZ and aug-cc-pVTZ basis sets increased significantly with respect to the cheaper 6-311+G(d,p) basis. IRC calculations or anharmonic frequency analysis took up to about one week for systems with 7-8 heavy atoms, obtaining no significant change in the resulting frequencies

and therefore zero point energies and rate constants. Therefore, this work mostly adopted the cheaper 6-311+G(d,p) basis set.

Finally, rate constant calculation for barrierless channels is the most demanding reaction type treated in this work in terms of both human hours and computational cost. The computational cost of VaReCoF calculations depends on the system size, the level of theory chosen for the sampling, and the number of surfaces and samplings selected. CASPT2 calculations for configuration sampling used smaller AS and basis sets with respect to high level energies (from (2e,2o) to (10e,8o), with cc-pVDZ basis set). A minimum of 200 samplings for each surface, was imposed, resulting generally in > 5000 samplings for each reaction. Calculations run in parallel on ~ 4 processors on ~ 4 – 10 nodes took up to one week for systems with 7–8 heavy atoms.

3.5.2 Uncertainty estimate for rate constants

Uncertainty quantification is an essential and often neglected part of theoretical kinetics and an increasingly important task for the construction of physically sound kinetic mechanisms [84]. The uncertainty of estimated kinetic parameters is used as a "degree of freedom" in the development of kinetic mechanisms, as well as in the interpretation of experimental data with small sub-mechanisms of few reactions. Similarly, kinetic parameters with negligible uncertainty (e.g., determined with very accurate experiments or theoretical methodologies) may be considered "fixed", thus helping to identify sources of higher uncertainty or missing reaction pathways.

The recent exponential increase in the number of theoretically derived kinetic parameters in global kinetic mechanisms, together with the automation of mechanism optimization, has made uncertainty quantification even more crucial. In fact, mechanism optimization relies on penalties assigned to rate constants based on their uncertainty [276], [277]. The work of Bertolino et al. [277] proposed for the first time the variation of uncertainty bounds based on the analysis of the level of theory used for the rate constant calculations.

Finally, estimating the uncertainty of the kinetic parameters of a reaction based on the theoretical methodology may even be used to decide whether it is worthwhile to perform theoretical calculations at all. In fact, in some cases rate-rule estimates and feasible theoretical calculations have comparable uncertainties, such that computational time may just be of better use for something else. For example, calculating rate constants of recombination reactions between radicals using low-level DFT methods and VTST with poor treatment of anharmonicities easily produces errors of one order of magnitude or larger, as well as an incorrect temperature dependence.

Unfortunately, assigning uncertainty to a theoretically derived rate constant is a critical and to some extent arbitrary task. ES methodologies are validated with large sets of experimental data (or directly parametrized on experiments [208]) or theoretical calculations at a higher level of theory [194]. Data types used for validation generally include excitation energies, reaction energies, or molecular spectra. However, these experimental data do have their own uncertainties and involve only limited classes of atoms and compounds. The application of a theoretical methodology to a new class of compounds or of reactions

may not be equally accurate: very few validation studies of theoretical methodologies are available for MAHs. Finally, exceptions do exist and therefore tested cases may have unexpectedly large uncertainty. For instance, in this work unsuspected MR or anharmonic effects were highlighted thanks to comparisons with experimental data. However, in the absence of experimental data the supposedly "gold standard" methodology adopted would have been considered reasonably accurate.

The choice of the kinetic theory also contributes to the uncertainty of the rate constant. For instance, a largely neglected source of uncertainty is that of energy transfer parameters.

Fortunately, error compensation effects can drastically reduce the inaccuracy of the kinetic parameters. While error cancellation is a well-known phenomenon in ES calculations, the simultaneous effects of different aspects of the calculation, e.g., compensation between overestimation of SPE and underestimation of ZPE, are almost unpredictable.

For all the reasons listed above, uncertainty of the calculated rate constants is often underestimated in the literature. Because of the high number of uncertainty sources, theoretical calculations should at least be performed with methodologies that are validated in the literature or considered appropriate for the type of reaction investigated. Different reaction types require different theoretical treatments, as summarized in Table 3.1. Important exceptions found in this work are also listed. This table is used as a reference for the discussion of this section about the impact of different aspects of theoretical calculations on the final rate constants.

TABLE 3.1: Recommended methodologies for ES and kinetic calculations by reaction type. Italics highlights the preferred method if more than one alternative is listed. M and R indicate molecules and radicals, respectively. CCSD(T)/CBS and spin split refer to the theoretical protocols of Eqn. (3.11), (3.16), respectively. * warns about possible need for MR geometry optimization.

REACTION TYPE	GEOMETRY FREQ.	ENERGY	KINETIC THEORY	EXCEPTIONS (require MR SPE)
ISOMERIZATION (H TRANSFER, RING OPENING)	DFT	CCSD(T)/CBS	CTST VTST	ring insertion* or opening involving C-O/O-O Formation of resonance involving C-O (through H transfer)
ISC	DFT <i>MR</i>	MR	NA-TST	
CONCERTED ELIMINATION (M/R→R+M)	DFT	CCSD(T)/CBS	CTST VTST	CO/CO ₂ elimination
ABSTRACTION (M+R→R+M)	DFT	CCSD(T)/CBS	VTST	ring excited states involved (A1-M+H) multiple oxygens interacting (A1,OH-M+OH*/O ₂)
ADDITION/BETASC. (M+M→M) (M+R→R)	DFT	CCSD(T)/CBS	VTST	
RECOMBINATION/ BONDFISSION (R+R→M)	DFT <i>MR</i>	MR CCSD(T)/CBS <i>+spin split</i>	VTST <i>VRC-TST</i>	
RADICAL ABSTRACTION (R+R→M+M)	DFT MR	<i>CCSD(T)/CBS</i> <i>+spin split</i> MR	VTST VRC-TST	

3.5.2.1 Geometry and vibrational frequencies

Geometry optimization and frequency calculation using DFT methodologies have reasonable accuracy. Notable exceptions where MR methods are preferred are radical-radical reactions, ISC, and reactions involving bond breaking/formation of oxygen atoms with significant state

mixing (see Table 3.1). In this work, the largest difference in the optimized geometry between DFT and MR levels was found for the H-atom abstraction reaction by OH from the hydroxy group of phenol (see marked* entries in Table 3.1), with differences in the resulting rate constants larger than one order of magnitude. Besides the exceptional case of oxygen insertion in the aromatic ring (Section 6.3.3), the DFT methods used in this work provided similar geometries when compared. The SPEs were almost insensitive to the choice of the functional / basis set within the chosen set.

On the other hand, vibrational frequencies and ZPEs and consequently energy barriers (SPE + ZPE) are more sensitive to the choice of the functional. In this work, it was found that ν_i for some torsional or bending modes may differ with the type of functional and basis set employed. B2PLYPD3 generally results in increased ZPEs, especially for TSs of unimolecular reactions, with the increase in the energy barrier being as large as 0.5 kcal/mol. The most notable difference was found between ω B97X-D and B2PLYPD3 results for the vibrational frequency of C₅H₅ associated with the Jahn-Teller distortion (Section 5.3.2.3), which probably relates to the peculiar nature of this motion. Instead, comparison between M06-2X and B2PLYPD3 in H-atom abstraction rate constants from benzene resulted in almost identical rate constants (differences of only a few %).

While B2PLYPD3 should provide higher accuracy than M06-2X and ω B97X-D due to its MP2 component, no systematic study on MAHs proves it. The performance of less expensive DFT methods such as ω B97X-D/6-311+G(d,p) seems to provide good accuracy based on comparisons with B2PLYPD3 and experimental data, and is probably preferred to the heavily parametrized M06-2X functional.

Vibrational frequencies derived at the CASPT2 level are even more sensitive to the choice of the AS and basis set. With the limited basis sets and ASs used in this work, CASPT2 frequencies are probably less accurate than those derived at DFT level (when appropriate). Additionally, convergence criteria implemented in Molpro are generally less restrictive and the output also requires more careful reading (e.g., warnings are provided for poor convergence, but no error message is shown).

Finally, it is highlighted that large errors generally arise from improper treatment of anharmonicities (see Section 3.5.2.4) rather than absolutely wrong values of the calculated frequencies.

3.5.2.2 Electronic energy

Determining accurate electronic energies along the MEP is essential to obtaining reliable rate constants and to deriving the correct temperature dependence. Because of the \sim exponential dependence of $k(T)$ on the apparent activation energy, errors in the energy barriers are often the largest source of uncertainty in theoretically-derived rate constants.

Table 3.1 shows that for many unimolecular (except for ISC) and molecule-radical reactions, the so called "gold standard" CCSD(T)/CBS methodology (Section 3.1.3.2) should suffice to derive accurate energy barriers. Comparison with experimental data performed in this work and other literature studies suggest that CCSD(T)/CBS barriers have errors below 1 kcal/mol for most H-atom abstraction, addition, and isomerization reactions. However,

channels with strong MR character were present also among these classes, as listed in the exceptions of Table 3.1. CCSD(T)/CBS discrepancies with respect to MR values are clearly case dependent, varying from 1–2 kcal/mol to above 10 kcal/mol. In most cases, MR character is highlighted by a high T1 diagnostic (Section 3.1.3.3). In this work, two TSs with high MR character and low T1 diagnostic were also found (H-atom abstraction by H from benzene, decarbonylation in phenol decomposition).

MR methods are instead always necessary to derive accurate SPEs for both radical-radical reactions and ISC. In the case of radical abstraction reactions, the spin splitting approach seems to be preferred to MR calculations on the low-spin PES. For barrierless reactions DFT methodologies may provide reasonable predictions of the geometries along the MEP, however energies generally have high errors and may even result in fake energy barriers along the MEP.

The accuracy in MR energies strongly depends on the AS and basis set selected. AS and basis set "convergence" may be checked by comparing energy barriers obtained by progressively increasing the basis set or AS size. As noted in Section 3.1.3.3, the π space must always be included in aromatic systems. RS2 calculations for oxygenated species require level shifts, which increase the energy barriers by up to 1–3 kcal/mol. Finally, state averaging is necessary for quasi-degenerate states and are often required for non-symmetrical wavefunctions including oxygen lone pairs. Overall, the uncertainty for energies computed at the CASPT2/aug-cc-pVTZ level with a converged AS may still be higher than 1 kcal/mol. The calculations of this work show that very good agreement with experimental data (factor < 2) can be obtained for barrierless recombination reactions. The highest uncertainty in the energy barriers investigated in this work is certainly that for the oxygen ring insertion on the $C_6H_5+O_2$ PES, also due to computational limitations (Section 6.3.3).

Finally, energy barriers for reactions involving PAHs were only treated with DFT methods, which are believed to achieve an accuracy of a few kcal/mol. In this work, the comparison between ω B97X-D/6-311+G(d,p) or M06-2X/6-311+G(d,p) and CCSD(T)/CBS energies for abstractions and additions on MAHs agree to within 1–2 kcal/mol. Assuming that DFT and CC methods have similar differences in larger PAHs, it may be possible to approach CCSD(T)/CBS accuracy from corrections derived for MAH systems (Sections 5.3.1.3, 6.4.4, and 6.5.3.1).

3.5.2.3 Kinetic theories

Table 3.1 shows that different reaction types also require the application of different kinetic theories. The uncertainty of the rates of ISC determined with NA-TST depends heavily on the system treated and is discussed separately in Section 6.3.1.

CTST is only appropriate for unimolecular reactions and elimination reactions with tight barriers such as H transfer or H_2O and CO_2 elimination, as clarified in Section 3.3.2.

VTST is needed for all other cases (barrierless recombination reactions are discussed later). The variational treatment may decrease the calculated rate constants by up to a factor of 2–4 with respect to CTST for reactions with flat barriers such as in H-atom abstractions by OH (see Sections 6.4 and 6.4.3.3). The accuracy of VTST depends on the accuracy in the

description of the energy and partition functions along the MEP. In this work, the energy along the MEP obtained at the DFT level for reactions with a barrier was scaled according to the HL - DFT energy difference at the TS. This approach provides good scaling when the electronic configuration does not change dramatically along the scanned MEP (an exception is discussed in Section 6.3.3.5).

As far as vibrational frequencies are concerned, their accuracy along the MEP depends both on the functional employed and on the selection of coordinates (Cartesian or internal) for the calculation of the Hessian outside of the TS. A density functional heavily parametrized on stationary points such as M06-2X is expected to perform worse at λ far from the TS. This is probably one of the reasons for the heavy variations observed between Cartesian and internal coordinate frequencies in H-atom abstraction reactions on MAHs (Sections 6.4 and 6.4.3.10). For these cases (and OH, O₂ abstractors in particular), the uncertainty in the rate constant is estimated to increase by a factor of 2. Another assumption potentially increasing the uncertainty of the partition functions along the MEP is that the hindered rotor potentials were considered equal to those at the TS. The validity of this assumption was not verified. However, it is not expected to produce dramatic variations in the partition functions in the present calculations.

VTST can also be applied to barrierless recombination reactions. In this work, VTST was used for the recombination of H with the phenoxy radical (Section 6.3.2). While the error in recombination rate constants computed with VTST is probably larger than careful VRC-TST calculations, VTST can provide accurate results when the vibrational frequencies along the MEP are meaningful (e.g., no second order saddle points) and the minimum of the flux is reached at relatively short λ in the temperature range of interest. For these conditions, VTST may vary with respect to VRC-TST by a factor < 2 .

VRC-TST is able to provide recombination rate constants of experimental accuracy (e.g., few % discrepancy with experimental results [200]). However, because of the poor automation of VRC-TST, results are currently very user-dependent. Each step of the calculation requires extremely careful checks in terms of e.g., active space selection, pivot point selection, convergence of ES calculations and of the flux on multifaceted surfaces, as well as the complexity of the reaction [278]. Using the procedure described in Section 3.3.2.4, in this work agreement within a factor of 1.3 from state-of-the-art theoretical calculations and experimental data was obtained.

3.5.2.4 Anharmonicities

Section 3.2.2 anticipates that anharmonicities may have a great impact on rate constants. Errors in the RRHO treatment derive from improper representation of potentials associated with internal motions having low barriers.

In aromatic hydrocarbons, anharmonic effects are less relevant than in other types of species such as alkanes due to their rigid structure. However, important anharmonic effects may result from the presence of lateral groups with hindered torsions, such as in phenol, catechol, toluene, etc., or in bimolecular reactions where TS structures have rotating groups, such as C₆H₆ + OH (Section 6.4.3.3).

When the number of HRs in the TS and in the reactant is different, or energy barriers for the respective HRs differ significantly, the HR treatment may change the rate constant by factors > 2 with respect to RRHO. Unfortunately, using HR models does not always guarantee accuracy. Strongly interacting groups (e.g., two adjacent OH groups in catechol) should be treated with 2DHR models, which sometimes differ substantially from 1DHR results. However, computational demand for such 2DHR treatments can be excessive. When the rotating group is asymmetric and large, the choice of the theoretical method used to determine the moments of inertia may also impact the results.

Finally, in TSs of bimolecular reactions where the rotating group in the torsional motion includes both fragments there may even be some arbitrariness in the choice of the vibrational frequency to be projected out of the Hessian. Examples from this work (Section 6.4) include $\text{OCH}_3\text{-CH}_3$, $\text{OCH}_3\text{-OH}$, $\text{OCH}_3\text{-O}_2$, $\text{CH}_3\text{-O}_2$ rotating groups in the H-atom abstractions from anisole by CH_3 , OH , O_2 and from toluene by O_2 , respectively. The chosen frequency associated to the torsion may be that of the single substituent (i.e., the same as that of the reactant), or that of the lateral substituent rotating together with the abstractor, which is generally lower and sometimes closer to a bending motion. The chosen frequency may even change along the MEP, as implemented in EStokTP and Auto-Mech subroutines (code available at <https://github.com/Auto-Mech/ProjRot>). Different choices have an impact up to a factor of 5–6 on the rate constant, as discussed in Section 6.4. In this work, the frequency chosen for projection was always that including both the substituent and the abstractor, consistent with the torsional potential derived. Comparisons with experimental data seem to confirm the appropriateness of this choice.

Finally, anharmonic corrections for the ZPEs are not expected to impact significantly the investigated rate constants. However, in the case of loose motions at the TS, corrections to ZPEs may need to be included. In this work, anharmonic frequency analyses were only performed for H-atom abstractions from benzene and toluene (Section 6.4), finding that anharmonic corrections to the ZPE are significant (up to 0.79 kcal/mol) for the OH abstractor.

3.5.2.5 Minor sources of uncertainty

Minor sources of uncertainty for the present rate constants not discussed in the previous sections include:

- **Tunneling effects:** tunneling effects (Section 3.3.3) are mostly relevant at low temperatures. At combustion conditions, they may increase the rate constant by a factor of 2–1.5 at 500 K for tight TSs (e.g., H-atom abstractions by H), while above 1000 K tunneling effects are generally below 30%. Tunneling corrections computed according to the asymmetric Eckart model as in this work are affected by the imaginary frequency at the TS and by the barrier height. Variations by 2–3 kcal/mol in the energy barriers for H-atom abstraction reactions related to the uncertainty in the DFT energy of van der Waals wells were found to have an impact of less than 10% on the estimated rate constants in the 500–2000 K range. The uncertainty in the imaginary frequency at

the TS might also impact the resulting tunneling corrections. Because of the difficult estimation of this uncertainty, this aspect was not quantified in this work.

- **Energy transfer parameters:** energy transfer parameters are essential to determining the pressure dependence of reactions occurring on multi-well PESs. Luckily, the pressure dependence for large bulky species is less sensitive to these parameters. In this work, reasonable estimates were mostly adopted from literature. Sensitivity to collisional efficiency and exponential down model parameters was tested for $\text{HO}_2 + \text{C}_5\text{H}_5$ and $\text{C}_6\text{H}_5 + \text{O}_2$ PESs (i.e., using parameters from different sources), resulting in negligible variations in the rate constants.
- **Fitting and lumping:** fitting quality can also affect the uncertainty in the rate constants obtained. Poor fitting quality of modified Arrhenius expressions can be amended by multiple (modified) Arrhenius expressions. In particular, rate constants from multi-well PESs involving the competition between well-skipping and thermalization reactions may result in strong non-Arrhenius temperature dependence and large values of the α exponent in Eqn. (2.3). All rate constants from theoretical calculations of this work also include the fitting quality in the form of R^2 .

A High uncertainty in kinetic modeling may also stem from rate constants defined over limited temperature ranges (Section 3.3.4.3). When isomers are lumped together, the temperature range where the pseudo-species is defined may increase, thus providing good approximations for a wider range of operating conditions (see Chapter 4). On the other hand, lumped rate constants intrinsically have additional errors that heavily depend on user choices. In this work, bad fitting quality of lumped rate constants at low temperatures (e.g., 500–700 K) was generally accepted for the sake of mechanism simplification. These aspects are discussed in Chapter 4.

3.5.2.6 Comparison with experimental data

The uncertainty of a theoretical methodology is mostly assessed by comparisons with microkinetic experimental data, i.e., experiments aiming at determining the rate constant of a single reaction channel or product branching fractions from the same entrance channel. The uncertainty in experimental measurements arises from many sources such as the type of experiment, purity of reagents, ideality of the reactor (e.g., homogeneity), setup, diagnostic methodology, data cleaning and interpretation, and experimentalist. Measurements of both experimental conditions (T, p) and species concentrations, or sometimes even species identification, may be sources of uncertainty.

Microkinetic data are most commonly obtained from shock tube experiments [279], which sometimes allow one to reach extremely diluted conditions, such that secondary reactions are suppressed. Measurements of rate constants are generally derived from fittings of species profiles as a function of t, T . In many cases, a small reaction mechanism has to be built for data interpretation, such that uncertainty of the results also depends on other reactions adopted in the small mechanism. Diagnostic techniques for species measurement include gas

chromatography, mass spectrometry, and absorption spectroscopy. Laser absorption spectroscopy is probably the most accurate diagnostic technique for ST experiments, however it requires accurate determinations of the absorption cross sections of species, which may be obtained from theoretical calculations combined with known parameters. Detection techniques for STs are also used in other reactor types simulated in this work to test the performance of the global reaction mechanism.

Low-pressure crossed laser beams are used because they allow one to reach quasi-collisionless conditions, such that bimolecular reactions other than that investigated should be completely suppressed. For instance, the cavity ring down method measures photon decay upon the crossing (and reaction) of two laser beams, relating the photon decay time with the absorption coefficients of the species. Another technique widely used to determine product distribution is crossed molecular beam (CMB) experiments. In CMB experiments, supersonic beams are crossed under single collision conditions, and species are detected with mass spectrometry combined with time of flight (TOF) analysis and with the angular and translational energies at the center of mass. Also in this case, species cross sections are required.

Each experimental work declares the estimated uncertainty, but these are commonly underestimated, just as in the case of theoretical works. Careful literature analysis should be conducted to gain insights on potentially higher uncertainty or errors in the datasets considered for comparison with theoretical calculations.

3.5.3 Contributions of this work

Table 3.2 lists the main reactions investigated in this work highlighting global reaction pathways, elementary reaction channels and corresponding theoretical methodologies, and the estimated uncertainty factor for the global reaction based on the discussion of this section. The table highlights how the theoretical treatment varies with the elementary reaction type. Hence, the theoretical treatment for the channels of a given PES should not be the same for all channels. Uncertainty estimates for each PES are discussed in more detail in the sections on theoretical calculations in Chapters 5 and 6. The uncertainty decreases for rate constants validated with experimental data.

Chapter 4

Bridging computational chemistry and kinetic modeling

This chapter presents MEL, a tool developed in this work for the integration of theoretically-derived rate constants into global kinetic mechanisms. The fundamental concepts of kinetic modeling and theoretical kinetics were presented in chapters 2 and 3. In particular, this chapter relies on the understanding of the relation between master equation simulations and phenomenological rate constants, treated in Section 3.3.4.3.

The motivation to develop MEL and the background on conventional lumping techniques are presented in Section 4.1. The methodology developed is discussed in Section 4.3.1, while the aspects of automated implementation are treated in Sections 4.3.2 and 4.3.3. Finally, successful examples of application are reported in Section 4.4, with particular focus on delicate user-dependent aspects in the use of MEL. The concluding Section 4.5 presents further considerations and future steps for the improvement of the MEL approach.

4.1 Motivation

As anticipated in Sections 1.3 and 1.4, the integration of *ab initio* derived theoretical rate constants into global kinetic mechanisms is one of the major current challenges in kinetic modeling. Detailed kinetics of MAHs and PAHs oxidation and growth involve extremely complex multi-well PESs with several reaction intermediates [140], [280]–[282]. However, ME simulations of the reactivity of PESs with N species produce up to $N(N - 1)$ phenomenological rate constants (Section 3.3.4.3), possibly resulting in hundreds of rate constants for complex PESs. The inclusion of these results into existing global kinetic mechanisms is necessary to understand their impact on macroscopic experimental trends. Besides their large number, the derived $k(T, p)$ do not always cover the full range of temperature and pressure of ME simulations (see Section 3.3.4.3). Additionally, the inclusion of the full set of reactions and intermediate species (often not present in the starting mechanism) may significantly increase the complexity of the reaction network, making the solution of even the simplest 0-D or 1-D reactive system tedious. A large number of new and relatively stable intermediate species also complicates the understanding of the macroscopic role of the investigated pathways.

A viable approach to reducing the number of isomers with similar structure and reactivity and consequently the number of reaction channels of large PESs is to lump them into pseudospecies. Figure 4.1 illustrates qualitatively the typical size of detailed, lumped, and reduced global kinetic mechanisms. The size of detailed kinetic mechanisms is reduced first via chemical lumping techniques and then by reduction techniques to be able to perform CFD simulations. Generally, detailed kinetic mechanisms are not derived entirely from first principles. Should this be the case, the number of species and reactions of the global kinetic mechanism would be even less manageable (ME output box in Figure 4.1). This motivates the need to bridge theoretically derived rate constants for a large number of isomers and global kinetic mechanisms with reasonable size. However, conventional lumping techniques are not well suited to this purpose (Section 4.2). Therefore, this thesis tackles this challenge with a new approach called master equation-based lumping (MEL).

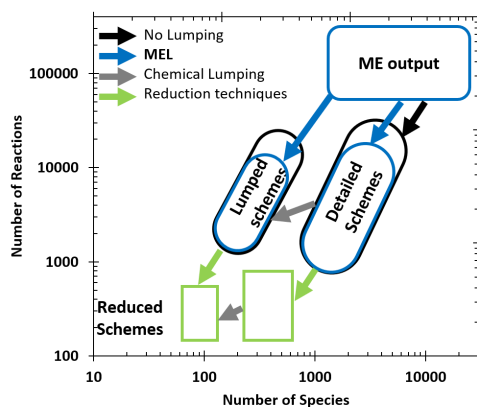


FIGURE 4.1: Qualitative representation of the typical number of reactions and species of detailed, lumped and reduced global kinetic mechanisms. Adapted from Ranzi et al. [65].

4.2 Conventional lumping techniques

Chemical lumping techniques derive equivalent rate constants for "pseudospecies", i.e., subsets of species of the detailed mechanism. The key of chemical lumping is the calculation of the contribution of each isomer to the total concentration of the pseudospecies $\tilde{c}_I = \sum_L c_L$ through coefficients $\alpha_L = \frac{c_L}{\sum_L c_L}$, where $0 \leq \alpha_L \leq 1$. The first methodologies proposed and largely applied by Ranzi et al. [63], [64], [77] lumped highly reactive radicals. α_L was found according to the pseudo steady-state approximation (PSSA) at fixed temperature, and the resulting $\tilde{k}_{IJ} = \sum_{L,J} \alpha_L k_{LJ}$ were optimized according to the selectivity of reaction products. The T -dependence of product selectivity may be introduced by fitting α_L with (modified) Arrhenius expressions, as in Chaos et al. [283]. This approach is clearly limited to highly reactive species with short lifetimes, i.e., not interacting with the rest of the reactive mixture.

A more rigorous but mathematically stringent approach was originally developed by Wei and Kuo [284], [285]. In this case, the size of the ordinary differential equation (ODE) system describing the chemical species mass balances was reduced through a lumping matrix. Although the solution of the system is exact, the detailed set of rate constants is subject

to several formal constraints and it excludes bimolecular reactions. A simplified and more flexible approach was proposed by Huang et al. [286], similar to that adopted by Nagy and Turanyi [287]. The analysis of the Jacobian of the system with e.g., principal component analysis, allows the removal of species and reactions unnecessary to the description of the global chemical reactivity. One of the downsides of this approach is that lumped groups may lose chemical significance as they are not necessarily comprised of isomers. Chemical significance is instead retained in the approach of Pepiot-Desjardins and Pitsch [288], where chemical structure determines the constituents of the pseudospecies [289]. However, in this case the results depend on the optimization subspace, i.e., on global kinetic simulations, which must be performed in a wide range of operating conditions. Similarly, the range of applicability of all the approaches mentioned is limited by the conditions of the kinetic simulations used for the derivation of the lumped kinetic parameters.

Despite the variety of chemical lumping methods widely used for the reduction of global kinetic mechanisms [66], such tools have never been specifically customized nor applied to the theoretical investigation of multi-well PESs.

4.3 A new approach: master equation-based lumping

4.3.1 Methodology

MEL is a general methodology to process phenomenological rate constants k_{IJ} obtained from ME simulations into a smaller set of equivalent rate constants $\tilde{k}_{\tilde{I}\tilde{J}}$ able to retain the accuracy of the detailed set of rate constants in the description of reactivity and products distribution. Since this procedure was specifically developed for - although not limited to - the lumping of the results of ME simulation, it is referred to as ME-based lumping (MEL). The MEL procedure is illustrated qualitatively in Figure 4.2. Starting from a PES with N species and $N(N - 1)$ rate constants k_{IJ} for the elementary reactions $I \rightarrow J$, the number of species is reduced to $\tilde{N} < N$ pseudospecies by either removing redundant species or grouping together species with similar chemical behavior. Rate constants $\tilde{k}_{\tilde{I}\tilde{J}}$ of lumped reactions $\tilde{I} \rightarrow \tilde{J}$ describe the new $\tilde{N}(\tilde{N} - 1)$ reactions of the lumped mechanism.

For better clarity, Table 4.1 summarizes the notations used for the description of the MEL approach in the rest of this chapter.

MEL addresses the two main issues described in Section 4.1 as it: 1) decreases the large number of rate constants derived with AI-TST-ME methodologies; 2) eliminates highly reactive species in the full temperature and pressure ranges considered. MEL solves an ODE system for N species, similar to conventional chemical lumping techniques:

$$\frac{d\mathbf{c}}{dt} = \mathbf{K}'\mathbf{c} \quad (4.1)$$

where \mathbf{c} is the concentration and t is the time, and then reduces it to the equivalent lumped system for $\tilde{N} < N$ pseudospecies:

$$\frac{d\tilde{\mathbf{c}}}{dt} = \tilde{\mathbf{K}}'\tilde{\mathbf{c}} \quad (4.2)$$

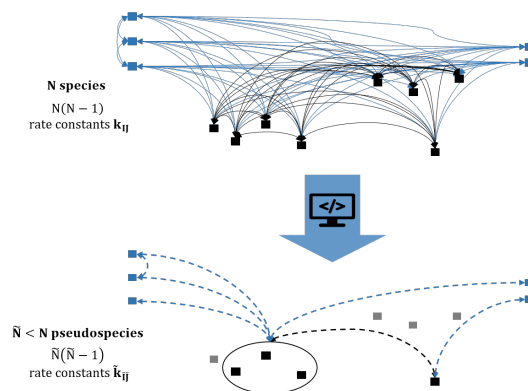


FIGURE 4.2: Qualitative representation of MEL procedure. Squares represent the species of the PES and arrows indicate reactions (solid lines for $N(N - 1)$ detailed reactions, dashed lines for $\tilde{N}(\tilde{N} - 1)$ lumped reactions). Shaded squares are redundant species, removed in the lumped mechanism; blue squares are bimolecular reactants/products; circles group isomers as one pseudospecies.

TABLE 4.1: Nomenclature and notations for MEL methodology.

c	Species concentration
I, J	Generic species. For bimolecular fragments $I + I_2$, I is the limiting reactant and I_2 is the excess reactant
k_{IJ}	Rate constant of reaction $I \rightarrow J$ also applies to bimolecular reactions
k'_{IJ}	Rate constant for a pseudo unimolecular reaction, i.e., $k_{IJ}c_{I_2}$ for bimolecular reactants $I + I_2$
N	Number of species
t	time
\sim	Accent indicating lumped quantities
L	Accumulating species of the detailed mechanism
IN SIMULATIONS FOR THE DERIVATION OF LUMPED RATE CONSTANTS:	
R	Generic reactant (from the set of L accumulating species) present in the system at $t = 0$
P	Generic non-reactive product (from the set of L accumulating species)

In the MEL approach, Eqn. (4.1) describes the phenomenological chemical evolution of the system as an initial value problem with initial conditions $\mathbf{c}(t = 0) = \mathbf{c}^0$. For a multi-well PES, \mathbf{K} contains the $N(N - 1)$ phenomenological rate constants k_{IJ} obtained as the output of ME simulations, which therefore have to be performed beforehand. The set of rate constants \mathbf{K} thus forms the "detailed mechanism", whose macroscopic performance has to be ideally reproduced by the lumped set of rate constants. Apex ' indicates that k_{IJ} of bimolecular reactions $I + I_2 \rightarrow J$ are multiplied by the concentration of the excess co-reactant $k'_{IJ} = k_{IJ}c_{I_2}$, thus becoming formally unimolecular. Therefore, \mathbf{K}' and consequently $\tilde{\mathbf{K}}'$ are pseudo-unimolecular rate constant matrices, similar to what was described by Wei and Kuo [284], [285]. The matrix \mathbf{K}' of pseudo-unimolecular rate constants is:

$$\mathbf{K}' = \begin{bmatrix} -\sum_{J \neq 1}^N k'_{1J} & k'_{21} & k'_{31} & \cdots & \cdots & \cdots & k'_{N1} \\ k'_{12} & -\sum_{J \neq 1}^N k'_{2J} & k'_{32} & \cdots & \cdots & \cdots & k'_{N2} \\ \cdots & \cdots & \ddots & \cdots & \cdots & \cdots & \cdots \\ k'_{1J} & k'_{2J} & k'_{3J} & -\sum_{J \neq I}^N k'_{IJ} & \cdots & \cdots & k'_{NJ} \\ \cdots & \cdots & \cdots & \cdots & \cdots & \ddots & \cdots \\ k'_{1N} & k'_{2N} & \cdots & \cdots & \cdots & k'_{(N-1)N} & -\sum_{J \neq N}^N k'_{NJ} \end{bmatrix} \quad (4.3)$$

The time evolution of the concentration of generic species I is described by:

$$\frac{dc_I}{dt} = \left(-\sum_{J \neq I}^N k'_{IJ} \right) c_I + \sum_{J \neq I}^N k'_{JI} c_J \quad ; \quad c_I(t=0) = c_I^0 \quad (4.4)$$

The MEL lumping procedure is initiated by subdividing the N species of the ME system into two groups, accumulating and non-accumulating species. Non-accumulating species, which are excluded from pseudospecies, include both wells not collisionally equilibrated in ME simulations (or equilibrated in very limited sets of operating conditions), and highly reactive species not accumulating in macroscopic kinetic simulations. Merging isomers of stable (accumulating) species is possible and advised, should they equilibrate very rapidly or show similar reactivity (i.e., similar characteristic times and product branching fractions). The ensemble of the merged and unmerged accumulating species constitutes the set of \tilde{N} pseudospecies: pseudospecies profiles $\tilde{c}_{\tilde{I}}$ of system (4.2) describe either unmerged or merged accumulating species profiles obtained from system (4.1): $\tilde{c}_{\tilde{I}} = \sum_L c_L$ for merged species, $\tilde{c}_{\tilde{I}} = c_L$ for unmerged species. In the following, index L refers only to accumulating species (see also Table 4.1). The procedure used to identify species groups is described in Section 4.3.3.

Equation (4.1) is then solved at an assigned (T, p) for each of the \tilde{N} pseudospecies, thus obtaining \tilde{N} sets of simulations. In each set, one selected accumulating pseudospecies acts as the reactant, i.e., is the only pseudospecies with a non-zero initial concentration, and is therefore indicated as \tilde{R} . It is recalled that \tilde{R} must be part of the accumulating species, and may be either unmerged (single species, $\tilde{c}_{\tilde{R}} = c_R$) or merged (multiple species, $\tilde{c}_{\tilde{R}} = \sum_R c_R$). The set of simulations having \tilde{R} as the reactant leads to the derivation of the lumped rate constants for reactions $\tilde{R} \rightarrow \tilde{P}$, where \tilde{P} indicates all the other "product" pseudospecies (i.e., all \tilde{I} except for \tilde{R}), therefore including accumulating species P (all L accumulating species except for R). All product species are forced to be non-reacting, such that c_P can only increase in time. This approximation is applied by modifying the \mathbf{K}' matrix (4.3) setting $k_{PJ} = 0$ (i.e., the columns corresponding to all P species are set to 0). This approach is similar to that implemented by Barbato et al. [107] to determine phenomenological rate constants from ME simulations, and results in the exponential decay of the concentration of the reacting pseudospecies $\tilde{c}_{\tilde{R}}$ according to the phenomenological law:

$$\begin{cases} \frac{d\tilde{c}_{\tilde{R}}}{dt} = \left(-\sum_{\tilde{P}} \tilde{k}'_{\tilde{R}\tilde{P}}\right) \tilde{c}_{\tilde{R}} & ; \tilde{c}_{\tilde{R}}(t=0) = \tilde{c}_{\tilde{R}}^0 \\ \frac{d\tilde{c}_{\tilde{P}}}{dt} = \tilde{k}'_{\tilde{R}\tilde{P}} \tilde{c}_{\tilde{R}} & ; \tilde{c}_{\tilde{P}}(t=0) = 0 \end{cases} \quad (4.5)$$

The analytical integration of Equation (4.5) describes the exponential decay for \tilde{R} . The unknown rate constants $\tilde{k}'_{\tilde{R}\tilde{P}}$ of reactions $\tilde{R} \rightarrow \tilde{P}$ (where \tilde{P} indicates a generic non-reactive pseudospecies other than \tilde{R}) at the assigned T, p value can then be derived from a differential fit of the product concentration profiles of Equation (4.5). For self-reactions $2\tilde{R} \rightarrow \tilde{P}$ and reactions with two products $\tilde{R} \rightarrow \tilde{P} + \tilde{P}_2$, the evolution of $\tilde{c}_{\tilde{P}}$ is described by $\frac{d\tilde{c}_{\tilde{P}}}{dt} = \tilde{k}'_{\tilde{R}\tilde{P}} \tilde{c}_{\tilde{R}}^2$ and $\frac{d\tilde{c}_{\tilde{P}}}{dt} = 2\tilde{k}'_{\tilde{R}\tilde{P}} \tilde{c}_{\tilde{R}}$, respectively. The coefficient of determination R^2 of the linear fits for $\tilde{k}'_{\tilde{R}\tilde{P}}$ provides a first estimate of the validity of the lumped model. Low values of R^2 may be caused by a wrong choice of the set of pseudospecies or of the constituents of merged pseudospecies and their composition.

A simple example of the application of MEL is illustrated starting from the PES qualitatively depicted in Figure 4.3. Bimolecular reactants $a + a_2$ and $b + b_2$ are accumulating species, and well w is possibly included among pseudospecies because of its low energy, while the shallow well s can be regarded as example of non-accumulating isomer. Excluding any species merging, in this case there are three pseudospecies, i.e., $\tilde{a} + \tilde{a}_2$, $\tilde{b} + \tilde{b}_2$, and \tilde{w} , corresponding to the unmerged accumulating species $a + a_2$, $b + b_2$, and w , respectively. Therefore, the goal of the lumping is to obtain equivalent rate constants $\tilde{k}_{\tilde{a}\tilde{b}}$, $\tilde{k}_{\tilde{a}\tilde{w}}$, $\tilde{k}_{\tilde{b}\tilde{a}}$, $\tilde{k}_{\tilde{b}\tilde{w}}$, $\tilde{k}_{\tilde{w}\tilde{a}}$, and $\tilde{k}_{\tilde{w}\tilde{b}}$ for global reactions skipping the unstable intermediate s , thus reducing the set of rate constants from 12 to 6.

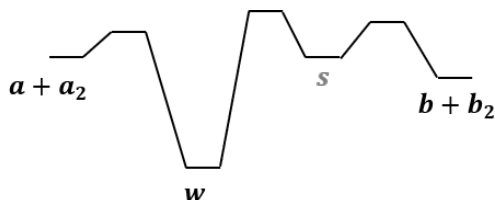


FIGURE 4.3: Qualitative PES for the reaction $a + a_2 = w = s = b + b_2$.

There are three different pseudospecies, therefore three different sets of simulations are required. For instance, the derivation of $\tilde{k}_{\tilde{a}\tilde{b}}$ and $\tilde{k}_{\tilde{a}\tilde{w}}$ requires to simulate a system where a is the reactant (corresponding to the R described above) and b and w are the non-reacting products (corresponding to the set of P described above), resulting in the following equations:

$$\begin{bmatrix} \frac{dc_a}{dt} \\ \frac{dc_w}{dt} \\ \frac{dc_s}{dt} \\ \frac{dc_b}{dt} \end{bmatrix} = \begin{bmatrix} -(k_{aw} + k_{as} + k_{ab})c_{a_2}^0 & 0 & k_{sa} & 0 \\ k_{aw}c_{a_2}^0 & 0 & k_{sw} & 0 \\ k_{as}c_{a_2}^0 & 0 & -k_{sa} - k_{sw} - k_{sb} & 0 \\ k_{ab}c_{a_2}^0 & 0 & k_{sb} & 0 \end{bmatrix} \begin{bmatrix} c_a \\ c_w \\ c_s \\ c_b \end{bmatrix}, \quad \begin{aligned} c_a^0 &= 10^{-5} c_{tot}^0 \\ c_{a_2}^0 &= c_{tot}^0 - c_a^0 \\ c_w^0, c_s^0, c_b^0, c_{b_2}^0 &= 0 \end{aligned} \quad (4.6)$$

If the assumption of fast reactivity of the intermediate s is correct, s does not accumulate significantly in the system and the profiles of $\tilde{c}_{\tilde{a}}$, $\tilde{c}_{\tilde{w}}$ and $\tilde{c}_{\tilde{b}}$ are well described by

$$\begin{cases} \frac{d\tilde{c}_a}{dt} = -(\tilde{k}_{a\tilde{w}} + \tilde{k}_{a\tilde{w}})\tilde{c}_{a_2}^0 \tilde{c}_a & ; \quad \tilde{c}_a^0 = 10^{-5}c_{tot}^0, \quad \tilde{c}_{a_2}^0 = c_{tot}^0 - \tilde{c}_a^0 \\ \frac{d\tilde{c}_{\tilde{w}}}{dt} = \tilde{k}_{a\tilde{w}}\tilde{c}_{a_2}^0 \tilde{c}_a & ; \quad \tilde{c}_{\tilde{w}}^0 = 0 \\ \frac{d\tilde{c}_b}{dt} = \tilde{k}_{a\tilde{w}}\tilde{c}_{a_2}^0 \tilde{c}_a & ; \quad \tilde{c}_b^0 = 0 \end{cases} \quad (4.7)$$

where \tilde{c}_a , $\tilde{c}_{\tilde{w}}$ and \tilde{c}_b derive from the solution of the detailed system (4.6). $\tilde{k}_{a\tilde{w}}$ and $\tilde{k}_{a\tilde{w}}$ are determined with a linear differential fit of $\frac{d\tilde{c}_{\tilde{w}}}{dt}$ and $\frac{d\tilde{c}_b}{dt}$ profiles in the lumped system (4.7), respectively.

Rate constants $\tilde{k}_{b\tilde{a}}$, $\tilde{k}_{b\tilde{w}}$, $\tilde{k}_{\tilde{w}a}$, and $\tilde{k}_{\tilde{w}b}$ are determined in a similar way. For instance, the determination of $\tilde{k}_{\tilde{w}a}$ and $\tilde{k}_{\tilde{w}b}$ requires the simulation of a system where well w acts as reactant R and a, b are non-reactive products P , such that the equations analogous to (4.6) are

$$\begin{bmatrix} \frac{dc_a}{dt} \\ \frac{dc_w}{dt} \\ \frac{dc_s}{dt} \\ \frac{dc_b}{dt} \end{bmatrix} = \begin{bmatrix} 0 & k_{wa} & k_{sa} & 0 \\ 0 & -(k_{wa} + k_{ws} + k_{wb}) & k_{sw} & 0 \\ 0 & k_{ws} & -(k_{sa} + k_{sw} + k_{sb}) & 0 \\ 0 & k_{wb} & k_{sb} & 0 \end{bmatrix} \begin{bmatrix} c_a \\ c_w \\ c_s \\ c_b \end{bmatrix}, \quad \begin{matrix} c_w^0 = c_{tot}^0 \\ c_a^0, c_{a_2}^0, c_s^0, c_b^0, c_{b_2}^0 = 0 \end{matrix} \quad (4.8)$$

The final rate constants are derived from the fitting of the differential product profiles from the set of equations

$$\begin{cases} \frac{d\tilde{c}_{\tilde{w}}}{dt} = -(\tilde{k}_{\tilde{w}a} + \tilde{k}_{\tilde{w}b})\tilde{c}_{\tilde{w}} & ; \quad \tilde{c}_{\tilde{w}}^0 = c_{tot}^0 \\ \frac{d\tilde{c}_a}{dt} = \tilde{k}_{\tilde{w}a}\tilde{c}_{\tilde{w}} & ; \quad \tilde{c}_a^0 = 0 \\ \frac{d\tilde{c}_b}{dt} = \tilde{k}_{\tilde{w}b}\tilde{c}_{\tilde{w}} & ; \quad \tilde{c}_b^0 = 0 \end{cases} \quad (4.9)$$

Finally, it is recalled that in this simple example $\tilde{c}_a = c_a$, $\tilde{c}_{\tilde{w}} = c_w$, and $\tilde{c}_b = c_b$, while in most cases each pseudospecies is formed by multiple isomers.

The methodology proposed has several advantages. Firstly, it requires only the output of ME simulations, being independent of kinetic simulations of experimental data, which usually limit the applicability range of the lumped rate constants. Then, in contrast with most chemical lumping approaches, MEL allows simultaneous elimination of redundant species and merging of accumulating isomers with similar reactivity, preserving the chemical meaning of the mechanism and easily including both unimolecular and bimolecular reaction channels.

4.3.2 Implementation

The MEL approach is implemented with an open-source in-house Python software (available at <https://github.com/lpratalimaffei/MEL>) and relies on OpenSMOKE++ [82] for the solution of the ODE system and, optionally, on OptiSMOKE++ [276] for further optimization of the lumped mechanism (see Section 2.7).

The flowchart in Figure 4.4 depicts the main steps performed by the code. Three main types of simulations can be run: "prescreening" analyzes the reactivity of species in the detailed mechanism; "lumping" derives the lumped rate constants from the reactivity of the selected pseudospecies (as described in Section 4.3.1); "validation" compares the reactivity

of the detailed mechanism with that of the lumped mechanism. The main steps are common to all simulation types. Input specifications include the set of reactants R and products P (i.e., the constituents of pseudospecies \tilde{R}, \tilde{P}), as well as the T, p range for the simulations. For a PES with \tilde{N} pseudospecies, lumping requires a total of $\tilde{N} \times N_p \times N_T$ sets of simulations performed at isobaric and isothermal conditions, where N_p and N_T are the number of nominal pressures and temperatures at which simulations are performed. The matrix \mathbf{K} of the ME system, namely $k_{IJ}|_{T,p}$ at the specified conditions, are extracted from ME output files. It is recalled that in lumping simulations products are treated as non-reacting, i.e., $k_{PJ} = 0$. Thermodynamics is irrelevant to the derivation of $\tilde{k}_{\tilde{I}\tilde{J}}$ because all $N(N-1)$ reactions are written irreversibly in the forward or backward direction, as also highlighted by Pepiot-Desjardins and Pitsch [288]. When a global kinetic scheme already includes reversible reactions of pseudospecies \tilde{I} , it is recommended to consider either the thermochemistry of the most stable isomer [289], or a weighted average of the thermochemistry of the isomers constituting the pseudospecies [288].

In each simulation, system (4.1) is solved with OpenSMOKE++ [82]. Initial conditions for the composition c_R^0 of the reactants are specified as follows:

- Unimolecular reactant R : for single reactant species, $c_R^0 = c_{tot}$; for merged species, $\sum_R c_R^0 = c_{tot}$, with c_R^0 derived from previous simulations (details in Section 4.3.3).
- Bimolecular reactants $R + R_2$: for single bimolecular deficient fragment R , $c_R^0 = 10^{-5}c_{tot}$; for merged fragments, $\sum_R c_R^0 = 10^{-5}c_{tot}$. The concentration of the excess fragment is approximately constant: $c_{R_2}^0 = c_{tot} - \sum_R c_R^0$. For self-reactions $2R \rightarrow P$, the total concentration is kept approximately constant by immersing R in an inert bath gas (e.g., Ar) consistent with that used for ME simulations: $c_R^0 = 10^{-5}c_{tot}$, and $c_{Ar}^0 = c_{tot} - c_R^0$ (see Section 4.4.3).

c_{tot} is derived from the equation of state in OpenSMOKE++ (e.g., p/RT for ideal gases), while $c_{I \neq R}^0 = 0$.

The resulting concentration profiles are then processed. Simulation times corresponding to less than 1% or more than 99% reactant consumption are excluded, so as to avoid numerical instabilities or non-exponential behavior due to initial population of the intermediate wells. Examples of the sensitivity of $\tilde{k}_{\tilde{R}\tilde{P}}$ to cutoff limits are provided in the results (Section 4.4.1). Then, merged pseudospecies profiles $\tilde{c}_{\tilde{I}} = \sum_L c_L$ (System (4.2)) are reconstructed if necessary. The the branching fractions (BFs) of constituent L in each merged pseudospecies \tilde{I} are computed as a time average weighted on the timeframe dt for each BF value:

$$\alpha_L|_{T,p} = \sum_{dt} \frac{c_L}{\tilde{c}_{\tilde{I}}} \Big|_{dt} \cdot \frac{dt}{t_{tot}} \quad (4.10)$$

where t_{tot} is the total simulation time considered, i.e., considering the concentration profiles cut at 1% and 99% reactant consumption, respectively, as described above; dt is the timeframe corresponding to each concentration c_L and $\tilde{c}_{\tilde{I}}$ read from the output of OpenSMOKE++ simulations. $\alpha_L|_{T,p}$ may be used for the selection of merged reactant composition, as depicted in Figure 4.4.

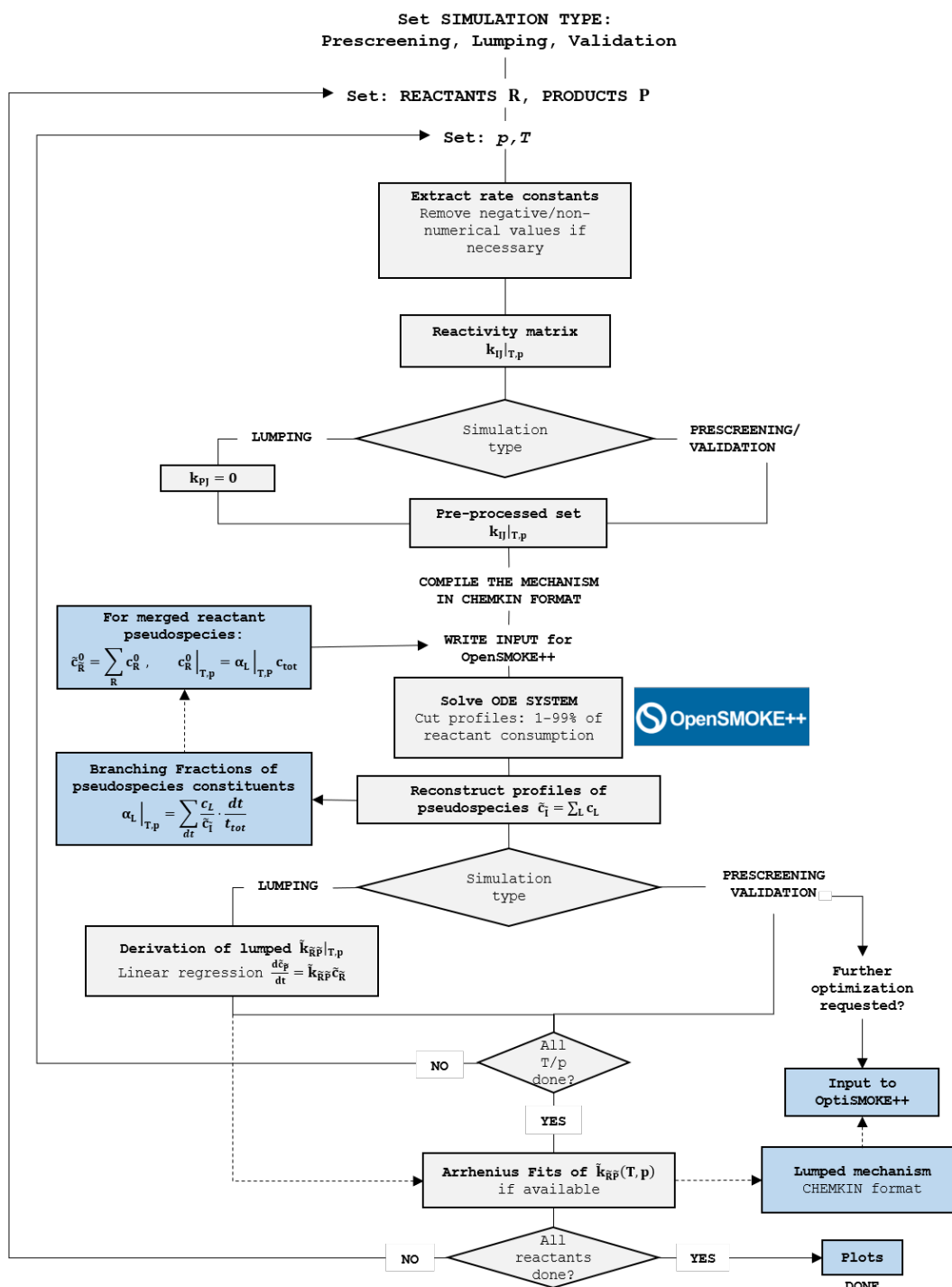


FIGURE 4.4: Flowchart of the algorithm used for the implementation of MEL. Blue boxes represent code outputs; dashed arrows indicate connections between portions of the code generated at different steps.

The steps described are repeated for the full set of operating conditions T, p specified in the input. For lumping simulations, the resulting $\tilde{k}_{\tilde{R}\tilde{P}}|_{T,p}$ are fitted according to modified Arrhenius expressions. Reiterating these steps for each set of reactants R results in the final lumped mechanism of $\tilde{N}(\tilde{N} - 1) \times \tilde{k}_{\tilde{I}\tilde{J}}$, which may be further optimized with tools such as OptiSMOKE++ [276], [277].

4.3.3 Species selection

Chemical structure and reactivity guide the selection of pseudospecies, as suggested by Ranzi et al. [63] and Pepiot-Desjardins and Pitsch [288]. Figure 4.5 summarizes the steps for the definition of the accumulating species (left) and the merged pseudospecies composition (right).

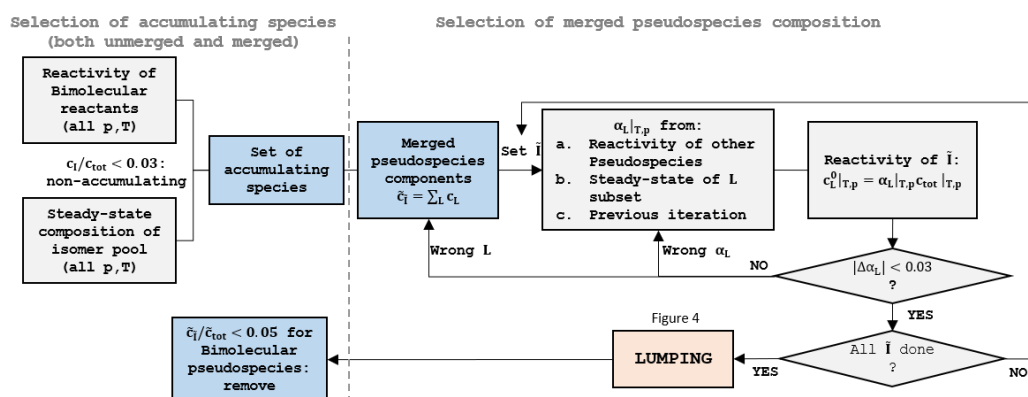


FIGURE 4.5: Diagram of the procedure of selection of accumulating species and merged pseudospecies composition. White boxes indicate the steps which require the use of the lumping code. The "LUMPING" box implies all the steps illustrated in the flowchart of Figure 4.4.

Bimolecular products are always included as pseudospecies in preliminary simulations, however they may be removed from the lumped kinetic mechanism when their production from all the other pseudospecies is negligible (e.g., $\tilde{c}_I/c_{tot} < 0.05$ at all operating conditions). An example is provided in Section 4.4.3.

The investigation of the accumulation of wells is performed in two steps. First, their production from bimolecular reactions is analyzed. Then, the steady-state composition of the set of wells is obtained with the detailed k_{IJ} including only isomerization reactions. A well with negligible accumulation at all T, p (in this work: $c_I/c_{tot} < 0.03$) is considered non-accumulating and is therefore not included in any pseudospecies. The lumping of the PES for CH_3COOH decomposition provides a straightforward example of non-accumulating species elimination (Section 4.4.1).

It must be noted that non-accumulating species might be produced by reactions of the target kinetic scheme occurring on a different PES. This species may be included among pseudospecies independently of its degree of accumulation. If the unimolecular decomposition of this species is extremely fast, replacing it with its decomposition products generally does not affect macroscopic performances of the kinetic mechanism.

Accumulating species with similar chemical structure (i.e., functionality) and reactivity should be merged into lumped groups of isomers (merged pseudospecies) according to a

given composition $\alpha_L|_{T,p}$ [63], [288]. The derivation of $\tilde{k}'_{IJ}|_{T,p}$ for pseudospecies \tilde{I} with $\tilde{c}_{\tilde{I}} = \sum_L c_L$ requires the definition of the initial concentration of each L for the solution of (4.1): $c_L^0|_{T,p} = \alpha_L c_{tot}|_{T,p}$. When equilibration between L species is fast, $\alpha_L|_{T,p}$ may be set as the steady-state composition of the lumped group. In fact, Wei and Kuo [284], [285] suggested that, for unimolecular reactions approaching equilibrium, a correct choice of $\alpha_L|_{T,p}$ produces negligible changes in the pseudospecies composition $\alpha_L|_{T,p}(t)$. In MEL, this condition is met through iterative simulations of the reactivity of L components using the full set of k_{IJ} ; iterations stop when the absolute change in the average $\alpha_L|_{T,p}$ (Eqn. (4.10)) with respect to the initial value $\Delta\alpha_L|_{T,p} = |\alpha_L - \alpha_L^0|_{T,p}$ is below a threshold (here set to 0.03). In all the other cases, $\alpha_L|_{T,p}$ is calculated with Eqn. (4.10) from the reactivity of the pseudospecies \tilde{R} contributing the most to the formation of the selected lumped group. An unphysical choice of the components of \tilde{I} results in non-exponential decays of L (and consequently of \tilde{I}), easily identified in the simulation profiles. Similarly, inconsistent composition $c_L^0|_{T,p} = \alpha_L c_{tot}|_{T,p}$ causes abrupt changes in $c_L(t)$ due to e.g., different characteristic times for L .

4.4 Application of MEL

4.4.1 CH₃COOH

The simplest MEL application of this work consists in the removal of one non-accumulating species in the PES for acetic acid (CH₃COOH) decomposition studied by Cavallotti et al. [290] (Figure 4.6). ME simulations cover temperature and pressure ranges of 800–2400 K and 0.1–100 atm.

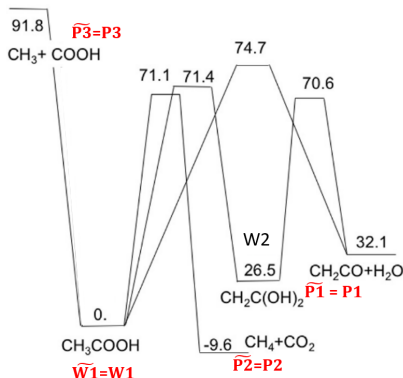


FIGURE 4.6: The PES for CH₃COOH decomposition reproduced from Cavallotti et al. [290]. Energies are in kcal/mol and are inclusive of zero point energies. Bold red names indicate accumulating species, and names with \sim are pseudospecies.

The selection of accumulating species starts with prescreening simulations of the reactivity of bimolecular reactions of $P1, P2, P3$ including all the rate constants derived from ME simulations (i.e., all accumulating species react). At every operating condition, the mole fraction of intermediate $W2$ is below 1%. The same result is obtained with steady-state simulations including only the isomerization reactions between $W1$ and $W2$. Therefore, $W2$

is not included among pseudospecies, while pseudospecies $\widetilde{W1}$, $\widetilde{P1}$, $\widetilde{P2}$, $\widetilde{P3}$ correspond to single (unmerged) species of the detailed set of rate constants, as indicated in Figure 4.6.

Lumped rate constants are derived as described in Section 4.3.2. All reactant decay profiles are pseudo-exponential, as expected. Variations of cutoff parameters initially set to 1-99% of reactant consumption do not significantly affect \widetilde{k}_{IJ} . In fact, the maximum discrepancies of 7% in $\widetilde{k}_{IJ}|_{1atm}$ obtained by setting the cutoff limits to 0.1-99% or 10-99% highlight the limited formation of $W2$ at the early stages of the reactivity. Reduction of the lower cutoff limit to 90% resulted instead in differences in $\widetilde{k}_{IJ}|_{1atm}$ below 1%. The Arrhenius parameters of \widetilde{k}_{IJ} obtained in these tests are found in the SM of the corresponding publication [291]. \widetilde{k}_{IJ} are validated by comparing the performances of the full detailed and lumped mechanisms, thus allowing for accumulation and consumption of all pseudospecies.

\widetilde{k}_{IJ} were further optimized with OptiSMOKE++ [276], [277], slightly increasing the accuracy of the predictions. The optimization of the lumped mechanism involved 96 active Arrhenius parameters (pre-exponential factor, temperature exponent and activation energy) in 8 pressure-dependent reactions, using the profiles generated with the full detailed mechanism as targets. The lumped rate constants were allowed to vary by a factor of 2 at most. Figure 4.7 shows profiles of $\widetilde{P1}$ reactivity at 10 atm, where the accumulation and consumption of $\widetilde{W1}$ at intermediate temperatures (800–1000 K) and of $\widetilde{P3}$ at higher temperatures (1600–2400 K) are well reproduced by the lumped model.

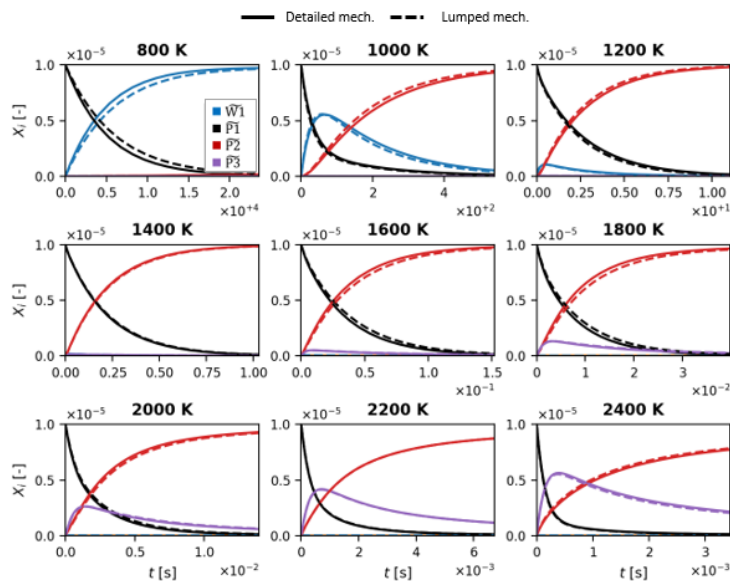


FIGURE 4.7: Profiles obtained from the reactivity of $\widetilde{P1}$ at 10 atm including all the reactions of the detailed (solid lines) and lumped (dashed lines) mechanisms.

4.4.2 C_5H_5+OH

The application of MEL to the C_5H_5OH PES studied by Galimova et al. [292] allows both the extension of the stability range of intermediate wells and the elimination of oscillatory behavior of the associated rate constants. Additionally, this example is particularly relevant to this thesis as a sensitive kinetic model update from lumped literature calculations (see

Sections 5.2 and 5.4). The lumping of this PES together with the other theoretical studies of cyclopentadienyl oxidation by Mebel et al. [293], [294] was crucial to the understanding of cyclopentadiene oxidation behavior.

The main reaction channels are depicted in Figure 4.8. OH recombination with C_5H_5 is followed by isomerization reactions between 6 different isomers ($W1$ – 6). C–H and O–H bond-fission lead to H ejection ($P2$, $P3$, $P5$, $P6$), while C–C bond-fission produces either HCO ($P4$) or CO ($P1$). Galimova et al. [292] recommend extra care in including the proposed rate constants into global kinetic schemes, due to the narrow range of thermal stability for the wells: at 0.01 atm, $W1$ and $W4$ exist thermodynamically and kinetically only below 1000 K, whereas k_{W5J} , k_{IW5} are available up to 1900 K. Furthermore, rate constants for the production of such isomers (e.g., k_{IW5} , k_{IW4} , k_{IW1}) show significant oscillations.

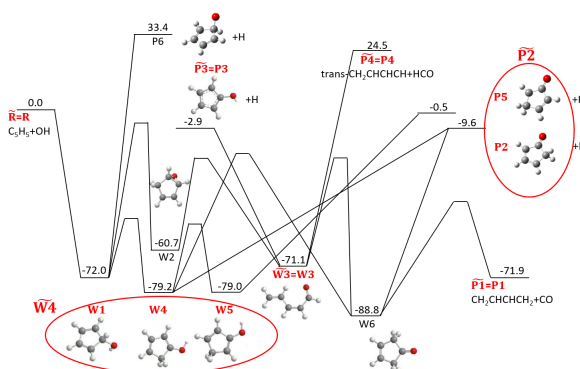


FIGURE 4.8: Simplified C_5H_5OH PES from the study of Galimova et al. [292]. Energies are in kcal/mol and inclusive of ZPE. Red names indicate accumulating species, and names with \sim are pseudospecies.

Species selection required several iterations. The analysis of the reactivity of bimolecular reactants $P1$ – 6 shows that $W2$ does not accumulate significantly in the system. As suggested by the reaction channels depicted in Figure 4.8, $W1$, $W4$, and $W5$ have compatible characteristic times and product BFs, therefore they are lumped together as $\widetilde{W4} : \widetilde{c}_{\widetilde{W4}} = c_{W1} + c_{W4} + c_{W5}$. On the contrary, $W6$ has different chemical functionality and reactivity. Since the accumulation of $W6$ above 600 K is significant only at 100 atm, $W6$ was excluded from pseudospecies and a temperature range of 600–2500 K was considered for the lumping. Finally, $W3$ constitutes a single unmerged pseudospecies $\widetilde{W3}$, being the only non-cyclic isomer, and it is produced in relevant amounts only by $P4$.

Lumping together $W1$, $W4$, $W5$ allows for an extension of the temperature range of $\widetilde{k}_{\widetilde{I}\widetilde{J}}$ with respect to the original k_{IJ} . Since k_{IJ} for $W1$ and $W4$ are unavailable above 1000 K at low pressures, $\widetilde{W4}$ is constituted only of $W5$ above 1000 K. The composition of $\widetilde{W4}$ was determined iteratively, reaching convergence in less than 10 iterations. The same method was used for the derivation of the composition of $\widetilde{P2}$, comprised of $P2$ and $P5$. \widetilde{R} , $\widetilde{P1}$, $\widetilde{P3}$ and $\widetilde{P4}$ are instead single unmerged pseudospecies. Finally, $P6$ was excluded from the pseudospecies. In fact, its production is negligible from all species of this PES, and the study of the $C_5H_5+O(^3P)$ PES by Ghildina et al. [293] highlights the instability of $P6$ with respect to $P2$ and $P5$.

MEL finally leads from 13 species and 156 k_{IJ} to 7 pseudospecies and 42 $\tilde{k}_{\tilde{I}\tilde{J}}$, further reduced to 27 by eliminating reaction channels of negligible importance (i.e., product BF < 1%). The final optimized mechanism reproduces well the results obtained with the detailed scheme, as shown in the SM of the corresponding paper [291]. The lumped mechanism shows lower accuracy at 600 K and 100 atm due to the exclusion of $W6$ from pseudospecies. This is an acceptable approximation in light of the good performances of the lumped mechanism at most of the operating conditions investigated.

The most interesting aspect of the MEL application in this case is its extension in the temperature range and its removal of the oscillatory behavior of some of the rate constants of the detailed ME mechanism. In particular, Figure 4.9 depicts the lumped $\tilde{k}_{\tilde{R}\tilde{W}_4}$ in comparison with the detailed $k_{R\ W_1}$, $k_{R\ W_4}$, $k_{R\ W_5}$.

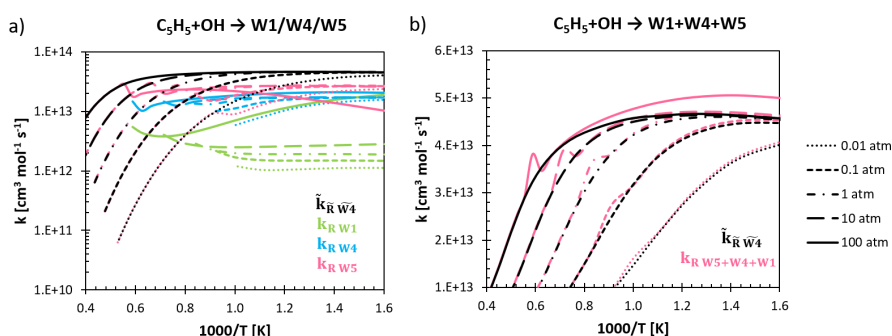


FIGURE 4.9: Comparison between the lumped rate constant $\tilde{k}_{\tilde{R}\tilde{W}_4}$ and the elementary rate constants $k_{R\ W_1}$, $k_{R\ W_4}$, $k_{R\ W_5}$ of MESS output as a function of pressure. a) Shows the single elementary rate constants and b) compares the lumped rate $\tilde{k}_{\tilde{R}\tilde{W}_4}$ with the sum of the single elementary rates $k_{R\ W_1} + k_{R\ W_4} + k_{R\ W_5}$.

At 0.01 atm, $\tilde{k}_{\tilde{R}\tilde{W}_4}$ corresponds approximately to the sum of the rate constants of the elementary reaction channels (Figure 4.9b). As the pressure increases, $\tilde{k}_{\tilde{R}\tilde{W}_4}$ is higher than $k_{R\ W_4} + k_{R\ W_5}$, and lower than $k_{R\ W_1} + k_{R\ W_4} + k_{R\ W_5}$, showing no oscillations thanks to the implicit inclusion of the reactivity of other intermediate channels. At higher temperatures, where intermediates $W1$ and $W4$ are kinetically and thermodynamically unstable, $\tilde{k}_{\tilde{R}\tilde{W}_4}$ becomes equal to $k_{R\ W_5}$, as expected.

The removal of the observed oscillatory behavior may also be obtained with the recently introduced well extension feature of MESS (activated through the WellExtension keyword in the input). The results obtained for the rate constants $k_{R\ W_1}$, $k_{R\ W_4}$, $k_{R\ W_5}$ are plotted in Figure 4.10a. Despite the strong non-Arrhenius behavior, the oscillations are strongly reduced and the total rate constant $k_{R\ W_1} + k_{R\ W_4} + k_{R\ W_5}$ has no oscillations. It is noted that this rate is extremely close to the lumped rate constant obtained from our original calculations $\tilde{k}_{\tilde{R}\tilde{W}_4}$, as shown in Figure 4.10b. The highest discrepancies (factor < 2) are found at 0.01 atm.

MESS well-extended results apparently produce a very different composition of the isomer pool formed by $W1$, $W4$ and $W5$, as highlighted in Figure 4.11. For instance, at high temperatures $W5$ contributes only about 60% of the total isomer pool. However, applying MEL to both the non-extended and the well-extended sets of rate constants k_{IJ} produces

two almost identical sets of lumped $\tilde{k}_{\tilde{T}J}$, with discrepancies within 15% for the main reaction channels. The similarity of the lumped results can be explained by carefully looking at the MESS log output file for the non-extended ME simulations, which reveals that $W1$, $W4$ and $W5$ are combined at high temperatures. In fact, when $W1$ and $W4$ disappear (i.e., no phenomenological rate constants are produced from MESS at high temperatures), $W5$ is actually the "assigned name" for the combination of these three species indicated. This confirms the validity of the MEL approach, showing that macroscopic results are consistent with lumping procedures implicitly considered in ME solution methodologies. Finally, these results warn that in some cases careful insight and interpretation of the output of ME simulations is required.

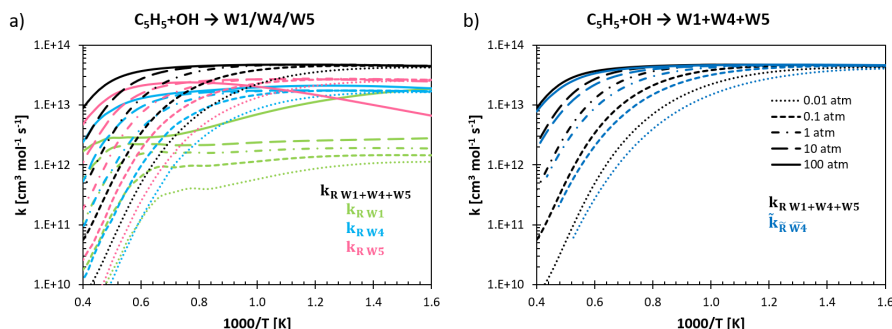


FIGURE 4.10: a) $k_{R,J}$ for $R \rightarrow W1/W4/W5$ obtained with the detailed mechanism using the WellExtension keyword in MESS input; b) comparison between the total rate $k_{R \rightarrow W1+W4+W5}$ obtained using the WellExtension keyword and the lumped rate constant of the $\tilde{R} \rightarrow \tilde{W4}$ equivalent reaction determined in this work.

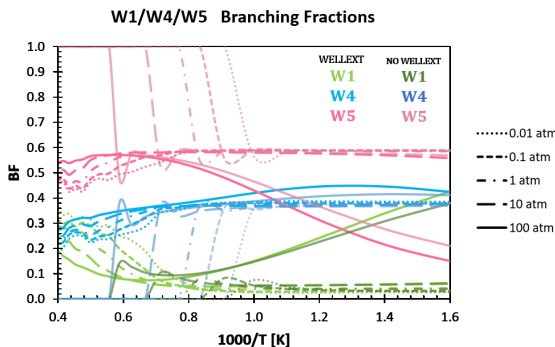


FIGURE 4.11: Branching fractions of $W1$, $W4$, $W5$ obtained from the detailed reactivity of R including the WellExtension keyword in MESS input (brighter lines) and from the detailed reactivity of R in the MESS calculations reproduced in this work as in [292] (shaded lines).

This set of reactions was included in the CRECK kinetic mechanism. The reactivity of newly introduced pseudospecies such as $\tilde{W4}$ and $\tilde{P2}$ was also considered, such as H-atom abstraction reactions on C_5H_6O isomers ($\tilde{W4}$) (See Section 5.2.1). The corresponding rate constants may be approximated according to the α_L of the constituents of the pseudospecies: $\tilde{k}_{Habs, \tilde{W4}} = \sum_L \alpha_L k_{Habs, L}$. Furthermore, unimolecular decomposition of C_5H_5O ($\tilde{P2}$) is relevant to the oxidation kinetics of C_5H_6 , as highlighted by Ghildina et al. [293]. This

required lumping C_5H_5O of the PES keeping the consistency of pseudospecies composition with the lumping of the PES explored in this section.

4.4.3 $C_5H_5 + C_5H_5$

The theoretically derived reactivity for the $C_{10}H_{10}$ and $C_{10}H_9$ PESs by Long et al. [295] consists of 328 reversible reactions and 31 species. MEL was applied to the two interconnected PESs, reducing the kinetic mechanism to 33 irreversible reactions and 8 pseudospecies; further elimination of all $C_{10}H_9$ isomers, which were found to react fast, resulted in a set of only 4 lumped reactions and 3 pseudospecies. The detailed and lumped rate constants were also included in the CRECK kinetic mechanism for additional validation of the lumping methodology. This section reports the study of the reactivity at 1 atm for simplicity. However, in the updated kinetic mechanism the full pressure dependent reactivity was considered.

Figure 4.12 shows a schematic representation of the two PESs (the original PES was provided in [295]). The recombination of two cyclopentadienyl radicals produces 16 $C_{10}H_{10}$ isomers. The prototype structures of the most stable wells, i.e., fulvalanes (6 species, alternatively named bicyclopentadienyl, see Appendix A) and azulanes (8 species), are shown in Figure 4.12. Overall, $C_{10}H_{10}$ PES has 23 species and its reactivity is described by 238 reversible reactions. Long et al. [295] suggest that at intermediate-to-low temperatures H-atom abstraction reactions from $C_{10}H_{10}$ are more relevant to the formation of $C_{10}H_9$ radicals (fulvalanyls and azulanyls) than bond-fission reactions. $C_{10}H_9$ isomers decompose via isomerization and β -scission reactions to fulvalene, azulene, and naphthalene. The $C_{10}H_9$ PES has 14 species (6 in common with $C_{10}H_{10}$ PES) and the corresponding detailed mechanism has 90 reversible reactions.

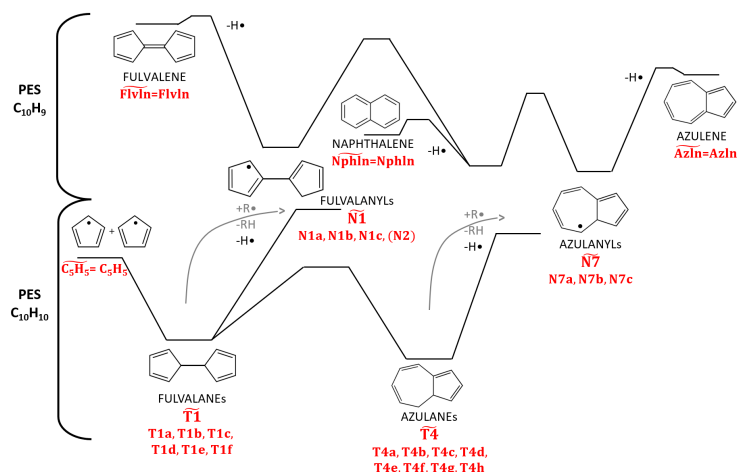


FIGURE 4.12: Scheme of the main reaction channels of the $C_{10}H_{10}$ and $C_{10}H_9$ PESs investigated by Long et al. [295]. Red names indicate accumulating species, and names with \sim are pseudospecies.

The lumping of the $C_{10}H_{10}$ PES starts with the selection of the accumulating isomers. The analysis of the reactivity of bimolecular reactants and the steady-state composition of the isomer pool allows for the elimination of three species. Cyclopentadienyl constitutes a single pseudospecies. $C_{10}H_{10}$ isomers are grouped into fulvalanes ($\widetilde{T1}$ consisting of 6 wells)

and azulanes ($\widetilde{T4}$ consisting of 8 wells) according to their chemical structure. Similarly, bimolecular reactants are lumped into fulvalanyls ($\widetilde{N1}$ consisting of 3 species) and azulanyls ($\widetilde{N7}$ consisting of 3 species). Further lumping of $\widetilde{T1}$ and $\widetilde{T4}$ into a single pseudospecies is discouraged by the large differences in the associated k_{IJ} (see Fig. 5B in the paper of Long et al. [295]).

Steady-state composition was used as a guess for α_L^0 of $\widetilde{T1}$ and $\widetilde{T4}$. Instead, α_L^0 for $\widetilde{N1}$ and $\widetilde{N7}$ was derived from the simulations of $\widetilde{T1}$ and $\widetilde{T4}$, respectively, as the main sources of the selected bimolecular products. Convergence of the final α_L was reached with less than 10 iterative simulations of the full detailed mechanism for each lumped reactant. It is noted that the reactivity of $\widetilde{T1}$ depends only slightly on α_L^0 , since fast isomerization reactions within $\widetilde{T1}$ lead to the steady-state composition much earlier than the initial cutoff time marking 1% of reactant consumption.

Overall, MEL allows for a reduction in the mechanism for the $C_{10}H_{10}$ PES from 23 species and 238 reversible reactions to 5 pseudospecies and 23 forward reaction channels. The plots of Figure 4.13 show the excellent results of the MEL for this case: simulation profiles obtained with the detailed and lumped kinetic models are mostly overlapped.

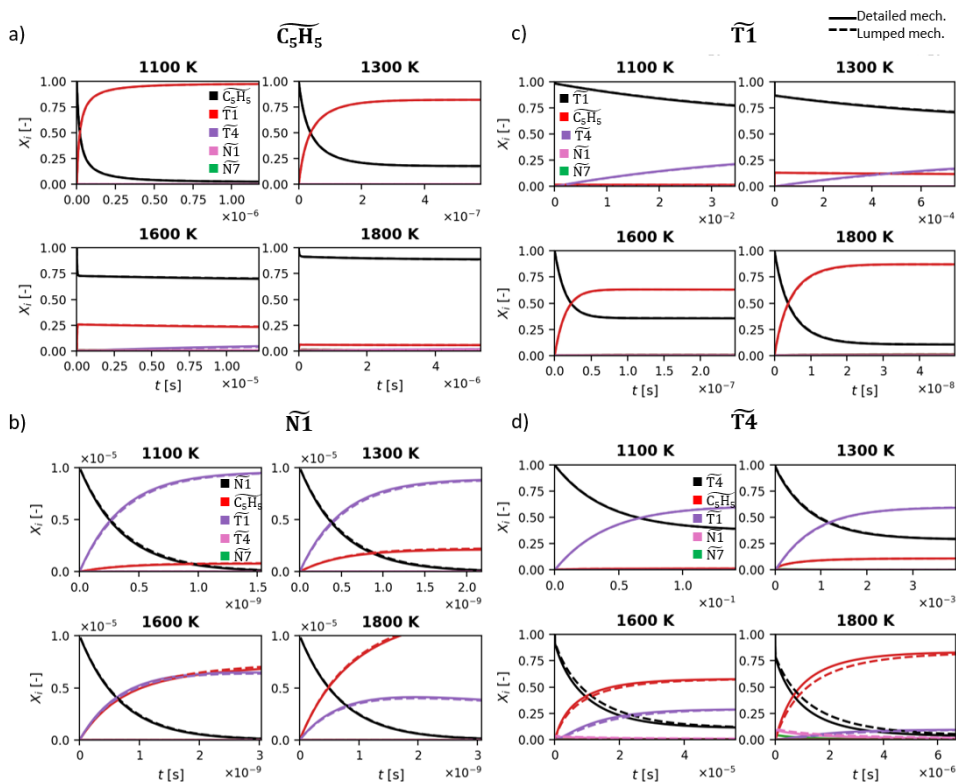


FIGURE 4.13: Comparison between the performances of the detailed (solid lines) and lumped (dashed lines) mechanisms in the 1000–1900 K range of the reactivity of pseudospecies C_5H_5 a), $\widetilde{N1}$ b), $\widetilde{T1}$ c), and $\widetilde{T4}$ d).

The lumping of the $C_{10}H_9$ PES was performed independently of the $C_{10}H_{10}$ PES. Nevertheless, fulvalanyls and azulanyls pseudospecies ($\widetilde{N1}$ and $\widetilde{N7}$) are common to both PESs, hence their lumping should be consistent.

Fulvalene, azulene and naphthalene are included as single unmerged pseudospecies. The remaining accumulating species are merged according to their chemical structure. $\widetilde{N7}$ has the same components as in the $C_{10}H_{10}$ PES, and is mostly comprised of $N7b$, like in the former PES. The behavior of the fulvalanyl group shows instead significant discrepancies with $\widetilde{N1}$ of the $C_{10}H_{10}$ PES. In fact, not only the isomer pool composition is different, but the correct reproduction of the profiles of the detailed mechanism requires the inclusion of one further species absent in the $C_{10}H_{10}$ PES ($N2$ in Figure 4.12). The consistency of this choice was verified by comparing kinetic simulations of the $C_{10}H_9$ detailed mechanism and a lumped version starting from the $\widetilde{N1}$ composition derived from the $C_{10}H_{10}$ PES. The performance of the two models was almost identical.

Overall, the application of MEL to $C_{10}H_9$ PES decreases the size of the associated mechanism from 14 species and 90 reversible reactions to 5 species and 20 irreversible reactions, which are further reduced to 13 when neglecting minor channels. Figure 4.14 reports comparisons between the detailed and lumped model performances for some pseudospecies: the profiles obtained are almost indistinguishable, supporting the accuracy of the approach proposed.

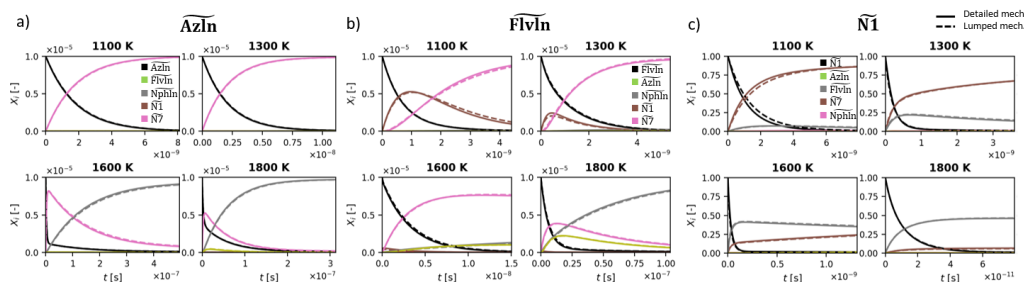


FIGURE 4.14: Comparison between the performance of the detailed (solid lines) and lumped (dashed lines) mechanisms in the 1100–1800 K range of the reactivity of pseudospecies \widetilde{Azln} a), \widetilde{Flvln} b), $\widetilde{N1}$ c), considering the full reactivity (no non-reacting species).

Finally, the new rate constants were integrated into the CRECK kinetic mechanism. Both cyclopentadienyl (C_5H_5) and naphthalene ($C_{10}H_8$) were already present in the target kinetic scheme, whereas the remaining 6 pseudospecies were added as $FC_{10}H_{10}$ ($\widetilde{T1}$), $AC_{10}H_{10}$ ($\widetilde{T4}$), $FC_{10}H_9$ ($\widetilde{N1}$) and $AC_{10}H_9$ ($\widetilde{N7}$), $Flvln$ (\widetilde{Flvln}) and $Azln$ (\widetilde{Azln}). Their thermodynamics corresponds to that of the most stable isomer constituting the pseudospecies. H-atom abstraction reactions from $FC_{10}H_{10}$ and $AC_{10}H_{10}$ by the main radicals were introduced using analogy rules from cyclopentadiene.

Relevant cyclopentadiene pyrolysis reactor data [296]–[298] were simulated with the target model updated with both the detailed and lumped sets of rate constants. $AC_{10}H_{10}$, all $C_{10}H_9$ isomers, azulene and fulvalene do not accumulate in relevant fractions in any of the cases tested, highlighting fast decomposition of $C_{10}H_{10}$ to $C_{10}H_8 + 2H$ and suggesting that the $C_{10}H_9$ reactivity may be entirely neglected. Hence, a further reduction was performed: the $C_{10}H_{10}$ PES was lumped considering only $FC_{10}H_{10}$ ($\widetilde{T1}$) and a single group of $C_{10}H_9 + H$ bimolecular products was always considered as non-reacting. Replacing $C_{10}H_9 + H$ with $C_{10}H_8 + 2H$ in the final model allowed complete removal of the $C_{10}H_9$ isomers. The final

lumped mechanism consists of only 3 species and 4 $\tilde{k}_{\tilde{I}\tilde{J}}$, an impressive reduction with respect to the detailed set of 31 species and 656 k_{IJ} . The performance of this lumped mechanism is almost identical to the first lumped version of 8 species and 33 reactions.

Figure 4.15 shows experimental data for the pyrolysis of C_5H_6 in a PFR in comparison with model performances of the original CRECK kinetic model, and of the model updated with the reactivity of the $C_{10}H_{10}/C_{10}H_9$ PESs [295]. The simulation profiles of the lumped and detailed kinetic schemes are almost superimposed, supporting the validity of the approach presented. Further validation with additional experimental datasets is reported in the SM of the corresponding paper [291].

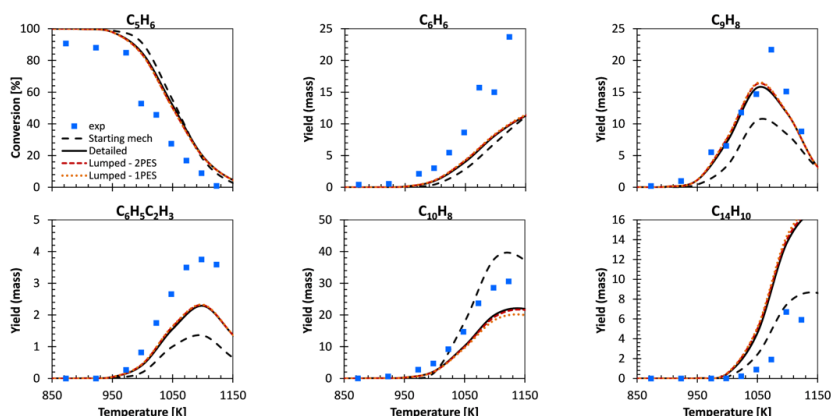


FIGURE 4.15: Experimental data for the pyrolysis of C_5H_6 in a plug flow reactor [296] compared to the profiles obtained from kinetic simulations with the CRECK kinetic model, with the updated detailed $C_{10}H_{10}/C_{10}H_9$ reactivity from Long et al. [295] (31 species, 656 reactions), and with the updated lumped reactivity (2PES: 8 species, 33 reactions; 1PES: 3 species, 4 reactions).

4.5 Summary and future perspectives

This section presented MEL, the first systematic approach specifically designed to process rate constants derived from master equation simulations and integrate them into global kinetic schemes. The main challenges addressed by MEL are:

1. The removal of several intermediate species often unnecessary to the macroscopic representation of the reactivity.
2. Discontinuities in rate constants and number of species originating from reactions involving highly reactive intermediates with comparable timescales for chemical reaction and rovibrational relaxation.

MEL retains features of lumping methodologies for both ME simulations and global kinetic schemes. The main idea is similar to chemical lumping of unimolecular reactions: a simple ODE system of equations describing time evolution of species concentration according to a detailed mechanism is reduced to an equivalent lumped system of a smaller set of pseudospecies. The derivation of lumped rate constants for pseudospecies is instead inspired

by the solution procedure of the non-conservative ME: simulations are run for each reactant pseudospecies imposing that all products are non-reactive, so that the reactant decays exponentially. Lumped rate constants are then derived from differential fits of the profiles of the product concentration. The constituents of the pseudospecies are selected according to their stability, chemical structure, and reactivity, while highly reactive non-accumulating species are excluded from the lumped mechanism. The final lumped mechanism may be further optimized against kinetic simulations of the full reactivity. All the operations listed above are performed with an in-house Python code relying on OpenSMOKE++ [82] and OptiSMOKE++ [276], [277] for kinetic simulations and optional mechanism optimization, respectively.

The approach proposed has several advantages:

1. Contrary to most chemical lumping approaches, it allows both species elimination and merging of species with similar structure and reactivity.
2. The applicability range of the lumped set of rate constants corresponds to that of the ME simulations.
3. The T, p range of validity for the lumped rate constants may be broader than that of the detailed rate constants.
4. Both bimolecular and unimolecular reaction channels are considered.

The validity of MEL is supported by three cases of application with increasing complexity. Lumping of the CH_3COOH PES shows how to remove a non-accumulating intermediate from the mechanism, still retaining implicitly its reactivity. The main challenge of including the reactivity of the $\text{C}_5\text{H}_5 + \text{OH}$ PES into a global kinetic scheme is the limited range of validity of the rate constants of the detailed mechanism, mostly related to the partial stability of the wells. Lumping together isomers with similar reactivity solves this issues, resulting in very similar performances of the lumped and detailed mechanisms. Finally, lumping $\text{C}_{10}\text{H}_{10}$ and C_{10}H_9 PESs allows one to dramatically decrease the initial set of 31 species and 328 reversible reactions to only 3 pseudospecies and 4 irreversible reactions, achieving excellent performances for the lumped kinetic mechanism.

The MEL approach constitutes an important step towards the systematic and rigorous integration of AI-TST-ME-derived rate constants into global kinetic schemes, effectively bridging the gap between the needs of kinetic model parameters of increasing accuracy and the necessity of producing predictive, reliable, physically meaningful, manageable and human readable global kinetic models. Hence, the MEL approach was extensively applied to all PESs theoretically investigated in this work (with the obvious exception of H-atom abstraction reactions). Additionally, MEL was also used to lump literature theoretical calculations to be included in the CRECK kinetic model, as highlighted in the tables of Section 5.2, 6.2.

MEL can also be used to process existing kinetic models rather than ME outputs, such as the complex kinetics of low temperature combustion of alkanes or other novel fuels. For instance, the methodology described was successfully applied to the low temperature oxidation mechanism of n-pentane of Bugler et al. [299]. This work was presented at the 10th

(Virtual) European Combustion Meeting (<https://www.ecm2021napoli.eu/proceedings/>, p. 171). The lumping of a portion of a mechanism larger than a single PES presents similar challenges to what was presented in Section 4.4.3, namely the consistent lumping of different connected PESs, especially in terms of pseudospecies composition selection. For instance, MEL was recently applied to the low-temperature oxidation mechanism of oxymethylethers (OMEs) [300]. In this case, the isomer pool composition of ROO radicals derived with the automatic pseudospecies selection of MEL failed, due to strong non-equilibrium effects and to the inconsistency of some of the reactions of the starting detailed mechanism (e.g., H-atom abstraction reactions producing different distributions of radical isomers depending on the abstractor). Therefore, composition of the selected isomer pool was fixed to a reasonable starting guess, and the resulting mechanism was consistently optimized with OptiSMOKE++ [276]. Besides the application of MEL to multiple PESs, another future development should include full automatization of the selection of pseudospecies and not only of their composition.

Chapter 5

Cyclopentadiene pyrolysis and oxidation

This chapter presents theoretical calculations and kinetic modeling results for the pyrolysis and oxidation of cyclopentadiene. A brief literature overview on the kinetics of cyclopentadiene combustion is presented in Section 5.1, focusing on general aspects of macroscopic combustion properties and product distribution, as well as commenting on the evolution of the interest in this molecule in recent years.

Section 5.2 explains the organization of the CRECK kinetic model according to the reaction classes for 5-membered rings formulated in this work. An extensive list of examples divided by class and highlighting the updates of this work is provided.

Theoretical calculations of relevant reactions in cyclopentadiene combustion mechanism are described in Section 5.3, showing how both detailed theoretical kinetics and analogy rules are used for mechanism development.

Finally, some of the kinetic modeling results of the global mechanism testing and validation are presented in Section 5.4, consistent with the class organization described.

5.1 Background and literature review

Cyclopentadiene (C_5H_6) is an unsaturated 5-membered ring with two double bonds. Cyclopentadienyl radical (C_5H_5) is obtained from H fission from cyclopentadiene. This radical is particularly interesting because of its strong resonance stabilization and its symmetric (D_{5h}) structure.

The first experimental study on cyclopentadiene bond dissociation energy dates back to the 1950s [301], while the first studies on other decomposition and growth pathways date back to the 1970s [163], [302]. The interest in cyclopentadiene and cyclopentadienyl mostly stems from their relevance as products of benzene oxidation through the decomposition of phenol and phenoxy radical, respectively [303], [304], and their significance in the formation of small linear C_1 – C_4 hydrocarbons.

Table 5.1 reports some of the relevant literature works published in the last 25 years on the reactivity of C_5H_6 , C_5H_5 , C_9H_8 . While this summary does not aim at being a full literature review, it highlights the evolution of the interest in 5-membered ring unsaturated

hydrocarbons as well as some of the main references for the update of the CRECK kinetic mechanism performed in this work.

The main decomposition products of cyclopentadiene were detected in studies from the 1990s, such as in the high-temperature shock tube study of Burcat et al. [305]. C_5H_6 decomposes to unsaturated C_2 – C_4 species and methane, and it can also grow to form benzene, as anticipated in kinetic modeling works for unsaturated cyclic species [163]. Burcat et al. also presented one of the first mechanisms for cyclopentadiene pyrolysis, postulating that smaller hydrocarbons derive from ring-opening processes, and highlighting the importance of cyclopentadienyl radical in the decomposition process. The C–H bond-fission to form cyclopentadienyl radical was studied with high temperature microkinetic experiments [306], [307], however in both cases the fitting through a small kinetic mechanism was required. The first theoretical studies on cyclopentadiene mostly focused on the reactivity of C_5H_5 [308]–[313]. The pioneering theoretical studies of Zhong and Bozzelli [310], [311] provide the first theoretical calculations for the reactions of C_5H_6 and C_5H_5 with important radicals. Their work was mostly motivated by the construction of a kinetic mechanism for the oxidation of cyclopentadiene within the context of MAHs combustion. In particular, they stressed the need for including reactions of cyclopentadienyl radical with H, OH, O, and O_2 to reproduce experimental product profiles of benzene oxidation.

Besides explaining the formation of linear hydrocarbons through ring-opening processes, the detection of PAHs formed in alkene flames led to the postulation that C_5 unsaturated rings may be important intermediates in MAH/PAH formation at sooting conditions in flames [314], [315]. The first postulated pathways for the formation of 1- and 2-ring aromatic species were $C_5H_5 + CH_3$ [312] (forming methyl-cyclopentadiene as an intermediate in ring-enlargement reactions) and the self-recombination of C_5H_5 [313], respectively. Both pathways were proved to be of key relevance in the formation of MAHs and PAHs, especially the latter, which was investigated numerous other times in the past two decades.

Between 2005–2018, a large number of both experimental and theoretical studies led to more comprehensive and physically based kinetic models for cyclopentadiene pyrolysis and oxidation. For instance, the combined experimental and kinetic modeling study of Vervust et al. [298] is an important reference for the kinetics of cyclopentadiene pyrolysis. The good variety of experimental flow reactor studies on cyclopentadiene oxidation did not encourage theoretical investigations, such that many of the kinetic parameters for oxidation reactions were based on estimates and analogies to well-investigated linear alkenes or best fits to experimental species profiles. On the other hand, theoretical investigations of growth pathways from cyclopentadiene and cyclopentadienyl radicals were conducted. In particular, the $C_5H_6 + C_5H_5$ addition was theoretically investigated multiple times [316]–[318] because of its key role in PAH formation from cyclopentadiene as a fuel. Additionally, recombination reactions of C_5H_5 with C_2H_2 and C_3H_3 were studied for their potential relevance in flames [319], [320].

Finally, in the past five years the interest in the combustion mechanism of cyclopentadiene has increased further, as highlighted by the consistent number of studies reported in

Table 5.1. Many theoretical studies provided more accurate calculations for reaction pathways already investigated in the literature. For instance, Long et al. [295] theoretically investigated the "well-known" cyclopentadienyl self-recombination. Mebel et al. [292]–[294] performed thorough theoretical investigations of the reaction pathways for the oxidation of cyclopentadienyl with relevant radicals. At the same time, theoretical investigations of primary reactions of cyclopentadiene oxidation such as H-atom abstraction or addition reactions with H, OH, and HO₂ were performed [321]–[323].

This renewed interest in the reactivity of 5-membered unsaturated rings is related to the relevance of cyclopentadiene in the combustion of new fuels as well as in the synthesis of new materials. In particular, cyclopentadiene is an important decomposition product of jet fuels (e.g., JP-10 [324], [325]), as well as of potential alternative fuels such as dimethylfuran [326]. Additionally, in recent years it was suggested that controlled combustion of rich flames might be used for the synthesis of new carbon nanomaterials, e.g., carbonaceous nanoparticles and graphene. The knowledge of the reactivity of the main functional groups present in these materials under combustion conditions is essential to control their formation. Recent experimental studies proved that 5-membered ring structures persist in large PAHs and incipient soot particles [57], [327], suggesting that such structures are essential in PAH nucleation and growth through radical chain reactions. It is also worth mentioning that 5-membered ring structures in carbonaceous nanoparticles also affect the resulting optical and electric properties. These aspects motivate detailed theoretical studies of the reactivity of C₅H₆ and C₅H₅, used as model compounds for the behavior of 5-membered rings in PAHs and soot.

Despite the numerous experimental, theoretical and kinetic modeling studies, the sub-mechanism of cyclopentadiene pyrolysis and oxidation is hardly ever fully updated in current kinetic mechanisms. For instance, even the most recent mechanism developed ad-hoc for cyclopentadiene [338] largely disregards recent literature theoretical investigations, and nonetheless performs well in reproducing many experimental datasets for cyclopentadiene oxidation. The lack of model updates also stems from the complex multi-well PESs describing the reactivity of cyclic species, which certainly discourages from including the corresponding rate constants in kinetic models. Additionally, the exponentially increasing number of publications together with the lack of unified conventions and public databases hinders a continuous and smooth update of the kinetic models available. Finally, it must be mentioned that updating a model with rate constants from different sources and with different degree of detail as well as different uncertainties generates imbalances in the kinetic model. This generally results in the "tuning" of the parameters of rate constants deemed as more uncertain for a best match with experimental data, possibly causing large errors in the modified kinetic parameters.

Table 5.1 also shows the main experimental and theoretical studies concerning indene (C₉H₈) formation and combustion reactions. Indene is the smallest PAH with a cyclopentadiene-like 5-membered ring, and is therefore used as a model compound for larger PAHs. In the combustion of cyclopentadiene, indene mostly derives from C₅ + C₅ reactions (included in the C₅H₆ section of Table 5.1). Table 5.1 also includes formation pathways

TABLE 5.1: Overview of some of the relevant theoretical and experimental works on cyclopentadiene and indene pyrolysis and oxidation from the 1990s on.

year	1995	2000	2005	2010	2015	2020
C₅H₆						
EXP (microkin.)	Roy [306], [328]	Kern [307]				Jin [329]
THEORY	BONDFISS. Zhong [310] C ₅ H ₆ +H /OH/O/HO ₂	BONDFISS. Moskaleva [330] HABS by H Bacskey [332] DECO	Harding [331] BONDFISS. Kislov [333] C ₅ H ₆ +C ₅ H ₅ Wang [317] C ₅ H ₆ +C ₅ H ₅	Cavallotti [318] C ₅ H ₆ +C ₅ H ₅		HABS by OH Baroncelli [321] HABS Mao unpub. C ₅ H ₆ +OH Mao [334] C ₅ H ₆ +H Xu [323] C ₅ H ₆ +HO ₂
REACTOR DATA	Burcat [305] pyrolysis		Orme [335] oxidation	Kim [296] pyrolysis Butler [336] oxidation	Djokic [297] pyrolysis Ji [337] oxidation	Vervust [298] pyrolysis Wang [338] oxidation Johnson [339] pyrolysis
C₅H₅						
EXP (microkin.)					Knyazev [340] C ₅ H ₅ +C ₅ H ₅	
THEORY	Bearpark [308] Thermo (C ₅ H ₅) Moskaleva [312] C ₅ H ₅ +CH ₃ Melius [313] C ₅ H ₅ +C ₅ H ₅	Kiefer [309] Thermo (C ₅ H ₅) Zhong [311] C ₅ H ₅ +H/OH /HO ₂ /O/O ₂	Cavallotti [319] C ₅ H ₅ +C ₂ H ₂	Sharma [341] C ₅ H ₅ +CH ₃ Robinson [343] C ₅ H ₅ +O/OH/O ₂ Sharma [320] C ₅ H ₅ +C ₃ H ₃	Cavallotti [342] C ₅ H ₅ +C ₅ H ₅	Long [295] C ₅ H ₅ +C ₅ H ₅ Mebel et al. [292]-[294] C ₅ H ₅ +O/OH/O ₂ Mao [322], [344] C ₅ H ₅ +C ₂ H ₂ DECO
C₉H₈						
EXP (microkin., formation)				Parker [345] C ₆ H ₅ +C ₃ H ₅ / C ₃ H ₄	Parker [346] C ₇ H ₇ +C ₂ H ₂	
EXP (microkin., growth/ox)						Jin [329] HABS by OH Zhao [347] C ₉ H ₇ +CH ₃
REACTOR DATA		Laskin [348] pyrolysis Lu [349] pyrolysis				Jin [337] pyrolysis
THEORY (formation)			Fascella [350] C ₄ H ₆ /C ₄ H ₅ + C ₆ H ₆ /C ₆ H ₅		Mebel [140] Mebel [281]	Mao [322] C ₇ H ₇ +C ₂ H ₂
THEORY (growth)		Mulholland [351] C ₅ H ₆ /C ₅ H ₅ +C ₉ H ₈ /C ₉ H ₇				Zhao [347] C ₉ H ₇ +CH ₃ Krasnoukhov [352] C ₉ H ₇ +C ₅ H ₅

more relevant in benzene and toluene pyrolysis and oxidation (discussed in Section 6.2.2). Indene is also an important precursor of larger PAHs. For instance, naphthalene (C₁₀H₈) can be formed through the ring enlargement pathway C₉H₇ + CH₃ [347], analogous to C₅H₅ + CH₃. Instead, indene and indenyl self reactions as well as reactions with C₅ rings result in the formation of 3 and 4 ring PAHs (e.g., [351]).

Because of the similarity between cyclopentadiene and indene, most of the reaction pathways studied for the former may be applied to the latter to build consistent kinetic mechanisms. Also the main theoretical studies of reactions relevant to indene decomposition and growth involve reaction pathways already identified for cyclopentadiene [347], [351]. However, it is still unclear whether analogy rules can be blindly applied to determine the reactivity of C₉H₈ from that of C₅H₆. The only experimental study addressing this aspect is the shock tube study of Jin et al. [329], who detected a difference of a factor of 2 in the total rate constants of OH + C₅H₆ / C₉H₈. Additionally, the presence of the aromatic ring does change the product distribution. In fact, the decomposition of the 5-membered ring results in the formation of substituted MAHs such as phenylacetylene and toluene, as confirmed by experimental studies on indene decomposition [337], [348]. These studies also detect 3 and 4 ring PAHs, as confirmed by the theoretical studies mentioned above. Finally, while accurate

theoretical calculations of the main reaction pathways involving cyclopentadiene are possible with the currently available computational resources, the same level of accuracy cannot generally be reached for indene due to its larger number of heavy atoms (see 3.5.1). Besides the computational cost, PESs for larger aromatics involve a larger number of isomers, formed for instance by H transfers to multiple ring sites, or ring opening at multiple locations, and consequently a larger number of reaction pathways.

As far as kinetic modeling is concerned, the recent combined experimental and kinetic modeling work of Jin et al. [337] provides the only detailed kinetic mechanism for indene pyrolysis, while neither experimental data nor kinetic models are available for indene oxidation.

In this context, this chapter revises the CRECK kinetic mechanism for cyclopentadiene and indene pyrolysis and oxidation based on both the available literature and new theoretical insights. The kinetic mechanism is organized according to relevant reaction classes identified for the formation, pyrolysis, oxidation and growth of cyclopentadiene-like rings as well as substituted unsaturated 5-membered rings such as $C_5H_5CH_3$, C_5H_5OH , C_9H_8 (Section 5.2) Accurate theoretical calculations are performed for some of the relevant classes to fill in knowledge gaps (Section 5.3) and to explore the uncertainty in extending the rate constants obtained to similar systems. The performance of the updated CRECK kinetic mechanism with regard to the available experimental data for cyclopentadiene and indene pyrolysis and oxidation is finally tested and discussed (Section 5.4).

5.2 Reaction classes and kinetic model updates by class

5.2.1 Decomposition and oxidation

This section lists the main reaction classes for the decomposition and oxidation of unsaturated 5-membered ring species of the CRECK kinetic mechanism, many of which were added in this work. Structures of the main species are found in appendix A. Tables 5.2 and 5.3 illustrate species, classes and reaction types identified according to the criteria presented in Section 2.6. For each reaction type, an example is provided together with the corresponding reaction parameters, their source, and indication of the updates performed in this work (boxes colored according to the type of update: theory from this work, theory/experiment from literature, theory + MEL from literature, estimate or analogy rules). Additionally, the elementary steps for each reaction class are listed. It is noted that most reaction types (except for bond-fission and H-atom abstraction reactions) consist of multiple elementary steps, and thus highlight the essential role of multi-well PESs. The identification of all elementary steps might be uncertain for some estimated lumped reactions. The attempt to specify the elementary steps for each reaction provides some guidance for relating the present classification with codes for automatic PES generation or ES calculations [94], [97], [98].

As explained in Section 2.6, the species type identifies the functional group that participates in the reactivity in a hierarchical way. It is noted that most of the examples for a species type refer to the same species, however the same reaction class is applied also to substituted or multiple ring species sharing the same chemical functionality. For instance, the simplest species of C5-M type is cyclopentadiene (C_5H_6 , see Table 5.2). Its reactivity is characterized by the presence of the unsaturated C_5 ring and the methylene group. Hence, its reaction classes also extend to substituted forms such as C_5H_5OH , $C_5H_5CH_3$, C_9H_8 .

The class type is mostly related to the reactants. The reaction types provide additional information about the main steps of multi-well PES reactivity or about the product channels. The main class types identified for C_5 species (which also apply to aromatic species of Section 6.2) are:

- **Decomposition** (DECO.): unimolecular reactions, may be molecular or radical decomposition steps. The elementary steps involved are generally H transfer, ring opening, elimination or β -scission in the case of radicals. The reaction type MOLEC_DECO mostly identifies CO elimination, common to both C_5 and C_6 rings (Section 6.2). For radicals, a common decomposition type is ROPEN, where the limiting step is the ring opening of the radical.
- **Bond-fission** (BONDFISS.): this class type identifies bond-fission reactions and is not grouped together with decomposition reactions because of its chain branching (or termination, depending on the direction in which it occurs) character. In this case, the reaction type also identifies the bond being broken, e.g., BONDFISSION_CH.
- **β -scission** (BETASCISS.): single-step β -scission reactions. Similarly to bond-fission reactions, the reaction type identifies the bond being broken.

- **Isomerization** (ISOM.): isomerization reactions that mostly indicate H atom transfer. The reaction type may also inform about the atoms involved in the H transfer (e.g., ISOM_OC indicates a transfer from an oxygen to a carbon atom). In a few cases, this reaction type indicates bimolecular well-skipping isomerization reactions aided by addition or recombination steps (e.g., ISOM_BIMOL_H in Table 5.3).
- **H-atom abstraction** (HABS): H-atom abstraction reactions, which may involve both molecule + radical and radical + radical reactions. They always occur in a single elementary step. The reaction type identifies the abstractor, i.e., HABS_X indicates abstractor X.
- **Ipsso substitution** (IPSO): ipso addition-elimination reactions consisting of two elementary addition/ β -scission steps. The reaction type identifies the radical being added, while the eliminated group can be retrieved from the species type. For instance, reaction class [C5,OH-M][IPSO_H] identifies the replacement of the OH group in a C₅-membered ring with an H atom.
- **Addition_X** (ADD_X): addition and recombination reactions with group X (generally a radical). The reaction type specifies both the nature of the addition, i.e., whether it is an addition or a recombination, and products or subsequent reaction steps, often common to unimolecular decomposition reactivity (e.g., ring opening, elimination). Instead, addition/recombination resulting in well stabilization is indicated as ADD/REC_WELL. REC_X_WELL is therefore the reverse of a bond-fission reaction.

The main classes identified for each species type are briefly commented on below. The smallest representative of species type C₅-M is cyclopentadiene. The identified reaction types are all bimolecular H-atom abstraction reactions or addition reactions. Unimolecular decomposition is instead described in the opposite direction, i.e., through growth reactions from C₂, C₃ species (Section 5.2.2) and H recombination with cyclopentadienyl radical ([C5-RSR][REC_H] in Table 5.3). H-atom abstraction reactions are the main consumption pathway of cyclopentadiene and rate constants were updated with theoretical calculations from the present work (Section 5.3.1) and from literature [321]. As far as addition reactions are concerned, both H and OH additions were found to be particularly relevant in cyclopentadiene oxidation. Rate constants for both class types were updated with the recent theoretical investigation of Mao et al. [334] (the latter is from an unpublished work) and lumped with MEL (Chapter 4). Addition reactions with O₂ and O(³P) (ADD_O2, ADD_O) only include well-skipping ring opening pathways estimated in older versions of the CRECK mechanism.

Reaction classes for substituted C₅ species (i.e., one or more of the H atoms bonded to sp² carbons in the ring are substituted) were identified for H₂, CH₃, OH, and ring (C₅, A1) substituents. The corresponding species types C₅,X-M only account for additional reactions characteristic of the X substituent and its interaction with the C₅ ring. For instance, all of the H-atom abstraction reactions refer to the X substituent. C₅,A1-M indicates an aromatic

substituent, and the simplest species of this type is indene (C_9H_8). In this case, since the individual C5-M and A1-M (Section 6.2) are already described, the C5,A1-M type only includes reaction classes deriving from simultaneous presence of the two rings. The prototypical species of C5,CH3-M type is 1,3- methylcyclopentadiene, especially relevant in cyclopentadiene pyrolysis. On the other hand, 1,3- C_5H_5OH is the simplest species of C5,OH-M type and was recently found to be formed upon OH recombination with cyclopentadienyl radical at intermediate temperatures [292]. Finally, cyclopentadienone (C_5H_4O) is the simplest species of C5O-M type. This species never gained a lot of attention in the kinetics community until recently as a potentially relevant product of benzene oxidation [353], and it was not present in the original version of the CRECK mechanism. Decomposition and H addition reactions were added from theoretical calculations [293], while all the other bimolecular reactions were estimated by analogy with aromatic systems. H-atom abstraction reactions are not reported because they were included according to the CRECK's automated rules; the corresponding radical is assumed to decompose directly to C_2/C_4 products.

C5-RSR (Table 5.3) is the representative of resonance-stabilized C_5 radicals such as cyclopentadienyl. The reaction classes of this type are particularly relevant as they serve as prototype for large PAHs [58]. All of the relevant reaction classes of cyclopentadienyl pyrolysis and oxidation in the CRECK mechanism were therefore updated with recent theoretical calculations as well as with theoretical calculations from the present work. All recombination classes include subsequent ring opening and elimination steps. The contribution of each class is extensively discussed in Section 5.4. The reactivity of substituted resonance-stabilized C_5 species such as C5H2-RSR and C5O-RSR (such as 1,3- C_5H_5O , which was recently identified as a relevant oxidation intermediate of cyclopentadienyl [292], [293]) was found to be extremely relevant to the radical pool in cyclopentadiene pyrolysis and oxidation at low and intermediate temperatures. In this work, the reactivity of these types was carefully introduced and revised in the CRECK kinetic mechanism.

The role and relevance of the identified classes and reaction types is discussed in the presentation of the results of kinetic simulations in Section 5.4.

TABLE 5.2: Reaction classes for decomposition and oxidation of C5,X-M species types. M, R, RSR indicate a molecule or resonantly stabilized radical, respectively, while X indicates a substituent. Colored boxes highlight the reaction classes updated in this thesis. For each example, kinetic parameters of the modified Arrhenius form $k = k_0 T^\alpha \exp(-\frac{E_A}{RT})$ are provided (units cal, mol, cm^3 , s, K, reference pressure of 1 atm for pressure-dependent reactions). Colored boxes indicate model updates performed in different ways: orange for theoretical calculations from this work, yellow for literature theoretical calculations, green for literature theoretical calculations lumped with MEL, blue for estimates from other mechanisms or analogy rules.

SPECIES TYPE:	C5-M	(C_5H_6)		
CLASS TYPE	REACTION TYPE	EXAMPLE	ELEM. STEPS	SOURCE
HABS	HABS_H	$H + C_5H_6 = H_2 + C_5H_5$ 5.71E+05 2.39 2176	H ABSTRACTION	THEORY This work
	HABS_CH3	$CH_3 + C_5H_6 = CH_4 + C_5H_5$ 4.45E+02 2.91 4728	H ABSTRACTION	THEORY This work
	HABS_OH	$C_5H_6 + OH = C_5H_5 + H_2O$ 3.00E+07 1.80 504	H ABSTRACTION	THEORY This work
	HABS_O	$C_5H_6 + O = C_5H_5 + OH$ 6.20E+06 2.12 4855	H ABSTRACTION	THEORY Baroncelli 2020 [321]
	HABS_HO2	$C_5H_5 + HO_2 = C_5H_6 + O_2$ 3.22E-03 4.25 -3202	H ABSTRACTION	THEORY This work

	HABS_HO2	$C_5H_6 + HO_2 = C_5H_5 + H_2O_2$ 6.0E-04 4.65 6909	H ABSTRACTION	THEORY Baroncelli 2020 [321]
	HABS_C2H3	$C_5H_6 + C_2H_3 = C_5H_5 + C_2H_4$ 1.4E+06 2.00 4871	H ABSTRACTION	CRECK ESTIMATE
ADD_H	ADD_H_WELL	$C_5H_6 + H = CYC_5H_7$ 1.76E+14 -0.68 -484 6.50E+72 -17.33 35535	ADDITION	THEORY Mao 2020 [334] + MEL
	ADD_H_ROPEN	$C_5H_6 + H = LC_5H_7$ 2.58E+21 -4.28 2290 5.00E+99 -24.96 56788 $C_5H_6 + H = C_3H_5-A + C_2H_2$ 3.70E+31 -4.60 34025 $C_5H_6 + H = C_3H_3 + C_2H_4$ 5.32E+23 -2.10 44897	ADDITION H TRANSFER RING OPENING	THEORY Mao 2020 [334]
ADD_OH	ADD_OH_WELL	$C_5H_6 + OH \rightarrow C_5H_6OH$ 3.20E+39 -8.4 8348	ADDITION H TRANSFER	THEORY Mao 2021, unpublished + MEL
	ADD_OH_EL_H	$C_5H_6 + OH \rightarrow C_5H_5OH + H$ 2.24E+12 0.25 12815 $C_5H_6 + OH \rightarrow 0.5C_5H_5OH$ +0.5C ₅ H ₅ O+1.5H 9.45E+12 -0.13 16085	ADDITION H TRANSFER BETASCISSION	THEORY Mao 2021, unpublished + MEL
	ADD_OH_ROPEN	$C_5H_6 + OH \rightarrow C_4H_6 + HCO$ 4.84E+33 -6.11 26064 $C_5H_6 + OH \rightarrow C_2H_2 + C_2H_4 + HCO$ 4.84E+33 -6.11 29064	ADDITION H TRANSFER RING OPENING BETASCISSION	THEORY Mao 2021, unpublished + MEL
ADD_O2	ADD_O2_ROPEN	$O_2 + C_5H_6 \rightarrow 2CO + C_3H_6$ 1.00E+13 .00 39000 $O_2 + C_5H_6 \rightarrow CO + HCO + C_3H_5-A$ 4.00E+13 .00 39000	ADDITION H TRANSFER RING OPENING ISOMERIZATION +?	CRECK ESTIMATE
ADD_O	ADD_O_ROPEN	$O + C_5H_6 \rightarrow CO + C_4H_6$ 2.00E+13 .00 0 $O + C_5H_6 \rightarrow CH_2CO + C_3H_4-A$ 3.00E+12 .00 0 $O + C_5H_6 \rightarrow CH_2CO + C_3H_4-P$ 3.00E+12 .00 0	ADDITION H TRANSFER RING OPENING ISOMERIZATION +?	CRECK ESTIMATE
ADD_HO2	ADD_HO2_EL_OH	$C_5H_6 + HO_2 \rightarrow C_4H_6 + CO + OH$ 1.10E+01 3.19 6913	ADDITION	THEORY Xu 2020 [323]
	ADD_HO2_EL_O2	$C_5H_6 + HO_2 = CYC_5H_7 + O_2$ 8.03E-01 3.23 7611	ELIMINATION ADDITION	THEORY Xu 2020 [323] + MEL
SPECIES TYPE:	C5,CH3-M	(C₅H₅CH₃)		
CLASS TYPE	REACTION TYPE	EXAMPLE	ELEM. STEPS	SOURCE
BONDFISS.	BONDFISSION_CH	$C_5H_5CH_3 \rightarrow FULVENE + 2H$ 7.35E+96 -24.40 116183 1.70E+110 -29.70 135237	BONDFISSION (H TRANSFER)	THEORY Sharma 2009 [341]
DECO.	EL_H2	$C_5H_5CH_3 \rightarrow FULVENE + H_2$ 7.75E+93 -25.07 118634	ELIMINATION (H TRANSFER)	THEORY Sharma 2009 [341]
IPSO	IPSO_H	$H + C_5H_5CH_3 \rightarrow CH_3 + C_5H_6$ 1.50E+13 .00 2000	ADDITION	CRECK ESTIMATE
HABS	HABS_H	$C_5H_5CH_3 + H \rightarrow H + FULVENE + H_2$ 0.80E+05 2.67 7645 $C_5H_5CH_3 + H \rightarrow H_2 + C_6H_6 + H$ 1.20E+07 2.00 2663	H ABSTRACTION	ESTIMATE LLNL MECH Ranzi 2012 [354]
	HABS_CH3	$C_5H_5CH_3 + CH_3 \rightarrow H + FULVENE + CH_4$ 2.50E+00 3.49 8599 $C_5H_5CH_3 + CH_3 \rightarrow CH_4 + C_6H_6 + H$ 3.60E+05 2.00 3778	H ABSTRACTION	ESTIMATE LLNL MECH Ranzi 2012 [354]
	HABS_OH	$C_5H_5CH_3 + OH \rightarrow H + FULVENE + H_2O$ 1.00E+06 2.11 1367 $C_5H_5CH_3 + OH \rightarrow H_2O + C_6H_6 + H$ 1.00E+07 2.0 -3152	H ABSTRACTION	ESTIMATE LLNL MECH Ranzi 2012 [354]
	HABS_O	$C_5H_5CH_3 + O \rightarrow H + FULVENE + OH$ 1.10E+09 1.32 5676 $C_5H_5CH_3 + O \rightarrow OH + C_6H_6 + H$ 0.75E+07 2.00 1356	H ABSTRACTION	ESTIMATE LLNL MECH Ranzi 2012 [354]
	HABS_O2	$C_5H_5CH_3 + O_2 \rightarrow H + FULVENE + HO_2$ 1.50E+13 .00 52000 $C_5H_5CH_3 + O_2 \rightarrow HO_2 + C_6H_6 + H$ 0.85E+07 2.00 38571	H ABSTRACTION	ESTIMATE LLNL MECH Ranzi 2012 [354]
	HABS_HO2	$C_5H_5CH_3 + HO_2 \rightarrow H + FULVENE + H_2O_2$ 2.06E+00 3.80 17470	H ABSTRACTION	ESTIMATE LLNL MECH

		$C_5H_5CH_3 + HO_2 \rightarrow H_2O_2 + C_6H_6 + H$ 2.71E+05 2.00 10318		Ranzi 2012 [354]
	HABS_C5-RSR	$C_5H_5 + C_5H_5CH_3 \rightarrow C_5H_6 + C_6H_6 + H$ 4.00E+05 2.0 16500	H ABSTRACTION	CRECK ESTIMATE
SPECIES TYPE:	C5,A1-M	(C₉H₈ indene)		
CLASS TYPE	REACTION TYPE	EXAMPLE	ELEM. STEPS	SOURCE
ADD_O	ADD_O_ROPEN	$O + INDENE \rightarrow C_6H_5CHO + C_2H_2$ 1.00E+013 0. 3000	ADDITION H TRANSFER RING OPENING INSERTION +?	CRECK ESTIMATE
SPECIES TYPE:	C5,C5-M	(FC₁₀H₁₀ fulvalene)		
CLASS TYPE	REACTION TYPE	EXAMPLE	ELEM. STEPS	SOURCE
DECO.	BONDFISSION_CH	$FC_{10}H_{10} \rightarrow 2H + C_{10}H_8$ 5.13E+17 -1.04 66694	BONDFISSION (H TRANSFER)	THEORY Long 2017 [5] +MEL
SPECIES TYPE:	C5,H2-M	(CYC₅H₈ cyclopentene)		
CLASS TYPE	REACTION TYPE	EXAMPLE	ELEM. STEPS	SOURCE
DECO.	EL_H2	$CYC_5H_8 = C_5H_6 + H_2$ 5.00E+12 0.00 58000	ELIMINATION	CRECK ESTIMATE
	ROPEN	$CYC_5H_8 \rightarrow 0.6LC_5H_8 + 0.4LC_5H_7 + 0.4H$ 8.00E+15 0.00 86000	RING OPENING	CRECK ESTIMATE
SPECIES TYPE:	C5,OH-M	(C₅H₅OH)		
CLASS TYPE	REACTION TYPE	EXAMPLE	ELEM. STEPS	SOURCE
DECO.	MOLEC_DECO	$C_5H_5OH \rightarrow C_4H_6 + CO$ 7.11E+33 -6.11 69496	H TRANSFER RING OPENING ELIMINATION	THEORY Galimova 2018 [292] + MEL
IPSO	IPSO_H	$H + C_5H_5OH \rightarrow C_5H_6 + OH$ 8.49E+27 -4.03 13697	ADDITION	THEORY Mao, unpubl. + MEL
HABS	HABS_H	$H + C_5H_5OH = H_2 + C_5H_5O$ 9.72E+02 3.06 2608	H ABSTRACTION	THEORY This work
	HABS_CH3	$CH_3 + C_5H_5OH = CH_4 + C_5H_5O$ 1.69E+02 2.91 6558	H ABSTRACTION	RATE RULE This work
	HABS_OH	$OH + C_5H_5OH = H_2O + C_5H_5O$ 2.96E+06 1.90 2834	H ABSTRACTION	RATE RULE This work
	HABS_O2	$O_2 + C_5H_5OH = HO_2 + C_5H_5O$ 6.46E+06 2.00 45830	H ABSTRACTION	RATE RULE This work
	HABS_O	$O + C_5H_5OH = OH + C_5H_5O$ 2.36E+06 2.12 6685	H ABSTRACTION	RATE RULE This work
	HABS_HO2	$HO_2 + C_5H_5OH = H_2O_2 + C_5H_5O$ 4.90E-05 4.65 8739	H ABSTRACTION	RATE RULE This work
SPECIES TYPE:	C5O-M	(C₅H₄O)		
CLASS TYPE	REACTION TYPE	EXAMPLE	ELEM. STEPS	SOURCE
DECO.	MOLEC_DECO	$C_5H_4O \rightarrow 2C_2H_2 + CO$ 3.37E+31 -4.84 87887	RING OPENING ELIMINATION	THEORY Ghildina 2017 [293] + MEL
ADD_H	ADD_H_WELL	$C_5H_4O + H = C_5H_5O$ 2.71E+43 -9.42 12697	ADDITION H TRANSFER	THEORY Ghildina 2017 [293] + MEL
	ADD_H_ROPEN	$C_5H_4O + H = C_5H_4OH$ 1.36E+42 -8.40 19450		
		$C_5H_4O + H = C_4H_5 + CO$ 5.58E+25 -3.15 14655	ADDITION H TRANSFER RING OPENING	THEORY Ghildina 2017 [293] + MEL
ADD_HO2	ADD_HO2_ROPEN	$C_5H_4O + HO_2 \rightarrow CO_2 + C_4H_4 + OH$ 2.00E+12 .00 16000	ADDITION H TRANSFER RING OPENING ELIMINATION +?	ANALOGY from A1-M ESTIMATE
	ADD_HO2_EL_OH	$C_5H_4O + HO_2 \rightarrow 2CO + C_3H_4-A + OH$ 2.00E+12 .00 16000	ADDITION H TRANSFER	ANALOGY from A1-M
		$C_5H_4O + HO_2 \rightarrow CO + CO_2 + C_3H_5-A$ 1.00E+12 .00 16000	RING OPENING ELIMINATION	ESTIMATE

				+?
ADD_O2	ADD_O2_ROPEN	$C_5H_4O+O_2 \rightarrow OH+HCCO+CO+C_2H_2$ 6.67E+13 .00 44000 $C_5H_4O+O_2 \rightarrow CO+CO_2+C_3H_4-A$ 6.67E+13 .00 44000	ADDITION H TRANSFER RING OPENING INSERTION +?	ANALOGY from A1-M ESTIMATE
ADD_OH	ADD_OH_ROPEN	$C_5H_4O+OH \rightarrow HCCO+C_2H_3CHO$ 9.50E+07 1.46 855 $C_5H_4O+OH \rightarrow C_4H_4+CO+OH$ 2.00E+07 1.46 2000	ADDITION H TRANSFER RING OPENING +?	ANALOGY from A1-M ESTIMATE
	ADD_OH_DECO	$C_5H_4O+OH \rightarrow HCCO+CO+C_2H_2+2H$ 6.94E+02 2.95 7067 $C_5H_4O+OH \rightarrow HCCO+CO+C_2H_4$ 3.00E+07 1.46 1000	ADDITION H TRANSFER RING OPENING ELIMINATION +?	ANALOGY from A1-M ESTIMATE
	ADD_OH_INSERT	$C_5H_4O+OH \rightarrow C_4H_5+CO_2$ 9.50E+07 1.46 855	ADDITION H TRANSFER INSERTION ELIMINATION +?	ANALOGY from A1-M ESTIMATE

TABLE 5.3: Reaction classes for decomposition and oxidation of C5,X-RSR species types. M, R, RSR indicate a molecule or resonantly stabilized radical, respectively, while X indicates a substituent. Colored boxes highlight the reaction classes updated in this thesis. For each example, kinetic parameters of the modified Arrhenius form $k = k_0 T^\alpha \exp(-\frac{E_A}{RT})$ are provided (units cal, mol, cm³, s, K, reference pressure of 1 atm for pressure-dependent reactions). For color codes see Table 5.2.

SPECIES TYPE:	C5-RSR	(C ₅ H ₅)		
CLASS TYPE	REACTION TYPE	EXAMPLE	ELEM. STEPS	SOURCE
RADICAL DECO.	ROPEN	$C_5H_5 \rightarrow C_2H_2+C_3H_3$ 3.27E+66 -14.55 114342	H TRANSFER RING OPENING BETASCISSION	THEORY Mao 2021 [344] + MEL
ADD_H	REC_H_WELL	$H+C_5H_5(+M)=C_5H_6(+M)$ 3.16E+13 0.28 -179.	RECOMBINATION	THEORY Harding 2007 [331]
ADD_CH3	REC_CH3_WELL REC_CH3_EL_H2	$C_5H_5+CH_3=C_5H_5CH_3$ 3.69E+105 -27.03 47902 $CH_3+C_5H_5 \rightarrow H_2+FULVENE$ 1.14E+15 -1.40 20266	RECOMBINATION (H TRANSFER) RECOMBINATION H TRANSFER ELIMINATION	THEORY Sharma 2009 [341] THEORY Sharma 2009 [341]
ADD_HO2	REC_HO2_EL_OH REC_HO2_EL_H2O	$C_5H_5+HO_2=C_5H_5O+OH$ 4.86E+18 -1.89 1874 2.43E+14 -0.47 5950 4.37E+61 -15.97 13112 $C_5H_5+HO_2 \rightarrow C_5H_4O+H_2O$ 1.46E+03 2.47 1550 4.59E+03 2.57 9741	RECOMBINATION H TRANSFER RECOMBINATION ELIMINATION	THEORY + MEL This work THEORY + MEL This work
ADD_O2	REC_O2_EL_OH REC_O2_ROPEN	$C_5H_5+O_2 \rightarrow C_5H_4O+OH$ 8.77E+01 3.11 23496 $C_5H_5+O_2 \rightarrow HCO+C_3H_4-P+CO$ 7.42E+08 0.65 23667 1.11E+12 -0.28 26565 $C_5H_5+O_2 \rightarrow HCO+CO+C_3H_3+H$ 5.45E+01 2.85 25001	RECOMBINATION ELIMINATION RECOMBINATION RING OPENING H TRANSFER BETASCISSION	THEORY Oleinikov 2018 [294] + MEL THEORY Oleinikov 2018 [294] + MEL
ADD_OH	REC_OH_WELL REC_OH_EL_H REC_OH_DECO	$C_5H_5+OH=C_5H_5OH$ 1.01E+52 -11.38 18934 5.00E+00 -26.79 32059 $C_5H_5+OH=C_5H_5O+H$ 5.70E+32 -5.09 22417 $C_5H_5+OH=C_5H_4OH+H$ 1.39E+30 -4.43 24237 $C_5H_5+OH \rightarrow C_4H_6+CO$ 1.47E+35 -6.11 21723	RECOMBINATION (H TRANSFER) RECOMBINATION H TRANSFER RECOMBINATION H TRANSFER CO ELIMINATION	THEORY Galimova 2018 [292] + MEL THEORY Galimova 2018 [292] + MEL THEORY Galimova 2018 [292] + MEL
ADD_O	REC_O_EL_H	$C_5H_5+O \rightarrow C_5H_4O+H$ 4.73E+10 0.67 167	RECOMBINATION H TRANSFER BETASCISSION	THEORY Ghildina 2017 [293] + MEL

	REC_O_ROPEN	$C_5H_5 + O \rightarrow C_4H_5 + CO$ 2.32E+13 -0.49 -2432 5.34E+15 -0.47 1214	RECOMBINATION H TRANSFER RING OPENING BETASCISSION	THEORY Ghildina 2017 [293] + MEL
SPECIES TYPE:	C5,A1-RSR	(C₉H₇ INDENYL)		
CLASS TYPE	REACTION TYPE	EXAMPLE	ELEM. STEPS	SOURCE
DECO.	ROPEN	INDENYL \rightarrow C ₅ H ₅ + C ₄ H ₂ 1.00E+13 0.00 78000	H TRANSFER ROPEN	CRECK ESTIMATE
SPECIES TYPE:	C5O-RSR	(C₅H₅O)		
CLASS TYPE	REACTION TYPE	EXAMPLE	ELEM. STEPS	SOURCE
RADICAL DECO.	ROPEN	C ₅ H ₅ O = C ₄ H ₅ + CO 1.17E+82 -19.99 81976 C ₅ H ₄ OH = C ₄ H ₅ + CO 6.08E+54 -12.19 77966	(H TRANSFER) RING OPENING BETASCISSION	THEORY Ghildina 2017 [293] + MEL
ADD_H	REC_H_WELL	C ₅ H ₅ O + H = C ₅ H ₅ OH 5.92E+49 -10.57 17832	RECOMBINATION	THEORY Galimova 2018 [292] + MEL
	REC_H_ROPEN	C ₅ H ₅ O + H \rightarrow C ₄ H ₆ + CO 8.65E+34 -5.61 23266 C ₅ H ₄ OH + H \rightarrow C ₄ H ₆ + CO 3.28E+35 -5.92 23022	RECOMBINATION H TRANSFER ELIMINATION (RING OPENING)	THEORY Galimova 2018 [292] + MEL
ISOM.	ISOM_OC	C ₅ H ₄ OH = C ₅ H ₅ O 4.82E+37 -8.04 60575	H TRANSFER	THEORY Galimova 2018 [292] + MEL
	ISOM_BIMOL_H	C ₅ H ₅ O + H = C ₅ H ₄ OH + H 3.06E+29 -4.07 23789	RECOMBINATION H TRANSFER	THEORY Galimova 2018 [292] + MEL
ADD_OH	REC_OH_EL_H2O	C ₅ H ₅ O + OH \rightarrow C ₅ H ₄ O + H ₂ O 2.17E+14 -0.82 44514 5.00E+12 .00 0	RECOMBINATION H TRANSFER ELIMINATION (H ABSTRACTION)	THEORY /ANALOGY This work
	REC_OH_DECO	C ₅ H ₅ O + OH \rightarrow 0.5C ₃ H ₅ -A + 0.5HCO + 0.5OH + 0.5C ₄ H ₅ + CO 4.5E+13.00 0 C ₅ H ₅ O + OH \rightarrow CH ₂ CHO + C ₂ H ₃ + CO 1.5E+13 .00 0 C ₅ H ₅ O + OH \rightarrow CH ₃ CO + C ₂ H ₂ + HCO 1.00E+13 .00 0	RECOMBINATION H TRANSFER RING OPENING	THEORY /ANALOGY This work
ADD_O2	REC_O2_ROPEN	C ₅ H ₅ O + O ₂ \rightarrow C ₃ H ₄ -A + HCO + CO ₂ 2.83E+06 1.37 17728	RECOMBINATION H TRANSFER RING OPENING +?	ANALOGY From C5-RSR
	REC_O2_EL_HO2	C ₅ H ₅ O + O ₂ \rightarrow C ₅ H ₄ O + HO ₂ 1.00E+06 1.37 11000	RECOMBINATION ELIMINATION (H ABSTRACTION)	ANALOGY From C5-RSR
HABS	HABS_O2	C ₅ H ₅ O + O ₂ = C ₅ H ₄ O + HO ₂ 8.05 2.83 7657	H ABSTRACTION	THEORY This work
SPECIES TYPE:	C5H2-RSR	(CYC₅H₇)		
CLASS TYPE	REACTION TYPE	EXAMPLE	ELEM. STEPS	SOURCE
RADICAL DECO.	ROPEN	CYC ₅ H ₇ = LC ₅ H ₇ 5.18E+36 -7.01 54800 CYC ₅ H ₇ \rightarrow C ₃ H ₃ + C ₂ H ₄ 1.34E+48 -10.10 93978	H TRANSFER RING OPENING H TRANSFER BETASCISSION	THEORY Mao 2020 [334] + MEL
HABS	HABS_H	C ₅ H ₅ O + H \rightarrow C ₅ H ₄ O + H ₂ 9.3E+06 1.92 -743	H ABSTRACTION	THEORY This work
	HABS_O	CYC ₅ H ₇ + O = C ₅ H ₆ + OH 1.00E+13 .00 0	H ABSTRACTION	CRECK ESTIMATE
	HABS_OH	CYC ₅ H ₇ + OH = C ₅ H ₆ + H ₂ O 3.5E+12 .00 0	H ABSTRACTION	THEORY This work
	HABS_C5-RSR	CYC ₅ H ₇ + C ₅ H ₅ = 2C ₅ H ₆ 1.0E+22 -2.72 3906	H ABSTRACTION	ANALOGY Jin 2019 [337]
SPECIES TYPE:	C5H2,A1-RSR	(C₉H₉ INDANYL)		
CLASS	REACTION TYPE	EXAMPLE	ELEM. STEPS	SOURCE

TYPE				
DECO.	ROPEN	$C_9H_9 \rightarrow C_5H_5 + C_4H_4$ 4.02E+43 -7.47 100072	H TRANSFER RING OPENING BETACISSION	THEORY Jin 2019 [337]
SPECIES TYPE:	C5OH-RSR	(C ₅ H ₆ OH)		
CLASS TYPE	REACTION TYPE	EXAMPLE	ELEM. STEPS	SOURCE
BETACISS.	BETACISSION_CH	$C_5H_6OH \rightarrow C_5H_5OH + H$ 8.07E+43 -9.12 60072 $C_5H_6OH \rightarrow 0.5C_5H_5OH$ +0.5C ₅ H ₅ O+1.5H 6.37E+33 -6.50 48788	H TRANSFER BETACISSION	THEORY Mao unpubl. + MEL

5.2.2 Growth

This section lists the main reaction classes for the growth from linear species to form C₅ unsaturated rings as well as the growth of C₅ species types to larger PAHs. The structure of Tables 5.4 and 5.5 is similar to that of Section 5.2.1. However, the elementary steps corresponding to each reaction type are not listed because most of the reference kinetic parameters derive from estimates and are not easily associated to a specific set of elementary steps. Relevant elementary steps identified in the literature theoretical studies are β -scission, recombination, H transfer, ring opening, concerted elimination, and isomerization reactions including torsions with large barrier heights.

The formulated reaction classes focus mostly on the formation of C₅ rings from linear species and on the growth of C₅ species (mostly cyclopentadiene-like). While this work only classifies formation and growth of C₅ species with a single ring, all the reaction classes also apply to PAHs containing C₅ rings, as explained in Section 2.6 and 5.2.1. It is recalled that reversible growth pathways can also be regarded as decomposition pathways. For instance, ring enlargement processes of C₅ species forming aromatic rings are also relevant in the decomposition process of the latter, which are essential in the study of PAHs and soot [59], [60].

In this section, also linear species types are also considered. The notation adopted for linear species follows the same logic of that for C₅ and aromatic rings, namely the species type is defined from the functional group participating in the reactivity. The format for linear species types is C_n.Z-M/R/RSR, where n is the number of carbon atoms of the functionality considered, Z provides information on the type of bonds in the species, i.e., the presence of double (D) or triple (T) bonds, M/R/RSR indicate molecules, radicals, and resonance-stabilized radicals, respectively. For instance, C3.D-M type identifies a C₃ linear group with a double bond in a molecule, such as in propene, 1-butene, butadiene, 1-pentene, etc. Similarly, C3.D-RSR identifies a resonance-stabilized C3 group with a double bond, such as in allyl (C₃H₅-A), 1-methyl-allyl (1,3-C₄H₇), etc., while C3.DD-RSR indicates the reactivity typical of propargyl radical (C₃H₃). While this classification is inaccurate with respect to the detailed univocal identifiers such as InChI, this notation is meant as a compromise between the generality of the reaction class and the specificity of the functionality considered.

The class types for growth reactions are more general than those used for decomposition and oxidation reactions as they do not provide specific information on the species being added. Class types are simply called GROWTH-S, where S is a generic species only indicating the number of carbon atoms of the species type being added, i.e., C₁–C₅. The only unimolecular reaction class (GROWTH-UNIMOL) describes the ring enlargement from substituted C₅ species (e.g., C₅CH₂) to A1. Additionally, growth classes are built so that the species being added (indicated by the class/reaction type) is always smaller than the species type. For instance, class [A1-M][GROWTH-C5] exists, however class [C5-M][GROWTH-A1] does not. When the two reacting species have the same number of carbon atoms, the one with the lower molecular weight defines the class type.

Reaction types provide additional information on the species being added. Reaction types may be ADD_S, REC_S, ENLARGE_S. ADD, REC stand for addition and recombination, while ENLARGE indicates ring enlargement reactions from C₅ to A1. The species type combined with the reaction type therefore provides complete information on the functional groups reacting. The lack of information about the products formed (in contrast with many reaction types defined in Section 5.2.1) is mostly related to the heavily lumped structure of growth reactions in the CRECK kinetic mechanism. In most cases, the intermediate species taking part in the growth process are not present in the kinetic mechanism.

Tables 5.4 and 5.5 show that the rate constants of most of the growth reaction classes identified in this work derive from estimates and only a few of them were updated with recent theoretical calculations. In fact, theoretical calculations for most of the growth classes identified are unavailable in the literature, while other reaction pathways were not included from theoretical calculations to avoid too extreme imbalances in the level of detail of similar reaction classes. Therefore, the growth classes presented here should be considered only as a general framework to help the understanding of relevant growth reaction pathways rather than a detailed set of classes.

As anticipated in Section 5.2.1, the unimolecular decomposition of cyclopentadiene is among the growth reactions, and is identified by [C3.DD-M][ADD_C2.T-M]. Growth classes from C5-M with C₁–C₅ species are found in Table 5.4. Growth classes with C₁–C₃ species only include enlargement reaction types, while an aromatic ring next to the C₅ ring can clearly be formed through GROWTH-C4 class types. A similar comment applies to the growth of A1-M (Section 6.2.2). Class type GROWTH-C5 is the most relevant in kinetic studies using cyclopentadiene as a fuel, as shown in the kinetic simulation in Section 5.4. The reaction classes for the growth of cyclopentadienyl radical (C5-RSR type) are more updated. In particular, one of the most sensitive reactions in cyclopentadiene pyrolysis and oxidation is the self-recombination of cyclopentadienyl radicals [C5-RSR][REC_C5-RSR], updated with recent theoretical calculations [295] (Section 4.4.3).

In a few cases, growth reactions from A1 species appear in the flux analysis of the kinetic simulations performed in this chapter (in particular for indene pyrolysis, Section 5.4.1). The logic for the definition of growth classes for aromatic species is that described in this section and is presented in more detail in Section 6.2.2.

TABLE 5.4: Reaction classes for the growth to C5 or from C5,X-M species types. M, R, RSR indicate a molecule, a radical, or a resonantly stabilized radical, respectively, while X indicates a substituent. Colored boxes highlight the reaction classes updated in this thesis. For each example, kinetic parameters of the modified Arrhenius form $k = k_0 T^\alpha \exp\left(-\frac{E_A}{RT}\right)$ are provided (units cal, mol, cm^3 , s, K, reference pressure of 1 atm for pressure-dependent reactions). For color codes see Table 5.2.

SPECIES TYPE:	C3.D-M	(C ₃ H ₆)	
CLASS TYPE	REACTION TYPE	EXAMPLE	SOURCE
GROWTH-C2	ADD_C2.D-R	C ₂ H ₃ +C ₄ H ₆ →CH ₃ +C ₅ H ₆ 1.00E+12 0.00 2000	CRECK ESTIMATE
SPECIES TYPE:	C3.DD-M	(C ₃ H ₄)	
CLASS TYPE	REACTION TYPE	EXAMPLE	SOURCE
GROWTH-C2	ADD_C2.T-M	C ₂ H ₂ +C ₃ H ₄ -A=C ₅ H ₆ 2.5E+11 0.00 22000	CRECK ESTIMATE
	ADD_C2.D-R	C ₂ H ₂ +C ₃ H ₄ -P=C ₅ H ₆ 2.5E+10 0.00 22000 !TOT: 3.6E+12 0.00 7500 C ₃ H ₄ -A+C ₂ H ₃ =LC ₅ H ₇ 1.13E+32 -5.83 16391 C ₃ H ₄ -P+C ₂ H ₃ →LC ₅ H ₇ 2.26E+60 -15.00 25788	THEORY Mao 2020 [334] + MEL
SPECIES TYPE:	C4.DT-M	(C ₄ H ₄)	
CLASS TYPE	REACTION TYPE	EXAMPLE	SOURCE
GROWTH-C1	ADD_C1-R	C ₄ H ₄ +CH ₃ →LC ₅ H ₇ 9.53E+77 -20.02 39093	THEORY Mao 2020 [334] + MEL
SPECIES TYPE:	C5-M	(C ₅ H ₆)	
CLASS TYPE	REACTION TYPE	EXAMPLE	SOURCE
GROWTH-C1	ENLARGE_C1-R	CH ₃ +INDENE→C ₁₀ H ₈ +H ₂ +H 3.00E+11 0.00 7600	CRECK ESTIMATE
GROWTH-C2	ENLARGE_C2.T-M	C ₂ H ₂ +C ₅ H ₆ →C ₇ H ₈ 3.00E+11 0.00 30000	CRECK ESTIMATE
	ENLARGE_C2.D-M	C ₂ H ₄ +C ₅ H ₆ →C ₆ H ₆ +CH ₃ +H 7.50E+10 0.00 30000	CRECK ESTIMATE
GROWTH-C3	ENLARGE_C3.D-R	C ₄ H ₅ +C ₅ H ₆ →C ₃ H ₅ -A+C ₆ H ₆ 1.00E+12 0.00 6000	CRECK ESTIMATE
	ENLARGE_C3.D-RSR	C ₅ H ₆ +LC ₅ H ₇ →C ₆ H ₆ +C ₂ H ₄ +C ₂ H ₃ 1.00E+12 0.00 16000	CRECK ESTIMATE
GROWTH-C4	ADD_C4.DD-M	C ₄ H ₆ +C ₅ H ₆ →INDENE+H ₂ +H ₂ 5.00E+11 0.00 30000	CRECK ESTIMATE
	ADD_C4.DT-R	C ₄ H ₃ +C ₅ H ₆ →INDENE+H 5.00E+11 0.00 5000	CRECK ESTIMATE
	ADD_C4.DD-R	C ₄ H ₅ +C ₅ H ₆ →INDENE+H+H ₂ 5.00E+11 0.00 3000	CRECK ESTIMATE
GROWTH-C5	ADD_C5-M	C ₅ H ₆ +C ₅ H ₆ →C ₁₀ H ₈ +2H ₂ 2.00E+11 0.00 35000	CRECK ESTIMATE
		C ₅ H ₆ +INDENE→FLUORENE+CH ₃ +H 1.25E+11 0.00 30000	CRECK ESTIMATE
	ENLARGE_C5-RSR	C ₅ H ₅ +C ₅ H ₆ →C ₆ H ₆ +C ₄ H ₅ 2.00E+13 0.00 25500	CRECK ESTIMATE
	ADD_C5-RSR	C ₅ H ₅ +C ₅ H ₆ →C ₁₀ H ₈ +H ₂ +H 2.00E+12 0.00 23000	CRECK ESTIMATE
		C ₅ H ₅ +C ₅ H ₆ →C ₁₀ H ₁₀ +H 3.00E+12 0.00 23000	CRECK ESTIMATE
		C ₅ H ₅ +INDENE→C ₁₄ H ₁₀ +H+H ₂ 4.00E+11 0.00 19000	CRECK ESTIMATE
		C ₅ H ₅ +C ₅ H ₆ →INDENE+CH ₃ 3.40E+11 0.00 15700	THEORY Cavallotti 2012 [318]
	ADD_DECO_C5-RSR	C ₅ H ₅ +C ₅ H ₆ →C ₆ H ₅ C ₂ H ₃ +C ₂ H ₃ 4.00E+12 0.00 25500	CRECK ESTIMATE

SPECIES TYPE:		C5H5 + C5H6 → C7H7 + C3H4 4.00E+12 0.00 25000	CRECK ESTIMATE
CLASS TYPE	REACTION TYPE	EXAMPLE	SOURCE
GROWTH-UNIMOL	ENLARGE	FULVENE=C6H5+H 2.24E+68 -14.65 142570 FULVENE=C6H6 1.44E+45 -8.90 96999	THEORY Miller 2003 [271]
GROWTH-H	ENLARGE_H	FULVENE+H=C6H6+H 7.26E+31 -4.75 18390	THEORY Jasper 2013 [355]

TABLE 5.5: Reaction classes for the growth to C5 or from C5,X-R/RSR species types. M, R, RSR indicate a molecule, a radical, or a resonantly stabilized radical, respectively, while X indicates a substituent. Colored boxes highlight the reaction classes updated in this thesis. For each example, kinetic parameters of the modified Arrhenius form $k = k_0 T^\alpha \exp\left(-\frac{E_A}{RT}\right)$ are provided (units cal, mol, cm³, s, K, reference pressure of 1 atm for pressure-dependent reactions). For color codes see Table 5.2.

SPECIES TYPE:		C3.D-RSR	(C3H5)	
CLASS TYPE	REACTION TYPE	EXAMPLE	SOURCE	
GROWTH-C2	ADD_C2.D-M	IC4H7+C2H4 → C5H6+CH4+H 1.05E+11 0.00 18000 C4H71-3+C2H4 → CH3+C5H6+H2 1.50E+11 0.00 13000	CRECK ESTIMATE	
	ADD_C2.T-M	C4H71-3+C2H2 → H+C5H5CH3 1.00E+12 0.00 14100 C3H5-A+C2H2=CYC5H7 1.04E+34 -6.98 21827 C3H5-A+C2H2=LC5H7 2.85E+41 -8.94 28110	THEORY anal. Mao 2021 [322] THEORY Mao 2020 [334] + MEL	
SPECIES TYPE:		C4.DT-R	(C4H3)	
CLASS TYPE	REACTION TYPE	EXAMPLE	SOURCE	
GROWTH-C1	REC_C1-R	CH3+C4H3 → C5H6 1.00E+13 0.00 0	CRECK ESTIMATE	
SPECIES TYPE:		C5-RSR	(C5H5)	
CLASS TYPE	REACTION TYPE	EXAMPLE	SOURCE	
GROWTH-C2	ENLARGE_C2.T-M	C5H5+C2H2=C7H7 1.92E+11 -6.85 24136	THEORY Mao 2021 [322] + MEL	
GROWTH-C3	ENLARGE_C3.DD-M	C3H4-P+INDENYL→C10H8+C2H3 C3H4-P+C5H5 → C6H5C2H3+H 3.00E+12 0.00 18000	CRECK RULE	
	ENLARGE_C3.D-RSR	C3H5-A+C5H5=C6H5C2H3+H2 C3H5-A+INDENYL=C10H7C2H5 5.00E+11 0.00 6000	CRECK RULE	
	ENLARGE_C3.DD-RSR	C3H3+C5H5 → C6H5C2H+H2 5.0E+12 0.00 6000 C3H3+C5H5 → C6H5C2H3 5.8E+11 0.00 -4273	CRECK RULE Theory Sharma 2010 [320] + MEL, tot	
	ENLARGE_C3.D-R	C4H5+C5H5 → C3H4-A+C6H6 2.00E+12 0.00 3000		
GROWTH-C4	REC_C4.DD-R	C4H5+C5H5 → INDENE+H2 5.00E+11/12 0.00 3000	CRECK RULE	
GROWTH-C5	REC_C5-RSR	C5H5+INDENYL→C14H10+H+H 5.0E+11/2E+12 0.00 6000 2C5H5=FC10H10 1.09E+21 -2.74 74	CRECK RULE THEORY Long 2018 [295]	

				+ MEL
SPECIES TYPE:	C5,A1-RSR	(C ₉ H ₇ INDENYL)		
CLASS TYPE	REACTION TYPE	EXAMPLE	SOURCE	
GROWTH-C5	REC_C5,A1-RSR	2INDENYL→C ₁₀ H ₈ +C ₆ H ₅ C ₂ H 1.00E+10 0.00 7000	CRECK RULE	

5.3 Theoretical calculations

5.3.1 H-atom abstraction reactions by H and OH from C₅H₆ and extension to C₉H₈ and C₅H₅OH

5.3.1.1 Motivation and literature review

H-atom abstraction reactions by H and OH from cyclopentadiene are an essential activation step for the formation of cyclopentadienyl radical in combustion systems, where C₅H₆ can be formed from small alkenes such as in C₂–C₃ flames, or from phenol molecular decomposition in OAHs pyrolysis or MAHs oxidation (Section 6.3.2). For instance, in this work it was found that the concentration of H atoms in phenol decomposition [132] is extremely sensitive to the rate constant of C₅H₆ + H = C₅H₅ + H₂ reaction .

No experimental data are available for the H-atom abstraction by H from cyclopentadiene. In kinetic mechanisms, the rate constant of this reaction is determined by analogy with smaller systems (e.g., 1,3-butadiene [356] or propene [310]), resulting in discrepancies of up to one order of magnitude in the rate constants implemented in different kinetic models. Moskaleva and Lin [330] performed one of the first theoretical studies of the PES for this reaction at the G2M(RCC,MP2)//B3LYP/6-311G(d,p) level of theory. They computed an energy barrier of 6.34 kcal/mol, with a declared uncertainty of 1–2 kcal/mol. Their RRKM rate constant is about a factor of 5–10 smaller than common estimates in kinetic models [46]. More recently, Baroncelli et al. [321] obtained a lower energy barrier of 5.2 kcal/mol at CCSD(T)/cc-pVTZ//M06-2X/6-311+G(d,p) level of theory. Their cTST rate constant agrees with [330] to within a factor of 2.

The only literature rate constants available for the H-atom abstraction by OH from cyclopentadiene are the theoretical calculations of Baroncelli et al. [321] and the recent reflected shock waves measurements of Jin et al. [329] in the 800–1400 K temperature range, which agree to within a factor of ~2.

This section presents high-level theoretical calculations of the rate constants for the H-atom abstraction reactions by H and OH from C₅H₆. The validity of these rate constants for different systems, namely larger systems (C₉H₈) and oxygenated systems (C₅H₅OH) is explored. The interest in C₉H₈ is obvious as it is the prototypical structure for large PAHs containing C₅ rings and is detected in large amounts in the combustion of linear and cyclic alkenes [357], [358] as well as of all aromatic hydrocarbons [359], [360]. On the other hand, C₅H₅OH was predicted as one of the main products of C₅H₅ + OH at intermediate temperatures [292], [293] (see also Section 4.4.2) and is therefore expected to accumulate significantly in systems where C₅H₆ oxidation plays a role.

5.3.1.2 Theoretical methodology

Electronic structure calculations were performed with EStokTP [97] as described in Section 3.4.1. ω B97X-D/aug-cc-pVTZ was adopted to compute geometries and vibrational frequencies at the stationary points. Additional calculations at M06-2X/6-311+G(d,p) and B2PLYPD3/6-311+G(d,p) levels were also performed for the H-atom abstraction by OH.

The energies of the stationary points were computed at the CCSD(T)/aug-cc-pVTZ level of theory [361], [362], and corrected for basis set size effects with the change between density fitted (DF) MP2 energy computed with aug-cc-pVQZ and aug-cc-pVTZ basis sets [363]. No MR calculations were performed as the T1 diagnostic at the TS was always below 0.02. On the other hand, the SPE for the H-atom abstractions by OH from C₉H₈ was obtained by correcting the L1 (ω B97X-D/aug-cc-pVTZ) energy according to the difference between HL (CCSD(T)/CBS) and L1 in the corresponding TS of C₅H₆ because of extremely high computational cost of the calculation. The same energy correction applied to the TS of the abstraction by H would result in an error of 0.1 kcal/mol with respect to the CCSD(T)/CBS energy.

The main purpose of the theoretical calculations for C₅H₅OH was the derivation of rate rules for the extension of C₅H₆ reactivity. Hence, rate constants were computed only for the H-atom abstraction by H from the most stable 1,3-C₅H₅OH and 1,4-C₅H₅OH isomers [292]. The cheaper M06-2X/6-311+G(d,p) level was used for geometry optimization, while SPEs were computed at CCSD(T)/CBS level. The H-atom abstraction rate constants of C₅H₆ + H performed using M06-2X/6-311+G(d,p) and ω B97X-D/aug-cc-pVTZ levels of theory showed maximum deviations of 28% at 2500 K, hence the M06-2X/6-311+G(d,p) level of theory is expected to be appropriate to investigate analogies between the two systems.

The partition functions for the torsional motion of the hydroxyl radical were determined according to the 1D hindered rotor model [106], and the corresponding torsional potentials were determined at 20° intervals at the level of theory used for geometry optimization.

Van der Waals wells that precede and follow the TSs were also determined, so as to compute properly the energy barrier for quantum tunneling corrections, determined using the Eckart model [263].

The rate constants of the investigated reactions were computed in the 500 – 2500 K temperature solving the one-dimensional ME as implemented in MESS [265]. It is recalled that abstraction reactions generally show no pressure dependence, however using a ME code instead of canonical TST allows to properly exclude from the rate constant calculation the contribution of reaction fluxes from energies below that of the reactants in the presence of submerged wells and saddle points. cTST was used for the H-atom abstraction by H, while variational effects were accounted for in the H-atom abstraction by OH, using IRC scans of 10 steps of 0.02 Å along the MEP in the direction of both reactants and products. Vibrational frequencies along the IRC path were computed using internal coordinates with the Hessian manipulation code that is part of EStokTP.

5.3.1.3 Rate constant calculations: cyclopentadiene and indene

Figure 5.1a presents the PES computed for H-atom abstraction reaction by H from C₅H₆ and C₉H₈ and the corresponding rate constants. The energy barrier of 5.5 kcal/mol for the abstraction from C₅H₆ agrees to within 0.8 kcal/mol with the G2M(RCC,MP2)//B3LYP/6-311G(d,p) calculations of Moskaleva and Lin [330] and to within 0.3 kcal/mol with the CCSD(T)/cc-pVTZ//M06-2X/6-311+G(d,p) results of Baroncelli et al. [321]. However, the discrepancy of the computed rate constants with the rate of Baroncelli et al. is up to a factor

of 2. This is not easily explained by the sensitivity to the level of geometry optimization, since the present rate constant derived at CCSD(T)/CBS//M06-2X/6-311+G(d,p) level is only about 30% higher than the rate plotted in Figure 5.1a. Finally, it is noted that all theoretical calculations strongly disagree with model estimates such as those of the starting CRECK model [46] of this work and that by Zhong and Bozzelli [310]. The H-atom abstraction reaction by H from indene is 2 kcal/mol more exothermic than that from cyclopentadiene due to the higher resonance stabilization in indenyl radical. This is mirrored in the energy barrier of 5.1 kcal/mol and in the resulting rate constant.

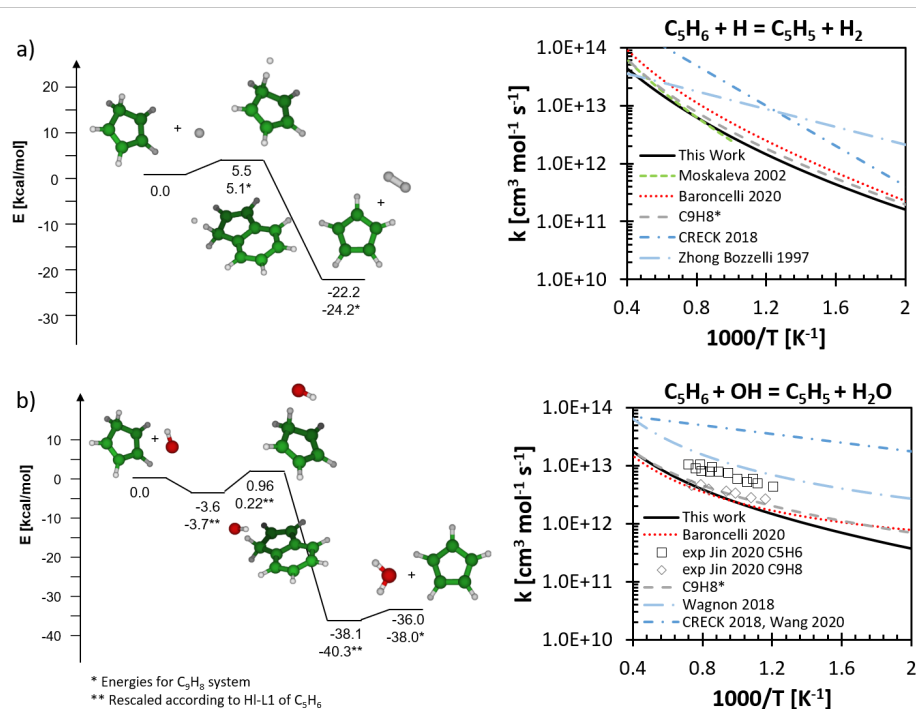


FIGURE 5.1: PES and rate constants for H-atom abstraction by a) H and b) OH from C_5H_6 and C_9H_8 in comparison with literature values [46], [50], [310], [321], [330], [338]

Figure 5.1b shows the results obtained for the abstraction by OH radical. Relatively deep van der Waals wells are formed for both the entrance and the exit channels. Additionally, the larger exothermicity of the reaction determines a larger difference (0.74 kcal/mol) between the TS energies for cyclopentadiene and indene. The resulting rate constants are compared with the recent experimental shock-tube data of Jin et al. [329], and with the theoretical calculations of Baroncelli et al. [321]. Additional comparisons with the rate constants present in the literature kinetic models for C_5H_6 are also provided [46], [50], [338], showing that only the kinetic model estimate of Wagnon et al. [50] agrees closely with the experimental data. The present rate constants for the H-atom abstraction from cyclopentadiene and indene are in close agreement with the calculations of Baroncelli et al. [321] and with the experimental data of Jin et al. [329], respectively. On the other hand, the experimental measurements of Jin et al. [329] for $C_5H_6 + OH$ are about a factor of 2 higher than the present calculations. While Jin et al. [329] attribute the difference between the rate constants for C_5H_6 and C_9H_8 to the different symmetry, this work finds that the overall TS/REAC symmetry of the

two systems is the same: in fact, the TS of $C_5H_6 + OH$ has two optical isomers which are however both included in the conformations sampled by the hindered rotor, hence the total TS/REAC symmetry number is 2. On the other hand, one of the two optical isomers of the TS of $C_9H_8 + OH$ is not compensated by the structures sampled in the HR, therefore the total TS/REAC symmetry number is still 2. Additional CASPT2(9e,8o)/aug-cc-pVTZ SPEs for $C_5H_6 + OH$ resulted in an even larger energy barrier (by 0.5 kcal/mol), which would increase the difference with the experimental data.

5.3.1.4 Rate rule extension to C_5H_5OH

Figure 5.2 presents the theoretical results for the H-atom abstraction rate constants by H from C_5H_5OH . C_5H_5OH isomers are lumped in the CRECK kinetic mechanism as described in Section 4.4.2. The isomer pool composition below 1500 K consists of comparable fractions (between 40 and 60%) of the two isomers, hence the rate constants of the H-atom abstractions from the two isomers were simply averaged for the inclusion in the kinetic mechanism. The average rate constant of the abstraction from the methylene group (CH_2) is extremely close to that from C_5H_6 , with maximum discrepancies below 30% at 500 K. Clearly, the abstraction from the hydroxy group cannot be compared to a C_5H_6 analogue. In this case, the rate constant for the H-atom abstraction from the meta isomer is significantly lower than that from the ortho isomer (about a factor of 5 at 500 K) due to the lower stability of the resonance-stabilized radical formed (see Figure 4.8). Hence, a difference of about 10 kcal/mol in the reaction energy results in a difference in the energy barrier of about 2 kcal/mol, consistent with what may be expected according to Evans-Polanyi rules.

For the purpose of extending the other rate constants of the H-atom abstraction reactions from C_5H_6 to this system, approximate scaling factors were derived on the basis of the present calculations. These approximate rate rules are probably accurate for the abstractions from the methylene group, however rate rules for the extension to the abstractions from the hydroxy group are expected to have larger uncertainty. Scaling factors were simply calculated by fitting with a 2-parameter Arrhenius expression the ratio between the rate constants obtained for the two systems $k_{C_5H_5OH}/k_{C_5H_6}$, thus obtaining

$$k_{CH_2,C_5H_5OH} = k_{CH_2,C_5H_6} \cdot 1.16 \cdot \exp\left(\frac{184}{T}\right)$$

$$k_{OH,C_5H_5OH} = k_{CH_2,C_5H_6} \cdot 0.38 \cdot \exp\left(-\frac{920}{T}\right)$$

where k_{CH_2} refers to the abstraction from the methylene group and k_{OH} to that from the hydroxy group.

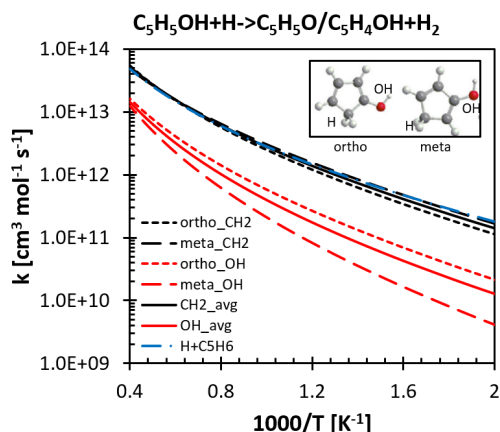


FIGURE 5.2: Rate constants for the H-atom abstraction by H from the CH₂ and OH groups of 1,3-C₅H₅OH and 1,4-C₅H₅OH in comparison with the results obtained for C₅H₆. avg refers to the average of the rate constants obtained for 1,3-C₅H₅OH and 1,4-C₅H₅OH.

5.3.2 C₅H₅ + HO₂

5.3.2.1 Motivation and state of the art

The interaction of the long-lived cyclopentadienyl radical with the radical pool in oxidative environments largely determines the competition between fuel decomposition to aliphatic species and growth to larger aromatics. In the intermediate-to-low temperature range, the recombination of C₅H₅ with the hydroperoxyl radical (HO₂) fosters its conversion via a pseudo chain-branching pathway to C₅H₅O and OH radicals [311]. Figure 5.3a,b shows that, according to the CRECK mechanism, this pathway is among the most sensitive reactions favoring CO₂ and decreasing C₁₀H₈ in the low temperature oxidation of C₅H₆. At higher temperatures (~1200 K), the C₅H₅ + HO₂ reaction becomes relevant also in the complex benzene oxidation mechanism (Figure 5.3c), as anticipated above.

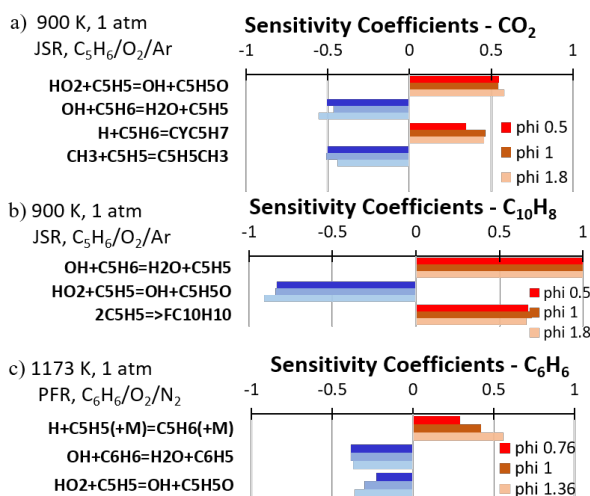


FIGURE 5.3: Sensitivity coefficients of a) CO₂ and b) C₁₀H₈ in cyclopentadiene oxidation in Wang jet stirred reactor [338] and of c) C₆H₆ at the oxidative conditions of the Princeton plug flow reactor [304] according to the CRECK mechanism.

Recent state-of-the-art theoretical calculations revealed the fate of C_5H_5 radical reaction with OH, 3O_2 , and $O(^3P)$ radicals [292]–[294]. However, no high-level theoretical calculations are available for the $C_5H_5 + HO_2$ potential energy surface. The main theoretical challenge in the study of this PES is that all of the most relevant reaction channels are barrierless, thus requiring multireference methodologies to determine the PES and complex theoretical methods to determine the rate constants, i.e., variable reaction coordinate transition state theory (VRC-TST) [234].

The first investigation of this PES was presented by Zhong and Bozzelli [311], who calculated the thermochemistry of the stationary points with group additivity methods and used literature analogies to estimate the rate constants of barrierless channels. They concluded that HO_2 and C_5H_5 recombine to form 2,4- C_5H_5OOH , which mostly dissociates through O–O bond-fission to 2,4- $C_5H_5O + OH$, while $C_5H_4O + H_2O$ is a possible high-temperature pathway. H-transfer from 2,4- C_5H_5OOH generates 1,3- and 1,4- C_5H_5OOH , which also undergo O–O bond-fission to the resonance-stabilized 1,3- and 1,4- C_5H_5O radicals. More recently, Robinson and Linstedt [343] re-investigated the primary reaction channels at the G4MP2 level. Rate constants for barrierless reactions were estimated from the properties of reactants and products. Compared to the previous work, $C_5H_4O + H_2O$ was found to be a minor product.

Literature findings in the reactivity $C_5H_5 + HO_2$ are in contrast with recent theoretical calculations of the $C_5H_5 + OH$ (Section 4.4.2) and $C_5H_5 + O(^3P)$ PESs [292], [293], where C_5H_5O radicals are also predicted to be among the main products. In these systems, 1,3- C_5H_5O and 1,4- C_5H_5O play a central role in the reactivity, whereas 2,4- C_5H_5O is unstable and rapidly converts to 1,3- C_5H_5O via H-transfer. Additionally, 1,3 and 1,4 isomers are predicted to be 30–40 kcal/mol more stable than 2,4- C_5H_5O , as opposed to the ~20 kcal/mol estimate of Zhong and Bozzelli [311]. Such discrepancies, together with attempts at simplifying the reactivity, result in different representations of the reactions of C_5H_5O radicals in global kinetic mechanisms. For instance, some models include 1,3 and 2,4 isomers only [337], [338], while in other models 1,3 and 1,4 isomers are lumped and the 2,4 isomer is excluded [67]. Finally, interconversion between isomers or reactions with other radicals are generally excluded.

In summary, the lack of high-level theoretical calculations and the resulting inconsistencies in the kinetic modeling of C_5H_6 and C_5H_5 oxidation highlight the need to revisit the reactivity on the $C_5H_5 + HO_2$ PES. This work presents high level theoretical calculations for this PES, which include VRC-TST treatment of barrierless channels, accurate thermochemistry, and master equation simulations. The impact of the new theoretical results is tested on the CRECK kinetic mechanism, and the accumulation of C_5H_5O is critically evaluated to assess both the relative amounts of the three isomers and the possible need for further theoretical studies. Kinetic simulations of Section 5.3.2.7 exemplify only a few cases of the influence of the present theoretical calculations on flow reactor simulations of cyclopentadiene and benzene oxidation, while more comprehensive simulation datasets are reported in Section 5.4, 6.6.

5.3.2.2 Theoretical methodology

The calculation of rate constants was performed according to the AI-TST-ME methodology using EStokTP, as described in Section 3.4.1. Geometry optimization and frequency calculations of the stationary points were performed at the DFT level using the B2PLYPD3 functional and the 6-311+G(d,p) basis set. SPEs were evaluated using Eqn. (3.11). When T1 diagnostic exceeded 0.02, high-level energies were determined at the CASPT2/aug-cc-pVTZ level. In particular, the energy of the TS for the water elimination channel and for the H-atom abstraction, and of 2,4-C₅H₅O + OH products, were all determined at CASPT2/aug-cc-pVTZ level. For the TS energies, an (8e,8o) AS was used, including all electrons of the breaking bonds and the π electrons of the ring. The energy of 2,4-C₅H₅O + OH was instead determined with a (10e,8o) active space including also the lone pairs of the oxygen radicals. In all cases, level shifts were used for energy calculations [204].

The thermochemistry for all species was computed from the partition functions and fitted to NASA polynomials with the Auto-Mech suite of codes [98] (Section 3.4.2). 0 K formation enthalpies were calculated through isogyric reactions using as reference the experimentally available formation enthalpy of C₅H₅ [117] (Section 3.2.3). Particular care was taken in reproducing the experimental results for the C₅H₅ radical entropy and enthalpy accounting for Jahn-Teller effects, as reported in Section 5.3.2.3.

Rate constants for the channels with well-defined barriers were treated with conventional transition state theory. Internal rotor partition functions were calculated using the 1D and, when needed, 2D coupled hindered rotor models. Torsional potentials were computed at 20° interval scans of the dihedral angles at the same level of theory used for geometry optimization. Tunneling corrections were evaluated using the Eckart model [263].

Barrierless C–O and O–O bond-fission were studied with VRC-TST [234] employing the two transition states model [278], [364] (see Section 3.3.2.4). For the short range calculations, pivot points were placed at the reacting atoms and then displaced by 0.1–0.3 Bohr along the direction of the molecular bonding orbital being broken in the reaction, while for the long range calculations pivot points were placed at the centers-of-mass of the fragments. A dynamical correction of 0.9 was included, as derived from trajectory simulations for simple model systems. Channel-specific details of the VRC-TST calculations performed for the C₅H₅ + HO₂, 2,4-C₅H₅O + OH and 1,3-C₅H₅O + OH channels are reported in the following. The discussion on the 1,4-C₅H₅O + OH channel is analogous to that on 1,3-C₅H₅O + OH and it is less interesting because of the small impact of 1,4-C₅H₅O on the overall reactivity of the system, hence it is not reported here.

For the C₅H₅ + HO₂ channel, fragment orientations were sampled at the CASPT2(2e,2o)/cc-pVDZ level, using fixed fragment geometries optimized at the CASPT2(1e,1o)/cc-pVDZ (HO₂) and CASPT2(5e,5o)/cc-pVDZ (C₅H₅) levels. The energies obtained from the sampling were corrected using a C–O distance-dependent potential. Geometry relaxation was accounted for as the difference between CASPT2(6e,6o)/cc-pVDZ energies obtained with both relaxed and constrained geometry optimizations along the minimum energy path. Basis set and AS corrections were computed as the difference

between CASPT2(6e,6o)/aug-cc-pVTZ and CASPT2(2e,2o)/cc-pVDZ energies calculated on MEP geometries.

Fragment orientations for the 2,4-C₅H₅O + OH recombination were sampled at the CASPT2(2e,2o)/cc-pVDZ level with fixed fragment geometries optimized at the CASPT2(1e,1o)/cc-pVDZ (OH) and CASPT2(5e,5o)/cc-pVDZ (2,4-C₅H₅O) levels. At separations larger than ~ 5 Å, the AS for the sampling was enlarged to (10e,8o) due to poor convergence of the CASSCF(2e,2o) reference wavefunction. The O–O distance-dependent correction for geometry relaxation was computed as described above. HL energy corrections along the MEP were computed at the CASPT2(10e,8o)/aug-cc-pVTZ level of theory, including the orbitals of the lone pairs of both oxygen atoms. The reference wavefunction was averaged over four states.

OH can recombine on either the oxygen or the ortho carbon site of 1,3-C₅H₅O. Fragment orientations were sampled at CASPT2(8e,7o)/cc-pVDZ level of theory using fixed fragment geometries optimized at CASPT2(1e,1o)/cc-pVDZ for the OH radical and CASPT2(5e,5o)/cc-pVDZ for the C₅H₅O radical, respectively. In the recombination on oxygen atom, the separation between the short and long range VRC-TST calculations is marked by the local minimum at an O–O distance of ~ 2.8 Å. Instead, for the recombination on the carbon site a hydrogen-bonded complex is formed at a C–O distance of about 4 Å. The energies obtained from the VRC-TST calculations were corrected with a distance-dependent potential. The geometry relaxation was calculated as discussed above, while HL MEP energies were computed at CASPT2(8e,7o)/aug-cc-pVTZ level of theory. The reference wavefunction was averaged over two states.

Pressure-dependent rate constants were computed in the 300–2500 K temperature range solving the multi-well one-dimensional ME as implemented in MESS [106] (see Section 3.3.4.3). Collisional energy transfer parameters in Ar bath gas were computed as suggested by Jasper [115]. The energy transfer parameters in the exponential down model were then fitted as $\langle \Delta E \rangle = 283 \left(\frac{T}{300} \right)^{0.62} \text{ cm}^{-1}$, while the collisional frequency was estimated with a Lennard-Jones model using $\sigma = 4.5$ Å and $\epsilon = 331$ K.

The impact of the new theoretical calculations was tested with kinetic simulations of experimental data from C₅H₆ and MAH/OAH oxidation using the CRECK mechanism. The full testing set is reported in the supplementary material of the corresponding publication [365]. Kinetic simulations with the Wang model [338], specifically developed for cyclopentadiene oxidation, were also performed. These results are not reported here for the sake of simplicity and brevity.

The CRECK model presented in this section already includes most of the literature updates of C₅H₆ oxidation mechanism listed in Section 5.2. In the starting CRECK model, the rate constant for the C₅H₅ + HO₂ = C₅H₅O + OH reaction channel was estimated as the high-pressure limit of the entrance channel, very similar to that of the present study. The updated model differs in the inclusion of the full ME pressure dependent results, as well as by the additional reactivity of C₅H₅O with OH (Section 5.3.2.6).

The rate constants obtained from MESS were lumped using MEL [291] (Section 4.3). It was thus possible to lump the 2,4-C₅H₅O reactivity into that of the 1,3 and 1,4 isomers, and

to merge these two species into a single C_5H_5O pseudospecies. The thermochemistry was assumed to be equal to that of the most stable 1,3- C_5H_5O isomer, since the contribution of 1,4- C_5H_5O to the C_5H_5O isomer pool computed with MEL is below 10% over the full range of operating conditions. This supports the lumping of the C_5H_5O and C_5H_6O PESs already included in the CRECK mechanism. Finally, it was assumed that 2,4- C_5H_5OOH rapidly decomposes to 1,3- $C_5H_5O + OH$ upon formation. The validity of the lumping procedure was verified by comparing the performance of the detailed and lumped versions of the model (e.g., see Section 4.4.3).

5.3.2.3 Thermochemistry of C_5H_5 radical

The thermochemistry of the cyclopentadienyl radical was carefully determined according to the indications reported in previous literature studies [308], [309], [341], [342], [366]. The formation enthalpy of C_5H_5 at 0 K available from the Active Thermochemical Tables of Ruscic et al. [117] is 65.61 kcal/mol. The same value was obtained at the level of theory described in Section 5.3.2.2 from the isogyric reaction $C_5H_5 \rightarrow 5CH_4 - 7.5H_2$ and the experimental values for CH_4 formation enthalpy. Table 5.6 shows that the C_5H_5 relative formation enthalpy (H-H(298 K)) calculated in this work at different levels of theory is in excellent agreement with CASSCF/cc-pVDZ results of Kiefer et al. [309], with discrepancies below 0.3 kcal/mol over the full range of temperature.

Particular care was taken in the derivation of the entropy of cyclopentadienyl radical. The Jahn-Teller distortion stabilizes $2A''$ (dienylic) and $2B'$ (allylic) states instead of the expected D_{5h} symmetry. The interconversion between these states affects the resulting entropy and may be treated as a pseudorotation [341], [366]. In particular, theoretical literature studies found that non-symmetric geometry optimization of this radical may result in a low frequency mode [341]. Replacing its contribution to the density of states with a pseudorotation with a rotational constant of 230 cm^{-1} , as suggested by Katzer and Sax [366], results in good agreement of the calculated entropy (differences below 1 cal/mol/K) with the values of Kiefer et al. [309], who accurately included the DOS of the Jahn-Teller modes.

Table 5.6 reports the results of this work obtained at different levels of theory in comparison with literature values. Interestingly, non-symmetric geometry optimization of cyclopentadienyl radical at B2PLYPD3/6-311+G(d,p) level resulted in the allylic distorted geometry, with no low frequencies and a calculated entropy matching the results of Kiefer et al. [309] within 1%. Removing the no-symmetry constraint in the geometry optimization at B2PLYPD3/6-311+G(d,p) level of theory resulted in the dienylic geometry with an imaginary frequency corresponding to a Jahn-Teller mode of about $400i \text{ cm}^{-1}$, consistently with literature results. In this case, the treatment of this normal mode as a pseudorotation is necessary to achieve consistent values of the entropy (B2PLYPD3/6-311+G(d,p) SYM+FREEROT in Table 5.6), showing maximum discrepancies with the results of Kiefer et al. [309] of 1.5 cal/mol/K at 300 K. A dienylic geometry with a low normal mode of about 70 cm^{-1} is instead obtained at ω B97X-D/6-311+G(d,p) level of theory. Also in this case, the high entropy estimated (ω B97X-D/6-311+G(d,p) LOWFREQ in Table 5.6)

must be corrected with the free-rotor treatment of the low normal mode (ω B97X-D/6-311+G(d,p) FREEROT in Table 5.6) to achieve better agreement with literature values. The B2PLYPD3/6-311+G(d,p) were used for the derivation of the thermochemical properties.

TABLE 5.6: Theoretical enthalpy (H) and entropy (S) variation of cyclopentadienyl radical with respect to that at 298 K (H–H(298), S–S(298), units are cal, mol, K) obtained by Kiefer et al. [309] and in this work. The levels of theory refer to geometry and frequency calculation. Bold columns indicate the final values used in this work. "LOWFREQ" indicates the results obtained with a harmonic oscillator treatment of the low frequency mode associated with the Jahn-Teller effect; "FREEROT" indicates that the density of states associated with the low frequency mode was treated as a pseudorotation.

T (K)	Kiefer et al. [309]	B2PLYPD3 /6-311+G(d,p) NOSYM	ω B97X-D /6-311+G(d,p) LOWFREQ	B2PLYPD3 /6-311+G(d,p) SYM+FREEROT
H–H(298)				
300	0.03	0.03	0.03	0.03
400	2.34	2.15	2.18	2.11
500	5.12	4.81	4.85	4.70
600	8.17	7.90	7.94	7.71
700	11.49	11.33	11.36	11.05
800	15.07	15.02	15.05	14.66
900	18.88	18.94	18.97	18.48
1000	22.9	23.04	23.07	22.50
1100	27.11	27.30	27.34	26.67
1200	31.48	31.71	31.74	30.98
1300	35.99	36.23	36.26	35.40
1400	40.62	40.85	40.88	39.93
1500	45.36	45.57	45.60	44.55
1600	50.19	50.36	50.39	49.25
1700	55.09	55.23	55.26	54.02
1800	60.07	60.15	60.18	58.85
1900	65.11	65.13	65.16	63.73
2000	70.2	70.16	70.19	68.66
S–S(298)				
300	63.5	63.6	64.9	66.7
400	70.1	69.7	70.8	72.8
500	76.3	75.6	76.5	78.7
600	81.8	81.2	82.0	84.3
700	86.9	86.5	87.2	89.6
800	91.7	91.4	92.0	94.5
900	96.2	96.0	96.5	99.2
1000	100.4	100.3	100.7	103.5
1100	104.4	104.4	104.7	107.5
1200	108.2	108.2	108.4	111.4
1300	111.9	111.8	112.0	115.0
1400	115.3	115.3	115.3	118.4
1500	118.6	118.5	118.5	121.7
1600	121.7	121.6	121.5	124.8
1700	124.7	124.6	124.4	127.7
1800	127.5	127.4	127.2	130.5
1900	130.2	130.1	129.8	133.2
2000	132.8	132.6	132.4	135.8

5.3.2.4 Potential energy surface

The portion of the $C_5H_5 + HO_2$ PES explored in this work is compared with previous theoretical estimates [293], [343] in Figure 5.4. The G4MP2 energies of Robinson and Lindstedt [343] agree to within 2 kcal/mol with the present calculations, and the calculations of Ghildina et al [293] are consistent with the relative energy of the C_5H_5O isomers obtained in this work. The group additivity estimates of Zhong and Bozzelli [311] reasonably predict the energies of all stationary points except for 1,4- C_5H_5O and 1,3- C_5H_5O .

HO_2 recombines on one of the five carbon sites of C_5H_5 to form 2,4- C_5H_5OOH . The backward H-atom abstraction to ${}^3O_2 + C_5H_6$ occurring on the triplet PES is expected to be irrelevant at intermediate temperatures with respect to the recombination channel due to its energy barrier of 2.6 kcal/mol (blue lines of Figure 5.4). The PES suggests that the product distribution is controlled by the competition between 2,4- C_5H_5OOH O–O bond-fission and its isomerization to 1,3- C_5H_5OOH , which rapidly decomposes to 1,3- $C_5H_5O + OH$. H_2O elimination might play a role at high temperatures, while hydrogen transfer from 1,3- C_5H_5OOH to 1,4- C_5H_5OOH is both energetically and entropically unfavored with respect to the dissociation channel. Consequently, the 1,4- $C_5H_5O + OH$ product channel is expected to be irrelevant even at high temperatures.

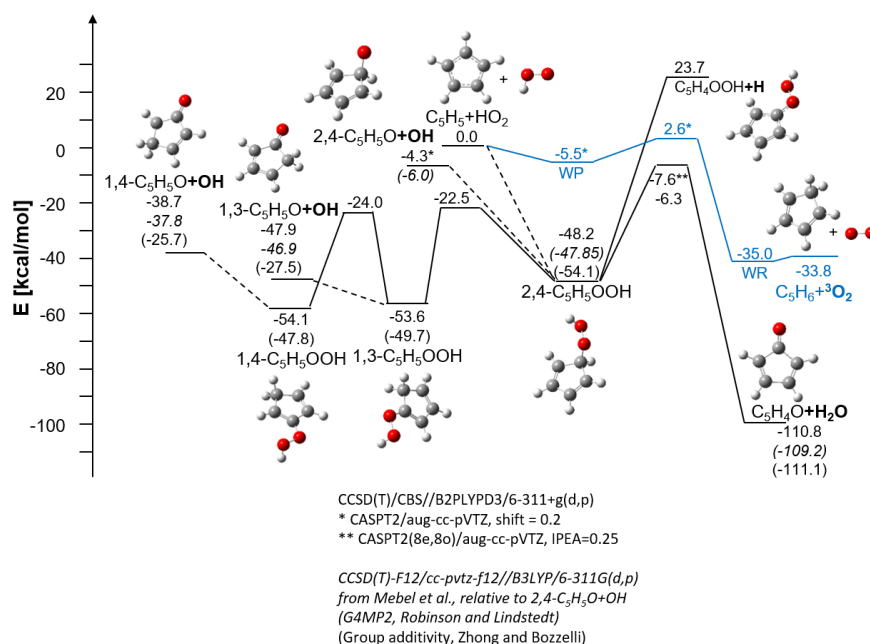


FIGURE 5.4: Potential energy surface of $HO_2 + C_5H_5$ reaction. Energies are corrected with ZPEs and are compared with the results of previous theoretical investigations [293], [311], [343].

5.3.2.5 Rate constants

Figure 5.5 shows the MEP computed along the C–O distance for HO_2 recombination with C_5H_5 . The interaction between the hydroperoxyl radical and the ring is significant even at large separations (~ 2 kcal/mol at 5 Å). HO_2 approaches the ring re-orienting from a vertical

to a quasi-parallel configuration with respect to C_5H_5 through a well with an interaction potential larger than 5 kcal/mol (C–O distance of 4 Å). Then, HO_2 rearranges laterally, overcoming a small barrier associated with the repulsion between the lone pairs of O and the electrons on the ring (C–O distance of 3.6 Å). This marks the separation between the inner and outer TS regions used in the VRC-TST simulations.

Figure 5.5b reports the resulting high-pressure limit rate constant together with that for $HO_2 + CH_3$ computed at the same level of theory and used for validation of the theoretical methodology. The latter rate constant slightly overestimates (25–40%) the literature value of Jasper et al. [367]. Compared to this reference, the rate constant for $C_5H_5 + HO_2$ has a stronger non-Arrhenius temperature dependence, decreasing from about $2 \times 10^{13} \text{ cm}^3 \text{ mol}^{-1} \text{ s}^{-1}$ at 300 K to $4 \times 10^{12} \text{ cm}^3 \text{ mol}^{-1} \text{ s}^{-1}$ at 2000 K. The previous estimate of Zhong and Bozzelli [311] is in reasonable agreement with the present calculations, while that of Robinson and Lindstedt [343] differs both qualitatively and quantitatively.

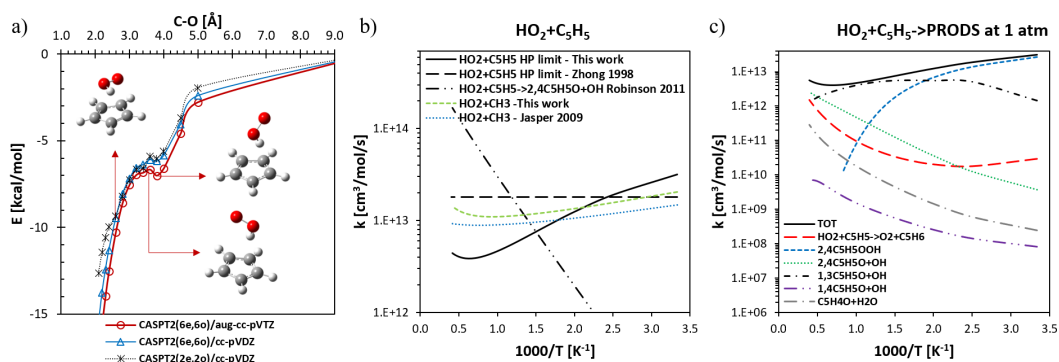


FIGURE 5.5: a) Minimum energy path for HO_2 recombination with C_5H_5 and b) resulting high-pressure limit rate constant in comparison with previous estimates [311], [343] and analogous reactions [367]; c) rate constants for the formation of products at 1 atm.

Figure 5.6a shows the MEP for O–O bond-fission in $2,4\text{-}C_5H_5OOH$. In this case, a hydrogen-bonded complex ~ 5 kcal/mol more stable than the separated fragments is formed in the long range region. Below 3 Å, the hydroxyl radical rearranges its orientation to favor the formation of the O–O bond. The minimum of the reactive flux is located in the long-range region below ~ 1000 K, while short-range interactions are limiting at higher temperatures. The MEP structures at O–O distances larger than those of the long-range well were determined through constrained optimizations fixing the OH orientation to avoid converging to the van der Waals wells of the other entrance channels. The high-pressure limit rate constant obtained (Figure 5.6b) is about one order of magnitude lower than the previous estimate of Zhong and Bozzelli [311], while it agrees to within a factor of ~ 3 with the rate constant of the similar $OH + CH_3O$ channel computed by Jasper et al. [367].

Figure 5.7a shows the MEP for the recombination channel of OH with the oxygen atom of $1,3\text{-}C_5H_5O$ at different levels of theory. The hydroxyl radical approaches $1,3\text{-}C_5H_5O$ from the side of the methylene group, forming a strong hydrogen bond of almost 8 kcal/mol at an O–O distance of ~ 2.8 Å. At shorter separations, the hydroxyl group is positioned above the O atom, perpendicular to the plane of the 5-membered ring. A local maximum at -2 kcal/mol with respect to the separated fragments is expected to limit the reactive flux at

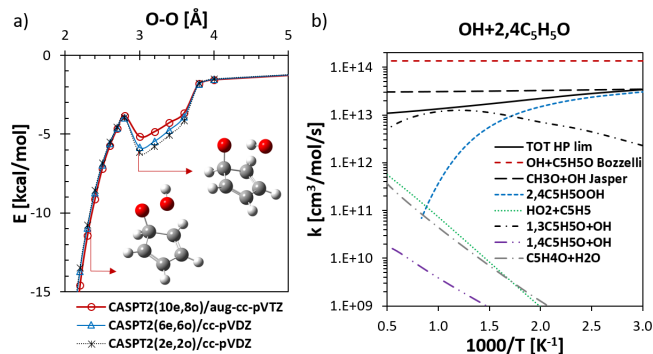


FIGURE 5.6: a) Minimum energy path of OH recombination with 2,4-C₅H₅O and b) high-pressure limit rate constant in comparison with previous estimates/analogue reactions and product-specific rate constants at 1 atm [311], [367].

high temperatures. An imaginary frequency corresponding to O–O stretching was found at a fairly short O–O separation of ~ 1.9 Å, thus allowing also a reasonable treatment of this channel with variational transition state theory. In VRC-TST calculations, a repulsive potential was placed on the carbon atoms close to the oxygen atom of the ring to exclude recombination on those sites.

It is noted that the MEP computed with HL and lower level energies is almost identical at O–O > 5 Å. At large separations, the calculation of the flux with VRC-TST resulted in electronic configurations having an attractive potential of 1.5 kcal/mol, in contrast with the expected lower values, which should converge asymptotically to 0 kcal/mol. This effect is probably due to poor convergence of the reference wavefunction or wrong active spaces, which was found to be affected by the relative orientation of the fragments. Trials with different ASs for VRC-TST samplings (e.g., 2e,2o or 4e,3o) resulted in a similar behavior. Therefore, VRC-TST calculations for the outer TS are expected to have a larger uncertainty and at low temperatures the actual rate constant might be smaller than the calculated values. Similar issues were encountered for the OH recombination on the carbon sites (see Section 5.3.2.6).

Figure 5.7b compares the high-pressure limit rate constants obtained with VTST and VRC-TST, showing smaller values than those of typical radical recombination reactions and a positive Arrhenius temperature dependence, attributed to the local maximum on the MEP at short separations. At 2000 K, the VTST and VRC-TST calculated rate constants have the same value of about 8×10^{11} cm³mol⁻¹s⁻¹, while at low temperatures the VRC-TST results are up to a factor of 2 lower than the VTST estimates. Despite the higher uncertainty in this rate constant, global rate constants for the C₅H₅ + HO₂ and 1,3-C₅H₅O + OH reactions are not strongly affected by this channel since 1) the rate limiting step to the formation of 1,3-C₅H₅O + OH is the H-transfer from 2,4-C₅H₅OOH and 2) OH mostly recombines on the carbon sites of 1,3-C₅H₅O (see Section 5.3.2.6).

Pressure-dependent rate constants were determined through ME simulations. Product-specific rate constants for C₅H₅ + HO₂ and 2,4-C₅H₅O + OH at 1 atm are shown in Figures 5.5c and 5.6b. In contrast with previous theoretical works and to most literature kinetic models [311], [337], [338], [343], the present calculations predict that the main bimolecular

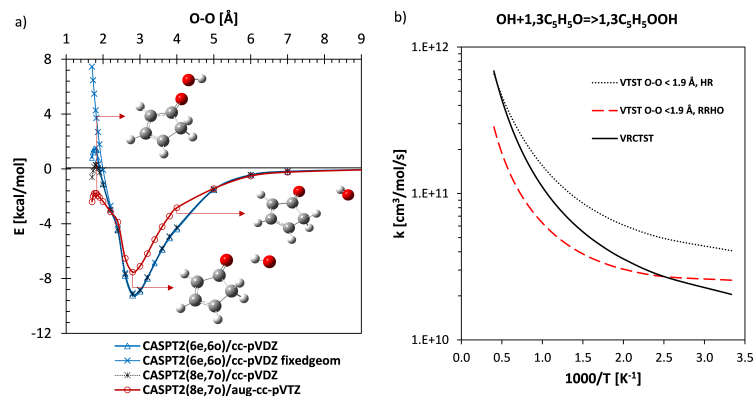


FIGURE 5.7: a) Minimum energy path and b) high-pressure limit rate constants for the recombination of OH with the oxygen atom of 1,3-C₅H₅O. VTST HR and RRHO indicate k calculated using VTST for MEP points with O-O distances below 1.9 Å with either RRHO approximation or 1DHR treatment of internal torsions, respectively.

product of C₅H₅ + HO₂ is 1,3-C₅H₅O + OH. The formation of 1,3-C₅H₅O + OH and 1,4-C₅H₅O + OH occurs entirely via well-skipping channels, as the corresponding wells are thermochemically and kinetically unstable over the full range of T, p investigated. The formation of 2,4-C₅H₅O + OH becomes competitive ($\sim 10\%$ of products BF) only above 1000 K, and prevails over that of 1,3-C₅H₅O + OH above 2000 K. Above 1500 K, the backward H-atom abstraction reaction to ³O₂ + C₅H₆ also contributes to the product distribution, reaching 20% at 2000 K. At 1 atm, 2,4-C₅H₅OOH collisionally stabilizes below 1000 K and becomes the main product below 500 K.

1,3-C₅H₅O + OH and 2,4-C₅H₅OOH are also the most relevant products also of the 2,4-C₅H₅O + OH reaction (Figure 5.6b). Above 1500 K, the C₅H₅ + HO₂ and H₂O + C₅H₄O reaction channels increase in relevance, becoming about 30% of the total products at 2500 K.

Pressure dependence is analyzed in Figure 5.8. As pressure increases, the stabilization of 2,4-C₅H₅OOH shifts to lower temperatures, thus decreasing the formation of bimolecular products. At 100 atm, the production of 2,4-C₅H₅OOH from both C₅H₅ + HO₂ and 2,4-C₅H₅O + OH prevails over that of bimolecular products already at 1100 K. Hence, at higher pressures the mid-to-low temperature reactivity of the system largely depends on the fate of 2,4-C₅H₅OOH. The reactivity of this well at 100 atm (also representative of lower pressures) is inspected in Figure 5.8c. The main product of 2,4-C₅H₅OOH is again 1,3-C₅H₅O + OH, while 2,4-C₅H₅O + OH plays a minor role at high temperatures, reaching about 12% of the product BF at 1600 K.

Overall, the main product of the C₅H₅ + HO₂ reaction network is 1,3-C₅H₅O + OH. The minor fraction of 2,4-C₅H₅O formed at high temperatures is rapidly converted to 1,3-C₅H₅O through either OH-assisted or direct isomerization [293]. 1,3-C₅H₅O is expected to accumulate in the system and successively react with radicals. This work predicts that the recombination of OH on the oxygen atom of 1,3-C₅H₅O to form 1,3-C₅H₅OOH is unfavored due to the low O-O bond energy of 5.6 kcal/mol. On the other hand, preliminary investigations of OH recombination to 1,3-C₅H₅O carbon sites revealed the formation of deep

wells with typical recombination rate constants of $2\text{--}5 \times 10^{13} \text{ cm}^3 \text{ mol}^{-1} \text{ s}^{-1}$ (Section 5.3.2.6). Potential bimolecular products of these reactions include $\text{C}_4\text{H}_5\text{OH} + \text{CO}$ and $\text{C}_5\text{H}_4\text{O} + \text{H}_2\text{O}$.

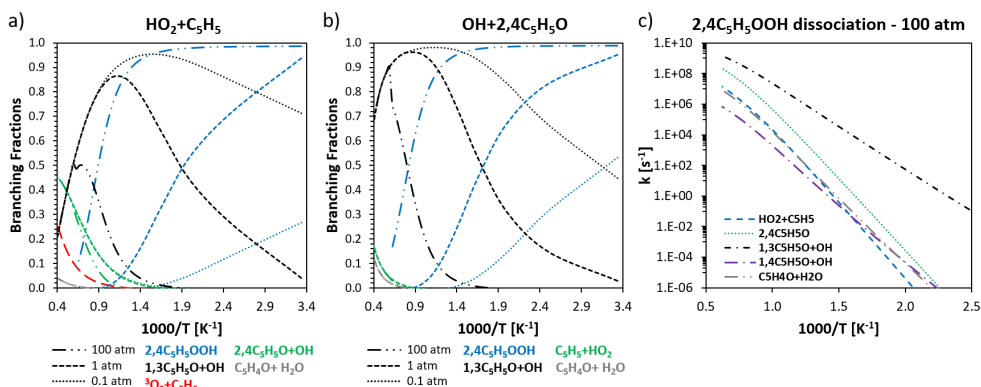


FIGURE 5.8: Pressure-dependent product branching fractions for a) $\text{C}_5\text{H}_5 + \text{HO}_2$ and b) $\text{OH} + 2,4\text{C}_5\text{H}_5\text{O}$ reactions. c) Rate constants for $2,4\text{C}_5\text{H}_5\text{OOH}$ dissociation at 100 atm.

5.3.2.6 Approximate reactivity of $\text{C}_5\text{H}_5\text{O}$ with OH radical

Because of the accumulation of $1,3\text{C}_5\text{H}_5\text{O}$ found in kinetic simulations of cyclopentadiene and benzene oxidation with both the CRECK and the Wang models, preliminary investigations of the $\text{C}_5\text{H}_5\text{OOH}$ PES accessed from $1,3\text{C}_5\text{H}_5\text{O} + \text{OH}$ were performed. Figure 5.9 shows that OH may recombine on both the ortho and meta carbon sites of $1,3\text{C}_5\text{H}_5\text{O}$. The recombination on the ortho site forms the stable W4-o (72.5 kcal/mol below the reactants). Theoretical calculations of some of the decomposition pathways of W4-o identified CO elimination as an important pathway. W4-m is formed from OH recombination on the meta carbon site. In this case, the favored channel may be H-transfer from the methylene group to the hydroxy group followed by water elimination. The other H-transfer and ring-opening channels investigated have higher energy barriers, however the high T1 diagnostic of CCSD(T)/CBS calculations reveal large uncertainties. MR calculations were not performed in this case, hence, it cannot be excluded that ring opening pathways might be competitive.

Figure 5.10 shows the results of the theoretical calculations for the recombination of OH on the ortho carbon site of $1,3\text{C}_5\text{H}_5\text{O}$. Figure 5.10a shows the MEP obtained by fixing the relative position of the O atom of the hydroxyl radical with respect to the C atom of the ring above 2.6 Å, while the MEP resulting from a C–OH distance constrained optimization is found in Figure 5.10b. In the latter, the H-bonded complex at around 3.5 Å resembles the structures obtained for the OH recombination on the oxygen atom (Figure 5.7). The separation between short and long range VRC-TST calculations was set to 4 Å for MEP a) and to 3 Å for MEP b). The contribution of the recombination channels on sites close to the ortho carbon was excluded by using a repulsive potential on the closest carbon atoms. Similar to the recombination of $1,3\text{C}_5\text{H}_5\text{O} + \text{OH}$ on the oxygen atom (Section 5.3.2.5), the long-range VRC-TST sampling resulted in an attractive potential between the two fragments of about 1.5 kcal/mol, which may lead to an overestimation of the resulting rate constant in the low temperature range. The rate constants obtained for both MEPs are reported

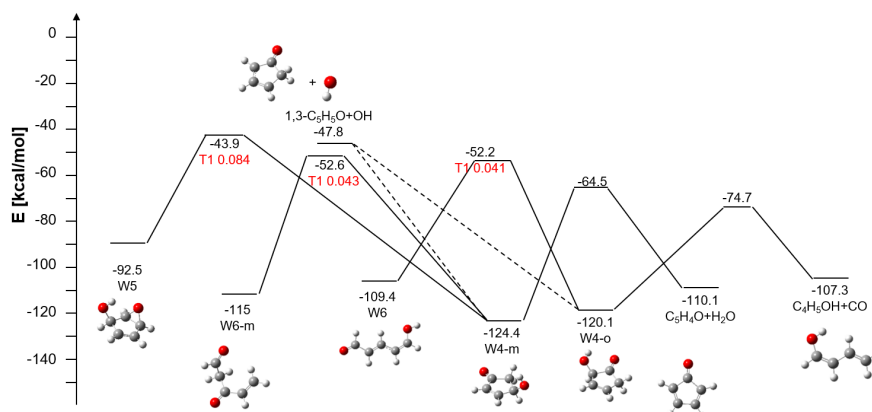


FIGURE 5.9: Investigation of possibly relevant reaction channels on the $1,3\text{-C}_5\text{H}_5\text{O} + \text{OH}$ PES. Dashed lines indicate barrierless channels investigated using VRC-TST. High values of T1 diagnostic obtained at CCSD(T)/aug-cc-pVTZ level of theory are marked in red.

in Figure 5.10c. Both rate constants are in the range of $1.5\text{--}4.5 \times 10^{13} \text{ cm}^3 \text{ mol}^{-1} \text{ s}^{-1}$. These values represent a likely range for the rate constant considered. The rate constants associated with the unconstrained MEP b) is lower because of the formation of the intermediate well. However, this configuration is similar to what was obtained for the OH recombination with the oxygen atom (Figure 5.7), thus raising the suspect that this well might lead to the recombination on a different site.

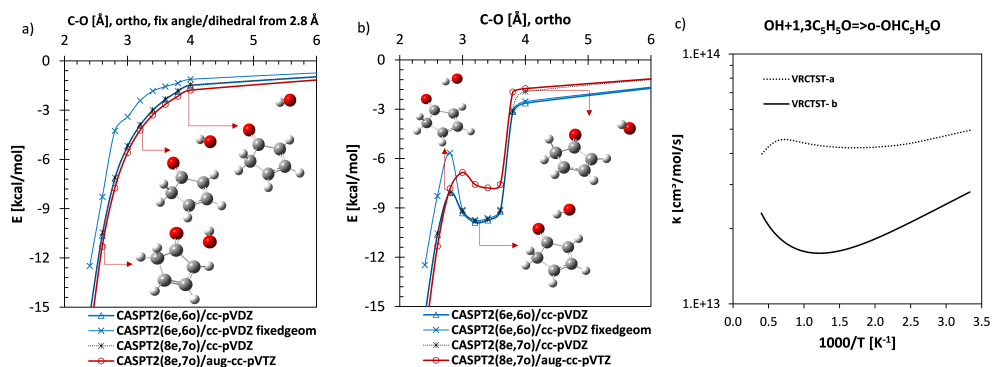
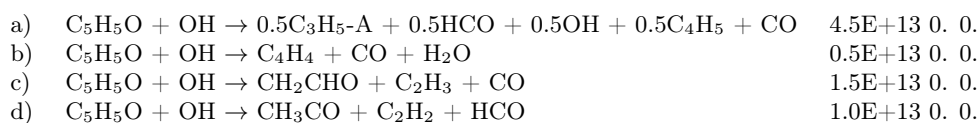


FIGURE 5.10: Minimum energy paths for the recombination of OH on the ortho carbon atom of $1,3\text{-C}_5\text{H}_5\text{O}$. MEP a) is obtained by constraining the position of the O atom of the OH radical with respect to the ring above 2.8 \AA , while MEP b) constrains only the C–OH distance. c) Shows the resulting VRC-TST rate constants.

Based on the results of the preliminary investigations of the $1,3\text{-C}_5\text{H}_5\text{O} + \text{OH}$ PES, approximate secondary reactivity was introduced into the kinetic mechanisms according to the following reaction parameters ($k = k_0 \cdot T^\alpha \cdot \exp\left(-\frac{E_A}{RT}\right)$ with units cm^3 , mol, s, cal, K):



Reaction a) derives from the recombination of OH in the ortho position. The total recombination rate constant is approximately the estimated upper limit. The main product $\text{C}_4\text{H}_5\text{OH} + \text{CO}$ was vertically lumped into its possible decomposition products $\text{C}_4\text{H}_5 + \text{OH}$ and

C_3H_5+HCO . Channels b-d instead derive from the estimates obtained for the recombination of OH in the meta position. Hence, the estimated upper limit rate constant was split among possible products. $C_4H_4+CO+H_2O$ derives from the channel to $C_5H_4O+H_2O$ found theoretically, where C_5H_4O is assumed to decompose due to the high exothermicity of the channel. Channels c,d instead result from the H-transfer from the hydroxyl group to the adjacent carbon atoms with successive ring opening, as exemplified in the scheme of Figure 5.11.

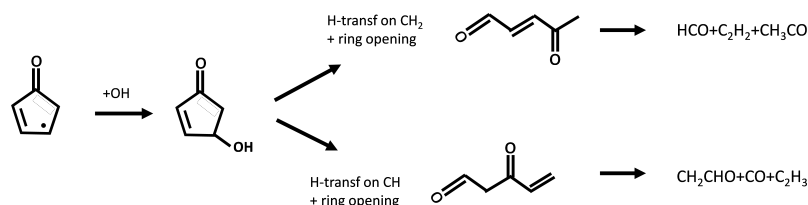


FIGURE 5.11: Possible H-transfer and ring opening pathways deriving from the OH recombination on the meta site of 1,3- C_5H_5O considered in this work for inclusion in global kinetic mechanism. The pathway on the bottom was also calculated (Figure 5.9).

5.3.2.7 Example of impact on kinetic simulations

The phenomenological rate constants obtained from the multi-well ME simulation, lumped using the MEL approach, were integrated into the CRECK mechanism. The lumped rate constants are found in Table 5.7. Thanks to MEL, the detailed set of 7 species and 10 (reversible) rate constants was reduced to 3 pseudospecies and 3 rate constants. The 1,3-/1,4- C_5H_5O isomers are lumped as a single C_5H_5O pseudospecies; 2,4- C_5H_5OOH decomposes directly to C_5H_5O+OH , while 2,4- C_5H_5O+OH was lumped according to the branching fractions to products. The impact of the present theoretical calculations was tested with kinetic simulations of experimental data of cyclopentadiene and benzene oxidation. In this section, examples of the updated CRECK model performances verify the suitability of the adopted lumping procedure and suggest directions for further model improvement.

Figure 5.12a shows the experimental and simulated mole fraction profiles of C_5H_6 , O_2 , C_5H_5 and $C_{10}H_8$ in the oxidation of cyclopentadiene in a JSR at stoichiometric conditions [338]. The corresponding flux analysis at 900 K is reported in Figure 5.12b. Profiles obtained with the detailed model are not depicted as they overlap with the lumped model. The concentration of C_5H_5 is mostly controlled by H-atom abstraction by OH from C_5H_6 . Additions of H and OH radicals are also competitive, resulting in an under-estimation of C_5H_5 and therefore of naphthalene ($C_{10}H_8$), produced via C_5H_5 self-recombination mechanism [295]. The updated reaction $C_5H_5 + HO_2 = C_5H_5O + OH$ consumes almost 50% of the C_5H_5 radical. In the detailed model (dotted arrows in Figure 5.12b), about 5% of C_5H_5 is consumed to produce 2,4- C_5H_5O and 2,4- C_5H_5OOH , which rapidly convert to 1,3- C_5H_5O via H-transfer [293] and O-O bond-fission, respectively. Hence, the concentration of these species is negligible. Similar behavior was found for the other tested cases and in the kinetic simulations performed (see also SM in [365]). This supports the adopted choices for lumping. C_5H_5O then recombines with O_2 forming $C_5H_4O + HO_2$ or smaller products derived

TABLE 5.7: Lumped set of rate constants for the calculated portion of the $C_5H_5 + HO_2$ PES. ** indicates the products from 2,4- C_5H_5OOH , while * indicates 2,4- $C_5H_5O + OH$ decomposed according to its product branching fractions. Pressure dependent reaction parameters are provided according to the modified Arrhenius expression $k = k_0 \cdot T^\alpha \cdot \exp(-\frac{E_A}{RT})$ in PLOG form, units are cm^3 , mol, s, cal, atm, K. The fitting range is 500–2500 K and R^2 is always > 0.99 except for $C_5H_5 + HO_2 = C_5H_5O + OH$ at 100 atm (0.96).

Reaction, pressure	k_0 (cm^3 , mol, s)	α	E_A (cal, mol)	
$C_5H_5 + HO_2 = C_5H_5O + OH$	3.95E+15	-1.0	-655	
PLOG/0.01	3.95E+15	-1.0	-655	/
PLOG/0.1	7.30E+15	-1.1	-449	/
PLOG/1.0	4.86E+18	-1.9	1874	/
PLOG/10.0	5.42E+23	-3.3	6884	/
PLOG/100.0	2.26E+23	-3.0	9840	/
DUP				
$C_5H_5 + HO_2 \rightarrow C_5H_5O + OH$	7.25E+11	0.2	3861	
*PLOG/0.01	7.25E+11	0.2	3861	/
**PLOG/0.01	1.02E+55	-15.6	8111	/
*PLOG/0.1	1.85E+12	0.1	4177	/
**PLOG/0.1	2.46E+63	-17.3	10972	/
*PLOG/1.0	2.43E+14	-0.5	5950	/
**PLOG/1.0	4.37E+61	-16.0	13113	/
*PLOG/10.0	8.78E+18	-1.7	10329	/
**PLOG/10.0	6.05E+48	-11.5	10960	/
*PLOG/100.0	2.68E+20	-2.0	14161	/
**PLOG/100.0	3.21E+34	-6.8	6884	/
DUP				
$C_5H_5 + HO_2 \rightarrow C_5H_4O + H_2O$	2.81E+00	3.2	-674	
PLOG/0.01	2.81E+00	3.2	-674	/
*PLOG/0.01	9.77E-03	4.1	5045	/
PLOG/0.1	7.21E+00	3.1	-350	/
*PLOG/0.1	9.12E-02	3.9	5815	/
PLOG/1.0	1.46E+03	2.5	1551	/
*PLOG/1.0	4.59E+03	2.6	9741	/
PLOG/10.0	1.32E+08	1.1	6166	/
*PLOG/10.0	2.32E+13	-0.1	18930	/
PLOG/100.0	1.28E+10	0.7	10277	/
*PLOG/100.0	7.54E+17	-1.2	27474	/
$C_5H_5O + OH \rightarrow C_5H_4O + H_2O$	3.30E+07	1.1	38940	
PLOG/0.01	3.30E+07	1.1	38940	/
PLOG/0.1	2.74E+09	0.5	40437	/
PLOG/1.0	2.17E+14	-0.8	44514	/
PLOG/10.0	6.16E+19	-2.3	50105	/
PLOG/100.0	1.02E+19	-2.0	52917	/

from ring-opening reactions. This results in a high concentration of C_5H_4O also for other experimental targets. At the conditions investigated, C_5H_4O is partially consumed only by addition with H (included from [293]) and OH (estimated). Since C_5H_4O is generally not detected in cyclopentadiene oxidation experiments (possibly also due to experimental difficulties), it might be worth exploring further both the reactivity of C_5H_5O with O_2 and the interactions of C_5H_4O with radicals.

The updated rate constants improve significantly the kinetic model predictions of C_5H_6 conversion in the Princeton plug flow reactor (PFR) data of cyclopentadiene oxidation [336], especially at fuel-lean conditions ($\Phi = 0.6$, $T = 1150$ K, $p = 1$ atm, Figure 5.12c). In the updated model, the production of C_2/C_4 species is mediated by C_5H_5O radicals, while in the original model it occurred directly from $C_5H_5 + HO_2$. Hence, the conversion decreases, contextually with an increase in the concentration of C_5H_5 and therefore of PAHs such as

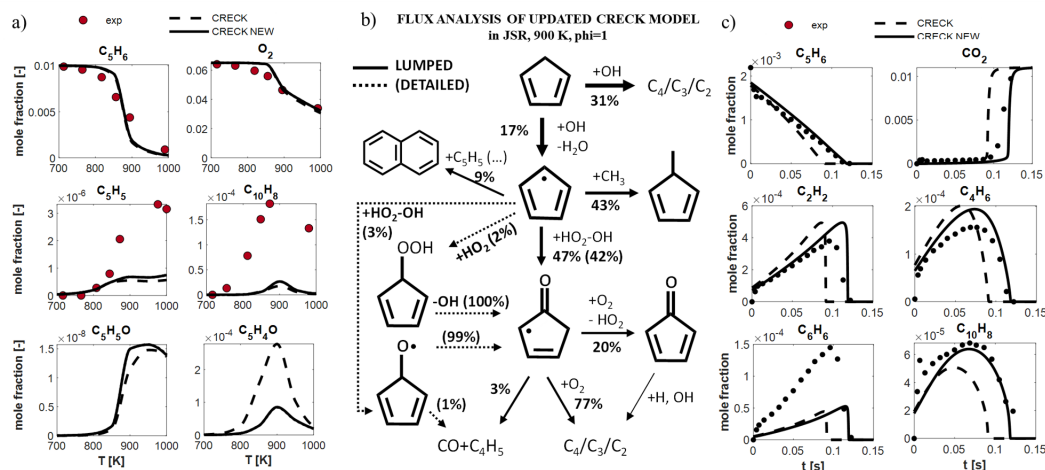


FIGURE 5.12: Experimental and simulated mole fraction profiles of significant species for C_5H_6 oxidation a) in the JSR of Wang et al. at $\Phi=1$ [338] and c) in the PFR of Butler et al. [336] at $T = 1150$ K, $\Phi=0.6$ (shift of -30 ms applied to the kinetic simulations) and b) flux analysis at 900 K in the JSR of Wang.

naphthalene, in accordance with the experimental data. The under-estimation of benzene may instead be related to the sub-mechanism of methylcyclopentadiene, through which it is produced.

Above 1000 K, the reactivity of $C_5H_5 + HO_2$ strongly affects kinetic simulations of benzene oxidation. In the PFR data of Lovell et al. [304] ($\Phi = 1.36$, $T = 1170$ K, $p = 1$ atm) benzene conversion slows down significantly in the updated CRECK model, thus improving the agreement with experiments (Figure 5.13a). In this system, C_5H_6 and C_5H_5 are mostly produced from phenol and phenoxy radical decomposition (Section 6.3.2). In the updated model, the concentration of C_5H_5 increases and that of OH decreases accordingly, thus reducing benzene consumption via H-atom abstractions by OH. The reactions of C_5H_5O with O_2 contribute to the production of CO together with phenoxy decomposition.

At fuel-lean conditions (Figure 5.13b), benzene conversion does not change dramatically compared to the original CRECK model, as OH radical pool is mostly unchanged. However, the higher concentration of C_5H_5 leads to a larger production of naphthalene, consistent with the observations made for C_5H_6 oxidation [336]. The consumption of C_5H_5O radical mostly occurs via O_2 addition, which also leads to the slight improvement in C_4H_4 predictions.

Finally, it must be mentioned that the results of the kinetic simulations presented in this section differ slightly from those presented in Sections 5.4 and 6.6, which instead include the complete set of kinetic mechanism updates of this work.

5.3.3 Reactivity of C_5H_5O

This section describes the additional reactivity calculated or introduced by analogy for the C_5H_5O resonance-stabilized radical, so as to exemplify more approximate calculation procedures and rate estimation based on analogy rules. The rate constants for other C_5 oxygenated species newly introduced in the CRECK kinetic mechanism in the course of this work (C_5H_5OH , C_5H_4OH , C_5H_4O) were mostly estimated by analogy with the non-oxygenated

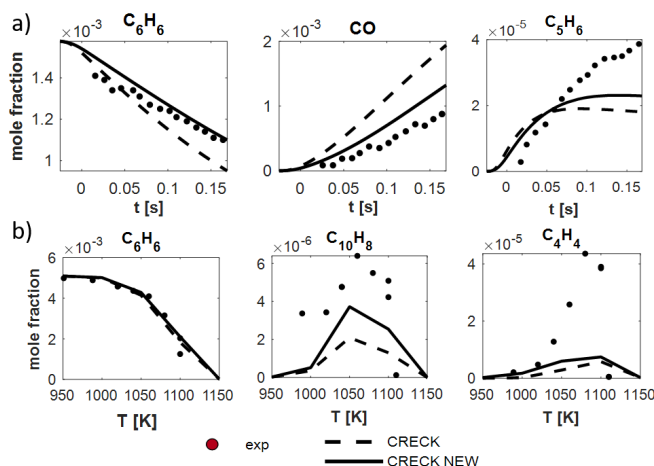


FIGURE 5.13: Experimental and simulated mole fraction profiles of relevant species in the oxidation of benzene in the Princeton PFR [304] (a, $T = 1170$ K, $\Phi = 1.36$) and in the Yale JSR (b, $T = 950$ – 1150 K, $\Phi = 0.19$, $p = 0.46$ atm [368]).

counterparts, similarly to what was described in Section 5.3.3.2. It is noted that in this section the structure of C_5H_5O is assumed to be that of 1,3- C_5H_5O , consistent with the findings of the previous section.

5.3.3.1 Radical H-atom abstractions by H, OH, and 3O_2

H-atom abstraction reactions from radicals are often neglected in kinetic mechanisms because radical recombination reactions are generally favored. However, rate constants for radical recombination with π resonance-stabilized radicals may have lower values than typical recombination rate constants for σ radicals (Section 5.3.2.5). Therefore, rate constants for H-atom abstraction reactions by H, OH and 3O_2 from the methylene group of 1,3- C_5H_5O were calculated and compared with the respective recombination rate constants to assess the relative importance of the two channels.

H-atom abstraction reactions from radicals are also interesting from a theoretical standpoint. In fact, the transition state structures for these reaction are not well described neither by low-spin MR calculations, nor by coupled cluster energies. Reasonable energy barriers can be obtained with the spin-splitting approach of Eqn. (3.16) (Section 3.1.3.3). Hence, the PESs were determined at the same level of theory described in Section 5.3.2.2, however energy barriers were refined with spin-splitting calculations.

Table 5.8 summarizes the energies of the stationary points and provides details about the selected active spaces for each reaction. Energy barriers were computed relative to the reactants. All ASs include the pi electrons of the ring (5e,5o) as well as the electrons of the C–H breaking bond (2e,2o). The lone pair of the oxygen atom was only included in the case of OH abstracting radical, consequently the reference wave function was weighted over two states. For H and OH abstracting radicals, the spin-splitting correction (CASPT2_{LS} – CASPT2_{HS}) was of 6.5 and 5.3 kcal/mol, respectively. On the other hand, the spin-splitting correction for 3O_2 abstracting radical was as high as ~ 61 kcal/mol. In this case, additional MR calculations were performed. The final triplet CASPT2(9e,9o)/aug-cc-pVTZ energy barrier

obtained considering the products as a reference (because of their closer electronic configuration to the TS) confirmed the value obtained using the spin-splitting approach, as shown in Table 5.8.

TABLE 5.8: Energies of the entrance well (WR), transition state (TS) and products (PRODS) of the radical H-atom abstraction reactions from C_5H_5O . Levels of theory L1, MR are specified in the text, while the spin-splitting level is described in the table (ATZ indicates aug-cc-pVTZ basis set).

ENERGIES	$C_5H_5O + H$	$C_5H_5O + OH$	$C_5H_5O + O_2$
WR	-1.6	-5.8	
TS - L1	4.9	-3.1	13.7
TS - SPIN SPLIT	0.9	-4.4	10.1
TS - MR			10.9
PRODS	-48.7	-62.8	6.5
SPIN SPLIT METHOD	CASPT2(8e,8o)/ATZ shift = 0.2	CASPT2(10e,9o)/ATZ shift = 0.2	CASPT2(9e,9o)/ATZ IPEA = 0.25

Figure 5.14 shows the rate constants obtained in comparison with the corresponding total recombination rate constants calculated in this work or obtained from literature [293], [294].

The radical H-atom abstractions by H and OH (Figure 5.14a) are significantly lower than the corresponding total rate constants for the recombination reactions and are therefore expected to play a negligible role in the reactivity. On the other hand, the radical abstraction by 3O_2 (Figure 5.14b) may be competitive with the reaction channels deriving from the recombination PES. The main reason lies in the different stability of the formed adduct for the recombination reactions: in fact, the recombination of H and OH on C_5H_5O form stable adducts which decompose to more stable products than the bimolecular reactants, whereas the less stable $C_5H_5O_2$ adduct results mostly in back-dissociation and the energy barriers to products are comparable or higher than that of the radical abstraction reaction.

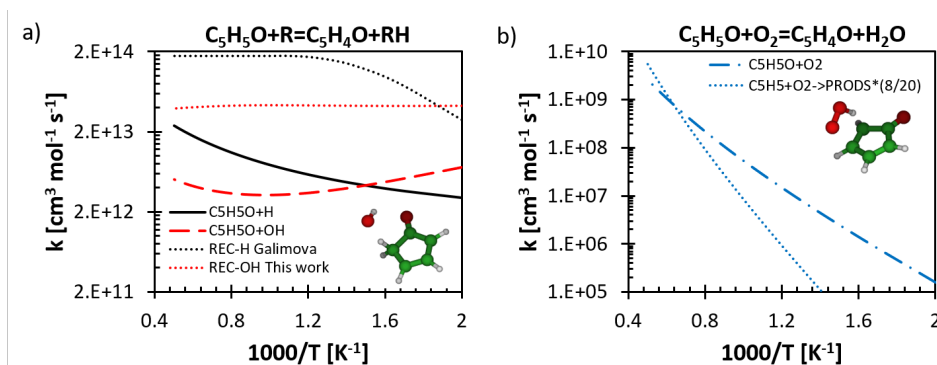


FIGURE 5.14: Rate constants of the radical H-atom abstractions by a) H and OH and b) 3O_2 from 1,3- C_5H_5O . Corresponding structures for the abstractions by OH and 3O_2 are also shown. Dotted lines refer to the recombination rate constants calculated in this work or in the literature [292], [294].

5.3.3.2 Approximate reactivity of C_5H_5O with molecular oxygen

The accumulation of C_5H_5O in benzene and cyclopentadiene oxidation encourages the inclusion in kinetic models of the reactivity of this resonance-stabilized radical with molecular oxygen. In this case, no theoretical calculations were performed. The reactivity of C_5H_5O with molecular oxygen was estimated by analogy with the $^3O_2 + C_5H_5$ system investigated

by Oleinikov et al. [294], included in this work after appropriate lumping with MEL. The lumping procedure resulted in 2 main reaction channels, namely OH elimination and ring opening. As anticipated in the previous section, both channels have positive energy barriers with respect to the reactants and therefore the corresponding rate constants are not typical total recombination rate constants.

The scaling of these rate constants to the C_5H_5O system was performed by analogy according to both symmetry and energy considerations. In particular, the total recombination rate constant was multiplied by a factor of 8/20 according to the following considerations: C_5H_5O has 2 recombination sites with 2 optical isomers for each TS (4); C_5H_5 has a symmetry factor of 10; in both cases, the symmetry of O_2 contributes by a factor of 2. This analogy rule is expected to be accurate as the same analogy applied to $C_5H_5O + OH$ with respect to $C_5H_5 + OH$ from [292] results in an error of less than 50% with respect to rate constant computed in this work.

The exothermicity of the formation of the adduct 1,3- $C_5H_5O-O_2$ from the recombination on the ortho site calculated at CCSD(T)/CBS//DFT level of theory is -15.8 kcal/mol, as opposed to the -10.4 kcal/mol of the $C_5H_5-O_2$ adduct calculated by Oleinikov et al. [294]. Hence, the activation energies of the two main channels lumped from the $C_5H_5 + {}^3O_2$ PES were rescaled by -5.5 kcal/mol.

An HO_2 elimination channel should also be considered for 1,3- $C_5H_5O-O_2$. In fact, this channel is common to the low-temperature mechanism of cycloalkenes such as cyclopentane [369]. The analogy with the cyclopentyl system allowed us to estimate a net energy barrier of about 11 kcal/mol. However, no accurate information for the pre-exponential factor and temperature-dependence were derived. Hence, for the other channels the parameters derived from cyclopentadienyl were adopted. The rate constant thus derived shows a discrepancy of less than a factor of 2 from that of the direct H-atom abstraction reaction by 3O_2 . This raises concern that the TS found for the radical H-atom abstraction reaction may be in fact that for HO_2 elimination from the adduct. However, given the similarity of the rate constants obtained and the number of approximations considered, these first estimates are considered reasonable for kinetic modeling purposes.

The final estimated rate constants are listed below:

a)	$C_5H_5O + O_2 \rightarrow 1.5CO + 0.5C_3H_4-A + 0.5CH_2CO + 0.5C_2H_2 + OH$	3.51E+01	3.11	17996
b)	$C_5H_5O + O_2 \rightarrow C_2H_3CHO + HCO + CO$	1.00E+06	1.37	17728
c)	$C_5H_5O + O_2 \rightarrow C_3H_4-A + HCO + CO_2$	1.00E+06	1.37	17728
d)	$C_5H_5O + O_2 \rightarrow C_5H_4O + HO_2$	1.00E+06	1.37	11000

A schematic representation of the reaction channels considered is provided in Figure 5.15. Channel a) may be accessed by internal H-atom abstraction from the intermediate 1,3- $C_5H_5O-O_2$ well followed by β -scission to OH and $C_5H_4O_2$, which might decompose according to the reaction pathways proposed at the bottom of Figure 5.15. $C_5H_4O_2$ might be an interesting intermediate to study, since it was detected in recent JSR experiments of anisole oxidation [370]. Channels b) and c) may be accessed from the O_2 recombination on the ortho site via internal addition of O to the adjacent carbon sites on the ring and successive ring opening, similarly to the investigated channels on ${}^3O_2 + C_5H_5$ PES [294]. Finally, channel

d) derives from the recombination of oxygen on the meta carbon site followed by a successive 5-membered ring internal abstraction reaction discussed above.

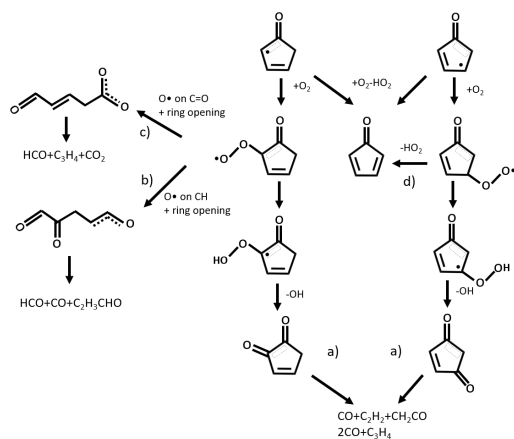


FIGURE 5.15: Speculated reaction pathways deriving from the recombination of ³O₂ on the ortho and meta carbon sites of 1,3-C₅H₅O.

5.4 Model performance and analysis

Table 5.9 lists the operating conditions for the experimental data on cyclopentadiene and indene pyrolysis and oxidation used for the testing of the updated CRECK kinetic mechanism. The results discuss most of the kinetic simulations performed.

TABLE 5.9: Simulation database of flow reactors included for the testing of the sub-mechanism of cyclopentadiene and indene. $\Phi = \text{inf}$ indicates pyrolysis conditions.

Inlet	Reactor type	T [K]	P [atm]	Φ	Residence time [s]	Reference
C ₅ H ₆ /N ₂	PFR	850–1160	1	inf	3	Kim 2010 [296]
C ₅ H ₆ /N ₂	PFR	850–1150	1	Inf	0.35–0.5	Djokic 2014 [297]
C ₅ H ₆ /C ₂ H ₄ /N ₂	PFR	900–1200	1.7	inf	0.3–0.5	Vervust 2018 [298]
C ₅ H ₆ /O ₂ /Ar	JSR	620–1070	1	0.5, 1.0, 1.8	–	Wang 2020 [338]
C ₅ H ₆ /O ₂ /N ₂	PFR	1100	1	0.6, 1.03, 1.6, 97.8	0.2	Butler 2009 [336]
C ₅ H ₆ /O ₂ /Ar	ST (IDT)	1100–1800	1	0.5, 1, 2	–	Orme 2005 [335]
C ₉ H ₈ /Ar	PFR	1000–1300	0.04, 1	inf	0.003–0.05	Jin 2019 [337]
C ₉ H ₈ /Ar	ST	1100–1900	4	inf	0.0015	Laskin 1998 [348]

5.4.1 Pyrolysis

This section presents kinetic modeling results for cyclopentadiene and indene pyrolysis, focusing on the interpretation of flux analysis and heat maps by reaction classes.

All three experimental datasets for cyclopentadiene pyrolysis investigate the 850–1150 K temperature range. Figure 5.16 shows the experimental and simulated species profiles in the PFR of Djokic et al. [297]. Cyclopentadiene starts converting around 1000 K. The main products are mostly polyaromatic species, primarily naphthalene, indene, and phenanthrene. The relevant MAH products instead include benzene, styrene and toluene. Overall, the agreement between experimental and simulated profiles is satisfactory. The most relevant discrepancy for the MAHs concerns the overestimation of benzene. However, at similar conditions in the PFR of Kim et al. [296] benzene is underestimated, while in the PFR of Vervust et al. [298] (Figure 5.17) the kinetic mechanism slightly overestimates C₆H₆ at lower temperatures while underestimating it at 1200 K.

The doping of C₅H₆ with C₂H₄ in the PFR of Vervust et al. [298] (Figure 5.17) does not significantly impact the product distribution. The presence of ethylene favors the formation of benzene and alkylated MAHs such as toluene and styrene. Additionally, the decomposition of ethylene leads to significant amounts of CH₄, which also fosters the production of methylcyclopentadiene.

Figure 5.18 shows the qualitative flux analysis of cyclopentadiene pyrolysis at 1000 K and about 50% conversion. All three PFRs investigated show very similar results in terms of the main reaction pathways, hence this analysis applies to all of them. The left panel shows that cyclopentadiene is converted to cyclopentadienyl mostly via H-atom abstraction reactions (updated in this work). Because of the high stability of cyclopentadienyl and the relatively low temperature, C₅ species do not decompose but add to form larger aromatics. In particular, C₅H₆ + C₅H₅ is a relevant consumption pathway for both species, thus forming MAHs (benzene and styrene) and 2-ring PAHs (indene, naphthalene, tetralin). Additionally, cyclopentadienyl recombination leads to fulvalene (FC₁₀H₁₀, see Section 4.4.3 and Appendix A), which dehydrogenates to naphthalene through bond-fission and subsequent β -scission

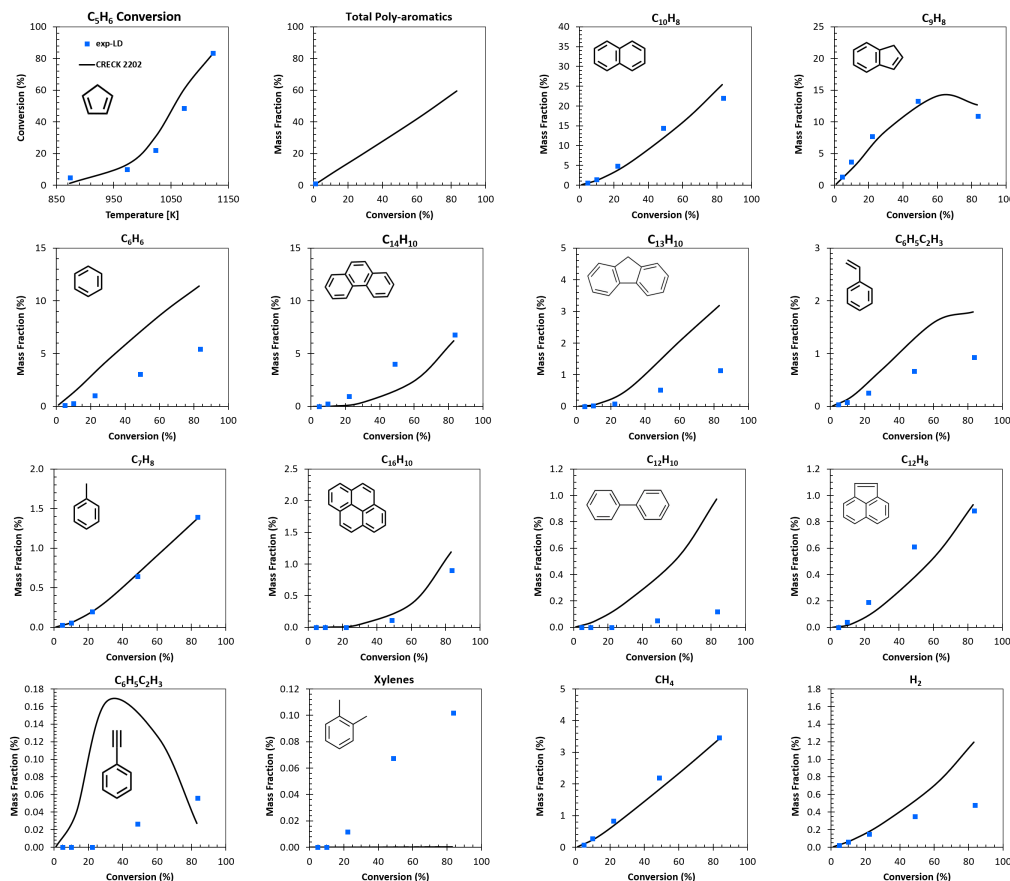


FIGURE 5.16: Experimental (dots) and simulated (lines) species profiles for cyclopentadiene pyrolysis in the PFR of Djokic et al. [297].

(see Section 4.4.3). $C_{10}H_{10}$ intermediates were only detected by Vervust et al. [298] (Figure 5.17). Upon ethylene doping, benzene is also formed via ring enlargement from $C_5H_6 + C_2H_4$, C_3H_5 , C_3H_7 . Finally, growth to PAHs with more than 2 rings occurs mostly from indene, indenyl and naphthalene via C_5H_6 and C_5H_5 additions.

The right panel of Figure 5.18 shows the flux heat maps (relative to the highest reaction flux for each species) organized by reaction class. It is immediately visible that C_5H_6 is mostly converted to C_5H_5 via abstraction reactions. The reaction class [C5-M][ADD_C5-RSR] corresponding to $C_5H_6 + C_5H_5$ is an equally relevant source of consumption of these two species, forming the above mentioned PAHs. Naphthalene is mostly formed via bond-fission from $FC_{10}H_{10}$, formed by [C5-RSR][REC_C5-RSR]. The formation of benzene and styrene are instead classified as [ENLARGE_C5-RSR] and [ADD_DECO_C5-RSR] because of the different nature of the respective reaction pathways. It is noted that the reaction class [C5-RSR][REC_C5-RSR], main formation pathway of phenanthrene, indicates the recombination of indenyl radicals, part of the [C5-RSR][REC_C5-RSR] class because of the cyclopentadienyl-like reactive moieties.

A useful application of heat maps is comparative analysis between similar operating conditions. For instance, the effect of temperature on the relevance of different class types for cyclopentadiene pyrolysis is considered in Figure 5.19. In particular, an increase from 1000

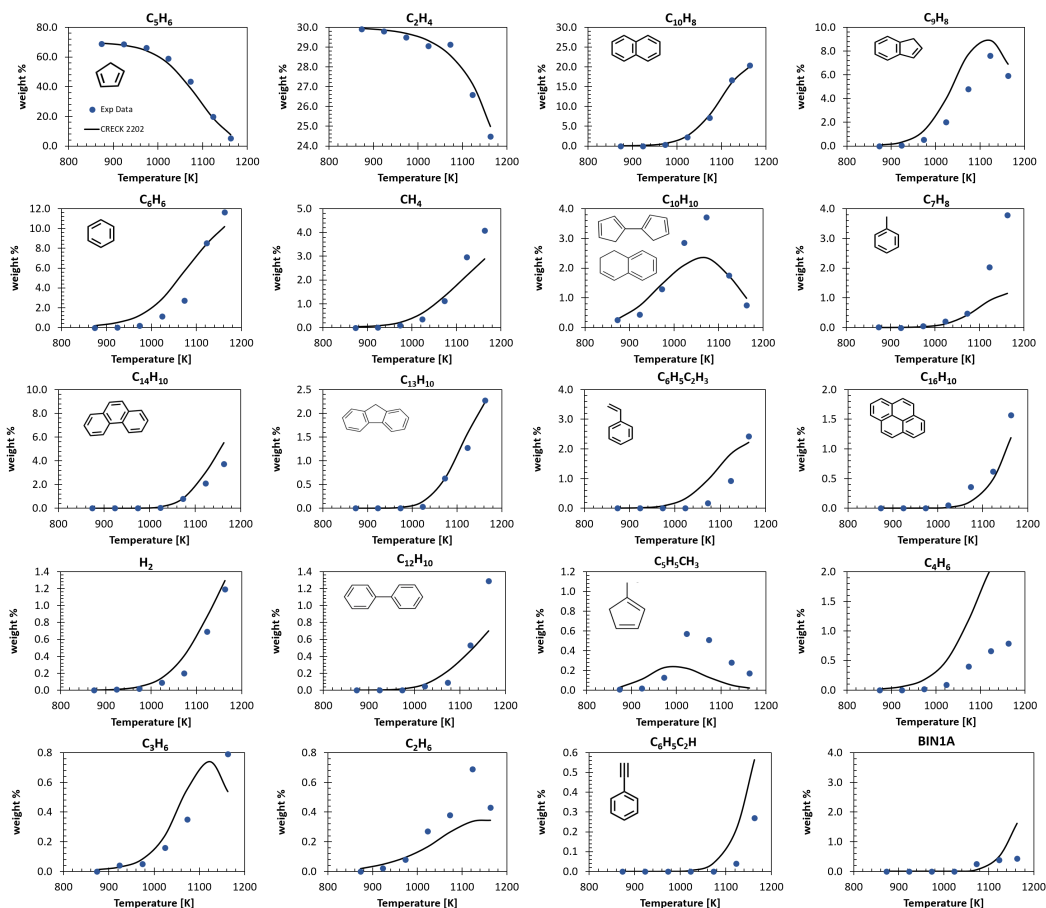


FIGURE 5.17: Experimental (dots) and simulated (lines) species profiles for cyclopentadiene pyrolysis doped with ethylene in the PFR of Vervust et al. [298].

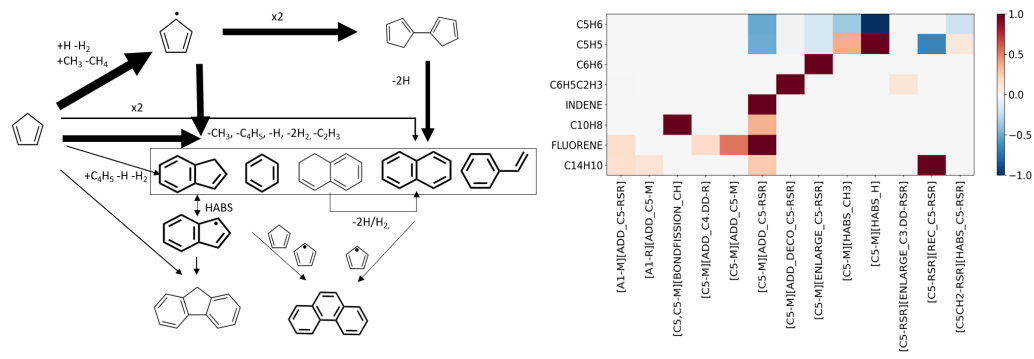


FIGURE 5.18: Global flux analysis for cyclopentadiene pyrolysis at 1000 K and $\sim 50\%$ conversion, including heat maps by reaction class (right panel) with a relative threshold of 10%.

K (conditions of the flux analyses presented in Figure 5.18) to 1500 K is considered. The 1000 K panel provides a more compact description of the considerations reported in Figure 5.18, highlighting the relevance of C_5 -type species [GROWTH- C_5] in reactant consumption as well as PAH formation. At higher temperature, the reactivity changes dramatically: in fact, the bond-fission of C_5H_6 to $C_5H_5 + H$ (ADD_H) as well as the unimolecular decomposition of C_5H_5 radical (DECOMPOSITION) to $C_2H_2 + C_3H_3$ become relevant. The C_2 and C_3 radicals formed upon C_5H_5 decomposition significantly contribute to MAHs and PAHs

formation. For instance, benzene is mostly produced via the recombination of C_3H_3 radicals (GROWTH-C3) as well as via $C_5H_4CH_2 + H$ (GROWTH-H), where $C_5H_4CH_2$ is also produced via recombination of propargyl radicals. Additionally, because of the larger amount of radicals, MAHs and PAHs are consumed more by H-atom abstraction reactions than in the 1000 K scenario. The effect of temperature on the type of growth reactions is analyzed in Figure 5.20, where bimolecular reactions of class types GROWTH-X and ENLARGE-X are arranged according to the nature of the reactants (M = molecule, R = radical, RSR = resonance-stabilized radical). At 1000 K, the M+RSR type (mostly corresponding to [C5-M][ADD_C5-RSR]) prevails. At 1500 K, C_5H_5 decomposition determines a broader distribution of growth reaction types, such that M+R or RSR+RSR reaction types also play a role. The presence of RSR prevents the R+R class from gaining relevance in growth reactivity.

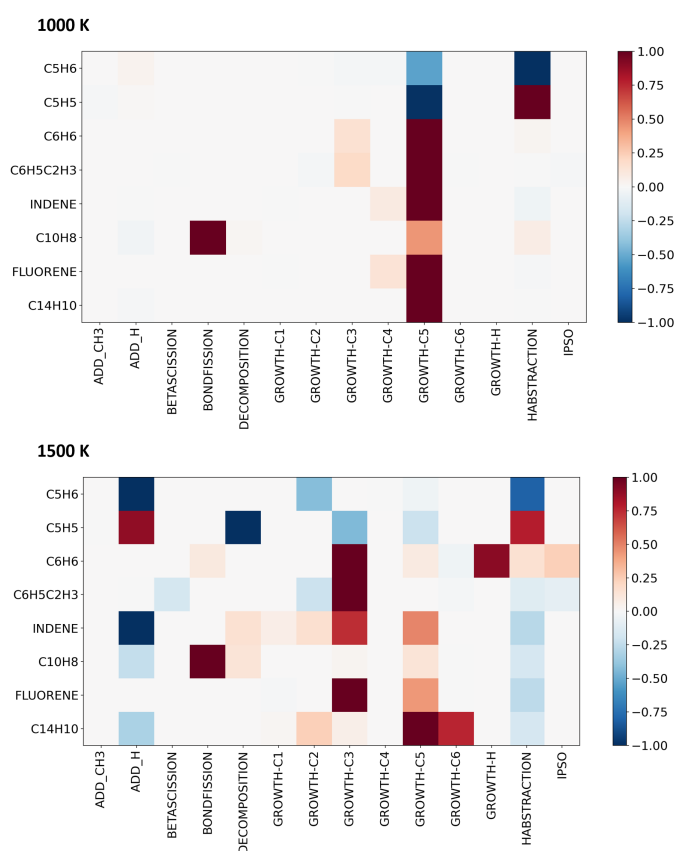


FIGURE 5.19: Flux analysis for cyclopentadiene pyrolysis at 1000 K and 1500 K organized by class type with a relative threshold of 1%.

More recently, theoretical and experimental studies also focused on the decomposition of indene. It is interesting to analyze the macroscopic model performance in terms of analogies and differences between the reactivity of cyclopentadiene and its smallest PAH counterpart. The primary products of indene decomposition were first identified by Laskin et al. [348], who performed a ST experimental investigation at 4 atm. Figure 5.21 shows that indene starts to convert around 1300 K. Laskin et al. mostly detected MAH products, namely benzene, phenylacetylene, and toluene, resulting from the decomposition of the C_5 ring. Naphthalene was also identified as a relevant product. A more comprehensive analysis was

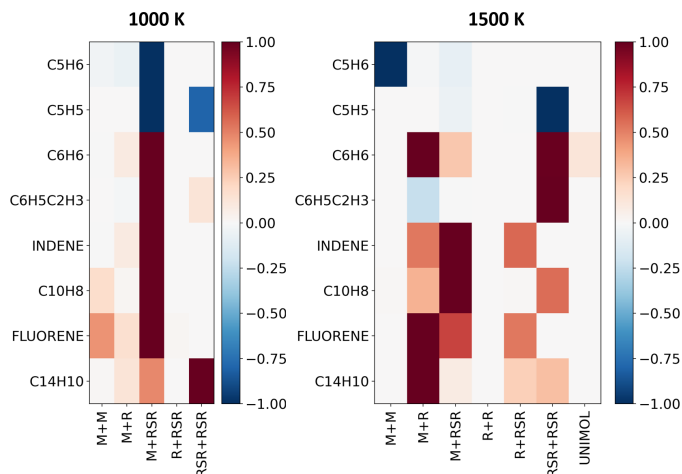


FIGURE 5.20: Flux analysis for growth reactions in cyclopentadiene pyrolysis at 1000 K and 1500 K organized by addition type (M, R, RSR indicate molecules, radicals, and resonance-stabilized radicals, respectively) with a relative threshold of 1%.

recently performed by Jin et al. [337], who studied indene decomposition at 0.03 and 1 atm in a PFR and were able to experimentally detect a large number of PAHs. Figure 5.22 reports some of the experimental species profiles in comparison with the kinetic simulations. Besides the products mentioned above, larger PAHs up to $C_{18}H_{14}$ were detected. At these conditions, conversion of indene starts around 1100 K, i.e., still at higher temperatures than cyclopentadiene.

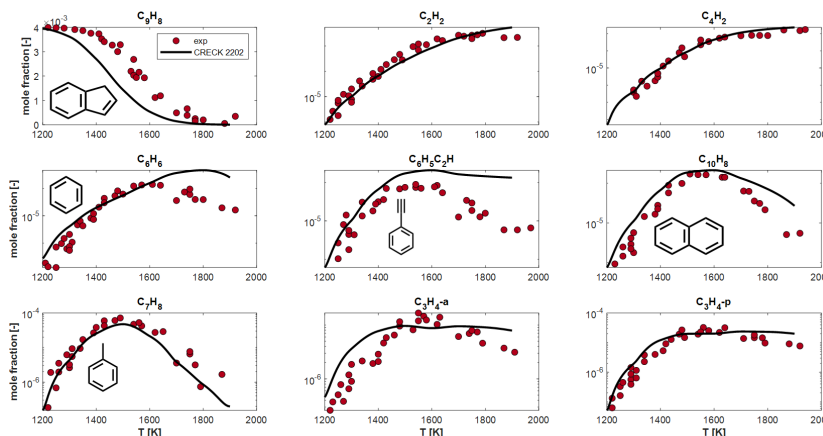


FIGURE 5.21: Experimental (dots) and simulated (lines) species profiles for indene pyrolysis at 1 atm in the ST of Laskin et al. [348]

The simulated profiles are able to reproduce reasonably the experimental results of Laskin et al. [348], despite the overestimation of indene conversion. Instead, the conversion in the PFR of Jin et al. [337] and the equilibrium between indene and indenyl is very well captured by the model. Only some of the experimental trends for decomposition products or larger PAHs are reproduced reasonably, such as those for C_7H_8 , C_5H_6 , $C_{10}H_{10}$ and $C_{18}H_{14}$. The indene sub-mechanism was mostly based on the analogous sub-mechanism of cyclopentadiene and on the theoretical calculations performed. Some of the indene and indenyl kinetics

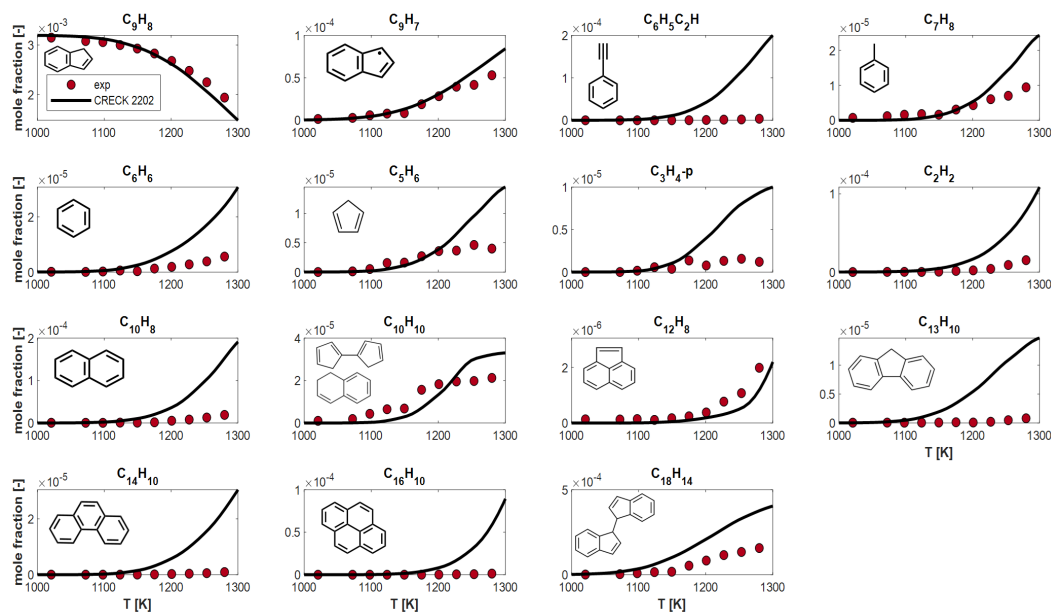


FIGURE 5.22: Experimental (dots) and simulated (lines) species profiles for indene pyrolysis at 1 atm in the PFR of Jin et al. [337].

proposed in the model developed by Jin et al. to interpret the experimental data were also integrated in the mechanism, with $\text{H} + \text{C}_9\text{H}_8 = \text{C}_9\text{H}_9$ and subsequent decomposition of C_9H_9 as well as $2\text{C}_9\text{H}_7 = \text{C}_{18}\text{H}_{10}$ being particularly relevant to capturing the main experimental trends.

The class-based flux analysis of Figure 5.23 helps guide the discussion about the main factors controlling indene reactivity according to the present kinetic simulations. First, the conversion from indene to indenyl occurs with almost equal contributions from H-atom abstraction by H and bond-fission, similarly to the high-temperature flux analysis proposed for cyclopentadiene pyrolysis (Figure 5.18). These classes, together with H addition on C_9H_8 mostly control the radical pool of H, C_9H_7 , C_5H_5 , and C_6H_5 , and consequently the reactivity of the whole system, as also highlighted by the sensitivity analysis of Jin et al. [337]. These radicals also act as the main abstractors on the stable molecular species. A notable difference between the reactivity of cyclopentadiene and indene is the behavior of the resonance-stabilized radicals formed. In the former case, the reactivity of $\text{C}_5\text{H}_6 + \text{C}_5\text{H}_5$ largely controls product distribution at lower temperatures. At higher temperatures, the decomposition of C_5H_5 into reactive small hydrocarbon species allows for new growth pathways. At the same time, MAHs and PAHs also start decomposing mostly via abstractions by H atoms. On the other hand, the decomposition of indenyl radical is less favored because of the stability associated with the aromatic ring. Hence, indene decomposition mostly occurs upon H addition: the decomposition pathways in Figure 5.23 mostly include C_9H_9 reactions. The opening of the C_5 ring moiety results in benzene or substituted MAHs. As a consequence, growth pathways via C_2 and C_3 species are less relevant than in cyclopentadiene pyrolysis, while growth through A1 moieties appears in the flux analysis (right panel of Figure 5.23). Indenyl is therefore consumed mostly via self-recombination. The overall reactivity of indene

is thus slower than that of cyclopentadiene, showing a shift in the conversion by about 50 K at the same experimental conditions. The discrepancy between the CRECK mechanism based modeling and the experimental data may be explained by missing or approximated radical-decomposition reactions and possibly too low radical concentrations, also suggested by the overestimation of most of the molecular species. For instance, the flux analysis of cyclopentadiene pyrolysis at high temperature shows that PAHs are consumed via H-atom abstraction reactions, while in the case of indene no significant PAH consumption is observed.

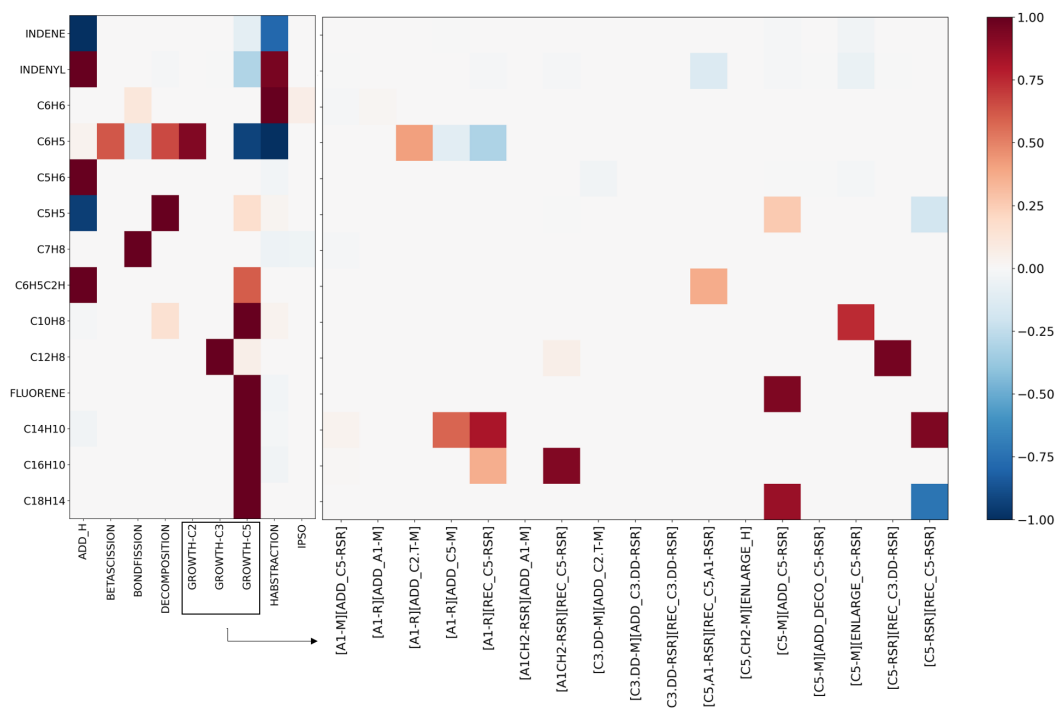


FIGURE 5.23: Flux analysis for indene pyrolysis in the PFR of Jin et al. [337] at 1300 K (30% conversion) organized by class type (left panel, relative threshold of 0.1%) with additional species + reaction type analysis for growth reactions (right panel, relative threshold of 1%).

5.4.2 Oxidation

This section presents the results from the kinetic modeling of cyclopentadiene oxidation in comparison with most of the experimental datasets considered in this work. Insights into the performance of the CRECK kinetic mechanism are provided by considering first speciation in low and high temperature oxidation, and then macroscopic properties such as the IDT and the LFS. The aspects concerning the oxidation and growth of MAHs formed during cyclopentadiene oxidation are only briefly mentioned in this section, while mechanistic insights are presented in Chapter 6. Only growth reactions involving C_5 species are discussed in this section, in accordance with the classes described in Section 5.2. Figure 5.24 shows kinetic simulations against the latest experimental data for low-temperature C_5H_6 oxidation from Wang et al. [338] at different equivalence ratios ($\Phi = 0.5, 1, 1.8$). The authors report an uncertainty in the mass balance for each species of 3% in comparison to C, H and O, whose balances have an uncertainty of 24%, 20% and 14%, respectively. The main decomposition

products detected besides CO, CO₂ and CH₄ are unsaturated C₂–C₄ species such as C₂H₄ and C₄H₆, identified mainly as 1,3-butadiene. Also aldehydes such as formaldehyde and acrolein contribute significantly to the product distribution. As far as aromatic species are concerned, the most abundant MAH detected is benzene, followed by styrene, toluene, and phenylacetylene, while the only PAHs are naphthalene and indene. The effect of the equivalence ratio seems to be mostly related to the conversion rather than to dramatic changes in the product distribution. At $\Phi = 0.5$, the mole fractions of H₂O and CO₂ are remarkably larger than at lower Φ ; the increase in CO₂ reasonably reflects the conversion of CO, which peaks around 950 K, as well as the oxidation of C₁–C₄ species. At $\Phi = 1.8$, the main difference in the product distribution besides H₂ and CH₄ is a slightly higher concentration of MAHs/PAHs, especially of C₅H₅ and C₆H₅C₂H at higher temperatures ($T > 1000$ K).

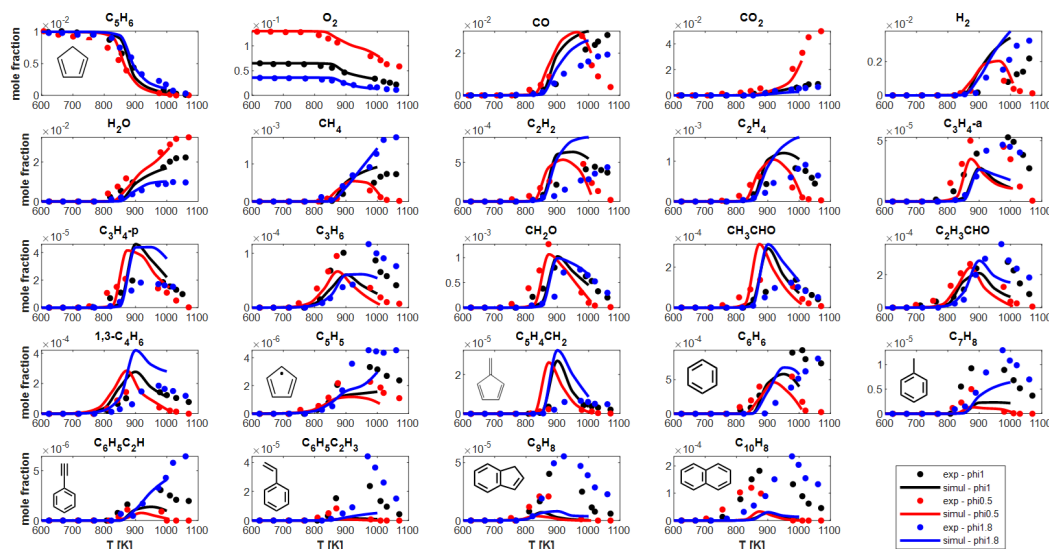


FIGURE 5.24: Experimental (dots) and simulated (lines) species profiles for cyclopentadiene oxidation at 1 atm in the JSR of Wang et al. [338] at $\Phi=0.5, 1, 1.8$.

The model predictions generally agree with experimental data, with some striking discrepancies. In particular, the model strongly overpredicts the concentration of H₂, CO and a few of the smaller products, while it underpredicts that of larger aromatics. Additionally, the slope of the modeled conversion of C₅H₆ is definitely sharper than that of the experimental results, especially at fuel-lean conditions. Such discrepancies seem to suggest potentially missing low-T oxidation pathways, possibly involving O₂ additions. The underprediction of cyclopentadienyl concentration probably explains the underpredicted concentrations of PAHs, in contrast with the good predictions of MAHs/PAHs in pyrolysis flow reactors at similar conditions (see Section 5.4.1).

The results of global flux analysis at about 50% conversion (~ 900 K) for $\Phi = 1.8, 0.5$ are presented in Figure 5.25. At $\Phi = 0.5$, class analysis by species and reaction types of C₅ species types is also included. Cyclopentadiene is mostly consumed by addition reactions ADD_H, ADD_OH, ADD_O2, ADD_O, as well as by H-atom abstractions by OH and H (see bottom right panel of Fig. 5.25). All of these classes except for

ADD_O2 and ADD_O were updated with theoretical calculations (Table 5.2). At fuel-lean conditions, the relevance of additions with OH and O₂ increases. ADD_HO2 instead produces cyclopentadiene as a result of the competition between ADD_HO2_EL_O2, which proceeds in the backward direction, and ADD_HO2_EL_OH, which decomposes cyclopentadiene to C₄H₆ [323] (see flux and reaction types on the right side of Figure 5.25). The H addition to CYC₅H₇ [C5-M][ADD_H_WELL] and subsequent radical abstraction by cyclopentadienyl [C5H2-RSR][HABS_C5-RSR] play a relevant role in determining cyclopentadiene conversion. O₂ addition on CYC₅H₇ is also an important formation pathway of unsaturated linear C₂-C₄ species. OH addition to cyclopentadiene forms C₅H₆OH, a resonance-stabilized radical which rapidly decomposes through β -scission. The main decomposition pathway of cyclopentadienyl radical at low temperatures is HO₂ recombination [C5-RSR][REC_HO2_EL_OH] (Section 5.3.2). The radical thus formed mostly decomposes via ring opening [C5O-RSR][ROPEN].

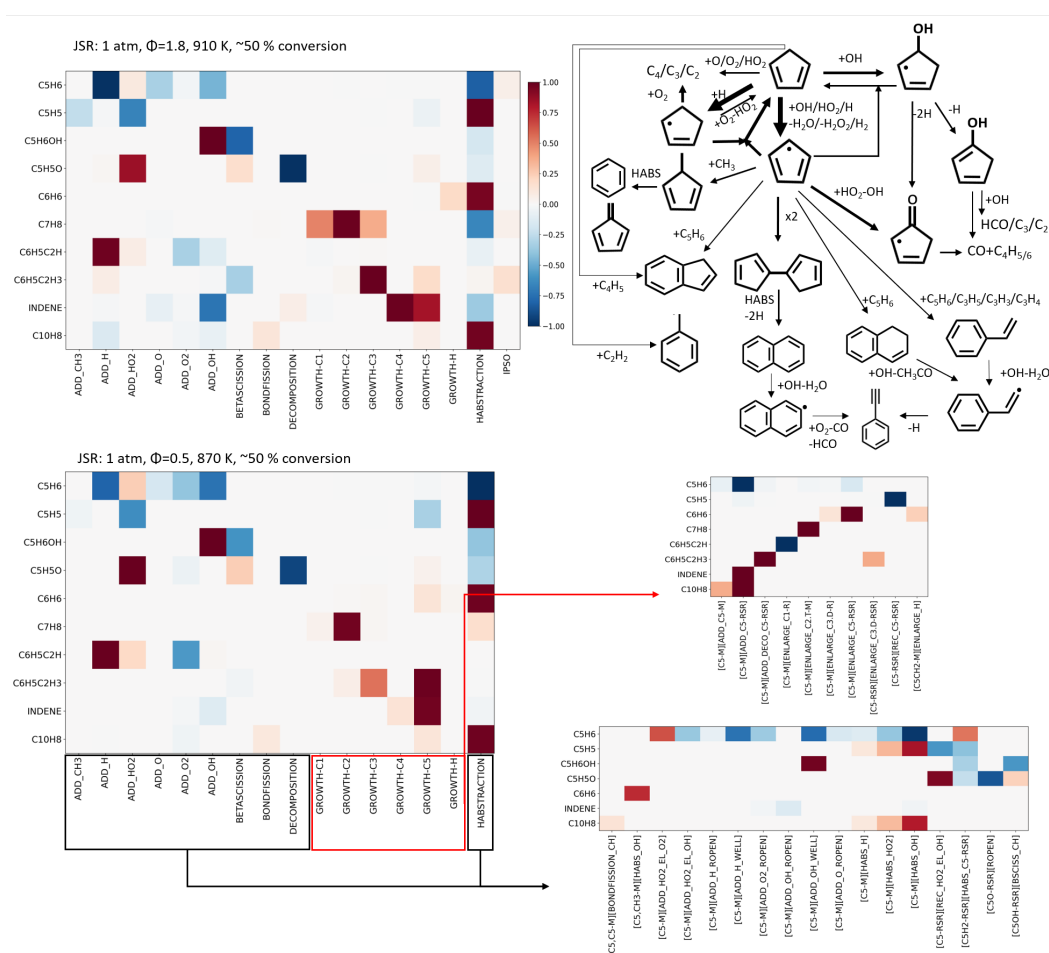


FIGURE 5.25: Schematic flux analysis for cyclopentadiene oxidation at ~ 900 K (50% conversion) in the JSR of Wang et al. [338]. Fluxes are organized by class type (left panel, relative threshold of 1%) at $\Phi = 1.8, 0.5$ with additional species + reaction type analysis for growth and oxidation reactions involving C₅ species (right panel, relative threshold of 5%).

With respect to the simple flux obtained for the pyrolysis case (Figures 5.18 and 5.19), where C₅ growth classes dominate, the larger concentration of smaller species and radicals in oxidative conditions change the relevant growth pathways, as shown in the bottom-right

panel of Figure 5.25. C_5 classes involving C5-M and C5-RSR species types still prevail in the formation of styrene and indene and play an important role in the formation of benzene and naphthalene. However, the latter are also produced from H-atom abstraction reactions by OH from methylcyclopentadiene and fulvalane, respectively. Because of the larger concentration of C_2 – C_3 species, ring enlargement reactions on both C5-M and C5-RSR species types significantly contribute to the formation of toluene and styrene (e.g., [ENLARGE_C2.T-M], [ENLARGE_C3.DD-RSR]). Finally, the formation of phenylacetylene is mediated by the oxidation of naphthalene (ADD_O2) as well as the decomposition of styrene parent radical through β -scission (ADD_H). In fuel-rich conditions, the larger concentration of MAHs and PAHs allows for their partial decomposition via either additions (ADD_O2, ADD_OH) or abstraction reactions.

Considering the flux analysis, discrepancies with experimental data might be explained by a wrong relative importance for some of the reactions determining cyclopentadienyl concentrations, as well as high uncertainties in growth reactions through C_2 – C_3 species (mostly estimated by analogy), not relevant in pyrolysis conditions. Finally, it is comforting to highlight that in benzene oxidation the shortcomings discussed in this section are not expected to be as relevant, since the concentration of C_5H_6 and C_5H_5 are mostly controlled by the decomposition of phenol and phenoxy radical, respectively.

The PFR data of Butler et al. [336] at 1150 K allows one to analyze the history of product formation in greater detail, thanks to the detection of the evolution of products at short times (< 0.02 s). Figure 5.26 compares experimental data at fuel-rich and fuel-lean conditions with kinetic simulations with the CRECK kinetic model presented in this work. It is noted that the PFR was simulated as isobaric and adiabatic, therefore a shift of -40 ms was applied to the kinetic simulation profiles to account for the length of the mixing zone, as suggested in [127], [371]. For illustrative purposes, species profiles are presented as a function of conversion, and simulation time at fuel-rich conditions was extended with respect to that of experiments so as to reach full conversion of benzene. The product distribution is similar to the low T case, with 2 main differences: aldehydic products were not detected (with a detection limit of the experimental apparatus of 20 ppmv), while methylcyclopentadiene was detected in large amounts. Less abundant new products instead include phenol and $C_{10}H_{10}$. Similarly to the low temperature experiments, the equivalence ratio does not affect dramatically the product distribution. As expected, at fuel-lean conditions the selectivity to MAHs and PAHs decreases in favor of some of the smaller alkenes (e.g., C_2H_6 , C_3H_6 , C_4H_6). On the other hand, methylcyclopentadiene decreases with increasing Φ , mirroring the decrease in methyl concentration. Similarly, benzene seems to be almost unaffected by the equivalence ratio, probably because of compensation effects for its competing formation pathways (i.e., from C_5 species and from cyclopentadiene). Finally, the fraction of phenol increases at fuel-lean conditions, since its formation is controlled by reactions of benzene oxidation. These mechanistic aspects are further expanded on below through the flux analysis.

Overall, the model reproduces experimental data satisfactorily, with good performances for the main MAH and PAH products such as $C_6H_5C_2H$, $C_6H_5C_2H_3$, C_9H_8 , $C_{10}H_8$, $C_{10}H_{10}$. Since the main formation pathways of these species involve reactions starting from C_5H_6

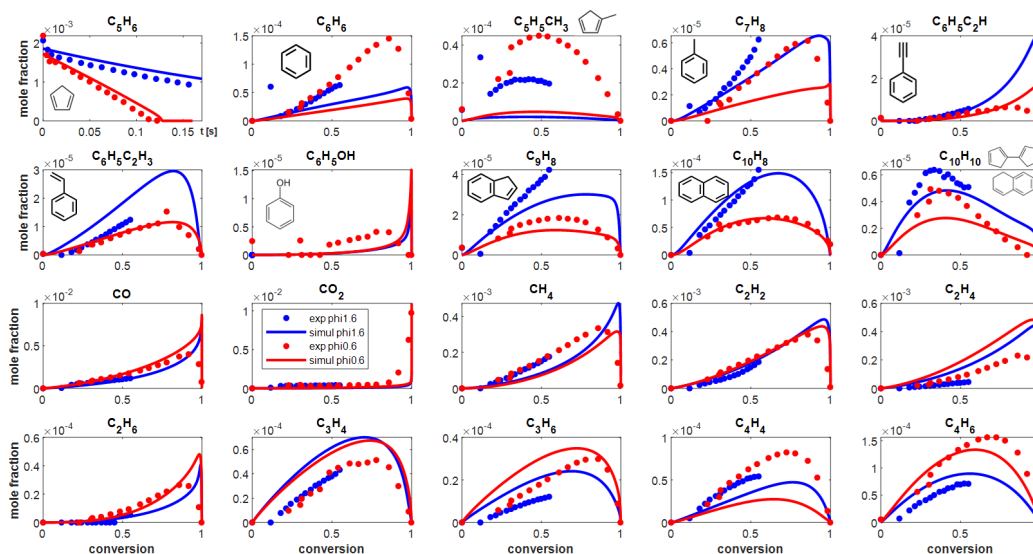


FIGURE 5.26: Experimental (dots) and simulated (lines) species profiles for cyclopentadiene oxidation at 1 atm in the PFR of Butler et al. [336] at $\Phi = 0.6, 1.6$. Simulated profiles for the fuel (first panel) were shifted by -0.04 s to account for back-diffusion effects. Other species are plotted as a function of the fuel conversion.

and C_5H_5 , the concentration of cyclopentadienyl radical is unlikely to be underpredicted at these experimental conditions. On the other hand, methylcyclopentadiene is strongly underpredicted, also causing the underprediction of benzene. In the kinetic model, reaction classes involving C_5, CH_3 -M species were estimated with analogy rules; additionally, the radicals formed from methylcyclopentadiene were lumped directly to fulvene and benzene. Hence, the sub-mechanism of methylcyclopentadiene certainly requires updates.

The flux analysis at $\Phi = 0.6$ is reported in Figure 5.27. Flux analysis by class type as well as more detailed reaction types involving C_5 species are reported at both 50% and 100% conversion. Flux analysis at $\Phi = 1.6$ is essentially identical, with stronger relative importance of GROWTH-C5 and DECO class types with respect to ADD_OX, HABS, GROWTH-C2, GROWTH-C3, due to the lower content of oxygen and radicals and therefore smaller extent of oxidation to C_2 - C_3 species.

The main class types dominating the consumption of cyclopentadiene at 50% conversion are similar to the low T case. However, at higher temperature H-atom abstraction reactions definitely prevail over addition reactions. This transition also explains the lack of aldehydic species, which are formed by oxidation addition reactions on C_3 - C_4 species. The analysis by species and reaction type (bottom right panel of Fig. 5.27) reveals that among oxidation addition reactions, the oxidation with atomic oxygen $[C_5-M][ADD_O_ROPER]$ gains relevance because of the higher concentration of radicals containing oxygen. Additionally, the higher temperature favors addition - decomposition reactions over well stabilization: for instance, reaction type ADD_R_ROPER prevails over ADD_R_WELL. Another consequence of the larger radical pool is the relevance of radical recombination reactions such as $[C_5-RSR][REC_H_WELL]$, which produces the reactant from its parent radical. The larger concentration of cyclopentadienyl can be explained by the fact that its production via

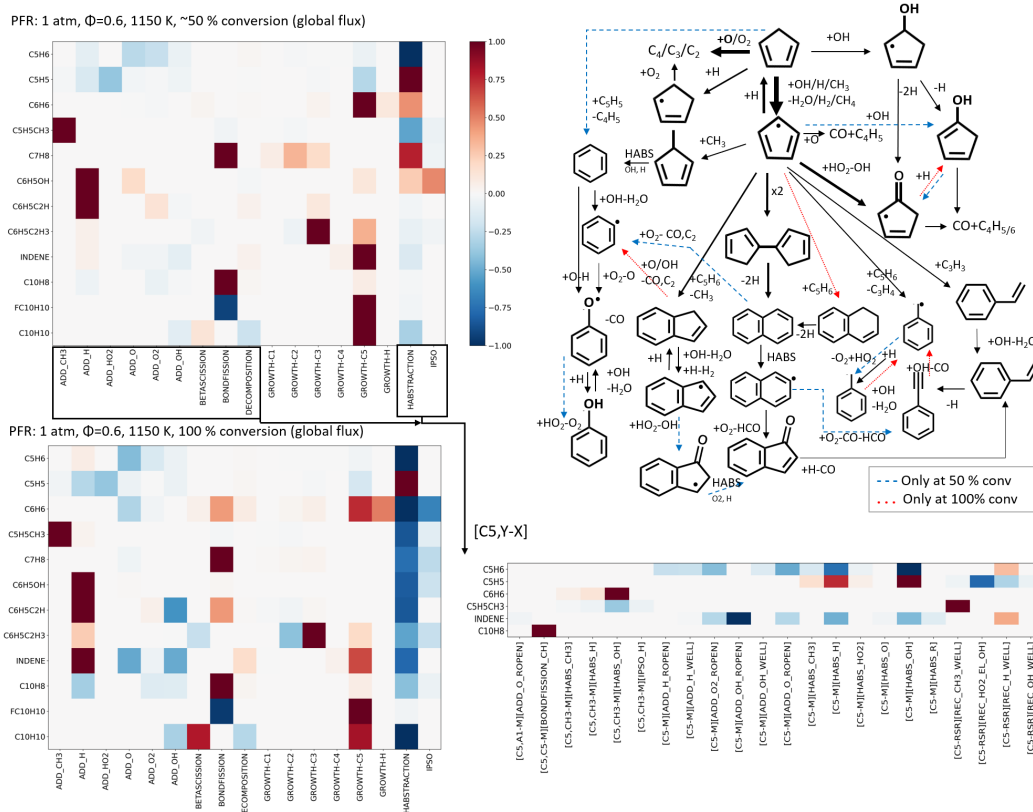


FIGURE 5.27: Schematic flux analysis for cyclopentadiene oxidation at ~ 1150 K in the PFR of Butler et al. [336] at $\Phi = 0.6$. Fluxes from the global flux analysis are organized by class type (left panel, relative threshold of 1%) at $\Phi = 0.6$ (50%, 100% conversion) with additional species + reaction type analysis for oxidation reactions involving C₅ species (right bottom panel, relative threshold of 5%).

H-atom abstraction reactions is not fully compensated by addition oxidation reactions.

The growth to MAHs and PAHs still occurs mostly via GROWTH-C5, with some relevance of GROWTH-C2 and GROWTH-C3 reaction classes. Compared to lower temperatures, M+R classes gain importance with respect to M+M classes. An interesting aspect related to the higher temperature as well as the larger radical pool is that the equilibrium between MAHs/PAHs and their parent radical starts becoming relevant. For instance, the fractions of indene, toluene and phenol are partially controlled by H-atom abstractions by H, OH and HO₂ as well as H recombinations on the parent radical (bottom right panel of Fig. 5.27). The analysis by class type at 100% conversion clearly highlights the higher importance of H-atom abstractions and H recombinations in MAH consumption and production, respectively. Finally, the presence of phenol is explained by the relevance of 1) atomic oxygen (adding to benzene) and 2) abstraction reactions (producing phenyl, oxidized to phenoxy radical). The aspects regarding benzene oxidation are thoroughly discussed in Chapter 6.

At 100% conversion, several changes are observed. Decomposition reactions (BETACISSION, BONDFISSION, DECOMPOSITION class types) play a relevant role in the reactivity; H-atom abstraction reactions heavily consume MAHs and PAHs, which mostly reach equilibrium with the parent radicals through bond-fission / recombination reactions. The

relative importance of growth classes decreases. Finally, the accumulated MAHs/PAHs start oxidizing via addition reactions (ADD_OH, ADD_O). With the exception of indene, most of these classes involve aromatic rings and are therefore discussed in Section 6.2 in more detail.

The complex reaction network described in this section shapes the global reactivity of the system and therefore the macroscopic combustion properties of the fuel. Figure 5.28 shows the CRECK model predictions for the ignition delay time conditions of Orme et al. [335] and for the laminar flame speed measurements of Ji et al. [372]. The model is in excellent agreement with the experimental data at stoichiometric and lean conditions, while the global reactivity at high temperature is overestimated at fuel-rich conditions. This behavior is not observed at the lower temperatures of the flow reactors presented above.

The reactivity at high temperature is mostly controlled by the first step of fuel decomposition, as well as the high temperature reactivity of its small decomposition products. The left panel of Figure 5.28a presents flux analysis by class type considering the same IDT value (about 300 μ s) at different equivalence ratios and therefore different temperatures (corresponding to the grey line of Fig. 5.28a). Similarly to the lower temperatures of the JSR/PFR experiments, H-atom abstraction reactions still prevail in determining the consumption of the fuel. However, the class types ADD_H, DECOMPOSITION, GROWTH_C2 gain relevance. All of these types can be interpreted in terms of decomposition: in fact, the main contribution to ADD_H class is that of $C_5H_5 + H = C_5H_6$ proceeding in the backward direction. Similarly, GROWTH-C2 is mostly $C_3H_4 + C_2H_2 = C_5H_6$, namely the molecular decomposition of the fuel. Compared to lower T, the ADD_O2, ADD_HO2 and GROWTH-C5 types almost disappear from the flux analysis. With increasing Φ and T, unimolecular decomposition reactions become more relevant with respect to bimolecular abstractions and addition reactions. In particular, the increased relevance of bond-fission is essentially an effect of temperature, while the decrease in bimolecular addition reactions is mostly due to the increase in the equivalence ratio, as highlighted by the class type analysis for different Φ at 1550 K (conditions corresponding to the green vertical dashed line in the IDT plot).

In LFS experiments (Figure 5.28b), temperatures up to 2300 K are reached at the flame front. The extremely high concentration of radicals suppresses the relevance of M+M reactions such as ADD_O2 or that of M+R/RSR+R reactions with less reactive radicals such as ADD_HO2. Additionally, unimolecular decomposition reactions (DECOMPOSITION, GROWTH-C2) are only relevant at fuel-rich conditions. Overall, only a few reaction classes contribute to the decomposition of the fuel, mostly H-atom abstraction reactions, H recombination, and additions of O atom. In contrast with the IDT simulations, the $C_5H_5 + H = C_5H_6$ reaction occurs in the direction of the recombination, due to the high concentration of H atoms. It is recalled that H atoms enhance the global reactivity of the system through the branching reaction $H + O_2 = O + OH$.

The class dependence on the equivalence ratio leads to similar considerations to those for the IDT simulations: at richer conditions, the relevance of ADD_O, ADD_OH decreases in favor of unimolecular decomposition. The analysis by species type and reaction type also shows that at increasing Φ the HABS_H classes naturally prevails over HABS_OH as a

consequence of the smaller O_2/OH concentration.

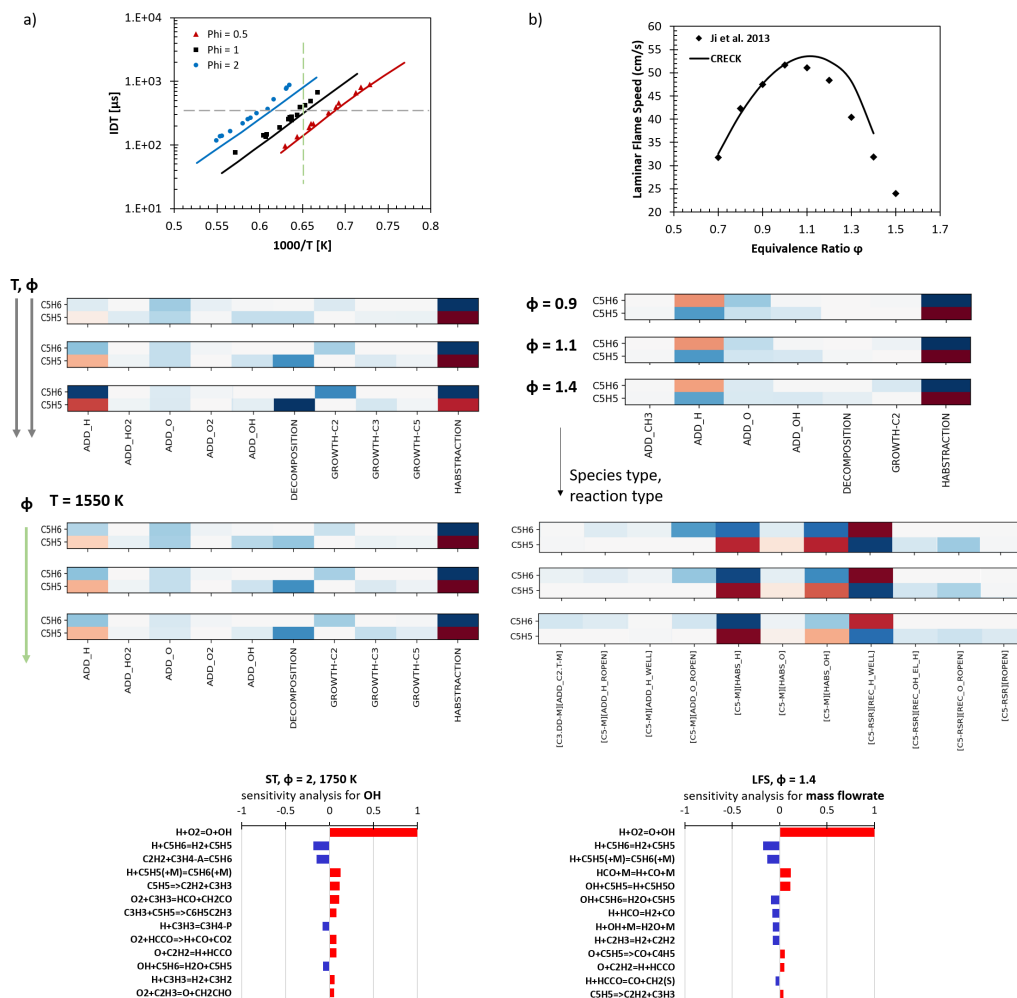


FIGURE 5.28: Experimental (dots) and simulated (lines) for a) the IDT [335] and b) the LFS [372] of cyclopentadiene, together with class type global flux analysis for C_5H_6 and C_5H_5 at different conditions (relative threshold of 5%). For the LFS, [species type][reaction type] analysis is also presented. Bottom plots show sensitivity analysis at fuel-rich conditions.

Finally, sensitivity analysis for the OH concentration in IDT experiments and mass flowrate for LFS experiments at fuel-rich conditions was performed in order to investigate the discrepancy between model predictions and experimental measurements. The bottom panels of Figure 5.28 shows that besides the $H + O_2 = O + OH$ branching reaction, H-atom abstractions by H and OH from the fuel both contribute to decreasing the reactivity. On the other hand, the $C_5H_5 + H$ recombination has opposite effects on the IDT and LFS experiments, as highlighted above. It is also intuitive that the unimolecular decomposition of C_5H_5 radical also increases the reactivity. Unimolecular decomposition reactions are more relevant in the IDT experiments, while the LFS is more sensitive to radical recombinations $C_5H_5 + H/OH/O_2$. In this work, all the fuel and fuel radical reactions appearing in both sensitivity analyses were updated with theoretical calculations, hopefully decreasing the uncertainty in the model. A higher uncertainty might be expected for the $C_3H_3 + C_5H_5$ reaction, updated from CBS-QB3 calculations of [320] and lumped as a single channel. Reactions involving

OH radicals and O atoms are more sensitive in fuel-lean conditions, where the model well reproduces experimental data, and therefore large errors in such reactions may be excluded. The sensitivity analysis performed here is therefore not easily interpreted in terms of a single culprit for the discrepancies observed. The core chemistry, particularly relevant at high temperatures, also plays an essential role in determining reactivity properties and its accuracy should be further assessed. Finally, it is noted that the large discrepancies in the LFS at fuel-rich conditions may also be related to faulty measurements: in fact, benzene LFSs measured in the same reactor [373] (Section 6.6.1.3) show a sharp decrease in the LFS at fuel-rich conditions that is not observed in other datasets [374], [375].

5.4.3 Summary

This section presented model testing for cyclopentadiene and indene pyrolysis and cyclopentadiene oxidation. A critical analysis of the model performance, focusing on relevant reaction classes at different operating conditions, guided the understanding of the mechanism.

In pyrolytic conditions, cyclopentadiene is mostly consumed by H-atom abstraction reactions. The small amount of ring-opening pathways determines the relevance of growth reactions via additions and recombinations of unsaturated C₅ rings. At higher temperatures, bond-fission in cyclopentadiene also contributes to the radical pool of cyclopentadienyl. The formation of PAHs also occurs through growth reactions with C₂/C₃ species produced from cyclopentadienyl decomposition. The larger radical pool also consumes PAHs by H-atom abstraction reactions or H additions. Overall, the kinetic mechanism reproduces well the experimental profiles.

Indene decomposition starts at higher temperatures than in the case of cyclopentadiene because of 1) the higher stability of indenyl radical and 2) stable aromatic products resulting from the decomposition of C₉ species (instead of C₂/C₃ species). Growth pathways of aromatic species occur from both cyclopentadiene-like and benzene-like moieties. Model predictions for indene pyrolysis are worse than those for cyclopentadiene pyrolysis. While the indene/indenyl concentrations seem to be well predicted, most MAHs and PAHs are overpredicted in the 1100–1300 K range, suggesting a wrong pool of smaller radicals. Finally, the different agreement between the model and the two datasets presented, which have different pressures, also indicate a potential misprediction in the pressure dependence of relevant indene decomposition reactions. Indeed, the sub-mechanism of indene decomposition requires further investigation in terms of the legitimacy of the analogies applied and the pressure dependence.

Oxidation of cyclopentadiene has a complex kinetics, involving several C₅ resonance-stabilized intermediate species. At low temperatures, cyclopentadiene is consumed by both additions and H-atom abstraction reactions. Additions with H atoms and OH radicals and the equilibrium with the resulting intermediates plays a relevant role in shaping the radical pool of the system. The main consumption reaction for the cyclopentadienyl radical is its recombination with HO₂ radicals, studied theoretically in this work. The higher concentration of C₂/C₃ species resulting from C₅ oxidation reactions results in a wider range of growth pathways to PAHs, involving also reactions poorly studied in the literature. Kinetic model

results at low temperatures predict a sharper slope of cyclopentadiene consumption, smaller cyclopentadienyl radical concentration, and consequently too low a concentration of PAHs. The analysis suggests that additional efforts should be put in determining more accurately reaction pathways affecting low-temperature cyclopentadienyl concentration, which are not as relevant in pyrolysis and high temperature conditions, namely oxidation addition reactions and some growth pathways with C_2/C_3 species. However, most of them were updated with recent theoretical calculations in this work, hence model optimization should also be considered.

Kinetic model results for high-temperature oxidation in both speciation and IDT/LFS experiments are in good agreement with experimental results. At higher temperatures, H-atom abstraction reactions, bond-fission from cyclopentadiene and direct decomposition almost completely control the reactivity. The larger radical pool results in formation and consumption of PAHs also through some oxidation pathways. The only significant discrepancy found in speciation measurements is the underprediction of benzene, methylcyclopentadiene, and toluene, which are probably all related to the sub-mechanism of $C_5H_5CH_3$, whose components were almost entirely estimated with analogy rules from a previous version of the CRECK mechanism and is in need for revision.

Chapter 6

MAHs pyrolysis and oxidation

This chapter presents theoretical calculations and kinetic modeling results for the pyrolysis and oxidation of MAHs and OAHs. A brief literature overview on important experimental and kinetic modeling results is presented in Section 6.1, focusing on general aspects of macroscopic combustion properties and product distribution.

Section 6.2 explains the organization of reaction classes for aromatic species formulated in this work, together with an extensive list of examples highlighting the updates of this work.

Theoretical calculations of relevant reactions in benzene and OAH combustion is presented in Section 6.3, showing both simpler reactions validated with a wide range of experimental data and more complex theoretical calculations with very high uncertainty.

This chapter also explores the formulation of ES-based rate rules with systematic theoretical calculations on substituted MAHs. In particular, H-atom abstraction reactions are treated in Section 6.4, while ipso addition-elimination reactions are presented in Section 6.5.

Finally, some kinetic modeling results for the global testing and validation of the mechanism are presented in Section 6.6.

6.1 Background and literature review

6.1.1 Benzene

Benzene is the simplest aromatic ring and is therefore prototypical of all aromatic hydrocarbons. Section 1.1 presented the main reasons for the interest in benzene combustion, namely its relatively large concentration in liquid fuels (both conventional and biomass-derived), its anti-knock properties, its crucial role in kinetic modeling of real fuel surrogates, its relevance as precursor of large PAHs and therefore soot, and finally its importance in interstellar and atmospheric chemistry.

This section presents an overview of relevant literature studies of the kinetics of benzene pyrolysis and oxidation, and therefore provides a background for the detailed theoretical calculations and the results of kinetic simulations. The simplified scheme of Figure 6.1 guides the discussion of the reaction pathways mentioned in this section.

Because of the substantial interest in the kinetics of benzene oxidation, first mechanistic developments date back to the 1930s–1960s [376]–[379], with a first global "detailed" mechanism proposed by Glassman in the 1970s [380].

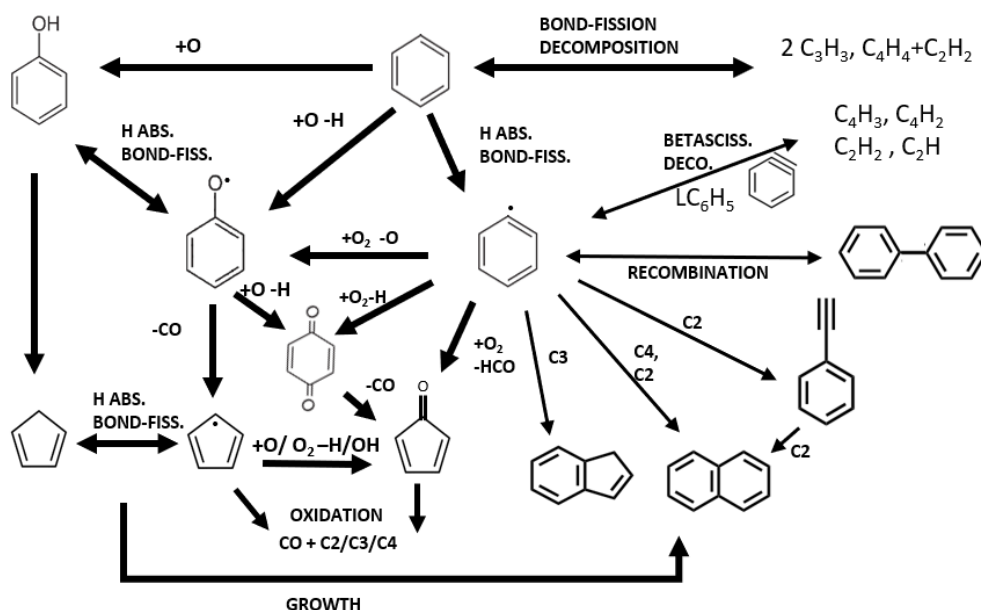


FIGURE 6.1: Schematic overview of relevant reaction pathways identified in the pyrolysis and oxidation of benzene in the literature.

A large number of flow reactor experiments were performed starting from the 1980s. Most of them were presented together with kinetic mechanisms or mechanistic insights to explain the experimental findings. The first ST experiments of high-temperature benzene pyrolysis (1200–2000 K) of Kern et al. [381] and Laskin et al. [382] monitored benzene decay and detected two main decomposition products, namely C_2H_2 (acetylene) and C_4H_2 (diacetylene). The formation of these products was explained with direct ring opening of benzene or bond-fission/H-atom abstraction to form phenyl radical and subsequent β -scission or ring opening, as shown in scheme 6.1. Laskin et al. [382] were the first to highlight the relevance of L- C_6H_5 ($\text{HCCCH}_2\text{CHCCH}$) as an intermediate in the decomposition to linear species. Additionally, Laskin et al. [382] detected biphenyl, supposedly formed by the recombination of phenyl radicals. In the same years, the theoretical calculations of Wang and Frenklach [138] suggested that the decomposition of phenyl to linear alkynes is mediated by CYC_6H_4 (o-benzyne). More recently, Sivaramakrishnan et al. [383] performed benzene pyrolysis experiments in a ST at extreme conditions ($T > 1200$ K, $p = 30$ – 50 bar) and confirmed the importance of o-benzyne in their kinetic mechanism.

All experimental ST studies for benzene pyrolysis noted consistent loss of the total carbon mass, probably due to the growth of PAHs and soot. Quantification of different PAHs was performed in the latest study of benzene pyrolysis, in the ST at CNRS [130]. Different 2-, 3-, and 4-ring PAHs were quantified and an older version of the CRECK kinetic mechanism was also updated with recent theoretical insights to reasonably reproduce the data. In the massive experimental and kinetic modeling work of Comandini et al., new high temperature growth pathways, e.g., through o-benzyne [384], were also highlighted.

Experimental and kinetic modeling works on benzene oxidation started even earlier [376]–

[380]. In these studies, it was postulated that benzene is mostly oxidized via H-atom abstractions by O_2 , while O_2 recombination with C_6H_5 forms C_6H_5OO phenylperoxy adduct, which transforms into phenoxy radical C_6H_5O through abstraction of an O and O–O bond-fission. Glassman also highlighted the importance of oxygenated species such as phenoxy radical, phenol and catechol.

The slow global reactivity of benzene relative to most aliphatic hydrocarbons was experimentally confirmed since the 1980s with IDT measurements in shock tubes [385], [386], and since the late 1990s with LFS measurements [373]–[375].

Measurements of product distributions in benzene oxidation started with the pioneering high T (> 1100 K) PFR experiments by Brezinsky et al. [304], [387], who then developed a small sub-mechanism (about 130 reactions) to model benzene and toluene oxidation based on their experimental findings [388], [389]. Experimentally detected products included C_5H_6 , C_6H_5OH , and C_4 and C_2 alkenes and alkynes. Their kinetic mechanism explained benzene consumption mostly via H-atom abstraction by OH and $O(^3P)$ addition to form $C_6H_5O + H$ (see scheme 6.1), estimated experimentally by Nicovich et al. [390]. The formation of phenol was easily explained by H recombination with phenoxy radical, while their decomposition led to C_5H_6 and C_5H_5 . Most of the reaction pathways of their model are also present in the latest literature kinetic mechanisms. PFR experiments at lower temperatures (900–1400 K) were then performed by Alzueta et al. [391]. Only cyclic C_5 and C_6 products were detected, namely cyclopentadiene, phenol, and benzoquinone ($C_6H_4O_2$). The formation of $C_6H_4O_2$, which had never been measured in previous studies, was attributed to $C_6H_5 + O_2$ as postulated by Frank et al. [303], while its decomposition to cyclopentadienone (C_5H_4O) and the oxidation of the latter also led to linear alkenes. Despite the fact that the formation of benzoquinone through this reaction pathway was proved wrong in later studies, the kinetic model proposed was fairly complete, hence it was extensively used in the development of later kinetic mechanisms.

In the late 1990s and early 2000s, experimental works also focused on benzene partial oxidation in the JSRs at intermediate and high temperatures (900–1400 K) [359], [368], [386], [392]. These measurements presented the widest range of products thus far, including linear alkenes and alkynes, and oxygenated C_2/C_3 species such as ketene (CH_2CO) and acrolein (C_2H_3CHO). Chai et al. [368] were also able to detect oxygenated cyclic species such as C_5H_4O and $C_6H_4O_2$, and 2-ring PAHs such as C_9H_8 , $C_{10}H_8$, $C_{10}H_{10}$, $C_{10}H_{12}$. The combined experimental and kinetic modeling studies at CNRS [359], [386] led to a kinetic mechanism of about 120 species and 900 reactions, where kinetic parameters mostly derived from estimates or experimental measurements, reaching reasonable but limited agreement with the experimental results. H-atom abstraction reactions from benzene, direct oxidation with $O(^3P)$, and oxidation of phenyl radical with O_2 , OH and HO_2 leading to C_6H_5O were marked as determining for benzene conversion. Formation of alkenes was mostly attributed to C_5H_5 oxidation and C_5H_4O decomposition. Da Costa et al. [386] highlighted the crucial role of C_5H_4O in the mechanism despite the impossibility of detecting it experimentally. Growth to aromatic species was explained via C_2/C_4 additions to phenyl, according to HACA and HAVA pathways.

Speciation measurements for oxidation at higher temperatures (up to 1800 K) and atmospheric to low pressures have been performed in premixed laminar flames since the 1980s [360], [393]–[395]. In many cases, the overall reactivity is also controlled by the core chemistry. Therefore, flames have not been widely used for understanding the first decomposition steps of the fuel. Most of the experimental investigations of flames at fuel-rich conditions [360], [394]–[398] detected a wide range of PAHs with 2–5 aromatic rings, providing insights into relative amounts and important structures of PAHs to be interpreted with kinetic modeling. It must be noted that benzene and PAH formation was also extensively studied in alkene flames [314], [315], so as to investigate their formation and growth mechanism in conventional fuels.

The recent kinetic modeling studies of Vourliotakis et al. [128] and Saggese et al. [127] (CRECK mechanism) built and validated a global mechanism for benzene oxidation. In both cases, good overall model performance was achieved. Both of these mechanisms adopted kinetic parameters mostly from estimates and microkinetic experiments, while very few theoretical calculations were available (and fewer were used) for the model development. The main reasons are 1) the objectively good agreement with experimental data obtained in non-fundamentally based kinetic models; 2) the challenge of theoretical calculations for aromatic hydrocarbons and the difficulty in reaching an agreement on rate constants and branching fractions for complex reaction pathways (Sections 6.3.1 and 6.3.3); 3) the shift in the focus of the application of theoretical methodologies from oxidation to growth reactions. The last point refers to the huge number of theoretical calculations over the past 20 years devoted to the investigation of new reaction pathways for PAH growth. Theoretical calculations for the well known HACA pathway, formulated in the late 1980s and early 1990s [137], [138], were only performed in 2017 [139]. Because of the inability of the HACA mechanism to fully account for PAH formation and growth, a lot of theoretical effort, in particular by the group of Mebel et al., focused on new reaction pathways, mostly involving aromatic rings, such as additions of C₃/C₄ unsaturated species [281], [282], [399], addition or recombination between aromatic rings such as phenyl addition cyclization (PAC) [400], [401], cycloaddition fragmentation processes through o-benzyne addition [384], [402], e-bridge formation [403], [404], and recombinations between resonance stabilized substituted MAHs [405].

In recent years, global kinetic mechanisms containing more or less updated benzene combustion sub-mechanisms were developed by the CRECK [56]; ITV [406], focusing on benzene formation in alkene flames; and LLNL [407]–[410] teams, mostly targeting the ignition behavior of fuels relevant to surrogate mixtures (i.e., toluene, tetralin, methylated aromatics). All three mechanisms included portions describing anisole and guaiacol pyrolysis and oxidation [45], [50], [131]. Other literature kinetic mechanisms focused on smaller subsets. For instance, at KAUST sub-mechanisms for PAH pyrolysis (e.g., indene [337], or other oxygenated PAHs [411]) were developed in detail. Instead, Comandini et al. [130], [412], [413] focused on improving the CRECK sub-mechanism of PAH growth in pyrolysis conditions.

The mechanisms available in the literature disagree on many relevant reaction pathways for benzene decomposition, oxidation and growth. It is recalled that one important reason for different predictions in different mechanisms is the difference in their core chemistry,

which largely shapes high temperature behavior. This might result in consistent differences also in primary reactions for fuel consumption. Additional complexity derives from the fact that combustion products experimentally detected may be formed directly or indirectly via a large number of reaction pathways - for instance, the early studies on benzene oxidation highlighted that cyclopentadienone may be formed directly from benzene or phenyl oxidation or indirectly from oxidation reactions of C₅ species. The LLNL mechanism is probably overall the most up-to-date with theoretical calculations, while the KAUST mechanism also presents various updates on PAH growth; however, many portions of these models show inconsistencies or very different levels of detail.

In this context, this chapter revises the CRECK kinetic mechanism for MAHs combustion based on theoretical insights (from literature and from this work, Sections 6.3, 5.3.1, and 6.5), with a particular focus on oxidation reactions. The organization in classes (Section 6.2) allows internal consistency in the kinetic mechanism for all substituted MAHs.

Finally, it must be mentioned that most of the kinetic mechanism structure and theoretical findings of this work were not only used for the update of the CRECK kinetic mechanism, but also for the development of C3MechV3.3 [67] within the computational chemistry consortium <https://fuelmech.org/>. The C3 effort led to a first consistent and working version of a unified kinetic mechanism bringing together several industrial and academic partners. The development of the C3 mechanism is not discussed here but is presented in the corresponding literature publications [67], [414].

6.1.2 Oxygenated MAHs

Oxygenated aromatic hydrocarbons (OAHs) are interesting for a number of reasons. The first OAHs studied for the kinetic modeling of combustion processes were phenol and phenoxy radical, because of their central role in the oxidation of benzene. For instance, phenoxy decomposition and recombination with H atoms are important sensitive reactions in both low-temperature reactors and laminar flame speed simulations [127], [128], [359], [374].

More recently, phenol and substituted phenolic species have gained attention as model compounds for the decomposition products of lignocellulosic biomass [42], [50]. In particular, phenol, catechol, anisole, guaiacol and vanillin are good candidates for fuel surrogate formulation of biomass-derived bio-fuels. It is noted that while anisole is not OH-substituted, its decomposition readily leads to phenoxy radical and therefore phenol, as described below. All these compounds are also potential anti-knocking additives.

Experimental measurements of the pyrolysis and oxidation of OAHs are often challenging: most OAHs are solid at room temperature; their high sooting tendency results in fouling of the reactor walls; OAHs like phenol are toxic and corrosive [126]. Due to both experimental difficulties and the only recent interest in OAH combustion, there are not as many experimental investigations as there are for benzene. This dearth of experimental data encourages theoretical investigations on these systems.

This section briefly reviews general literature knowledge on the kinetic mechanism of pyrolysis and oxidation of phenol, catechol, anisole, guaiacol and vanillin. Common features of the reactivity of these compounds are the central role of phenoxy-like radicals and

the similarity in the kinetics of pyrolysis and oxidation [45], [46], as clarified below. Other relevant OAH types are CHO-substituted MAHs such as benzaldehyde (C_6H_5CHO) and salicylaldehyde ($o\text{-}HOC_6H_5CHO$), relevant in the sub-mechanism of methyl-substituted MAHs (toluene, cresols), not extensively treated in this work. Table 6.1 presents some of the relevant experimental and kinetic modeling studies on OAH combustion from the last 40 years. Figure 6.2 is used as a reference for the description of the main reaction pathways relevant in OAH combustion according to literature studies.

TABLE 6.1: Overview of some of the relevant **experimental** and **kinetic modeling** (or combined) works on the pyrolysis and *oxidation* of oxygenated aromatics.

Phenol	Catechol	Anisole	Guaiacol	Vanillin
Manion 1989 [415] Brezinsky 1998 [125] Horn 1998 [132]	Wornat 2001 [418] Wornat et al. 2002-4 [421]–[423] Thomas 2007 [424] Wornat et al. 2008-11 [426]–[428] Ranzi 2012 [354]	Mackie 1989 [416] Arends 1993 [417] Pecullan 1997 [419]		Shin 2001 [420]
Khachatryan 2008 [425] Scheer 2012 [429]		Nowakowska 2014 [51] Shu 2017 [430] Herzler 2017 [431] Wagnon 2018 [50] Pelucchi 2018 [131] Bierkanth 2019 [432] Zare 2019 [434] Yuan 2019 [435] Pelucchi 2019 [46] Büttgen 2020 [55] Chen 2021 [370]	Nowakowska 2018 [45] Yerrayya 2019 [433]	
Büttgen 2019 [54]	Pelucchi 2019 [46]		Pelucchi 2019 [46]	Pelucchi 2019 [46]

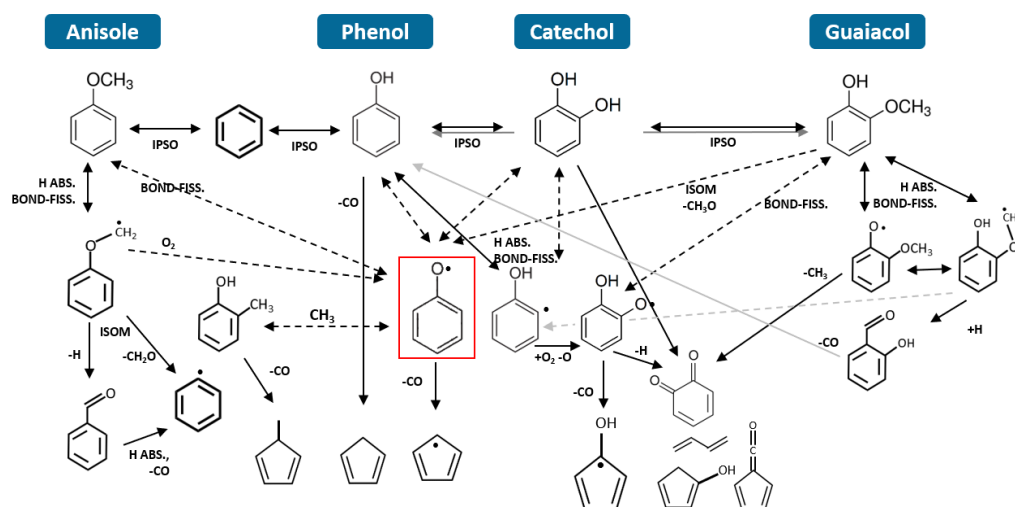


FIGURE 6.2: Schematic overview of the relevant reaction pathways identified in the literature for the pyrolysis and oxidation of phenol, catechol, anisole, and guaiacol; highlighting the relevance of phenoxy-like radicals (dashed arrows).

6.1.2.1 Phenol

Phenol (C_6H_5OH) is the simplest phenolic compound. The reactivity of phenol pyrolysis was studied several times in the literature [54], [125], [132], [415], [425], [429]. The main products detected experimentally are cyclopentadiene and CO [125], [132], as shown schematically in

Figure 6.2. $C_5H_6 + CO$ may be formed directly via molecular decomposition of phenol through a enol/keto tautomerization, as confirmed theoretically by Scheer et al. [429]. At higher temperatures, the same products may be formed via bond-fission to $C_6H_5O + H$, and C_6H_5O decomposition to C_5H_5 . The relative importance of these two pathways is still debated in the literature and is theoretically investigated in this work (Section 6.3.2).

The pyrolysis experiments by Brezinsky et al. [125] and hydrogenolysis experiments by Manion and Louw [415] detected large amounts of benzene and naphthalene, as well as minor fractions of other substituted MAHs and PAHs in the latter. Benzene formation is mostly explained by H ipso substitution (depicted in Figure 6.2 and investigated in Section 6.5) in competition with H-atom abstraction reactions. Also in this case, experimental studies struggled to interpret the relative importance of the two competing pathways again due to the fast subsequent reactivity [436], [437]. Furthermore, the few theoretical investigations available in the literature [438], [439] only led to partial agreement with experimental data. These reaction channels are critically assessed in this work (Sections 6.4.3.4 and 6.5.2.2).

Finally, only one flow reactor study is available for phenol oxidation [125]. The product distribution does not change significantly compared to pyrolysis conditions, as is generally the case for OAHs. Phenyl-like oxidation pathways may originate from hydroxy-phenyl (C_6H_4OH), formed at higher temperature from H-atom abstraction reactions from the aromatic ring. For instance, Prendergast et al. [440] found that O_2 recombination with o- C_6H_4OH generates $C_6H_4O_2$ and C_5H_4O products, however the same authors [441] also found that o- C_6H_4OH has short lifetimes due to rapid isomerization to phenoxy radical. However, kinetic models which include the oxidation of C_6H_4OH generally assume analogies with the corresponding pathways in phenyl [45], [50], without distinguishing between the reactivity of the three hydroxyphenyl isomers.

The only kinetic model specifically developed for phenol pyrolysis is that of Scheer et al. [429]. However, the sub-mechanism of phenol pyrolysis and oxidation is included in kinetic mechanisms for anisole [50], [435] or multi-substituted OAHs [45], [46].

6.1.2.2 Catechol

Catechol is the common name for 1,2-benzenediol ($C_6H_4(OH)_2$). The group of Wornat et al. put a lot of effort into identifying both the decomposition products and the PAHs growing during the pyrolysis of catechol as a model fuel for wood and biomass. In their flow reactor experiments, they detected several different PAHs and identified more than 60 different structures, including benzenoid, cyclopenta-fused, cyclopentadiene-like, and alkyl-substituted PAHs (with methyl, vinyl, and ethynyl groups) [418], [422], [423]. Among non-oxygenated aromatic products, benzene, naphthalene, indene and 3-ring PAHs showed the highest yields.

In JSR pyrolysis experiments it was found that catechol decomposes at a temperature in the range of 900–950 K, producing large amounts of butadiene, acetylene, and CO [421], [424]. While these studies did not develop a full kinetic mechanism, it was postulated [421] that catechol decomposes via bond-fission and H-atom abstraction reactions to o- OC_6H_4OH , an OH-substituted phenoxy-like radical (see scheme in Figure 6.2), which then decomposes to

C_5H_4OH (OH-substituted cyclopentadienyl-like) and eventually to C_4H_6 . Another suggested production route for C_4/C_2 species was catechol C–OH bond-fission or H ipso substitution to phenoxy radical and phenol, respectively, with further decomposition to C_5H_5/C_5H_6 . This latter hypothesis is also supported by the relatively high amounts of phenol and cyclopentadiene detected by Thomas et al. [424].

Catechol co-pyrolysis with unsaturated linear hydrocarbons (C_2H_2 , C_3H_4 -P, C_4H_6) [426]–[428] revealed strong non-linear mixing effects. In fact, the weak O–H bond in catechol produces H atoms which accelerate the reactivity of alkenes and alkynes. Overall, the detected PAHs were higher than what was predicted by a simple linear combination of the reactivity. In particular, catechol mixtures yield larger amounts of benzene, indene, and substituted PAHs attributed for instance to C_7H_7 (benzyl) + C_2H_2 and C_6H_5 + C_3H_3 .

Thomas et al. [424] also investigated catechol oxidation at different equivalence ratios. Similarly to phenol, no significant difference in the product distribution between pyrolysis and oxidation conditions was found, with the exception of smaller relative amounts of C_4H_6 and C_5H_6 and overall accelerated conversion (possibly by H-atom abstractions by O_2).

Successive theoretical investigations [134], [442] provided mechanistic insights into the elementary steps for catechol unimolecular decomposition and reactivity with H atom. In particular, Altarawneh et al. [134] found that H migration followed by ring opening and CO elimination to produce $C_4H_6 + 2CO$ or $C_5H_5OH + CO$ is the most relevant pathway at intermediate temperatures, while H_2O elimination to C_5H_4CO prevails above 1000 K (see bottom of Scheme 6.2). A more recent study of Furutani et al. [442] reached similar conclusions, highlighting unimolecular decomposition to $C_5H_5OH + CO$ (analogous to phenol) as the most important channel. Direct H_2 elimination to form *o*- $C_6H_4O_2$ was instead deemed as unimportant. Both theoretical studies agreed that the reactivity with H atoms mostly leads to phenol through H ipso substitution (top of Scheme 6.2) and *o*- OC_6H_4OH via H-atom abstraction reactions.

Some of the theoretical findings listed above were successfully included into the CRECK kinetic mechanism [46], [354] to explain experimental trends for the pyrolysis and oxidation of catechol.

6.1.2.3 Anisole

Anisole (methoxybenzene, $C_6H_5OCH_3$) is the simplest aromatic containing a methoxy functional group OCH_3 . The low bond dissociation energy (~ 65 kcal/mol) of the O– CH_3 bond largely determines the reactivity, as found by early theoretical and experimental studies in the late 1980s [416], [443], such that anisole starts decomposing already around 800 K. In particular, Scheme 6.2 shows that O– CH_3 bond-fission produces phenoxy radical, crucial to anisole reactivity, and methyl radical, which can recombine on the carbon sites of phenoxy radical to produce cresol.

The main products and the main steps in the reactivity of anisole decomposition were already identified in the first combined experimental and kinetic modeling studies of Arends et al. [417] and Pecullan et al. [419]. The main detected products were CO, phenol, cresol, benzaldehyde, benzene, cyclopentadiene and methylcyclopentadiene, and dibenzofuran as the

most abundant PAH. Methylcyclopentadiene was postulated to derive from molecular decomposition of cresol, in analogy to phenol, or from CH_3 recombination with C_5H_5 . Instead, benzaldehyde is produced from the $\text{C}_6\text{H}_5\text{OCH}_2$ radical, which isomerizes to $\text{C}_6\text{H}_5\text{CH}_2\text{O}$ via a 3-membered ring TS and loses an H atom. The same intermediate may also decompose directly to phenyl, as depicted in Scheme 6.2. Finally, dibenzofuran ($\text{C}_{12}\text{H}_8\text{O}$) was postulated to derive from the recombination of phenoxy radicals [417]. The experimental study of Pecullan et al. [419] also explored oxidative conditions, finding no significant differences in product distribution (however, CO_2 was not measured).

Experimental studies of almost 20 years later performed together with more fundamentally-based kinetic modeling (see Table 6.1) mostly confirmed the results of previous studies. The experimental JSR studies of Nowakowska et al. [51] and Wagnon et al. [50] also detected a wider range of substituted MAHs and PAHs, such as toluene, phenylacetylene, indene, tetralin, benzofuran. Nowakowska et al. [51] highlighted the sensitivity of the kinetic mechanism not only to the rate constant for O- CH_3 bond-fission, but also to those for the bond-fission of C_5H_6 and $\text{C}_5\text{H}_5\text{CH}_3$, indicating the strong interconnection with cyclopentadiene. They also attributed the early formation of naphthalene to cyclopentadienyl radical recombination. The kinetic mechanism developed by Wagnon et al. [50] is one of the most detailed in the literature. Both Wagnon et al. [50] and Büttgen et al. [55] suggested low- T oxidation pathways for anisyl radical leading to phenoxy or phenylperoxy radicals (see Figure 6.2), however they confirmed that pyrolysis reactions prevail in oxidative conditions even at 800 K. The more recent mechanisms of Yuan et al. [435] and Chen et al. [370] also added reaction pathways for the formation of oxygenated PAHs (benzofuran, dibenzofuran) from oxygenated MAHs. An unexplained experimental trend by all models is the early formation of CO_2 even in pyrolysis conditions [50], also common to other experimental findings for phenolic species [136], [424].

The only experimental data for anisole flames are the low-pressure rich flames of Bierkandt et al. [432]. In this case, a very wide range of products was detected, including several intermediate resonance-stabilized radicals and oxygenated cyclic species. While the first steps of the reactivity seem to be analogous to those of importance at low temperatures, the product distribution is now mostly dominated by anisole decomposition and by the oxidation of its decomposition products. The high concentration of methylcyclopentadiene detected in the flame is also attributed to the higher relevance of methyl radical in high-temperature environments.

Finally, IDT and LFS measurements were only performed recently. Wagnon et al. [50] and Zare et al. [434] found that anisole LFS is significantly higher than that of benzene and toluene, as expected. Similar results were obtained for IDT measurements and model predictions [50], [55]. In particular, Wagnon et al. [50] found that a key reaction in determining anisole faster global reactivity is phenoxy radical addition to O_2 to produce o-benzoquinone and OH radical, while the isomerization between $\text{C}_6\text{H}_5\text{OCH}_2$ and $\text{C}_6\text{H}_5\text{CH}_2\text{O}$ slows it down significantly.

The starting anisole sub-mechanism of this work is that of Pelucchi et al. [46]. This mechanism, which is fairly lumped, e.g., $\text{C}_6\text{H}_5\text{OCH}_2$ and $\text{C}_6\text{H}_5\text{CH}_2\text{O}$ radicals are lumped to

decomposed products, obtains reasonable performances with experimental data. This work does not heavily modify this mechanism, however some mechanistic insights are presented in Section 6.6.2.

6.1.2.4 Guaiacol and Vanillin

Guaiacol has one hydroxy and one methoxy group in the ortho position with respect to one another. Table 6.1 shows that only a few experimental and kinetic modeling studies are available for the pyrolysis and oxidation of guaiacol, which is also interesting as a potential surrogate component for biomass-derived bio-fuels.

Kinetic models for guaiacol pyrolysis and oxidation were derived from those of anisole, phenol and catechol. The O-CH₃ BDE in guaiacol is even lower than that of anisole [45], [46], [433] (~58 kcal/mol), such that the decomposition of guaiacol starts at around 700–750 K. Its decomposition reactivity is mostly dominated by OH-substituted species (see Figure 6.2), which may convert to cresols via CH₃ ipso substitution. As a result, the most abundant aromatic product detected in both pyrolysis and oxidation conditions is catechol [45], [433], and phenol and cresols are also abundant. Another relevant aromatic product is salicylaldehyde (CHOC₆H₄OH), formed with a similar reaction pathway to that of benzaldehyde in anisole pyrolysis. Tri-substituted MAHs such as methylcatechol were also detected, while benzene is less relevant than in anisole pyrolysis because ipso substitution reactions still form substituted MAHs and OAHs. Similarly to all other OAHs, O₂ does not significantly change the product distribution, but it enhances the reactivity, such that guaiacol decomposes already at 650–700 K. None of the kinetic models developed reproduces the experimental data very well because of the lack of knowledge regarding the fate of OAHs.

Finally, vanillin has the structure of guaiacol with an additional CHO substituent in para position with respect to OH. The only flow reactor study (of Shin et al. [420]) identified primary (vanillin), secondary (guaiacol, catechol, salicylaldehyde) and tertiary (phenol, benzene) products. Initial mechanistic studies [46] highlighted that the reactivity is probably dominated by O-CH₃ bond-fission, similar to guaiacol, producing other tri-substituted OAHs such as dihydroxybenzaldehyde. Recent theoretical studies [444], [445] highlighted that H-atom abstraction reactions are also relevant in the production of different radicals and therefore in the formation of products.

In summary, kinetic mechanisms for the pyrolysis and oxidation of multi-substituted OAHs are extremely approximate, despite the general ability to reproduce experimental trends [46]. Theoretical insights, including those of this work (Section 6.5), will contribute to more physical and fundamentally-based kinetic mechanisms. Such fundamentally based kinetic mechanisms should provide better extrapolations to conditions outside those for which the experimental validations were performed.

6.2 Reaction classes and kinetic model updates by class

6.2.1 Decomposition and oxidation

This section lists the main reaction classes for the decomposition and oxidation of C₆ membered ring species relevant to the combustion of MAHs. The structure of this section is the same as Section 5.2. Explanations for the main class types and the structure of the tables is not repeated here. Structures for the main species are found in appendix A.

The species type characterizing the reactivity of the aromatic ring is indicated with A1-M, while phenyl-like radicals are represented as A1-R. A1,X-M and A1,X-R refer to X-substituted aromatic rings: for these types, the reactivity of A1 is implicitly accounted for with A1-M and A1-R classes, while additional reactions for the X substituent are specified. The reactivity of resonance-stabilized aromatic rings behaving differently from phenyl are classified separately. The main types considered are A1CH₂-RSR (benzyl-like) and A1O-RSR (phenoxy-like), deriving from e.g., bond-fission reactions from A1,CH₃-M (toluene-like) and A1,OH-M (phenol-like) species types.

Table 6.2 shows the main classes for the pyrolysis and oxidation of A1-M. Consumption pathways involve the formation of A1-R through bond-fission [A1-M][BONDFISSION_CH] (at high temperatures) and H-atom abstraction reactions [A1-M][HABS_R]. Most of these reaction pathways were updated with theoretical calculations from literature or from this work. Benzene direct decomposition via ring opening is instead included as a growth reaction from linear species (Section 6.2.2). [ADD_H] and [ADD_OH] glass groups have minor relevance in the reactivity compared to C₅ species due to the higher stability of the aromatic ring. On the other hand, addition with atomic oxygen [ADD_O] is one of the main benzene consumption pathways at most combustion operating conditions. Compared to C₅-species, new class types involving intersystem crossing [ADD_O_ISC], [ADD_O_ISC_DECO] determine product branching fractions. This important class type was studied theoretically in this work (Section 6.3.1). Table 6.2 also includes reaction classes for A2-M (deriving from the presence of an additional aromatic ring, such as in naphthalene), A1,H₂,H₂-M, and A2,H₂,H₂-M. The identified classes were not reconsidered in the present work and are all estimated from previous works of the CRECK group. Similarly to classes for substituted C₅ rings, the presence of methylene groups allows for decomposition via H₂ elimination. On the other hand, the second aromatic ring allows for ring-opening pathways aided by the addition of H, OH, and O₂.

The presence of substituents in the aromatic ring may substantially change the reactivity. Classes for A1,X-M species types with alkyl substituents are listed in Table 6.3. Fuel consumption is generally governed by reactions specific to the substituents because of the lower BDE in the substituent compared to aromatic C–H bonds. For instance, in A1,M-CH₃ (toluene-like) aromatics the resonance stabilized A1CH₂-RSR radical (benzyl-like, Table 6.6) is easily formed by H-atom abstraction reactions (studied theoretically in [129] and in Section 6.4). Due to the presence of the weaker C–C bond, ipso substitution reactions are also relevant, especially with H atom [A1,CH₃-M][IPSO_H] (updated from this work, see Section 6.5). It is noted that the [A1,CH₃-M][IPSO_O] reaction class was estimated by

analogy from theoretical calculations for [A1-M][IPSO_O]; this reaction channel is CH₃-specific, while A1-M channels are still included for species such as toluene according to the hierarchical structure of the classes presented. Similar considerations apply to A1,C2H-M and A1,C2H3-M species types. In these cases, the interaction of the lateral substituents with radicals also result in new addition-decomposition classes.

Table 6.4 lists the main reaction classes for A1,X-M with oxygenated X substituents. The significant update of classes for A1,OH-M species type, i.e., phenol-like aromatics, is particularly evident. Compared to alkyl-substituted aromatics, the OH substituent changes the reactive behavior mostly through the [A1,OH-M][MOLECULAR_DECO] class (theoretical calculations in 6.3.2), characteristic of A1,OY-M substituted aromatics. Molecular decomposition in A1,OH-M, A1,OCH3-M, A1,O2-M, and A1,O,CH2-M types forms C₅ rings, which therefore control the subsequent oxidation or growth reactions. In contrast, the peculiar molecular decomposition in catechol, i.e., A1,OH,OH-M species type, leads to direct decomposition to alkenes (C₄H₆ in the case of catechol), such that C₅ ring species are less relevant in the following oxidation process. Some of the rate constants of the A1,OH-M class were extended from phenol to catechol according to theoretical findings. For instance, the activation energy of rate constants of bimolecular reactions adopted from A1,OH-M was decreased by 2 kcal/mol according to what was observed for H-atom abstraction and ipso substitutions (Section 6.5.2.4). In the absence of theoretically based rules, rate constants were simply adopted by analogy.

The A1,OCH3-M species type has additional reactions related to the facile dissociation of the O-CH₃ bond, i.e., [A1,OCH3-M][BONDFISSION_CO] and new reaction channels for ipso substitution reactions. As a result, the A1O-RSR radical type is key to the reactivity. Instead, H-atom abstraction reactions abstract the hydrogen atom from the methyl group (see calculations in Section 6.4). It is noted that the resulting A1OCH2-RSR species type is not included in the CRECK kinetic mechanism, hence in the case of anisole C₆H₅OCH₂ is written as decomposed lumped products (see Table 6.4). Also H-atom abstractions from the aromatic ring are excluded, such that A1-M classes do not apply to anisole. Indeed, a further level of detail should be included in the mechanism. The simplest A1,CHO-M species is benzaldehyde, an important intermediate in the oxidation of toluene. In this case, the weak H-CO bond in the lateral substituent mostly controls the reactivity through abstractions and bond-fission reactions. Finally, the A1,O2-M and A1,O,CH2-M species types are relevant to the oxidation of all aromatics and A1,CH3,Y-M species, respectively. The corresponding decomposition mechanisms are poorly studied and only estimates are included in the CRECK mechanism.

Table 6.5 lists the main reaction classes identified for A1-R, A2-R, and A1,X-R radical species. OH, HO₂ and O atom recombination reactions on phenyl-like rings form resonance-stabilized A1O-RSR and C5-RSR species with recombination and elimination or decomposition reactions. Rate constants were estimated from the literature (e.g., from the ITV mechanism [446]). Instead, the mechanism for the crucial O₂ recombination classes is more complex, involving the competition between well stabilization [REC_O2_WELL], bond-fission [REC_O2_EL_O], and oxygen insertion in the aromatic ring [REC_O2_INSERTION].

This set of reactions is widely debated in the literature and it was carefully investigated in this work (Section 6.3.3). While the oxygen insertion into the aromatic ring is typically included only for aromatic ring reactivity, it was recently suggested that a similar mechanism is possible for C₅ radicals such as C₅H₃O [447], produced by H-atom abstractions from cyclopentadienone and not included in this work.

In A1,CH3-R, additional OH elimination classes derive from the interaction between O₂ and the lateral substituent in the ortho position (therefore, rate constants are scaled by 1/3 according to the lumped isomer pool). To maintain consistency with the rate constants obtained for the corresponding A1-R reaction class [A1-R][REC_O2], the rate constants obtained for the A1-R class were rescaled to account for the new [A1,CH3-R][REC_O2_EL_OH] channel according to the branching fraction obtained by Da Silva and Bozzelli [448]. It is noted that this class is not present in A1,OH-R because the ortho isomer is lumped together with A1O-RSR types due to the fast isomerization to the latter. Finally, in A1,OH-R isomerization to the A1O-RSR and well-skipping decomposition to C5-RSR [RADICAL_DECO] lead to the formation of resonance-stabilized species.

Table 6.6 shows the main reaction classes of A1CH2-RSR (benzyl-like resonance-stabilized radicals), the main radicals formed from toluene-like species. The full set of A1CH2-RSR was recently updated by Pelucchi et al. [129], and was therefore only mildly updated in this work. Classes [ADD_HO2] and [ADD_O2] include reaction channels unique to the A1CH2-RSR reactivity: the recombination of oxygenated radicals on the resonance-stabilized CH₂ group allow facilitated O/OH transfers or elimination and bond-fission channels to form aromatic species containing formyl or carboxyl groups.

Finally, Table 6.7 contains reaction classes for oxygenated resonance stabilized aromatic radicals. The sub-mechanism of the crucial A1O-RSR (phenoxy-like) radicals was almost entirely updated in this work with theoretical calculations (Sections 6.3.3 and 6.3.2) or analogy estimates. Similarly to their molecular counterparts, the presence of C–O allows radical decomposition to C₅ species [A1O-RSR][RADICAL_DECO]. Similar reaction pathways are accessed by recombinations with radicals (H, CH₃, O, OH, HO₂). In some cases, ring opening reactions also occur, in contrast with the A1CH2-RSR counterparts. The presence of a lateral OH substituent A1O,OH-RSR mostly results in new elimination or ring opening pathways through e.g., REC_O. In the absence of theory based guidance, these rate constants were estimated as ring opening channels from the analogous A1O-RSR system. It is noted that many products of oxidation recombination reactions are written as lumped decomposed fragments, such that corresponding multi-substituted C₅ species are not considered, as they are not included in the CRECK mechanism. Finally, only two classes are identified for the A1CO-RSR species type. In fact, in this case the extremely weak C–C bond results in quasi-instantaneous β -scission, such that the inclusion of additional reactions has no effect on macroscopic kinetic simulations. Even O₂ recombination reaction has a null impact in low-temperature oxidation kinetics [449].

The role and relevance of the identified classes and reaction types is discussed in more detail in the presentation of the kinetic simulations in Section 6.6.

TABLE 6.2: Reaction classes for decomposition and oxidation of molecular species types: A1-M, A1,H2,H2-M, A2-M, A2,H2,H2-M. Colored boxes highlight the reaction classes updated in this thesis. For each example, kinetic parameters of the modified Arrhenius form $k = k_0 T^\alpha \exp\left(-\frac{E_A}{RT}\right)$ are provided (units cal, mol, cm³, s, K, reference pressure of 1 atm for pressure-dependent reactions). For color codes see Table 5.2.

SPECIES TYPE:		A1-M	(C ₆ H ₆)		
CLASS TYPE	REACTION TYPE	EXAMPLE	ELEM. STEPS	SOURCE	
BONDFISS.	BONDFISSION_CH	C ₆ H ₆ =C ₆ H ₅ +H 6.31E+60 -12.40 148070	BONDFISSION	THEORY Miller 2003 [271]	
HABS	HABS_H	C ₆ H ₆ +H=C ₆ H ₅ +H ₂ 3.59E+08 1.89 16052	H ABSTRACTION	THEORY This work	
	HABS_CH3	C ₆ H ₆ +CH ₃ =C ₆ H ₅ +CH ₄ 5.05E+02 3.19 13738	H ABSTRACTION	THEORY This work	
	HABS_OH	C ₆ H ₆ +OH=C ₆ H ₅ +H ₂ O 4.72E+05 2.35 2560	H ABSTRACTION	THEORY This work	
	HABS_O	C ₆ H ₆ +O=C ₆ H ₅ +OH 4.08E+06 2.29 10073	H ABSTRACTION	CHECK ESTIMATE	
	HABS_HO2	C ₆ H ₆ +HO ₂ =C ₆ H ₅ +H ₂ O ₂ 2.22E+03 3.09 24005	H ABSTRACTION	CHECK ESTIMATE	
	HABS_O2	C ₆ H ₆ +O ₂ →C ₆ H ₅ +HO ₂ 2.98E+08 1.89 58953 C ₆ H ₅ +HO ₂ →C ₆ H ₆ +O ₂ 2.59E+05 2.11 -4778	H ABSTRACTION	THEORY This work	
	HABS_A1O-RSR	C ₆ H ₆ +C ₆ H ₅ O→C ₆ H ₅ +C ₆ H ₅ OH 4.32E+05 2.00 20655	H ABSTRACTION	CHECK ESTIMATE	
ADD_H	ADD_H_WELL	H+C ₁₀ H ₈ →0.5RTETRALIN+0.5C ₁₀ H ₇ 5.00E+12 0.00 2500	BONDFISSION	CHECK ESTIMATE	
		H+C ₁₄ H ₁₀ →0.69C ₁₄ H ₉ +0.43RTETRALIN 1.00E+13 0.00 3500			
ADD_O	ADD_O_ISC_DECO	C ₆ H ₆ +O→CO+C ₅ H ₆ 1.45E+32 -5.44 24217	BONDFISSION ISC H TRANSFER RING CLOSURE ELIMINATION	THEORY + MEL This work	
	ADD_O_ISC	C ₆ H ₆ +O→C ₆ H ₅ OH 1.24E+14 -0.78 3522 0.52E+48 -10.40 21217	BONDFISSION ISC	THEORY + MEL This work	
IPSO	IPSO_O	C ₆ H ₆ +O=C ₆ H ₅ O+H 7.14E+07 1.91 6209	BETACISSION	THEORY + MEL This work	
ADD_O2	ADD_O2_EL_OH	O ₂ +C ₆ H ₆ →OH+C ₆ H ₅ O 1.50E+14 0.00 44000	BONDFISSION ELIMINATION	CHECK ESTIMATE	
SPECIES TYPE:		A1,H2,H2-M	(CYC ₆ H ₈)		
CLASS TYPE	REACTION TYPE	EXAMPLE	ELEM. STEPS	SOURCE	
DECO.	EL_H2	C ₁₀ H ₁₀ =C ₁₀ H ₈ +H ₂ CYC ₆ H ₈ =C ₆ H ₆ +H ₂ 1.00E+14 0.00 70000	ELIMINATION	CHECK ESTIMATE	
HABS	HABS_H	H+TETRALIN=H ₂ +RTETRALIN 3.00E+07 2.00 3951	H ABSTRACTION	CHECK ESTIMATE	
ADD_H	ADD_H_WELL	H+C ₁₀ H ₁₀ →RTETRALIN 1.00E+13 0.00 3500	ADDITION		
ADD_OH	ADD_OH_INSERT	OH+C ₁₀ H ₁₀ →BZLFUR+C ₂ H ₄ +H 2.00E+12 0.00 2000	ADDITION H TRANSFER INSERTION BETACISSION	CHECK ESTIMATE	
SPECIES TYPE:		A2-M	(C ₁₀ H ₈)		
CLASS TYPE	REACTION TYPE	EXAMPLE	ELEM. STEPS	SOURCE	
ADD_H	ADD_H_ROPEN	H+C ₁₀ H ₈ →C ₆ H ₅ +C ₄ H ₄ 5.00E+12 0.00 5000	ADDITION H TRANSFER RING OPENING BETACISSION	CHECK ESTIMATE	
ADD_O2	ADD_O2_ROPEN	O ₂ +C ₁₀ H ₈ →C ₆ H ₅ +2CO+C ₂ H ₂ +H 8.00E+13 0.00 38000	as above	CHECK ESTIMATE	
ADD_OH	ADD_OH_DECO	OH+C ₁₄ H ₁₀ →FLUORENE+CO+H	ADDITION	CHECK	

SPECIES TYPE:	A2,H2,H2-M	(C ₁₀ H ₁₀)	H TRANSFER RING OP/CLOSE BETACISSION	ESTIMATE
CLASS TYPE	REACTION TYPE	EXAMPLE	ELEM. STEPS	SOURCE
ADD_OH	ADD_OH_ROPEN	OH+C ₁₀ H ₁₀ →CH ₃ C ₆ H ₄ +C ₂ H ₃ CHO OH+C ₁₀ H ₁₀ →CH ₃ CHO+C ₆ H ₅ C ₂ H ₂ 5.00E+12 0.00 0	ADDITION H TRANSFER RING OPENING BETACISSION	CRECK ESTIMATE

TABLE 6.3: Reaction classes for decomposition and oxidation of molecular species types: A1,CH3-M, A1,C2H-M, A1,C2H3-M. Colored boxes highlight the reaction classes updated in this thesis. For each example, kinetic parameters of the modified Arrhenius form $k = k_0 T^\alpha \exp\left(-\frac{E_A}{RT}\right)$ are provided (units cal, mol, cm³, s, K, reference pressure of 1 atm for pressure-dependent reactions). For color codes see Table 5.2.

SPECIES TYPE:	A1,CH3-M	(C ₇ H ₈)		
CLASS TYPE	REACTION TYPE	EXAMPLE	ELEM. STEPS	SOURCE
BONDFISS.	BONDFISSION_CH	C ₇ H ₈ (+M)=C ₇ H ₇ +H(+M) 5.6E+15 0.17 91168	BONDFISSION	THEORY Klippenstein 2007 [450]
	BONDFISSION_CC	C ₇ H ₈ (+M)=CH ₃ +C ₆ H ₅ (+M) 1.95E+27 -3.16 107447	BONDFISSION	THEORY Klippenstein 2007 [450]
HABS	HABS_H	H+C ₇ H ₈ =C ₇ H ₇ +H ₂ 3.10E+04 2.76 3992	H ABSTRACTION	THEORY This work
	HABS_CH3	CH ₃ +C ₇ H ₈ =C ₇ H ₇ +CH ₄ 2.10E+01 3.38 7299	H ABSTRACTION	THEORY This work
	HABS_OH	OH+C ₇ H ₈ =C ₇ H ₇ +H ₂ O 4.21E+07 1.70 563	H ABSTRACTION	THEORY This work
	HABS_O2	O ₂ +C ₇ H ₈ =C ₇ H ₇ +HO ₂ 2.18E+07 2.50 46045	H ABSTRACTION	EXPERIMENT Oehlschlaeger 2006 [451]
	HABS_HO2	HO ₂ +C ₇ H ₈ =C ₇ H ₇ +H ₂ O ₂ 2.72 3.55 11324	H ABSTRACTION	THEORY Pelucchi 2018 [129]
	HABS_O	O+C ₇ H ₈ =C ₇ H ₇ +OH 4.91E+07 1.63 3796	H ABSTRACTION	THEORY Pelucchi 2018 [129]
IPSO	IPSO_H	H+C ₇ H ₈ =C ₆ H ₆ +CH ₃ 5.28E+07 1.71 4387	ADDITION BETACISSION	THEORY + MEL This work
	IPSO_O	C ₇ H ₈ +O=C ₆ H ₅ O+CH ₃ 2.38E+07 1.91 6209	ADDITION BETACISSION	ANALOGY This work
	IPSO_OH	OH+C ₇ H ₈ =C ₆ H ₅ OH+CH ₃ 7.83E+02 2.88 3221	ADDITION BETACISSION	THEORY Seta 2006 [452]
SPECIES TYPE:	A1,C2H-M	(C ₆ H ₅ C ₂ H)		
CLASS TYPE	REACTION TYPE	EXAMPLE	ELEM. STEPS	SOURCE
ADD_H	ADD_H_WELL	H+C ₆ H ₅ C ₂ H=C ₆ H ₅ C ₂ H ₂ 1.59E+62 -14.5 31760 H+C ₆ H ₅ C ₂ H=C ₆ H ₄ C ₂ H ₃ 4.96E+78 -19.1 46600	ADDITION	THEORY Mebel 2017 [139]
ADD_O2	ADD_O2_EL_HCO	O ₂ +C ₆ H ₅ C ₂ H→C ₆ H ₅ +CO+HCO 3.00E+11 0.00 22000	ADDITION H TRANSFER BETACISSION	CRECK ESTIMATE
ADD_OH	ADD_OH_DECO	OH+C ₆ H ₅ C ₂ H→CH ₂ CO+C ₆ H ₅ 5.00E+12 0.00 2000 OH+C ₆ H ₅ C ₂ H→C ₇ H ₇ +CO 1.00E+13 0.00 7000	ADDITION H TRANSFER BETACISSION	CRECK ESTIMATE
SPECIES TYPE:	A1,C2H3-M	(C ₆ H ₅ C ₂ H ₃)		
CLASS TYPE	REACTION TYPE	EXAMPLE	ELEM. STEPS	SOURCE
IPSO	IPSO_H	H+C ₆ H ₅ C ₂ H ₃ =C ₆ H ₆ +C ₂ H ₃ 1.20E+13 0.00 5500	ADDITION BETACISSION	CRECK ESTIMATE
HABS	HABS_R	R+C ₆ H ₅ C ₂ H ₃ →RH+C ₆ H ₅ C ₂ H ₂	H ABSTRACTION	CRECK RULE
ADD_OH	ADD_OH_DECO	OH+C ₆ H ₅ C ₂ H ₃ →C ₇ H ₇ +CH ₂ O 1.00E+11 0.00 0.00	ADDITION H TRANSFER	CRECK ESTIMATE

BETACISSION

TABLE 6.4: Reaction classes for decomposition and oxidation of molecular species types A1,X-M, with X = oxygenated group (OH, CHO, O, OCH3). Colored boxes highlight the reaction classes updated in this thesis. * indicates adjustment with respect to literature references. For each example, kinetic parameters of the modified Arrhenius form $k = k_0 T^\alpha \exp\left(-\frac{E_A}{RT}\right)$ are provided (units cal, mol, cm^3 , s, K, reference pressure of 1 atm for pressure-dependent reactions). For color codes see Table 5.2.

SPECIES TYPE:	A1,OH-M	(C ₆ H ₅ OH)				
CLASS TYPE	REACTION TYPE	EXAMPLE	ELEM. STEPS	SOURCE		
BONDFISS.	BONDFISSION_OH	C ₆ H ₅ OH → C ₆ H ₅ O + H 6.58E+38 -6.88 97738	BONDFISSION	THEORY + MEL This work		
	BONDFISSION_CO	C ₆ H ₅ OH = OH + C ₆ H ₅ 1E+16 0. 111000	BONDFISSION	CHECK ESTIMATE		
DECO.	MOLEC_DECO	C ₆ H ₅ OH → CO + C ₅ H ₆ 9.30E+23 -3.12 78585	H TRANSFER RING CLOSURE ELIMINATION	THEORY + MEL This work		
	EL_H2O	C ₆ H ₅ OH → CYC ₆ H ₄ + H ₂ O 4.36E+20 -2.19 90188	ELIMINATION	THEORY This work		
HABS	HABS_H	C ₆ H ₅ OH + H = C ₆ H ₅ O + H ₂ 3.62E+03 2.94 5616 1.42E+07 2.15 15835	H ABSTRACTION	THEORY This work		
	HABS_CH3	C ₆ H ₅ OH + CH ₃ = C ₆ H ₅ O + CH ₄ 1.60E+00 3.58 4694 1.02E+02 3.24 13605	H ABSTRACTION	THEORY This work		
	HABS_OH	C ₆ H ₅ OH + OH = C ₆ H ₅ O + H ₂ O 3.89E+05 2.30 -1062 5.18E+03 2.54 237	H ABSTRACTION	THEORY This work		
	HABS_O	O + C ₆ H ₅ OH = OH + C ₆ H ₅ O 1.64E+07 1.64 3795	H ABSTRACTION	ANALOGY FROM TOL./3		
	HABS_HO2	C ₆ H ₅ OH + HO ₂ = C ₆ H ₅ O + H ₂ O ₂ 2.60E-08 5.80 1543	H ABSTRACTION	THEORY This work		
	HABS_O2	HABS_O2	C ₆ H ₅ OH + O ₂ → C ₆ H ₅ O + HO ₂ 6.11E+07 1.52 32968 4.76E+05 2.40 57738 C ₆ H ₅ O + HO ₂ → C ₆ H ₅ OH + O ₂ 3.89E+06 1.54 -5223	H ABSTRACTION	THEORY This work	
			HABS_A1-R	C ₆ H ₅ OH + C ₆ H ₅ → C ₆ H ₅ O + C ₆ H ₆ 3.00E+08 1.00 1355	H ABSTRACTION	CHECK ESTIMATE
			HABS_C5-RSR	C ₆ H ₅ OH + C ₅ H ₅ = C ₅ H ₆ + C ₆ H ₅ O 3.00E+12 0.00 25000	H ABSTRACTION	CHECK ESTIMATE
	IPSO	IPSO_H	H + C ₆ H ₅ OH = C ₆ H ₆ + OH 5.37E+07 1.71 5900	ADDITION BETACISSION	THEORY + MEL This work	
IPSO_C2H3		C ₂ H ₃ + C ₆ H ₅ OH = C ₆ H ₅ C ₂ H ₃ + OH 1.00E+12 0.00 6000	ADDITION BETACISSION	CHECK ESTIMATE		
IPSO_O		C ₆ H ₅ OH + O = C ₆ H ₅ O + OH 2.38E+07 1.91 6209	ADDITION BETACISSION	CHECK ESTIMATE		
SPECIES TYPE:	A1,OH,OH-M	(CATECHOL)				
CLASS TYPE	REACTION TYPE	EXAMPLE	ELEM. STEPS	SOURCE		
DECO.	MOLEC_DECO	CATECHOL → C ₄ H ₆ + 2CO 6.00E+11 0.61 67000	CONCERTED H TRANSFER RING OPENING	THEORY* Altarawneh 2010 [134]		
	EL_H2O	CATECHOL → 0.5C ₂ H ₂ + 0.5C ₃ H ₂ + 0.5CYC ₅ H ₄ + CO + H ₂ O 8.00E+11 1.18 82200 CATECHOL → CYC ₅ H ₄ CO + H ₂ O 3.00E+11 1.18 82200	H TRANSFER ELIMINATION	THEORY Furutani 2017 + MEL [442]		
ADD_O2	ADD_O2_DECO	O ₂ + CATECHOL → CO + 2CH ₂ CO + H + HCO 1.00E+17 0.00 62000	ADDITION RING OPENING BETACISSION ?	CHECK ESTIMATE		
SPECIES TYPE:	A1,OCH3-M	(C ₆ H ₅ OCH ₃)				
CLASS TYPE	REACTION TYPE	EXAMPLE	ELEM. STEPS	SOURCE		
BONDFISS.	BONDFISSION_CO	C ₆ H ₅ OCH ₃ = C ₆ H ₅ O + CH ₃	BONDFISSION	ESTIMATE*		

		2.00E+15 0.00 63700	Yuan 2019 [435]	
DECO.	MOLEC_DECO	$C_6H_5OCH_3=C_6H_6+CH_2O$ 3.00E+14 0.00 69000 $C_6H_5OCH_3=CO+C_5H_5CH_3$ 1.50E+14 0.00 64000	H TRANSFER BOND FISSION CH ₃ MIGRATION RING CLOSURE ELIMINATION	CHECK ESTIMATE
IPSO	IPSO_H	$H+C_6H_5OCH_3=C_6H_6+CH_3O$ 4.86E+07 1.71 5173 $H+C_6H_5OCH_3=C_6H_5OH+CH_3$ 1.00E+13 0.00 6000	ADDITION BETASCISSION BETASCISSION	THEORY + MEL This work CHECK ESTIMATE
	IPSO_CH3	$CH_3+C_6H_5OCH_3=C_7H_8+CH_3O$ 7.50E+11 0.00 15000	ADDITION BETASCISSION	CHECK ESTIMATE
	IPSO_OH	$OH+C_6H_5OCH_3=C_6H_5OH+CH_3O$ 1.00E+13 0.00 5000	ADDITION BETASCISSION	CHECK ESTIMATE
HABS	HABS_H	$C_6H_5OCH_3+H\rightarrow H_2$ +0.85(C_6H_5CHO+H)+0.15($HCO+C_6H_6$) 1.10E+06 2.33 5342	H ABSTRACTION	THEORY This work
	HABS_CH3	$C_6H_5OCH_3+CH_3\rightarrow CH_4$ +0.85(C_6H_5CHO+H)+0.15($HCO+C_6H_6$) 1.35E+01 3.46 8093	H ABSTRACTION	THEORY This work
	HABS_OH	$C_6H_5OCH_3+OH\rightarrow H_2O$ +0.85(C_6H_5CHO+H)+0.15($HCO+C_6H_6$) 6.40E+05 2.29 -291	H ABSTRACTION	THEORY This work
	HABS_O2	$C_6H_5OCH_3+O_2\rightarrow HO_2$ +0.85(C_6H_5CHO+H)+0.15($HCO+C_6H_6$) 1.28E-01 4.40 42190	H ABSTRACTION	THEORY This work
SPECIES TYPE:	A1,CHO-M	(C₆H₅CHO)		
CLASS TYPE	REACTION TYPE	EXAMPLE	ELEM. STEPS	SOURCE
BONDFISS.	BONDFISSION_CC	$C_6H_5CHO=C_6H_5+HCO$ 5.00E+15 0.00 98900	BONDFISSION	CHECK ESTIMATE
	BONDFISSION_CH	$C_6H_5CHO=H+C_6H_5CO$ 3.00E+15 0.00 89300	BONDFISSION	CHECK ESTIMATE
HABS	HABS_H	$H+C_6H_5CHO=H_2+C_6H_5CO$ 1.04E+06 2.30 1792	H ABSTRACTION	THEORY This work
	HABS_CH3	$CH_3+C_6H_5CHO=CH_4+C_6H_5CO$ 8.37E+00 3.44 4471	H ABSTRACTION	THEORY This work
	HABS_OH	$OH+C_6H_5CHO=H_2O+C_6H_5CO$ 5.11E+05 2.15 -2412	H ABSTRACTION	THEORY This work
	HABS_O2	$O_2+C_6H_5CHO=HO_2+C_6H_5CO$ 7.30E+06 2.05 37428	H ABSTRACTION	THEORY This work
	HABS_HO2	$HO_2+C_6H_5CHO=H_2O_2+C_6H_5CO$ 9.88E-02 4.07 6187	H ABSTRACTION	THEORY This work
	HABS_C5-RSR	$C_5H_5+C_6H_5CHO=C_5H_6+C_6H_5CO$ 2.72E+05 2.00 12130	H ABSTRACTION	CHECK ESTIMATE
	HABS_A1CH2-RSR	$C_7H_7+C_6H_5CHO=C_7H_8+C_6H_5CO$ 1.08E+05 2.00 14063	H ABSTRACTION	CHECK ESTIMATE
	HABS_A1O-RSR	$C_6H_5O+C_6H_5CHO=C_6H_5OH+C_6H_5CO$ 1.44E+05 2.00 10683	H ABSTRACTION	CHECK ESTIMATE
IPSO	IPSO_H	$H+C_6H_5CHO=HCO+C_6H_6$ 7.5E+07 1.71 4699	ADDITION BETASCISSION	THEORY + MEL This work
	IPSO_CH3	$CH_3+C_6H_5CHO=HCO+C_7H_8$ 1.20E+12 0.00 15200	ADDITION BETASCISSION	CHECK ESTIMATE
	IPSO_O	$O+C_6H_5CHO=HCO+C_6H_5O$ 1.50E+12 0.00 4000	ADDITION BETASCISSION	CHECK ESTIMATE
	IPSO_OH	$OH+C_6H_5CHO=HCO+C_6H_5OH$ 4.70E+12 0.00 8600	ADDITION BETASCISSION	CHECK ESTIMATE
SPECIES TYPE:	A1,O2-M	(C₆H₄O₂)		
CLASS TYPE	REACTION TYPE	EXAMPLE	ELEM. STEPS	SOURCE
DECO.	MOLEC_DECO	$C_6H_4O_2\rightarrow C_5H_4O+CO$ 7.40E+11 0.00 59400 $C_6H_4O_2\rightarrow 2C_2H_2+2CO$ 7.40E+11 0.00 59400	RING CLOSURE ELIMINATION	CHECK ESTIMATE CHECK ESTIMATE
	ROPEN	$C_6H_4O_2\rightarrow CO_2+C_3H_2+C_2H_2$ 3.50E+12 0.0 67000	H TRANSFER RING OPENING ELIMINATION	CHECK ESTIMATE
HABS	HABS_DECO	$R+C_6H_4O_2\rightarrow RH+C_2H_2+C_2H+2CO$	H ABSTRACTION DECOMPOSITION	CHECK RULE
ADD_H	ADD_H_DECO	$C_6H_4O_2+H\rightarrow C_5H_4OH+CO$ 5.35E+15 -0.45 47148	ADDITION H TRANSFER RING CLOSURE	THEORY This work + MEL

			ELIMINATION	
ADD_HO2	ADD_HO2_DECO	$\text{HO}_2 + \text{C}_6\text{H}_4\text{O}_2 \rightarrow 2\text{CO} + \text{C}_2\text{H}_2 + \text{CH}_2\text{O} + \text{HCO}$ 5.00E+12 0.00 13000	ADDITION RING OPENING H TRANSFER ELIMINATION	
SPECIES TYPE:	A1,O,CH2-M	(OC₆H₄CH₂)		
CLASS TYPE	REACTION TYPE	EXAMPLE	ELEM. STEPS	SOURCE
DECO.	MOLEC_DECO	$\text{OC}_6\text{H}_4\text{CH}_2 = 0.5\text{FULVENE} + 0.5\text{C}_6\text{H}_6 + \text{CO}$ 6.31E+14 0.00 67160	RING CLOSURE ELIMINATION	ESTIMATE Yuan 2015 [453], [454]

TABLE 6.5: [Reaction classes for decomposition and oxidation of radical species types A1-R, A2-R, A1,X-R with X = 3H2, CH3, OH. Colored boxes highlight the reaction classes updated in this thesis. For each example, kinetic parameters of the modified Arrhenius form $k = k_0 T^\alpha \exp(-\frac{E_A}{RT})$ are provided (units cal, mol, cm³, s, K, reference pressure of 1 atm for pressure-dependent reactions). For color codes see Table 5.2.

SPECIES TYPE:	A1-R	(C₆H₅)		
CLASS TYPE	REACTION TYPE	EXAMPLE	ELEM. STEPS	SOURCE
BETASCISSION	BSCISS_CH	$\text{C}_6\text{H}_5 = \text{CYC}_6\text{H}_4 + \text{H}$ $\text{C}_6\text{H}_5 \rightarrow \text{H} + \text{C}_4\text{H}_2 + \text{C}_2\text{H}_2$ 5.00E+12 0.62 77302	BETASCISSION	THEORY Wang 1994 [138]
DECO.	ROPEN	$\text{C}_6\text{H}_5 + \text{M} = \text{LC}_6\text{H}_5 + \text{M}$ 5.00E+18 0.00 67000	RING OPENING	CRECK ESTIMATE
ADD_O2	REC_O2_WELL	$\text{C}_6\text{H}_5 + \text{O}_2 = \text{C}_6\text{H}_5\text{O}_2$ 6.39e+52 -12.51 14603	RECOMBINATION	THEORY + MEL This work
	REC_O2_EL_O	$\text{C}_6\text{H}_5 + \text{O}_2 = \text{C}_6\text{H}_5\text{O} + \text{O}$ 2.76E+28 -4.47 13101	RECOMBINATION	THEORY + MEL This work
	REC_O2_INSERTION	$\text{C}_6\text{H}_5 + \text{O}_2 \rightarrow \text{C}_5\text{H}_4\text{O} + \text{HCO}$ 3.87E+29 -4.91 14033	RECOMBINATION RING CLOSURE RING INSERTION RING OPENING RING TORSION BETASCISSION	THEORY + MEL This work
	RO2_INSERTION	$\text{C}_6\text{H}_5\text{O}_2 \rightarrow \text{C}_5\text{H}_4\text{O} + \text{HCO}$ 1.08E+47 -10.29 50061	as above	THEORY + MEL This work
ADD_OH	REC_OH_EL_H	$\text{C}_6\text{H}_5 + \text{OH} = \text{C}_6\text{H}_5\text{O} + \text{H}$ 3.00E+13 0.00 0	BONDFISSION	ESTIMATE ITV MECH.
ADD_HO2	REC_HO2_EL_OH	$\text{C}_6\text{H}_5 + \text{HO}_2 = \text{C}_6\text{H}_5\text{O} + \text{OH}$ 3.00E+13 0.00 0	BONDFISSION	ESTIMATE ITV MECH.
ADD_O	REC_O_DECO	$\text{O} + \text{C}_6\text{H}_5 \rightarrow \text{C}_5\text{H}_5 + \text{CO}$ 5.00E+13 0.00 0	BONDFISSION	ESTIMATE
SPECIES TYPE:	A2-R	(C₁₀H₇)		
CLASS TYPE	REACTION TYPE	EXAMPLE	ELEM. STEPS	SOURCE
ADD_O2	REC_O2_ROPEN	$\text{O}_2 + \text{C}_{10}\text{H}_7 \rightarrow \text{C}_6\text{H}_5\text{C}_2\text{H} + \text{HCO} + \text{CO}$ $\text{O}_2 + \text{C}_{16}\text{H}_9 \rightarrow \text{C}_{14}\text{H}_9 + \text{CO} + \text{CO}$ 1.00E+12 0.00 3000	BONDFISSION H TRANSFER RING OPENING ELIMINATION ?	CRECK ESTIMATE
SPECIES TYPE:	A1,3H2-R	(RTETRALIN)		
CLASS TYPE	REACTION TYPE	EXAMPLE	ELEM. STEPS	SOURCE
DECO.	RADICAL_DECO	$\text{RTETRALIN} \rightarrow \text{INDENE} + \text{CH}_3$ 1.00E+13 0.00 31000	H TRANSFER RING CLOSURE BETASCISSION ?	CRECK ESTIMATE
BETASCISS.	BSCISS_CH	$\text{RTETRALIN} \rightarrow \text{C}_{10}\text{H}_{10} + \text{H}$ 3.00E+14 0.00 38000	BETASCISSION	
SPECIES TYPE:	A1,CH3-R	(C₆H₄CH₃)		

CLASS TYPE	REACTION TYPE	EXAMPLE	ELEM. STEPS	SOURCE
BETACISS.	BSCISS_CC	$\text{CH}_3\text{C}_6\text{H}_4(+\text{M})=\text{CYC}_6\text{H}_4+\text{CH}_3(+\text{M})$ 4.3E+12 0.62 67449	BETACISSION	ESTIMATE From A1-M
ISOM.	ISOM_CC	$\text{CH}_3\text{C}_6\text{H}_4=\text{C}_7\text{H}_7$ 5.58E+45 -9.83 57617	H TRANSFER	THEORY Dames 2013 [455]
REC_O2	REC_O2_EL_OH	$\text{CH}_3\text{C}_6\text{H}_4+\text{O}_2=\text{OC}_6\text{H}_4\text{CH}_2+\text{OH}$ 1.40E+29 -4.93 10243	BONDFISSION H TRANSFER BETACISSION	RULE from THEORY This work ($\text{C}_6\text{H}_5+\text{O}_2$) Da Silva 2007 [448]
	RO2_EL_OH	$\text{O}_2\text{C}_6\text{H}_4\text{CH}_3=\text{OC}_6\text{H}_4\text{CH}_2+\text{OH}$ 6.77E+44 -10.17 40220	H TRANSFER BETACISSION	ESTIMATE Bounaceur 2005 [456]
	REC_O2_INSERTION	$\text{O}_2+\text{CH}_3\text{C}_6\text{H}_4=\text{C}_6\text{H}_4\text{O}_2+\text{CH}_3$ 6.0E+13 0.00 9000	BONDFISSION INSERTION RING OPENING BETACISSION	
SPECIES TYPE:	A1,OH-R	($\text{C}_6\text{H}_4\text{OH}$)		
CLASS TYPE	REACTION TYPE	EXAMPLE	ELEM. STEPS	SOURCE
BETACISS.	BSCISS_CO	$\text{C}_6\text{H}_4\text{OH}(+\text{M})=\text{CYC}_6\text{H}_4+\text{OH}(+\text{M})$ 4.3E+12 0.62 75702	BETACISSION	ESTIMATE From A1-M
DECO.	RADICAL_DECO	$\text{C}_6\text{H}_4\text{OH}\rightarrow\text{C}_5\text{H}_5+\text{CO}$ 3.00E+04 -8.11 84286	H TRANSFER RING CLOSURE BETACISSION	THEORY + MEL This work
ISOM.	ISOM_OC	$\text{C}_6\text{H}_4\text{OH}=\text{C}_6\text{H}_5\text{O}$ 1.84E+42 -8.73 71944	H TRANSFER	THEORY + MEL This work
REC_O2	REC_O2_INSERTION	$\text{O}_2+\text{C}_6\text{H}_4\text{OH}=\text{C}_6\text{H}_4\text{O}_2+\text{OH}$ 6.0E+13 0.00 9000	BONDFISSION INSERTION RING OPENING BETACISSION	ANALOGY A1- CH_3 This work

TABLE 6.6: Reaction classes for decomposition and oxidation of resonantly-stabilized species types: A1CH2-RSR, A1CH2,OH-RSR. Colored boxes highlight the reaction classes updated in this thesis. For each example, kinetic parameters of the modified Arrhenius form $k = k_0 T^\alpha \exp(-\frac{E_A}{RT})$ are provided (units cal, mol, cm^3 , s, K, reference pressure of 1 atm for pressure-dependent reactions). For color codes see Table 5.2.

SPECIES TYPE:	A1CH2-RSR	(C_7H_7)		
CLASS TYPE	REACTION TYPE	EXAMPLE	ELEM. STEPS	SOURCE
BETACISS.	BSCISS_CC	$\text{C}_7\text{H}_7=\text{CYC}_6\text{H}_4+\text{CH}_3$ 5.5E+89 -20.8 141680	H TRANSFER BETACISSION	THEORY Derudi 2011 [457]
ADD_H	REC_H_EL_CH3	$\text{C}_7\text{H}_7+\text{H}=\text{C}_6\text{H}_5+\text{CH}_3$ 5.83E+67 -14.15 68330	BONDFISSION	THEORY Klippenstein 2007 [450]
ADD_CH3	REC_CH3	$\text{C}_7\text{H}_7+\text{CH}_3=\text{C}_6\text{H}_5\text{C}_2\text{H}_5$ 1.16E+14 -0.27 -483	BONDFISSION	ESTIMATE LLNL MECH.
ADD_HO2	REC_HO2_WELL	$\text{C}_7\text{H}_7+\text{HO}_2=\text{BZCOOH}$ 1.88E+30 -6.00 2300	BONDFISSION	ESTIMATE LLNL MECH.
	REC_HO2_EL_OH	$\text{C}_7\text{H}_7+\text{HO}_2=\text{C}_6\text{H}_5\text{CH}_2\text{O}+\text{OH}$ 2.26E+24 -3.15 9500 1.63E+02 2.40 9841	BONDFISSION (OH TRANSFER)	THEORY Da Silva 2009 [458]
	REC_HO2_EL_H2O	$\text{C}_7\text{H}_7+\text{HO}_2=\text{C}_6\text{H}_5\text{CHO}+\text{H}_2\text{O}$ 2.51E+09 0.61 9474	BONDFISSION ELIMINATION	THEORY Da Silva 2009 [458]
	ROOH_EL_OH	$\text{BZCOOH}=\text{C}_6\text{H}_5\text{CH}_2\text{O}+\text{OH}$ 1.48E+50 -10.77 55271 3.94E+36 -7.71 63309	BONDFISSION (OH TRANSFER)	THEORY Da Silva 2009 [458]
	ROOH_EL_H2O	$\text{BZCOOH}=\text{C}_6\text{H}_5\text{CHO}+\text{H}_2\text{O}$ 3.91E+36 -7.41 56430	ELIMINATION	THEORY Da Silva 2009 [458]
ADD_O2	REC_O2_WELL	$\text{C}_7\text{H}_7+\text{O}_2=\text{C}_7\text{H}_7\text{O}_2$ 2.80E+36 -7.92 7185	BONDFISSION	THEORY Pelucchi 2018 [129]
	REC_O2_EL_OH	$\text{C}_7\text{H}_7+\text{O}_2=\text{C}_6\text{H}_5\text{CHO}+\text{OH}$ 3.54E+06 1.48 16508	BONDFISSION ELIMINATION	THEORY Pelucchi 2018 [129]
	REC_O2_ISOM_O	$\text{C}_7\text{H}_7+\text{O}_2=\text{C}_6\text{H}_5\text{O}+\text{CH}_2\text{O}$ 2.581E+09 0.42 20714	BONDFISSION O TRANSFER BETACISSION	THEORY Pelucchi 2018 [129]
	RO2_EL_OH	$\text{C}_7\text{H}_7\text{O}_2=\text{C}_6\text{H}_5\text{CHO}+\text{OH}$ 1.59E+39 -9.52 41350	ELIMINATION	THEORY Pelucchi 2018 [129]
	RO2_ISOM_O	$\text{C}_7\text{H}_7\text{O}_2=\text{C}_6\text{H}_5\text{O}+\text{CH}_2\text{O}$	O TRANSFER	THEORY

		2.72 0.74 13991	BETASCISSION	Pelucchi 2018 [129]
RO2_SEC.	RO2_REC_H	C ₇ H ₇ O ₂ +H=C ₆ H ₅ CH ₂ O+OH 3.80E+14 -0.19 1890	RECOMBINATION	THEORY Da Silva 2009 [459]
		C ₇ H ₇ O ₂ +H=BZCOOH 4.35E+60 -15.92 11400	RECOMBINATION	THEORY Da Silva 2009 [459]
		C ₇ H ₇ O ₂ +H=C ₇ H ₇ +HO ₂ 1.96E+04 2.47 1430	RECOMBINATION	THEORY Da Silva 2009 [459]
	RO2_DISP	C ₇ H ₇ O ₂ +C ₇ H ₇ O ₂ → 2C ₆ H ₅ CH ₂ O+O ₂ 6.30E+10 0.00 -725	DISPROPORTION.	ESTIMATE Herbinet 2013 [460]
	RO2_HABS	C ₇ H ₇ O ₂ +HO ₂ =BZCOOH+O ₂ 2.00E+11 0.00 -1300	H ABSTRACTION	ESTIMATE Herbinet 2013 [460]
		C ₇ H ₇ O ₂ +C ₇ H ₈ =C ₇ H ₇ +BZCOOH 4.00E+11 0.00 14000	H ABSTRACTION	ESTIMATE Bounaceur 2005 [456]
SPECIES TYPE:	A1CH2,OH-RSR	(HOC₆H₄CH₂)		
CLASS TYPE	REACTION TYPE	EXAMPLE	ELEM. STEPS	SOURCE
ISOM.	ISOM_OC	HOC ₆ H ₄ CH ₂ →OC ₆ H ₄ CH ₃ 1.75E+03 1.92 19234	H TRANSFER	THEORY This work
REC_O	REC_O_EL_OH	O+HOC ₆ H ₄ CH ₂ →C ₆ H ₅ CHO+OH 5.00E+14 0.00 0	RECOMBINATION H TRANSFER BETASCISSION	CRECK ESTIMATE

TABLE 6.7: [Reaction classes for decomposition and oxidation of resonantly-stabilized oxygenated species types: A1O-RSR, A1O,OH-RSR, A1O,CH3-RSR, A1CO-RSR. Colored boxes highlight the reaction classes updated in this thesis. For each example, kinetic parameters of the modified Arrhenius form $k = k_0 T^\alpha \exp\left(-\frac{E_A}{RT}\right)$ are provided (units cal, mol, cm³, s, K, reference pressure of 1 atm for pressure-dependent reactions). For color codes see Table 5.2.

SPECIES TYPE:	A1O-RSR	(C₆H₅O)		
CLASS TYPE	REACTION TYPE	EXAMPLE	ELEM. STEPS	SOURCE
DECO.	RADICAL_DECO	C ₆ H ₅ O→CO+C ₅ H ₅ 3.45E+2 -3.62 57325	RING CLOSURE BETASCISSION	THEORY + MEL This work
ADD_H	REC_H_WELL	C ₆ H ₅ O+H→C ₆ H ₅ OH 2.16E+33 -5.65 7614	BONDFISSION (H TRANSFER)	THEORY + MEL This work
	REC_H_DECO	C ₆ H ₅ O+H=CO+C ₅ H ₆ 1.94E+11 0.31 3494	BONDFISSION H TRANSFER	THEORY + MEL This work
		7.26E+34 -5.67 18932	RING CLOSURE ELIMINATION	
ADD_CH3	REC_CH3_WELL	CH ₃ +C ₆ H ₅ O=CRESOL 1.00E+13 0.00 0	BONDFISSION	CRECK ESTIMATE
	REC_CH3_DECO	CH ₃ +C ₆ H ₅ O→CO+C ₅ H ₅ CH ₃ 5.00E+14 0.00 20000	RECOMBINATION H TRANSFER RING CLOSURE ELIMINATION	CRECK ESTIMATE
ADD_O	REC_O_WELL	C ₆ H ₅ O+O=C ₆ H ₅ O ₂ 8.89E+46 -10.66 13400	BONDFISSION H TRANSFER	THEORY + MEL This work
		C ₆ H ₅ O+O→OC ₆ H ₄ OH 4.06E+62 -15.41 20928		
		3.16E+62 -15.76 16550		
	REC_O_ROPEN	C ₆ H ₅ O+O→C ₅ H ₄ O+HCO 4.67E+16 -1.06 666	BONDFISSION H TRANSFER	THEORY + MEL This work
		3.67E+58 -15.42 11300	RING OPENING	
		C ₆ H ₅ O+O→C ₅ H ₅ +CO ₂ 7.41E+48 -13.24 3635	BETASCISSION ELIMINATION	
		C ₆ H ₅ O+O→FURAN+HCCO 3.21E+09 0.91 -109		
	REC_O_EL_H	C ₆ H ₅ O+O→C ₆ H ₄ O ₂ +H 2.97E+12 0.14 -831	BONDFISSION H TRANSFER	THEORY + MEL This work
		2.15E+15 -0.64 6854	BETASCISSION	
ADD_OH	REC_OH_WELL	OH+C ₆ H ₅ O=CATECHOL 5.05E+51 -11.38 18934	BONDFISSION H TRANSFER	ANALOGY C ₅ -RSR/2
		2.50E+00 -26.79 32059		
	REC_OH_DECO	OH+C ₆ H ₅ O→C ₅ H ₅ OH+CO 7.35E+34 -6.11 21723	BONDFISSION H TRANSFER RING CLOSURE	ANALOGY C ₅ -RSR/2

			ELIMINATION	
ADD_HO2	REC_HO2_EL_OH	HO ₂ +C ₆ H ₅ O→OH+HCO+C ₅ H ₄ O 1.00E+12 0.00 3000 HO ₂ +C ₆ H ₅ O→OH+HCO+2C ₂ H ₂ +CO 1.00E+12 0.00 6000 HO ₂ +C ₆ H ₅ O→OH+H+C ₆ H ₄ O ₂ HO ₂ +C ₆ H ₅ O→OH+OC ₆ H ₄ OH 1-2.00E+12 0.00 8000	BONDFISSION H TRANSFER RING CLOSURE BETACISSION ELIMINATION	ESTIMATE similar to C ₅ -RSR
IPSO	IPSO_OH	OH+C ₆ H ₅ O=OC ₆ H ₄ OH+H 2.85E+32 -5.09 22417 6.95E+29 -4.43 24238	BETACISSION	ANALOGY C ₅ -RSR/2
SPECIES TYPE:	A1O,CH3-RSR	(OC₆H₄CH₃)		
CLASS TYPE	REACTION TYPE	EXAMPLE	ELEM. STEPS	SOURCE
ISOM.	ISOM_CO	OC ₆ H ₄ CH ₃ →HOC ₆ H ₄ CH ₂ 4.63E+01 2.50 23488	H TRANSFER	THEORY This work
SPECIES TYPE:	A1O,OH-RSR	(OC₆H₄OH)		
CLASS TYPE	REACTION TYPE	EXAMPLE	ELEM. STEPS	SOURCE
ADD_O2	REC_O2_EL_OH	O ₂ +OC ₆ H ₄ OH→3CO+OH+C ₃ H ₄ 3.00E+11 0.00 16500 O ₂ +OC ₆ H ₄ OH→2CO+OH +C ₂ H ₂ +CH ₂ CO 3.00E+11 0.00 15000	BONDFISSION H TRANSFER RING CLOSURE ELIMINATION	CRECK ESTIMATE
	REC_O2_EL_HO2	O ₂ +OC ₆ H ₄ OH→2CO+0.7C ₄ H ₄ +0.6C ₂ H ₂ +HO ₂ 1.00E+13 0.00 14000	BONDFISSION ELIMINATION	CRECK ESTIMATE
ADD_O	REC_O_ROPEN	OC ₆ H ₄ OH+O→2C ₂ H ₂ +OH+2CO 4.06E+62 -15.41 20928 3.16E+62 -15.76 16550	BONDFISSION H TRANSFER RING OPENING BETACISSION ELIMINATION	ANALOGY from A1O-RSR
ADD_SELF	REC_DISP_DECO	2OC ₆ H ₄ OH→C ₆ H ₅ C ₂ H ₃ +4CO+2H 3.00E+13 0.00 7000 2OC ₆ H ₄ OH→C ₆ H ₅ C ₂ H+4CO+H ₂ +2H 2.00E+13 0.00 7000	BONDFISSION H TRANSFER RING CLOSURE ELIMINATION ??	CRECK ESTIMATE
SPECIES TYPE:	A1CO-RSR	(C₆H₅CO)		
CLASS TYPE	REACTION TYPE	EXAMPLE	ELEM. STEPS	SOURCE
BETACISS.	BSCISS_CC	C ₆ H ₅ CO→CO+C ₆ H ₅ 5.80E+14 0.00 23000	BETACISSION	CRECK ESTIMATE
ADD_O2	REC_O2_ISOM_O	C ₆ H ₅ CO+O ₂ =C ₆ H ₅ O+CO ₂ 5.00E+10 0.00 0		ESTIMATE from THEORY Zhao 2020 [461]

6.2.2 Growth

This section lists the main reaction classes for the growth from linear species to form aromatic rings as well as the growth of A1 species types to larger PAHs. The structure of the tables, the notation for species types and the rationale for growth class definition are analogous to those of Sections 5.2.2 and 6.2.1 and are therefore not repeated here.

Similarly to Section 5.2.2, Tables 6.8 and 6.9 present the main reaction classes identified for the growth to and from molecular and radical aromatic species, respectively. Growth reaction pathways were not updated with all of the recent literature studies to preserve model simplicity and consistency (as well as for human time limitations). Therefore, the classes listed only provide a general classification for growth pathways to form up to three aromatic rings. Contrary to growth classes presented in Section 5.2.2, A1 species have no ring enlargement reaction classes, as 7-membered rings are not detected as stable species

in fuel-rich sooting flames and therefore are not present in the CRECK mechanism (or are implicitly included as intermediates).

As anticipated in Section 6.2.1, the decomposition of benzene is classified among the growth reactions as [C4.DT-M][ADD_C2.T-M]. The formation of the aromatic ring from linear species occurs via $C_3 + C_3$ or $C_4 + C_2$ reactions. Among these reactions, probably the most relevant to benzene formation in alkene flames are the recombination of propargyl radicals [C3.DD-RSR][REC_C3.DD-RSR] and acetylene addition [ADD_C2.T-M] to C_4 unsaturated species, i.e., C4.DT-M, C4.DD-R, C4.DT-R. These pathways are also relevant decomposition pathways in benzene flames (obviously occurring in the reverse direction). Rate constants for most of these pathways were derived from the literature.

The A1-R species type generally dominates the growth of aromatic rings at combustion temperatures. The growth pathways to indene and naphthalene recently described by Mebel et al. [140] are all included. In particular, rate constants for growth pathways through HACA [A1-R][ADD_C2.T-M] and HAVA [A1-R][ADD_C4.DT-M] derive from literature theoretical calculations. Instead, growth with C_4H_6 to indene [A1-R][ADD_C3.D-M] and naphthalene [A1-R][ADD_C4.D-M] are included from CRECK estimates. It is noted that the former is classified as [ADD_C3.D-M] because only three of the carbon atoms in C_4H_6 contribute to form the 5-membered ring in indene. Finally, among recombination pathways, the [A1-R][REC_C3.DD-RSR] pathway is probably the most interesting due to the high concentration of propargyl radical in flames, together with phenyl recombination to biphenyl [A1-R][REC_A1-R].

In the present version of the CRECK mechanism, all reaction classes considered for the growth of A1 are also applied to growth reactions from larger PAHs in the gas phase, i.e., up to 5 rings. The additional uncertainty of this strong assumption is still unclear, however recent theoretical calculations [58] suggest that the reactivity of 2 and 3-ring PAHs might differ, and that the increasing resonance stabilization for a larger number of rings indeed affects the reactive behavior.

TABLE 6.8: Reaction classes for the growth of CY,X-M species to A1 or from A1,X-M species types. M, R, RSR indicate a molecule, a radical, or a resonantly stabilized radical, respectively, while X indicates a substituent. Colored boxes highlight the reaction classes updated in this thesis. For each example, kinetic parameters of the modified Arrhenius form $k = k_0 T^\alpha \exp(-\frac{E_A}{RT})$ are provided (units cal, mol, cm^3 , s, K, reference pressure of 1 atm for pressure-dependent reactions). For color codes see Table 5.2.

SPECIES TYPE:	C3.D-M	(C ₃ H ₆)	
CLASS TYPE	REACTION TYPE	EXAMPLE	SOURCE
GROWTH-C3	ADD_C3.DD-RSR	$C_3H_3 + C_4H_6 = C_7H_8 + H$ 2.0E+11 0.00 5000	CRECK ESTIMATE
SPECIES TYPE:	C3.DD-M	(C ₃ H ₄)	
CLASS TYPE	REACTION TYPE	EXAMPLE	SOURCE
GROWTH-C3	ADD_C3.DD-RSR	$C_3H_3 + C_3H_4-A = C_6H_6 + H$ 1.40E+12 0.00 10000	CRECK ESTIMATE
	ADD_C3.D-RSR	$C_3H_4-A + C_4H_7-1-3 \rightarrow C_6H_6 + H_2 + CH_3$ 2.00E+12 0.00 18000	CRECK ESTIMATE
SPECIES TYPE:	C4.DT-M	(C ₄ H ₄)	

TYPE:			
CLASS TYPE	REACTION TYPE	EXAMPLE	SOURCE
GROWTH-C2	ADD_C2.T-M	$C_4H_4 + C_2H_2 = C_6H_6$ 4.50E+11 0.00 30010	EXP. ESTIMATE Chanmugathas 1986 [462]
	ADD_C2.D-M	$C_4H_4 + C_4H_4 \rightarrow C_6H_6 + C_2H_2$ 2.50E+14 0.00 44000	CRECK ESTIMATE
	ADD_C2.D-R	$C_2H_3 + C_4H_4 \rightarrow C_6H_6 + H$ 1.00E+12 0.00 6000	CRECK ESTIMATE
SPECIES TYPE:	C4.DD-M	(C₄H₆)	
CLASS TYPE	REACTION TYPE	EXAMPLE	SOURCE
GROWTH-C2	ADD_C2.D-M	$C_4H_6 + C_4H_6 \rightarrow C_6H_5C_2H_3 + 2H_2$ 1.25E+12 0.00 31000 $C_4H_6 + C_4H_6 \rightarrow C_6H_5C_2H_5 + H_2$ 2.00E+12 0.00 36000	CRECK ESTIMATE CRECK ESTIMATE
	ADD_C2.D-R	$C_2H_3 + C_4H_6 \rightarrow C_6H_6 + H_2 + H$ 5.62E+11 0.00 3240	EXP. ESTIMATE Laskin 1996 [382]
	ADD_C2.T-R	$C_2H + C_4H_6 \rightarrow C_6H_6 + H$ 3.00E+11 0.00 8000	CRECK ESTIMATE
SPECIES TYPE:	A1-M	(C₆H₆)	
CLASS TYPE	REACTION TYPE	EXAMPLE	SOURCE
GROWTH_C3	ADD_C3.DD-RSR	$C_3H_3 + C_6H_6 \rightarrow INDENE + H$ 4.00E+11 0.00 19000	CRECK ESTIMATE
	ADD_C3.D-RSR	$C_3H_5-A + C_6H_6 \rightarrow INDENE + H + H_2$ 4.00E+11 0.00 19000	CRECK ESTIMATE
GROWTH_C4	ADD_C4.DD-M	$C_4H_6 + C_6H_6 \rightarrow C_{10}H_8 + H_2 + H + H$ 1.00E+11 0.00 30000	CRECK ESTIMATE
	ADD_C4.DT-R	$C_4H_3 + C_6H_6 \rightarrow C_{10}H_8 + H$ 5.00E+11 0.00 5000	CRECK ESTIMATE
	ADD_C4.D-RSR	$C_4H_7 1-4 + C_6H_6 \rightarrow H + C_{10}H_8 + 2H_2$ 4.50E+11 0.00 6000	CRECK ESTIMATE
GROWTH_C5	ADD_C5-M	$C_5H_6 + C_6H_6 \rightarrow C_{10}H_8 + CH_3 + H$ 2.00E+11 0.00 30000 $C_5H_6 + C_{10}H_8 \rightarrow C_{14}H_{10} + CH_3 + H$ 2.50E+11 0.00 41000	CRECK ESTIMATE CRECK ESTIMATE
	ADD_C5-RSR	$C_5H_5 + C_6H_6 \rightarrow C_{10}H_8 + CH_3$ 2.00E+12 0.00 23000 $C_5H_5 + C_6H_6 \rightarrow INDENE + C_2H_3$ 4.00E+11 .00 19000.	CRECK ESTIMATE CRECK ESTIMATE

TABLE 6.9: Reaction classes for the growth of CY,X-R/RSR species to A1 or from A1,X-R/RSR species types. M, R, RSR indicate a molecule, a radical, or a resonantly stabilized radical, respectively, while X indicates a substituent. Colored boxes highlight the reaction classes updated in this thesis. For each example, kinetic parameters of the modified Arrhenius form $k = k_0 T^\alpha \exp\left(-\frac{E_A}{RT}\right)$ are provided (units cal, mol, cm³, s, K, reference pressure of 1 atm for pressure-dependent reactions).

For color codes see Table 5.2.

SPECIES TYPE:			
CLASS TYPE	REACTION TYPE	EXAMPLE	SOURCE
GROWTH-C3	REC_C3.DD-RSR	$C_3H_3 + C_3H_3 = C_6H_5 + H$ 8.50E+47 -9.98 36800	THEORY Miller 2003 [271]
SPECIES TYPE:	C3.D-RSR	(C₃H₅)	
CLASS TYPE	REACTION TYPE	EXAMPLE	SOURCE
GROWTH-C3	REC_C3.DD-RSR	$C_3H_3 + C_3H_5-A \rightarrow FULVENE + H + H$ 6.23E+38 -7.77 11442	THEORY Miller 2010 [463]

	REC_C3.D-RSR	1.92E+38 -7.53 23903 C ₄ H ₇ 1-3+C ₄ H ₇ 1-3→CH ₃ +H+C ₇ H ₈ +H ₂ 7.50E+11 0.00 0	MEL, tot upper lim. CHECK ESTIMATE
SPECIES TYPE:	C4.DD-R	(C₄H₅)	
CLASS TYPE	REACTION TYPE	EXAMPLE	SOURCE
GROWTH-C2	ADD_C2.T-M	C ₂ H ₂ +C ₄ H ₅ =H+C ₆ H ₆ 1.38E+16 -1.00 8900	THEORY Senosiain 2007 [464]
	REC_C2.T-R	C ₂ H+C ₄ H ₅ →C ₆ H ₆ 1.00E+13 0.00 0	CHECK ESTIMATE
	REC_C2.D-R	C ₄ H ₅ +C ₂ H ₃ =C ₆ H ₆ +H ₂ 1.84E-12 7.07 -3611	EXP. ESTIMATE Laskin 1996 [382]
SPECIES TYPE:	C4.DT-R	(C₄H₃)	
CLASS TYPE	REACTION TYPE	EXAMPLE	SOURCE
GROWTH-C2	ADD_C2.T-M	C ₄ H ₃ +C ₂ H ₂ =C ₆ H ₅ 9.60E+70 -17.77 31300	EXP. ESTIMATE Laskin 1996 [382]
	ADD_C2.D-M	C ₄ H ₃ +C ₂ H ₄ →C ₆ H ₆ +H 5.00E+11 0.00 5000	CHECK ESTIMATE
	REC_C2.D-R	C ₄ H ₃ +C ₂ H ₃ →C ₆ H ₆ 1.50E+13 0.00 0	CHECK ESTIMATE
SPECIES TYPE:	A1-R	(C₆H₅)	
CLASS TYPE	REACTION TYPE	EXAMPLE	SOURCE
GROWTH_C2	ADD_C2.T-M (HACA)	C ₂ H ₂ +C ₆ H ₅ =C ₆ H ₅ C ₂ H ₂ 1.91E+16 -14.50 28610 C ₂ H ₂ +C ₆ H ₅ =C ₆ H ₄ C ₂ H ₃ 1.36E+75 -18.40 40880 C ₂ H ₂ +C ₁₂ H ₇ →C ₁₄ H ₉ 3.00E+12 0.00 6000	THEORY Mebel 2017 [140] THEORY Mebel 2017 [140] CHECK ESTIMATE
	ADD_C2.D-M	C ₂ H ₄ +C ₆ H ₅ =C ₆ H ₅ C ₂ H ₃ +H 2.50E+12 0.00 6190 C ₆ H ₄ C ₂ H+C ₂ H ₄ =C ₁₀ H ₈ +H 4.64E+49 -10.80 46180 1.65E+68 -15.70 55945	CHECK ESTIMATE THEORY Mao 2022 unpublished
GROWTH_C3	ADD_C3.D-M	C ₄ H ₆ +C ₆ H ₅ →INDENE+CH ₃ 5.00E+11 0.00 6000	CHECK ESTIMATE
	ADD_C3.DD-M	C ₃ H ₄ -A+C ₆ H ₅ →INDENE+H 3.00E+12 0.00 5000	CHECK ESTIMATE
	REC_C3.D-RSR	C ₃ H ₅ -A+C ₆ H ₅ →INDENE+2H 5.00E+12 0.00 3000	CHECK ESTIMATE
	REC_C3.DD-RSR	C ₃ H ₃ +C ₆ H ₅ →INDENE 5.00E+12 0.00 3000	CHECK ESTIMATE
GROWTH_C4	ADD_C4.DT-M (HAVA)	C ₄ H ₄ +C ₆ H ₅ →C ₁₀ H ₈ +H 1.26E+04 2.61 1430	THEORY Aguilera 2007 [465]
	ADD_C4.DD-M	C ₄ H ₆ +C ₆ H ₅ →C ₁₀ H ₈ +H+H ₂ 5.00E+11 0.00 6000	CHECK ESTIMATE
	REC_C4.DD-R	C ₄ H ₅ +C ₆ H ₅ →C ₁₀ H ₈ +H+H 5.00E+12 0.00 1000	CHECK ESTIMATE
GROWTH_C5	ADD_C5-M	C ₅ H ₆ +C ₆ H ₅ →C ₁₀ H ₈ +CH ₃ 1.00E+12 0.00 8000	CHECK ESTIMATE
	REC_C5-RSR	C ₅ H ₅ +C ₆ H ₅ →C ₁₀ H ₇ CH ₃ 2.00E+12 0.00 3000	CHECK ESTIMATE
GROWTH_C6	ADD_A1-M	C ₆ H ₅ +C ₆ H ₅ C ₂ H →C ₁₄ H ₁₀ +H 1.00E+12 0.00 8000	CHECK ESTIMATE
	REC_A1-R	C ₆ H ₅ +C ₆ H ₅ =BIPHENYL 7.34E+20 -2.33 4125 C ₆ H ₅ +CH ₃ C ₆ H ₄ →FLUORENE+H+H 5.00E+12 0.00 0	THEORY Tranter 2010 [466] CHECK ESTIMATE
SPECIES TYPE:	A1CH2-RSR	(C₇H₇)	
CLASS TYPE	REACTION TYPE	EXAMPLE	SOURCE
GROWTH_C2	ADD_C2.T-M	C ₇ H ₇ +C ₂ H ₂ →INDENE+H 2.92E+22 -3.24 15073	THEORY Mao 2021 [322]

			+ MEL
GROWTH_C3	ADD_C3-DD-M	$C_3H_4-P + C_7H_7 \rightarrow INDENE + CH_3$ 3.00E+12 0.00 18000	CRECK ESTIMATE
GROWTH_C5	ADD_C5-M	$RXYLENE + INDENE \rightarrow C_{16}H_{10} + 2H_2 + CH_3$ $C_5H_6 + C_7H_7 \rightarrow BIPHENYL + H_2 + H$ 4.00E+11 0.00 19000	CRECK ESTIMATE
	REC_C5-RSR	$C_5H_5 + C_7H_7 \rightarrow BIPHENYL + H + H$ 5.00E+11 0.00 6000 $C_5H_5 + C_7H_7 \rightarrow C_{12}H_8 + H_2 + H + H$ 2.00E+12 0.00 7000	CRECK ESTIMATE CRECK ESTIMATE
GROWTH_C6	ADD_A1-M	$C_6H_6 + C_7H_7 = C_6H_5CH_2C_6H_5 + H$ 4.00E+11 0.00 19000	CRECK ESTIMATE
	REC_A1-R	$C_6H_5 + C_7H_7 = C_6H_5CH_2C_6H_5$ 2.00E+12 0.00 3000	CRECK ESTIMATE

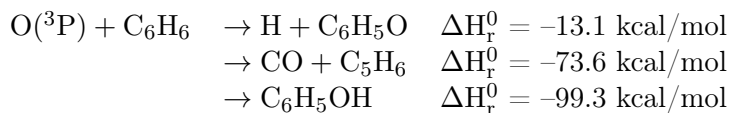
6.3 Theoretical calculations

6.3.1 $\text{C}_6\text{H}_6 + \text{O}({}^3\text{P})$

6.3.1.1 Literature review

The addition of atomic oxygen to the benzene ring is an essential benzene oxidation pathway, especially at low temperatures and lean conditions [127]. Compared to substituted aromatics, in the case of benzene the high C–H bond strength favors addition reactions over H-atom abstraction reactions. Hence, is more sensitive to $\text{O}({}^3\text{P})$ addition in benzene than in substituted MAHs. This reaction pathway was also highlighted as an effective step PAH and soot oxidation mechanisms [467].

The addition of $\text{O}({}^3\text{P})$ to the benzene ring is challenging to study theoretically. In fact, while the addition occurs on the triplet state, the resulting adduct may undergo intersystem crossing to the singlet state [468], [469]. The final reaction products can be rationalized in terms of two main pathways: chain branching to the phenoxy radical and atomic hydrogen (occurring mostly on the triplet surface but also possibly on the singlet surface), and termination, leading to either phenol or cyclopentadiene and CO [468], [470]:



The competition between termination and branching impacts the concentration of radicals in the reaction environment, thus affecting significantly the reactivity of the system. However, the quantitative reaction parameters and channel branching fractions in the literature [468], [469], [471] are in poor agreement. In particular, the relative importance of the branching and termination channels has been widely controversial. Crossed molecular beam work suggested that the major pathway leads to the formation of $\text{H} + \text{C}_6\text{H}_5\text{O}$ [472], while a recent combined experimental and theoretical work suggests that at about 1000–1200 K the chain termination dominates [468]. It should be noted though that, because of the complexity of the experiments [468], the error bars of the measured branching fractions are rather high. Theoretically, the system reactivity was recently investigated in two studies [468], [469]. However, in both cases the extent of ISC was included in the models only indirectly, and the corresponding rate was tuned to match the experimental estimates.

Additionally, despite the fact that the theoretical and experimental investigation of spin-forbidden reactions has been a rich and active theoretical and experimental research subject in the past decades, there is a need to identify model systems that can be used to check the quality of the theoretical and experimental approaches developed to study them. The $\text{O}({}^3\text{P}) + \text{C}_6\text{H}_6$ reaction has the possibility of becoming one such model system, as benzene is the simplest aromatic species and the number of reaction channels is limited.

In this framework, this study determines at a high level of accuracy channel-specific rate constants for the title reaction including explicitly, for the first time, ISC kinetics in the theoretical model by coupling AI-TST-ME with non adiabatic transition state theory (NA-TST), as described in Section 3.3.2.6 and reference [200]. The theoretical results are

compared with new CMB experiments reported in detail in dedicated publications [255], [473]. The contribution of the author of this thesis to this study was mostly the identification of guess geometries for the MECP(s) and final ME simulations of the full system. This section discusses the triplet PES region and the ISC, while Section 6.3.2 describes the complex singlet PES leading to termination channels, which is also a subject of debate in the literature.

6.3.1.2 Theoretical Methodology

Structures and vibrational frequencies on the triplet PES were determined using density functional theory at the unrestricted ω B97X-D/6-311+G(d,p) level, energies of saddle points at the CASPT2/aug-cc-pVTZ level, and energies of wells at the CCSD(T)/aug-cc-pVTZ level, using DF-MP2/aug-cc-pVQZ – DF-MP2/aug-cc-pVTZ level corrections for basis size effects (CCSD(T)/CBS).

The addition of atomic oxygen on the aromatic ring and the ejection of the H atom from the adduct included both $3A'$ and $3A''$ states. The energy difference between them was determined at the CASPT2/aug-cc-pVTZ level using a (10e,9o) active space, consisting of the (4e,3o) p electrons and orbitals of oxygen and of the 3 π and π^* bonding and anti-bonding orbitals of benzene (6e,6o). A 0.25 IPEA shift was used for all CASPT2 calculations. The same theoretical approach also proved successful in the study of the $O(^3P) + 1-C_4H_8$ reaction, with stationary point energies usually within 1 kcal/mol or better with respect to those determined using CASPT2 geometries and larger active spaces [474].

For the MECP, a (8e,7o) active space, state averaged over two states, was used to determine the CASSCF wave function adopted to compute Spin-Orbit coupling energies. The (8e,7o) AS consisted of the two unpaired electrons and orbitals (2e,2o), of the two π and π^* bonding and anti-bonding orbitals of benzene (4e,4o), and of the oxygen lone pair (2e,1o).

Structure and vibrational frequencies of stationary points on the singlet PES were determined at the same level of theory as the triplet PES, using a restricted wavefunction. The TS connecting the benzoxide intermediate (W7) formed upon ISC to the rest of the singlet PES (described in Section 6.3.2) was found to have a strong multireference character. Its energy was determined at the CASPT2/aug-cc-pVTZ level using a (12e,11o) AS, consisting of the (4e,3o) p electrons and orbitals of oxygen, the 3 π and π^* bonding and anti-bonding orbitals of benzene (6e,6o), and the σ and σ^* bonding and anti-bonding orbitals of the C–C bond of the benzoxide 3-membered ring (2e,2o). The treatments of the other MR channels of the PES for phenol decomposition are described in Section 6.3.2.

The rate of ISC between triplet and singlet PESs was determined using NA-TST [99], [257], [259]. As explained in Section 3.3.2.6, the determination of MECPs between two PESs can be formulated in terms of minimization of the energy on a PES under the constraint that the energies of both PESs are equal. This constrained local minimum search was performed from a manually selected guess, then interfacing EStokTP to NLopt, an open source library for non-linear optimization (<http://github.com/stevengj/nlopt>). MECPs were determined using energies and analytical gradients evaluated at the ω B97X-D/6-311+G(d,p) level using an unrestricted formalism for the triplet PES and both unrestricted and restricted formalisms for the singlet PES. MECPs were searched between both triplet $3A'$ and $3A''$ PESs

and the singlet ground state. Optimizations were started from the structure of the triplet adduct and converged within about 50 steps, with an accuracy of 10^{-10} Hartrees using 10^{-4} tolerances. SOCs were then evaluated at the MECPs [475] (see Section 3.3.2.6). Vibrational frequencies at the MECP were computed using the Hessian suggested by Harvey et al. [257], after projection of rotational and translational motions, as well as of the motion along the reaction coordinate.

Master equation simulations were performed using a single exponential down model, with the same average collision downward energy transfer ΔE_{down} parameter of $260(\frac{T}{300})^{0.875}$ (recommended by Klippenstein and Cavallotti [200]) used in the ME investigation of phenol decomposition (Section 6.3.2). ME simulations were performed with the MCRRKM code of Barbato et al. [107]. The termination threshold for Monte Carlo simulations was 10^4 reactive events.

The main computational uncertainties are related to the estimation of energy barriers for reactions with multireference character, the estimation of the rate constant for ISC, and the parameters used in the ME simulations (see Section 3.5.2). The computational uncertainty related to the estimation of the rate of ISC crossing is due to the fact that a thorough assessment of the level of accuracy of NA-TST theory coupled with Landau-Zener estimation of ISC probabilities is presently missing. The many parameters that must be accurately determined to calculate the crossing rates, such as the energy barrier at the MECP, the ZPE, the SO coupling energy, and the fact the ISC is considered only at the MECP, and not along other non stationary points on the crossing seams, suggests that the uncertainty factor may be large (a factor of 10 or more). However, the success of the theoretical methodology adopted in the determination of ISC rates for analogous system suggests that the uncertainty of the calculated ISC rate is about a factor of 3, as larger values would lead to a very poor fit of experimental evidences. Finally, there is also uncertainty about the ΔE_{down} parameter used in ME simulations. In particular it is interesting to notice that a smaller ΔE_{down} (and a higher ISC rate) would improve the agreement between the predictions of the present calculations and the product branching fractions measured by Taatjes et al. [468].

6.3.1.3 PES and entrance channel rate constant

The triplet $\text{C}_6\text{H}_6\text{O}$ PES and a portion of the singlet PES are shown in Figure 6.3. The reactivity on the triplet PES is controlled by a limited number of reactions. The addition of $\text{O}(^3\text{P})$ to benzene leads to the formation of a $\text{C}_6\text{H}_6\text{O}$ adduct W1-T of C_5 symmetry having two close lying $3A'$ and $3A''$ electronic states. W1-T can then decompose to $\text{C}_6\text{H}_5\text{O} + \text{H}$, perform ISC to the singlet PES, or decompose back to reactants. Each one of these reactions can take place either on the $3A'$ or $3A''$ PES.

It was found that the T1 ground state of the entrance well has $3A'$ symmetry, and that the energy gap with the T2 $3A''$ state is 4.2 kcal/mol, slightly smaller than the 5.2 kcal/mol and 6.1–6.9 kcal/mol energy gaps determined by Nguyen et al. [469] and Taatjes et al. [468], respectively. The energy barriers for $\text{O}(^3\text{P})$ addition are 3.8 and 4.5 kcal/mol on the $3A'$ and $3A''$ PESs, which are similar to the energy barriers determined in ref. [469] (4.1 and 4.3 kcal/mol) and smaller than the 5.7 kcal/mol found in ref. [468].

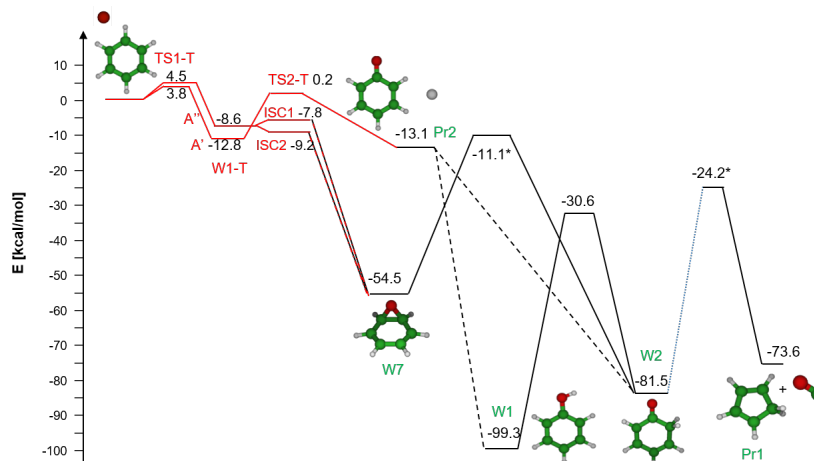


FIGURE 6.3: Potential energy surface for the $O(^3P) + C_6H_6$ reaction. Energies marked with * were computed at the CASPT2/aug-cc-pVTZ level. The triplet PES is highlighted in red and the corresponding stationary points are labeled as -T, while the main channels for the singlet PES are highlighted in black (the full singlet PES is described in Section 6.3.2). Dashed lines highlight barrierless channels and blue dotted line indicates multiple steps (the TS depicted is the rate determining one).

The calculated total addition rate constant is compared with selected experimental data in Figure 6.4. The largest discrepancy is a factor of 1.4 at 1300 K from the experimental data of Ko et al. [471], while the agreement with the results of Nicovich et al. [390] is quantitative. The agreement is good also with the total rate constants evaluated in previous theoretical studies [468], [469], even though they only considered the $3A'$ PES. However, Fig. 6.4 shows that the contribution of the reaction flux on the $3A''$ PES cannot be neglected, especially above 1000 K. Decomposition of W1-T to phenoxy + H through TS2-T (see Figure 6.3) requires the overcoming of a barrier of 13.0 kcal/mol on the $3A'$ PES, while the barrier for this channel on the $3A''$ PES is much higher [469] and was therefore not investigated.

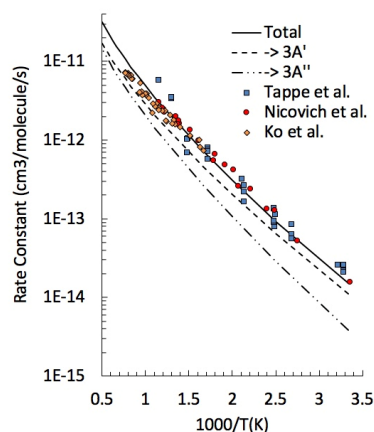


FIGURE 6.4: Total rate constant for the reaction of $O(^3P)$ addition to C_6H_6 calculated in this work compared with selected literature experimental data of Tappe et al. [476] (270–850 Torr in He), Nicovich et al. [390] (100 Torr in Ar), and Ko et al. [471] (180–450 Torr in Ar). The separate contributions of the $3A'$ and $3A''$ entrance channels are also reported as dashed and dot-dashed lines, respectively.

6.3.1.4 ISC and comparison with experimental results

The use of the restricted and unrestricted wavefunctions for the singlet PES leads to the optimization of two different MECPs for the $3A''$ state. The optimized MECP structures and the calculated SOCs are shown in Figure 6.5a. The T1/S0 structure (1) has C_S symmetry and a 101° O–C–H angle, characteristic of this electronic state [468]. The calculated SOC is very small (0.6 cm^{-1}), indicating that the contribution to reactivity of this pathway is negligible. The T2/S0 structures (2) and (3) have larger O–C–H angles and C–O distances than the T1/S0 MECP, and much larger SOCs of $\sim 35\text{ cm}^{-1}$. The difference in geometries and SOCs is related to the difference between the $3A'$ and $3A''$ electronic structures, and in particular to the different filling of the oxygen in-plane and out-of-plane lone pairs. In fact, in the $3A''$ state the in-plane oxygen lone pair is doubly occupied, hence the resulting repulsion increases the O–C–H angle and therefore SOC. The two T2/S0 structures differ in their symmetry. The T2/S0 C_1 structure, determined using a restricted wave function for the singlet state, has the O atom displaced from the symmetry plane towards the nearest C atom of the phenyl ring. Geometric considerations suggest that the $3A''$ triplet adduct is connected through the T2/S0 C_1 MECP (ISC2) to singlet benzene oxide (W7 of the PES in Figure 6.3), and through the T2/S0 C_S MECP (ISC1) to a singlet diradical.

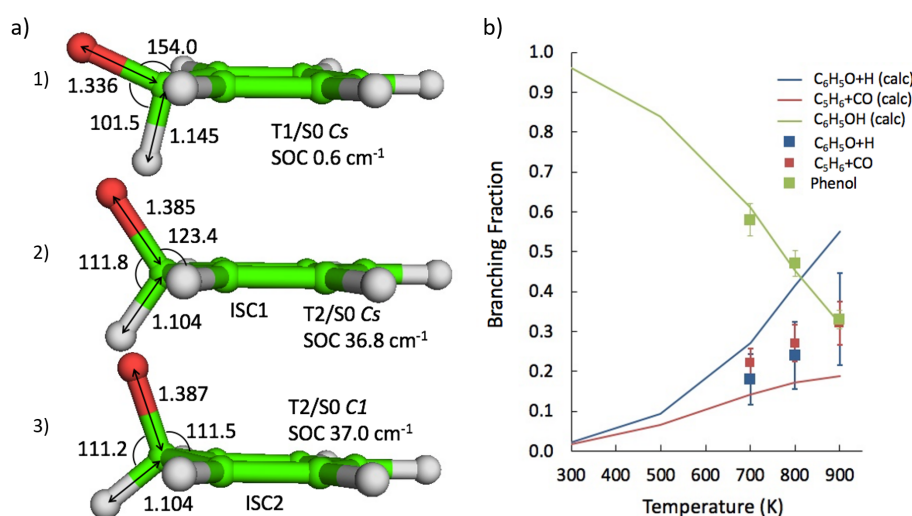


FIGURE 6.5: a) Triplet-singlet MECP geometries and corresponding SOCs (distances in Å, angles in $^\circ$), and b) comparison between branching fractions calculated using ME simulations at 4 Torr and 300–900 K and experimental data measured in a flow reactor [468].

The energies of the ISC1 and ISC2 MECPs are 5.0 and 3.6 kcal/mol above that of W1-T, respectively. Notably, the energy of ISC2 is slightly lower than that of the $3A'$ W1-T well, which is a result of the smaller ZPE corrections for the MECP, while the electronic energy is, as expected, slightly higher. Between the MECPs found, ISC1 has larger ISC rates despite the higher energy. In fact, in the Landau-Zener formula (3.42) the ISC probability shows exponential dependence on the off-diagonal spin-orbit coupling elements (H_{SO} , similar for ISC1 and ISC2) and on the relative slope of the triplet and singlet PESs at the MECP (ΔF). This last term was determined as the difference of the norms of the gradient determined in mass-weighted Cartesian coordinates at the MECP on the singlet and the triplet PESs. ISC2

has considerably larger gradients than ISC1 because of the significant displacement from the minimum energy configuration. Therefore, the C_{LZ} of Eqn. (3.42) decreases significantly from 0.298 cm^{-1} for ISC1 to 0.078 cm^{-1} for ISC2.

The reactivity on the singlet PES shown in Figure 6.3 is more complex than on the triplet PES, even though there are only two exit channels: decomposition to $\text{C}_6\text{H}_5\text{O} + \text{H}$ and to $\text{C}_5\text{H}_6 + \text{CO}$. A detailed analysis of the singlet PES is provided in Section 6.3.2. The only additional channel considered here is the formation of benzene oxide (W7), which is then converted to 2,4- $\text{C}_6\text{H}_6\text{O}$ (2,4-cyclohexadienone). 2,4- $\text{C}_6\text{H}_6\text{O}$ then may isomerize to $\text{C}_6\text{H}_5\text{OH}$ (W1), or decompose to either $\text{C}_6\text{H}_5\text{O} + \text{H}$ or $\text{C}_5\text{H}_6 + \text{CO}$.

The derivation of the product branching fractions with the MCRRKM code was initially performed for the flow reactor of Taatjes et al. [468], who measured the branching fractions of this reaction at 300–900 K and 1–10 Torr. The comparison between the calculated and experimental BFs measured by Taatjes et al. is shown in Figure 6.5b. There is good agreement between the predicted and measured $\text{C}_6\text{H}_5\text{OH}$ BF, while the yields of the $\text{C}_5\text{H}_6 + \text{CO}$ and $\text{C}_6\text{H}_5\text{O} + \text{H}$ channels are slightly underestimated and overestimated, respectively. However, the difference from the bounds of the experimental uncertainties is not large, with maximum deviations in the BF of <0.06 at 900 K, easily accounted for by considering computational uncertainties. One interesting result from the present simulations is that the $\text{C}_6\text{H}_5\text{O} + \text{H}$ channel has contributions from both the triplet and singlet PES. In particular, at 4 Torr and 800 K the ratio of the triplet to singlet contributions to formation of $\text{C}_6\text{H}_5\text{O} + \text{H}$ is about a factor of 2, as highlighted in Table 6.10. This means that the extent of ISC is still large (above 50%) at 1100 K, a temperature at which benzene oxidation experiments are typically conducted [359], [387]. Hence, the $\text{C}_6\text{H}_6 + \text{O}(^3\text{P})$ system and therefore benzene combustion properties are strongly affected by quantum effects.

As anticipated, this work also includes comparison with new CMB experiments. These were performed specifically for the validation of the theoretical results, using mass-spectrometric detection and time-of-flight analysis at a collision energy $E_c = 8.2 \text{ kcal/mol}$, similarly to recent successful experiments for reactions of $\text{O}(^3\text{P})$ with a variety of aliphatic unsaturated hydrocarbons [250], [258], [474], [475], [477]–[479]. Details of the experiments can be found in the dedicated publication [255]. The methodology for the derivation of experimental product branching fractions from CMB experiments is described in detail in [478].

The experimental product BFs are reported in Table 6.10, together with selected thermal data measured in conditions where the BF for the $\text{C}_5\text{H}_6 + \text{CO}$ channel is comparable. The present experimental results confirm that $\text{C}_6\text{H}_5\text{O} + \text{H}$ is partly produced from the direct adiabatic reaction of $\text{O}(^3\text{P})$ on the triplet PES ($\text{BF} = 0.48 \pm 0.14$) and partly from the non-adiabatic reaction via ISC to the singlet PES ($\text{BF} = 0.18 \pm 0.06$), with a total BF of $\text{C}_6\text{H}_5\text{O} + \text{H}$ of 0.66 ± 0.20 . The ME and experimental CMB results are in reasonable agreement, although the computational predictions underestimate the $\text{C}_6\text{H}_5\text{O} + \text{H}$ experimental BF, falling, however, within the lower end of the experimental uncertainty. Notably, the ME simulation overestimates the experimental thermal data at 800 K. This means that any modification of the ME simulation parameters that would lead to an improvement of the

agreement with CMB data would also lead to a worsening of the predictions of the thermal data, thus suggesting that the present ME kinetic simulations offer a reasonable compromise for the interpretation of both experiments. The ME simulations confirm the pronounced pressure dependence found by Taatjes et al. [468]. This is mostly determined by the reactivity on the singlet PES as the ISC is fast, with an average lifetime on the triplet surface of about 10 ps (7 ps at 800 K). Also, the theoretical results confirm that the dominant product at 10 Torr is phenol, as suggested by Taatjes, who could not, however, rule out minor contributions from other isomers. The present theoretical calculations find that at 800 K and 4 Torr about 5% of 2,4-C₆H₆O (W2) is produced from collisional stabilization.

TABLE 6.10: History of the branching fractions of the O(³P) + C₆H₆ reaction and present experimental and theoretical estimates.

Product channel	Sibener et al. [472] CMB	Taatjes et al. [468] 800 K, 4 Torr	This work ME/ 800 K, 4 Torr	New CMB [255]	This work ME/CMB
C ₆ H ₅ O + H (triplet) (singlet via ISC)	major	0.24±0.10	0.40 (0.26) (0.14)	0.66±0.20 (0.48±0.14) (0.18±0.06)	0.52 (0.22) (0.30)
CO + C ₅ H ₆ (singlet via ISC)	≤5%	0.27±0.06	0.16	0.32±0.16	0.48
C ₆ H ₅ OH (singlet via ISC)	small	0.47±0.07	0.44	0.02±0.01	0.0

Table 6.11 reports the rate constants calculated in this work and implemented in the CRECK mechanism. Phenomenological rate constants were lumped using MEL, such that unstable intermediates are implicitly included in the lumped rate constants. It is noted that phenol also includes the 2,4-C₆H₆O isomer, as explained more extensively in Section 6.3.2.

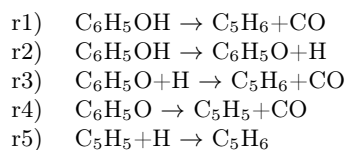
TABLE 6.11: Fits of the modified Arrhenius expressions $k = k_0 \cdot T^\alpha \cdot \exp\left(-\frac{E_A}{RT}\right)$ for the rate constants of O(³P) addition to benzene. Pressure dependent reaction parameters are provided in PLOG form, units are cm³, mol, s, cal, atm, K. Fitting quality and temperature range are also provided.

Reaction	<i>p</i>	<i>k</i> ₀	α	<i>E</i> _A	<i>R</i> ²	<i>T</i> Range
C ₆ H ₆ + O → C ₆ H ₅ O + H	0.01	2.88E+08	1.68	6522	1.00	300–2200
	1	4.76E+07	1.91	6209	1.00	300–2200
	10	3.39E+08	1.66	6704	1.00	300–2200
	100	2.56E+09	1.41	7478	1.00	300–2200
C ₆ H ₆ + O → CO + C ₅ H ₆	0.01	6.29E+18	-1.77	11232	0.98	300–2200
	1	1.45E+32	-5.44	24217	1.00	700–2200
	10	8.16E+34	-6.05	33005	0.98	800–2200
	100	2.89E+49	-9.85	55232	0.99	1200–2200
C ₆ H ₆ + O → C ₆ H ₅ OH	0.01	1.63E+16	-6.73	-14031	0.98	300–2200
	1	2.48E+14	-0.78	3522	0.98	300–2200
	10	3.01E+17	-1.58	5066	1.00	300–2200
	100	1.68E+17	-1.35	5515	1.00	300–2200
DUPLICATE	0.01	4.30E+35	-6.92	13025		
	1	1.03E+48	-10.4	21217		
	10	2.16E+36	-6.88	16364		
	100	6.00E+38	-7.6	18628		

6.3.2 C₆H₅OH and C₆H₅O decomposition

6.3.2.1 Literature review

Phenol molecular decomposition is one of the most sensitive reactions in benzene oxidation and the most sensitive reaction in phenol pyrolysis. Section 6.1.2 anticipated that the main decomposition pathway of phenol is still debated in the literature. Flow reactor experiments of Lovell et al. [126], Manion and Louw [415], and Brezinsky et al. [125] and ST experiments of Horn et al. [132] were unable to reach an agreement on whether phenol decomposition occurs directly or through a sequence of steps involving initial bond-fission, as both pathways seem to result in equal accordance with experimental data:



where r1, r2+r3, r2+r4+r5 all result in the same global decomposition reaction. Hence, all experimental studies presented different estimates for the rate constants r1-r3 depending on the chosen reaction steps. More recently, Scheer et al. [429] combined theoretical calculations with experiments in a microtubular reactor at 475–1575 K, where they detected the product species with photoionization mass spectroscopy and matrix isolated infrared spectroscopy. They were able to confirm the relevance of the enol/keto tautomerization of phenol to 2,4-C₆H₆O, the first intermediate of phenol molecular decomposition (r1), and they found that the radical decomposition pathway (r2+r3) is of minor importance in the investigated temperature range, as also stated by Horn et al. [132].

Theoretical calculations shed light on the elementary steps of phenol molecular decomposition. The first reconstruction of the PES by Zhu and Bozzelli [480] at the CBS-QB3 level highlighted that 2,4-C₆H₆O may stabilize in the absence of radical reactivity. This intermediate further isomerizes to the meta conformer and eventually forms cyclopentadiene via 3/5-membered ring closure and successive decarbonylation. Xu and Lin [481] investigated the PES at the more accurate G2M//B3LYP/6-311G(d,p) level of theory, revealing that the rate determining step for r1 is the decarbonylation, with a barrier of about 75 kcal/mol. They computed pressure dependent rate constants for r1-2 using RKKM theory and microcanonical VTST for barrierless reactions at $T = 800\text{--}2000$ K and $p = 0.001\text{--}100$ atm, obtaining good agreement with [132] for r1 and strong disagreement (one order of magnitude) with [126] for r2. The following experimental and theoretical study of Scheer et al. [429] highlighted that this discrepancy might be due to the missing channels of H recombination with phenoxy to form 2,4-C₆H₆O and 2,5-C₆H₆O. However, this latter study only provided approximate rate constants (CBS-QB3 PES, QRRK rate constants with no variational effects). Finally, none of the theoretical studies considered the well-skipping channel r3, which was instead found to be relevant in kinetic simulations of phenol pyrolysis and benzene oxidation. Overall, despite the experimental and theoretical modeling efforts to determine the kinetics of phenol decomposition, some aspects of reactions r1-3 are still not fully understood.

The decomposition of phenoxy radical *r4* is key not only to phenol decomposition, but it is also the main connection between aromatic and C_5 intermediates in benzene oxidation. *r4* proceeds via a bicyclic intermediate that forms a 2,4-cyclopentadiene carbonyl radical which decarbonylates, similar to phenol. The first theoretical study of Olivella et al. [482] determined the PES at the CASPT2/6-31+G(d,p)//CASSCF/6-31G(d) level of theory, showing that the decarbonylation step controls the reactivity. The first pressure-dependent theoretical study by Liu et al. [483] revealed a significant pressure dependence of the decomposition kinetics, thus explaining the difference between the 60 kcal/mol of activation energy theoretically determined and the 44 kcal/mol experimentally estimated at atmospheric pressure. The effect of pressure was further analyzed by Carstensen et al. [484], who investigated the PES at the CBS-QB3//B3LYP/6-311G(2d,p) and CBS-QB3//QCISD/6-31G(d) levels with MP2 extrapolations to the complete basis set limit and computed rate constants with ME solvers that implement QRRK and RRKM theories. This study concluded that the discrepancies between the values of the experimental datasets cannot simply be explained as an effect of slightly different pressures, however no final indication was provided on the most reliable rate constant. Finally, the most recent theoretical rate constant from Shu et al. [430] at G4 level of theory agrees well with their own experimental data and is about twice the value proposed by Frank et al. [303] and Carstensen et al. [484]. In all the mentioned theoretical studies, the temperature range of the theoretical calculations was relatively narrow (900 – 1600 K), resulting in unreliable predictions when the rate constant is extrapolated. In conclusion, none of the theoretical rate constants computed is accurate enough to be safely implemented in kinetic models to be used in a wide range of operating conditions, if the target uncertainty is less than a factor of 2.

6.3.2.2 Theoretical Methodology

The rate constants of the selected reaction pathways were computed with AI-TST-ME using EStokTP (Section 3.4.1), at the level of theory described in Section 6.3.1.

Rate constants for the three H-loss barrierless decomposition pathways were evaluated using VTST, determining structures and harmonic frequencies along the minimum energy path at the ω B97X-D/6-311+G(d,p) level and energies at the CASPT2 level. The selected AS included (8e,8o), namely the 6 π and π^* bonding and anti-bonding orbitals of the aromatic ring, and the σ and σ^* bonding and anti-bonding orbitals of the breaking bond (O–H for phenol, and C–H for 2,4- C_6H_6O and 2,5- C_6H_6O). The energies along the MEP were computed with respect to $C_6H_5O + H$, with the H atom positioned at 10 Å from the oxygen atom in the case of phenol and from the carbon atom in the case of 2,4- C_6H_6O and 2,5- C_6H_6O .

Despite the fact that no stationary point exhibited a T1 diagnostic larger than the reference thresholds (Section 3.1.3.2 and 3.1.3.3), MR methods proved necessary to study properly the concerted decarbonylation step of the molecular decomposition of phenol. In particular, this was revealed by the total atomization energy (%TAE), the M diagnostic (based on the occupation of the frontier orbitals), and C02 diagnostic (where C0 is the coefficient of the Hartree-Fock determinant in the multi-configuration expansion) [485], [486]. More details

about the different types of diagnostics are provided in the results. The geometry and the vibrational frequencies of the TS were computed at the CASPT2/aug-cc-pVTZ level with an active space of (6e,6o), whereas for the calculation of the energies the selected active space was increased to (12e,11o). The energy change from the (6e,6o) to the (12e,11o) AS was smaller than 0.5 kcal/mol, indicating that the AS is converged with the system size. The smaller AS included the σ and σ^* bonding and anti-bonding orbitals of the CO detaching moiety (4e,4o), and the C–C bond between the 5-membered ring and the 3-membered ring (2e,2o). In the larger AS, the electrons of the π orbitals on the ring and the forming C–O π bond were also added (6e,5o). Calculations were performed using an IPEA shift of 0.25. The energy barrier was computed with respect to the reactant, optimized at the same level of theory.

Torsional motions were treated according to the 1DHR approximation (Section 3.2.2), and the rotation potential was computed scanning the torsional angle with 20° intervals. For all reaction channels, intrinsic reaction coordinate calculations were performed, taking 10 steps of 0.02 Å along the MEP in the direction of both reactants and products (Section 3.3.2.2).

The rate constants for the reaction pathways investigated were computed in the 300–2500 K temperature and 0.1–100 atm pressure ranges using MESS. Collisional energy transfer parameters were already described (Section 6.3.1). The phenomenological rate constants obtained were lumped using MEL [291], as extensively reported in Chapter 4. The lumping allowed to preserve only chemical species already present in the CRECK kinetic mechanism. For the phenol PES, the lumped C₆H₅OH pseudospecies also contains a fraction of the 2,4-C₆H₆O and 2,5-C₆H₆O isomers. On the other hand, in the PES for phenoxy decomposition C₆H₅O and o-C₆H₄OH were lumped together. In this case, the fraction of o-C₆H₄OH is negligible as it rapidly isomerizes to C₆H₅O. On the other hand, the m-C₆H₄OH and p-C₆H₄OH isomers were lumped together as C₆H₄OH. All the other intermediate wells of both PESs were implicitly included in the reactivity. The composition of pseudospecies was also made to be consistent with the rest of the mechanism: for instance, H-atom abstractions from C₆H₅OH producing C₆H₅O and o-C₆H₄OH (Section 6.4) were included as duplicate reactions producing the same pseudospecies.

6.3.2.3 PESs and rate constants

The PES for phenol decomposition is shown in Figure 6.6. The investigated reaction channels were limited to those found to contribute significantly to the reactivity in previous theoretical studies [429], [480], [481].

The initial reactivity of phenol is controlled by the competition between isomerization to 2,4-cyclohexadienone (W2), with an energy barrier of 68.7 kcal/mol, and dissociation to phenoxy radical + H (Pr2). The O–H bond dissociation energy (BDE) was predicted to be 86.2 kcal/mol at 0 K, in excellent agreement with the dissociation energy of 86.5 ± 0.4 kcal/mol calculated from the ATcT tables [117]. 2,4-C₆H₆O lies 17.9 kcal/mol above C₆H₅OH, consistent with the 18.7 kcal/mol value determined by Zhu and Bozzelli at the CBS-Q// B3LYP/6-31G(d,p) level using isodesmic reactions [480]. W2 can undergo C–H

bond-fission to $C_6H_5O + H$, isomerize to W3, or form an unsaturated ketene (W5) through ring opening. W3 is particularly unstable due to its diradical nature, and rapidly isomerizes to either W4 or 2,5- C_6H_6O (W6). W6 lies only 16.4 kcal/mol above W1, and is about 1 kcal/mol more stable than W2, similar to what was found by Xu and Lin [481] and by Scheer et al. [429]. The energy barrier between W3 and W4 is 0.7 kcal/mol smaller than that to W6. However, the latter channel is entropically favored, such that W6 is expected to contribute significantly to the formation of phenoxy radical, as already indicated by Scheer et al. [429]. While Xu and Lin proposed that W5 can decompose directly to cyclopentadiene and CO [481], in the present study a saddle point with a similar structure (TS10) was found to connect, as determined through an IRC analysis, W5 to W4, where the formation of W4 is limited by the high energy barrier. Finally, W4 decarbonylates to $C_5H_6 + CO$. As found by Xu and Lin [481], two different transition states for the final decarbonylation step were identified, indicated as TS4 and TS11 in Figure 6.6. The lower-lying TS4 contributes the most to the formation of CO. The CCSD(T)/CBS energy of TS4 is 78.7 kcal/mol, thus significantly higher than the 74–76 kcal/mol determined by Xu and Lin and by Scheer et al. [429], [481].

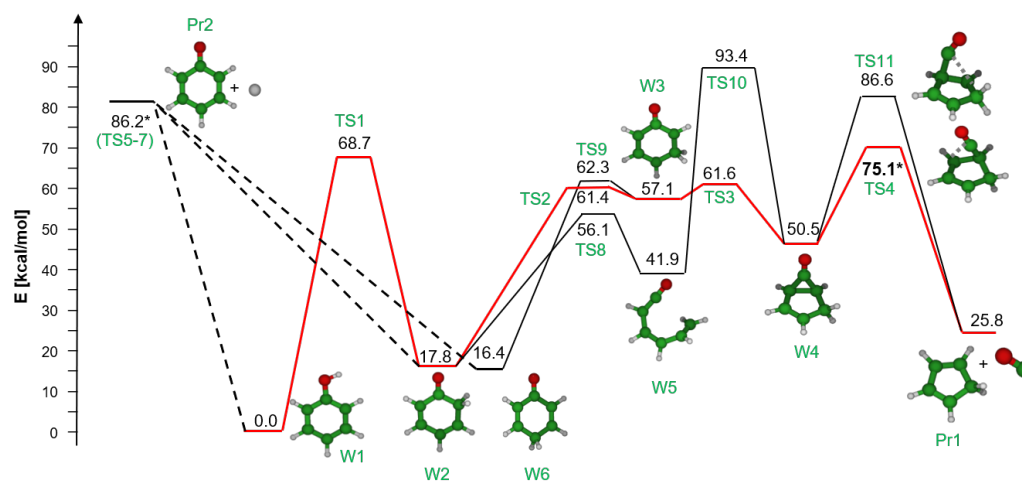


FIGURE 6.6: PES for phenol decomposition. The energies include ZPEs. * indicates MR energies. The main channels, marked in bold, are homolytic decomposition to phenoxy radical (black dashed) and molecular decomposition to $CO + C_5H_6$ (red).

W4 decomposition to cyclopentadiene is a concerted reaction, where the formation and disruption of bonds takes place contextually in a single step, as in Diels-Alder reactions. Often these reactions exhibit a significant multireference character. Hence, a thorough MR diagnostics analysis was performed, similar to that by Grambow et al. [487] which follows the recommendation listed by Jalan et al. [488]. The results are summarized in Table 6.12.

The B1 diagnostic [489] is based on the energy difference obtained with B1LYP and BLYP and is computed as $(B1LYP//BLYP-BLYP//BLYP)/n$, where n is the number of bonds broken (in this case, 2). Calculations using two different basis sets (6-311+G(d,p) and 6-311+G(2df,2p)) resulted in close values of about 2.7 kcal/mol, well below the recommended threshold of 10 kcal/mol.

Instead, the total atomization energy (TAE) diagnostic proposed by Karton and coworkers [485] revealed the significant MR character of the TS. In particular, the %TAE(SCF) compares the TAE obtained at the highest level of theory used (CCSD(T)/aug-cc-pVTZ in this case) with the TAE obtained by a single-reference SCF calculation. %TAE(SCF) was thus computed as $(\text{TAE}(\text{CCSD}(\text{T})) - \text{TAE}(\text{HF})) / \text{TAE}(\text{CCSD}(\text{T})) * 100\%$ using the aug-cc-pVTZ basis set, on the geometries optimized at $\omega\text{B97X-D}/6\text{-}311\text{+G}(\text{d,p})$ level. The resulting %TAE(SCF) of 28% indicates a fairly large amount of non-dynamical correlation (see Table 6.12). The %TAE[(T)] diagnostic instead accounts for the contribution of the perturbative triples (T) to the RCCSD(T) energy compared to the RCCSD one, and is defined as $(\text{TAE}(\text{RCCSD}(\text{T})) - \text{TAE}(\text{RCCSD})) / \text{TAE}(\text{RCCSD}(\text{T})) * 100\%$. In this case, the 2.4% value computed for the present system is slightly higher than the recommended threshold of 2%, and therefore indicates a mild MR character.

The M diagnostic [486] is defined as $(2 - n(\text{MCDONO}) + n(\text{MCUNO})) / 2$, where $n(\text{MCDONO})$ is the lowest occupation of all doubly occupied natural orbitals, whereas $n(\text{MCUNO})$ is the highest occupation of the unoccupied natural orbitals. The M value obtained with an active space of (2e,2o) was 0.08, increasing to 0.11 when using an AS of (6e,6o). Both values are above the recommended 0.04 threshold. Finally, the C0_2 diagnostic, where C0 is the coefficient of the HF determinant in the multi-configuration expansion, resulted in a value of 0.96, higher than the recommended threshold of 0.9. Due to the positive results of some of the MR diagnostic methods, this channel was treated at the CASPT2 level of theory.

TABLE 6.12: Multireference diagnostics and recommended values for the decarbonylation channel on phenol PES.

Diagnostic	Value	Recommendation (non-MR if.)	MR?
B1	2.7 kcal/mol	< 10 kcal/mol	NO
%TAE(SCF)	28%	> 66.7%	YES
%TAE[(T)]	2.4%	< 2%	YES,MILD
M	0.08	< 0.04	YES
C0_2	0.96	> 0.9	NO

Table 6.13 and 6.14 report the energies obtained for different levels of theory at the DFT and CASPT2 geometries, respectively. The small difference (< 0.4 kcal/mol) in energy between the (6e,6o) and (12e,11o) ASs shows proper AS convergence. The difference in energy between the DFT and CASPT2 structures is about 0.5 kcal/mol. The final energy of 75.1 kcal/mol (with respect to phenol) is 3.6 kcal/mol lower than that obtained at the CCSD(T) level. The impact on the rate constant is partially compensated by the higher vibrational frequencies found at the CASPT2 level with respect to those determined at the DFT level, through a sort of enthalpy-entropy compensation effect. For instance, the lowest vibrational frequency increases from 66 cm^{-1} ($\omega\text{B97X-D}/6\text{-}311\text{+G}(\text{d,p})$), to 117 cm^{-1} (CASPT2/aug-cc-pVTZ).

Rate constants were determined by solving the ME as a function of temperature and pressure, as explained in Section 6.3.2.2. Concerning the stabilization of the intermediate

TABLE 6.13: Energy barriers [kcal/mol] for the decarbonylation channel at the DFT geometry. ATZ indicates aug-cc-pVTZ basis set.

ZPE	CCSD(T)/ CBS	RS2C(6e,6o)/ ATZ	RS2C(12e,11o)/ ATZ	RS2C(12e,11o)/ ATZ shift 0.2	RS2C(12e,11o)/ ATZ IPEA 0.25
ΔE_{TS}	29.91	27.15	24.81	25.05	25.74
ΔH_{TS}	28.18	25.42	23.08	23.32	24.01

TABLE 6.14: Energy barriers [kcal/mol] for the decarbonylation channel at the CASPT2 geometry optimized at the CASPT2(6e,6o)/aug-cc-pVTZ level. ATZ indicates aug-cc-pVTZ basis set.

ZPE	RS2(6e,6o)/ ATZ	RS2C(12e,11o)/ ATZ	RS2C(12e,11o)/ ATZ shift 0.2	RS2C(12e,11o)/ ATZ IPEA 0.25
ΔE_{TS}	25.91	25.52	25.74	26.25
ΔH_{TS}	24.22	23.84	24.06	24.57

species on the PES, 2,4-C₆H₆O and 2,5-C₆H₆O exist as thermodynamically stable intermediates over an extended temperature range, even at atmospheric pressure (up to 2200 K and 1900 K, respectively). All other intermediate wells are stable only below 1000 K. For both kinetic modeling purposes and consistent comparisons with microkinetic literature data, which do not account explicitly for intermediate species, global rate constants were determined with MEL and are reported in Table 6.15.

Figure 6.7 compares the main global rate constants r_1 and r_2 with data from the literature and from the initial version of the CRECK kinetic mechanism [46]. Figure 6.7a shows the results obtained for r_1 . The rate constant calculated in the present work is a factor of 3–4 lower than that of Xu and Lin [481] and differs from the experimental estimate of Horn et al. [132] by up to a factor of 4. The rate constant for the bond-fission reaction (r_2) (Figure 6.7b) agrees well with both the predictions of Xu and Lin [481] and Zhu and Bozzelli [480] and with the experimental estimate of Horn et al. [132]. At lower temperatures, the estimate of Lovell et al. [126] is in better agreement with the present calculations (a factor of 2–2.5) than with previous theoretical calculations (> factor of 10). Finally, the rate of recombination of H with phenoxy radical (Figure 6.7c) differs by less than a factor of 2 from that obtained by the RRKM calculation of Davis et al. [374], previously adopted by the CRECK kinetic mechanism. It is highlighted that the most relevant contributions to the rate constants are the C–H bond-fissions of W2 and W6 (up to 60% and 40%, respectively).

Overall, the main difference between the present calculations and literature data consists in the lower rate found for the production of C₅H₆ and the higher one for the production of phenoxy radical. The latter is due to the contribution of intermediate species, especially 2,5-C₆H₆O (W6), which was not considered in the work of Xu and Lin [481]. The experimental estimate of Horn et al. [132] shows some discrepancy with the present calculations. In their work, r_1 and r_2 were obtained fitting the CO and H profiles at different temperatures using a simplified kinetic mechanism that assumed r_1 as the initial step of phenol decomposition, and estimated that r_2 cannot exceed $0.15 \cdot k_{r1}$ in the investigated temperature range (1477–1536 K). On the other hand, the present theoretical calculations predict that the rates of r_1 and r_2 are comparable in this temperature range, thus contradicting one of the hypotheses

on which the experimental data interpretation was based. Despite this difference, the CO and H profiles measured in the ST experiments of Horn are in excellent agreement with the kinetic simulations performed using the present rate constants for kinetic modeling (Section 6.6.2.1).

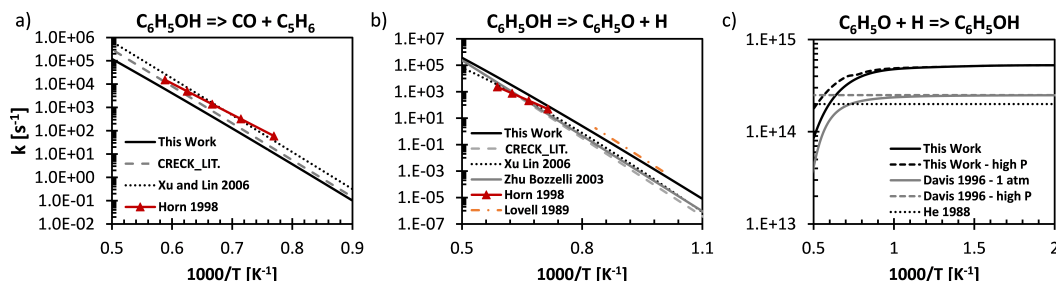


FIGURE 6.7: Global rate constants for the decomposition of phenol (1 atm) and comparison with available literature data [126], [132], [436], [480], [481], [490].

Figure 6.8 shows the PES diagram for phenoxy decomposition to $C_5H_5 + CO$ and a comparison between the present decomposition rate constant and literature experimental and theoretical values. The PES diagram also reports the energies of the main decomposition channel from previous theoretical estimates [430], [482], [484]. There is reasonable agreement with all the previous works, with a maximum discrepancy of 2.5 kcal/mol with the CBS-QB3 method. The most striking difference is the 0 K global reaction enthalpy that, though in quite good agreement with the ATcT value of 21.4 kcal/mol [117], differs by 3.5 kcal/mol from the CBS-QB3 estimate.

Phenoxy decomposition involves a ring closure reaction to form a 5-membered ring (TS1), followed by the successive two step cleavage of the two C–C bonds of the 3-membered ring (TS3, TS6). The first C–C cleavage may be considered as the rate determining step, hence it directly affects the activation energy found for the high pressure limit rate constant (53.3 kcal/mol), in good agreement with the previous calculations of Carstensen and Dean (55.2 kcal/mol) [484]. The 2 kcal/mol discrepancy derives from the systematic overprediction of the energy barriers that are sometimes observed at the CBS-QB3 level of theory [491].

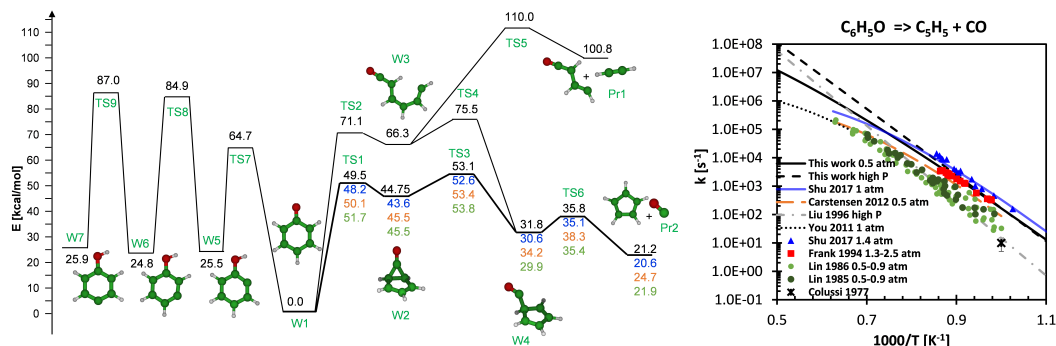


FIGURE 6.8: PES for phenoxy decomposition and the corresponding global rate constant. Energies are compared with previous works: G4 (blue, Shu 2017 [430]), CBS-QB3 (orange, Carstensen 2012 [484]), CASPT2/6-31+G(d,p) (green, Olivella 1995 [482]).

The calculated global decomposition rate constant (right side of Figure 6.8) is in excellent agreement with the experimental data of Frank et al. [303] (factor < 1.3) and with the recent experiments of Shu et al. [430] (factor of ~ 2), whereas there is a larger discrepancy with the data of Lin et al. [443] (factor of 2–5). The largest discrepancy may be attributed to the effect of secondary reactions, which are possibly relevant at the high phenoxy concentration of the experimental study [443]. As regards the theoretical rates reported in the literature, the present calculations agree to a factor of ~ 2 with the work of Carstensen and Dean [484] and of Shu et al. [430] in the 900–1300 K range. The significant difference with the rate constant of You et al. [492] (factor of 4–7) can instead be related to the lower level of theory used, B3LYP/6-311G(d,p), which may lead to an uncertainty in the final rate constant estimation of up to one order of magnitude. At high temperatures, the rate constant calculated in the present work shows a smaller decrease in the apparent activation energy with respect to the literature theoretical calculations mentioned above. This is probably due to the consideration of the dependence on temperature of the collisional energy transfer parameter, neglected in the previous theoretical studies. The modified Arrhenius fits for the global decomposition rate constant at different pressures are provided in Table 6.15.

Figure 6.8 also shows the isomerization channels from the phenoxy radical to the ortho, meta, and para isomers of C_6H_4OH . None of the previous theoretical studies included them in the PES, in fact the isomerization barrier from phenoxy to *o*- C_6H_4OH is significantly higher than for decomposition (r3). Nevertheless, when these radicals are present in the system, for instance resulting from C–H bond-fission or H-atom abstraction reactions of phenol, they may either isomerize to phenoxy or decompose. In this respect, Hemberger et al. [493] conducted a combined experimental and theoretical study concerning the stability of the *o,m,p*- C_6H_4OH radicals. The enthalpies of both *o,m,p*- C_6H_4OH and the relative TSs are in reasonable agreement with the G3X-K energies calculated by Hemberger et al. [493] (< 0.2 kcal/mol and < 1.9 kcal/mol, respectively). Their experimental results reveal that the ortho isomer is short-lived, as it rapidly isomerizes to phenoxy, whereas the meta and para isomers may be considered as stable species in pyrolysis systems. Additionally, they highlighted that, as the isomerization barrier from *m,p*- C_6H_4OH to phenoxy lie higher than the barrier to the decomposition products, the well-skipping decomposition channel of *m,p*- C_6H_4OH to $C_5H_5 + CO$ should also be included in kinetic models. The present ME simulations confirm the instability of *o*- C_6H_4OH compared to its meta and para isomers. Unimolecular reactions of *m,p*- C_6H_4OH radicals, lumped as C_6H_4OH , did not dramatically change simulation results of the available flow reactor studies of phenol pyrolysis and oxidation around 1200 K, however they may be more relevant at higher temperatures or with higher radical concentrations.

TABLE 6.15: Arrhenius fits in the form $k_0 \cdot T^\alpha \cdot \exp\left(-\frac{E_A}{RT}\right)$. Units: cal, mol, s, cm³. The range of the Arrhenius fits is 300–2500 K, with the exception of $\text{H} + \text{C}_6\text{H}_5\text{O} \rightarrow \text{C}_6\text{H}_5\text{OH}$ and the backward rate where it was reduced to 500–2500 K. R^2 indicates 1 minus the square residuals of the fitting.

reaction	P [atm]	k_0	α	E_A	R^2
$\text{C}_6\text{H}_5\text{OH} \rightarrow \text{CO} + \text{C}_5\text{H}_6$	0.1	9.19E+28	-4.7	80342	1.00
	1	9.30E+23	-3.1	78585	1.00
	10	5.79E+21	-2.4	78076	1.00
	100	3.28E+19	-1.8	77021	1.00
$\text{C}_6\text{H}_5\text{OH} \rightarrow \text{H} + \text{C}_6\text{H}_5\text{O}$	0.1	8.29E+48	-9.9	102202	1.00
	1	6.58E+38	-6.9	97738	1.00
	10	1.32E+32	-4.9	94606	1.00
	100	1.14E+29	-4.0	93140	1.00
$\text{H} + \text{C}_6\text{H}_5\text{O} \rightarrow \text{C}_6\text{H}_5\text{OH}$	0.1	2.45E+42	-8.4	11212	0.92
	1	2.16E+33	-5.7	7614	0.91
	10	4.11E+27	-3.9	5237	0.92
	100	1.50E+25	-3.2	4211	0.94
$\text{H} + \text{C}_6\text{H}_5\text{O} \rightarrow \text{CO} + \text{C}_5\text{H}_6$	0.1	4.47E+05	2.3	874	R^2 of k1+k2 1.00
	1	1.94E+11	0.3	3494	1.00
	10	3.85E+19	-12.3	-26471	0.99
	100	1.03E+31	-4.8	18368	0.97
duplicate	0.1	6.60E+35	-6.0	19124	
	1	7.26E+34	-5.7	18932	
	10	1.20E+30	-4.3	16758	
	100	1.17E+32	-4.8	18409	
$\text{C}_6\text{H}_5\text{OH} \rightarrow \text{H}_2\text{O} + \text{C}_6\text{H}_4$	0.1	5.49E+29	-5.0	93271	1.00
	1	4.36E+20	-2.2	90188	1.00
	10	1.44E+15	-0.5	88550	1.00
	100	3.01E+11	0.6	86989	1.00
$\text{C}_6\text{H}_5\text{O} \rightarrow \text{CO} + \text{C}_5\text{H}_5$	0.1	9.76E+30	-5.4	58903	1.00
	1	3.44E+25	-3.6	57326	1.00
	10	3.49E+21	-2.4	56115	1.00
	100	5.19E+16	-0.9	54427	1.00
$\text{C}_6\text{H}_4\text{OH} = \text{C}_6\text{H}_5\text{O}$	0.1	1.77E+61	-14.8	78066	1.00
	1	1.84E+42	-8.7	71944	1.00
	10	4.01E+25	-3.6	65314	1.00
	100	6.69E+14	-0.4	60507	1.00
$\text{C}_6\text{H}_4\text{OH} = \text{C}_5\text{H}_5 + \text{CO}$	0.1	2.15E+48	-10.1	81081	1.00
	1	3.00E+42	-8.1	84286	1.00
	10	3.92E+26	-3.35	82093	1.00
	100	1.09E+01	3.96	73261	1.00

6.3.3 $C_6H_5+O_2$ and $C_6H_5O+O(^3P)$

6.3.3.1 Motivation and literature review

The reaction of phenyl radical with O_2 is one of the most significant reactions in the mechanism for benzene oxidation. In fact, in combustion conditions, benzene is largely converted to phenyl radical via H-atom abstraction reactions (Section 6.4). Then, phenyl reacts with molecular oxygen to oxygenated aromatic and 5-membered ring products. The $C_6H_5 + O_2$ reaction was therefore fundamental in the development of kinetic mechanisms for benzene oxidation [127], [128], [303]. This reaction is also of relevance to tropospheric and atmospheric chemistry, where benzene is partially consumed via H-atom abstraction by OH [391], [494]–[496]. The total rate constant of $C_6H_5 + O_2$ and its branching fractions to products determine the subsequent reactivity of the system and therefore also macroscopic ignition properties. However, the kinetics of $C_6H_5 + O_2$ is probably the most debated reaction in the literature of MAHs oxidation. Microkinetic experimental studies were hindered by difficulties in isolating the phenyl precursor, probing intermediates as well as products [496], [497], achieving small concentrations in flow reactors, reactor fouling, overlap in the absorption spectra of products [497]. Similarly, obtaining accurate theoretical rate constants for this system is extremely challenging because of the large number of heavy atoms and therefore the high computational cost, the multireference character of many relevant stationary points (and large AS required), complex unconventional multi-step reaction channels such as oxygen insertion in the ring, the numerous recombination reactions involving oxygen atoms, and the large number of reaction channels on the PES (in the order of 40–50 [353], [498]–[500]).

Despite the numerous theoretical and experimental efforts of the last 30 years, many aspects of the kinetics of $C_6H_5 + O_2$ are still unclear. This section summarizes the main literature experimental and theoretical evidences, focusing on the main reaction channels and on the dilemmas that emerged.

Figure 6.9 represents schematically the main reaction channels of $C_6H_5 + O_2$ and $C_6H_5O + O(^3P)$ reactions and guides the discussion of this section. The recombination of phenyl with molecular oxygen produces a phenylperoxy (C_6H_5OO) radical. The first experimental studies in the 1990s and early 2000s focused on room-temperature rate constants for the adduct formation, as summarized in Table 6.16. The low pressure experiments of Yu and Lin [501] and Tonokura et al. [497] found lifetimes longer than 1×10^{-8} s for the phenylperoxy radical. The more recent study of Tanaka et al. [502] confirmed that at 298 K the high pressure limit of the recombination rate constant is reached already at very low pressures (0.01 atm) because of the slow reactivity of the adduct. These studies [497], [501], [502] also agree on the total recombination rate constant estimates of $1.2\text{--}2.1 \times 10^{-11}$ cm³/molec/s ($\sim 7\text{--}12 \times 10^{12}$ cm³/mol/s).

At higher energies and temperatures, CMB experiments observed that the phenylperoxy radical decomposes to $C_6H_5O + O(^3P)$ [503]–[505], as summarized in Table 6.17. In the experiments of Gu et al. [503], performed at high temperature (1350 K) and with high collision energy (25.6 kcal/mol), the lifetime of the phenylperoxy radical was shorter than its rotational timescale, thus dissociating directly to $C_6H_5O + O(^3P)$, as confirmed by the

high translational energy in the products (53%). At lower temperature (298 K) and lower collisional energy (5–15 kcal/mol) the lifetime of phenylperoxy radical was found to be longer than the rotational timescale of 1 ps [504], [505], possibly allowing for isomerization reactions. No other products than $C_6H_5O + O(^3P)$ were detected in the experiments.

TABLE 6.16: Summary of literature experimental studies on the $C_6H_5 + O_2$ recombination channel highlighting the main findings.

ENTRANCE	CHANNEL Exp. Technique	$C_6H_5 + O_2$ P [atm]	T [K]	Inlet	Finding	Rate [cm^3/s]
Yu 1994 [501]	cavity-ring-down	0.02–0.1	297–473	$C_6H_5NO/O_2/Ar$	Adduct stabilizes	$1.2–2.1 \times 10^{-11}$
Tonokura 2002 [497]	cavity-ring-down +laser photolysis	0.01–0.06	298	$C_6H_5NO/O_2/N_2$	lifetime of C_6H_5OO 1.4×10^{-8} s	$1.4 \pm 0.4 \times 10^{-11}$
Tanaka 2011 [502]	cavity-ring-down	0.04	296	$C_6H_5Cl/O_2/N_2$	Adduct stabilizes	$1.2 \pm 0.1 \times 10^{-11}$

TABLE 6.17: Summary of literature CMB experiments conducted for the $C_6H_5 + O_2$ reaction.

CMB	Coll. energy [kcal/mol]	T [K]	P [atm]	C_6H_5OO lifetime [s]		Product	Trasl. En. in $C_6H_5O + O$
Gu 2007 [503]	25.6	1350	0.72	1×10^{-14}	<rot. period	$C_6H_5O + O$	53%
Albert 2010 [504]	15.3	298	0.06	1×10^{-12}	>rot. period	$C_6H_5O + O$	19%
Parker 2011 [505]	5.0	298	0.72	–	>rot. period	$C_6H_5O + O$	28%

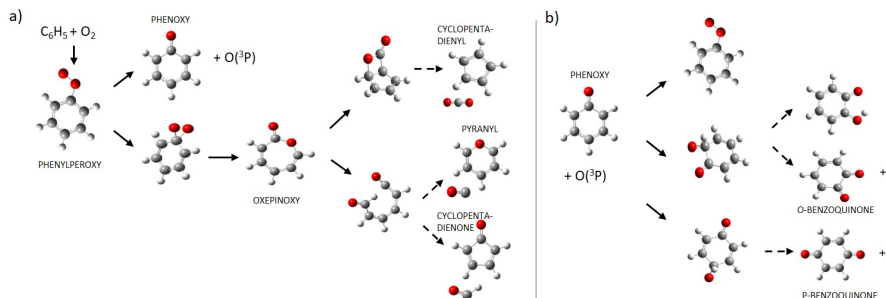


FIGURE 6.9: Scheme of the main channels for the a) $C_6H_5 + O_2$ and b) $C_6H_5O + O(^3P)$ PES identified in the literature. Solid lines indicate connections through direct TSs, while dashed lines refer to multi-step reaction channels. Some relevant species names are also reported.

The first (and only) microkinetic studies of $C_6H_5 + O_2$ in the diluted shock tube experiments of Frank et al. [303] and Kumaran and Michael [506] provided additional information on product branching fractions. Experimental conditions are presented in Table 6.18. In both works, the O and H atom mole fraction profiles were measured, and a small mechanism of 8–9 reactions was used to interpret experimental data. Best fits of the experimental profiles for the two reactions $C_6H_5 + O_2 \rightarrow C_6H_5 + O(^3P)$ / $C_6H_4O_2 + H$, assumed as the main source of O and H, respectively, resulted in very similar rate constants of $2.4/0.9 \times 10^{12}$ [303] and $2.6/1.1 \times 10^{12}$ $cm^3/mol/s$ [506] at 1300 K. Therefore, the BF of the O and H channels is about 70% and 30%, respectively. The more diluted experiments of Kumaran and Michael [506] are probably less affected by secondary reactions. The authors estimated that about 75% conversion of C_6H_5 occurs through the fitted reactions, while the remaining 25% might lead to the stabilization of isomers of C_6H_5OO . On the other hand, Frank et al. [303] indicated that simulated O and H profiles were partially affected by other reactions in the mechanism, namely $C_6H_5 + O(^3P) \rightarrow C_6H_5O$ and $C_5H_5 + O(^3P) \rightarrow C_5H_4O + H$ for the

former and $C_6H_5 + H \rightarrow C_6H_6$, $C_5H_5 + H \rightarrow C_5H_6$ for the latter. It is noted that neither of the sub-mechanisms included $C_6H_5O + O(^3P)$ reactions.

While the first experimental and theoretical studies postulated that H atoms were produced from $C_6H_4O_2 + H$, later experimental and theoretical evidence revealed that H atoms are probably produced through a multi-step process: one oxygen atom inserts in the aromatic ring to produce oxepinoxy radical, which rearranges and dissociates to $C_5H_4O + HCO$ (see Figure 6.9), such that the low dissociation threshold of HCO easily leads to H atoms. The presence of oxepinoxy was experimentally confirmed in the low temperature matrix isolation experiments of Mardyukov et al. [495]. Then, Kirk et al. [496] identified with ion-trap mass spectrometry both the presence of intermediate isomers and of C_5H_4O in room temperature distonic radical ion experiments. The authors applied the same technique also to methylphenyl radicals [440], observing the same class of products (substituted cyclopentadienone structures).

Finally, the recent nozzle reactor experiments of Parker et al. [507] coupled vacuum ultraviolet photoionization with mass spectroscopic detection of photoionized products in the $873\text{--}1000 \pm 150$ K temperature range. A large variety of products such as phenol, phenoxy, cyclopentadienyl, cyclopentadienone, furan (C_4H_4O), benzoquinone, and decomposed products such as acrolein (C_2H_3CHO), vinylacetylene (C_4H_4), ketene (CH_2CO) and acetylene were detected. However, the large uncertainty in the temperature, and the difficult understanding and simulation of experimental conditions, where oxygen was used as bath gas, prevent a clear interpretation of the data.

TABLE 6.18: Literature flow reactor "microkinetic" experiments for $C_6H_5 + O_2$ reaction. Main detected species and operating conditions are listed.

Lit. source	Reactor type	Detects	T [K]	P [bar]	τ [s]	Inlet [mole frac]
Frank 1994 [303]	ST	O, H	1320	2.36	1.0×10^{-3}	$0.15/2.50 \times 10^{-4}$
Kumaran 1997 [506]	ST	O, H	1068–1403	0.36–0.56	1.0×10^{-3}	C_6H_5NO/O_2 in He $0.026/6.32 \times 10^{-4}$
Parker 2015 [507]	Supersonic nozzle	various $C_2\text{--}C_6$ products	873, 1003 \pm 150	0.4	?	C_6H_5I/O_2 in Kr 0.001/0.999 C_6H_5/O_2

Because of the experimental difficulties in determining product fractions of the $C_6H_5 + O_2$ reaction, theoretical studies have been performed in parallel to the experiments. Figure 6.9 and Table 6.19 summarize the main reaction channels and the theoretical methodologies and main findings.

Carpenter [508] was the first to postulate the oxygen ring insertion mechanism to form oxepinoxy radical, in analogy to the $C_2H_3 + O_2$ PES. Then, Hadad et al. [499], [510], [511] investigated the fate of oxepinoxy radical at the DFT level, concluding that the main decomposition pathway proceeds through ring opening, torsions, ring closure, and β -scission to produce pyranyl + CO. Channels to furan, cyclopentadienyl, and linear hydrocarbons were also investigated, but were deemed less energetically or entropically favored in the temperature range investigated (1000–1250 K). These studies also highlight that the competition between the O–O bond-fission in phenylperoxy radical and the ring insertion steps ultimately determine the distribution of products.

TABLE 6.19: Summary of the main literature theoretical investigations for the $C_6H_5+O_2$ PES including information on the theoretical methodology for electronic structure (ES) calculations, rate constant calculations, and findings on product fractions.

PES	Focus on	Theory (ES)	Theory (Kin)	Findings on products
Carpenter 1993 [508]	oxepinoxy formation	PM3/UHF	-	oxepinoxy stabilizes $C_5H_5+CO_2$ unfavored
Mebel 1994 [509]	C_6H_5OO isomers	PUMP3//UHF/6-31G(d)	-	<i>o</i> - C_6H_4OH most stable $H+o/p-C_6H_4O_2$ possible
Lin 1995 [498]	$O+C_6H_5O$ PES	PUMP3//UHF/6-31G(d)	RRKM	<i>o</i> - C_6H_4OH dominates $H+o/p-C_6H_4O_2$ minor
Barckholtz 1999 [510]	C_6H_5OO decomposition	B3LYP/6-311+G(d,p)//B3LYP/6-31G(d)	-	$C_6H_5OO \rightarrow$ oxepinoxy, C_6H_5O+O oxepinoxy $\rightarrow C_5H_5+CO_2$, pyranyl+CO
Fadden 2000 [511]	C_6H_5OO decomposition	B3LYP/6-311+G(d,p)//B3LYP/6-31G(d)	-	pyranyl+CO, C_6H_5O+O (high T); ring opening to $C_5H_5+CO_2$ unfavored
Fadden 2000 [499]	oxepinoxy decomposition	B3LYP/6-311+G(d,p)//B3LYP/6-31G(d)	-	ring opening: C_5H_5O+CO , C_4H_5+2CO
Tokmakov 2005 [500]	Complete PES and product branching	G2M(MP2)//B3LYP/6-311++G(d,p)	-	Ring insertion controls BF oxepinoxy $\rightarrow C_5H_5+CO_2$, pyranyl+CO, <i>o</i> - $C_6H_4O_2+H$ C_6H_5O+O main product
Sebbar 2007 /2008 [512], [513]	first rate constants	G3	RRKM-ME	
Tanaka 2011 [502]	few channels for exp. comparison	CBS-QB3	RRKM-ME	C_6H_5O+O main product Insertion at lower P
Kislov 2015 [514]	$C_6H_5+O_2$ total rate product branching	G2M(MP2)//B3LYP/6-311++G(d,p)	VRC-TST/ RRKM-ME	$C_6H_5O+O >80\%$ pyranyl+CO $< 10\%$ at $T > 1500$ K
Morozov 2021 [353]	Full set of accurate rate constants; product branching	CCSD(T)-F12/cc-pVTZ-F12//B3LYP/6-311++G(d,p); CASPT2(15e,13o)/CBS//B3LYP/6-311++G(d,p)	CTST, VTST, VRC-TST/ RRKM-ME	C_5H_4O+HCO main product; C_6H_5O+O mostly produce $C_6H_4O_2+H$, C_5H_4O+HCO

Starting from the findings of Hadad et al. [499], [511], Tokmakov et al. [500] performed an extensive theoretical investigation of more than 40 reaction channels at the G2M(MP2) level of theory, presenting a detailed analysis of the ring insertion pathway. In particular, the authors proposed the O–O bond breaking of the 3-ring intermediate depicted in Figure 6.9a as the limiting step in the complex ring insertion process. At the B3LYP/6-311++G(d,p) level, this structure has C_{2V} symmetry ($2B'$ electronic state), while the TSs for the subsequent C_{2V} and C_S symmetry breaking have lower energies. The complexity of this pathway was highlighted by the presence of other quasi-degenerate electronic states and by the difficulty in reaching satisfactory theoretical accuracy for this energy barrier, as computational resources were unable to reach a minimal AS for an appropriate CASPT2 treatment. The estimated G2M barrier for the analogous TS in the vinyl + O_2 system was 24.0 kcal/mol, as opposed to the 16.9 kcal/mol obtained at the MRCI+Q(9e,9o) level of theory. Tokmakov et al. also performed a structural analysis for the O–O bond-fission channel from the peroxy radical (Figure 6.9, Table 6.21), identifying a non-planar submerged TS.

The following theoretical studies providing the first rate constants estimates mostly relied on the PES described by Tokmakov et al. [500]. Sebbar et al. [512], [513] found that the main competing pathways above 700 K are the stabilization of the phenylperoxy intermediate and the formation of phenoxy radical, while rate constants for the ring insertion products were more than one order of magnitude smaller. Similarly, the high temperature RRKM/ME investigation of Kislov et al. [514] found a branching fraction for the $C_6H_5O + O(^3P)$ channel higher than 80% at $T > 1500$ K, as opposed to a fraction of pyranyl + CO below 10% in the 0.01–10 atm range.

The reactivity of the system was completely reconsidered in the recent work of Morozov et al. [353]. The energies for the PES for Tokmakov et al. [500] were refined at the

CCSD(T)-F12/cc-pVTZ-F12 level of theory, while SPEs for channels with high multireference character were computed at the CASPT2(15e,13o)/cc-pVDZ level (including in both cases extrapolation to CBS), as summarized in Tables 6.19, 6.20, and 6.21). New channels were also investigated. While the energy for the O–O bond-fission channel of the C_6H_5OO intermediate agrees with previous results [500], [515], multireference calculations for the TS of the oxygen insertion in the aromatic ring resulted in a significant decrease in the energy barrier (from 12.7 to 8.1 kcal/mol at G2M [500] and CASPT2 [353] level, respectively), thus changing completely the product distribution. Additionally, the investigation of a new channel for oxepinoxy radical decomposition revealed that the main product resulting from the ring insertion channel is $C_5H_4O + HCO$, as supported by some experimental findings [387], [440], [496], [507].

The final rate constants obtained from the ME simulations by Morozov et al. [353] question most of the previous theoretical and experimental results in terms of product branching fractions. In fact, $C_5H_4O + HCO$ is predicted as the main product channel almost up to 2500 K. This result is not corroborated by any of the high-temperature experiments. On the other hand, the negligible product BF's of furan, acrolein and ketene suggest that the experimental results of Parker et al. [507] are strongly affected by secondary reactions, as expected from the high oxygen concentration.

Accurate determination of rate constants for the bond-fission channels is essential to obtaining reliable and predictive kinetics. Table 6.20 lists the theoretical studies for the total rate constant of $C_6H_5 + O_2$. All theoretical studies confirmed a planar structure for the TS. The VTST rate constant of Da Silva and Bozzelli [515] found strong variation of the C–O distance with temperature (2.56–2.16 Å in the 2000–300 K range) and reasonable agreement with room temperature data. The VRC-TST study of Kislov et al. [514] found instead a positive temperature dependence in the rate constant, resulting in significant underestimation of low temperature experimental data. Finally, Zhang et al. [241] performed VRC-TST calculations for the recombination of several aromatic radicals with O_2 . The $C_6H_5 + O_2$ rate constant showed quantitative agreement with the available experimental data (factor < 2) and was also adopted in the work of Morozov et al. [353].

Less attention was dedicated to the study of this PES from the $C_6H_5O + O(^3P)$ entrance channel. Most theoretical studies only derived the rate constant for the O–O bond-fission determining product distribution of $C_6H_5 + O_2$, as reported in Table 6.21. All theoretical studies found a relatively tight TS for this bond-fission [353], [498], [500], [515], occurring through symmetry breaking from the plane and the formation of a weak Van der Waals complex [500]. The VTST rate constant of Morozov et al. [353] is probably the most accurate theoretical estimate available in the literature (theoretical details in Table 6.21). Their calculated rate constant is a factor of 3–20 smaller than the estimate of Da Silva and Bozzelli [515].

The work of Morozov et al. [353] also determined for the first time rate constants and product branching fractions for the $O(^3P)$ recombination on the ortho and para carbon sites of C_6H_5O . Rate constants for the entrance channels were determined using VRC-TST, analyzing MEP distances up to 3 Å and using correction potentials for geometry and energy

(see Section 3.3.2.4). They found that the recombination of $O(^3P)$ on the carbon atoms is favored with respect to that on the oxygen atom of phenoxy radical, as anticipated by Lin et al. [498]. Some relevant channels in the reactivity of the intermediates formed by $C_6H_5O + O(^3P)$ were also investigated. While the recombination with the ortho carbon mostly proceeds via ring-opening and eventually forms $C_5H_4O + HCO$, the recombination with the para carbon produces $p-C_6H_4O_2 + H$ (see Figure 6.9). The authors did not investigate the formation of $o-OC_6H_4OH$ via H-transfer, identified as potentially relevant by Mebel et al. [498], [509].

TABLE 6.20: Summary of literature theoretical studies of the $C_6H_5 + O_2$ recombination channel. The theoretical methodology for electronic structure (ES) calculations, rate constant calculation, and main findings are listed.

Lit. source	Theory (ES)	Theory (Kin)	Finding
Tokmakov 2005 [500]	G2M(MP2)//B3LYP/6-311++G(d,p)	-	Confirmed barrierless Cs, symmetry allowed
Da Silva 2008 [515] Kislov 2015 [514] Zhang 2017 [241]	G3B3//O3LYP/6-31G(d) CASPT2(19e,14o)//CASSCF(9e,9o)/aug-cc-pVDZ CCSD(T)-F12/CBS + spin split at CASPT2(7e,5o)/CBS	VTST VRC-TST (Cs fixed) VRC-TST; sampling at CASPT2(7e,5o)/cc-pVDZ	Negative T dependence Positive T dependence? Agreement with exp data

TABLE 6.21: Literature theoretical studies of the $C_6H_5O + O(^3P)$ recombination channel. The theoretical methodology for electronic structure (ES) calculations, rate constant calculation, and main findings are listed.

Lit. source	Theory (ES)	Theory (Kin)	Channels	Finding
Lin 1995 [498]	PUMP3//UHF/6-31G(d)	RRKM	O-O	tight TS for O-O fission
Tokmakov 2005 [500]	G2M(MP2)//B3LYP/6-311++G(d,p)	-	O-C, ortho O-O	rec. on C favored Symmetry breaking non-planar TS energy below products
Da Silva 2008 [515]	G3B3//O3LYP/6-31G(d)	VTST	O-O	Confirmed barrierless relatively tight TS
Morozov 2021 [353]	CASPT2(15e,13o)/CBS// CASSCF(15e,13o)/DZP CASPT2(5e,4o)/cc-pVDZ	VTST VRC-TST	O-O O-C, ortho O-C, para	relatively tight TS Ortho recombination: largest rate

Overall, strong discrepancies in theoretical and experimental observations for the study of C_6H_5OO PES are still unexplained. This work re-investigates the main channels and additional channels on this PES with state-of-the-art theoretical methodologies and presents critical analysis of the crucial aspects determining global rate constants and product branching fractions. Detailed rate constants obtained from the ME simulations are lumped for easy integration into the CRECK kinetic mechanism. Kinetic simulations of the available microkinetic experiments are used to assess the uncertainty and validity of the results and provide interesting insights into the unsolved mysteries of the C_6H_5OO PES.

6.3.3.2 Theoretical methodology

The calculation of rate constants was performed according to the AI-TST-ME methodology using EStokTP (see Section 3.4.1). Geometry optimization and frequency calculations of the stationary points were performed at ω B97X-D/6-311+G(d,p) level, and SPEs were refined at the CCSD(T)/CBS level (Eqn. (3.11)).

Thermochemistry of all species was computed from the partition functions and fitted to NASA polynomials with the Auto-Mech suite of codes [98] (Section 3.4.2). 0 K formation

enthalpies were calculated through isogyric reactions, considering tabulated enthalpies of ATcT tables [117] for reference species.

In the following, species labels refer to the PESs described in Section 6.3.3.3 and depicted in Figures 6.10, 6.11, and 6.12.

The energy barrier for relevant reaction channels with high multireference character (T1 diagnostic of CC calculations > 0.03) was refined at the CASPT2/aug-cc-pVTZ (CASPT2/ATZ) level of theory, using an IPEA shift and 4-state averaging of the reference wavefunction when oxygen lone pairs were included. The results were compared with CASPT2/cc-pVTZ (CASPT2/TZ) and CASPT2/cc-pVQZ (CASPT2/QZ) energies extrapolated to the CBS using $0.4*(QZ - TZ)$ extrapolation (similar to [353]), finding a maximum discrepancy of 0.5 kcal/mol for an H transfer reaction. The active space (AS) for each reaction channel was visually inspected. Energies were determined with respect to the well closest in energy to the TS, i.e., considering the reaction barrier for the exothermic channel. In the following, DZ, TZ, QZ, ATZ indicate cc-pVDZ, cc-pVTZ, cc-pVQZ, aug-cc-pVTZ basis sets, respectively, while CASPT2/TZ calculations with $0.4*(QZ - TZ)$ extrapolation are indicated as CBS.

The reaction channel for the formation of the O–C–O ring intermediate (W3) from the phenylperoxy radical (W1) was investigated using a (15e,13o) AS, including the π space of the ring (5e,5o), the σ , σ^* C–O and O–O bonding and anti-bonding orbitals (6e,6o) and the oxygen lone pairs (4e,2o). The H transfer of the adduct formed upon O(3P) recombination with the para carbon of C₆H₅O (W1-p) to the meta carbon (W19) was inspected with a (13e,11o) AS, including the π space of the ring and of the C=O bond (6e,6o), the σ , σ^* C–H and C–O bonding and anti-bonding orbitals (4e,4o) and the oxygen radical and lone pair (3e,2o). The corresponding H transfer from the adduct formed upon O(3P) recombination with the ortho carbon of C₆H₅O (W1-o) was treated with a smaller (9e,8o) AS, including the π space of the ring (4e,4o), the C–H σ , σ^* orbitals (2e,2o), and the (3e,2o) space of the oxygen on the sp³ carbon site.

Several theoretical methodologies were used for the complicated TS describing the ring insertion in the aromatic ring. Starting from the guess C_{2v} geometry obtained at B3LYP/6-311++G(d,p) by Tokmakov et al. [500], saddle point optimization at the ω B97X-D/6-311++G(d,p) level resulted in a non-symmetrical geometry. A second order saddle point was found in constrained C_s TS optimization. Additional tests were performed first at the DFT level using B2PLYPD3/jun-cc-pVTZ, which also found a symmetrical saddle point structure. MR geometry optimization was attempted along the MEP for the scission of the O–O bond, highlighted by previous studies as the bottleneck of the reaction [500]. Geometry optimization at fixed OCO angles was performed at the CASPT2/cc-pVDZ and CASPT2/cc-pVTZ levels progressively increasing the AS from (3e,3o) to (7e,7o) and (11e,9o). The largest AS selected included the π space of the aromatic ring (5e,5o), the O–O σ , σ^* orbitals (2e,2o) and oxygen lone pairs (4e,2o). MR calculations highlighted 8 states very close in energy (within few kcal/mol) in the OCO = 95–115° region. However, all MR saddle point optimizations failed. Therefore, the MEP was mapped from the TS found at ω B97X-D/6-311++G(d,p) level with IRC calculations, and energies at each point were refined at the

CASPT2(15e,13o)/ATZ level (i.e., with the same AS used for W3→W1 described above), with 8-state averaging for the reference wavefunction. Finally, SPE calculations at the maximum obtained at the DFT level were also performed at the MRCI+Q(7e,5o)/cc-pVDZ level. The uncertainty in the resulting energy barrier seems extremely large, with variations in SPEs up to 10 kcal/mol for the same structure treated with DFT or MR methods, and large discrepancies with the recent results of Morozov et al. [353]. The results are discussed in greater detail in Section 6.3.3.5.

Rate constants for the channels with well-defined barriers were treated with conventional transition state theory. Partition functions for the internal rotations were calculated from a 1DHR model, using torsional potentials computed at 20° interval scans of the dihedral angles at the same level of theory used for the geometry optimization. Tunneling corrections were evaluated using the Eckart model [263].

The O–O bond-fission channel of phenylperoxy radical (W1) was treated using VTST. The MEP was optimized at constrained O–O distances in the range of 1.7–2.4 Å at both ω B97X-D/6-311++G(d,p) and CASPT2(11e,10o)/cc-pVTZ levels of theory. Energies were refined at the CASPT2(11e,10o)/aug-cc-pVTZ level of theory and compared with those obtained at CBS level. The (11e,10o) AS included the π space of the atomic oxygen (3e,2o) and of the aromatic ring (6e,6o), and σ , σ^* bonding and anti-bonding orbitals of the O–O breaking bond (2e,2o). 2-state averaging of the reference wavefunction was enough for the description of the TS region (with differences between the second and third state always above 10 kcal/mol), while the reference energy for the separated fragments was computed considering 3-state averaging. An IPEA shift of 0.25 was used. The lone pair of the oxygen atom in phenoxy radical was excluded because of 1) the high computational cost preventing the use of larger basis sets, and 2) its irrelevance in the description of the MEP found for the analogous vinoxy + O(³P) channel [198]. The potential for the C–OO hindered rotor was scanned at ω B97X-D/6-311++G(d,p) level of theory at different distances along the MEP (1.8, 2.0, 2.1, 2.2 Å), constraining also the O–O distance.

Barrierless C–O bond-fission channels were studied with VRC-TST [234] employing the two TS model (Section 3.3.2.4). For the short-range TS, pivot points were placed at the reacting atoms and then displaced by 0.1–0.3 Bohr along the direction of the molecular bonding orbital being broken in the reaction. For the latter, pivot points were placed at the center-of-mass of the fragments. A dynamical correction of 0.9 was included.

For the O₂ + C₆H₅ channel, fragment orientations were sampled at the CASPT2(7e,5o)/cc-pVDZ level (as in [241]), using fixed fragment geometries optimized at the CASPT2(6e,4o)/cc-pVDZ (O₂) and CASPT2(1e,1o)/cc-pVDZ (C₆H₅) levels. The energies obtained from the sampling were corrected with a C–O distance-dependent potential accounting for both geometry relaxation (difference between CASPT2(7e,5o)/cc-pVDZ energies obtained with both relaxed and constrained optimizations) and basis set/AS effects (difference between CASPT2(13e,11o)/aug-cc-pVTZ and CASPT2(7e,5o)/cc-pVDZ SPEs on optimized MEP geometries). The (13e,11o) AS included the full π space of O₂ (6e,4o) and of the aromatic ring (6e,6o) and the radical of phenyl (1e,1o).

Fragment orientations for the O(³P) recombination on the ortho and para carbon sites of

phenoxy were sampled at the CASPT2(5e,4o)/cc-pVDZ level (using a 2-state averaged reference wavefunction) with fixed fragment geometries optimized at ω B97X-D/6-311++G(d,p) level of theory. The AS included the (4e,3o) π space of the atomic oxygen and the radical on phenoxy (1e,1o). The C–O distance-dependent correction for geometry relaxation was computed from the energy difference between MEP geometries optimized at ω B97X-D/6-311++G(d,p) level and structures obtained optimizing only the transitional modes using fixed fragment geometries. Geometry optimization for the recombination on the ortho site was performed fixing the angle and the dihedral of the oxygen atom for C–O distances beyond 2.8 Å (i.e., with the oxygen approximately perpendicular to the aromatic ring). High level energy corrections along the MEP were computed at the CASPT2(11e,10o)/aug-cc-pVTZ level of theory, adding the rest of the π space of phenoxy (6e,6o). In this case, the reference wavefunction was averaged over 3 states at C–O distances > 3.2 Å, where the energy difference between the second and third state was below 5 kcal/mol. A C–O distance of ~ 4 Å marked the separation between the short and long range VRC-TST simulations. The flux for the recombination on the selected site was isolated by placing a repulsive potential on adjacent sites. The instability of the wavefunction in both the DFT and MR calculations is probably due to state mixing required significant additional effort for the selection of physically meaningful reference wavefunctions. The guess = read option in Gaussian and *ad hoc* AS guesses and orbital rotations in Molpro calculations were extensively used. In automated MR calculations for VRC-TST, the (5e,4o) AS selection was facilitated by an initial (7e,4o) guess adopted for all samplings.

Pressure-dependent rate constants were computed in the 300–2500 K temperature range solving the multi-well one-dimensional ME as implemented in MESS [106] (Section 3.3.4.3). Energy transfer parameters in Ar were adopted from the $C_6H_5C_2H_2/Ar$ system [139], as in Morozov et al. [353]. Collisional parameters in the Lennard-Jones model were $\sigma = 4.46$ Å and $\epsilon = 317$ K; the average energy transferred in collisions according to the exponential down model was set to $\langle \Delta E \rangle = 375 \left(\frac{T}{300} \right)^{0.61} \text{ cm}^{-1}$.

The complex set of phenomenological rate constants obtained was lumped with MEL [291] (see Chapter 4). Besides the bimolecular fragments, only two of the 25 intermediate wells were retained. The phenylperoxy radical accumulates at temperatures as high as 1400 K at 100 atm and was therefore included in the lumped set of rate constants. Both oxepinoxy (W4) and C_5H_4OCHO (W11) generated from phenylperoxy or from $O(^3P) + C_6H_5O$ channels partially accumulate below 1200 K. However, their reactivity to bimolecular products is faster than 1×10^{-5} at 1000 K, therefore they were directly replaced with their main products. o- OC_6H_4OH (W12 + W13) accumulates from $O(^3P) + C_6H_5O$ and is also generated from other reactions in the CRECK kinetic mechanism (i.e., the catechol sub-mechanism). Therefore, its lumped reactions were included. In contrast, a minor fraction of p- OC_6H_4OH (W16 + W19) is only produced from $O + C_6H_5O$ below 800 K, hence its unimolecular reactivity was not considered for the global mechanism. Finally, benzoquinone is produced significantly only from the recombination of O on the para position of phenoxy radical. Hence, the only $C_6H_4O_2$ isomer included was p- $C_6H_4O_2$. The lumped set of rate constants was integrated in the CRECK kinetic mechanism, analog with the rest of the theoretical calculations from this

work. Additional kinetic simulations were also performed using other sets of rate constants to compare model performances with microkinetic experiments.

6.3.3.3 Potential energy surface

Figure 6.10 shows the main reaction channels investigated in the present work for the C_6H_5OO PES accessed from $C_6H_5 + O_2$. Almost all of the reaction channels were already investigated in previous works [353], [500]. The energies are compared with those of Morozov et al. [353] or with those of Tokmakov et al. [500] for channels not re-investigated in [353].

The most relevant pathways on the C_6H_5OO PES for Figure 6.10 are highlighted with thicker lines. As found in previous works, the recombination of molecular oxygen on phenyl produces the stable phenylperoxy adduct (W1). The fate of phenylperoxy is controlled by the competition of three channels, i.e., back-dissociation to reactants, O–O bond-fission to $C_6H_5O + O(^3P)$, and isomerization to W3, followed by the ring insertion to form oxepinoxy radical (W4). The energy of the TSs for the O–O bond-fission and for the W1→W3 isomerization are in very good agreement with previous works. On the other hand, the energy found for the W3→W4 ring insertion TS, key to determining the branching fractions of O and H atoms and the product distribution, strongly disagrees with previous results and significantly varies with the theoretical methodology: * indicates CASPT2(15,13o)/ATZ energies found as the maximum on the IRC pathway computed at the DFT level (−1.9 kcal/mol) or at the DFT optimized saddle point (−15.0 kcal/mol), while** refers to the former structure including MRCI+Q(7e,5o) corrections (−7.2 kcal/mol). All results strongly differ from one another, and most importantly are all at least 6.5 kcal/mol higher than the energy barrier found by Morozov et al [353]. A detailed separate discussion is presented in Sections 6.3.3.5 and 6.3.3.6.

$C_5H_4O + HCO$ (P8) is the favored pathway for oxepinoxy (W4) decomposition, in agreement with Morozov et al. [353]. The energies of the W4→W7→W11→P8 channels all agree to within 1 kcal/mol with [353], with the W11→P8 TS being rate determining (energy of −56.4 kcal/mol). While the barrier to $C_5H_5 + CO_2$ (W4→W5) has a lower energy of −59.5 kcal/mol, this channel is highly disfavored entropically, as it closes the 7-membered ring of oxepinoxy into an intermediate with two rings. Therefore, it is not predicted to contribute to the reactivity [353].

Ring closure of the W7 intermediate in Figure 6.10 can also form W1-o, the same well resulting from $O(^3P)$ recombination on the ortho carbon of C_6H_5O . The main reaction channels of W1-o are depicted in Figure 6.11. The main competitive pathways are the H-transfer to W12, dissociating to ortho-benzoquinone $o-C_6H_4O_2 + H$, and ring opening to W7, eventually forming $C_5H_4O + HCO$. Comparisons between the energy barriers for these channels and those of Morozov et al. [353] suggest that in the present work the contribution of the latter channel to the product distribution will be even larger. At higher temperatures, the formation of $o-OC_6H_4OH$ and its decomposition to $C_5H_4OH + CO$, investigated in this work for the first time, might also play a role. The investigation of this portion of the PES

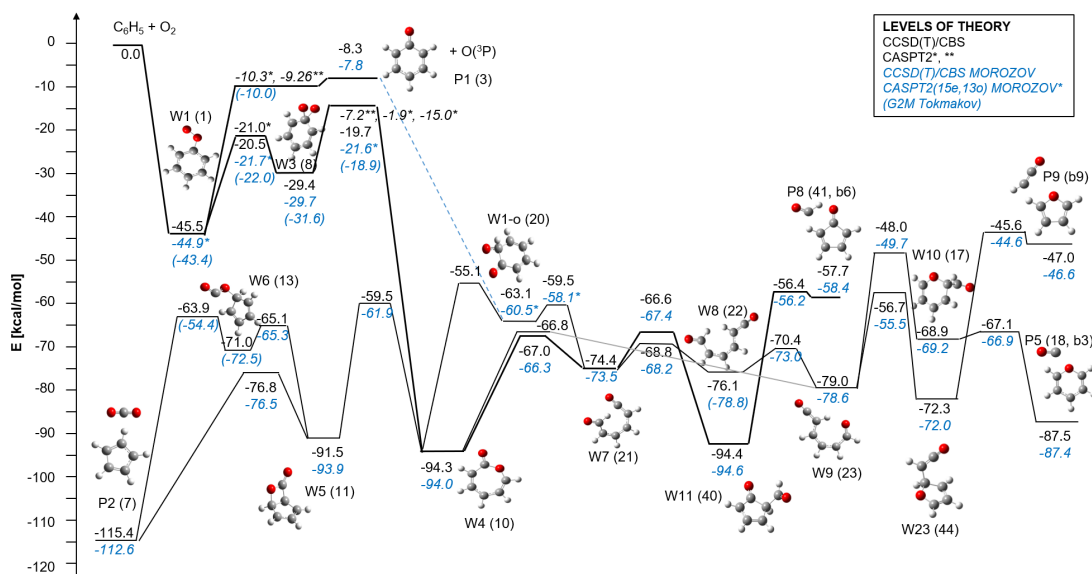


FIGURE 6.10: Main channels of C_6H_5OO PES accessed from $C_6H_5 + O_2$. Energies in kcal/mol include zero point energies (ZPE). Comparison with previous works [353], [500] are shown in italics (in blue), while species names of [353], [500] are in brackets. Thicker lines highlight more relevant pathways. For the difference between * and** CASPT2 levels, see the main text.

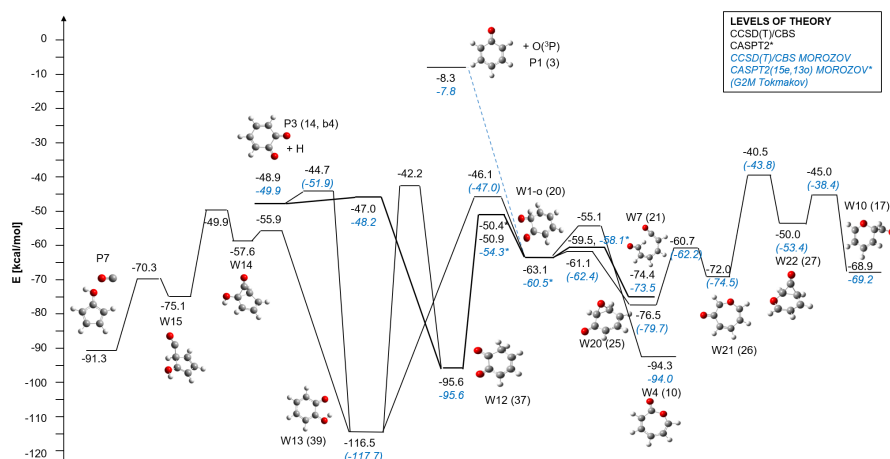


FIGURE 6.11: Main channels of C_6H_5OO PES accessed from $O(^3P)$ recombination on the ortho carbon of C_6H_5O . Energies in kcal/mol include zero point energies. Comparison with previous works [353], [500] are shown in italics (in blue), while species names of [353], [500] are in brackets. Thicker lines highlight more relevant pathways.

is also useful to determine radical decomposition rate constants for $o\text{-OC}_6\text{H}_4\text{OH}$, the main radical formed in the pyrolysis and oxidation of catechol (Sections 6.1.2 and 6.6.2.2).

Finally, Figure 6.12 shows the PES accessed from $O(^3P)$ recombination on the para carbon site of C_6H_5O . The main reaction channel is H transfer from W1-p to W19, which undergoes β -scission to $p\text{-C}_6\text{H}_4\text{O}_2 + \text{H}$. This pathway is more energetically favored than the direct C–H β -scission from W1-p, i.e., the only reaction channel studied in [353], [500]. Nevertheless, the global reactivity of $C_6H_5O + O(^3P)$ is not expected to change dramatically with respect to previous works [353], [500], since the main product channel remains the

same and the energy barriers to products are all lower in energy than the entrance channel. This work also investigates for the first time the formation of $p\text{-OC}_6\text{H}_4\text{OH}$ (W16) and its decomposition to either $p\text{-C}_6\text{H}_4\text{O}_2 + \text{H}$ (P4) or $\text{C}_5\text{H}_4\text{OH} + \text{CO}$ (P7) through a multi-step process analogous to that of phenoxy radical [470] (Section 6.3.2). The energy barrier for the rate determining step of the latter is comparable to that for the decomposition of the unsubstituted phenoxy radical (3 kcal/mol higher, see Section 6.3.2.3), in contrast with that of $o\text{-OC}_6\text{H}_4\text{OH}$ (W13), which is significantly higher (~ 10 kcal/mol higher than that for $p\text{-OC}_6\text{H}_4\text{OH}$) due to the stabilization of W13 through H-bonding between the adjacent C–OH and C=O groups.

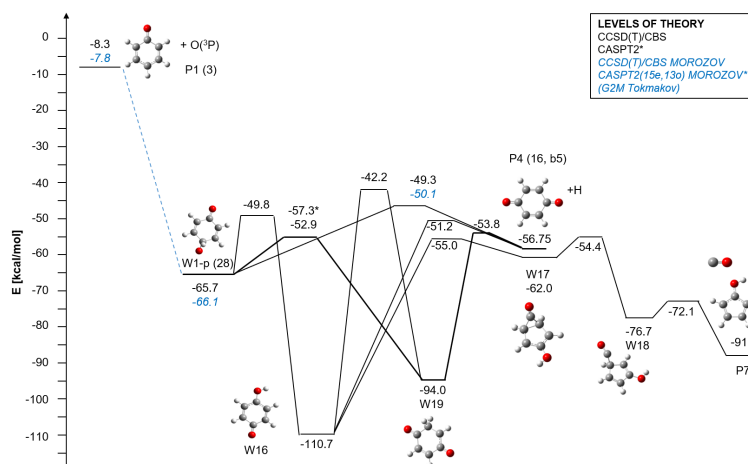


FIGURE 6.12: Main channels of $\text{C}_6\text{H}_5\text{OO}$ PES accessed from $\text{O}(^3\text{P})$ recombination on the para carbon atom of $\text{C}_6\text{H}_5\text{O}$. Energies in kcal/mol include zero point energies. Comparison with previous works [353], [500] are shown in italics (in blue), while species names of [353], [500] are in brackets. Thicker lines highlight more relevant pathways.

6.3.3.4 Recombination rate constants

Figure 6.13a shows the minimum energy path for the formation of phenylperoxy radical from $\text{C}_6\text{H}_5 + \text{O}_2$. The MEP is relatively flat until ~ 3 Å. All optimized structures along the MEP are planar, as also found by Tokmakov et al. [500]. The minimum of the flux in VRC-TST calculations was reached at distances of 2.0–2.8 Å at 2500–300 K, i.e., in the short range region, also corresponding to planar structures. Figure 6.13b compares the HP limit rate constant computed in this work with previous literature results. The present values agree to within 34% with the recent VRC-TST calculations of Zhang et al. [241] (see Table 6.20), where the final rate was obtained as an averaging of VRC-TST calculations on MEPs computed using CASPT2-based and MRCI-based spin-splitting approaches. Reasonable agreement (factor < 2.5) is also found with the VTST calculations of Da Silva and Bozzelli [515]. However, the present VTST calculations, which agree to within a factor of 2 from the VRC-TST results, strongly disagree with [515], probably due to the single-reference treatment of the MEP of the latter (see Table 6.20). Finally, the present rate constant is in excellent agreement with the room temperature experimental estimates of Tonokura et al.

[497] and Tanaka et al. [502], while slightly larger disagreement - but almost always within the error bars - is found with the higher temperature data of Yu et al. [501].

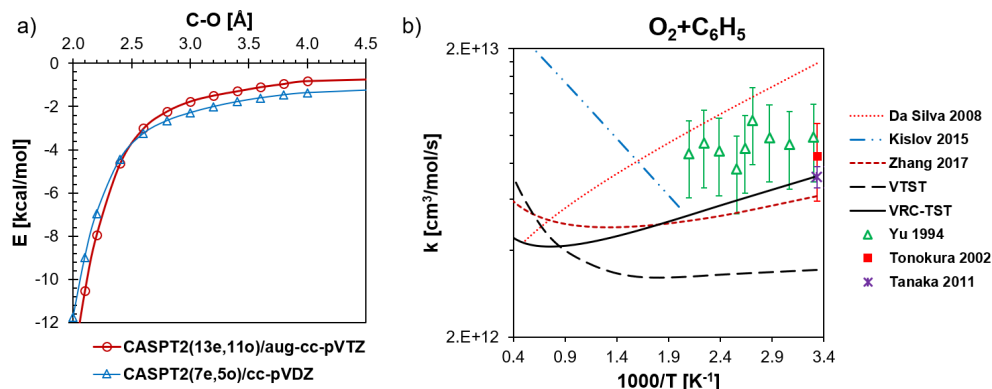


FIGURE 6.13: a) Minimum energy path (including ZPEs) and b) high-pressure limit rate constant for the recombination of molecular oxygen on phenyl. b) also reports comparison with experimental [439], [501], [502] and theoretical [241], [514], [515] literature data.

Figure 6.14a shows the minimum energy path for the recombination of $O(^3P)$ on the oxygen of phenoxy radical. Both the DFT and CCSD(T)/CBS MEPs have a maximum at 1.9 Å O–O distance, similar to the DFT results of Da Silva and Bozzelli [515] and to the G2M calculations of Tokmakov et al. [500]. As in these two works, the geometry of the maximum along the MEP is non-planar, confirming that the reaction occurs through symmetry breaking. Nevertheless, in the present results (both in the DFT and CASPT2 calculations) the C–O–O dihedral angle is perpendicular to the aromatic ring, as also found in the recent work of Morozov et al. [353]. MR calculations on both the DFT and CASPT2 geometries result in a flatter MEP and a shift in the region of the maximum to O–O distances of 2.1–2.2 Å. Figure 6.14a also compares energies obtained at the CASPT2(13e,11o) level using different basis sets and reference geometries. The use of the CASPT2 or DFT geometries and frequencies seems to have a negligible impact on the final MEP energies, especially in the region determining the minimum of the flux. On the other hand, the size of the basis set significantly affects the shape of the MEP: for instance, at O–O distances between 1.9 and 2.2 Å, energies vary up to 3 kcal/mol from ATZ to DZ basis sets.

The high-pressure limit rate constants obtained at different levels of theory are shown in Figure 6.15b. The higher energy predicted for the CASPT2/CBS MEP results in lower rate constants than those obtained using the CASPT2/ATZ energies by a factor of 2.5–1.29 in the 500–2000 K range. In contrast, the use of the DFT or CASPT2 geometries has an impact of < 20% on the resulting rate constant. All rate constants agree to within a factor of 1.7 with the results of Morozov et al. [353] (level of theory in Table 6.21).

Figure 6.14b, c show the MEPs for the recombination of $O(^3P)$ on the ortho and para carbon sites of C_6H_5O , respectively. In both cases, the level of theory strongly affects the predicted energies, probably due to the limited ability of the (5e,4o) AS to describe the evolution of the electronic configuration. It is also recalled that 3-state averaging was only used for the high level energies. This resulted in correction potentials for VRC-TST calculations between 0.5 and 6.5 kcal/mol at C–O distances of 3.8 and 2.4 Å, where the

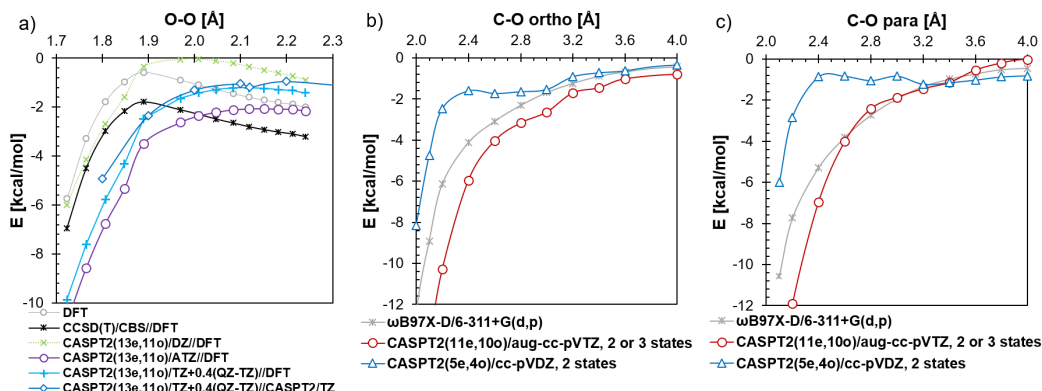


FIGURE 6.14: Minimum energy paths (including ZPEs) for the recombination of $O(^3P)$ on different sites of phenoxy radical: a) oxygen atom to form phenylperoxy, b) carbon atom in the ortho position, c) carbon atom in the para position). In panel a), DFT indicates the ω B97X-D/6-311+G(d,p) level of theory; CASPT2/TZ refers to an optimized geometry at the CASPT2(13e,11o)/TZ level; 0.4(QZ-TZ) refer to basis set extrapolation (see main text).

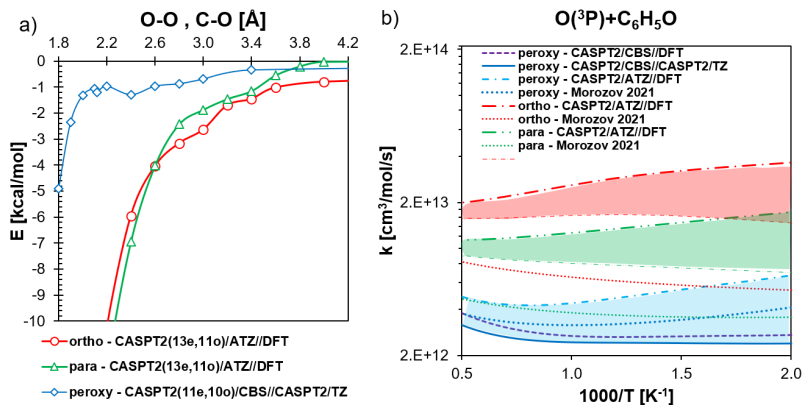


FIGURE 6.15: a) Selected MEPs for the recombination of $O(^3P)$ on different sites of the phenoxy radical and b) resulting high-pressure limit rate constants in comparison with literature results [353], highlighting uncertainty bands (see main text for details). DFT indicates the ω B97X-D/6-311+G(d,p) level of theory; CASPT2/TZ refers to an optimized geometry at the CASPT2(13e,11o)/cc-pVTZ level; CBS refers to basis set extrapolation as described in the main text.

minimum flux was reached at 500 K and above 1000 K, respectively. In this range, the energies on the MEP for the recombination on the para site are slightly higher, as shown in Figure 6.15a. Therefore, a smaller rate constant for the oxygen attack on the para carbon is expected for both energy and symmetry considerations. A similar relative behavior of the two MEPs at CASPT2(15e,13o)/CBS//CASSCF(13e,13o)/DZP (where extrapolation to CBS was based on DZ, TZ, QZ basis sets and the (7e,5o) AS) was obtained by Morozov et al. [353].

The resulting rate constants are compared in Figure 6.15b. Predicted rate constants for the recombination on the ortho and para carbon sites are in the $2\text{--}3.6 \times 10^{13}$ and $1.1\text{--}1.7 \times 10^{13}$ $\text{cm}^3/\text{mol}/\text{s}$ range, respectively, with a slightly negative temperature dependence. Shaded areas in Figure 6.15b highlight an uncertainty of ~ 0.9 kcal/mol in the energy barriers,

related to instabilities in the selected wavefunction for VRC-TST calculations. In particular, it is noted that 1) the predicted energy in the long range was always below 0, and 2) geometries minimizing the flux above $\sim 3 \text{ \AA}$ had the oxygen atom tilted away from the plane perpendicular to the aromatic ring, where the correction potential was derived. In both cases, the present rate constants are significantly higher than the results of Morozov et al. [353], i.e., a factor of 5–2 in the 500–2000 K range, reduced to a factor of ~ 2 considering the lower limit of the estimated uncertainty. This result is not very surprising, considering the high sensitivity in the energies to the selected AS, basis set, guess wavefunction, and structure. In this work, the recombination of the oxygen atom on the carbon sites is strongly favored over that on the oxygen atom, which is consistent with the optimized MEPs and with the reaction exothermicity. Similar trends are also observed in the theoretical work of Morozov et al. [353]. However in their theoretical predictions the rate constant for the formation of phenylperoxy is almost comparable to that of the recombination on the para carbon site.

6.3.3.5 Ring insertion TS

The ring insertion pathway (W3 \rightarrow W10) proceeds through 1) O–O bond-fission of W3, 2) symmetry breaking to a C_S structure with non-symmetric angles for the $2\times C-O$ bonds, and 3) symmetry breaking to a C_1 structure where one oxygen inserts in the ring. The careful B3LYP/6-311++G(d,p) investigation of Tokmakov et al. [500] essentially concluded that the rate determining step for this reaction is the first O–O bond breaking (C_{2V} symmetry, $2B'$ state), with an energy barrier of 12.7 kcal/mol (computed at G2M level). Morozov et al. [353] refined this energy barrier at the CASPT2(15e,13o)/CBS level of theory, obtaining a much smaller value of 8.1 kcal/mol.

In this work, B3LYP/6-311++G(d,p) and ω B97X-D/6-311++G(d,p) optimization resulted in two different saddle point structures, having C_{2V} and C_S symmetry, respectively, with the latter being about 6 kcal/mol higher in energy than the former (at the DFT level). Relevant structural parameters are depicted in Figure 6.16 (structures 1 and 2). Symmetry-constrained saddle point optimization at ω B97X-D/6-311++G(d,p) level of theory led to a second order saddle point ($2A''$ state), with the two imaginary frequencies corresponding to O–C–O scissoring and rocking on the O–C–O plane. In both cases, the imaginary frequency corresponds to O–C–O scissoring, however in the ω B97X-D structure C_{2V} symmetry breaking has already occurred. Further tests at B2PLYPD3 level of theory resulted in C_{2V} and C_S structures using 6-311+G(d,p) and jun-cc-pVTZ basis sets, respectively.

Another remarkable difference with the results of Morozov et al. [353] is the energy barrier computed at the CASPT2(15e,13o)/ATZ level of theory. The present calculations predict an energy barrier of 13.1 kcal/mol, 5 kcal/mol higher than in [353], despite the fact that the AS selected should be the same. Figure 6.17 shows the AS and orbital occupations for the AS selected for the calculation of the energy of $2B'$ state on the B3LYP/6-311+G(d,p) geometry. Orbitals were visually inspected also for C_1 symmetry wavefunctions (used for instance on the ω B97X-D/6-311++G(d,p) geometry), confirming the selection of the same

orbitals. Morozov et al. [353] describe that their AS selection was performed from the SCF wavefunction obtained in DFT calculations. The same procedure in this work led to an energy barrier of 8.9 kcal/mol, much closer to the literature value. However, visual inspection of the orbitals at the TS revealed that the AS includes σ , σ^* orbitals of C–C bonds (2e,2o) and a Rydberg-like orbital (with a high eigenvalue of 1.21), while two π , π^* orbitals corresponding to electrons on the aromatic ring were excluded. Significant differences in the energy for the reactant (W3) are excluded in light of the good agreement of the energy barrier for W3→W1 (also computed at the CASPT2 level in both cases).

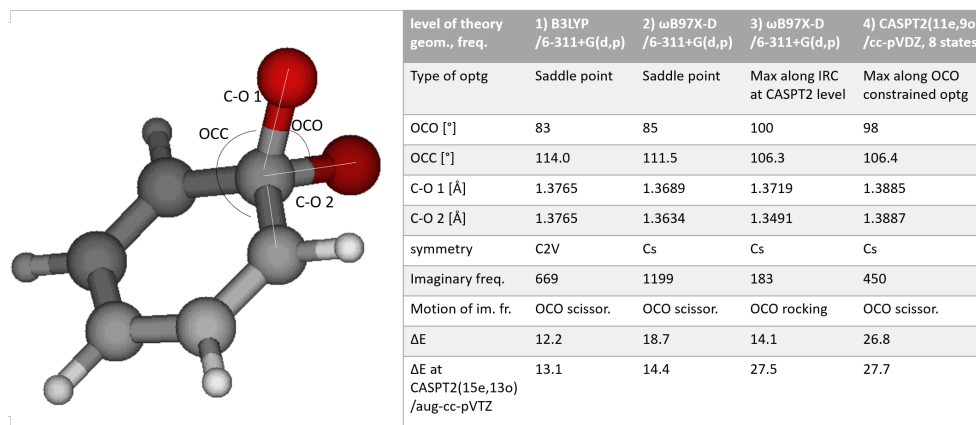


FIGURE 6.16: Main geometry parameters, imaginary frequencies, and energy barriers for the TS corresponding to the oxygen insertion in the aromatic ring obtained at different levels of theory and with different theoretical protocols.

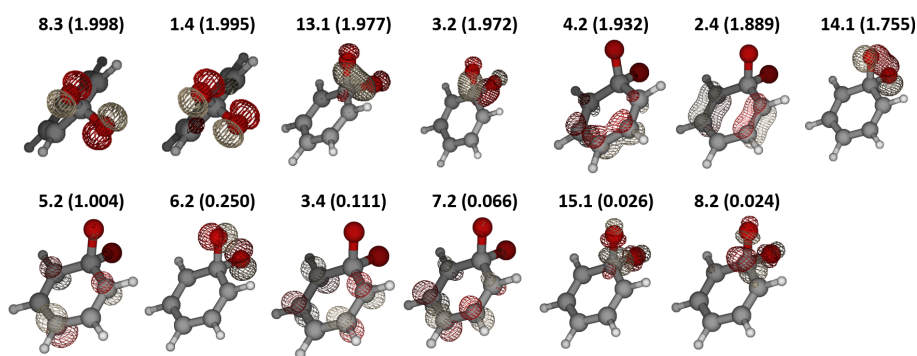


FIGURE 6.17: 15e,13o active space and corresponding orbital occupations for the oxygen ring insertion in the aromatic ring on the C_{2V} geometry obtained at the B3LYP/6-311+G(d,p) level of theory. X.1, 2, 3, 4 are orbitals in $2A'$, $2B'$, $2B''$, $2A''$ symmetry, respectively.

Further investigation of the AS and basis set sensitivity for the energy barrier computed at B3LYP and ω B97X-D geometries to the AS and basis set is shown in Table 6.22. The use of symmetry for the wavefunction on the same B3LYP structure results in discrepancies below 0.2 kcal/mol. Energy barriers obtained using different ASs with the ATZ basis set all agree to within 2.7 kcal/mol. The TZ, QZ and ATZ energies using the same AS (also for small ASs, not shown in the table) are extremely close (differences < 0.35 kcal/mol). In contrast, the CASPT2(15e,13o)/DZ energy barrier computed for the ω B97X-D geometry is about 2 kcal/mol lower than that obtained using the ATZ basis set. Despite the higher

energy obtained for the ω B97X-D structure, all energies agree to within 1.5 kcal/mol at the same level of theory, showing only relative sensitivity to the level of geometry optimization.

Finally, the energy barriers obtained can be compared to those for the oxygen ring insertion in the analogous $C_2H_3 + O_2$ system: Goldsmith et al. [198] obtained 17.7 kcal/mol at the CASPT2(13e,11o)/CBS//CASPT2(9e,8o)/TZ level of theory, within 1 kcal/mol to their results using the spin-splitting approach, while the G2M energy barrier was 24.0 kcal/mol [516], [517]. With respect to the (13e,11o) AS used by Goldsmith et al. [198], this work excludes the C–C bonds, which affected their energy barrier by about 1 kcal/mol.

TABLE 6.22: Energy barriers [kcal/mol] for the TS of oxygen insertion in the aromatic ring at the CASPT2 level using DZ, TZ, QZ, ATZ basis sets and different active spaces (AS). The level of theory used for geometry optimization and the corresponding wavefunction symmetry are also specified (i.e., structure 1 and 2 of Figure 6.16).

AS	basis	B3LYP, C_{2V}	B3LYP, nosym	ω B97X-D, nosym
15e,13o	TZ	13.45	13.31	14.73
15e,13o	QZ	13.50	13.42	14.88
15e,13o	DZ			12.29
15e,13o	ATZ	13.11	13.05	14.39
11e,11o	ATZ	13.13		
11e,9o	ATZ	15.80		17.12
7e,7o	ATZ	14.90		
7e,5o	ATZ			14.67
3e,3o	ATZ	15.24		
15e,13o as in [353]	ATZ	8.94		

Because of the peculiarity of this TS, CASPT2 geometry optimization was also attempted. CASPT2 geometry optimizations at constrained values of the OCO angle in the 80–115° range were conducted using ASs of 3e,3o (radical on the ring and O–O breaking bond), 7e,7o (adding a 4e,4o π space from the aromatic ring), 11e,9o (adding the oxygen lone pairs) using DZ and TZ basis sets. (3e,3o) and (7e,7o) optimizations were performed constraining C_S symmetry and including a single (A') electronic state. The (3e,3o) optimization highlighted a maximum around $OCO = 100^\circ$, corresponding to a C_{2V} geometry and with an imaginary frequency ($1127i \text{ cm}^{-1}$) associated with O–O bond breaking; at larger angles, the symmetry breaks to C_s , as the radical shifts from the ring to one oxygen. At 108° , C_S symmetry breaks ($307i \text{ cm}^{-1}$ for OCO out of plane) at a lower energy with respect to the C_{2V} breaking (by about 1.5 kcal/mol). A similar behavior was observed for the (7e,7o) AS.

Inspection of multi-state wavefunctions using (3e,3o) and (7e,7o) ASs revealed two nearly-degenerate states in the region of the maximum. Therefore, additional (C_s) constrained optimization was performed at the CASPT2(11e,9o)/DZ level using 4-state averaged wavefunctions for both A' and A'' states. Figure 6.18 shows that the A' and A'' MEPs intersect at $OCO = 98^\circ$, corresponding to an intersection of the ground A' state and the first two A'' states. In the $OCO = 98$ – 112° region, all 8 states are very close in energy (within 10 kcal/mol). The MEP was therefore optimized also without symmetry constraints for the geometry and wavefunction including the first 8 reference states, obtaining the MEP shown as black line in Figure 6.18. The maximum is 26.8 kcal/mol above the reactant W3, and its imaginary frequency corresponds to O–O breaking (parameters of structure 4 in Figure

6.16). The geometry is slightly distorted with respect to C_{2V} , with OCC angles differing by $\sim 1^\circ$.

Despite the steps for the ring insertion seem relatively clear, no unconstrained saddle point optimization along the investigated MEPs succeeded, and all frequency calculations showed poor convergence. CASPT2(15,13o)/ATZ energy calculations for the maximum found at the CASPT2(11e,9o)/DZ level resulted in an energy barrier of 27.7 kcal/mol, definitely larger than any literature value. CASPT2(15e,13o) SPE calculations were also performed on the IRC path computed at ω B97X-D level of theory. Also on DFT geometries, the maximum was found at a high OCO angle of 100.1° (structure c in Figure 6.16), with a CASPT2(15,13o)/ATZ energy barrier of 27.5 kcal/mol. Energies computed in this region are also shown as the red MEP of Figure 6.18.

Finally, further CASPT2(7e,5o) and MRCI+Q(7e,5o) (using 4-state averaging) calculations were performed on the maximum found along the IRC pathway (structure c in Fig. 6.16) to try to better estimate the uncertainty of this energy barrier. Table 6.23 reports that MRCI+Q energies are about 5 kcal/mol lower than CASPT2 energies obtained at the same level of theory. Approximate AS correction from CASPT2 values (i.e., from 7e,5o to 15e,13o, see Table 6.23) applied to MRCI+Q energy with the smaller AS suggests an energy barrier around 22 kcal/mol (indicated as CASPT2+CI in the following).

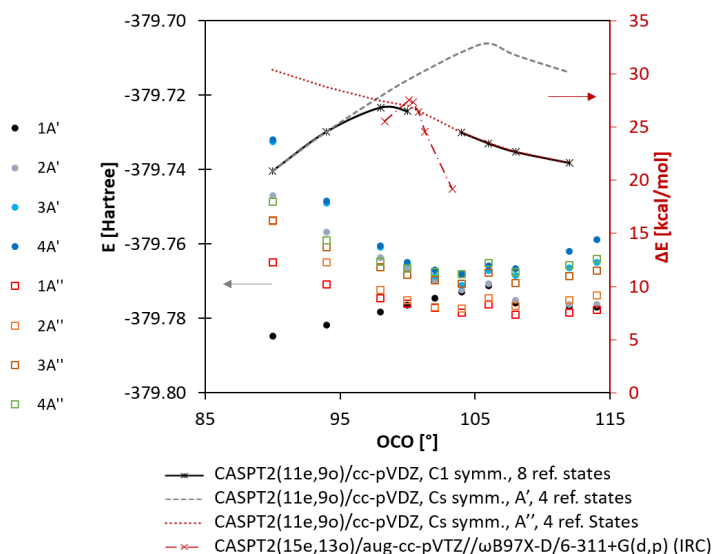


FIGURE 6.18: MEP along the OCO angle for the oxygen ring insertion. Symbols are energies in Hartree (left axis) of the four lowest A' and A'' states obtained with C_S optimizations. The interrupted black line is due to convergence failure at 102° .

6.3.3.6 Rate constants: reconciling theory and experiments

The huge variations obtained for the TS of the oxygen ring insertion do not allow to provide a best estimate for the energy barrier for this TS. However, comparison with the microkinetic ST experiments of Frank et al. [303] and Kumaran and Michael [506] helps to decrease the uncertainty in the final rate constants obtained. Of all the reaction channels computed on

TABLE 6.23: Energy barrier for the oxygen ring insertion TS at the CASPT2 maximum found along the IRC path (geometries and frequencies at ω B97X-D/6-311+G(d,p) level, OCO angle of 100.1°).

basis set	15e,13o CASPT2	7e,5o CASPT2	7e,5o MRCI+Q	MRCI+Q(7e,5o)+ (CASPT2(15e,13o)-(7e,5o))
DZ	24.7	27.4	23.2	20.5
TZ	27.8	31.2	25.6	22.3
QZ	28.0	31.6	25.8	22.3
ATZ	27.5	30.9	25.6	22.2

the $C_6H_5 + O_2$ PES, kinetic simulations of these experimental data are only sensitive to the branching fractions of $C_6H_5O + O$ vs $C_5H_4O + HCO$ from $C_6H_5 + O_2$ and $C_6H_5O_2$. Hence, a reduced set of rate constants obtained from ME simulations considering only the $C_6H_5 + O_2$, W1, P1, and W4 (assumed to fully decompose to $C_5H_4O + HCO$) from the PES depicted in Figure 6.10 was integrated into the CRECK kinetic mechanism to simulate these sets of experiments. The W1→P1 bond-fission rate constant used for the simulations was the CASPT2/CBS//CASPT2/TZ described in Section 6.3.3.4 (solid blue line in Figure 6.15b). Later kinetic simulations confirmed that the results obtained are identical to those simulated with the full set of rate constants.

Figure 6.19a-c show the experimental and simulated O and H atom profiles at the experimental conditions reported in Table 6.18. The level of theory adopted for the TS of the oxygen ring insertion is also specified. ME simulations were also performed adopting the B3LYP structure (1 in Figure 6.16) and the energy barrier of 8.1 kcal/mol computed by Morozov et al. [353]. The calculated BFs of $C_6H_5 + O_2 \rightarrow C_6H_5O + O / C_5H_4O + HCO$ (main sources of O and H atoms, respectively) obtained from ME simulations are also depicted in Figure 6.19d.

The experiments of Kumaran and Michael [506] are the most diluted available in the literature and therefore the least sensitive to secondary reactions. They predict O and H BFs of about 70% and 30% in the 1000–1400 K temperature range. The simulated profiles of Figure 6.19a,b show that the 8.1 and 14.4 kcal/mol energy barriers obtained for structure 1 by Morozov et al. [353]) and for structure 2 in this work, are incompatible with experimental trends, as they predict that H prevails or is comparable to O (consistent with the BFs of Figure 6.19d). Using the CASPT2+CI estimate of 22.3 kcal/mol for the ring insertion barrier on structure 3 results in better agreement with the experimental trends, however the slope for the generation of H atoms at 1400 K (Figure 6.19b) suggests that the rate constant for the oxygen ring insertion is underpredicted. All simulated profiles predict a stronger temperature dependence than that of the experiments.

The O and H experimental profiles measured by Frank et al. [303] (Figure 6.19c) lead to similar conclusions. However, in this case the simulated profiles seem to vary less with the level of theory, probably due to the increased effects of secondary reactions.

A best fit of the experimental profiles (solid lines in Figure 6.19) was obtained by decreasing the CASPT2+CI insertion barrier obtained on structure 3 by 2 kcal/mol, resulting in a weaker temperature dependence for the $C_6H_5 + O_2 \rightarrow C_6H_5O + O$ and $C_5H_4O + HCO$ branching fractions, which are approximately 70% and 30%. Similar profiles were obtained

by increasing the O ring insertion barrier at the CASPT2(15e,13o) level on structure 2 by 2 kcal/mol and using the upper limit rate constant found for the O–O bond-fission channel (light blue dash-dotted line of Figure 6.15b). This best fit barrier was chosen for the final ME simulations to derive phenomenological rate constants.

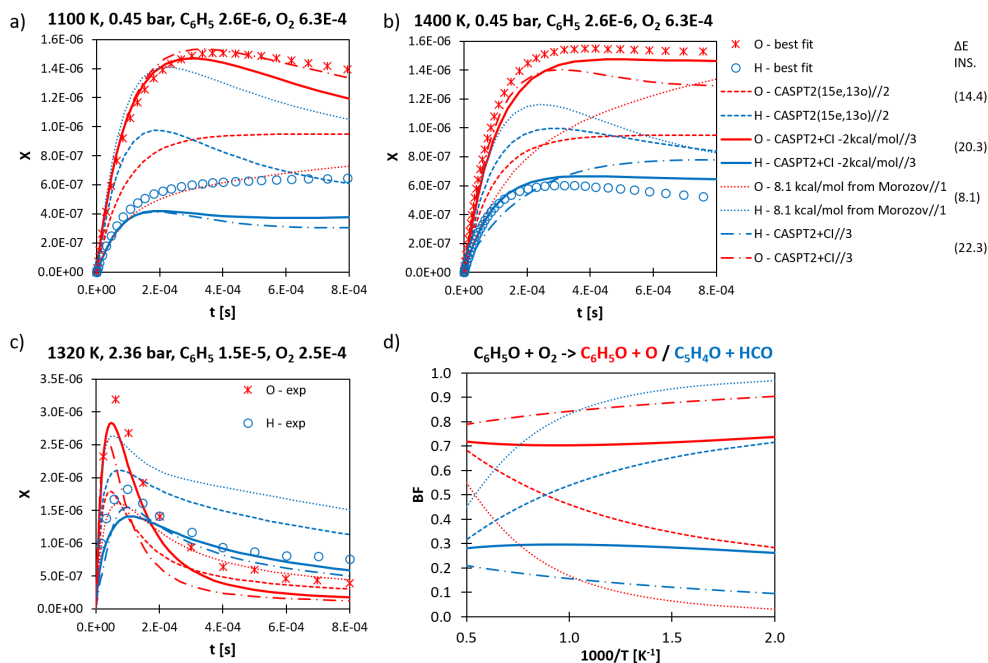


FIGURE 6.19: Experimental and simulated O and H profiles in the ST experiments of a,b) Kumaran and Michael [506] and c) Frank et al. [303] (operating conditions in Table 6.18). Data points of Kumaran and Michael [506] were retrieved from their small mechanism presented as best-fit of experimental profiles. d) Shows the branching fractions for the O and H generation channels from $C_6H_5 + O_2$ at 1 atm. In the legend, levels of theory refer to the theoretical treatment of the ring insertion TS on structures of Figure 6.16, with corresponding energy barriers specified in brackets.

The profiles of Frank et al. [303] (Figure 6.19c) show a peak in H and O profiles, followed by an inversion in their concentrations. This behavior, as well as the peaks obtained in some of the simulated H and O profiles of Figure 6.19a,b clearly highlight the influence of secondary reactions. Figure 6.20 depicts the main pathways involving the production and consumption of O and H atoms according to the CRECK mechanism. The concentration of O is primarily produced from $C_6H_5 + O_2 \rightarrow C_6H_5O + O$, and it is partially consumed (25%–35% at 1300 K) by $O + C_5H_5$. In the ST of Frank et al. [303], atomic oxygen is also consumed directly by $O + C_6H_5 \rightarrow C_5H_5 + CO$, thus also enhancing the $O + C_5H_5$ reaction. It is noted that the relevance of the $O + C_6H_5$ and $O + C_5H_5$ reactions was already highlighted in the corresponding experimental works, however the main product of $O + C_5H_5$ was assumed to be $C_5H_4O + H$. In this work, the total rate constant for $O + C_5H_5$ (lumped from [293]) is 1.5 times higher than the estimate in [303], [506], while that for $O + C_6H_5$ is a factor of 2 smaller than the best fits in [303], [506].

The reaction network for H atom production and consumption is more complex, as shown in the scheme of Figure 6.20. In both sets of kinetic simulations, up to $\sim 70\%$ of H production is from HCO dissociation, i.e., directly from $C_6H_5 + O_2$. However, β -scission from C_4H_5 also plays a key role in its production, resulting in almost 50% of H production in the simulated

ST of Frank et al. [303]. Since C_4H_5 is almost entirely produced from $O + C_5H_5$, where C_5H_5 derives from phenoxy decomposition, H concentration ends up depending indirectly on that of O. Additionally, in both sets of simulations H is largely consumed (30–80% in the more and less diluted conditions, respectively) by $H + C_5H_5$. Finally, at higher temperatures and concentrations the recombination of H with phenyl and phenoxy radicals also contributes to H consumption. Despite the complexity of this network, the predictions of H profiles using the best fit of this work (solid lines in Figure 6.19) are satisfactory.

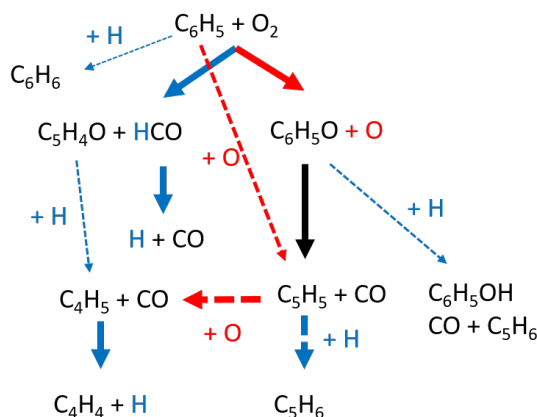


FIGURE 6.20: Main production (solid lines) and consumption (dashed lines) pathways of O (red) and H (blue) atoms in the microkinetic ST experiments of Kumaran and Michael [506] and of Frank et al. [303].

The chosen barrier for O ring insertion was used for the final ME simulations and the derivation of the lumped rate constants. The plots of the lumped rate constants for the main reaction pathways from $C_6H_5 + O_2$ and $C_6H_5O + O(^3P)$ are shown in Figure 6.21. The corresponding modified Arrhenius expressions in PLOG format are listed in Table 6.24, which also includes rate constants for the reactivity of *o*- OC_6H_4OH and *p*- $C_6H_4O_2$.

Figure 6.21a shows that the predicted fraction of $C_6H_5O + O$ and $C_5H_4O + HCO$ from $C_6H_5 + O_2$ does not vary strongly with temperature and pressure. The phenylperoxy radical only stabilizes below 1000 K at lower pressures, however at 10 atm it accumulates up to 1300 K. The product fractions of $C_6H_5O_2$ are similar to those from $C_6H_5 + O_2$, as the back-dissociation to reactants plays a negligible role at the conditions investigated.

The main product channel of $C_6H_5O + O$ is $C_5H_4O + HCO$ (Figure 6.21b). In fact, the recombination on the ortho carbon site prevails, and the adduct formed mostly undergoes ring opening to a precursor of $C_5H_4O + HCO$ (see PESs of Figure 6.10, 6.11). Rate constants for other pathways derived from the recombination on the ortho site are generally more than one order of magnitude slower. At low temperatures, *o*- OC_6H_4OH stabilizes, while at high temperatures the channel to furan becomes accessible, in contrast with predictions of previous works. The recombination of atomic oxygen on the para site of phenoxy radical instead mostly produces *p*- $C_6H_4O_2 + H$. At low temperatures, *p*- OC_6H_4OH also accumulates. Both *o*- OC_6H_4OH and *p*- OC_6H_4OH isomers either lose an H or decompose to $C_5H_4OH + CO$, similar to phenoxy (Section 6.3.2). This work presents for the first time decomposition rate constants for OH-substituted species.

Comparisons of the global mechanism with experimental benzene flow reactor and flames measurements are presented in Section 6.6.1. Further discussion on the effect of the rate constants adopted is provided (especially in relation to their sensitivity to the benzene laminar flame speed predictions 6.6.1.4).

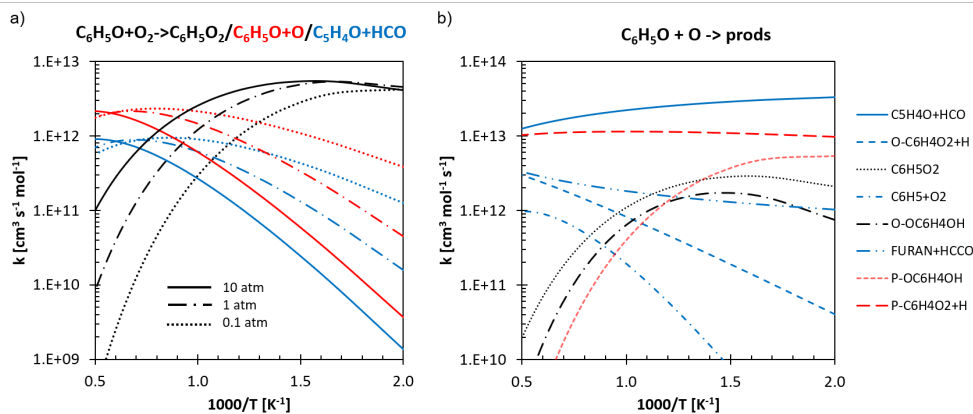


FIGURE 6.21: Lumped rate constants for a) $C_6H_5 + O_2$ using the BF from the solid lines of Figure 6.19d (see text for details) and for b) the main channels of $C_6H_5O + O$ at 1 atm.

TABLE 6.24: Lumped set of rate constants for the $O_2 + C_6H_5$, $O + C_6H_5O$, $C_6H_5O_2$, $o-OC_6H_4OH$, $H + p-C_6H_4O_2$ reaction channels for the CRECK mechanism. Pressure dependent reaction parameters are provided according to the modified Arrhenius expression $k = k_0 \cdot T^\alpha \cdot \exp(-\frac{E_A}{RT})$ in PLOG form, units are cm^3 , mol, s, cal, atm, K. Fitting quality and temperature range are also provided.

Reaction, p	k_0	α	E_A	R^2	T range	
$C_6H_5 + O_2 = C_6H_5O_2$	0.01	5.45E+68	-18.2	16500	1.00	500–1100
	0.1	2.52E+62	-15.8	16445	1.00	500–1200
	1	6.39E+52	-12.5	14603	0.99	500–1400
	10	7.76E+40	-8.7	11023	0.97	500–1600
	100	1.06E+29	-5.0	6692	0.83	500–1800
$C_6H_5 + O_2 = C_6H_5O + O$	0.1	1.41E+23	-3.1	7621	0.96	500–2000
	1	2.76E+28	-4.5	13101	1.00	500–2000
	10	1.91E+26	-3.7	15265	0.99	500–2000
	100	1.48E+14	-0.1	12119	0.99	500–2000
$C_6H_5 + O_2 \rightarrow C_5H_4O + HCO$	0.01	5.13E+25	-4.0	7133	0.93	500–2000
	0.1	2.92E+26	-4.1	9579	1.00	500–2000
	1	3.87E+29	-4.9	14033	1.00	500–2000
	10	1.65E+27	-4.1	16115	0.99	500–2000
	100	4.31E+15	-0.7	13346	0.99	500–2000
$C_6H_5O_2 \rightarrow C_5H_4O + HCO$	0.01	5.59E+66	-16.8	54804	1.00	500–1100
	0.1	8.29E+56	-13.5	52690	1.00	500–1200
	1	1.08E+47	-10.3	50061	1.00	500–1400
	10	4.16E-13	7.2	17574	0.97	500–1600
	100	5.87E-08	5.8	21364	0.98	500–1800
$C_6H_5O + O = C_6H_5O_2$	0.01	6.05E+65	-16.9	17820	1.00	500–1100
	0.1	1.32E+56	-13.7	15742	0.99	500–1200
	1	8.89E+46	-10.7	13400	0.98	500–1400
	10	2.10E+36	-7.3	9870	0.95	500–1600

	100	1.11E+26	-4.1	5978	0.90	500-1800
<hr/>						
C ₆ H ₅ O+O → o-OC ₆ H ₄ OH						
	0.01	3.50E+75	-20.6	20319	1.00	500-1900
	0.1	5.33E+74	-19.6	23105	1.00	500-2000
	1	4.06E+62	-15.4	20928	0.98	500-2000
	10	4.62E+40	-8.5	13031	0.92	500-2000
C ₆ H ₅ O+O → C ₅ H ₄ O+HCO						
	0.01	3.23E+16	-1.0	538	1.00	500-2000
	0.1	3.26E+16	-1.0	544	1.00	500-2000
	1	4.67E+16	-1.1	667	1.00	500-2000
	10	2.84E+20	-2.1	3709	0.98	500-2000
	100	7.04E+21	-2.4	8125	0.99	500-2000
dup. *from C ₅ H ₄ OCHO						
	0.1	1.24E+55	-14.9	13858	1.00	500-1300
	1	3.67E+58	-15.4	11300	1.00	500-1400
	10	8.05E+65	-16.7	17887	1.00	500-1600
	100	7.64E+49	-11.2	14693	0.99	500-1900
C ₆ H ₅ O+O → C ₅ H ₅ +CO ₂						
*form C ₅ H ₄ OCHO						
	0.1	2.47E+44	-12.3	6173	1.00	500-1300
	1	7.41E+48	-13.2	3635	1.00	500-1400
	10	9.13E+57	-15.0	10739	1.00	500-1600
	100	8.59E+42	-9.9	7856	0.99	500-1900
<hr/>						
C ₆ H ₅ O+O → FURAN+HCCO						
	0.01	1.37E+09	1.0	-419	1.00	500-2000
	0.1	1.45E+09	1.0	-397	1.00	500-2000
	1	3.21E+09	0.9	-109	1.00	500-2000
	10	1.24E+12	0.2	2155	1.00	500-2000
	100	1.64E+11	0.5	3946	1.00	500-2000
<hr/>						
C ₆ H ₅ O+O → p-C ₆ H ₄ O ₂ +H						
	0.01	2.97E+12	0.1	-831	1.00	500-2000
	0.1	4.50E+12	0.1	-694	1.00	500-2000
	10	3.90E+14	-0.4	1957	0.97	500-2000
	100	9.00E+08	1.2	-759	0.98	500-2000
C ₆ H ₅ O+O → P-OC ₆ H ₄ OH						
	0.01	5.44E+70	-19.6	16356	1.00	500-1700
	0.1	1.24E+71	-18.9	18913	1.00	500-1900
	1	3.16E+62	-15.8	16550	1.00	500-2000
	10	7.52E+53	-12.7	15318	0.99	500-2000
	100	3.81E+36	-7.3	9192	0.98	500-2000
<hr/>						
o-OC ₆ H ₄ OH → C ₆ H ₄ O ₂ +H						
	0.01	1.65E+60	-13.7	92610	1.00	500-1900
	0.1	2.49E+49	-10.3	89229	1.00	500-2000
	1	3.18E+29	-4.4	77779	0.99	500-2000
	10	4.03E+17	-0.8	73085	1.00	500-2000
	100	4.47E+08	1.9	69013	1.00	500-2000
o-OC ₆ H ₄ OH → C ₅ H ₄ O+HCO						
	0.01	4.24E+62	-14.6	92466	1.00	500-1900
	0.1	8.45E+57	-12.9	93895	1.00	500-2000
	1	4.07E+44	-8.9	88518	0.99	500-2000
	10	3.97E+33	-5.4	88441	1.00	500-2000
	100	1.52E+07	2.4	79183	1.00	500-2000
o-OC ₆ H ₄ OH → C ₅ H ₄ OH+CO						
	0.01	2.08E+53	-11.8	84369	1.00	500-1900
	0.1	1.24E+146	-37.8	148564	0.98	500-2000
	1	3.02E+149	-38.5	153510	0.97	500-2000
	10	6.68E+172	-45.0	170880	0.96	500-2000

	100	1.62E+07	2.0	62290	1.00	500–2000
<hr/>						
p-C ₆ H ₄ O ₂ +H → C ₅ H ₄ OH+CO						
*second set from P-OC ₆ H ₄ OH						
	0.01	7.28E+66	-16.2	24812	0.96	500–1700
	0.01	2.31E+37	-6.4	28351	1.00	500–2000
	0.1	1.44E+59	-13.7	23181	0.92	500–1900
	0.1	6.88E+31	-4.7	28866	1.00	500–2000
	1	3.53E+49	-10.6	20100	0.81	500–2000
	1	3.96E+18	-0.8	25105	1.00	500–2000
	10	9.47E+31	-5.3	12772	0.80	500–2000
	10	1.20E+01	4.3	18491	1.00	500–2000
	100	1.76E+17	-0.8	6167	0.99	500–2000
	100	1.29E-14	8.5	12420	1.00	500–2000
<hr/>						

6.4 Theoretical calculations by reaction class: H-atom abstraction reactions from mono-substituted MAHs

6.4.1 Motivation

H-atom abstraction reactions are the most important radical formation reactions in combustion systems. In aromatic systems, hydrogen abstractions from the aromatic ring are the first step of the HACA mechanism leading to phenyl-like radical and successive acetylene addition and PAH growth [62]. On the other hand, abstractions from substituted MAH functional groups may lead to resonance-stabilized radicals such as benzyl, also key in PAH growth via recombination reactions [405], or phenoxy, key to benzene oxidation and PAH growth [295], [350], [518]. Nevertheless, no systematic theoretical investigation of the H-atom abstractions from aromatic hydrocarbons is available in the literature except for the recent work on H-atom abstraction from OAHs by Wang et al. [519]. This calls for an extensive theoretical work for a consistent kinetic model update and the exploration of rate rule formulation by reaction class. Hence, this work investigates H-atom abstraction reactions by H, CH₃, OH, and ³O₂ from benzene, toluene, phenol, and anisole, using the AI-TST-ME method. H-atom abstractions by OH and ³O₂ from toluene were revised from the recent theoretical investigation of Pelucchi et al. [129]. The large set of 52 rate parameters reported is useful both for direct implementation in existing kinetic models and for analogy-based extension to MAHs with multiple substitutions, or PAHs with the same functional groups, as explored in Section 6.4.5. This section also assesses the accuracy of the theoretical methodology adopted both by comparison with the available literature data and by testing the role of variational treatment, torsional anharmonicities, internal coordinates and of different levels of theory for single point energy calculations. Finally, it is recalled that, as reported in the previous sections, the rate constants from the functional group of benzaldehyde C₆H₅CHO were also calculated at the same level of theory and the kinetic model was updated with the results of the calculations, while the rate constants of the H-atom abstractions from the aromatic ring were not calculated. The observations for this set of rate constants are redundant with what was already reported in this section and are therefore not discussed.

6.4.2 Theoretical methodology

Electronic structure calculations were performed with EStokTP as in the rest of this work. The M06-2X functional [208] and 6-311+G(d,p) basis set were used for geometry optimization and frequency calculations for stationary points, since this methodology was proved to be accurate in the calculation of H-atom abstraction reactions from toluene [129] and to perform best among a selection of DFT methods in estimating the energy barriers for H-atom abstraction reactions by H from benzene and larger aromatics [520]. SPEs were refined at the CCSD(T)/aug-cc-pVTZ level of theory, and corrected for basis set effects with the change between density fitted (DF) MP2 energy computed with aug-cc-pVQZ and aug-cc-pVTZ basis sets. CASPT2/aug-cc-pVTZ level of theory was instead used for reaction pathways with TSs having large T1 diagnostic (Section 3.1.3.2). This was the case for the TSs of the H-atom

abstractions by $^3\text{O}_2$ and OH from the phenol hydroxy group (T1 diagnostic of 0.034 and 0.077, respectively). The selected active space for the former reaction included 10 electrons in 10 orbitals (10e,10o), namely the 6 π and π^* bonding and anti-bonding orbitals of the aromatic ring (6e,6o), the bonding and anti-bonding orbitals of the O–H breaking bond, and the two singly-occupied orbitals of $^3\text{O}_2$. The energies of the entrance van der Waals well and of the product (with HO_2 positioned at 10 Å from the O of the phenoxy radical), with respect to which the energy barrier was computed, were determined using the same AS. The AS for H-atom abstraction by OH on phenol included 13 electrons in 11 orbitals (13e,11o), namely 6 π and π^* bonding and anti-bonding orbitals of the aromatic ring (6e,6o), the σ and σ^* bonding and anti-bonding orbitals of the breaking O–H bond (2e,2o), the singly-occupied orbital of the OH (1e,1o), and the lone pairs of the phenolic oxygen and of the OH radical (4e,2o). The energies of the reactants (with the OH positioned at 10 Å from the H atom abstracted from phenol) and of the intermediate entrance van der Waals well were computed with the same AS. Calculations were performed using an IPEA shift of 0.25. The AS was considered well converged, with energy differences of about 1–1.5 kcal/mol with respect to the simpler CASPT2(9e,9o)/aug-cc-pVTZ, CASPT2(9e,9o)/cc-pVDZ and CASPT2(13e,11o)/cc-pVDZ levels of theory. Due to the peculiar structure of this TS, further geometry optimization at the CASPT2(13e,11o)/jun-cc-pVTZ level of theory was performed and energies were refined at the CASPT2(13e,11o)/aug-cc-pVTZ level of theory using an IPEA shift of 0.25.

For the H-atom abstractions by H, CH_3 , OH from benzene, as well as some other H-atom abstractions from the methyl and methoxy groups of toluene and anisole, respectively, the impact of higher levels of theory used for the calculation of geometries, frequencies and single point energies was tested. In particular, the structures and vibrational frequencies were computed at the B2PLYPD3/jun-cc-pVTZ level of theory [521]–[524]. Energies were further refined by including corrections for the core electrons as the difference between CCSD(T),core/cc-pCVTZ and CCSD(T)/cc-pCVTZ energies. The rate constants obtained at this higher level of theory are marked with * in the text.

Finally, because of the high computational efficiency of the recently developed PNO-LCCSD(T)-F12 methodology implemented in the latest release of Molpro [147], [202], the performance of this method for both the energy barriers and the reaction energies was tested on a large subset of the reactions investigated in this work. In particular, the energies of all stationary points of all H-atom abstractions from phenol, toluene and anisole functional groups and from the benzene ring were computed at PNO-LCCSD(T)-F12/cc-pCVTZ-F12 level of theory. Extrapolation to the basis set limit was obtained with density fitted PNO-LMP2-F12 energies using cc-pCVQZ-F12 and cc-pCVTZ-F12 basis sets. The results of this investigation are reported in Section 6.4.4.

The partition functions for torsional motions were determined according to the 1D or, in a few cases, 2D hindered rotor model [106], and the corresponding torsional potentials were determined at 20° intervals at the M06-2X/6-311+G(d,p) level. For all reaction channels, intrinsic reaction coordinate calculations were performed (as described in Section 3.3.2.2), considering at least 10 steps of 0.02 Å along the minimum energy path in the direction of both reactants and products.

Van der Waals wells that precede and follow the TSs were also determined so as to compute properly the energy barrier for quantum tunneling corrections, determined using the Eckart model [263]. In some cases, to reduce computational time, the energies of the van der Waals wells were calculated at the DFT level of theory of geometries and frequencies. For the 54 van der Waals complexes for which HL SPEs were computed, the DFT energies underestimate the CCSD(T)/aug-cc-pVTZ energy by an average of 1.2 kcal/mol, with maximum discrepancy of 2.2 kcal/mol. In the latter cases, the calculated rate varies by less than 10% above 500 K, which supports the accuracy of the adopted approach.

The rate constants of the investigated reactions were computed in the 500 – 2000 K temperature range by solving the one-dimensional ME as implemented in MESS [265] (Section 3.3.4.3). It is recalled that abstraction reactions generally show no pressure dependence (as confirmed also in this work), however using a ME code allows one to properly exclude from the rate constant calculation the contribution of reaction fluxes from energies below that of the reactants when the saddle point energy is submerged. All rate constants were computed using both microcanonical conventional TST and its variational implementation (VTST), both in internal (VTST-int) and Cartesian coordinates (VTST-xyz). Vibrational frequencies in internal coordinates were computed with the Hessian manipulation code that is part of EStokTP and using the Z-Matrix automatically set up from the reactants by EStokTP. The transitional modes involved in the reaction TS are automatically identified and thus included in the B-Matrix used to compute the internal vibrational frequencies. It is expected that this approach is physically more consistent than the Cartesian coordinate representations and therefore this is the set finally implemented in the kinetic model. Comparisons among the different kinetic theories adopted are provided in the next sections.

6.4.3 Rate constant calculations

This section presents an overview from the results of the theoretical calculations. The following subsections instead provide detailed comparisons with literature calculations and considerations about the methodologies adopted. The observations for all H-atom abstractions from benzene also apply to abstraction reactions from the aromatic ring of all substituted MAHs, as highlighted in Section 6.4.4. Table 6.25 reports the Arrhenius parameters for the rate constants calculated in this study for both the forward and backward directions. Figure 6.22 shows all the rate constants computed in this work grouped by abstracting radical, together with literature data not specifically addressed in the next sections. The rate constants for H-atom abstractions from substituted rings are plotted as the sum of the rate constants for all ring sites, hence they are easily compared to the reference rates of the H-atom abstractions from benzene. The rate constants for the H-atom abstractions by $^3\text{O}_2$ vary by many orders of magnitude and therefore their differences would hardly be visible in the plot, hence they are plotted in the reverse direction.

Figure 6.22 highlights one of the most important aspects of this work, namely the internal consistency of the set of rate constants presented. In fact, all of the rate constants for the H-atom abstractions from the ring sites agree to within a factor of ~ 2 , supporting the use of the rate constants from benzene as a reference for all aromatic rings. The total rate

constants for the abstraction by OH from phenol and anisole rings (Figure 6.22d) are lower than that from benzene (by a factor of ~ 3) because of the significantly lower contribution of the abstraction from the ortho sites.

Another useful takeaway of this set of plots relates to the competition of H-atom abstractions from the ring and from the functional groups in substituted MAHs. In most cases, H-atom abstractions from the functional groups are favored mostly because of the lower bond energies of the breaking bonds, as a consequence of the formation of resonance-stabilized π systems. Consequently, it is expected that in oxidation conditions the reactivity of the phenyl-like radicals formed from substituted MAHs will be less relevant than that of the MAH-specific radicals such as phenoxy or benzyl. In contrast, at high temperatures also H-atom abstractions from the aromatic ring may become competitive, as clearly indicated by all plots. This trend is particularly relevant in the case of phenol: considering an H abstracting radical (Figure 6.22a), the abstraction from the aromatic ring prevails over that from the hydroxy group above 1400 K. This point is of vital importance to the understanding of global combustion mechanisms for MAHs and PAHs.

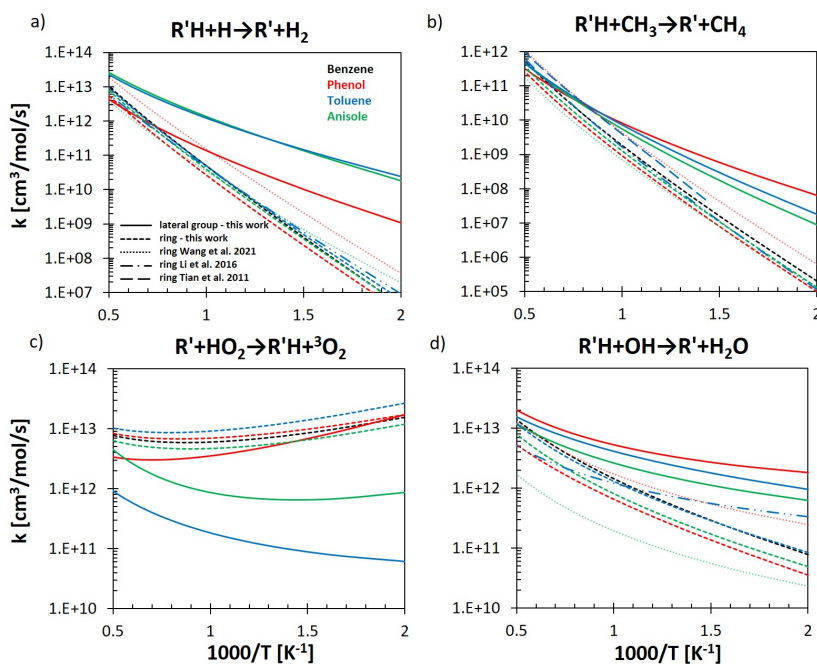


FIGURE 6.22: Calculated rate constants for different abstracting radicals (a) H, b) CH_3 , c) OH and d) $^3\text{O}_2$) on the functional groups (solid lines) and on the aromatic ring (sum of ortho, meta, para with dashed lines), in comparison with some of the available theoretical literature data [519], [525], [526].

6.4.3.1 $\text{C}_6\text{H}_6+\text{H}$

The H-atom abstraction reaction by H from benzene has been studied both experimentally and theoretically. Figure 6.23 compares the rate constant computed in this work with previous estimates. TST and VTST refer to the rate constant calculated in this work with conventional and variational transition state theory, respectively, whereas the suffix -xyz and

TABLE 6.25: Arrhenius fits in the 500–2000 K temperature range of the calculated rate constants for H-atom abstraction reactions by H, CH₃, OH, and ³O₂ on benzene, phenol, anisole, and toluene. $k = k_0 T^\alpha \exp(-\frac{E_A}{RT})$, units are cal, mol, cm, s. $R^2 > 0.99$ for every reaction. Rates with * were refined at a high level of theory; rates with *' were rescaled to the same level of * (see the main text for details). Rates with** were calculated in [129] and are updated according to the internal coordinate treatment. Rates with*** were revised with respect to previous work.

Reaction	Forward			Backward		
	k ₀	α	E _A	k ₀	α	E _A
C ₆ H ₆ +H=C ₆ H ₅ +H ₂ *	3.59E+08	1.89	16052	2.63E+04	2.55	6197
C ₆ H ₅ OH+H=C ₆ H ₅ O+H ₂	3.62E+03	2.94	5616	3.29E+01	3.39	21518
C ₆ H ₅ OH+H=o-C ₆ H ₄ OH+H ₂ *'	1.42E+07	2.15	15835	1.15E+04	2.65	5307
C ₆ H ₅ OH+H=m-C ₆ H ₄ OH+H ₂ *'	1.90E+07	2.10	15150	4.13E+03	2.76	5501
C ₆ H ₅ OH+H=p-C ₆ H ₄ OH+H ₂ *'	1.24E+07	2.09	15881	3.39E+03	2.80	5056
C ₆ H ₅ CH ₃ +H=C ₆ H ₅ CH ₂ +H ₂	4.68E+04	2.76	3992	5.93E+03	2.74	17114
C ₆ H ₅ CH ₃ +H=o-C ₆ H ₄ CH ₃ +H ₂ *'	1.66E+07	2.12	14821	3.26E+03	2.78	5386
C ₆ H ₅ CH ₃ +H=m-C ₆ H ₄ CH ₃ +H ₂ *'	1.82E+07	2.10	15009	3.93E+03	2.76	5497
C ₆ H ₅ CH ₃ +H=p-C ₆ H ₄ CH ₃ +H ₂ *'	6.74E+06	2.14	15245	3.30E+03	2.78	5303
C ₆ H ₅ OCH ₃ +H=C ₆ H ₅ OCH ₂ +H ₂	2.10E+06	2.33	5342	3.17E+02	3.09	10713
C ₆ H ₅ OCH ₃ +H=o-C ₆ H ₄ OCH ₃ +H ₂ *'	1.22E+07	2.09	16085	1.02E+04	2.58	6519
C ₆ H ₅ OCH ₃ +H=m-C ₆ H ₄ OCH ₃ +H ₂ *'	1.30E+07	2.15	14786	1.61E+03	2.87	5278
C ₆ H ₅ OCH ₃ +H=p-C ₆ H ₄ OCH ₃ +H ₂ *'	1.14E+08	1.83	15959	3.56E+04	2.52	5181
C ₆ H ₆ +CH ₃ =C ₆ H ₅ +CH ₄	5.05E+02	3.19	13738	2.54E+01	3.51	5545
C ₆ H ₅ OH+CH ₃ =C ₆ H ₅ O+CH ₄	1.60E+00	3.58	4694	9.05E+00	3.71	22034
C ₆ H ₅ OH+CH ₃ =o-C ₆ H ₄ OH+CH ₄	1.02E+02	3.24	13605	5.72E+01	3.41	4545
C ₆ H ₅ OH+CH ₃ =m-C ₆ H ₄ OH+CH ₄	1.58E+02	3.20	13562	2.09E+01	3.54	5351
C ₆ H ₅ OH+CH ₃ =p-C ₆ H ₄ OH+CH ₄	1.12E+03	2.85	14725	1.87E+02	3.24	5335
C ₆ H ₅ CH ₃ +CH ₃ =o-C ₆ H ₅ CH ₂ +CH ₄	2.10E+01	3.38	7299	1.80E+03	3.02	21875
C ₆ H ₅ CH ₃ +CH ₃ =o-C ₆ H ₄ CH ₃ +CH ₄	1.05E+02	3.23	13309	1.38E+01	3.56	5325
C ₆ H ₅ CH ₃ +CH ₃ =m-C ₆ H ₄ CH ₃ +CH ₄	8.01E+01	3.28	13468	1.14E+01	3.61	5413
C ₆ H ₅ CH ₃ +CH ₃ =p-C ₆ H ₄ CH ₃ +CH ₄	4.75E+01	3.26	13720	1.37E+01	3.58	5204
C ₆ H ₅ OCH ₃ +CH ₃ =C ₆ H ₅ OCH ₂ +CH ₄	1.35E+01	3.46	8094	3.24E+01	3.55	14425
C ₆ H ₅ OCH ₃ +CH ₃ =o-C ₆ H ₄ OCH ₃ +CH ₄	1.71E+03	2.84	14783	8.75E+02	3.01	6654
C ₆ H ₅ OCH ₃ +CH ₃ =m-C ₆ H ₄ OCH ₃ +CH ₄	4.82E+02	3.05	13717	3.48E+01	3.46	5637
C ₆ H ₅ OCH ₃ +CH ₃ =p-C ₆ H ₄ OCH ₃ +CH ₄	3.12E+02	3.02	14611	5.80E+01	3.40	5261
C ₆ H ₆ +OH=C ₆ H ₅ +H ₂ O*	4.72E+05	2.35	2560	6.29E+02	2.83	7709
C ₆ H ₅ OH+OH=C ₆ H ₅ O+H ₂ O*	3.89E+05	2.30	-1062	1.15E+04	2.71	29693
C ₆ H ₅ OH+OH=o-C ₆ H ₄ OH+H ₂ O*'	5.18E+03	2.54	237	7.57E+01	2.87	4504
C ₆ H ₅ OH+OH=m-C ₆ H ₄ OH+H ₂ O*'	8.60E+06	1.81	3227	3.07E+04	2.31	8354
C ₆ H ₅ OH+OH=p-C ₆ H ₄ OH+H ₂ O*'	2.50E+06	1.86	3351	1.07E+04	2.42	7286
C ₆ H ₅ CH ₃ +OH=C ₆ H ₅ CH ₂ +H ₂ O**	4.21E+07	1.70	563	9.67E+07	1.51	28476
C ₆ H ₅ CH ₃ +OH=o-C ₆ H ₄ CH ₃ +H ₂ O***	8.64E+04	2.40	1843	2.73E+02	2.91	7184
C ₆ H ₅ CH ₃ +OH=m-C ₆ H ₄ CH ₃ +H ₂ O***	1.05E+05	2.40	2321	4.04E+02	2.89	7598
C ₆ H ₅ CH ₃ +OH=p-C ₆ H ₄ CH ₃ +H ₂ O***	3.80E+04	2.43	2366	2.99E+02	2.92	7190
C ₆ H ₅ OCH ₃ +OH=C ₆ H ₅ OCH ₂ +H ₂ O	3.17E+05	2.29	-291	8.42E+02	2.88	19875
C ₆ H ₅ OCH ₃ +OH=o-C ₆ H ₄ OCH ₃ +H ₂ O*	1.07E+03	2.81	1540	1.36E+01	3.13	6810
C ₆ H ₅ OCH ₃ +OH=m-C ₆ H ₄ OCH ₃ +H ₂ O*	6.53E+04	2.45	2152	1.26E+02	3.02	7413
C ₆ H ₅ OCH ₃ +OH=p-C ₆ H ₄ OCH ₃ +H ₂ O*	1.61E+04	2.52	2361	6.94E+01	3.08	6313
C ₆ H ₆ +O ₂ =C ₆ H ₅ +HO ₂	2.98E+08	1.89	58953	2.59E+05	2.11	-4778
C ₆ H ₅ OH+O ₂ =C ₆ H ₅ O+HO ₂	6.64E+05	2.12	32125	6.15E+04	2.14	-6072
C ₆ H ₅ OH+O ₂ =o-C ₆ H ₄ OH+HO ₂	4.76E+05	2.40	57738	4.15E+03	2.47	-6894
C ₆ H ₅ OH+O ₂ =m-C ₆ H ₄ OH+HO ₂	3.55E+07	2.02	58875	8.38E+04	2.25	-4869
C ₆ H ₅ OH+O ₂ =p-C ₆ H ₄ OH+HO ₂	1.35E+10	1.21	61078	3.78E+07	1.50	-3857
C ₆ H ₅ CH ₃ +O ₂ =C ₆ H ₅ CH ₂ +HO ₂ **	1.86E+02	3.40	39311	4.56E+01	3.05	-2028
C ₆ H ₅ CH ₃ +O ₂ =o-C ₆ H ₄ CH ₃ +HO ₂ ***	1.01E+09	1.63	58815	1.98E+06	1.88	-4713
C ₆ H ₅ CH ₃ +O ₂ =m-C ₆ H ₄ CH ₃ +HO ₂ ***	9.02E+08	1.64	58863	2.25E+06	1.86	-4711
C ₆ H ₅ CH ₃ +O ₂ =p-C ₆ H ₄ CH ₃ +HO ₂ ***	3.72E+08	1.66	59313	1.68E+06	1.90	-4730
C ₆ H ₅ OCH ₃ +O ₂ =C ₆ H ₅ OCH ₂ +HO ₂	1.28E-01	4.40	42190	2.04E-04	4.73	-6522
C ₆ H ₅ OCH ₃ +O ₂ =o-C ₆ H ₄ OCH ₃ +HO ₂	9.01E+06	2.17	58807	7.51E+04	2.24	-4874
C ₆ H ₅ OCH ₃ +O ₂ =m-C ₆ H ₄ OCH ₃ +HO ₂	1.85E+07	2.10	58551	5.06E+04	2.39	-4986
C ₆ H ₅ OCH ₃ +O ₂ =p-C ₆ H ₄ OCH ₃ +HO ₂	1.52E+08	1.72	60142	9.34E+05	2.00	-4762

-int indicate that vibrational frequencies were computed using Cartesian or internal coordinates, respectively. In this case, the impact of internal coordinates is minimal (10-30%). The forward rate is below the upper limit indicated by Nicovich et al. [527], and it overpredicts the high temperature estimates of Giri et al. [528] and of Kiefer et al. [529] by maximum

factors of 2 and 4, respectively. The latter difference may be explained by the large declared uncertainty in the experimental results of Kiefer et al., who estimated the rate through a fit of a simple mechanism of four reactions.

The calculated reverse rate constant (Figure 6.23b) shows instead a larger overprediction of the available experimental data, reaching up to a factor of 5 at 600 K. This disagreement suggests that the reverse energy barrier may be underestimated by about 2 kcal/mol, which is above the expected uncertainty for CCSD(T)/CBS with small T1 diagnostic (0.014 for the TS of this reaction). The 0 K reaction enthalpy is in excellent agreement with the one calculated from ATcT database (7.97 kcal/mol versus 8.08 kcal/mol [117]), thus excluding significant errors in the calculation of the reaction energy.

The effect of the choice of the density functional was tested by more accurate CCSD(T)/CBS//B2PLYP-D3/jun-cc-pVTZ calculations, resulting in a slight increase in both the energy barrier and in the reaction enthalpy (by 0.5 and 0.2 kcal/mol, respectively) mostly due to the higher contribution of the ZPE. This value is still insufficient to account for the discrepancies observed with the experimental data: the rate constants obtained, shown in Figure 6.23 as VTST-int*, are extremely close to the original values. Finally, the energy barrier was computed at the CASPT2 level using a (9e,9o) active space and the aug-cc-pVTZ basis set, which raised its value by 1.7 kcal/mol. The agreement with the experimental data is in this case quantitative. For consistency, energy barriers for all H-atom abstractions from substituted MAHs were increased by 1.7 kcal/mol, since MR calculations are expected to produce an analogous increase as in benzene (see Table 6.25).

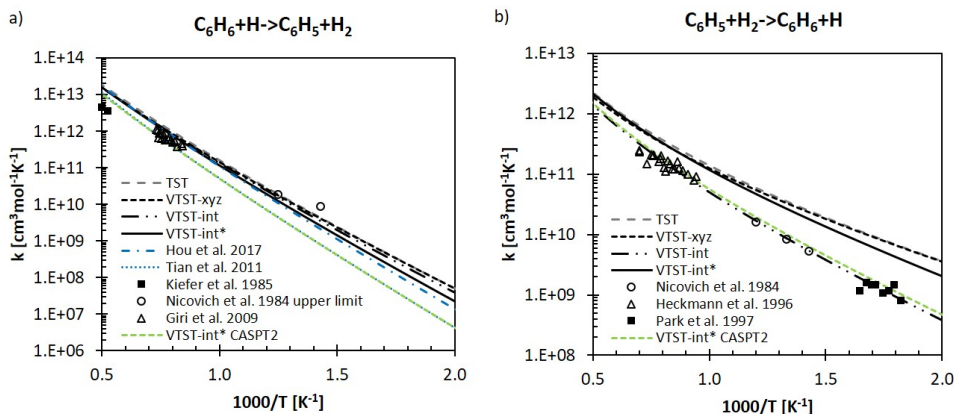


FIGURE 6.23: a) forward and b) backward rate constants of the H-atom abstraction reaction by H from benzene. The plots show the impact of the use of conventional and variational TST (TST, VTST-xyz) and of the use of internal coordinates (VTST-int). VTST-int* is the rate constant computed at the highest level of theory (see main text). Comparisons with the available literature data are provided [520], [525], [527]–[531].

6.4.3.2 $C_6H_6 + CH_3$

The calculated rate constant for the H-atom abstraction by CH_3 from the benzene ring (Figure 6.24a) is in excellent agreement with the available experimental measurements of Krech et al. and of Zhang et al. [532], [533], overestimating both datasets by less than 30%.

The calculated rate also agrees reasonably with the calculations by Tian et al. [525] (within a factor of 1.2–2.4) and with the rates computed at the CCSD(T)/CBS//BH&HLYP/cc-pVDZ level by Mai et al. [534] (factor of 1.4–2.4) and at the G3(MP2,CC)//B3LYP/6-311+G(d,p) level by Kislov and Mebel [316] (factor of 1.5–3.1). The rates computed according to TST, VTST-xyz and VTST-int differ by less than 3%; therefore only the VTST-int rate is shown.

Larger discrepancies are found between the present reverse rate constant (Figure 6.24b) and other available experimental data. The rate constant computed in this work is within the experimental uncertainty of the data of Heckmann et al. [530] (factor of 3.4 at 1400 K), however this is not the case for the more recent estimates of Tokmakov et al. [535], which are overpredicted here by a factor of 4–5. Both datasets were derived through fitting a reaction mechanism of at least four reactions, including $2\text{C}_6\text{H}_5 = \text{C}_{12}\text{H}_{10}$, $\text{C}_6\text{H}_5 + \text{CH}_3 = \text{C}_6\text{H}_5\text{CH}_3$, $\text{CH}_3 + \text{CH}_3 = \text{C}_2\text{H}_6$. The resulting rate constant for the reaction $\text{C}_6\text{H}_5 + \text{CH}_4 = \text{C}_6\text{H}_6 + \text{CH}_3$ was found to be particularly sensitive to the recombination rate of phenyl radicals, whose estimate varied between $1 \times 10^{14} \text{ cm}^3 \text{ mol}^{-1} \text{ s}^{-1}$ (as assumed in Duncan et al. [536]) and $5.7 \times 10^{12} \text{ cm}^3 \text{ mol}^{-1} \text{ s}^{-1}$ (Heckmann et al. [530]). Both Heckmann and Tokmakov reinterpreted the experimental values of Duncan et al. [536], as depicted in Figure 6.24b. The resulting rate varies by about one order of magnitude, providing a rough quantification of the uncertainty of this dataset. The rate constant of phenyl recombination used by Tokmakov et al. as from Park et al. [531] is in close agreement with the recent theoretical rate constants reported by Tranter et al. [466]. Hence, also given the detailed discussion of Tokmakov et al. [535], their dataset may be the most reliable.

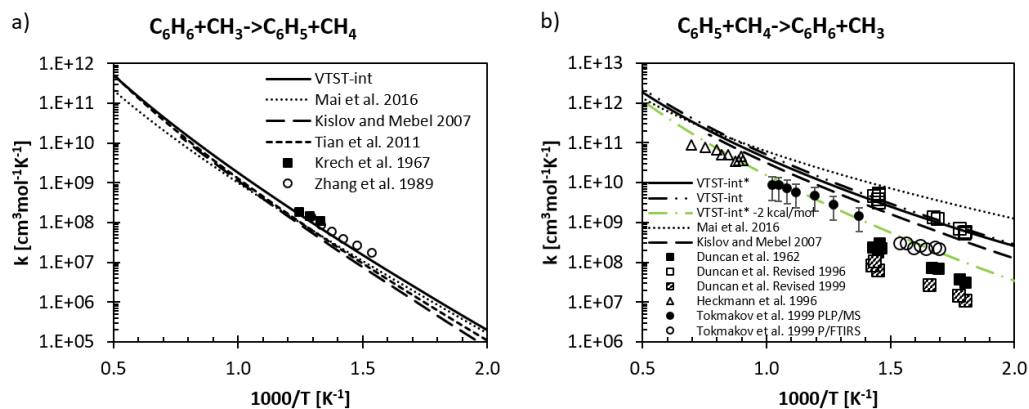


FIGURE 6.24: Comparison between the present calculations for the forward a) and backward b) rate constants of the reaction $\text{C}_6\text{H}_6 + \text{CH}_3 = \text{C}_6\text{H}_5 + \text{CH}_4$ and the available literature data [525], [530], [532]–[536].

Overall, the experimental data would suggest that the calculated reverse energy barrier is underestimated by about 2 kcal/mol. However, the reaction energy at both the CCSD(T)/CBS//B2PLYPD3/jun-cc-pVTZ and the CCSD(T)/CBS//M06-2X/6-311+G(d,p) levels of theory agree to within 0.5 kcal/mol with the value derived from the ATcT database [117]. In addition, the uncertainty of the forward energy barrier should not exceed 1 kcal/mol. This is also supported by the agreement of the forward rate constant with the available experimental data (Figure 6.24a). Also, the energy barrier calculated at

the CASPT2/aug-cc-pVTZ level using a (9e,9o) active space on B2PLYPD3 geometries, similar to what was done for C_6H_6+H , is only 0.5 kcal/mol smaller than that determined at the CCSD(T)/CBS level; thus in reasonably good agreement. Finally, an anharmonic analysis was also performed at the B2PLYPD3/6-311+G(d,p) level of theory, resulting in a decrease in the energy barrier by 0.3 kcal/mol. Neither of the refinements considered leads to quantitative agreement with the datasets of Tokmakov [535] and Duncan [536].

6.4.3.3 C_6H_6+OH

Figure 6.25 compares the computed rate constant for $OH + C_6H_6 = C_6H_5 + H_2O$ with experimental data [452], [537]–[539] and the Baulch recommendation [540], showing the high impact of using internal coordinates with respect to Cartesian coordinates. The former is lower than the latter by a factor of ~ 1.75 at 2000 K and up to a factor of ~ 3.4 at 500 K, due to an increase in the effective energy barrier from 4.2 kcal/mol to 5.5 kcal/mol, attributed to the higher vibrational frequencies. The same effect is observed in the rate constant calculated at the higher level of theory VTST-int*, which is almost identical to the VTST-int one.

The impact of the internal coordinate treatment on the energy barriers for this transition state is also observed in all H-atom abstractions by OH from mono-substituted rings, as highlighted in Section 6.4.3.10. This is the origin of discrepancies with theoretical literature data where conventional TST and Cartesian coordinates were used. For instance, the rate for the H-atom abstraction from phenol ring found by Wang et al. [519] overestimates that of the present work by almost one order of magnitude at low temperatures (Figure 6.22d) due to the combined effect of the use of internal coordinates and the higher energy barriers (about 1 kcal/mol).

The agreement between the rate constant obtained and the experimental measurements is already satisfactory, with maximum deviations of a factor of 2. To further investigate the reasons for the discrepancies, an anharmonic analysis was performed at the B3LYPD3/6-311+G(d,p) level of theory. Interestingly, the resulting ZPE correction on the energy barrier is as high as -0.79 kcal/mol. The final ZPE-corrected rate constant is in excellent agreement with the experimental data. The results suggest that this correction should also be applied to all H-atom abstractions from substituted aromatic rings, which all show very similar values and the same behavior also in terms of differences between Cartesian and internal coordinate treatments. Finally, the energy barrier for this TS was also evaluated at the CASPT2/aug-cc-pVTZ level of theory using an (11e,10o) active space including all the π electrons of the aromatic ring, the (2e,2o) space of the breaking C–H bond, and the (3e,2o) space of the OH radical and lone pairs. The reference wavefunction was averaged over two states and a level shift of 0.2 was used for the calculations. The obtained energy barrier of 4.32 kcal/mol confirms the CCSD(T) result of 4.11 kcal/mol (obtained for both B2PLYPD3/jun-cc-pVTZ and M06-2X/6-311+G(d,p) reference geometries).

Figure 6.25 also includes the contribution of the OH addition channel, which is indistinguishable from the abstraction channel in the low temperature experiments of Tully et al. [537]. While at $T > 800$ K only the H-atom abstraction channel contributes to the OH decay in experimental measurements, at lower temperatures the contribution from OH addition is

not negligible. In fact, the total rate constant including both the H-atom abstraction and the OH addition channels at $p = 0.1$ bar (blue dashed-dotted line in Figure 6.25), agrees better with the experimental observations. The OH addition channel was calculated as the reverse channel of the H ipso addition-elimination reactions presented in Section 6.5.

In light of the results of this analysis, all the energy barriers for H-atom abstractions from the substituted aromatic rings were corrected by -0.79 kcal/mol (see Table 6.25).

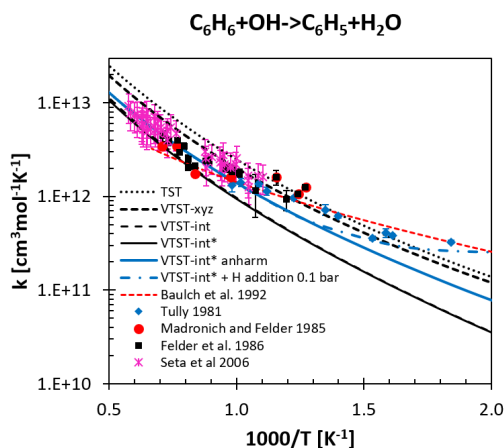


FIGURE 6.25: Comparison of the calculated rate constant for $\text{OH} + \text{C}_6\text{H}_6 = \text{C}_6\text{H}_5 + \text{H}_2\text{O}$ with experimental measurements [452], [537]–[539] and the Baulch recommendation (red dashed line, [540]) at $T = 500$ – 2000 K. Solid line: this work at B2PLYPD3/6-311+G(d,p) level for geometries and frequencies*; solid blue line includes anharmonic treatment; dashed-dotted line: sum of H-atom abstraction and OH addition ($p = 0.1$ bar).

6.4.3.4 H-atom abstraction by H from toluene and phenol

Figure 6.26a presents the results obtained for the rate constants of $\text{H} + \text{C}_6\text{H}_5\text{OH} = \text{C}_6\text{H}_5\text{O} + \text{C}_6\text{H}_4\text{OH} + \text{H}_2$. For the purpose of comparison with the experimental measurements of He et al. [436], which consider the global rate constant, the sum of all abstractions (from OH and from the ring sites) is plotted. It is observed that the use of internal coordinates has a negligible impact on the vibrational frequencies along the MEP, resulting in less than 8% variation in the predicted rate constants. The calculated rate constant is in excellent agreement (factor < 1.2) with the measurements of He et al, while it is about a factor of 3 lower than the recent results of Wang et al. [519], who derived the PES at the ROCBS-QB3//M06-2X/cc-pVTZ level of theory. This difference is explained by both the slightly higher energy barrier found in this work (11.05 kcal/mol versus 10.7 kcal/mol in [519]) and by the higher vibrational frequencies of the TS optimized at the M06-2X/6-311+G(d,p) level with respect to those calculated at the M06-2X/cc-pVTZ level. Figure 6.26a shows that geometry optimization at M06-2X/cc-pVTZ level (VTST-int cc-pVTZ) results in maximum differences of factors of 1.05 at low temperatures and 2.5 at high temperatures. High temperature discrepancies may instead be due to a different treatment of hindered rotors.

Figure 6.26b compares the rate constant for the H-atom abstraction by H from the toluene methyl group. Similar to all H-atom abstractions by H investigated in this work, both the

variational implementation of TST and the internal coordinate treatment do not affect the rate constant significantly (<15% differences), therefore only the VTST-int rate is shown. The theoretical rate constant obtained provides an excellent estimate of all the available experimental datasets [451], [541]–[543], with maximum discrepancies below 50%, as well as good agreement (factor <2) with the CSB-QB3 calculations of Tian et al. [525] and with the G4//B3LYP/6-31G(2df,p) calculations of Li et al. [526].

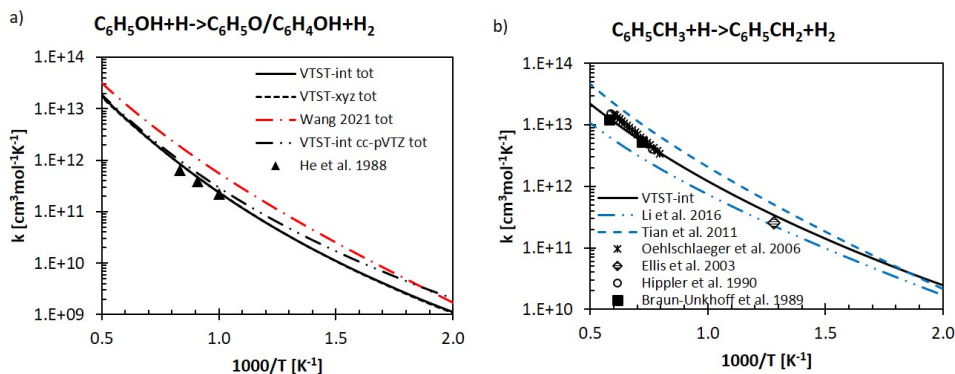


FIGURE 6.26: a) total rate constant for the H-atom abstraction by H from phenol and b) rate constant of H-atom abstraction by H from the toluene methyl group in comparison with available literature data [436], [451], [519], [541]–[543].

6.4.3.5 H-atom abstraction by H, OH and CH₃ from anisole: impact of hindered rotors

This section presents the results for the rate constants of H-atom abstractions by H, OH and CH₃ from the methoxy group of anisole, with a focus on the impact of the choices related to hindered rotor treatment.

Figure 6.27a shows the rate constant calculated for $\text{C}_6\text{H}_5\text{OCH}_3 + \text{H} = \text{C}_6\text{H}_5\text{OCH}_2 + \text{H}_2$ in comparison with the recent calculations of Wang et al. [519] and CBS-QB3 rates of Büttgen et al. [55]. The rate constant labelled VTST-int 2HR (as reported in Table 6.25) treats the vibrational frequencies of the torsional motions of both methoxy group ($\sim 90 \text{ cm}^{-1}$) and methyl group including the abstracting radical ($\sim 180 \text{ cm}^{-1}$) according to the 1D hindered rotor model. An RRHO treatment for the latter frequency decreases the rate constant by a factor of 2 (VTST-int 1HR), which is closer to previous theoretical estimates. On the other hand, the projection of the vibrational frequency of the stand-alone methyl group ($\sim 540 \text{ cm}^{-1}$) rather than the chosen one of 180 cm^{-1} would lead to increasing the rate constant by a factor of 3 (VTST-int 2HR proj2). However, this representation is inconsistent with the calculated PES for methyl torsion, which in fact includes the abstracting radical in the torsional motion. Therefore, VTST-int 2HR rate is believed to be the most physically consistent rate.

Literature data for the rate constant calculated for $\text{C}_6\text{H}_5\text{OCH}_3 + \text{CH}_3 = \text{C}_6\text{H}_5\text{OCH}_2 + \text{CH}_4$ (Figure 6.27b) are extremely scattered. In fact, the theoretical rate constant of Wang et al. [519] is almost 2 orders of magnitude higher (factor of 30–80) than that obtained by Büttgen et al. [55]. Both estimates fall out of the declared range of uncertainty of the

experimental data of Mulcahy et al. [544], which lie somewhere in between the calculated rates. On the other hand, the rate constant VTST-int 3HR calculated in this work (black solid line in Figure 6.27b) is in excellent agreement with the experimental data. Rate constants computed using TST and VTST-xyz are almost identical to the VTST-int rate (< 10% difference), therefore they are not shown. The large discrepancies among the theoretical calculations may be attributed to the choices related to the treatment of low vibrational frequencies. In particular, Figure 6.27b shows the impact of 1DHR treatment for the vibrational frequencies associated with the torsional motions of the methyl abstracting radical ($\sim 80 \text{ cm}^{-1}$), of the anisole methoxy group ($\sim 40 \text{ cm}^{-1}$), and of the anisole methyl group ($\sim 80 \text{ cm}^{-1}$). Including only the first torsion (VTST-int 1HR) results in a similar rate constant to that obtained by Büttgen et al. The inclusion of the second (VTST-int 2HR) and finally the third (VTST-int 3HR) torsional motions according to the 1DHR model increase the rate constant by a factor of 3–4, producing good agreement with the experimental results. As in the case of the H-atom abstraction by H, the torsion of the anisole methyl group also includes the motion of the abstracting radical. Instead, projecting the high vibrational frequency of the stand-alone methyl group ($\sim 690 \text{ cm}^{-1}$) would cause the rate constant to increase by more than one order of magnitude (VTST-int 3HR proj2), yielding results close to those presented by Wang et al.

Further inspection of the low normal modes at the saddle point was performed by optimizing the structure using different functionals (M06-2X, ω B97X-D, B2PLYPD3) and different basis sets (6-311+G(d,p), jun-cc-pVTZ). The PES for the torsional potentials were also re-optimized at the same level of theory of the saddle point. The lowest vibrational frequencies are reported in Table 6.26. It is found that different density functionals result in extremely different low normal modes, especially for the vibrational frequency associated with the torsion of the methyl abstracting radical, which varies from 52.5 cm^{-1} to 78.4 cm^{-1} . Nevertheless, the resulting rate constants vary by less than 50% because the lowest normal modes are projected out as hindered rotors.

The above discussion about the effect of hindered rotors also holds for the rate constant for $\text{C}_6\text{H}_5\text{OCH}_3 + \text{OH} = \text{C}_6\text{H}_5\text{OCH}_2 + \text{H}_2\text{O}$. Figure 6.27c shows that the 1DHR model progressively applied to the torsional motions of hydroxyl radical (VTST-int 1HR), of the anisole methoxy group (VTST-int 2HR) and of the anisole methyl group (VTST-int 3HR) increases the rate constant by a factor of 2–4. In contrast with the previous cases, the influence of the use of internal coordinates with respect to Cartesian coordinates (VTST-xyz 3HR rate of Figure 6.27c) is not negligible: in fact, the higher vibrational frequencies obtained with the former method decrease the final rate constant by about 20% at high temperatures up to 80% at low temperatures.

6.4.3.6 H-atom abstraction by CH_3 from the functional groups of toluene and phenol

Figure 6.28 shows the rate constants for CH_3 H-atom abstraction from the toluene and phenol functional groups. In both cases, the use of VTST and of internal coordinates impact the calculated rate constants by less than 30%, hence only the VTST-int rates are shown. In

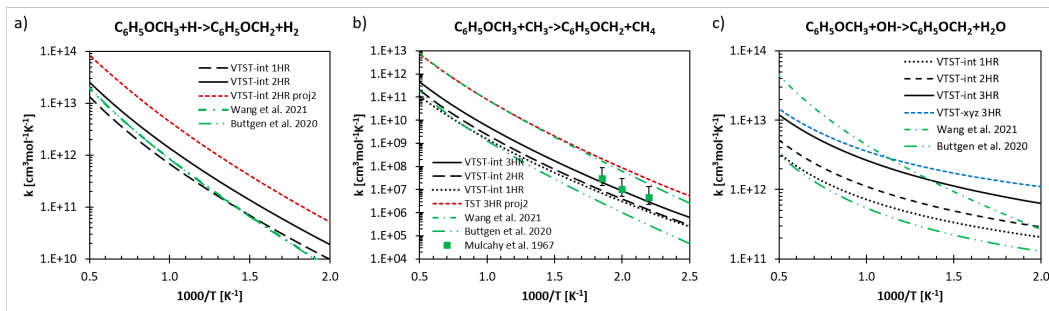


FIGURE 6.27: Rate constants for the H-atom abstraction by a) H, b) CH₃, c) OH from the anisole methoxy group (black solid line) in comparison with literature experimental data [544] and recent theoretical estimates [55], [519]. 3HR, 2HR and 1HR indicate the number of torsional motions included as hindered rotors according to the 1DHR model. Proj2 refers to the projection of the frequency of the independent methyl torsion. Solid lines highlight the rate constants adopted.

TABLE 6.26: Seven lowest vibrational frequencies at the saddle point of the PES for C₆H₅OCH₃ + CH₃ = C₆H₅OCH₂ + CH₄ reaction obtained using different DFTs and basis sets. Units are cm⁻¹.

M06-2X/ 6-311+G(d,p)	M06-2X/ jun-cc-pVTZ	ωB97X-D/ jun-cc-pVTZ	ωB97X-D/ 6-311+G(d,p)	B2PLYPD3/ 6-311+G(d,p)
41.8	42.7	44.4	42.7	36.7
78.4	76.2	53.8	52.5	53.6
81.0	79.1	77.8	79.6	70.3
136.5	136.5	143.2	142	135.6
242.1	243.1	244.2	242.5	232.8
271.9	273.1	268.6	267.8	264.9
373.2	371.5	376.3	376.0	370.0

addition, it was verified that the coupling between the hindered rotations of the abstracting radical and of the functional groups is relatively small. In fact, the rate constants were also calculated using the 2D hindered rotor model (dashed black lines in Figure 6.28). The resulting discrepancies are limited to about 30–50% at temperatures below 1700 K, reaching a maximum of 90% only at 2000 K. Similar to observations for the case of CH₃ abstracting from the anisole methoxy group arise in relation to the hindered rotors treatment.

Figure 6.28b exemplifies this behavior in toluene: the vibrational frequency of the torsion describing the toluene methyl group, which includes the motion of the CH₃ abstracting radical, is ~ 40 cm⁻¹ at the saddle point, whereas that of the stand-alone toluene methyl group is ~ 320 cm⁻¹. The rate constants resulting from the projection of the former and of the latter frequencies differ by a factor of 5–6 (solid and dotted line, respectively). It was chosen to project the lower frequency, because it is more representative of the calculated PES for the corresponding torsion. Overall, the very good agreement with the available experimental data [533], [545]–[548] also seem to favor this choice, and the former theoretical calculations of Li et al. [526] and Tian et al. [525] lie between the VTST-int and VTST-int-proj2 estimates. The largest discrepancy of a factor of 4 with the data of Zhang et al. [533] is still reasonable, since the authors measured the rate constant relative to the methyl H-atom abstraction from ethylene, declaring an uncertainty of about one order of magnitude. It is noted that all the other available experimental estimates were obtained as fittings to simple kinetic mechanisms.

As far as the H-atom abstraction from phenol is concerned (Figure 6.28a), the calculated

rate constant is in excellent agreement with the experimental measurement of Mulcahy et al [549], while it is about a factor of 5 lower than the recent theoretical calculations of Wang et al [519]. This is due to both the higher energy barrier obtained in this work (about 1.5 kcal/mol than in [519]) and probably to the different treatment of the hindered rotors. In fact, Figure 6.28a shows that projecting the high vibrational frequency associated with the torsional motion of the stand-alone phenol hydroxy group (VTST-xyz proj2) rather than that of the hydroxy group moving together with the abstracting radical (VTST-int) produces values much closer to those of Wang et al.

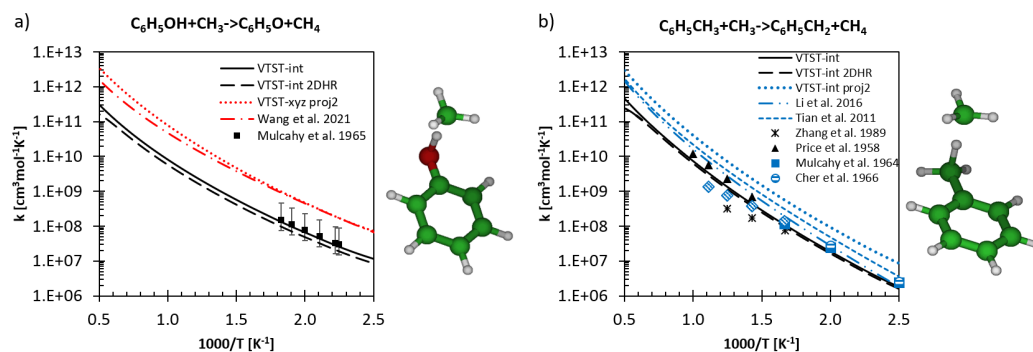


FIGURE 6.28: TS structure and rate constant of H-atom abstraction by CH_3 from a) the phenol hydroxy group and b) the toluene methyl group. The computed rate constants (black solid line) are compared with available experimental and theoretical estimates [519], [525], [526], [533], [545]–[548]. 2DHR refers to the rate constant computed using the 2D hindered rotor treatment, whereas proj2 considers the projection of the torsion of the functional group independent of the abstracting radical.

6.4.3.7 H-atom abstraction by OH from toluene revised

Figure 6.29 compares the total rate constant of the H-atom abstraction from toluene revised in this work (VTST-int) with a previous estimate (VTST-xyz) [129], with the recent calculations of Zhang et al. [217], and with the available experimental data [452], [537], [550]–[553]. For a complete comparison with the latter low-temperature data, the range of the rate constant was extended to 300 K. The newly calculated rate (VTST-int) shows less than 30% deviation from the high-temperature estimates of Vasudevan et al. [551]. However, the use of internal coordinates decreases the total rate constant significantly at low temperatures, worsening the overall agreement with the experimental data below 500 K (factor of ~ 3 lower than the experiments of Tully et al [537] and of Perry and Atkinson [553]). In particular, the rate of the H-atom abstraction from the toluene methyl group decreases by a factor of ~ 3 at 300 K with respect to the Cartesian coordinate treatment. The impact of internal coordinates is enhanced for the abstractions from the ring sites, being as high as a factor of ~ 2 – 7 at 2000 K and at 300 K, respectively, similar to the H-atom abstraction by OH from benzene (Section 6.4.3.3). In both cases, the decrease in the rate constant is due to higher vibrational frequencies and zero-point energies compared to those obtained using Cartesian coordinates. Multireference effects for H-atom abstractions by OH from the ring were excluded in the analysis performed for benzene (Section 6.4.3.3). As far as

the abstraction from the methyl group is concerned, the relatively low 0.02 T1 diagnostic of the CCSD(T)/aug-cc-pVTZ calculations at the TS suggests small MR effects. This was confirmed by calculating the energy barrier for this reaction at the CASPT2(11e,10o)/aug-cc-pVTZ level of theory. The (11e,10o) AS included all the π electrons of the aromatic ring, the (2e,2o) AS of the breaking C–H bond, and the (3e,2o) AS of the OH radical and lone pair. The reference wavefunction was averaged over two states and a level shift of 0.2 was used for the calculations. The energy barrier obtained was 1.24 kcal/mol, in good agreement with CCSD(T)/CBS results.

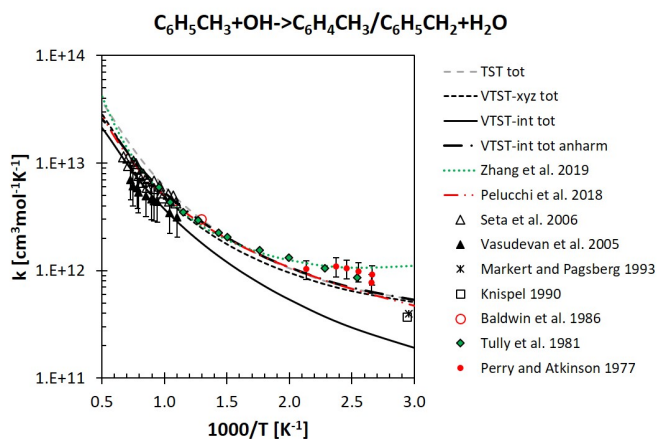


FIGURE 6.29: Total rate constant for H-atom abstraction by OH from toluene calculated at different levels of theory in comparison with the available experimental [452], [537], [550]–[553] and theoretical [129], [217] literature data. VTST-xyz corresponds to the results of Pelucchi et al. [129]. VTST-int tot anharmonic is the final rate constant proposed in this work accounting for anharmonic corrections.

The theoretical rate constant of Zhang et al. [217] shows excellent agreement with the experimental data. They derived the PES at the CCSD(T)-F12/jun-cc-pVTZ//M06-2X/MG3S level of theory, whereas the rate constant was calculated with multi-structural canonical VTST with small curvature tunneling (MS-CVT/SCT). The 0 K enthalpies of all stationary points agree with the present work within to 0.3 kcal/mol. In their work, the variational correction to the rate constant is comparable to the VTST-xyz/TST-xyz ratio of this work, although it is slightly higher for the H-atom abstraction from the methyl group (up to a factor of 2 at 2000 K). The SCT correction of Zhang et al. is similar to the Eckart tunneling correction obtained in this work (factor of 1.5 and 2, respectively). In addition, Zhang et al. found that properly accounting for anharmonicities through specific-reaction-parameter scaling factors for the vibrational frequencies and ZPEs is essential to quantitatively reproduce the experimental data [216]. In particular, the higher anharmonicity of the TS with respect to the other stationary points produces a decrease in the scaling factor for the vibrational frequencies from 0.970 (the standard value for M06-2X/MG3S [215]) to 0.960 for the H-atom abstraction from methyl and to ~ 0.965 for the abstractions from the ring sites. These observations are analogous to the analysis performed in Section 6.4.3.3 on the H-atom abstraction by OH from the benzene ring, where the inclusion of anharmonic corrections led to better agreement with the experimental data, as well as a decrease in the apparent activation energy. To deepen this point, an anharmonic analysis was performed computing

anharmonic vibrational frequencies and using the resulting ZPEs to correct the energy barrier. The anharmonic corrections were determined at the B2PLYPD3/6-311+G(d,p) level of theory, as the M06-2X/6-311+G(d,p) anharmonic analysis found four imaginary frequencies at the TS structure. The anharmonic analysis leads to a -0.68 kcal/mol correction to the harmonic ZPE for H-atom abstraction from the methyl group and -0.79 kcal/mol from the ring sites (already derived for benzene). The rate constant thus obtained (VTST-int tot anharm, dash-dotted line in Figure 6.29) shows excellent agreement with the available experimental data.

6.4.3.8 H-atom abstraction by OH from the phenol hydroxy group

Figure 6.30 shows the rate constants and the TS structures for $\text{C}_6\text{H}_5\text{OH} + \text{OH} = \text{C}_6\text{H}_5\text{O} + \text{H}_2\text{O}$. A large scatter in the available literature estimates is observed. In particular, experimental results suggest much larger values than theoretical calculations: at 500 K, the experimental data of Knispel et al. [550] and He et al. [436] are faster than the theoretical calculations of Wang et al. [519] by more than one order of magnitude, while the theoretical results of Xu et al. [554] are lower than the experiments by a factor of 4–5.

Two different saddle point structures were found in theoretical calculations. Structure a) of Figure 6.30, found also in Xu et al. [554] at MPWB1K/6-311+G(3df,2p) level, possesses a significant multireference character (T1 diagnostic of 0.077). MR calculations described in the methodology resulted in an increase in the energy barrier of 2 kcal/mol with respect to that obtained using coupled cluster. Wang et al. [519] instead considered a different structure (b in Figure 6.30) where the C–O–H angle is less strained and the abstracting radical interacts more significantly with the benzene ring. In this case, the lower 0.040 T1 diagnostic might lead to adopt CCSD(T)/CBS energy barrier of 0.7 kcal/mol, resulting in a higher rate constant (one order of magnitude at 500 K) closer to the experimental estimates (rate b in Figure 6.30). However, the energy of this structure at both M06-2X/6-311+G(d,p) and CASPT2(13e,11o)/aug-cc-pVTZ levels is significantly higher than structure a (2 and 5 kcal/mol, respectively).

Further inspection of the influence of the level of theory was performed by optimizing the saddle point at the CASPT2(13e,11o)/jun-cc-pVTZ level of theory. The optimized structure is shown in Figure 6.30c. Interestingly, both the bond distances and angles differ substantially from those of the structure obtained with DFT, and consequently the energy barrier changes completely. The resulting energy barrier is 0.6 kcal/mol and the calculated rate constant shows quantitative agreement with the experimental estimates (factor of ~ 2).

6.4.3.9 PES for the H-atom abstraction by $^3\text{O}_2$ from phenol

Figure 6.31 shows the peculiar PES for the H-atom abstraction by $^3\text{O}_2$ from phenol reactive sites. H-atom abstractions by $^3\text{O}_2$ to form HO_2 and a resonance stabilized radical (in this case $\text{C}_6\text{H}_5\text{O}$) lack a pronounced maximum (right side of Figure 6.31) [129]. The reaction is however not barrierless because of the exit van der Waals well, which lies 3.9 kcal/mol below the TS and 9.5 kcal/mol below the products. Consequently, the equilibrium constant strongly

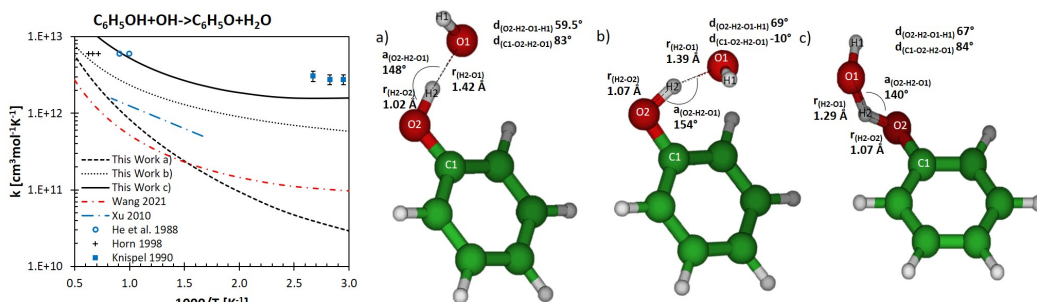


FIGURE 6.30: Rate constant of H-atom abstraction by OH from the hydroxy group of phenol. Structures a), b), and c) (with r , a , and d indicating structural parameters for distances, angles and dihedral angles, respectively) correspond to the black dashed, dotted, and solid rate constants, respectively. Rate constant c) was computed using CASPT2(13e,11o)/ aug-cc-pVTZ energies over structures optimized at the CASPT2(13e,11o)/jun-cc-pVTZ level, while rate constant a) was computed at the CASPT2(13e,11o)/aug-cc-pVTZ//M06-2X/6-311+G(d,p) level. The rates are compared with the available experimental and theoretical estimates [132], [436], [550], [554].

depends on temperature, and the reaction may either enhance or decrease the reactivity acting as initiation or termination step within a relatively small temperature window (1000–1400 K), as in the case of toluene [129] and as reported in the kinetic simulation Section 6.6.2.

The difference between the 0 K reaction enthalpies of $\text{C}_6\text{H}_5\text{OH} + {}^3\text{O}_2 = \text{C}_6\text{H}_5\text{O} + \text{HO}_2$ (~ 38.2 kcal/mol) and $\text{C}_6\text{H}_5\text{CH}_3 + {}^3\text{O}_2 = \text{C}_6\text{H}_5\text{CH}_2 + \text{HO}_2$ (~ 40.5 kcal/mol [129]) reflects the difference between the bond dissociation energies of the O–H (86.5 ± 0.4 kcal/mol [117]) and C–H (89.1 ± 0.2 kcal/mol [117]) bonds in phenol and toluene, respectively, within the expected accuracy of the adopted methods (< 1 kcal/mol [87]). This is however not the case for the energy barriers. In fact, the energy barrier for $\text{C}_6\text{H}_5\text{OH} + {}^3\text{O}_2 = \text{C}_6\text{H}_5\text{O} + \text{HO}_2$ computed at the CASPT2/aug-cc-pVTZ (10e,10o) level of theory (31.4 kcal/mol) is 8.4 kcal/mol lower than that calculated for the analogous benzyl radical formation channel in toluene (39.8 kcal/mol) [129]. This effect is not only due to the ~ 2 kcal/mol of higher stabilization of the formed RSR, but mostly to the hydrogen bonding between the hydrogen of the HO_2 moiety and the oxygen of the forming phenoxy radical. The latter effect is also found in the H-atom abstraction on the ortho position of the phenol ring, as the stability of the TS with respect to the products increases by ~ 2 kcal/mol with respect to the corresponding channel in toluene. In the case of phenol, the importance of the channels leading to the formation of hydroxyphenyl radicals ($\text{C}_6\text{H}_4\text{OH}$) is further reduced by the increased rate of abstraction from the hydroxy moiety.

o

6.4.3.10 Impact of the variational treatment and internal coordinates

The effect of the use of variational TST (VTST) and of Cartesian or internal coordinates for the calculation of vibrational frequencies (-xyz and -int) with respect to conventional transition state theory is summarized in Table 6.27.

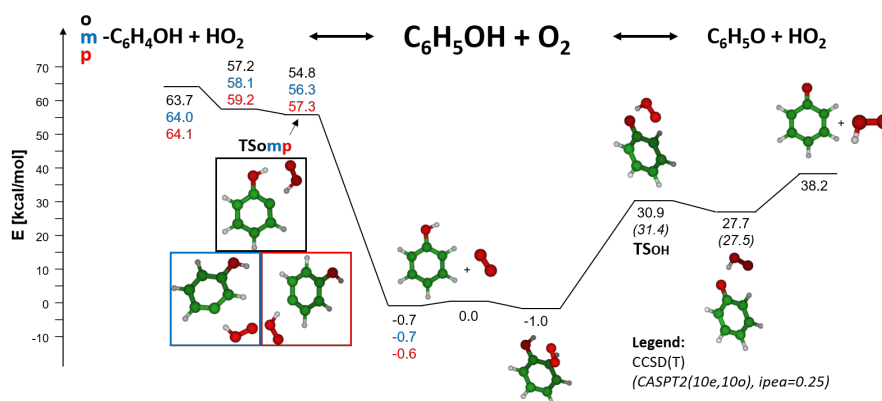


FIGURE 6.31: Potential energy surface for the ${}^3\text{O}_2 + \text{C}_6\text{H}_5\text{OH}$ reaction. Energies in kcal mol^{-1} are relative to the reactants. Numbers in parentheses are CASPT2/aug-cc-pVTZ (10e,10o) values.

In general, the effect of both the variational implementation of TST and of internal coordinate treatment is negligible for the H-atom abstractions by H atoms and CH_3 radicals, generally reducing the rate constants by less than 30%.

For the H-atom abstractions by H from the aromatic rings, internal coordinates lead to larger vibrational frequencies and consequently larger ZPEs, such that at low temperatures the rate constants decrease up to 40%. It is noted that in these cases VTST-int rates become closer to TST values as the temperature increases, as opposed to VTST-xyz rates.

On the other hand, as discussed in Section 6.4.3.3, the VTST-int rate constants for the abstractions by OH from the aromatic rings are much smaller than their TST and VTST-xyz counterparts, reaching differences of a factor of ~ 4 at 500 K. Again, this is caused by an increase in the energy barriers along the MEP due to higher ZPE values (0.5–1 kcal/mol higher than at the saddle point). Although this effect may be expected also in VTST-xyz rates, the vibrational frequencies computed in Cartesian coordinates often become imaginary, and thus unphysical, as the system evolves towards the reactant configuration, so that they cannot be used for rate constant calculations. Interestingly, these configurations correspond often to the minimum flux obtained with the VTST-int model.

Finally, opposite trends are observed for the H-atom abstractions by ${}^3\text{O}_2$: in most cases, the variational implementation of TST decreases the rate constants up to factors of 3–4. However, the vibrational frequencies computed using internal coordinates are lower than those obtained in Cartesian coordinates, resulting in larger TST/VTST-int ratios than the TST/VTST-xyz counterparts. Further inspection of the normal modes along the MEP using Cartesian coordinates revealed that in some cases the projection of the vibrational frequencies associated with the hindered rotors involving ${}^3\text{O}_2$ failed to select the correct normal mode, thus adding a further critical aspect to the use of Cartesian coordinates to determine variational effects.

The same trends observed for the H-atom abstractions from the aromatic ring generally apply also to the H-atom abstraction reactions from the functional groups. The main exception concerns the H-atom abstraction by OH, where the dramatic increase of the vibrational frequencies in internal coordinates typical of the abstractions from the aromatic ring is not

observed. Finally, the ratio between VTST-xyz and VTST-int in H-atom abstractions by $^3\text{O}_2$ from the methoxy group of anisole follows opposite trends compared to the other similar systems, with VTST-int being larger than VTST-xyz corrections. This change in trends is related to the fact that significant interactions are established in the proximity of the transition state between the OOH product and the phenyl side chain. These interactions impact the torsional projection differently from what was observed for the other reactions involving $^3\text{O}_2$.

TABLE 6.27: Impact on the rate constants computed in this work of the use of variational transition state theory (Vxyz) and of variational transition state theory with internal coordinate treatment (Vi) with respect to conventional TST (C), reported as ratios between the rate constants obtained using different methods (C/Vxyz, C/Vi) at 500, 1000, 1500 K.

Abstractor		H		CH ₃		OH		³ O ₂	
Site	T [K]	C/Vxyz	C/Vi	C/Vxyz	C/Vi	C/Vxyz	C/Vi	C/Vxyz	C/Vi
Benzene	500	1.02	1.29	1.00	1.04	1.16	3.91	3.78	2.14
	1000	1.12	1.16	1.00	1.03	1.24	2.59	3.35	1.87
	1500	1.17	1.13	1.00	1.04	1.27	2.37	2.96	1.69
Toluene ortho	500	1.04	1.34	1.02	1.05	1.05	3.33	3.19	1.72
	1000	1.14	1.20	1.03	1.08	1.11	2.31	3.20	1.55
	1500	1.19	1.17	1.03	1.08	1.14	2.18	3.34	1.40
Phenol ortho	500	1.07	1.42	1.02	1.06	1.00	2.48	1.25	1.55
	1000	1.19	1.25	1.02	1.07	1.01	2.05	1.04	1.38
	1500	1.25	1.22	1.01	1.07	1.02	2.02	1.00	1.24
Anisole ortho	500	0.98	1.36	1.02	1.07	1.03	3.71	3.17	2.30
	1000	1.00	1.12	1.02	1.05	1.04	3.05	2.46	1.75
	1500	1.03	1.09	1.02	1.09	1.05	3.09	2.14	1.55
Toluene meta	500	1.04	1.37	1.08	1.15	1.18	4.21	3.07	1.66
	1000	1.14	1.22	1.08	1.17	1.27	2.70	2.92	1.46
	1500	1.19	1.19	1.09	1.17	1.31	2.50	2.57	1.32
Phenol meta	500	1.04	1.34	0.96	0.99	1.17	3.74	3.62	2.00
	1000	1.13	1.19	0.95	1.00	1.25	2.53	2.92	1.59
	1500	1.18	1.16	0.95	1.00	1.28	2.36	2.54	1.42
Anisole meta	500	1.00	1.29	1.00	1.02	1.16	3.97	3.26	2.23
	1000	1.08	1.14	0.99	1.04	1.25	2.67	2.47	1.65
	1500	1.12	1.10	0.99	1.05	1.28	2.49	2.15	1.45
Toluene para	500	1.04	1.38	1.01	1.09	1.20	4.31	4.32	1.91
	1000	1.17	1.24	1.02	1.10	1.29	2.83	4.52	1.81
	1500	1.24	1.21	1.02	1.11	1.33	2.67	4.03	1.65
Phenol para	500	1.02	1.29	1.00	1.08	1.21	4.08	2.46	1.78
	1000	1.17	1.16	1.00	1.05	1.30	2.82	2.51	1.73
	1500	1.24	1.13	1.00	1.05	1.34	2.65	2.17	1.54
Anisole para	500	1.02	1.29	1.01	1.10	1.15	3.97	2.62	1.95
	1000	1.14	1.14	1.00	1.07	1.22	2.72	2.57	1.82
	1500	1.21	1.11	0.99	1.06	1.26	2.58	2.27	1.63
Toluene CH ₃	500	1.05	1.16	1.18	1.20	1.09	1.81	3.52	2.48
	1000	1.07	1.12	1.23	1.17	1.26	1.34	2.83	1.91
	1500	1.09	1.11	1.27	1.25	1.32	1.30	2.78	1.83
Phenol OH	500	1.17	1.09	1.06	0.99	1.02	1.80	3.14	1.82
	1000	1.11	1.05	1.07	1.01	1.06	1.29	3.43	1.73
	1500	1.10	1.05	1.08	1.03	1.10	1.22	3.18	1.59
Anisole OCH ₃	500	1.02	1.02	1.08	1.10	1.04	1.81	1.69	3.16
	1000	1.01	1.03	1.06	1.05	1.00	1.35	1.39	2.47
	1500	1.01	1.03	1.06	1.04	1.01	1.27	1.36	2.36

6.4.4 Systematic trends

To provide a synoptic view of the outcomes of the present study towards the definition of rate rules for H-atom abstraction reactions from mono-aromatic hydrocarbons, Figure 6.32 shows that activation energies and reaction enthalpies for H-atom abstractions by H, CH₃, OH, and ³O₂ on the functional groups (-H, -OH, -OCH₃ and -CH₃) of benzene, phenol, anisole, and toluene follow an Evans-Polanyi correlation ($E_A = \alpha\Delta H_r + \beta$).

As expected from resonance stabilization of the phenoxy and benzyl radicals, reactions involving phenol and toluene show the lowest enthalpy of reaction for each abstracting radical. Reactions involving OH and ³O₂ are the most exothermic and endothermic, respectively. Figure 6.32 also reports linear fits for the different mono-aromatic hydrocarbons. The impact of enthalpy changes on activation energies is noticeably less for the more exothermic reactions, i.e., those involving the formation of a resonance-stabilized radical. The slope of the Evans-Polanyi (EP) correlation, α , increases gradually moving from the most stable phenoxy radical ($\alpha = 0.40$), to benzyl radical ($\alpha = 0.57$), to anisyl radical ($\alpha = 0.62$), to the least stable phenyl radical ($\alpha = 0.75$). It is noted that the slope α of the EP correlation in phenol is significantly lower than that of toluene, in contrast with what is expected by looking at the relative stability of the phenoxy and benzyl radicals. This variation is due to the peculiarities of the TS of the H-atom abstraction by ³O₂ from phenol hydroxy group, as discussed above. However, this aspect warns against full extrapolation of this EP correlation to other abstracting radicals, as the EP correlation is actually based on the analogy of TS structures. Hence, Figure 6.32 reports additional points for the energy barriers for the H-atom abstractions from the toluene methyl group by O(³P) and HO₂ radical computed by Pelucchi et al. [129], where only the latter TS structure shows similar interactions with the aromatic ring as in the case of ³O₂. The calculated barriers agree satisfactorily with the correlation, with discrepancies within 2 kcal/mol.

Overall, the obtained EP correlations provide guidelines for the development of rate rules for this reaction class as well as a useful tool to check the consistency of the calculations of reaction barriers for H-atom abstractions by other abstracting radicals.

From the perspective of extending the present calculations to MAHs with multiple substituents or to PAHs, it is useful to inspect the performance of less computationally demanding methodologies for electronic structure calculations than the CCSD(T)/CBS level, as well as potential systematic trends in energy barriers and rate constants.

Tables 6.28 and 6.29 report the differences between M06-2X/6-311+G(d,p) (DFT) and PNO-LCCSD(T)-F12/CBS (PNO) estimates of the energy barriers and 0 K reaction enthalpies with respect to the CCSD(T)/CBS (HL) benchmark for all H-atom abstractions from the benzene ring and from each functional group of the mono-substituted rings.

As far as the energy barriers are concerned, DFT provides reasonable estimates of the HL values with errors generally below 1 kcal/mol, with the exception of H-atom abstraction by OH from phenol hydroxy group. In addition, differences between DFT and HL are systematic for the H-atom abstractions from the aromatic ring, as shown in Table 6.30, always showing standard deviations below 0.12 kcal/mol. This finding encourages the use of M06-2X/6-311+G(d,p) for reasonable estimates of energy barriers for H-atom abstractions from PAHs,

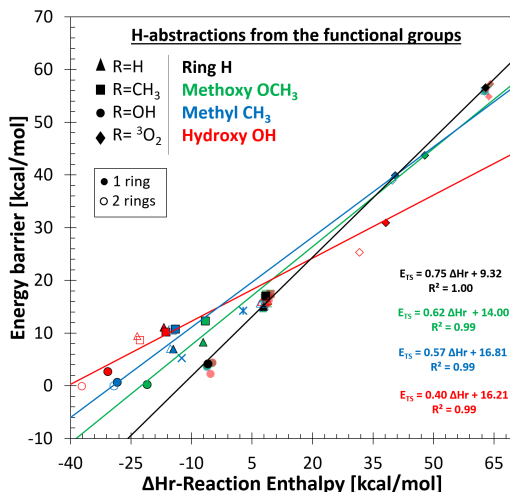


FIGURE 6.32: Relation between the energy barriers and 0 K reaction enthalpy for H-atom abstractions by H (triangles), OH (circles), CH₃ (squares), and ³O₂ (diamonds) from the functional groups of anisole (-OCH₃, blue), phenol (-OH, red), toluene (-CH₃, green), and benzene (-H, black). Transparent symbols refer to the abstraction of the H atoms on the mono-substituted rings. Empty symbols refer to the results obtained for 2 ring PAHs (Section 6.4.5). x and * refer to the barriers for the H-atom abstraction by O(³P) and HO₂ from the toluene methyl group [129].

as well as the scaling of DFT energy barriers with the systematic differences found in this work. Similar trends were also found for the estimates of the energy barriers for H-atom addition reactions on mono-substituted MAHs at ω B9X-D/6-311+G(d,p) (Section 6.5).

The accuracy of the PNO approximation is comparable to DFT for the H-atom abstractions by H and CH₃, while larger discrepancies are observed in the predictions of the energy barriers for the H-atom abstractions by OH and ³O₂. On the other hand, the PNO approach generally performs better than DFT in determining the 0 K reaction enthalpies (Table 6.29), with deviations generally below 1 kcal/mol. DFT discrepancies with respect to the HL benchmark reach about 2 kcal/mol for the estimate of the reaction enthalpies of the abstractions by OH and ³O₂. The approximation of the reaction enthalpies for the H-atom abstractions from phenol is less satisfactory for both DFT and PNO levels, with discrepancies of 2–3 kcal/mol. Overall, PNO does not seem to increase the precision of DFT estimates significantly. Hence, for the reactions investigated in the present work, the M06-2X functional represents a reasonable choice for the study of the same reaction class for larger PAHs.

TABLE 6.28: Difference between the energy barriers at PNO-LCCSD(T)-F12/CBS (PNO) and M06-2X/6-311+G(d,p) (DFT) levels and the benchmark values at the CCSD(T)/CBS level of theory (HL).

abstractor	H		CH ₃		OH		³ O ₂	
	PNO-HL	DFT-HL	PNO-HL	DFT-HL	PNO-HL	DFT-HL	PNO-HL	DFT-HL
Benzene	0.56	1.05	0.68	-0.37	1.27	-0.23	1.50	0.25
Phenol-OH	-2.53	-0.46	-2.68	-1.58			-1.09	-0.47
Toluene-CH ₃	0.67	1.01	0.72	-0.55	1.12	-0.21	2.77	-0.79
Anisole-OCH ₃	0.63	0.83	0.77	-0.88	1.49	-0.60	1.98	-1.18

Finally, common trends are expected for the rate constants of the H-atom abstractions from the aromatic rings. In fact, the rate constants of the H-atom abstractions by each

TABLE 6.29: Difference between the 0 K enthalpy of reactions at the PNO-LCCSD(T)-F12/CBS (PNO) and M06-2X/6-311+G(d,p) (DFT) levels and the benchmark values at the CCSD(T)/CBS level of theory (HL).

<i>abstractor</i>	H		CH ₃		OH		³ O ₂	
<i>site</i>	PNO-HL	DFT-HL	PNO-HL	DFT-HL	PNO-HL	DFT-HL	PNO-HL	DFT-HL
Benzene	0.01	-0.14	0.16	-1.00	-0.10	0.40	0.54	0.54
Phenol-OH	-3.66	2.18	-3.52	1.32			-3.13	2.86
Toluene-CH₃	0.73	1.52	0.87	0.66	0.84	2.06	1.25	2.20
Anisole-OCH₃	-0.02	0.61	0.13	-0.25	0.10	1.15	0.51	1.29

TABLE 6.30: Differences in energy barriers (ΔH TS) and 0 K reaction enthalpies (ΔH_r) between the CCSD(T)/CBS and M06-2X/6-311+G(d,p) levels of theory (HL-L1, see main text) for all the reactions investigated in this work. Energies are in kcal/mol.

<i>abstractor</i>	H		CH ₃		OH		³ O ₂	
<i>site (ring)</i>	ΔH TS HL-L1	ΔH_r HL-L1	ΔH TS HL-L1	ΔH_r HL-L1	ΔH TS HL-L1	ΔH_r HL-L1	ΔH TS HL-L1	ΔH_r HL-L1
Benzene	-1.05	0.14	0.37	1.00	0.23	-0.40	-0.25	-0.54
Phenol - o	-1.20	0.08	0.25	0.94	0.61	-0.46	-0.53	-0.60
Phenol - m	-1.06	0.21	0.35	1.07	0.21	-0.33	-0.20	-0.47
Phenol - p	-1.13	0.15	0.24	1.01	0.19	-0.39	-0.29	-0.53
Toluene - o	-1.10	0.07	0.35	0.93	0.32	-0.47	-0.30	-0.61
Toluene - m	-1.08	0.15	0.31	1.01	0.21	-0.39	-0.27	-0.53
Toluene - p	-1.09	0.14	0.29	1.00	0.22	-0.40	-0.25	-0.54
Anisole - o	-0.99	0.51	0.55	1.37	0.53	-0.03	-0.24	-0.17
Anisole - m	-1.11	0.21	0.29	1.07	0.17	-0.33	-0.27	-0.47
Anisole - p	-1.14	0.17	0.29	1.03	0.19	-0.37	-0.28	-0.51
average	-1.10	0.18	0.33	1.04	0.29	-0.36	-0.29	-0.50
std	0.06	0.12	0.09	0.12	0.16	0.12	0.09	0.12
<i>site (lateral)</i>								
Phenol - OH	0.46	-2.18	1.58	-1.32	3.98	-2.72	0.47	-2.86
Toluene - CH ₃	-1.01	-1.52	0.55	-0.66	0.21	-2.06	0.79	-2.20
Anisole - OCH ₃	-0.83	-0.61	0.88	0.25	0.60	-1.15	1.18	-1.29

radical from the single sites of all mono-substituted MAHs generally agree to within a factor of 2 with the reference rates of benzene, encouraging the adoption of similar values for substituted MAHs and potentially for PAHs.

The few observed deviations of more than a factor of 2 are caused by peculiar interactions between the abstracting radicals and the functional groups or by high steric hindrance. For these cases, correction factors with respect to the reference abstraction reaction from one benzene ring site are summarized in Table 6.31.

A significant decrease in the rate constant (up to a factor of 3–5) may be caused by H-bonding like interactions, such as for phenol and anisole functional groups in the vicinity of OH or ³O₂. The anisole methoxy group also causes a systematic decrease in the rate constants for the H-atom abstractions by ³O₂, whereas this effect is only observed for the abstractions from the ortho positions in the case of H and CH₃ abstracting radicals. Interestingly, the decrease in the activation energies obtained for C₆H₅OH + OH and C₆H₅OCH₃ + CH₃ is extremely close to that found for the H ipso substitutions on o-OHC₆H₄OH and o-CH₃C₆H₄OCH₃ with respect to the mono-substituted counterparts C₆H₅OH and C₆H₅OCH₃ (Section 6.5), suggesting similar types of interactions across different reaction classes.

Table 6.31 is therefore useful to build consistent kinetic schemes: the rate parameters for all H-atom abstractions by H, CH₃, OH and ³O₂ from aromatic ring sites may be set equal to benzene (from Table 6.25) and corrected according to the factors of Table 6.31 in the presence of interactions of the same kind. Potential applications to PAHs are investigated in the next section.

TABLE 6.31: Approximate corrections to the pre-exponential factors and activation energies of the Arrhenius fits for $C_6H_5Y + R = C_6H_4Y + RH$ reactions with differences of a factor >2 with respect to the reference abstraction reaction from benzene. $k = k_0 \cdot T^\alpha \cdot \exp(-\frac{E_A}{RT})$, units of E_A are cal/mol.

Interaction type	Reaction	correction	
		k_0	E_A
H-bonding like	$C_6H_5OH + OH = o-C_6H_4OH + H_2O$	0.15	-1950
	$C_6H_5OH + ^3O_2 = o-C_6H_4OH + HO_2$	0.30	0
	$C_6H_5OCH_3 + OH = o-C_6H_4OCH_3 + H_2O$	0.30	0
Steric hindrance	$C_6H_5OCH_3 + ^3O_2 = o-C_6H_4OCH_3 + HO_2$	0.56	0
	$C_6H_5OCH_3 + H/CH_3 = o-C_6H_4OCH_3 + H_2/CH_4$	0.61	-660

6.4.5 Exploration of rate extension to two ring PAHs

The analysis of the rate constants derived for MAHs revealed some systematic trends. In particular, EP correlation is generally valid, and systematic energy scaling from DFT (M06-2X) to CCSD(T)/CBS applies to a given TS type. Hence, the extension of the calculated rate constants to α -naphthol and α -methylnaphthalene (top of Figure 6.33) through the systematic trends found was explored.

In particular, H-atom abstractions by H, CH_3 , OH and 3O_2 from the functional groups of α -naphthol and α -methylnaphthalene were calculated at the M06-2X/6-311+G(d,p) level of theory. For abstractions by H atoms and OH radicals, the H-atom abstractions from the ring sites closest to the functional groups (i.e., ortho and ortho-edge positions highlighted in Figure 6.33) were also computed. The single point energies were shifted according to the HL-L1 energy differences for the corresponding MAH structures reported in Table 6.30.

The resulting energies for the H-atom abstractions from the functional groups are plotted in Figure 6.32 so as to highlight similarities and differences with the corresponding MAHs. The energy barriers for the H-atom abstractions from the aromatic rings are well aligned with those from the corresponding MAHs, with discrepancies generally below 0.5 kcal/mol. Both the reaction energies and the energy barriers for H-atom abstractions from the methyl group of α -methylnaphthalene agree to within 1 kcal/mol with those of toluene, and follow closely the EP correlation found. On the other hand, the second aromatic ring in α -naphthoxy produces a significantly higher resonance stabilization than phenoxy radical, resulting in a exothermicity for the corresponding H-atom abstraction reactions that is higher by 6.5 kcal/mol. The energy barriers are in overall agreement with the EP relation found for phenol, with discrepancies of only 1–2 kcal/mol. In contrast, the energy barrier for the H-atom abstraction by 3O_2 would be overestimated by the EP relation by more than 3 kcal/mol.

A test of the validity of the HL-L1 scaling relations adopted was performed for the H-atom abstraction by H from naphthol hydroxy group. In particular, SPEs of the corresponding PESs for both α -naphthol and phenol were also calculated at the CCSD(T)/aug-cc-pVDZ level of theory, with extrapolations to the basis set limit calculated at (MP2/aug-cc-pVTZ – MP2/aug-cc-pVDZ) level. The calculated energy barriers for phenol were about 4 kcal/mol lower than the CCSD(T)/CBS values. This result reveals the inadequacy of CCSD(T)/aug-cc-pVDZ to calculate accurate energies for this system. Furthermore, the (CCSD(T) –

M06-2X) values for both methodologies are extremely close in phenol and α -naphthol, with discrepancies below 0.3 kcal/mol. This provides an estimate of the error committed in the proposed HL-L1 scaling relations of Table 6.30.

Figures 6.33a,b show the rate constants obtained for the H-atom abstractions by H from α -naphthol (A2OH) and α -methylnaphthalene (A2CH3) compared to the 1-ring counterparts (A1OH, A1CH3) presented in the previous sections. Additionally, the rate constants rescaled from the 1-ring rates according to the EP relations of Figure 6.32 are also shown (dotted lines). In these cases, the activation energy of the 1-ring rate constant was simply shifted by the reaction energy difference between the 2-ring and 1-ring cases multiplied by the slope of the EP relations. Rate constants for A2CH3 are in excellent agreement with the results for A1CH3. The EP-rescaled rate almost overlaps with the calculated one. The rate constants for the abstractions from the A2CH3 ring are about a factor of 1.2–2 lower than that from a single ortho site in toluene. In particular, the rate constant on the ortho edge site in A2CH3 is about a factor of 2 smaller than the respective rate constant in toluene. This may be explained by the slightly larger rotational barriers for the methyl group in A2CH3. The total rate constant for the H-atom abstraction from the ring may therefore be derived as $A1CH3 \cdot 7/5$. If higher rotational barriers are considered, a scaling of 7/10 may be applied. However, such effects are expected to be relevant only for the ortho-edge site. In the case of A2OH, the calculated rate constants for the abstractions from the ring almost overlap with those of the A1OH counterpart. The total rate constant for the H-atom abstraction from the ring may be derived as $A1OH \cdot 7/5$, i.e., just accounting for the change in the number of sites.

Figure 6.33c shows the results for the H-atom abstractions by CH_3 . The A2CH3 rate for the abstraction from the aromatic ring is identical to that of A1CH3. In contrast, the rate constant for A2OH is slightly higher than that for A1OH because of the decrease in the energy barrier by 1 kcal/mol. This increase is partially compensated by the increase in the torsional barriers of the OH- CH_3 group due to the hindrance of the second aromatic ring. This effect is not captured by the rate constant simply derived through the EP relation for the barrier heights, which in fact overestimates the rate constant.

Figure 6.33d shows the results obtained for the reverse rate constants of the H-atom abstractions by 3O_2 . The A2CH3 rate is about a factor of 2–3 lower than that for A1CH3 because of the increase in both the energy barrier (0.4 kcal/mol for the reverse direction) and of the torsional barrier for the CH_3-O_2 group. Only the former effect is captured by the EP-corrected rate. The A2OH rate is lower than that of A1OH by a factor of ~ 4 –5 as a result of the increase in the reverse energy barrier by about 1.5 kcal/mol and to the high torsional barriers in A2OH. The EP-corrected rate constant is in partial agreement with the calculations, mostly because the overestimation of the energy barrier (Figure 6.32) partially accounts for the effect of the higher torsional barriers. The agreement worsens at low temperatures, where the EP-corrected rate is smaller than the calculated one by about a factor of 4.

Finally, Figures 6.33e,f show the results for the H-atom abstractions by OH. For the abstractions from the aromatic ring sites, similar considerations to the abstractions by an

H atom apply. A slight decrease in the energy barriers for the H-atom abstractions from A2OH is observed. The energy barrier in A2CH3 decreases exactly according to the EP relation of Figure 6.32. However, the corresponding rate constant decreases because of the steric hindrance of the second aromatic ring, which produces higher torsional barriers by 1–3 kcal/mol compared to A1CH3. The rate constants of the H-atom abstraction from A2OH hydroxy group is not shown because of the complexity found for the A1OH counterpart. Geometry optimization resulted in different structures with very different energies in A2OH which indeed encourages further exploration.

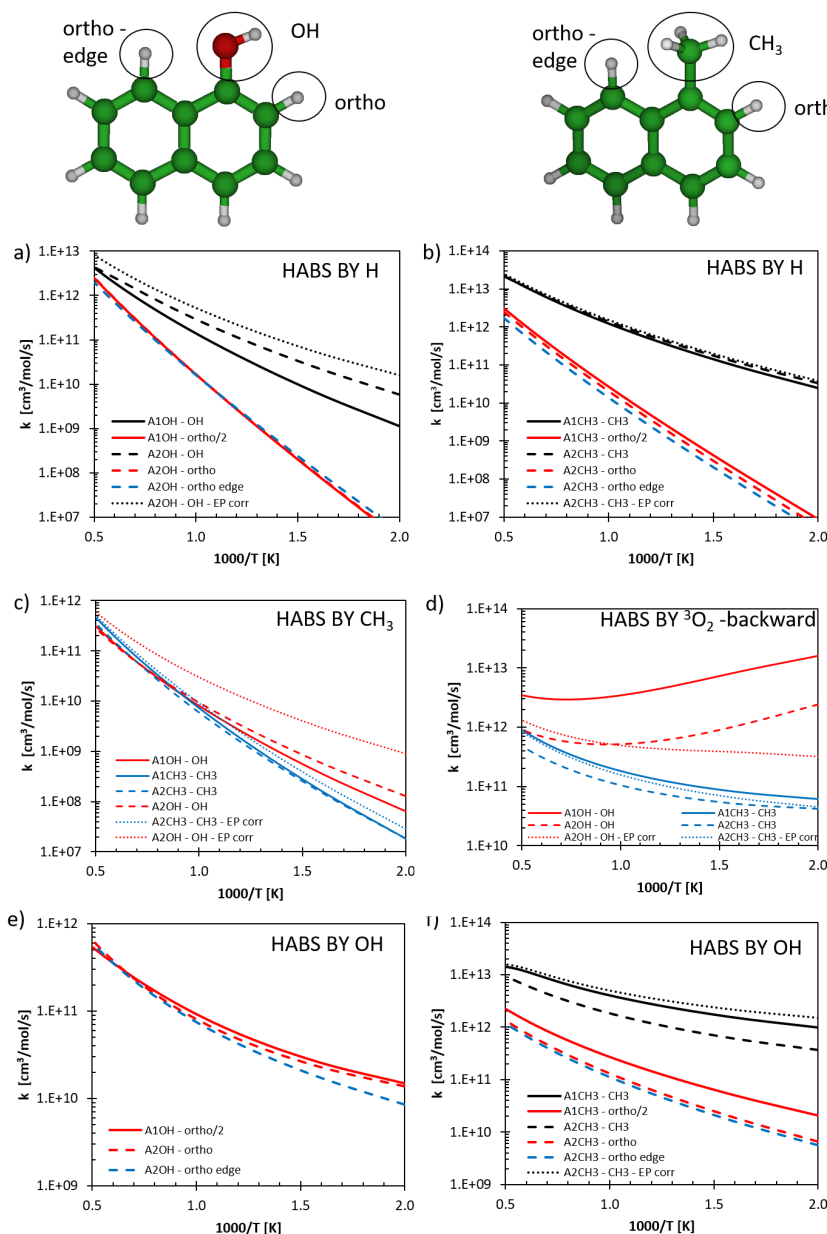


FIGURE 6.33: Rate constants for H-atom abstractions by H (a,b), CH₃ (c), ³O₂ (d), and OH (e,f) from different sites (OH, ortho, ortho-edge) of α -naphthol and α -methylnaphthalene (A2OH, A2CH3, dashed lines) in comparison with the MAHs counterparts (A1OH, A1CH3, solid lines) and rates obtained from the latter by shifting the energy barriers according to EP rules (dotted lines, rules from Figure 6.32).

6.4.6 Summary

This section presented a comprehensive theoretical investigation of the rate constants for H-atom abstraction reactions from MAHs by H, CH₃, OH, and ³O₂, overcoming the lack of systematic studies on reactions relevant in the pyrolysis and oxidation of aromatic hydrocarbons. In particular, benzene, toluene, phenol, and anisole were considered as reference for H-atom abstractions on the -H, -CH₃, -OH and -OCH₃ functional groups, respectively. A set of 52 rate constants were obtained with high-level AI-TST-ME calculations. The accuracy of the method, already discussed in a previous work on H-atom abstractions from toluene [129], was confirmed by the overall good agreement (generally factor < 2) with the available experimental data. The use of internal coordinates for the calculation of the rate constants resulted in significant differences for some of the abstractions by CH₃, OH, and ³O₂ abstracting radicals. Additionally, the impact of anharmonic analysis for the H-atom abstractions by OH from benzene and toluene was discussed, revealing that including anharmonic corrections to the ZPES for these reactions allow a closer agreement with the experimental datasets.

From the perspective of deriving rate-rules for this reaction class, Evans-Polanyi relations were built considering all H-atom abstractions on the functional groups, finding that the slope of the Evans-Polanyi correlation is inversely proportional to the stability of the formed radical. The case of phenol is peculiar in that it shows an increased stability of the TS for the H-atom abstraction by ³O₂ on the hydroxy group, mostly due to the H-bonding between the hydroxy moiety and the abstracting radical. Interestingly, systematic differences between CCSD(T) (HL) and DFT (L1) energies were found, suggesting that calculations on larger PAHs may be conducted at a lower level of theory and then shifted to the HL. Hence, H-atom abstractions from the 2-ring PAHs α -naphthol (A2OH) and α -methylnaphthalene (A2CH3) were also calculated at the DFT level. It was found that H-atom abstractions from the aromatic rings may in general be derived from the monoaromatic counterparts if the number of sites and symmetry corrections are accounted for. As for the abstractions from the functional groups, EP relations may be inaccurate in predicting the rate constants for 2-ring PAHs, especially when the abstracting radical is bulky. In fact, the steric hindrance of the second ring causes an increase in the TS torsional barriers, often decreasing the rate constant with respect to the MAH counterpart. Hence, EP relations may be a useful starting point to check the consistency of energy approximations and low level theoretical calculations, but they are not recommended for rate constant scaling to larger substituted PAHs.

6.5 Theoretical calculations by reaction class: ipso addition-elimination reactions on mono and di-substituted MAHs

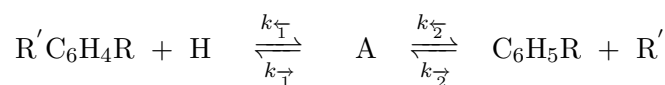
This section presents a set of theoretically coherent rate constants for H ipso addition-elimination reactions, or H ipso substitutions, on MAHs and OAHs with single and double substituents (C_6H_5OH , $C_6H_5CH_3$, *o*-,*m*-,*p*- $C_6H_4(OH)_2$ *o*-,*m*-,*p*- $CH_3C_6H_4OH$, and *o*-,*m*-,*p*- $C_6H_4(CH_3)_2$), and rate-rule extension to OCH_3 , CHO and C_2H_5 substituents.

6.5.1 Motivation and background

The choice of H ipso substitutions stems from their significant contribution to the fuel reactivity in both pyrolysis and combustion conditions, in particular at intermediate-to-low temperatures ($T \sim < 1500$ K). In MAHs, H ipso substitutions are key to fuel decomposition to less substituted MAHs. For instance, H ipso substitution on toluene and ethylbenzene constitutes the main source of benzene in their oxidation process, both in premixed flames and flow reactors [402], [525], [555], [556], favoring the cycloaddition/fragmentation steps in the formation of PAH intermediates [402]. Similarly, in MAHs with multiple substituents such as *o*-xylene, H ipso substitution determines the concentration of toluene and methyl radicals [557]. Furthermore, in ethylbenzene pyrolysis and oxidation, H ipso substitution is responsible for up to 10% of the fuel consumption below 1100 K [541], [558], [559]. H ipso substitution on phenol and catechol contributes up to 10% of the fuel consumption in both pyrolysis and oxidation [46], [470]. Similarly to MAHs, the concentration of benzene in flow reactors largely depends on ipso substitution reactions, as was found in benzaldehyde oxidation [449]. In addition, the product distribution of the pyrolysis of OAHs with multiple substituents such as vanillin was found extremely sensitive to H ipso substitutions [46], [420]. In the combustion of both anisole and guaiacol, this reaction plays a key role not only in terms of product distribution but also in determining the ignition properties of the fuel [45], [50].

Finally, H ipso substitutions are studied in the field of atmospheric chemistry. In particular, OH ipso substitution on benzene initiates its oxidation at low temperatures, and the formation of OH-aromatic adducts accounts almost for the whole benzene and toluene reactivity at room temperature and pressure [560], [561]. Hence, the rate constants computed in this work are also useful to study the oxidation of MAHs in the atmosphere. However, since the main focus of this thesis is combustion chemistry, only the H substitution channel will be discussed.

H ipso substitution reactions occur in two elementary steps, namely H-atom addition forming adduct A and its β -scission:



R' indicates the group replaced by H and R represents a side group in the ortho, meta, or para position, consistent with the notation used in the rest of this Section. k_{\uparrow} , k_{\downarrow} and k_{-1} , k_{-2} are the forward and backward rate constants of the elementary steps. The qualitative

potential energy surface (PES) for the generic reaction is depicted in Figure 6.34. In the case of OH elimination, the β -scission of the adduct (step2) may also involve the formation of a van der Waals well, as shown in the figure.

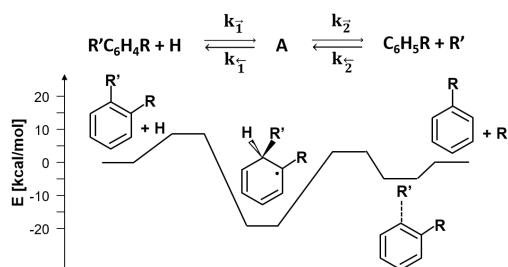
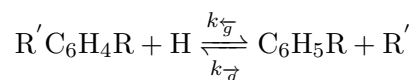


FIGURE 6.34: Qualitative PES for the H ipso substitution on the generic doubly-substituted aromatic $R'C_6H_4R + H$ to form well A and the products $C_6H_5R + R'$.

Adduct A is generally unstable at conditions of interest for combustion (> 800 K), and its secondary reactivity is expected to play a marginal role, therefore in most combustion kinetic mechanisms H ipso substitution reactions are only included as a "global" step:



The impact of ipso substitution by H or R' on the overall reactivity of the system depends on its competition with H-atom abstractions by H or R' , respectively. The rate $k_{\overleftarrow{g}}$ of ipso substitution by hydroxyl and methyl radicals ($R' = OH, CH_3$) is always negligible in comparison with H-atom abstraction by the same radicals, whereas the rate of the elementary addition step $k_{\overrightarrow{g}}$ may be comparable to or higher than the H-atom abstraction channel [439].

In contrast, ipso substitution by H may even prevail over H-atom abstraction by H at low temperatures. For instance, Ellis et al. [541] experimentally highlighted that around 800 K H ipso substitution on toluene accounts for more than 50% of H consumption, in competition with the formation of benzyl radical via H-atom abstraction. In the case of H ipso substitution on phenol, He et al. [436] determined experimentally that H consumption by ipso substitution prevails over H-atom abstraction also at 1000–1150 K (65–55% of the total H-atom addition and abstractions). Hence, this work mostly focuses on the global rate constants $k_{\overrightarrow{g}}$ of the chosen set of H ipso substitutions.

Only experimental measurements of the rate constants for H ipso substitutions on phenol and toluene are available in the literature [436], [541], [562]. In fact, the high reactivity of products and the competition between addition and abstraction channels complicates the determination of the branching fractions to products. Therefore, the rate constants of H ipso substitution on anisole, benzaldehyde, and ethylbenzene in kinetic models are estimates based on analogous reactions or recommended values [414], [558], [563]. Similar considerations apply to MAHs with multiple substituents [45], [557]. These aspects motivate the use of state-of-the-art theoretical methods for the investigation of the rate constants of H ipso substitutions on MAHs and OAHs with single and double substituents, so as to derive a consistent set of rate constants to be implemented in kinetic models.

This section investigates with AI-TST-ME method the replacement of OH and CH₃ with H assessing the impact of one additional side group (R = CH₃, OH) on the rate constant. Section 6.5.2.2 presents the rate constants for H ipso substitutions on phenol and toluene, providing evaluation of the accuracy of the theoretical approach adopted. Section 6.5.2.3 presents rate constants for H ipso substitutions on *o*-,*m*-,*p*-C₆H₄(OH)₂, *o*-,*m*-,*p*-CH₃C₆H₄OH, and *o*-,*m*-,*p*-C₆H₅(CH₃)₂, focusing on the role of the effect of the second side group on the energy barriers for the addition channel. This systematic approach provides guidelines for the analogy-based extension of the rate constants for H ipso substitutions to MAHs and PAHs with the same functional groups. Section 6.5.3 formulates electronic structure-based rate rules for 5 different reaction classes, namely OH, CH₃, OCH₃, CHO, and C₂H₅ replacement with H in MAHs with double OH/CH₃/OCH₃/CHO/C₂H₅ substituents. Additional calculations for the reference reactions for mono-substituted MAHs and a few additional rate constants for di-substituted MAHs allowed for the derivation of an internally-consistent set of 80 rate constants, for the reactions *o*-,*m*-,*p*-R'₂C₆H₄R → C₆H₅R+R' with R' = OH/CH₃/OCH₃/CHO/C₂H₅ substituents and R = H/OH/CH₃/OCH₃/CHO/C₂H₅ side groups in ortho, meta and para position (Section 6.5.3.2). An error analysis is carefully considered in Section 6.5.3.3.

6.5.2 Rate constant calculation

6.5.2.1 Theoretical methodology

The rate constants for all the considered reaction channels were computed using the AI-TST-ME method using EStokTP (Chapter 3). The derivation of the PESs was performed at the same level of theory successfully adopted for phenol and phenoxy decomposition (Section 6.3.2.2), hence in this section only additional considerations are reported.

Only the TSs for the OH addition channel to the sites of C₆H₅OH showed relatively high T1 values (up to 0.03). Hence, the energy barriers were also computed at the multireference CASPT2/aug-cc-pVTZ level. The selected AS included 7 electrons in 7 orbitals (7e,7o), namely the 6 π and π* orbitals of the aromatic ring (6e,6o), and the singly occupied p orbital of OH (1e,1o). Calculations were performed using an IPEA shift of 0.25. The multireference treatment resulted in a maximum difference in the energy barriers of 1 kcal/mol for the addition on the ortho carbon site, and to a lower discrepancy of 0.3 kcal/mol in the case of the meta and para carbon sites.

The rate constants were computed by implementing one-dimensional or, for the H+*o*-,*m*-C₆H₄(OH)₂ PESs, two-dimensional hindered rotor models, with the latter resulting in correction factors of about 1.2 with respect to rate constants determined with the one-dimensional rotor treatment [106]. For the OH addition channels, the structures of the entrance van der Waals wells were also determined, however ME simulations revealed that the entrance well does not stabilize below 1000 atm in any case, hence van der Waals complexes were excluded in the final ME simulations. The rate constants of the investigated reaction pathways were computed in the 300–2500 K temperature and 0.1–100 atm pressure

ranges, solving the multi-well one-dimensional master equation with the chemically significant eigenvalues method, as implemented in MESS (Section 3.3.4.3). Collisional parameters adopted were the same as those used for phenol decomposition. All MESS input files are attached as SM to the corresponding publication [564]. The intermediate adduct does not stabilize at the conditions of interest to combustion processes. According to the present ME simulations, at 1 atm the adduct is thermochemically stable only below 800–900 K for all reactions investigated, however well skipping channels still prevail at ~ 700 K. Therefore, in this work only global rate constants are presented, i.e., including the adduct formation implicitly upon lumping with MEL (Chapter 4). Lumping also flattens the pressure dependence of the reactions. Therefore, the global $k_{\rightarrow}^{\bar{g}}$, $k_{\leftarrow}^{\bar{g}}$ reported are independent of pressure.

The appropriateness of the adopted methods stems from the success in their application to similar systems in previous works [97], [129], [470], [565], and from literature recommendations [200]. Estimated uncertainties are about 50% in pre-exponential factors and 0.5–1 kcal/mol in energy barriers, as confirmed by the good agreement with the available experimental data of all the calculations presented in this work. The energy barriers for OH addition channels are assigned a larger uncertainty of 1–1.5 kcal/mol because of the MR treatment.

Finally, it is important to highlight that the value of the set of theoretical rate constants reported herein also resides in their internal consistency and coherence. In fact, the uncertainties of the rate constants will be mostly systematic, as also highlighted by the scaling relations developed in this work. Hence, the rate rules developed within this set of data are expected to be representative of the physical behavior of the system, at least in relative terms.

6.5.2.2 H ipso substitutions on phenol and toluene

The potential energy surfaces for H ipso substitution on phenol (a) and toluene (b) are shown in Figure 6.35. The product formation enthalpies at 0 K are consistent with the values reported in the ATcT tables [117], with discrepancies within 0.5–0.8 kcal/mol. Some evaluations of the PES for OH ipso substitution to benzene are available in the literature due to the interest of this reaction channel in the atmospheric oxidation of benzene. The energies computed in this work agree to within 1.5 kcal/mol of those computed at the G3 level of theory by Tokmakov and Lin [439] and from the best estimates of Seta et al. [452], where CBS-QB3 calculations were adjusted so as to reproduce high-temperature rate constants of the considered reaction channels. A similar agreement is also reached with the theoretical calculations of Hollman et al. [565], who investigated the PES with different DFT methods. In this case however, a discrepancy of 3 kcal/mol is found for the barrier for H-atom addition to phenol. The comparison between the PESs of Figure 6.35 highlights that, despite some similarity in the energies of both TS1 (8.0 and 5.9 kcal/mol) and TS2 (–0.6 and 1.4 kcal/mol) in the reaction of OH and CH₃ substitution with H, the reaction enthalpy is remarkably different (–1.7 and –9.8 kcal/mol) due to the different dissociation energies of the C–O and C–C bonds, clearly indicated by the optimized bond lengths of the adducts (1.44 and 1.55 Å, respectively). Therefore, the OH and CH₃ addition channels show substantial differences

in the energy barriers. The detailed analysis provided by Tokmakov and Lin and Hollman et al. highlight weak interactions between OH and the aromatic ring at distances of 5 Å [439], [565]. This leads to the formation of a symmetric C_s pre-reaction complex (WR of Figure 6.35a), which preserves the covalent-like bonding nature of TS2 [565]. Tokmakov and Lin [439] attribute these interactions to the overlap of the frontier orbitals of benzene and OH, which generates a charge transfer that involves also the benzene ring. Contrary to the other OH addition channels investigated in this work, this is the only case in which the pre-reaction complex stabilizes, although the stabilization range is narrow.

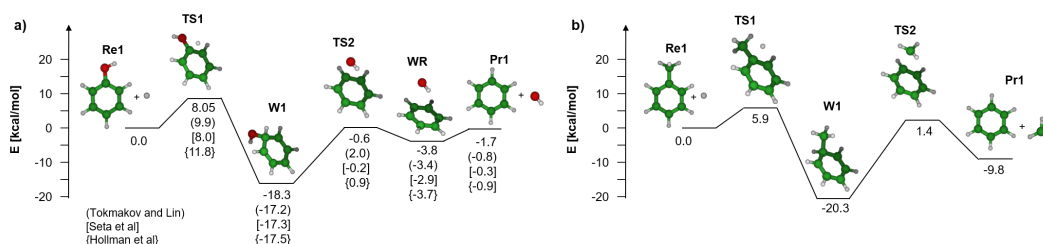


FIGURE 6.35: PES for H ipso substitution on phenol a) and toluene b). Energies in kcal/mol are computed with respect to the reactants and are inclusive of zero point energies. PES a) also shows the comparison of the energies with previous works [439], [452], [565].

Figure 6.36 shows the computed global rate constants for H ipso substitution on phenol and toluene in comparison with the available experimental and theoretical estimates, as well as the rate constants for the total H-atom abstraction by H on the side groups, calculated in [129], [470].

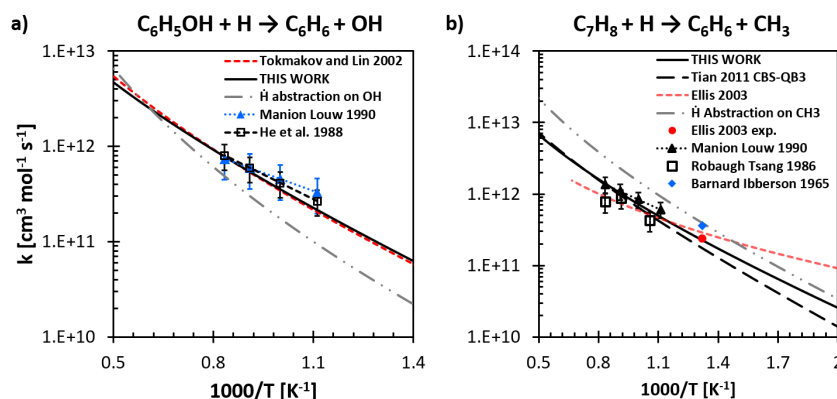


FIGURE 6.36: Computed global rate constants (solid black lines) for H ipso substitution reactions on phenol a) and toluene b) in comparison with the available experimental data [379], [436], [437], [439], [541], [562] (symbols) and with the rate for the total H-atom abstraction reactions by H (dash-dotted grey lines) from the side hydroxy and methyl groups [129], [470].

The global rate constant for OH replacement by H in phenol (a) Figure 6.36 is in excellent agreement with the recommended experimental estimates, with a discrepancy of less than a factor of 1.5 with the experiments of Manion and Louw [437] and <1.2 with the experiments of He et al. [436]; well within the reported experimental uncertainties. The present rate constant also agrees to within a factor of 1.25 with the theoretical calculations of Tokmakov and Lin [439], where the barrier for the H-atom addition channel was adjusted to 8 kcal/mol

to obtain the best fit to the experimental data. Also the calculated rate constant for CH₃ replacement by H in toluene (Figure 6.36b) agrees to within a factor of 1.7 with the experimental estimates of Barnard and Ibberson, and of Robaugh and Tsang [379], [562]. This discrepancy decreases to a factor of 1.3 for the experimental data of Manion and Louw, and of Ellis et al. [437], [541]. Though the calculated apparent activation energy is higher than the value recommended by Ellis et al., the disagreement between the rate constants is below a factor of 1.8 above 700 K. Similarly, the theoretical rate constant computed at the CBS-QB3 level in the work of Tian et al. [525] shows a maximum discrepancy of a factor of 2.4 at low temperature (400 K), decreasing to 1.5 in the range of interest to combustion processes. The overall good agreement with the available literature values for the reference rate constants for the reaction classes of OH and CH₃ replacement by H confirms the accuracy of the theoretical approach proposed and also supports its application to the other systems reported in this work, for which experimental measurements are not available. A similar agreement is obtained with the available literature data for the rate constants of OH and CH₃ ipso substitutions. These additional comparisons are reported in the supplementary material of the corresponding publication [564].

6.5.2.3 Rate constants and effects of OH and CH₃ side groups

A generalized PES diagram for H ipso substitution on *o*-R'C₆H₄R is shown in Figure 6.37, while the calculated global rate constants are reported in Figure 6.38 on a per site basis, together with those for *m*-R'C₆H₄R and *p*-R'C₆H₄R.

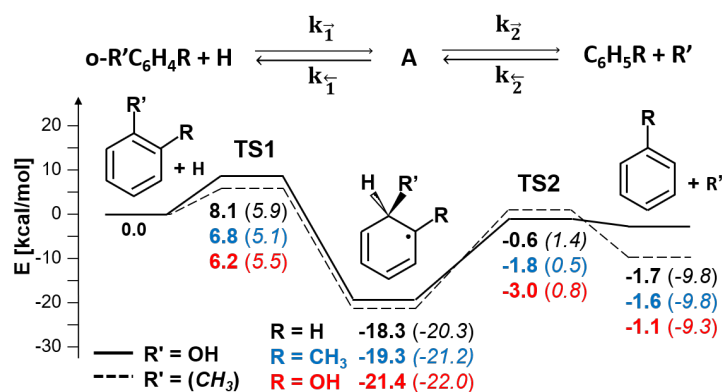


FIGURE 6.37: PES for the H-atom addition reactions to *o*-OHC₆H₄R (solid lines and bold numbers) and to *o*-CH₃C₆H₄R (dashed lines and italic numbers in brackets) and β-scission of the adduct A to C₆H₅ + OH and C₆H₅ + CH₃, respectively. R indicates the different side group in ortho position, and TS1/TS2 indicate the TSs of the addition and β-scission channels, respectively. Energies are computed with respect to the reactant *o*-R'C₆H₄R + H and are inclusive of zero point energies.

The PES diagrams show clearly that for the replacement of both OH and CH₃, the H-atom addition step is rate limiting because of the associated high energy barrier. Furthermore, with respect to TS1 energy barriers, the replacement of the methyl group is slightly favored over that of the hydroxy group, hence the rate constants for CH₃ replacement are consistently faster than those for OH replacement. This means for example that for all the isomers of cresol (CH₃C₆H₄OH) H ipso substitution will largely favor the formation of

phenol over that of toluene. However, as noticed in the previous section, the 0 K reaction enthalpy change for OH replacement by H is about 8 kcal/mol less exothermic than that for CH₃. Therefore, the global rate constants for OH ipso substitutions, are higher by orders of magnitude than those of CH₃ ipso substitutions.

The presence of vicinal OH and CH₃ groups in ortho positions have a significant impact on the energies of the PES stationary points, which decrease with respect to those of the mono-substituted MAHs (R = H). In particular, in catechol (o-C₆H₄(OH)₂) the side group R has the strongest impact, as both TS1 and the adduct A are 2 kcal/mol more stable than the corresponding stationary points of the PES for H-atom addition to phenol. This increased stability is due to the hydrogen bonding between the two hydroxy groups, which is preserved in the structures of both TS1 and a. As a consequence, the lateral hydroxy group assumes an out-of-plane configuration, contrary to what is observed in the meta and para isomers. On the other hand, the hydrogen bonding leads to an increase of the rotational barriers for the hydroxy groups, partially compensating the effect of the lower energy barrier on the addition step. Overall, the presence of a side group in the ortho position causes a significant increase of the H ipso substitution rate constants $k_{\vec{T}}$. Figure 6.38 shows that the H ipso substitution rate at 500 K increases by more than a factor of 3 compared to that of its mono-substituted counterpart, i.e., phenol, further increasing to a factor of 6.6 at 300 K. A similar impact is observed when the methyl group is in the ortho position. Figure 6.38b,c show the rate constants for H ipso substitutions on m-RC₆H₄R' and p-RC₆H₄R', respectively. It is evident that the difference between the global rates $k_{\vec{T}}$ of the doubly substituted MAHs and their mono-substituted counterparts is more limited than for H ipso substitutions on o-RC₆H₄R' (factor of 0.8–2.8 in the full 300–2500 K temperature range). Additionally, the impact of the side groups in the meta position is almost negligible, as opposed to the ortho and para side groups. Hence, the rate constants for H ipso substitutions on m-RC₆H₄R' may be derived with from those for the mono-substituted R'C₆H₅, introducing appropriate corrections on the pre-exponential factors for the number of reacting sites.

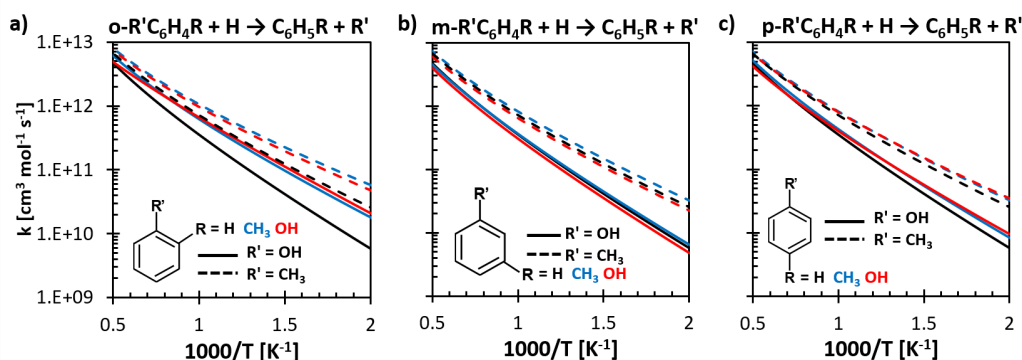


FIGURE 6.38: Forward global rate constants $k_{\vec{T}}$ for H ipso substitutions on a) o-R'C₆H₄R + H, b) m-R'C₆H₄R + H and c) p-R'C₆H₄R + H. The rate constants are reported per-site basis (i.e., when R' = R, the rate constant was divided by 2).

The 3-parameter Arrhenius fits, $k = k_0 \cdot T^\alpha \cdot \exp\left(-\frac{E_A}{RT}\right)$, for the rate constants presented in this section are provided in Table 6.32. It was found that the high-pressure limit

rate constants for the H-atom addition channel $k_{\overline{\uparrow}}$ provide very good estimates of the global rate constants $k_{\overline{\downarrow}}$, with average deviations below 10% ($\pm 4\%$) in the 300–2000 K range, which decrease to 3% ($\pm 1\%$) below 1700 K. The corresponding 3-parameter Arrhenius fits are found in Table 6.32. For the sake of simplicity, the following H-atom addition reactions are indicated by the reactants only, using the notation $R'C_6H_4R + H$. It is recalled that R' indicates the group being replaced by H, whereas R indicates the side group in ortho, meta or para position with respect to R' . Furthermore, "R' reaction class" will refer to the set of rate constants for R' replacement in both mono and di-substituted $R'C_6H_4R + H$.

TABLE 6.32: Arrhenius fits in the 300–2500 K range of the calculated forward and backward global rate constants for H ipso substitution on C_6H_5OH , $C_6H_5CH_3$, o-,m-,p- $C_6H_4(CH_3)_2$, o-,m-,p- $CH_3C_6H_4OH$, o-,m-,p- $C_6H_4(OH)_2$. $k = k_0 \cdot T^\alpha \cdot \exp(-\frac{E_A}{RT})$, units are cm^3 , mol, s, cal. $R^2 > 0.99$ for all reactions. The rate constants are on a single-site basis (i.e., when $R = R'$, k_0 was divided by 2).

R/R'	Reaction	Forward			Backward		
		k_0	α	E_A	k_0	α	E_A
R=OH	$C_6H_5OH + H \leftrightarrow C_6H_6 + OH$	2.29E+08	1.51	6102	1.04E+03	2.95	7067
R=CH ₃	o- $CH_3C_6H_4OH + H \leftrightarrow C_7H_8 + OH$	2.80E+08	1.48	5015	3.58E+02	2.92	5771
	m- $CH_3C_6H_4OH + H \leftrightarrow C_7H_8 + OH$	3.57E+08	1.44	6001	5.58E+02	2.88	6862
	p- $CH_3C_6H_4OH + H \leftrightarrow C_7H_8 + OH$	2.29E+08	1.51	5750	2.55E+02	2.90	7232
R=OH	o- $OHC_6H_4OH + H \leftrightarrow C_6H_5OH + OH$	6.56E+07	1.68	4785	2.77E+02	2.91	5667
	m- $OHC_6H_4OH + H \leftrightarrow C_6H_5OH + OH$	4.09E+08	1.42	6294	3.62E+02	2.92	7269
	p- $OHC_6H_4OH + H \leftrightarrow C_6H_5OH + OH$	4.70E+08	1.38	5529	5.92E+03	2.58	8575
R=CH ₃	$C_7H_8 + H \leftrightarrow C_6H_6 + CH_3$	8.70E+07	1.62	4388	5.23E+02	2.85	13091
R=CH ₃	o- $CH_3C_6H_4CH_3 + H \leftrightarrow C_7H_8 + CH_3$	9.83E+07	1.61	3579	4.98E+01	2.97	12614
	m- $CH_3C_6H_4CH_3 + H \leftrightarrow C_7H_8 + CH_3$	8.66E+07	1.63	4179	1.74E+02	2.86	12913
	p- $CH_3C_6H_4CH_3 + H \leftrightarrow C_7H_8 + CH_3$	1.19E+08	1.59	4208	1.24E+02	2.81	13070
R=OH	o- $CH_3C_6H_4OH + H \leftrightarrow C_6H_5OH + CH_3$	1.44E+08	1.56	3852	2.43E+02	2.78	12347
	m- $CH_3C_6H_4OH + H \leftrightarrow C_6H_5OH + CH_3$	9.66E+07	1.60	4464	1.99E+02	2.82	13062
	p- $CH_3C_6H_4OH + H \leftrightarrow C_6H_5OH + CH_3$	1.24E+08	1.57	4062	1.82E+02	2.74	13282

6.5.2.4 Competition with H-atom abstractions

The competition between H ipso substitutions and H-atom abstractions by H plays an important role in determining the product distribution of the pyrolysis and combustion of mono-substituted MAHs. Figure 6.36 reveals that, in the case of phenol, H ipso substitution prevails over almost the whole range of temperatures, and the rate of H-atom abstraction becomes comparable to that of addition only around 1500 K. In the 1000–1200 K range, the branching fraction of H ipso substitution is 61–67%, consistent with the experimental estimate of He et al. [436]. On the other hand, the rate constant for H-atom abstraction by H from the methyl group of toluene is higher than H ipso substitution over the full 300–2500 K range. The contribution of H ipso substitution is however still significant, as it is responsible for 21–43% of the total consumption of H. The branching fraction for H ipso substitutions with respect to the total H-atom abstraction by H, including also abstraction on the ring sites, is shown in Figure 6.39. The total rate constants for H-atom abstractions by H from phenol and toluene were taken from previous works [129], [470].

These product branching fractions may also be valid for aromatics with multiple substituents. Figure 6.39 shows the results obtained for o- $C_6H_4(OH)_2$ and o- $C_6H_4(CH_3)_2$. The rate constants for H-atom abstractions by H on the ring sites were estimated by analogy with the mono-substituted counterparts, whereas the rate constants for H-atom abstractions by H from the OH and CH_3 substituents were calculated here as described in Section 6.4. Interestingly, the average branching fractions obtained for the di-substituted MAHs differ

by less than 0.1 from that of the mono-substituted MAHs. In the case of catechol, the significant increase in the rate constant for the H ipso substitution channel is compensated by a similar increase in the rate for H-atom abstraction by H from the hydroxyl substituent due to the energy barriers for both channels being lower by about 2 kcal/mol with respect to the corresponding reactions on phenol. This analysis suggests that the effects of the side groups may be comparable in ipso substitutions and H-atom abstractions and in general across different reaction classes.

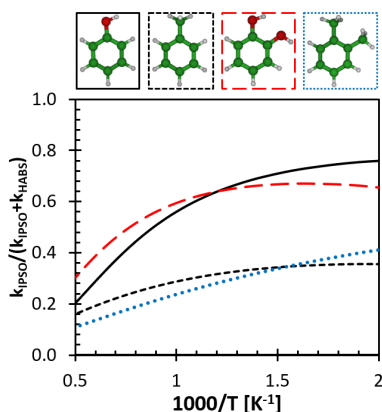


FIGURE 6.39: Branching fraction for H ipso substitution channel with respect to the total rate for H ipso substitution and H-atom abstractions by H from all available sites (ring substituents and aromatic H-atoms). The molecules considered are phenol (black line), toluene (black dashed line), catechol (red dashed line), and o-xylene (blue dotted line).

6.5.3 Determination of rate rules

6.5.3.1 Analysis of systematic trends

In order to devise rate rules for this reaction class, which is one of the aims of this study, it is important to analyze in detail the Arrhenius parameters of Table 6.32. For the sake of simplicity and of easy comparisons, new coefficients for the Arrhenius fits of comparable quality were obtained by fixing $\alpha = 1.71$ (the average of the α coefficients of forward rate constants of the considered set). This value can be also supported by theoretical considerations. According to TST and neglecting for simplicity electronic, symmetry, and tunneling contributions, the rate constant for a bimolecular reaction can be expressed as a function of the reactants and transition state translational, vibrational, and rotational partition functions as in Equation (3.34). The product between the ratio of the translational partition functions of the TS and the reactants $Q_{tr}^{\ddagger}/Q_{tr}^{react}$ and the frequency factor in bimolecular reactions $k_B T/h$ results in $\alpha = -0.5$. The contribution of the rotational partition functions is 0, as the H atom has no rotational partition function, while the contribution of the vibrational partition functions is significant. In all the cases investigated, the two transitional motions of the reaction have small and approximately constant vibrational frequencies of 400–500 cm^{-1} . Therefore, their contribution to the vibrational partition function $\frac{1}{1 - \exp\left(-\frac{h\nu}{k_B T}\right)}$ is reasonably approximated by $\frac{k_B T}{h\nu}$ (ν is small enough that the expression is expanded according to a first-order

Taylor expansion). This results in a temperature dependence of T^2 that, when combined with the $T^{-0.5}$ proportionality derived from the contribution of the frequency factor and the translational partition functions, leads to $\alpha = 1.5$, consistent with the trend found for the examined reactions. This re-fitting results in similar values for the pre-exponential factor in all considered reactions ($4.3\text{--}5.5 \cdot 10^7 \text{ cm}^3/\text{mol/s}$). Furthermore, the relative decrease in the apparent activation energy E_A ($\Delta E_{A,R-H}^{OH}$ and $\Delta E_{A,R-H}^{CH_3}$) of $\text{OHC}_6\text{H}_4\text{R} + \text{H}$ ($E_{A,R}^{OH}$) and $\text{CH}_3\text{C}_6\text{H}_4\text{R} + \text{H}$ ($E_{A,R}^{CH_3}$) with respect to the mono-substituted $\text{OHC}_6\text{H}_5 + \text{H}$ ($E_{A,H}^{OH}$) and $\text{CH}_3\text{C}_6\text{H}_5 + \text{H}$ ($E_{A,H}^{CH_3}$) reactions shows analogies in the impact of the side group R on the apparent activation energies E_A of the two reaction classes, as shown in Figure 6.40.

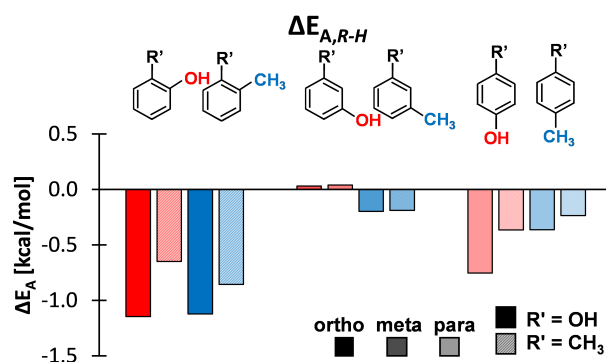


FIGURE 6.40: Effect of the R side group (CH_3 in blue, OH in red) in the ortho, meta, and para positions on the relative increase of the apparent activation energies ΔE_A of the H-atom addition channel $\text{R}'\text{C}_6\text{H}_4\text{R} + \text{H}$ with respect to the mono-substituted molecule ($\text{R} = \text{H}$).

As expected, the presence of the OH and CH_3 side groups at the ortho position has the strongest impact on the activation energies, which decrease by about 1.1 kcal/mol with respect to the mono-substituted $\text{R}'\text{C}_6\text{H}_5 + \text{H}$, while the presence of R groups at the meta position has the smallest impact.

An important feature observed in the bar chart of Figure 6.40 is that the impact of the R groups in the ortho and para positions on E_A for the replacement of R' with H varies linearly from $R' = \text{OH}$ to $R' = \text{CH}_3$, as highlighted in Figure 6.41.

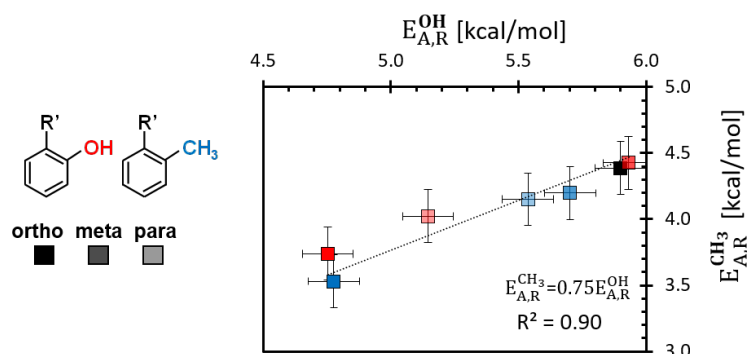


FIGURE 6.41: Apparent activation energies E_A of H-atom addition channel in the CH_3 replacement by H $E_{A,R}^{\text{CH}_3}$ as a function of that in the OH replacement by H $E_{A,R}^{\text{OH}}$. Error bars were set to 0.2 kcal/mol.

All the activation energies lay approximately on the line $E_{A,R}^{CH_3} = 0.75E_{A,R}^{OH}$. Similar accuracy in prediction is obtained by considering the change in the energy barrier relative to the mono-substituted counterpart, namely $\Delta E_{A,R-H}^{CH_3}$ and $\Delta E_{A,R-H}^{OH}$. Interestingly, the slope of the line (0.75) corresponds exactly to the ratio between the activation energies of the H-atom addition reaction on the mono-substituted MAHs $CH_3C_6H_5 + H$ and $OHC_6H_5 + H$. This means that the change in the apparent activation energy in the two reaction classes ($R' = CH_3$ and $R' = OH$) is approximately independent of the side group R. This finding suggests that the impact of a given side group R on the energy barriers for $R'C_6H_4R + H$ may be similar for different substituents R' , namely for different reaction classes, provided that a shifting on the activation energy of the class R' is considered. This would mean that the impact of a given side group R on the energy barriers for $o,m,p-R'C_6H_4R + H$ for a given reaction class R' , for instance $OHC_6H_4R + H$ ($R' = OH$), may also be valid for other R' classes. Systematic trends are also found for pre-exponential factors. In fact, k_0 of $R'C_6H_4R + H$ is, on average, $0.95 \pm 0.07 k_{0,H}$, where $k_{0,H}$ indicates the pre-exponential factor of the reference reaction in each class, namely the rate of the mono-substituted $R'C_6H_5 + H$.

The analysis reported above indicates that rate constant extrapolation is possible, but it requires some additional electronic structure calculations. The most computationally intensive step of the adopted computational protocol is the determination of high level energies. However, a systematic difference between energies computed at the $\omega B97X-D/6-311+G(d,p)$ level of theory (E_{L1}) and those computed at the CCSD(T)/CBS level (E_{HL}) was found. Figure 6.42 shows the difference ΔE_{HL-L1} for the stationary points of the PESs for OH and CH_3 replacement by H. Except in a few cases, such as the energy barrier for the OH addition to the ortho ring site of phenol, the values ΔE_{HL-L1} are consistent for each type of stationary point. Most importantly, the differences in TS1 energies (the controlling step for the reactivity) shows the smallest variability, being -1.8 ± 0.1 for $R' = OH$ and -1.95 ± 0.06 for $R' = CH_3$. These relations are used in the following sections to derive approximate energy barriers for the H-atom addition channels $R'C_6H_4R + H$ within the same reaction class R' from energies computed at the lower level of theory $\omega B97X-D/6-311+G(d,p)$. Validation of this relation performed in four arbitrary cases resulted in discrepancies below 0.15 kcal/mol, as explained in more detail in the next section.

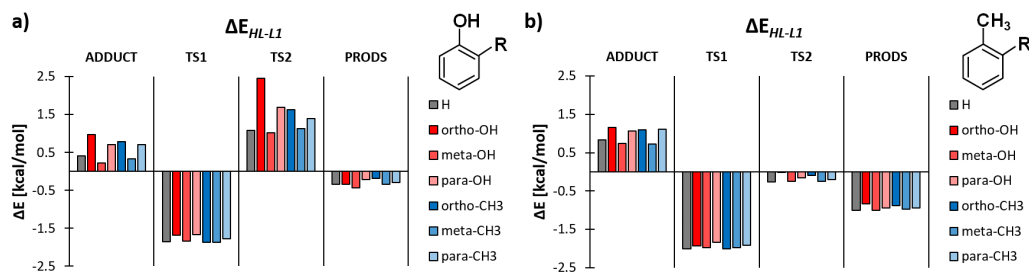


FIGURE 6.42: Energy differences ΔE_{HL-L1} between 0 K energies at the CCSD(T)/CBS (HL) and $\omega B97X-D/6-311+G(d,p)$ (L1) levels of theory for all 14 PESs computed in this work. a) refers to the $R' = OH$ class and b) to the $R' = CH_3$ class.

6.5.3.2 Methodology for rate rule derivation

The rate rules derived in this work allow one to extrapolate from a reference system the necessary activation energies and pre-exponential factor corrections for a large number of reactions from a limited set of electronic structure calculations, therefore they are called "electronic structure-based" rate rules. The general approach to rate-rule derivation was already presented in Section 2.6. The main work inspiring the present findings is that of Carstensen and Dean [165] and of Truong et al. [566], [567] on electronic structure-based rate rules through either group additivity (GA) or Reaction Class-TST/Structure Activity Relationship. However, their methodologies were not applied to any aromatic systems and were mostly successful in rate-rule derivation for H-atom abstraction reactions.

The basic idea behind the rate rule derivation protocol proposed in this work stems from the observation that pre-exponential factors of $R'C_6H_4R + H$ with R' , $R = OH/CH_3$ are all similar and that the activation energies E_A follow two systematic trends. First, the shifting of ΔE_{HL-L1} for TS1 is approximately the same for each R' , independent of the side group R ; second, the impact of a given side group R on E_A is the same independent of R' , as long as a proper constant shifting factor is accounted for.

Hence, in order to determine the rate constants for $R'C_6H_4R + H$, where R' and R can be any of $OH/CH_3/OCH_3/CHO/C_2H_5$, two additional theoretical calculation steps are required. The first one is the calculation of the rate constants for $R'C_6H_5 + H$ for the missing substituents $R' = OCH_3/CHO/C_2H_5$, to be used as a reference for the new reaction classes. Secondly, the calculation of the PES for $R'C_6H_4R + H$ with $R = OCH_3/CHO/C_2H_5$ for an arbitrary reaction class ($R' = OH$ was chosen), so as to derive shifting factors for E_A to be used transversally for all the other R' . This second set of rate constants may be computed at a lower level of theory, and the energies of TS1 may thus be shifted with ΔE_{HL-L1} . This allows us to account for nearest-neighbor interactions, as opposed to approaches such as GA, because corrective factors for side groups R are derived from reactions on di-substituted MAHs. Furthermore, the energy shifting ΔE_{HL-L1} , specific for each reaction class R' , allows us to save considerable computational resources. Finally, an important innovation is the use of corrective factors for the same group R across different reaction classes R' .

Simplifying, the overall rate constant estimation procedure can be summarized as follows:

- Full high-level AI-TST-ME calculations for reference rate constants, i.e., H ipso substitution on mono-substituted aromatics ($R' = CH_3/OH/OCH_3/CHO/C_2H_5$; $R = H$). These rate constants were also used to derive shifting factors ΔE_{HL-L1} for the energy barriers within each R' class.
- Rate constants for $R'C_6H_4OH + H$ and $R' = OH/CH_3/OCH_3/CHO/C_2H_5$ and of $OHC_6H_4R + H$, with $R = OH/CH_3/OCH_3/CHO/C_2H_5$ were computed using AI-TST-ME. In most cases, $\omega B97X-D/6-311+G(d,p)$ energy barriers were scaled according to the ΔE_{HL-L1} rules determined for each class. The first set of $R'C_6H_4OH + H$ rate constants allowed us to confirm that systematic trends for pre-exponential factors and activation energies exist for all the investigated reaction classes. The second set for

$\text{OHC}_6\text{H}_4\text{R} + \text{H}$ was used to derive shifting factors for the activation energies for all R side groups.

- The accuracy of the rate rules estimations was checked by (Section 6.5.3.3):
 1. Comparison with the original dataset of rate constants used for the construction of the rate rules, re-calculated from the mono-substituted reference species.
 2. Comparison with additional ab-initio calculations, i.e., 14 rate constants derived at the $\omega\text{B97X-D}/6\text{-311+G(d,p)}$ level of theory, using the scaling of TS1 energies $\Delta E_{\text{HL-L1}}$ proposed. This set also included reactions where potentially large deviations from the proposed rules are expected.

Section 6.5.2.2 presented the reference rate constants for H ipso substitutions in phenol and toluene. Figure 6.43 presents instead the reference rate constants for H ipso substitution on $\text{OCH}_3\text{C}_6\text{H}_5$, CHOC_6H_5 , and $\text{C}_2\text{H}_5\text{C}_6\text{H}_5$. The corresponding Arrhenius fits of the forward and backward global rate constants $k_{\vec{r}}$ are reported in Table 6.33.

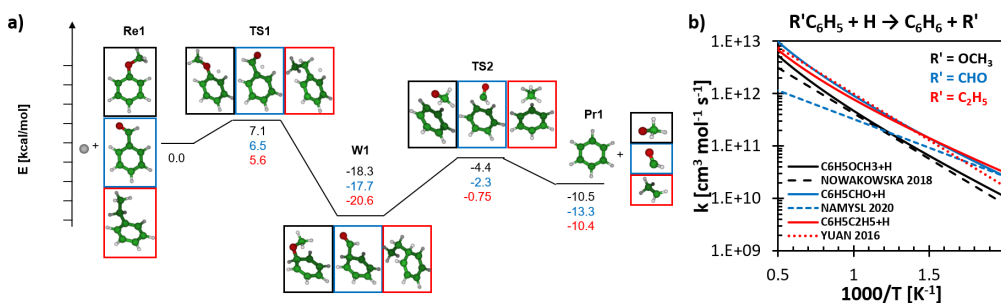


FIGURE 6.43: a) PESs for the $\text{R}'\text{C}_6\text{H}_5 + \text{H} = \text{C}_6\text{H}_6 + \text{R}'$ reactions with $\text{R}' = \text{OCH}_3/\text{CHO}/\text{C}_2\text{H}_5$ and b) corresponding global rate constants $k_{\vec{r}}$ in comparison with the recent literature estimates [45], [449], [558].

TABLE 6.33: Arrhenius fits in the 300–2500 K range of the calculated global rate constants for H ipso substitution on $\text{C}_6\text{H}_5\text{OCH}_3$, $\text{C}_6\text{H}_5\text{CHO}$, and $\text{C}_6\text{H}_5\text{C}_2\text{H}_5$. $k = k_0 \cdot T^\alpha \cdot \exp\left(-\frac{E_A}{RT}\right)$, units are mol, s, cal, K. $R^2 > 0.99$ for all reactions.

R'	Reaction	Forward			Backward		
		k_0	α	E_A	k_0	α	E_A
$\text{R}' = \text{OCH}_3$	$\text{C}_6\text{H}_5\text{OCH}_3 + \text{H} \leftrightarrow \text{C}_6\text{H}_6 + \text{OCH}_3$	$7.45\text{E}+07$	1.70	4674	$2.90\text{E}-01$	3.79	17054
$\text{R}' = \text{CHO}$	$\text{C}_6\text{H}_5\text{CHO} + \text{H} \leftrightarrow \text{C}_6\text{H}_6 + \text{CHO}$	$1.49\text{E}+08$	1.55	5335	$2.03\text{E}+01$	3.33	15786
$\text{R}' = \text{C}_2\text{H}_5$	$\text{C}_6\text{H}_5\text{C}_2\text{H}_5 + \text{H} \leftrightarrow \text{C}_6\text{H}_6 + \text{C}_2\text{H}_5$	$1.01\text{E}+08$	1.60	4166	$7.02\text{E}+00$	3.33	14056

As expected, the energy barrier for H-atom addition to anisole ($\text{OCH}_3\text{C}_6\text{H}_5$, where this notation highlights the replaced R' group, consistent with the $\text{R}'\text{C}_6\text{H}_5$ notation used above) is the highest, being about 1 kcal/mol lower than the barrier for H-atom addition to phenol. The energy barriers for H-atom addition to benzaldehyde (CHOC_6H_5) and ethylbenzene ($\text{C}_2\text{H}_5\text{C}_6\text{H}_5$) are similar to that for H-atom addition to toluene (less than 0.6 kcal/mol discrepancy), resulting in differences in the global rate constants of less than a factor of 1.5 in both cases. Because of the lack of both experimental and theoretical literature data for these rate constants, Figure 6.43 compares the predicted values with the recent literature

estimates in combustion mechanisms. The rate constant for $\text{OCH}_3\text{C}_6\text{H}_5 + \text{H} = \text{C}_6\text{H}_6 + \text{OCH}_3$ agrees to within a factor of 2 with the estimate of the model from Nowakowska et al. [45], who assumed this rate to be the same as phenol. A similar agreement is found between the calculated rate constant for $\text{C}_2\text{H}_5\text{C}_6\text{H}_5 + \text{H} = \text{C}_6\text{H}_6 + \text{C}_2\text{H}_5$ and the estimate from Baulch et al. [563], used by all recent models for ethylbenzene oxidation [558], [559]. A larger discrepancy is instead found between our rate constant for $\text{CHOC}_6\text{H}_5 + \text{H} = \text{C}_6\text{H}_6 + \text{CHO}$ and the only literature estimate of Namysl et al. [449], with discrepancies of up to one order of magnitude evident at high temperatures. This large discrepancy suggests the importance of revising this rate constant in kinetic models, where benzaldehyde plays a key role as both fuel and oxidation intermediate.

Also for this set of reference rate constants, the high pressure limit rate constants for the H-atom addition channel are in excellent agreement with the global H ipso substitution rate constants, with discrepancies below 6% in the 300–2000 K range. The calculations of these rate constants also allowed us to derive approximate corrections $\Delta E_{HL-L1}(\text{TS1})$, consistent with the procedure described above. The calculated $\Delta E_{HL-L1}(\text{TS1})$ values are similar to those found for $\text{R}' = \text{OH}$ and $\text{R}' = \text{CH}_3$: -1.82 , -1.92 and -1.92 kcal/mol for $\text{R}' = \text{OCH}_3$, CHO , and C_2H_5 , respectively.

After computing the reference rate constants for $\text{R}' = \text{OCH}_3/\text{CHO}/\text{C}_2\text{H}_5$, the trends observed for $\text{R}' = \text{OH}/\text{CH}_3$ were also verified for these systems. In particular, the initial set of rate constants for $\text{R}, \text{R}' = \text{OH}/\text{CH}_3$ suggests that the energy barriers for the generic rate of $\text{R}'\text{C}_6\text{H}_4\text{R} + \text{H}$ may be derived from a reference reaction class (in this case, $\text{R}' = \text{OH}$) assuming that the energy change $\Delta E_{A,R-H}^{\text{R}'}$ scales with the ratio between the activation energies of the rate constants for the mono-substituted MAHs: $\Delta E_{A,R-H}^{\text{R}'} = \Delta E_{A,R-H}^{\text{OH}} \cdot E_{A,H}^{\text{R}'}/E_{A,H}^{\text{OH}}$. To verify this aspect, the rate constants for $\text{o-R}'\text{C}_6\text{H}_4\text{OH} + \text{H}$ and $\text{o-R}'\text{C}_6\text{H}_4\text{CH}_3 + \text{H}$, with $\text{R}' = \text{OCH}_3/\text{CHO}/\text{C}_2\text{H}_5$, were derived. The ortho position of the substituents was chosen because nearest-neighbor interactions have the largest impact. The ES calculations were performed at L1 and the energy barriers were rescaled according to the ΔE_{HL-L1} values determined for each class R' . For a more consistent comparison of the activation energies E_A , the temperature dependence T^α in the fit was fixed to 1.71, as done for $\text{R}, \text{R}' = \text{OH}/\text{CH}_3$. The pre-exponential factors for H-atom addition rate constants on the di-substituted MAHs $\text{R}'\text{C}_6\text{H}_4\text{R}$ were $(0.93 \pm 0.11)k_{0,H}^{\text{R}'}$, where $k_{0,H}^{\text{R}'}$ is the pre-exponential factor of the reference rate constant in each class (fixed R' , $\text{R} = \text{H}$). Hence, the pre-exponential factors were also fixed to 0.93. The resulting $\Delta E_{A,R-H}^{\text{R}'}$ were compared with those obtained from the relation $\Delta E_{A,R-H}^{\text{R}'} = \Delta E_{A,R-H}^{\text{OH}} \cdot E_{A,H}^{\text{R}'}/E_{A,H}^{\text{OH}}$ (tables reported in the supplementary material of the corresponding publication [564]). This scaling relation provides excellent predictions for the activation energies, resulting in discrepancies of less than 0.1 kcal/mol, with the exception of $\text{o-CHOC}_6\text{H}_4\text{OH}$. In fact, the strong H-bond formed between OH and CHO substituents, revealed also by the extremely high rotation barriers for the OH and CHO groups (up to 10–15 kcal/mol), is unique to this structure. The final change $\Delta E_{A,OH-H}^{\text{CHO}}$ is almost negligible, as found also for CHO replacement in $\text{m-CHOC}_6\text{H}_4\text{OH}$ and $\text{p-CHOC}_6\text{H}_4\text{OH}$. Overall, the results confirm that the proposed scaling rule for $\Delta E_{A,R-H}^{\text{R}'}$ reasonably predicts activation energies for $\text{R}'\text{C}_6\text{H}_4\text{R} + \text{H}$.

TABLE 6.34: Corrections $\Delta E_{A,R-H}^{R'}$ to the energy barriers (kcal/mol) for the H-atom addition reaction to $R'C_6H_4R$ with respect to the reference $R'C_6H_5$ obtained with the rate rules derived in this work. The shaded values were used as a reference for the rate rules and therefore correspond to the original values $\Delta E_{A,R-H}^{R'}$ of the 3-parameter Arrhenius fits $0.93k_{0,R=H}T^{1.71}\exp(-\frac{E_A}{RT})$ reported in Table 6.36. The values in brackets correspond to the actual values obtained from *ab initio* calculations.

R = CH ₃				
R' = OH	R' = CH ₃	R' = OCH ₃	R' = CHO	R' = C ₂ H ₅
-1.2	-0.9 (-0.9)	-1.0 (-0.9)	-0.9 (-0.9)	-0.8 (-0.8)
-0.2	-0.2 (-0.3)	-0.2	-0.2	-0.2
-0.5	-0.3 (-0.3)	-0.4	-0.4	-0.3
R = OH				
R' = OH	R' = CH ₃	R' = OCH ₃	R' = CHO	R' = C ₂ H ₅
-1.2	-0.9 (-0.7)	-1.1 (-1.2)	0	-0.9 (-0.8)
0.1	0.1 (0.0)	0.1 (0.3)	0.0 (-0.2)	0.1 (0.1)
-0.6	-0.4 (-0.3)	-0.5 (-0.6)	0.0 (-0.1)	-0.4 (-0.4)
R = OCH ₃				
R' = OH	R' = CH ₃	R' = OCH ₃	R' = CHO	R' = C ₂ H ₅
-1.1	-0.8 (-1.0)	-1.0 (-1.2)	-0.9	-0.8
0	0	0	0	0
-0.9	-0.7	-0.8	-0.7	-0.7
R = HCO				
R' = OH	R' = CH ₃	R' = OCH ₃	R' = CHO	R' = C ₂ H ₅
-0.2	-0.7	-0.9	-0.8 (-0.7)	-0.7
0.3	0.3	0.3	0.3	0.3
0	0	0	0	0
R = C ₂ H ₅				
R' = OH	R' = CH ₃	R' = OCH ₃	R' = CHO	R' = C ₂ H ₅
-0.8	-0.6 (-0.5)	-0.7 (-0.7)	-0.6	-0.6 (-0.8)
-0.2	-0.2	-0.2	-0.2	-0.2 (-0.2)
-0.4	-0.3	-0.4	-0.3	-0.3 (-0.2)

The scaling factors for the activation energies of the side groups R = OCH₃/ CHO/ C₂H₅ in ortho, meta and para positions were derived from newly calculated rate constants for OHC₆H₄R + H. The values obtained confirm the trends observed in terms of pre-exponential factors and coefficients. In fact, the same average values of $k_{0,H}^{R'} = (0.93 \pm 0.11)$ and $\alpha = 1.71$ are obtained from the set of 33 rate constants considered. The corresponding values of $\Delta E_{A,R-H}^{OH}$ are reported in Table 6.34, together with all the scaling values obtained for the energy barriers for the reaction classes investigated. The OCH₃ methoxy group lowers the energy barriers considerably: the impact of R = OCH₃ in the ortho position is comparable to that of CH₃ and OH groups, whereas in the meta position the change in the energy barrier is negligible (below 0.1 kcal/mol). Interestingly, the effect of OCH₃ in an R of the para position is almost comparable to that in the ortho position ($\Delta E_{A,OCH_3-H}^{OH} = -0.9$ kcal/mol). These kinds of non-nearest neighbor interactions are generally neglected in GA approaches. The effect of R = C₂H₅ on the energy barriers $\Delta E_{A,C_2H_5-H}^{OH}$ is comparable to that of R = CH₃, with a smaller decrease in the ortho position. Finally, the impact of R = CHO on the energy barriers is extremely small. However, due to the peculiar interactions between OH and CHO substituents in the ortho position highlighted above, the energy barrier for o-CH₃C₆H₄CHO+H was also calculated, obtaining $\Delta E_{A,CHO-H}^{CH_3} = -0.7$ kcal/mol. Since no such interactions as those in o-OHC₆H₄CHO+H are expected for other R' substituents, $\Delta E_{A,CHO-H}^{CH_3}$ was used as a reference for the scalings of $\Delta E_{A,CHO-H}^{R'}$.

As far as pre-exponential factors are concerned, $k_{0,R}^{R'}$ for di-substituted MAHs (R ≠ H) are slightly lower than those for their mono-substituted counterparts (R = H): $k_{0,R}^{R'} =$

$(0.93 \pm 0.11)k_{0,H}^{R'}$. Consistent variations in the pre-exponential factors may be determined by tunneling corrections, variational effects, hindered rotations, or vibrational partition functions. In this case, the imaginary frequencies for the reaction coordinate of the adding H are very similar, with maximum differences in tunneling effects of about 30% at 300 K within each class, decreasing below 10% already at 500 K. This variability is comparable to the errors of literature correlations between tunnelling factors and activation energies [179], [190], hence here no specific correction for tunneling effects was derived. Concerning variational effects, the treatment with internal coordinates results in a decrease in the rate constant by within a factor of 1.2 for all rate constants, with small variations within each class R' . Regarding hindered rotations, no significant change in the rotational barriers of the reactants and the transition state is expected. In fact, hydrogen is not bulky and therefore should not result in too high hindrance of the substituents, as also noted in previous works [179], [189], [190], [566]. This trend was generally confirmed, though higher rotational barriers and higher corresponding vibrational frequencies for internal rotations were found when R and R' substituents are in the ortho position, due to the stronger interactions between substituents. This variation generally explains the decrease of the pre-exponential factor when a side group R is present. Furthermore, as expected, the bulkier the side group R, the lower the pre-exponential factor, due to the steric demand of the substituent and the consequent entropy decrease in the TS, as also noted in previous works on carbon-centered radical additions on unsaturated hydrocarbons [190], [568]. An important exception to this trend is $o\text{-OCH}_3\text{C}_6\text{H}_4\text{OH} + \text{H}$: in fact, in this case the pre-exponential factor is about $0.6k_{0,H}^{\text{OCH}_3}$. This is due to the significant change in the vibrational frequency for the internal rotation of the methoxy group, which increases significantly from 74 cm^{-1} to about 100 cm^{-1} in the TS. This peculiarity results in a lower accuracy of the predicted rate constant (see Table 6.36), with deviations as high as a factor of 1.4 at 2000 K.

The evidences led to the formulation of the following rate rule to derive the rate constants for H ipso substitutions on $R'\text{C}_6\text{H}_4\text{R}$ with $R', R = \text{OH}/\text{CH}_3/\text{OCH}_3/\text{CHO}/\text{C}_2\text{H}_5$:

$$k_R^{R'} = 0.93k_{0,H}^{R'} T^{1.71} \exp\left(-\frac{E_{A,H}^{R'} + \Delta E_{A,R-H}^{R'}}{RT}\right) \quad (6.1)$$

where $k_{0,H}^{R'}$ is the pre-exponential factor of the rate of the mono-substituted MAH in each class, and $\Delta E_{A,R-H}^{R'}$ is the impact of the R side group on the activation energy. The values of this correction (listed in Table 6.34) are derived from the known energy scaling for the side group R of a reference reaction class (in this case, REF=OH, except for the case of $o\text{-R}'\text{C}_6\text{H}_4\text{CHO}$ where REF=CH₃):

$$\Delta E_{A,R-H}^{R'} = c_{R'} \cdot \Delta E_{A,R-H}^{\text{REF}} \quad (6.2)$$

$\Delta E_{A,R-H}^{\text{REF}}$ is independent of the reaction class, whereas the coefficient $c_{R'}$ accounts for the different impact of the R' substituents. In particular, for R side groups in the meta position $c_{R'} = 1$, because the corresponding $\Delta E_{A,R-H}^{R'}$ corrections are small (about 0–0.3 kcal/mol), hence their values are comparable to the uncertainties in energy barriers. On the

other hand, for R substituents in ortho and para positions $\Delta E_{A,R-H}^{REF}$ was scaled according to the ratio between the energy barrier for H-atom addition to the mono-substituted $R'C_6H_5$ and that of the chosen reference reaction class:

$$c_{R'} = \frac{E_{A,H}^{R'}}{E_{A,H}^{REF}} \quad (6.3)$$

The proposed rate rule is therefore the following:

- The pre-exponential factors $k_{0,R}^{R'}$ of the rate constants for H-atom addition to di-substituted MAHs scale with a constant factor of 0.93 with respect to the mono-substituted reference $k_{0,H}^{R'}$.
- The temperature dependence of the pre-exponential factors T^α is $T^{1.71}$ for all H-atom additions to substituted MAHs. This result is theoretically supported by the evidence that the vibrational frequencies for the transitional degrees of freedom of the H atom undergoing addition are all small and equal to about 400–500 cm^{-1} .
- For each reaction class R' , the change in the activation energy with respect to the mono-substituted counterpart $\Delta E_{A,R-H}^{R'}$ is proportional to $\Delta E_{A,R-H}^{REF}$. The proportionality coefficient $c_{R'}$ increases with the activation energy for H-atom addition to the mono-substituted MAH of each class $E_{A,H}^{R'}$ (Equation (6.2), (6.3)).

The proposed rate rule has several advantages. First, it is extremely simple, because it does not require additional electronic structure calculations for each pre-exponential factor, in contrast with approaches like RC-TST/SAR. At the same time, the scaling factors proposed for the pre-exponential factors and the temperature dependence are physically meaningful, as they relate to the steric hindrance of di-substituted MAHs (lower pre-exponential factor) and to systematic corrections for the partition functions. The relation proposed to estimate the activation energies $\Delta E_{A,R-H}^{R'}$ is applicable to all the considered reaction classes R' , thanks to a simple scaling factor $c_{R'}$. In addition, deriving the corrections $\Delta E_{A,R-H}^{REF}$ allows us to partially account for the interactions between R and R' substituents, in contrast with truncated GA approaches.

6.5.3.3 Rate rules validation and error analysis

The 80 rate constants for $R'C_6H_4R + H$ ipso substitution reactions estimated according to the rate rules developed in this work are reported in Table 6.36, together with the 3-parameter Arrhenius fits of the calculated rate constants. All the calculations are summarized in Table 6.35. To verify the accuracy of the proposed rate rules, 14 additional rate constants were calculated. In particular, the rate constants necessary to complete the $R'C_6H_4OH + H$ set were determined, so as to provide a complete overview of the impact of a specific side group throughout different reaction classes. Then, 6 rate constants for $o-R'C_6H_4R + H$ with R'/R substitutions in the ortho position were calculated, namely where large deviations with respect to the mono-substituted counterpart are expected.

TABLE 6.35: Schematic representation of the rate constant calculations for the reactions o-,m-,p-R'C₆H₄R + H → C₆H₅R + R' performed in this work, where R' refers to the different reaction classes (columns), whereas R is the side group (rows). HL indicates CCSD(T)/CBS PESs, L1 indicates ωB97X-D/6-311+G(d,p) with shifting of the TS1 barrier to HL (see main text). Dark and light shaded areas highlight rate constants used for rate rule derivation and validation, respectively. * refers to the validation of the rules for HL–L1 energy shifting.

R'		OH	CH ₃	OCH ₃	CHO	C ₂ H ₅
H		HL	HL	HL	HL	HL
OH	o	HL	HL	L1	L1	L1
	m	HL	HL	L1	L1	L1
	p	HL	HL	L1	L1	L1
CH ₃	o	HL	HL	L1	L1	L1
	m	HL	HL			
	p	HL	HL			
OCH ₃	o	L1*	L1	L1		
	m	L1				
	p	L1				
CHO	o	L1	L1		L1*	
	m	L1*				
	p	L1				
C ₂ H ₅	o	L1	L1	L1		L1
	m	L1				L1
	p	L1				L1

TABLE 6.36: Arrhenius expressions for the rate constants k_{rule} of H addition to o-,m-,p-R'C₆H₄R, (R, R' = OH/CH₃/OCH₃/CHO/C₂H₅) in the 300–2000 K range obtained with the rate rules derived in this work. $k = k_0 \cdot T^\alpha \cdot \exp(-\frac{E_A}{RT})$, units are cm³, mol, s, cal. Where available, the original fit ($R^2 > 0.998$ for all reactions) and the corresponding deviations k_{rule}/k_{calc} at 500, 1000, and 2000 K are also shown. The rate constants are reported on a per site basis (i.e., when R' = R, the rate was divided by 2).

R'C ₆ H ₄ R+H→C ₆ H ₅ +R'	Reaction	$k_{rule}, k_{calc} \cdot 1E+07$			k_{rule}/k_{calc}		
		k_0	α	E_A	500	1000	2000
R' = OH (ref)	C ₆ H ₅ OH+H→C ₆ H ₆ +OH	5.37	1.71	5900	1.02	1.03	1.04
R = CH ₃	o-OHC ₆ H ₄ CH ₃ +H→C ₆ H ₅ CH ₃ +OH	5.96	1.69	5910			
		5.01	1.71	4716	1.02	1.00	1.00
	m-OHC ₆ H ₄ CH ₃ +H→C ₆ H ₅ CH ₃ +OH	7.17	1.67	4826			
		5.01	1.71	5732	1.00	1.02	1.07
	p-OHC ₆ H ₄ CH ₃ +H→C ₆ H ₅ CH ₃ +OH	10.3	1.61	5826			
		5.01	1.71	5442	1.03	0.99	0.98
R = OH	o-OHC ₆ H ₄ OH+H→C ₆ H ₅ OH+OH	6.94	1.67	5574			
		5.01	1.71	4684	1.03	1.00	1.00
	m-OHC ₆ H ₄ OH+H→C ₆ H ₅ OH+OH	6.56	1.68	4785			
		5.01	1.71	5981	1.00	1.03	1.09
	p-OHC ₆ H ₄ OH+H→C ₆ H ₅ OH+OH	10.8	1.6	6067			
		5.01	1.71	5325	0.98	1.08	1.16
R = OCH ₃	o-OHC ₆ H ₄ OCH ₃ +H→C ₆ H ₅ OCH ₃ +OH	6.07	1.66	5198			
		5.01	1.71	4795	1.02	1.03	1.04
	m-OHC ₆ H ₄ OCH ₃ +H→C ₆ H ₅ OCH ₃ +OH	4.56	1.72	4753			
		5.01	1.71	5924	1.01	1.03	1.05
	p-OHC ₆ H ₄ OCH ₃ +H→C ₆ H ₅ OCH ₃ +OH	5.14	1.7	5900			
		5.01	1.71	4984	0.99	1.04	1.12
R = CHO	o-OHC ₆ H ₄ CHO+H→C ₆ H ₅ CHO+OH	11.5	1.59	5039			
		5.01	1.71	5679	1.02	1.06	1.05
	m-OHC ₆ H ₄ CHO+H→C ₆ H ₅ CHO+OH	2.76	1.78	5515			
		5.01	1.71	6231	1.04	0.98	0.97
	p-OHC ₆ H ₄ CHO+H→C ₆ H ₅ CHO+OH	8.60	1.65	6431			
		5.01	1.71	5900	1.01	1.03	1.06
R = C ₂ H ₅	o-OHC ₆ H ₄ C ₂ H ₅ +H→C ₆ H ₅ C ₂ H ₅ +OH	8.13	1.64	5962			
		5.01	1.71	5126	0.99	1.07	1.14
	m-OHC ₆ H ₄ C ₂ H ₅ +H→C ₆ H ₅ C ₂ H ₅ +OH	7.50	1.64	5069			
		5.01	1.71	5737	1.04	0.99	0.97
	p-OHC ₆ H ₄ C ₂ H ₅ +H→C ₆ H ₅ C ₂ H ₅ +OH	5.54	1.7	5836			
		5.01	1.71	5469	1.04	0.98	0.97
R' = CH ₃ (ref)	C ₆ H ₅ CH ₃ +H→C ₆ H ₆ +CH ₃	5.28	1.71	4387	1.03	1.04	1.01
R = CH ₃	o-CH ₃ C ₆ H ₄ CH ₃ +H→C ₆ H ₅ CH ₃ +CH ₃	2.40	1.81	4234			
		4.93	1.71	3507	1.03	1.03	1.00
	m-CH ₃ C ₆ H ₄ CH ₃ +H→C ₆ H ₅ CH ₃ +CH ₃	2.48	1.8	3395			
		4.93	1.71	4220	0.9	0.92	0.89
	p-CH ₃ C ₆ H ₄ CH ₃ +H→C ₆ H ₅ CH ₃ +CH ₃	1.79	1.85	3985			

R/C ₆ H ₄ R+H→C ₆ H ₅ +R'	Reaction	k _{rule} , k _{calc} 1E+07			k _{rule} /k _{calc}			
		k ₀	α	E _A	500	1000	2000	
R = OH	p-CH ₃ C ₆ H ₄ CH ₃ +H→C ₆ H ₅ CH ₃ +CH ₃	4.93	1.71	4046	1.05	1.01	0.96	
	o-CH ₃ C ₆ H ₄ OH+H→C ₆ H ₅ OH+CH ₃	4.93	1.71	3483	1.28	1.14	1.06	
	m-CH ₃ C ₆ H ₄ OH+H→C ₆ H ₅ OH+CH ₃	4.93	1.71	4468	0.99	1.03	1.01	
	p-CH ₃ C ₆ H ₄ OH+H→C ₆ H ₅ OH+CH ₃	4.93	1.71	3959	1.13	1.10	1.08	
	R = OCH ₃	o-CH ₃ C ₆ H ₄ OCH ₃ +H→C ₆ H ₅ OCH ₃ +CH ₃	4.93	1.71	3565	0.9	0.94	0.93
		m-CH ₃ C ₆ H ₄ OCH ₃ +H→C ₆ H ₅ OCH ₃ +CH ₃	4.93	1.71	4411			
		p-CH ₃ C ₆ H ₄ OCH ₃ +H→C ₆ H ₅ OCH ₃ +CH ₃	4.93	1.71	3706			
	R = CHO	o-CH ₃ C ₆ H ₄ CHO+H→C ₆ H ₅ CHO+CH ₃	4.93	1.71	3565	1.04	0.99	0.97
		m-CH ₃ C ₆ H ₄ CHO+H→C ₆ H ₅ CHO+CH ₃	4.93	1.71	4718			
		p-CH ₃ C ₆ H ₄ CHO+H→C ₆ H ₅ CHO+CH ₃	4.93	1.71	4387			
	R = C ₂ H ₅	o-CH ₃ C ₆ H ₄ C ₂ H ₅ +H→C ₆ H ₅ C ₂ H ₅ +CH ₃	4.93	1.71	3812	1.12	1.2	1.2
		m-CH ₃ C ₆ H ₄ C ₂ H ₅ +H→C ₆ H ₅ C ₂ H ₅ +CH ₃	4.93	1.71	4224			
p-CH ₃ C ₆ H ₄ C ₂ H ₅ +H→C ₆ H ₅ C ₂ H ₅ +CH ₃		4.93	1.71	4067				
C ₆ H ₅ OCH ₃ +H→C ₆ H ₆ +OCH ₃		4.86	1.71	5173	1.02	1.03	1.04	
R' = OCH ₃ (ref)	o-OCH ₃ C ₆ H ₄ CH ₃ +H→C ₆ H ₅ CH ₃ +OCH ₃	4.53	1.71	4135	1.15	1.06	1.01	
	m-OCH ₃ C ₆ H ₄ CH ₃ +H→C ₆ H ₅ CH ₃ +OCH ₃	4.53	1.71	5006				
	p-OCH ₃ C ₆ H ₄ CH ₃ +H→C ₆ H ₅ CH ₃ +OCH ₃	4.53	1.71	4771				
	o-OCH ₃ C ₆ H ₄ OH+H→C ₆ H ₅ OH+OCH ₃	4.53	1.71	4107	0.77	1.07	1.4	
	m-OCH ₃ C ₆ H ₄ OH+H→C ₆ H ₅ OH+OCH ₃	4.53	1.71	5254	1.25	1.2	1.16	
	p-OCH ₃ C ₆ H ₄ OH+H→C ₆ H ₅ OH+OCH ₃	4.53	1.71	4669	0.87	1.00	1.06	
	o-OCH ₃ C ₆ H ₄ OCH ₃ +H→C ₆ H ₅ OCH ₃ +OCH ₃	4.53	1.71	4204	0.8	0.92	0.98	
	m-OCH ₃ C ₆ H ₄ OCH ₃ +H→C ₆ H ₅ OCH ₃ +OCH ₃	4.53	1.71	5197				
	p-OCH ₃ C ₆ H ₄ OCH ₃ +H→C ₆ H ₅ OCH ₃ +OCH ₃	4.53	1.71	4369				
	o-OCH ₃ C ₆ H ₄ CHO+H→C ₆ H ₅ CHO+OCH ₃	4.53	1.71	4304				
	m-OCH ₃ C ₆ H ₄ CHO+H→C ₆ H ₅ CHO+OCH ₃	4.53	1.71	5504				
	p-OCH ₃ C ₆ H ₄ CHO+H→C ₆ H ₅ CHO+OCH ₃	4.53	1.71	5173				
o-OCH ₃ C ₆ H ₄ C ₂ H ₅ +H→C ₆ H ₅ C ₂ H ₅ +OCH ₃	4.53	1.71	4494	0.96	1.14	1.3		
m-OCH ₃ C ₆ H ₄ C ₂ H ₅ +H→C ₆ H ₅ C ₂ H ₅ +OCH ₃	4.53	1.71	5010					
p-OCH ₃ C ₆ H ₄ C ₂ H ₅ +H→C ₆ H ₅ C ₂ H ₅ +OCH ₃	4.53	1.71	4795					
R' = CHO (ref)	C ₆ H ₅ CHO+H→C ₆ H ₆ +CHO	7.50	1.71	4699	1.03	1.04	1.02	
	o-CHOC ₆ H ₄ CH ₃ +H→C ₆ H ₅ CH ₃ +CHO	6.99	1.71	3756	1.01	1.04	1.08	
	m-CHOC ₆ H ₄ CH ₃ +H→C ₆ H ₅ CH ₃ +CHO	6.99	1.71	4531				
	p-CHOC ₆ H ₄ CH ₃ +H→C ₆ H ₅ CH ₃ +CHO	6.99	1.71	4334				
	o-CHOC ₆ H ₄ OH+H→C ₆ H ₅ OH+CHO	6.99	1.71	4683	1.06	0.96	0.91	
	m-CHOC ₆ H ₄ OH+H→C ₆ H ₅ OH+CHO	6.99	1.71	4699	0.84	0.91	0.93	
	p-CHOC ₆ H ₄ OH+H→C ₆ H ₅ OH+CHO	6.99	1.71	4699	0.95	0.97	0.98	
	o-CHOC ₆ H ₄ OCH ₃ +H→C ₆ H ₅ OCH ₃ +CHO	6.99	1.71	3819				
	m-CHOC ₆ H ₄ OCH ₃ +H→C ₆ H ₅ OCH ₃ +CHO	6.99	1.71	4722				
	p-CHOC ₆ H ₄ OCH ₃ +H→C ₆ H ₅ OCH ₃ +CHO	6.99	1.71	3969				
	o-CHOC ₆ H ₄ CHO+H→C ₆ H ₅ CHO+CHO	6.99	1.71	3910	1.11	1.18	1.13	
	m-CHOC ₆ H ₄ CHO+H→C ₆ H ₅ CHO+CHO	6.99	1.71	5030				
p-CHOC ₆ H ₄ CHO+H→C ₆ H ₅ CHO+CHO	6.99	1.71	4699					
o-CHOC ₆ H ₄ C ₂ H ₅ +H→C ₆ H ₅ C ₂ H ₅ +CHO	6.99	1.71	4082					
m-CHOC ₆ H ₄ C ₂ H ₅ +H→C ₆ H ₅ C ₂ H ₅ +CHO	6.99	1.71	4536					
p-CHOC ₆ H ₄ C ₂ H ₅ +H→C ₆ H ₅ C ₂ H ₅ +CHO	6.99	1.71	4355					
R' = C ₂ H ₅ (ref)	C ₆ H ₅ C ₂ H ₅ +H→C ₆ H ₆ +C ₂ H ₅	4.96	1.71	4193	1.04	1.05	1.00	
	o-C ₂ H ₅ C ₆ H ₄ CH ₃ +H→C ₆ H ₅ CH ₃ +C ₂ H ₅	4.62	1.71	3352	1.02	1.12	1.10	
	m-C ₂ H ₅ C ₆ H ₄ CH ₃ +H→C ₆ H ₅ CH ₃ +C ₂ H ₅	4.62	1.71	4026				
	p-C ₂ H ₅ C ₆ H ₄ CH ₃ +H→C ₆ H ₅ CH ₃ +C ₂ H ₅	4.62	1.71	3868				
	o-C ₂ H ₅ C ₆ H ₄ OH+H→C ₆ H ₅ OH+C ₂ H ₅	4.62	1.71	3329	1.06	1.07	1.04	
	m-C ₂ H ₅ C ₆ H ₄ OH+H→C ₆ H ₅ OH+C ₂ H ₅	4.62	1.71	4274	1.04	1.05	1.00	
	p-C ₂ H ₅ C ₆ H ₄ OH+H→C ₆ H ₅ OH+C ₂ H ₅	4.62	1.71	3784	1.03	1.06	1.03	
	o-C ₂ H ₅ C ₆ H ₄ OCH ₃ +H→C ₆ H ₅ OCH ₃ +C ₂ H ₅	4.62	1.71	3408				
	m-C ₂ H ₅ C ₆ H ₄ OCH ₃ +H→C ₆ H ₅ OCH ₃ +C ₂ H ₅	4.62	1.71	4217				

R'C ₆ H ₄ R+H→C ₆ H ₅ +R'	Reaction	k _{rule} , k _{calc} 1E+07			k _{rule} /k _{calc}		
		k ₀	α	E _A	500	1000	2000
R = CHO	p-C ₂ H ₅ C ₆ H ₄ OCH ₃ +H→C ₆ H ₅ OCH ₃ +C ₂ H ₅	4.62	1.71	3542			
	o-C ₂ H ₅ C ₆ H ₄ CHO+H→C ₆ H ₅ CHO+C ₂ H ₅	4.62	1.71	3489			
	m-C ₂ H ₅ C ₆ H ₄ CHO+H→C ₆ H ₅ CHO+C ₂ H ₅	4.62	1.71	4525			
R = C ₂ H ₅	p-C ₂ H ₅ C ₆ H ₄ CHO+H→C ₆ H ₅ CHO+C ₂ H ₅	4.62	1.71	4193			
	o-C ₂ H ₅ C ₆ H ₄ C ₂ H ₅ +H→C ₆ H ₅ C ₂ H ₅ +C ₂ H ₅	4.62	1.71	3643	0.74	1.01	1.07
		0.45	1.98	2677			
	m-C ₂ H ₅ C ₆ H ₄ C ₂ H ₅ +H→C ₆ H ₅ C ₂ H ₅ +C ₂ H ₅	4.62	1.71	4030	1.01	1.01	0.97
		1.73	1.84	3843			
	p-C ₂ H ₅ C ₆ H ₄ C ₂ H ₅ +H→C ₆ H ₅ C ₂ H ₅ +C ₂ H ₅	4.62	1.71	3887	1.16	1.09	1.01
	1.79	1.83	3847				

The comparison between the rate rule estimates and the values calculated using the full computational protocol (k_{rule}/k_{calc}) are provided in Table 6.36 at 500 K, 1000 K, and 2000 K. The rate rules proposed provide excellent predictions for the rate constants of H ipso substitutions on di-substituted MAHs R'C₆H₄R, generally resulting in errors below 20% over the whole temperature range considered. Higher discrepancies are found mostly in the predictions for o-R'C₆H₄R + H with bulkier R'/R substituents, as expected. In fact, the derivation of the set of rate constants from the reference OHC₆H₄R + H allows us to account for interactions between R' and R substituents only partially. In particular, the largest deviations are found for OCH₃ replacement in o-OCH₃C₆H₄OH + H (maximum factor of 1.4) and in o-OCH₃C₆H₄C₂H₅+H (maximum factor of 1.3), and o-C₂H₅C₆H₄C₂H₅ + H (maximum factor of 1.35). The first case was discussed in the previous section. In the other two cases, the deviations are due to the underestimation of the energy change $c_{R'} \cdot \Delta E_{A,R-H}^{OH}$ by about 0.2 kcal/mol (see Table 6.34), indicating an underestimation of the interactions between the substituents.

An overview of the comparison between the rate constants estimated with rate rules and the calculations presented in this work is shown in the parity plots of Figure 6.44.

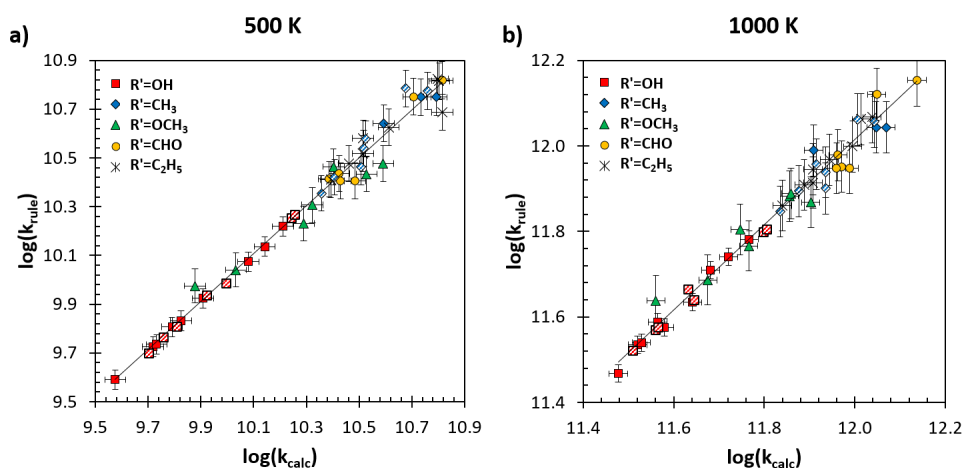


FIGURE 6.44: Parity plots of the rate constants of H-atom addition to R'C₆H₄R predicted by the rate rules derived in this work versus the calculated rate constants. Points with partial filling indicate the original set of 14 rate constants (R, R' = OH/CH₃) derived at a higher level of theory. Error bars are estimated as described in the text.

The error bars are derived according to the level of theory used for the calculation of the rate constants. The calculated rate constants for H-atom addition to R'C₆H₄R with R', R = OH/CH₃, have no error bars, because the energy barriers were computed at the highest level

of theory used in this work. For all the other k_{calc} , an uncertainty of 0.1 kcal/mol is estimated for the energy barriers, in accordance with the standard deviations of ΔE_{HL-L1} found for R' , $R = OH/CH_3$. For additional validation of the rule used for the scaling of the energy, the energy barriers for $o\text{-OHC}_6\text{H}_4\text{OCH}_3 + \text{H}$, $m\text{-OHC}_6\text{H}_4\text{CHO} + \text{H}$, $o\text{-CHOC}_6\text{H}_4\text{CH}_3 + \text{H}$ and $\text{C}_2\text{H}_5\text{C}_6\text{H}_4\text{OH} + \text{H}$, were refined at the CCSD(T)/CBS level, obtaining deviations of 0.15, 0.1 and 0.0 kcal/mol, respectively.

The errors in k_{rule} were set as those of k_{calc} for $\text{OHC}_6\text{H}_4\text{R} + \text{H}$, because $R' = OH$ was used as the reference set of rate constants and deviations may only be due to the fitting errors. In the other cases, error propagation from the scaling of activation energies ($c_{R'} \cdot \Delta E_{A,R-H}^{REF}$) and pre-exponential factors ($0.93k_{0,H}^{R'}$) were considered. The correction $y_1 = c_{CH_3} \cdot \Delta E_{A,R-H}^{OH}$ resulted in deviations of $\delta y_1 = 0.14$ kcal/mol with respect to the calculated values, whereas the average deviations for the pre-exponential factors $y_2 = k_{0,R}^{R'}/k_{0,H}^{R'}$ were $\delta y_2 = 0.93 \pm 0.11$. Hence, the overall uncertainty was computed as $\sqrt{\left(\frac{\partial k_R^{R'}}{\partial y_1} \delta y_1\right)^2 + \left(\frac{\partial k_R^{R'}}{\partial y_2} \delta y_2\right)^2}$ according to the theory of error propagation for random and independent uncertainties. Hence, relative uncertainties in k_{rule} are 18% and 14% at 500 K and 1000 K, respectively. The rate constants represented in the parity plots (Figure 6.44) are all in good agreement with the theoretical calculations. The points falling out of the uncertainty ranges are those mentioned above. Another exception is given by the rate for $o\text{-CH}_3\text{C}_6\text{H}_4\text{OH} + \text{H}$, which shows discrepancies of almost 30% with respect to the calculated value. This stems from the different interaction between the two hydroxy groups in catechol and the hydroxy and methyl groups in $o\text{-CH}_3\text{C}_6\text{H}_4\text{OH}$.

Overall, the rate rules proposed provide excellent estimates, with errors generally below 20% in the temperature range of interest to combustion conditions. Considering a maximum uncertainty for the original set of 14 rate constants of a factor of 2, and maximum discrepancies within the set of rate rules proposed below a factor of 1.5, the final uncertainty of the whole set of rate rules proposed is below a factor of 3 in the 500–2000 K range, and probably much smaller for reactions belonging to the same R' class.

6.5.3.4 Perspectives for the application to tri-substituted MAHs

The rate rules proposed may be extended to H ipso substitutions on tri-substituted MAHs. In particular, Equation (6.1) was applied to compute the rate constants for H ipso substitutions on vanillin (4-hydroxy-3-methoxybenzaldehyde), which is particularly interesting due to its relevance as a reference component for surrogate mixtures of bio-oils from the fast pyrolysis of biomass [46]. Equation (6.1) may be extended to a MAH with three substituents by computing the energy correction as the sum of the contributions for the two lateral substituents R_i as:

$$k_R^{R'} = 0.93k_{0,H}^{R'} T^{1.71} \exp\left(-\frac{E_{A,H}^{R'} + \sum_{R_i} \Delta E_{A,R_i-H}^{R'}}{RT}\right) \quad (6.4)$$

The accuracy of the predictions was checked with theoretical calculations at the ω B97X-D/6-311+G(d,p) level of theory, rescaling the energy barriers according to the ΔE_{HL-L1} of each class R' , as explained above. The resulting rate constants and the discrepancies between the estimated and the calculated values are provided in Table 6.37. Overall, the rate rules provide satisfactory predictions, with maximum discrepancies for the rate of OCH_3 replacement in line with the findings for the rate constant of OCH_3 replacement by H in *o*- $OCH_3C_6H_4OH$. The errors are not larger than those of the predictions for di-substituted aromatics, supporting the accuracy of the rate rules proposed and encouraging their application to other MAHs with more than 2 substituents.

As far as ipso substitutions with radicals different from H are concerned, more significant modifications to the proposed rate rules are needed, as significant changes in the pre-exponential factors and in the coefficients α are expected.

TABLE 6.37: Arrhenius expressions for the rate constants k_{rule} of H-atom addition to vanillin in the 300–2000 K range obtained with the rate rules derived in this work. $k = k_0 \cdot T^\alpha \cdot \exp(-\frac{E_A}{RT})$, units are cm^3 , mol, s, cal. The original fits and the corresponding deviations k_{rule}/k_{calc} at 500, 1000, and 2000 K are shown.

	$R' C_6H_4R + H \rightarrow C_6H_5 + R'$	$k_{rule}, k_{calc} 1E + 07$			k_{rule}/k_{calc}		
R'	Reaction	k_0	α	E_A	500	1000	2000
OH	VANILLIN+H→ <i>m</i> -CHOC ₆ H ₄ OCH ₃ +OH	5.37 2.10	1.71 1.80	4795 4592	1.11	1.15	1.14
OCH ₃	VANILLIN+H→ <i>p</i> -CHOC ₆ H ₄ OH+OCH ₃	4.86 9.17	1.71 1.57	4438 4562	1.30	1.35	1.43
CHO	VANILLIN+H→ <i>o</i> -OHC ₆ H ₄ OCH ₃ +CHO	7.50 5.68	1.71 1.70	4723 4216	0.77	1.00	1.14

6.5.4 Summary

The recent interest in bio-oils combustion and the key role of MAHs in existing kinetic models both as surrogate components and as precursors of PAHs and soot, motivates the current systematic theoretical investigation of a reaction class relevant to the description of their pyrolysis and oxidation, namely ipso substitution by H atoms. This section presented state-of-the-art AI-TST-ME calculations for the rate constants of H ipso substitution on phenol, toluene, *o*-,*m*-,*p*- $C_6H_4(OH)_2$, *o*-,*m*-,*p*-cresol ($CH_3C_6H_4OH$), and *o*-,*m*-,*p*-xylene ($C_6H_4(CH_3)_2$), for a total of 47 potential energy surfaces. Comparisons with available experimental measurements proved the accuracy of the adopted methods, with deviations smaller than a factor of 2. Global rate constants derived assuming a negligible stabilization of the intermediate well at conditions relevant to combustion applications were provided for direct implementation in existing kinetic models.

For the PES for OH and CH_3 replacement by H, the H-atom addition step shows a higher energy barrier than that of the following β -scission reaction, so that it is expected to be rate limiting. Indeed, it was found that the high pressure limit rate constants for H-atom addition provide excellent estimates to the global rate constants of OH and CH_3 replacement by H, with errors below 10% in the 300–2000 K range. The presence of OH and CH_3 side groups lowers the energy barriers for both the addition and decomposition steps compared

to mono-substituted MAHs (phenol/toluene). This effect is particularly relevant when the side group is in the ortho position.

The analysis of the results highlights systematic effects within the reaction classes $\text{OHC}_6\text{H}_4\text{R} + \text{H}$ and $\text{CH}_3\text{C}_6\text{H}_4\text{R} + \text{H}$:

- The energies for the stationary points of the PESs of OH and CH_3 replacement by H vary systematically from the $\omega\text{B97X-D}/6\text{-311+G(d,p)}$ to the CCSD(T)/CBS levels of theory, independent of the lateral group R (-1.8 kcal/mol and -1.95 kcal/mol for $\text{R}' = \text{OH}, \text{CH}_3$, respectively).
- The energy barriers for H-atom addition with methyl replacement by H scale approximately linearly with those for hydroxy replacement with H (proportionality coefficient of 0.75, which corresponds to $E_{A,H}^{\text{CH}_3}/E_{A,H}^{\text{OH}}$).
- The pre-exponential factors and temperature dependence of the rate constants for H-atom addition follow similar trends: in particular, the temperature dependence T^α is about 1.7, whereas the pre-exponential factors within each class R' are all similar.

These trends encouraged the formulation of a protocol for the computation of rate constants for MAH with other R'/R substituents. This protocol was used to estimate the rate constants for a total set of 80 H ipso substitution rate constants: 5 rate constants for $\text{R}'\text{C}_6\text{H}_5 + \text{H}$, and 75 rate constants for di-substituted $\text{R}'\text{C}_6\text{H}_4\text{R} + \text{H}$, with R' , $\text{R} = \text{OH}/\text{CH}_3/\text{OCH}_3/\text{CHO}/\text{C}_2\text{H}_5$. In the whole rate rule derivation procedure, only the H-atom addition channels were considered, as they provide excellent estimates (error below 10%) of the global H ipso substitution rate constants. The adopted procedure and the main findings are summarized below:

- Reference rate constants for mono-substituted aromatics were computed at a high level of theory. These rate constants are in general agreement with previous literature estimates. The energy shifting $\Delta E_{HL-L1}(\text{TS1})$ is consistent for all classes (about -1.9 kcal/mol) and was used as a reference for the scaling of the energy barriers for the other calculations performed within each R' class.
- A lower level of theory $\omega\text{B97X-D}/6\text{-311+G(d,p)}$ was used for the rate constants of H-atom addition to $\text{o-R}'\text{C}_6\text{H}_4\text{OH}$ and $\text{o-R}'\text{C}_6\text{H}_4\text{CH}_3$, with $\text{R}' = \text{OCH}_3/\text{CHO}/\text{C}_2\text{H}_5$, and to $\text{OHC}_6\text{H}_4\text{R}$, with $\text{R} = \text{OCH}_3/\text{CHO}/\text{C}_2\text{H}_5$ (16 H-atom addition channels in total) scaling the energy barriers according to the ΔE_{HL-L1} derived for each class. It was verified that the change in the activation energy $\Delta E_{A,R-H}^{\text{R}'}$ is proportional to $\Delta E_{A,R-H}^{\text{REF}}$ according to the relation between the activation energies of the classes $E_{A,H}^{\text{R}'}/E_{A,H}^{\text{REF}}$, with the exception of $\text{o-OHC}_6\text{H}_4\text{CHO}$, because of the extremely strong interactions between the lateral substituents.
- The rate constants for H-atom addition to $\text{OHC}_6\text{H}_4\text{R}$, with $\text{R} = \text{OCH}_3/\text{CHO}/\text{C}_2\text{H}_5$ allowed us to derive the energy corrections $\Delta E_{A,R-H}^{\text{OH}}$ for each side group R, which are used as a reference $\Delta E_{A,R-H}^{\text{REF}}$ for energy scaling factors of the other R' reaction classes.

The most notable results were the negligible impact of $R = \text{CHO}$ in all positions and the high stabilization effects of the methoxy group in the para position.

The averaging of the pre-exponential factors and temperature coefficients α for the whole set of 33 reactions considered, together with the observations of the systematic impact of each side group R on the activation energies, led to the rate rule formulated in Equation (6.1). This rate rule was used to estimate the whole set of 75 rate constants for di-substituted aromatics $R'C_6H_4R + H$, using $R' = \text{OH}$ as a reference. An additional set of 14 rate constants was computed for further validation of the proposed rate rules. With few exceptions, the rate rules provide excellent predictions of the computed rate constants, with errors below 20%. Considering a maximum uncertainty for the rate constants of the original set below a factor of 2, the maximum uncertainty in the predictions of the whole set of rate constants is estimated to be below a factor of 3. The most important feature of the set computed remains its internal consistency, such that relative errors within this set are expected to be extremely small. The same considerations apply to the extension of the rate rule proposed for H ipso substitutions on MAHs with more than two substituents. The resulting predictions for vanillin + H agree to within a factor of 1.4 with theoretical calculations performed using the full computational protocol, in accordance with the estimated uncertainty.

This systematic and coherent theoretical investigation of H ipso substitution reactions on MAHs with single and double substituents constitutes a step forward towards an improved understanding of MAHs kinetics, based on reaction classes and fundamentally-based reference kinetic parameters.

6.6 Model performance and analysis

This section presents an examination of the kinetic mechanism performance in simulations of experimental data for benzene and OAH pyrolysis and oxidation, in order to critically assess the impact of the kinetic model updates performed and identify relevant reaction classes and uncertain kinetic parameters for future studies. Tables 6.38, 6.39, and 6.40 list the operating conditions for the datasets tested.

TABLE 6.38: Simulation database of flow reactor results included for the testing of the sub-mechanism of benzene. $\Phi = \text{inf}$ indicates pyrolysis conditions.

Inlet	Reactor	T [K]	p [atm]	Φ	τ [s]	Reference
C ₆ H ₆ /Ar	ST	1200–1800	20	Inf	0.004	Sun 2021 [130]
C ₆ H ₆ /Ar	ST	1300–2100	5	Inf	0.002	Laskin 1996 [382]
C ₆ H ₆ /Ar	ST	1200–2000	30–50	Inf	0.0013	Sivaramakrishnan 2006 [383]
C ₆ H ₆ /Ar	ST	1700–2200	0.4	Inf	0.001	Kern 1984 [381]
C ₆ H ₆ /O ₂ /N ₂	PFR	1150	1	0.76, 1, 1.35	0.2	Lovell 1989 [304]
C ₆ H ₆ /O ₂ /N ₂	PFR	1120	1	0.4	0.1	Venkat 1982 [387]
C ₆ H ₆ /O ₂ /N ₂	JSR	900–1300	1	0.3, 0.5, 1, 1.5	0.07	Ristori 2001 [359]
C ₆ H ₆ /O ₂ /Ar	JSR	900–1250	0.46	0.19, 1.02	0.05	Chai 1998 [368]
C ₆ H ₆ /O ₂ /N ₂	JSR	900–1200	10	0.5, 1.5	0.7	Marchal 1995 [392]
C ₆ H ₆ /O ₂ /He	JSR	923	1	1.9, 3.6	1 — 10	Da Costa 2003 [386]
C ₆ H ₆ /O ₂ /He	ST (IDT)	1230–1970	6.5–9.5	0.3–1	—	Da Costa 2003 [386]
C ₆ H ₆ /O ₂ /Ar	ST (IDT)	1200–1750	2.44–6.2	0.25–2	0.01	Burcat 1986 [385]

TABLE 6.39: Simulation database of measurements in laminar flames included for the testing of the sub-mechanism of benzene. PFI and LFS indicate speciation or flame speed in laminar premixed flames, respectively.

Inlet	Reactor	T [K]	p [atm]	Φ	Reference
C ₆ H ₆ /O ₂ /Ar	PFI	400–1600	0.03	1.8	Bittner 1981 [393]
C ₆ H ₆ /air	PFI	500–1800	1	1.8, 1.92	Tregrossi 1999 [394]
C ₆ H ₆ /O ₂ /Ar	PFI	700–1800	0.05	2	Defoieux 2005 [396]
C ₆ H ₆ /CH ₄ /O ₂ /N ₂	PFI	450–1500	0.05	1	Bakali 2006 [360]
C ₆ H ₆ /O ₂ /Ar	PFI	700–1750	0.045	0.7–2	Detilleux 2009 [395]
C ₆ H ₆ /air	PFI	1100–1810	1	1.98	Russo 2012 [397]
C ₆ H ₆ /O ₂ /Ar	PFI	400–1600	0.04	1.25, 1.75, 2	Yang 2015 [398]
C ₆ H ₆ /air	LFS	298–2300	1	0.7–1.7	Davis 1998 [374]
C ₆ H ₆ /air	LFS	353–2350	1	0.7–1.5	Ji 2012 [373]
C ₆ H ₆ /air	LFS	450–2450	3	0.8–1.4	Johnston 2005 [375]

TABLE 6.40: Simulation database of flow reactor and laminar flame measurements included for the testing of the sub-mechanism of OAHs.

Inlet	Reactor	T [K]	P [atm]	Φ or mole frac	τ [s]	Reference
C ₆ H ₅ OH/Ar	ST	1500	2	inf	0.001	Horn 1998 [132]
C ₆ H ₅ OH/H ₂ /H ₂ O	PFR	1000–1200	1	inf	3.5	Lovell 1989 [126]
C ₆ H ₅ OH/N ₂ /O ₂	PFR	1100–1200	1	0.64, 1.03, 1.73, inf	0.15	Brezinsky 1998 [125]
C ₆ H ₅ OH/N ₂ /O ₂	RCM	950–1100	10, 20	0.5, 1	—	Büttgen 2019 [54]
C ₆ H ₅ CHO/He/O ₂	JSR	700–1100	1	0.5, 1, 2	0.7	Namysl 2020 [449]
o-HOC ₆ H ₄ OH/N ₂ /O ₂	PFR	770–1270	1	0.92, 0.58, 0.22, inf	0.3	Thomas 2007 [424]
o-HOC ₆ H ₄ OH/C ₂ H ₂ /N ₂	PFR	950–1300	1	0.11/0.14/99.75	0.3	Thomas 2008 [426]
o-HOC ₆ H ₄ OH/C ₄ H ₆ /N ₂	PFR	950–1300	1	0.11/0.13/99.76	0.3	Thomas 2009 [427]
C ₆ H ₅ OCH ₃ /N ₂	ST	1000–1270	1.3–1.6	inf	0.001	Shu 2017 [430]
C ₆ H ₅ OCH ₃ /N ₂	PFR	800–950	1.3	inf	1	Pelucchi 2018 [131]
C ₆ H ₅ OCH ₃ /He,Ar/O ₂	JSR	670–1170	1	1, inf	2	Nowakowska 2014 [51]
C ₆ H ₅ OCH ₃ /N ₂ /O ₂	JSR	775–1275	1	0.5, 1, 2, inf	0.07	Wagnon 2018 [50]
C ₆ H ₅ OCH ₃ /N ₂ /O ₂	JSR	600–1000	0.92	1	1.5	Chen 2021 [370]
C ₆ H ₅ OCH ₃ /Ar/O ₂	PFI	500–2300	0.04	1.2, 1.6	6 cm	Bierkanth 2019 [432]
C ₆ H ₅ OCH ₃ /N ₂ /O ₂	ST (IDT)	760–1600	10, 20, 40	0.5, 1	—	Herzler 2017 [431]
C ₆ H ₅ OCH ₃ /N ₂ /O ₂	ST, RCM	800–1300	10, 20, 40	0.5, 1, 2	—	Büttgen 2020 [55]
C ₆ H ₅ OCH ₃ /N ₂ /O ₂	LFS	358	1	0.6–1.2	—	Wagnon 2018 [50]
o-HOC ₆ H ₄ OCH ₃ /He/O ₂	JSR	650–950	1.06	inf	2	Nowakowska 2018 [45]
o-HOC ₆ H ₄ OCH ₃ /He	PFR	723–923	0.4, 1	inf	1.4	Yerrayya 2019 [433]

6.6.1 Benzene

6.6.1.1 Pyrolysis

The pyrolysis of benzene was only studied in high-temperature ($T > 1200$ K) shock tubes [130], [381]–[383], mostly at high pressures (see Table 6.38). Figure 6.45 shows the model simulations compared to the ST data of Laskin et al. [382] (a) and Sun et al. (b) [130], who detected the widest range of products. Experimental benzene conversion starts at ~ 1550 K at lower pressure (4 bar in [382]) and at ~ 1500 K at higher pressure (20 bar in [130]). The main decomposition products detected are acetylene and diacetylene, while the main aromatic products are phenylacetylene and biphenyl. While the relative amounts of $C_6H_5C_2H$ and $C_{12}H_{10}$ are comparable in [382], the latter prevails in [130]. The kinetic mechanism performs reasonably well in predicting the conversion and the main product profiles. However, benzene conversion is overpredicted for the set of Laskin et al. [382] and underpredicted for the set of Sun et al. [130]. Strong underprediction of benzene conversion is also observed in kinetic simulations of the high-pressure ST measurements of Sivaramakrishnan [383] and in the low p , high T ST experiments of Kern et al. [381]. While experimental results suggest that high p (20–50 bar) can shift the conversion of benzene from ~ 1500 to ~ 1350 K, this effect is not captured by the model.

The main pathway for benzene consumption (and the most sensitive for benzene conversion) is the H-atom abstraction by H, which was computed in this work (Section 6.4), followed by H bond-fission and decomposition to propargyl (included in the model from theoretical calculations of [271]). Phenyl radical mostly dissociates to $LC_6H_4 + H$ or directly to C_2/C_4 products, while a minor fraction is converted to CYC_6H_4 . In the lower pressure experiments of Laskin et al. [382], the model also predicts that a significant fraction of benzene is converted directly to biphenyl via $C_6H_5 + C_6H_6$. This is also the main production pathway of biphenyl in [130]. Phenylacetylene is formed by typical HACA reactions (C_2H and C_2H_2 additions to phenyl), while naphthalene is formed mostly by diacetylene addition to phenyl, and then grows through HACA reactions to $C_{12}H_8$ and $C_{14}H_{10}$. The main formation pathway for indene is instead propargyl radical addition to phenyl and benzene; the same reaction class [A1-R][REC_C3.DD-RSR] also determines naphthyl growth to fluorene. Finally, larger PAHs (C_{16} and C_{18}) are formed from additions and recombinations of aromatic rings.

In the ST of Laskin et al. [382] the higher conversion of benzene results in higher amounts of phenyl radical, which converts to a linear radical (according to a rate constant estimated and included as pressure-dependent in the mechanism) more slowly than at higher pressures, and favors the formation of aromatic species. This conversion partially explains the underestimation of most PAHs in the ST of Sun et al. [130]. As far as growth pathways are concerned, only rate constants for HACA reactions were recently updated from theoretical calculations, while reaction parameters for growth reactions via $C_6 + C_3$ producing C_5 rings or benzene + phenyl reactions derive from estimates or old literature. It is noted that indene and naphthalene underestimation is also common to many kinetic simulations of high-temperature benzene flames (Section 6.6.1.3), while predictions of biphenyl are generally

in better agreement with experimental data. The recent revision of growth reactions in the CRECK mechanism performed by Sun et al. [130], [412], [569]–[571] will help improve model predictions.

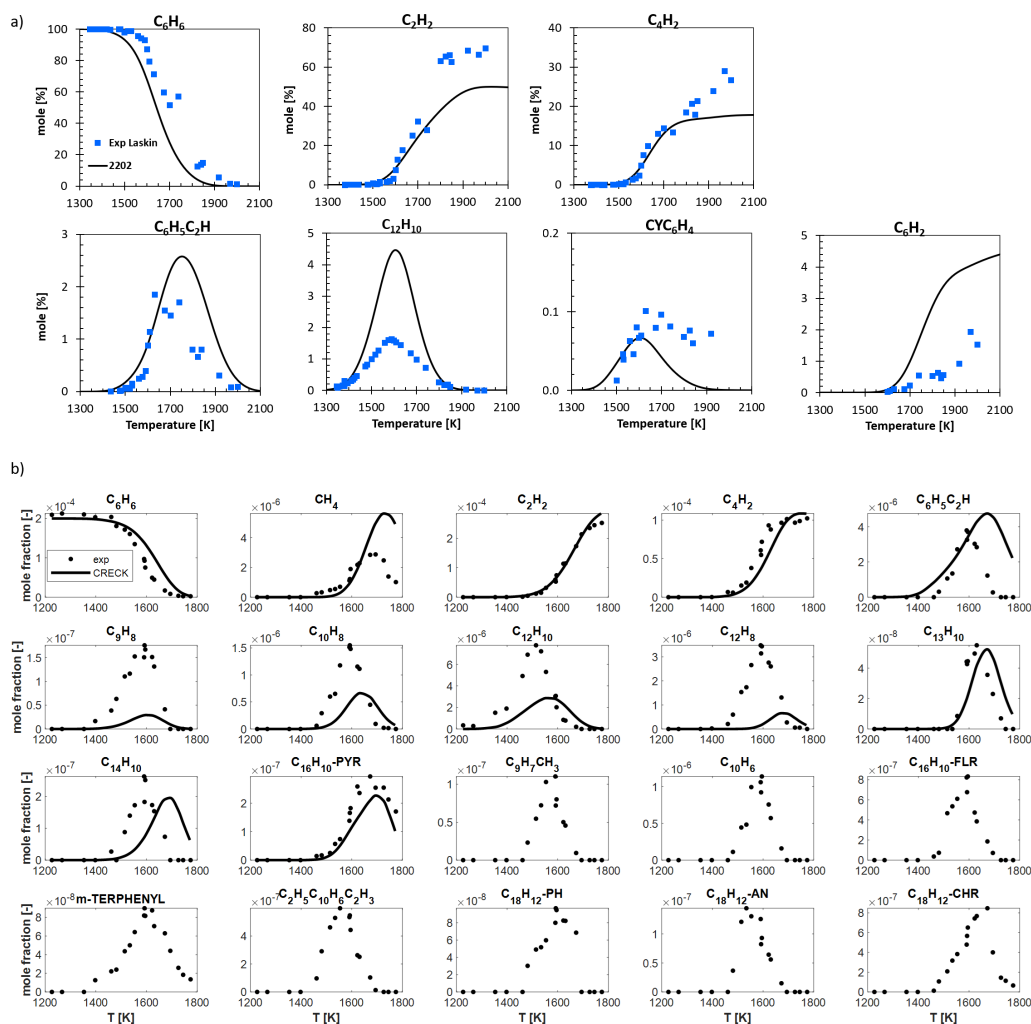


FIGURE 6.45: Experimental (dots) and simulated (lines) species profiles for benzene pyrolysis in the ST of a) Laskin et al. [382] and b) Sun et al. [130].

6.6.1.2 Oxidation in flow reactors

Figure 6.46 shows kinetic simulations of the oxidation of benzene in the JSR experiments of Ristori et al. [359] at different equivalence ratios. Benzene conversion starts at around 1050 K at fuel-lean conditions, while at fuel-rich conditions benzene starts being converted only above 1200 K. C_2H_2 and C_2H_4 are the main linear hydrocarbon products, while the main unsaturated cyclic products are C_6H_5OH and C_5H_6 . The yields of phenol, butadiene and C_3 species do not change dramatically with equivalence ratio. Instead, the selectivity to non-oxygenated species decreases at lower Φ in favor of oxygenated products, namely CH_2O , CO , CO_2 .

Overall, the model predicts reasonably well the experimental trends. The most evident discrepancy is the underestimation of benzene consumption at $\Phi = 1$ and its overestimation

at $\Phi = 1.5$. Phenol and cyclopentadiene profiles show opposite trends: at fuel-lean conditions, they are slightly overestimated and underestimated, respectively, while the reverse applies to rich conditions. Smaller hydrocarbons are well predicted, however C_3H_4 and C_4H_6 are underpredicted at fuel-lean conditions.

The flux analysis of Figure 6.47 guides the understanding of key steps in the mechanism. Benzene is mostly consumed to phenyl radical through H-atom abstraction reactions, while large amounts of phenoxy radicals are produced through both O_2 recombination with phenyl and direct O addition to benzene (in class type IPSO). Conversion between phenol and phenoxy is mostly controlled by H-atom abstractions by H, OH and O_2 , and bond-fission as the reverse of ADD_H. Phenol can also be formed via O addition to benzene followed by ISC. Phenoxy largely decomposes to cyclopentadienyl radical, which can be oxidized by HO_2 or recombine with H to form cyclopentadiene, which is in turn is mostly oxidized via O addition. The formation of linear alkenes occurs mainly from the oxidation of C_5 species (C_5H_6 , C_5H_5O , C_5H_4O).

Heat maps comparing the main class types at $\Phi = 1.5-0.3$ show the effect of the higher concentration of O_2 and therefore of H and oxygenated radicals at fuel-lean conditions: consumption of benzene via ADD_O and IPSO, and of C_5H_5 via ADD_HO2 increase. The larger amount of phenoxy radical (accumulated through IPSO_O) is consumed via recombination with H atom ADD_H, which increases its contribution to phenol production with respect to other classes. Phenol is slightly consumed by IPSO_O. Lean conditions have an opposite effect on cyclopentadiene: because of the larger concentrations of O and H atoms, its consumption via ADD_O increases, in contrast to its production via bond-fission ADD_H, which also explains the decrease in its concentration at fuel-lean conditions.

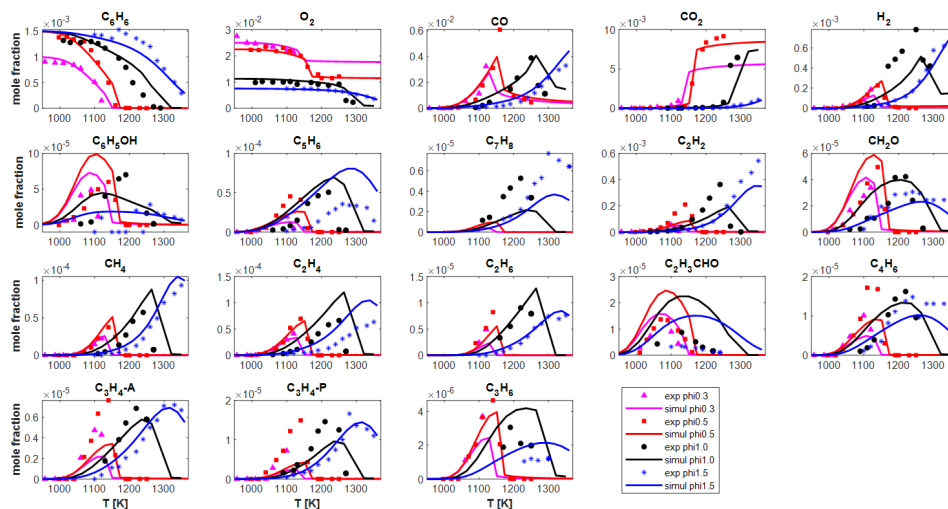


FIGURE 6.46: Experimental (dots) and simulated (lines) species profiles for benzene oxidation in the JSR of Ristori et al. [359].

The only intermediate- T flow reactor experiments detecting a wider range of aromatic species is the set of Chai et al. [368], which are compared with the kinetic simulations in Figure 6.48. The relevant C_5 and C_6 cyclic products besides phenol and cyclopentadiene are benzoquinone $C_6H_4O_2$ and cyclopentadienone C_5H_4O ; among the radicals, significant

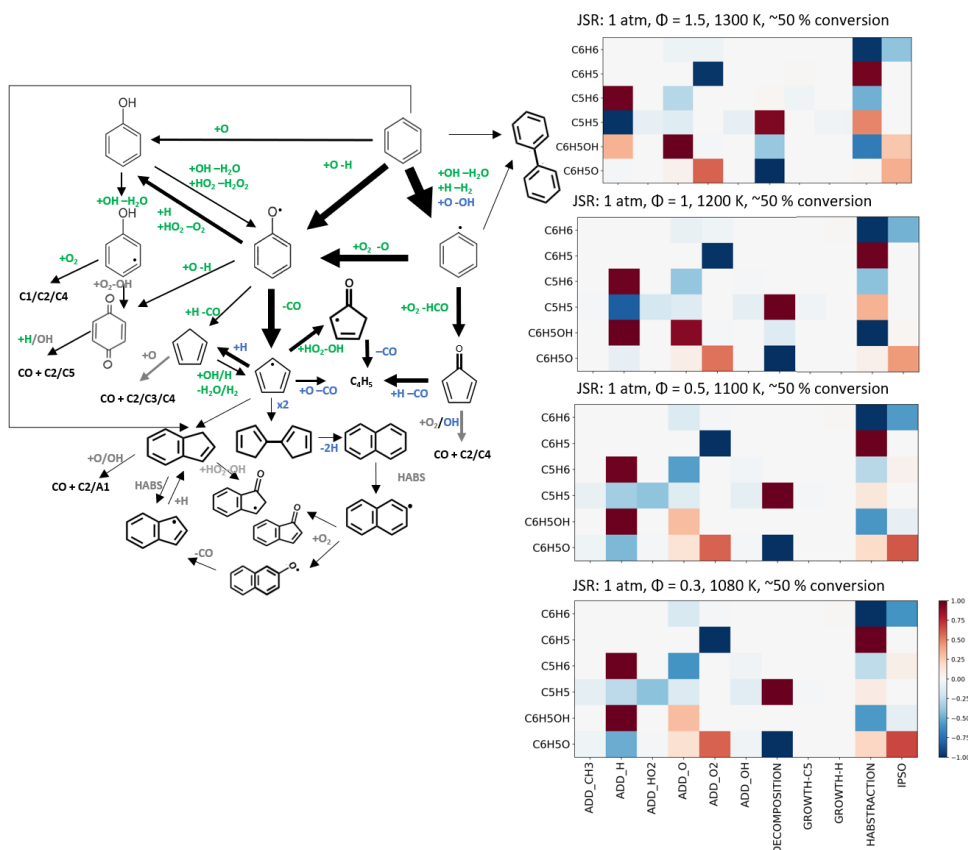


FIGURE 6.47: Schematic flux analysis for benzene oxidation at 1100–1200 K (50% conversion) in the JSR of Ristori et al. [359]. Colors of the reactions indicate the type of update: from theoretical calculations of this work (green), from literature theoretical calculations (blue), from rate rules or approximations (grey). Heat maps by class type for relevant species are also presented (flux relative to the highest flux of each species, with a threshold of 1%).

amounts of C_6H_5O and C_5H_5 were detected, while C_5H_5O was only measured at $\Phi = 0.19$. Measured PAHs were indene, naphthalene, $C_{10}H_{10}$, and biphenyl, which were all observed in comparable amounts.

Kinetic simulations overpredict benzene conversion at stoichiometric conditions, as compared to the experimental dataset of Ristori et al. [359]. At both stoichiometric and lean conditions, phenol is dramatically overpredicted, while the disagreement with experimental data is lower for C_5H_6 (particularly overestimated at fuel-lean conditions), C_5H_5 , and C_6H_5O . It is observed that slight mispredictions in radical concentrations (C_5H_5 , C_6H_5O) cause much larger discrepancies in the parent molecules (C_5H_6 , C_6H_5OH). Also C_5H_4O , which is directly produced from $C_6H_5 + O_2$, is overestimated. In this case, consumption reactions in the model were all estimated with the exception of unimolecular decomposition and H-atom addition (from [293]), and H-atom abstraction reactions lead directly to decomposed products. Further investigations should indeed be performed. In contrast, $C_6H_4O_2$ is well predicted by the model. This species is produced from $C_6H_4OH + O_2$ (Figure 6.47). At fuel-lean conditions, C_5H_5O is hardly accumulating in the model. C_5H_5O is entirely consumed by unimolecular decomposition (see Figure 6.47), suggesting that the corresponding rate constant (from [292]) is too high or, more likely, that production pathways are missing in

the mechanism. Overprediction of C_5/C_6 species is related to the underprediction of C_2/C_4 species, which suggests missing decomposition pathways or wrong equilibrium in the radical pool.

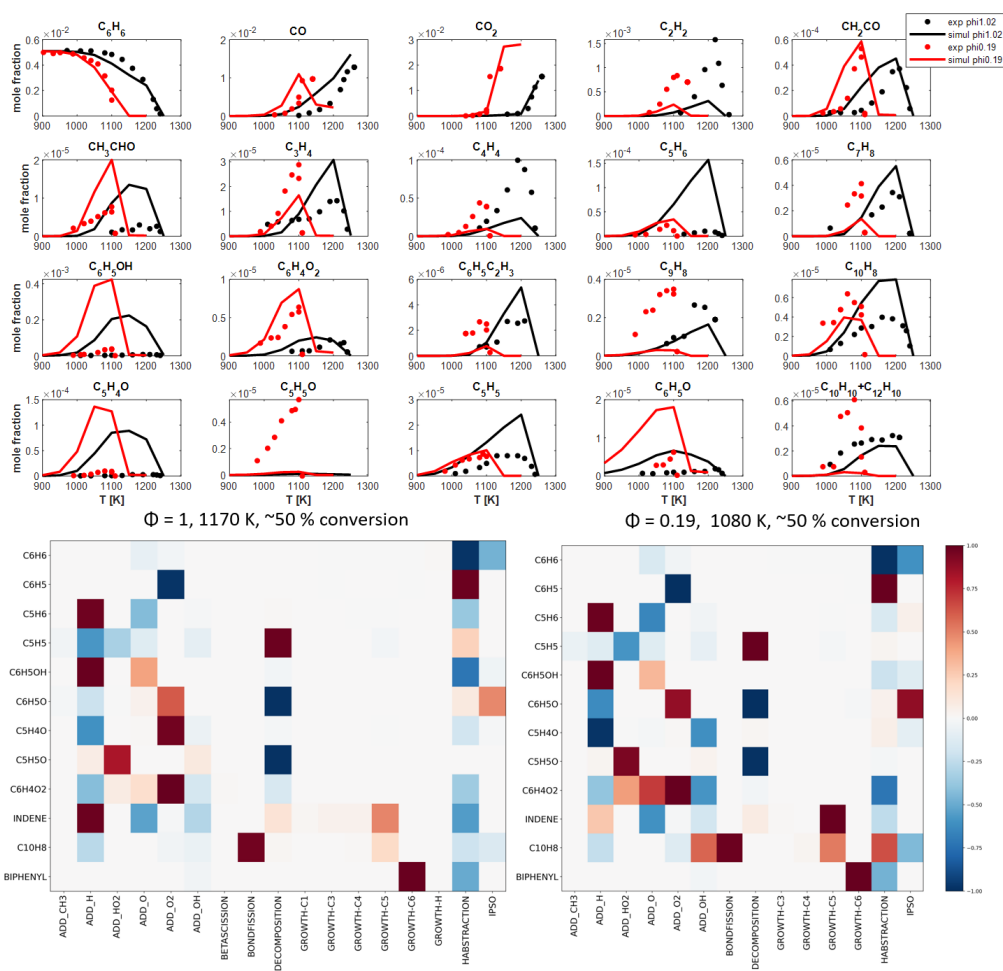


FIGURE 6.48: Experimental (dots) and simulated (lines) species profiles for benzene oxidation in the JSR of Chai et al. [359] with class-type flux analysis for the relevant species (flux relative to the highest flux of each species, with a threshold of 1%).

The class-type flux analysis presented at the bottom of Figure 6.48 highlights that benzene decomposition pathways are essentially identical to those observed in the previous experimental dataset. On the other hand, the consumption of C_5H_5 via `ADD_H` and `ADD_OH` is less relevant compared to `ADD_HO2`. Similarly, the relative importance of phenol consumption via `HABS` is also smaller than in the JSR of Ristori et al. [359]. The sensitivity analysis for C_5H_6 and C_6H_5OH at stoichiometric conditions and 50% of benzene conversion in both reactors is presented in Figure 6.49. No striking difference is observed. However, in the JSR of Chai phenol is more sensitive to H-atom abstraction reactions and H recombination with phenoxy radical, while the primary consumption reactions of benzene are more important in the JSR of Ristori. The cyclopentadiene concentration is extremely sensitive to O addition, which is the only reaction among the sensitive ones that was not investigated theoretically. In the Yale JSR [368], C_5H_6 shows higher sensitivity to HO_2 and O_2 reactions, while in the sensitivity for the JSR of Ristori H-atom abstraction by OH from benzene also contributes

to cyclopentadiene indirect production. Overall, the production and consumption of $C_5/A1$ species seems to be controlled by the complex radical pool of OH, O_2 , H, and HO_2 . In the JSR of Chai et al., the pressure is slightly lower, however the total mole fractions of benzene and O_2 are five times larger than in the reactor of Ristori et al. In Chai, the trends observed might be due to an underestimation of H and overestimation of O/OH concentrations, which does not enhance consumption.

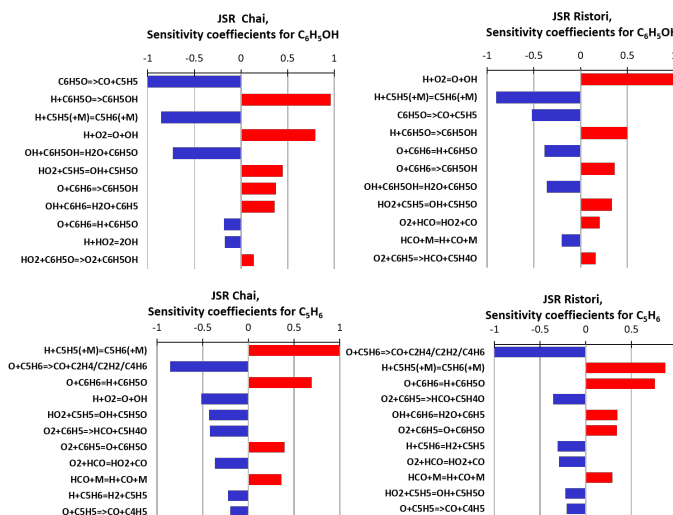


FIGURE 6.49: Normalized sensitivity coefficients for phenol and cyclopentadiene concentrations in the JSR of Chai et al. [368] and Ristori et al. [359] at 50% conversion and stoichiometric conditions (around 1200 K).

The flux analysis of Figure 6.47 and the heat maps of Figure 6.48 also describe formation of naphthalene, indene, and fulvalane ($FC_{10}H_{10}$). Fulvalane and naphthalene mostly grow from C_5H_5 recombination, as observed in Section 5.4. Indene instead is formed by $A1 + C_5$ (GROWTH- C_5) or from indenyl. The latter is produced through naphthalene oxidation, with analogous reaction pathways to benzene oxidation, as highlighted in Figure 6.47, in line with the consistent structure of the mechanism. Finally, biphenyl is produced from $C_6H_5 + C_6H_6$, as in pyrolysis. Model predictions of PAHs are satisfactory, however indene and C_{10}/C_{12} are underestimated at fuel-lean conditions, possibly in relation to the higher importance of oxidation pathways and consequently the lower concentrations of C_5H_5 and C_6H_5 .

Marchal et al. [392] investigated intermediate- T benzene oxidation in a JSR at higher pressure (10 atm). Figure 6.50 shows that overall good agreement is reached between the model simulations and experimental data, with an overestimation of the phenol peak of about a factor of 2. Conversion of benzene seems to be overestimated at low temperatures, however this contrasts the good agreement –or slight overestimation– with O_2 profiles. The flux analysis shows that at these conditions C_5H_6 consumption with ADD_O is more relevant than in the other experimental datasets. At the same time, C_5H_5 is more significantly consumed by ADD_HO2 . This also explains the production of C_5H_6 via H-atom abstraction reactions: because of the high HO_2 concentration, the H-atom abstraction reaction $C_5H_6 + O_2 = C_5H_5 + HO_2$ proceeds in the reverse direction. The same effect is observed for

$C_6H_5OH + O_2 = C_6H_5O + HO_2$ at fuel-lean conditions. Compared to the flux analysis of Ristori, the role of ADD_H and ADD_O classes for phenol and phenoxy radicals change: in fuel-rich conditions, ADD_H is essential for the conversion of phenol to phenoxy; at fuel-lean conditions, the relevance of ADD_H decreases in favor of H-atom abstraction and ADD_O class. This change in the radical pool may also be attributed to the effects of pressure.

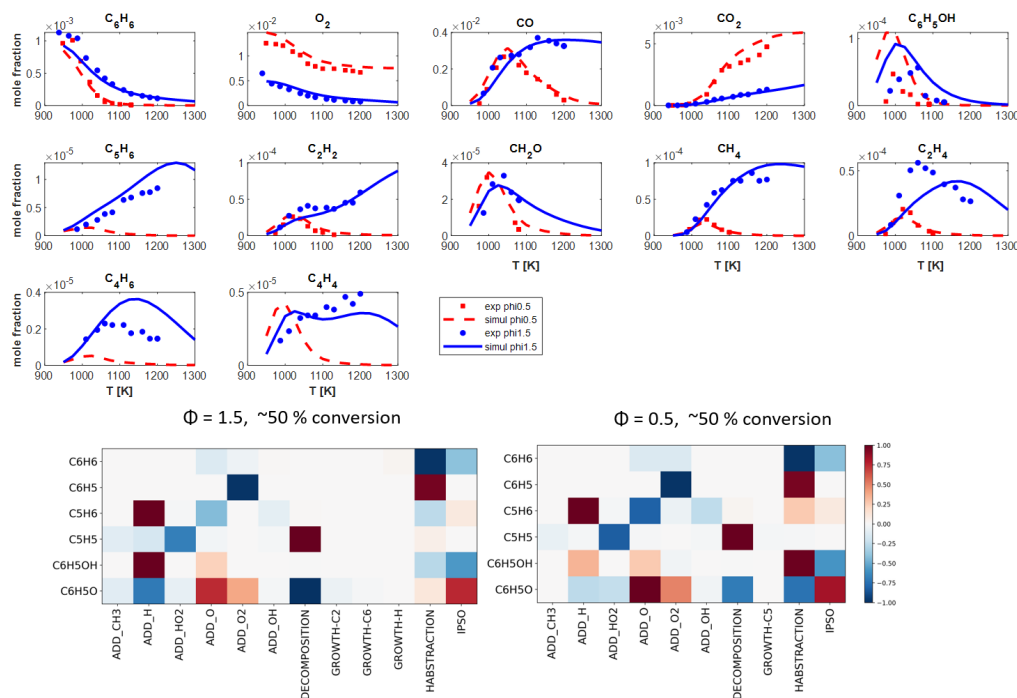


FIGURE 6.50: Experimental (dots) and simulated (lines) species profiles for benzene oxidation in the JSR of Marchal et al. [392] with class-type flux analysis for the relevant species (flux relative to the highest flux of each species, with a threshold of 1%).

Figure 6.51 shows the profiles of the main species detected in the JSR of Da Costa et al. [386] (1 atm, 920 K) at fuel-rich conditions as a function of time. The model agrees with the main trends. However, it fails to reproduce the sharper onset in the conversion corresponding to ~ 3 s of residence time. Sensitivity analysis at 2 s reveals that the most sensitive reaction in benzene consumption is $C_6H_6 + O_2$ producing phenoxy radical, together with $C_6H_5O + HO_2 \rightarrow C_6H_5OH + O_2$. This is also highlighted by class group analysis: the ADD_O2 class consumes C_6H_6 , in contrast with all the flux analyses presented above. Additionally, C_6H_5OH and C_6H_5O are produced and consumed by the H-atom abstraction class, respectively. A similar trend is observed for C_5H_6 and C_5H_5 : in this case, radical abstractions between C_5H_5 and C_5H_5O/CYC_5H_7 , accumulating due to the low temperature, significantly contribute to the consumption and production of these species. The rate constants for these abstractions were estimated, so it might be worth attempting more accurate estimates, also in light of the competition between these reactions and recombination to grow to C_{10} species. Finally, it is noted that C_5H_6 is also produced through ADD_HO2, i.e., the reverse reaction of $C_5H_6 + HO_2 = CYC_5H_7 + O_2$.

Finally, Figure 6.52 compares the PFR data of Lovell et al. [304] at ~ 1100 K with kinetic simulations using the updated CRECK mechanism. The need to shift the kinetic

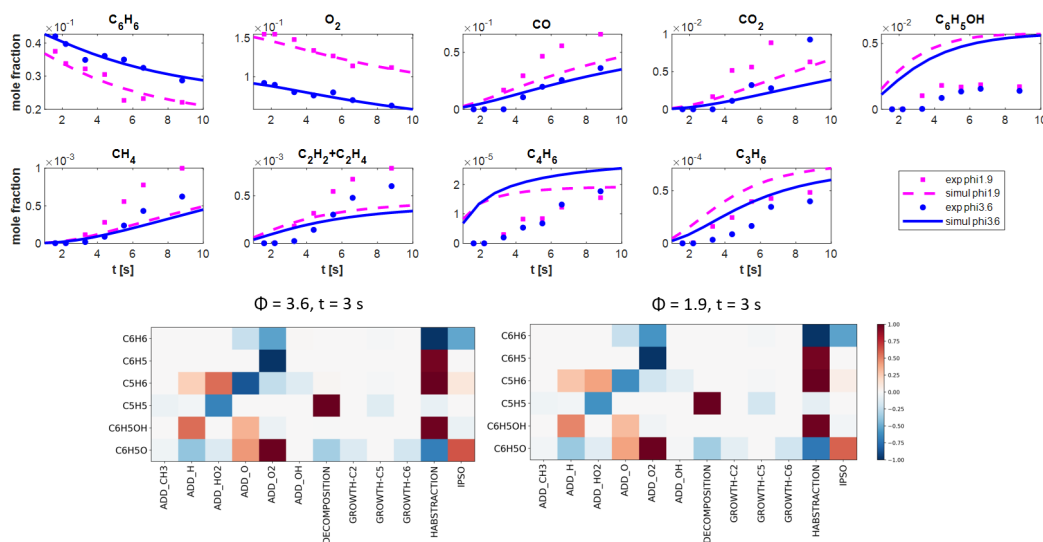


FIGURE 6.51: Experimental (dots) and simulated (lines) species profiles for benzene oxidation in the JSR of Da Costa et al. [386] with class-type flux analysis for the relevant species (flux relative to the highest flux of each species, with a threshold of 1%). JSR were simulated at different residence times parametrically.

simulations (in this case by -0.02 s) to account for the mixing effects of the experimental facility [127], [371] makes the interpretation of the results arbitrary to some extent. The slope of the conversion seems to be well captured by the model. Applying the same shift at all equivalence ratios results in an underprediction of the conversion at both lean and rich conditions. Overall, experimental trends are reproduced by the kinetic simulations. The underestimation of C_2/C_4 species is consistent with the trends observed in the JSR simulations discussed above. Similarly, C_5H_6 is slightly overpredicted by the model. On the other hand, this is the only case where phenol is underestimated by the model, with largest discrepancies observed at fuel-rich conditions. Flux analysis by class group at all equivalence ratios is very similar to that obtained for the JSR of Ristori et al. [359] at fuel-lean conditions (Fig. 6.47), which shares the same temperature of the PFR experiments. In the PFR, phenol consumption via H-atom abstraction reactions by OH is less relevant, and its formation via ADD_O increases at fuel-rich conditions, similar to the trends observed in Figure 6.47. The analysis of the H and O atom and of the OH and HO_2 radical profiles in the two reactors reveal that despite similar concentrations of O_2 and HO_2 , in the PFR the mole fractions of H, OH and O are about one order of magnitude smaller, probably limiting the conversion from phenoxy to phenol, since the concentration of phenoxy radical is significantly larger than that of H, in contrast with the JSR. This behavior is strictly related to the sub-mechanism of cyclopentadiene, which directly consumes HO_2 via recombination with cyclopentadienyl, producing H atoms.

Overall, the flow reactor experiments presented show a general overestimation of phenol, particularly at fuel-lean conditions, and of cyclopentadiene, especially at fuel-rich conditions; decomposition to C_2 – C_4 species seems to be underpredicted, with the exception of the JSR data of Marchal et al. [392]. Model predictions at fuel-rich conditions are overall in better

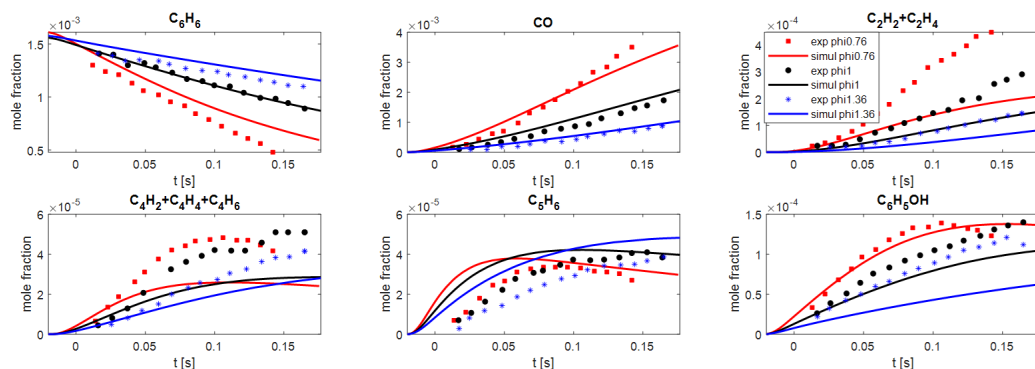


FIGURE 6.52: Experimental (dots) and simulated (lines) species profiles for benzene oxidation in the PFR of Lovell et al. [304] (1100 K, 1 atm). Simulations were shifted by -0.02 s to account for mixing effects of the experimental facility.

agreement with experimental data. The flux analysis showed that the radical pool is controlled by the complex interplay of H-atom abstraction reactions, recombination reactions with O_2 , HO_2 , H, and additions with O, O_2 , H. At higher pressure and rich conditions, HO_2 higher concentration results in reverse H-atom abstraction reactions by O_2 . The radical pool generated through these reactions does not always seem to be correct, generating inconsistent trends in the simulated data with the equivalence ratio. These discrepancies might however also be attributed to uncertainties in the experimental measurements. Among interesting species and reactions poorly studied, probably C_5H_5O production reactions, C_5H_4O abstractions and following oxidation kinetics, $C_5H_6 + O$, radical abstraction reactions between resonance-stabilized C_5 species, and $C_6H_6 + O_2$ require further investigation. These simulations also highlight the close interconnection between benzene and the sub-mechanism of C_5 oxidation.

6.6.1.3 Premixed laminar flame speciation

High-temperature sooting flames (mostly at fuel-rich conditions, often at low pressures) are widely used to quantify PAHs produced from benzene oxidation.

Among the flames simulated to test the kinetic mechanism, only those of Tregrossi et al. [394] and Russo et al. [397] are at atmospheric pressure (see Table 6.39). Figure 6.53 shows kinetic simulations and class type flux analysis for the former dataset (the latter shares the same trends). Overall, the model captures well the experimental data. The most evident differences are the strong overestimation of C_4H_2 and the slight overestimation of C_5H_6 , C_6H_5OH , and $C_{10}H_8$.

The flux analysis highlights that the relevance of H-atom abstraction reactions is significantly larger than in the flow reactor oxidation of Section 6.6.1.2, while ipso substitutions including the O addition to benzene contribute less to the reactivity. Benzene and C_5H_5 are also partially consumed with unimolecular decomposition reactions. The ADD_H class, which mostly includes H recombinations, is among the main sources of C_5H_6 , C_6H_5OH , and indene, while it consumes naphthalene via addition/decomposition pathways. The ADD_O2 class remains the main consumption pathway for phenyl radical. The decomposition of the

resulting C_6H_5O and C_5H_4O produces C_4H_5 , CO , and H (from $C_5H_5 + O$, $C_5H_4O + H$, and C_5H_5O decomposition, see Figure 6.47). Bond-fission, oxidation and decomposition reactions from C_4H_5 , C_4H_4 and C_4H_3 eventually form C_4H_2 . The misprediction of C_4H_2 as opposed to other C_4 species might be due to poor representation in the model of C_5 decomposition or of the interconversion between these species.

The formation of naphthalene and indene occurs through similar pathways to those described above (Figure 6.47). However, in the flame H-atom abstractions largely consume these species, and naphthalene can decompose via H and OH additions (e.g., to $C_4H_4 + C_6H_5$). New formation pathways are active, such as $C_6H_5C_2H + CH_3$ and $C_6H_5 + C_3H_3$ (GROWTH-C1, GROWTH-C3) in the case of indene. $C_6H_5C_2H$ was not detected in this dataset, however it plays a crucial role in the mechanism, as highlighted by high- T pyrolysis experiments (Section 6.6.1.1) and other flame experiments. Class type analysis of Figure 6.53 shows that $C_6H_5C_2H$ is mostly formed via ADD_H, BONDFISSION, and GROWTH-C2 classes. While the last one is easily identified with the HACA mechanism, the first two are actually $C_6H_5C_2H + H = C_6H_5C_2H_2$ (proceeding in the reverse direction) and $C_6H_5C_2H = C_6H_4C_2H + H$, also going in the reverse direction, i.e., also part of the HACA pathway. Phenylacetylene can also decompose back to C_6H_5 via OH addition.

Figure 6.54 shows kinetic simulations for the low-pressure (0.03 atm) rich flame of Bittner et al. [393]. Benzene conversion and the main product species, including H atoms and OH radicals, are very well predicted by the model. Conversely, CH_4 , C_2H_4 , C_3H_3 , C_5H_6 , C_6H_5OH , and C_7H_8 are overpredicted, in contrast with the underestimation of the main PAHs (naphthalene, indene, and acenaphthylene). The trends observed for cyclopentadiene, phenol and PAHs are consistent with observations in flow reactor experiments. Mispredictions may be related to the overestimation of the C_6H_5 concentration by about a factor of 2. Compared to the higher pressure, direct decomposition of phenyl to C_2/C_4 products plays a more important role, such that the main production pathways of C_2/C_4 species are related to A1 instead of C_5 mechanism. On the other hand, C_2H_4 , which is strongly overestimated by the model, derives from C_4H_5 , which in turn is mostly produced from C_5 oxidation, and that is consistent with the high predicted concentration of cyclopentadiene.

Similar results were obtained in other rich low-pressure flames [395], [396], [398]. Figure 6.55 shows model predictions for the rich low-pressure flame of Dettleux et al. [395]. While benzene conversion is slightly underpredicted by the model, mole fractions of CH_4 , C_3H_4 , C_5H_6 and substituted MAHs are overpredicted. On the other hand, C_4H_6 is underestimated, similar to [398] and in contrast with the flame of Bittner et al. [393]. In this flame, butadiene is mostly produced from $C_3H_3 + CH_3$, while C_5 oxidation reactions are less relevant. Additionally, the radical consumption mostly occurs via H-atom addition. It is noted that in this case H_2 concentration is underestimated by the model, as opposed to the overestimation in [393], possibly shifting the reactivity to growth reactions rather than H-atom addition/decomposition.

Another relevant difference with respect to the previous dataset is the strong overestimation of phenylacetylene, which is also observed in the simulations of the flame of Defoeux et

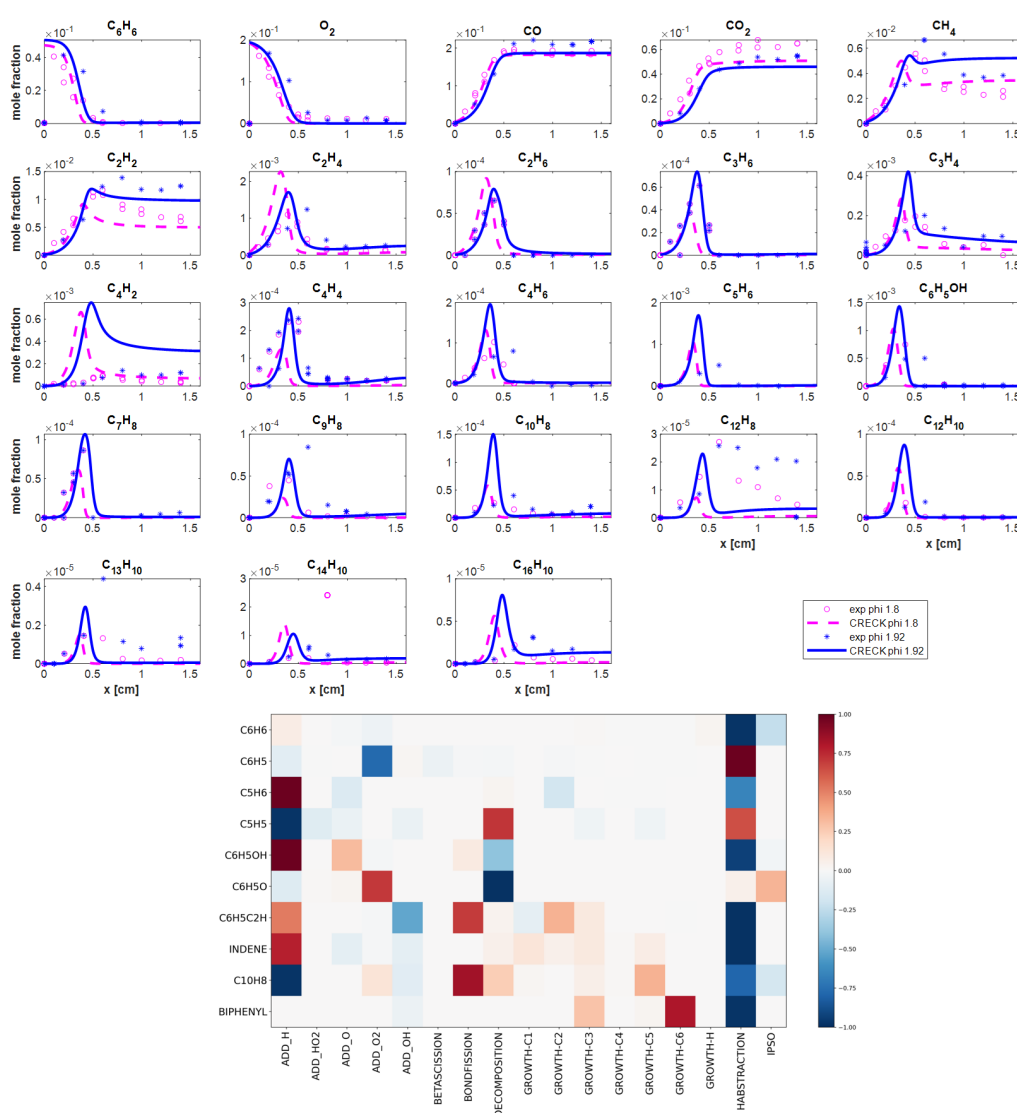


FIGURE 6.53: Experimental (dots) and simulated (lines) species profiles for benzene oxidation in the premixed rich atmospheric flame of Tregrossi et al. [394] with class-type flux analysis for the relevant species (flux relative to the highest flux of each species, with a threshold of 1%).

al. [396] and Yang et al. [398] (not plotted for brevity). The heat map class analysis of Figure 6.55 shows that essentially formation and consumption pathways for $C_6H_5C_2H$ are the same as at atmospheric pressure, with BONDFISSION prevailing over other classes. Also for phenylacetylene, the radical pool controls its formation and consumption via β -scission, bond-fission and H-atom abstractions by H and OH, respectively. In the flame of Bittner et al. [393], where phenylacetylene concentration is well predicted, the temperature is lower, and H-atom abstraction reactions contribute more significantly to its consumption.

Finally, comparing heat maps class analysis at atmospheric and low pressures of Figure 6.53, 6.55, respectively, the effect of pressure is evident. In fact, at lower pressure the relative importance of ADD_H is significantly smaller, while that of decomposition reactions increases. Additionally, at low pressures direct decomposition of cyclopentadiene and phenyl (BETACISSION and GROWTH-C2) also plays a more relevant role.

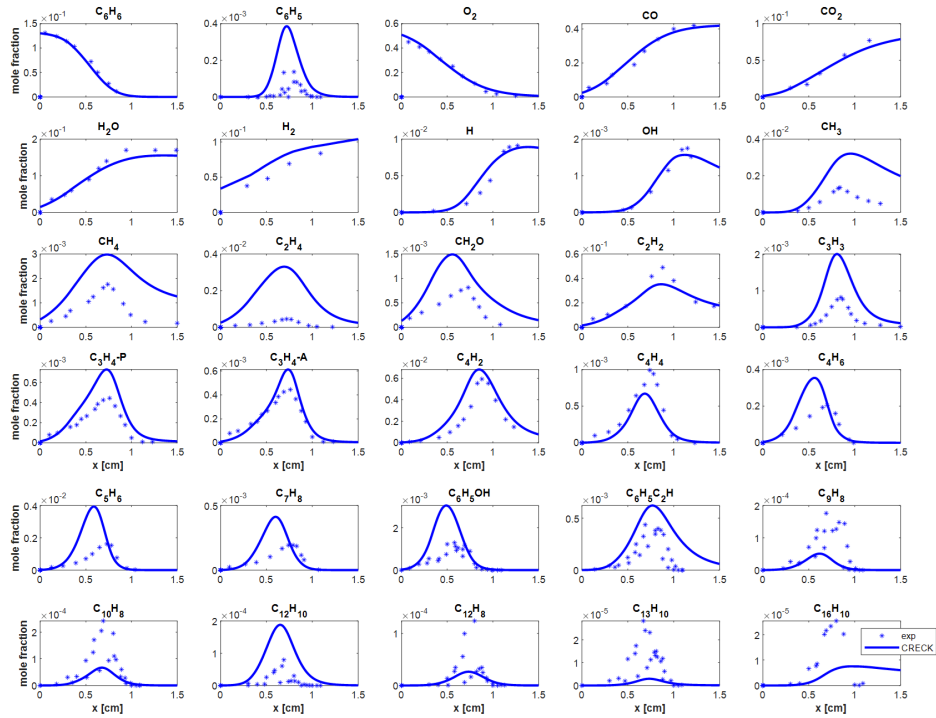


FIGURE 6.54: Experimental (dots) and simulated (lines) species profiles for benzene oxidation in the premixed rich low- p flame of Bittner et al. [393].

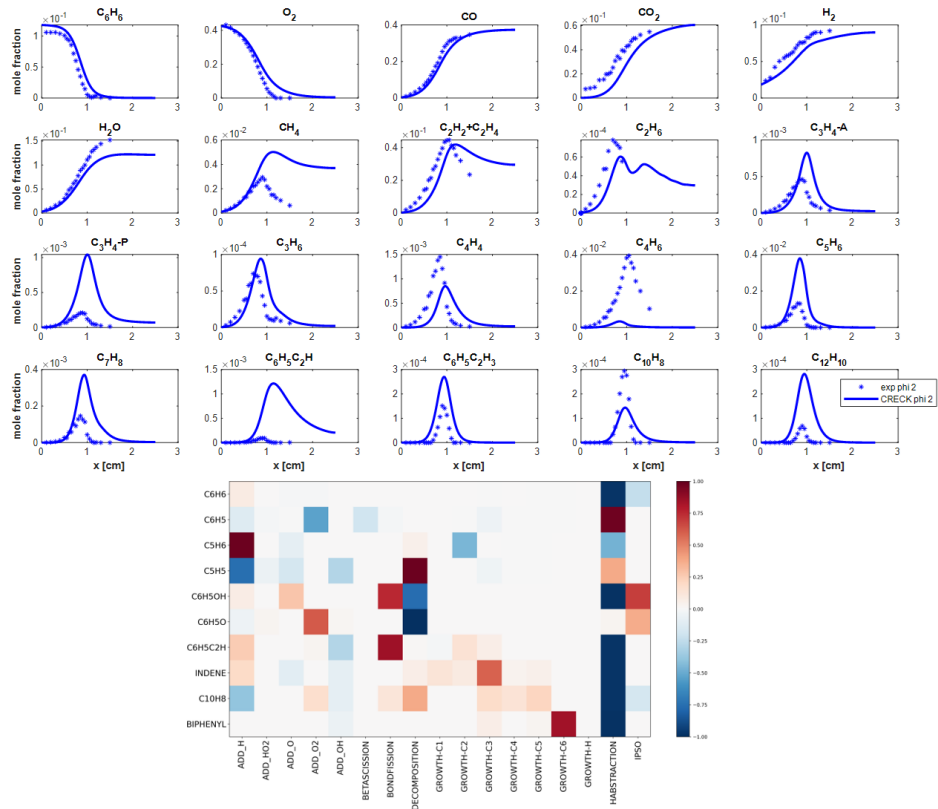


FIGURE 6.55: Experimental (dots) and simulated (lines) species profiles for benzene oxidation in the premixed rich low-pressure flame of Detilleux et al. [395] with class-type flux analysis for the relevant species (flux relative to the highest flux of each species, with a threshold of 1%).

6.6.1.4 Global oxidation reactivity

Figure 6.56 shows kinetic simulations of the IDT for benzene oxidation in the ST experiments of Burcat et al. [385] and Da Costa et al. [386]. Kinetic simulations reproduce well the experimental data, underestimating the IDT (by a factor < 2) at fuel-rich conditions in the ST of Burcat et al. [385], similar to the trends observed in cyclopentadiene (Section 5.4.2). The slope for the benzene reactivity in the ST data of Da Costa et al. [386] is not very well captured by the model, especially at stoichiometric conditions. However, the data are also considerably scattered, suggesting high uncertainty.

The class type flux analysis at different Φ for the operating conditions of Burcat et al. [385] (2.44 atm, 1450 K) shows a similar scenario to that observed in flames, with smaller relevance for H-atom abstraction and bond-fission reactions in favor of decomposition and ipso substitution reactions. The relevant classes for cyclopentadiene and phenoxy radical are essentially unchanged with the equivalence ratio, with GROWTH-C2 (i.e., C_5H_6 decomposition) decreasing its importance at fuel-lean conditions in favor of ADD_O, similar to what was observed in cyclopentadiene oxidation. It is noted that both of these reactions were estimated. Phenol and cyclopentadienyl reactivity instead change more substantially with the equivalence ratio. Phenol decomposition is essentially irrelevant at fuel-lean conditions, while its production from ipso addition (from $C_6H_6 + O$) at fuel-rich conditions is replaced by consumption by the same class at fuel-lean conditions (see also Fig. 6.47). In fact, while $C_6H_6 + O$ is still active, phenol is largely consumed by $C_6H_5OH + H$ ipso substitution, producing $C_6H_6 + OH$. It is also noted that phenol is produced also from BONDFISSION $C_6H_5OH = C_6H_5 + OH$. This reaction was estimated (only at the high-pressure limit) in a previous version of the mechanism and certainly needs revision: VRC-TST calculations for this channel would enable ME simulations of the full C_6H_5OH PES studied in Section 6.3.2. At fuel-lean conditions, phenol is mostly produced by H recombination with phenoxy radical.

It is interesting to compare the reactivity of C_5 species with that in the IDT simulations for cyclopentadiene presented in Section 5.4.2. The main difference is that in benzene oxidation cyclopentadienyl radical is produced first (by decomposition of phenoxy radical). Additionally, the ADD_H pathway is reversed compared to C_5H_6 oxidation, i.e., it consumes C_5H_5 . Instead, H-atom abstraction reactions follow similar trends (although they are less relevant than in C_5H_6 oxidation) as well as ADD_O and ADD_OH.

Flux analysis by bimolecular reaction type highlights the increasing importance of unimolecular reactions at fuel-rich conditions, as well as of M+R (mostly H-atom abstraction and ipso substitution reactions) as opposed to R+R and R+RSR (recombinations), which prevail at fuel-lean conditions due to the larger radical pool.

Finally, the effect of pressure is shown in the comparison of heat maps at stoichiometric conditions and 1450 K at 2.44 atm and 8.5 atm (bottom panel of Figure 6.56). The faster reactivity at 8.5 atm is related to the higher H concentration, resulting in a more significant contribution of ADD_H and of phenol consumption by H ipso substitution and cyclopentadiene conversion via H-atom abstractions.

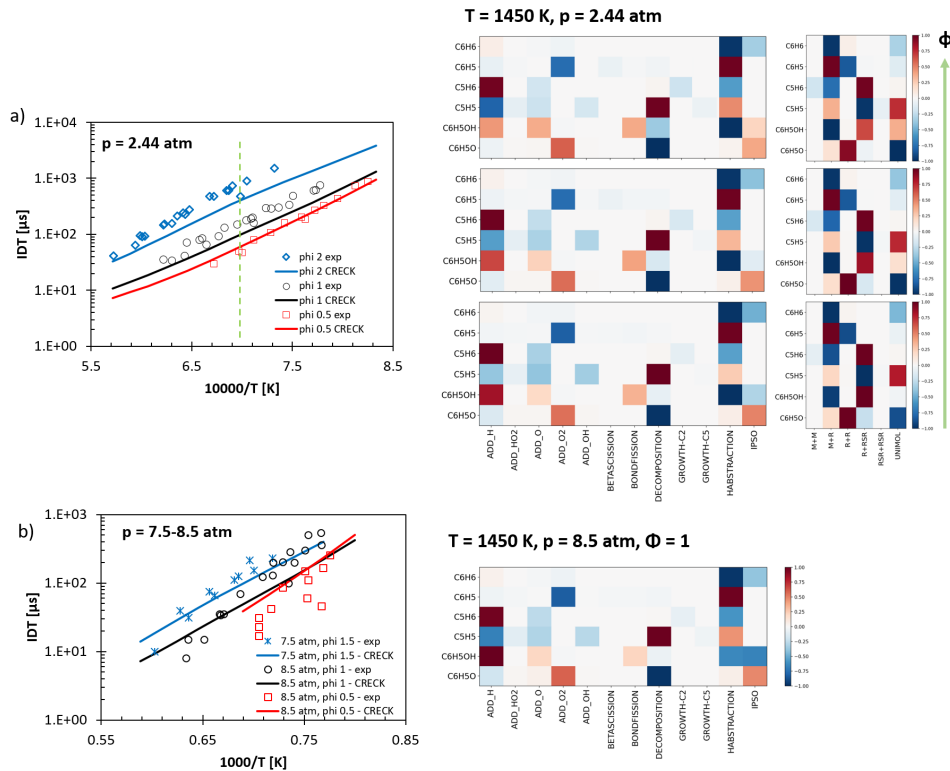


FIGURE 6.56: Experimental (dots) and simulated (lines) IDTs for benzene oxidation in the STs of a) Burcat et al. [385] and b) Da Costa et al. [386] with class-type flux analysis for the relevant species (flux relative to the highest flux of each species, with a threshold of 1%).

Figure 6.57a shows kinetic simulations of benzene laminar flame speeds at different initial temperatures from three different datasets [373]–[375] (see Table 6.39). The kinetic mechanism underestimates the LFS at fuel-lean conditions, with a shift in the peak of the LFS to $\Phi = 1.1$ – 1.2 , while better agreement is obtained at fuel-rich conditions. It is also noted that the apparent overestimation of the LFS measured by Ji et al. [373] at high Φ is probably due to difficulties in the experimental measurements, considering the consistency in the trends of Davis et al. [374] and of Johnston et al. [375], as well as the fact that experimental measurements of cyclopentadiene LFSs in the same reactor produced similar trends (Section 5.4.2).

The class type flux analysis of Figure 6.57b shows that the reactivity is similar to what was observed in IDT measurements, where the mechanism presents good agreement with experimental results at fuel-lean conditions, while it is too fast at fuel-rich conditions. This trend is consistent with what was observed for LFS predictions, however it is more evident in the LFS simulations. Compared to the IDT flux analysis, it is observed that 1) bimolecular reactions such as H-atom abstractions, ADD_H, ADD_O, and ADD_OH are more relevant in this case; 2) the effect of the equivalence ratio is stronger, such that ADD_O, ADD_O2, ADD_OH, and IPSO contribute to the consumption of species much more at fuel-lean conditions. This trend suggests that the underestimation of the LFS at fuel-lean conditions is probably related to ADD_O, ADD_OH or ADD_O2 classes, and in particular to a shift in the radical pool to oxygenated radicals rather than H atoms, which was also postulated

for some speciation premixed flame experiments.

Further inspection of the flaws of the model was performed with kinetic simulations where the $C_6H_5 + O_2$ reactivity (i.e., the main oxidation pathway of benzene) was replaced with a) the subset computed in this work using the $C_6H_5O + O / C_5H_4O + HCO$ BFs obtained from the calculations of Morozov et al. [353], favoring H production in the full range of temperatures (Section 6.3.3); and b) rate constants from the previous version of the CRECK mechanism, where the main products were $C_6H_4O_2 + H$ and $C_6H_5O + O$ (as in [303]), where the latter almost entirely reacts according to $C_6H_5O + O \rightarrow C_4H_5 + 2CO$ at a very high rate. Rate constants of this latter set are compared with the results of the present theoretical calculations in Figure 6.57c. Results obtained for the higher T flame are shown with dash-dotted and dotted lines in Figure 6.57a, respectively. It is interesting to note that changing the H/O BFs only decreases the LFS at fuel-rich conditions, thus slightly shifting the peak but not increasing the LFS. In fact, H production from $C_5H_4O + HCO$ is compensated by its consumption in the decomposition of the latter according to $C_5H_4O + H \rightarrow C_4H_5 + CO$. Other relevant consumption pathways for C_5H_4O are H-atom abstraction reactions by OH radicals, H and O atoms, which lead to decomposed product species. It must be mentioned that if C_5H_3O radical was included in the mechanism, its oxidation kinetics might be similar to that of C_6H_5 , as recently studied theoretically [447]. On the other hand, the subset of phenyl oxidation from the previous version of the CRECK mechanism results in excellent LFS predictions. This is due to the fact that the sub-mechanism for C_5 oxidation is completely "skipped", because of phenoxy radical direct decomposition to $C_4H_5 + 2CO$. Hence, the production of H atom is not compensated by subsequent reactions, while O atoms are largely consumed by $C_6H_5O + O$, which was however overestimated by one order of magnitude with respect to the present calculations (see Figure 6.57c). The present results again highlight the close interconnection between C_5 and MAH oxidation and suggest the need for further investigation of oxidation addition reactions, as well as H-atom abstraction from cyclopentadienone and possibly C_5H_3O oxidation with O_2 .

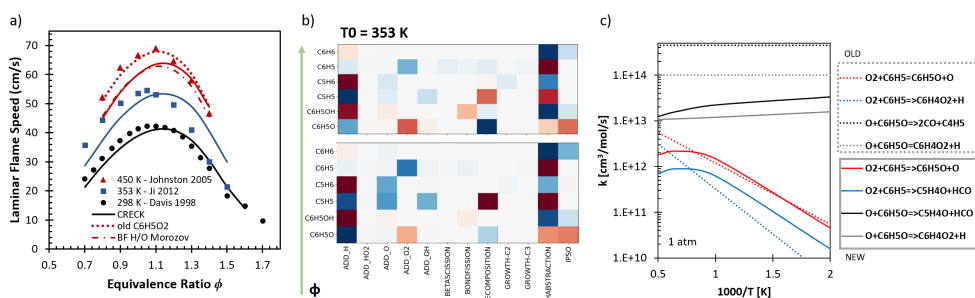


FIGURE 6.57: a) Experimental (dots) and simulated (lines) LFS of benzene at atmospheric pressure and different inlet temperatures (298 K [374], 353 K [373], 450 K [375]) with b) class-type flux analysis for the relevant species (flux relative to the highest flux of each species, with a threshold of 1%). Dotted and dash-dotted lines are modified versions of the mechanism (see main text for details). c) Compares the rate constants at 1 atm for $O + C_6H_5O$ and $O_2 + C_6H_5$ in the present (solid lines) and older (dotted lines) versions of the CRECK kinetic mechanism.

6.6.2 Oxygenated aromatics

6.6.2.1 Phenol

The kinetics of phenol pyrolysis is relatively simple. Kinetic simulations at the experimental conditions of the PFR of Brezinsky et al. [125] are compared with experimental measurements in Figure 6.58. The most abundant products are C_5H_6 and CO, followed by C_6H_6 , CH_4 , and C_2H_2 . The kinetic mechanism reproduces experimental profiles very accurately, with the exception of methane.

Heat maps and the schematic flux analysis of Figure 6.58 show that phenol is mostly consumed by unimolecular decomposition to cyclopentadiene and CO, which largely determine the corresponding product profiles. A significant fraction of phenol is consumed via bond-fission to phenoxy radical, which is also produced by H-atom abstractions by H and OH. Abstraction by OH in pyrolysis conditions is made possible by H ipso substitution on phenol, which ejects OH and produces benzene. Phenoxy radical decomposes to cyclopentadienyl radical, as in benzene oxidation, and cyclopentadienyl radical mostly grows to naphthalene via self-recombination or transforms into C_5H_6 via ADD_H, which converts back to C_5H_5 via H-atom abstraction reactions. The good agreement with experimental data is determined by 1) phenol molecular decomposition and bond-fission, which determine the generation of H atoms in the system, 2) probably correct balance in H consumption/production by H ipso substitution, recombination, and H-atom abstraction reactions. All of the reaction pathways relevant for the determination of H atom concentration shown in Figure 6.58 were computed theoretically in this work, with the exception of $C_5H_5 + H$. Underestimation of methane is related to CH_3 radicals. CH_3 is produced from $C_5H_5 + C_5H_6 \rightarrow C_9H_8 + CH_3$, from tetralin decomposition, and from $C_3H_4-P + H$, where the latter comes from cyclopentadiene decomposition. The estimated rate of cyclopentadiene unimolecular decomposition was already highlighted as a potential source of uncertainty in the cyclopentadiene subsystem.

The species type heat map analysis of Figure 6.58 also shows that the reactivity is dominated by A1,OH-M, A1O-RSR, and C5X species types. Hence, phenol decomposition is almost entirely controlled by the presence of the hydroxy substituent.

Another validation for the reactions theoretically computed in this work was obtained by comparing simulated and experimental CO and H profiles in the high- T diluted ST experiments of phenol decomposition by Horn et al. [132], as shown in Figure 6.59. In this case, bimolecular reactions play a minor role in the reactivity due to the very diluted conditions. It is noted that the M+R class of the heat map forms radicals, i.e., it proceeds in the direction of bond-fission. Phenol consumption in this case is dominated by bond-fission, due to the higher temperature. The good agreement of both CO and H profiles supports the validity of the theoretical calculations integrated in the mechanism.

The relevance of benzene in phenol decomposition increases in the presence of hydrogen, due to the higher rates for H ipso substitutions. This is evident in the PFR experiments of Manion and Louw [415], who diluted phenol and water ($\sim 6\%$ and $\sim 3\%$) in hydrogen. Species profiles of Figure 6.60 show that benzene is the main product (40–50% of carbon selectivity), followed by C_5H_6 and CO. Despite the overprediction of phenol conversion in the

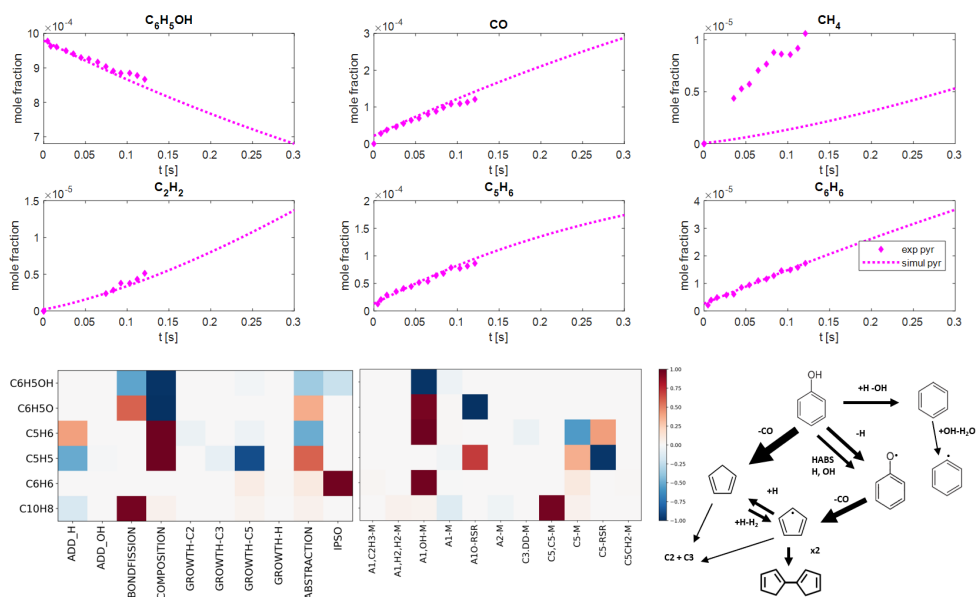


FIGURE 6.58: Experimental (dots) and simulated (lines) species profiles of phenol pyrolysis in the PFR of Brezinsky et al. [125] with class-type and species-type global flux analysis (flux relative to the highest flux of each species, with a threshold of 1%).

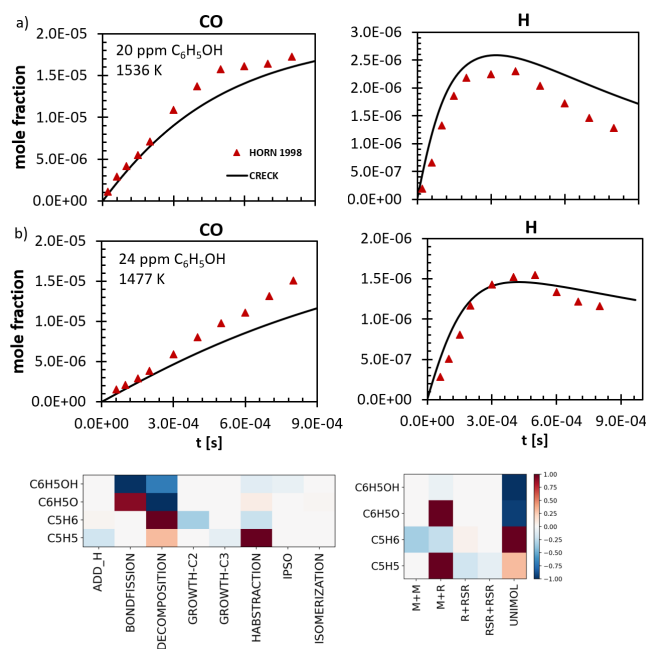


FIGURE 6.59: Experimental (dots) and simulated (lines) CO and H profiles from phenol pyrolysis in the ST of Horn et al. [132] with class-type and bimolecular type global flux analysis for the relevant species (flux relative to the highest flux of each species, with a threshold of 1%) at 1536 K (conditions of plot a).

kinetic simulations, the simulated profiles of the main products are in very good agreement with experimental data.

The heat map class type analysis of Figure 6.60 shows that compared to pyrolysis conditions, H ipso substitution is the main phenol consumption pathway, followed by H-atom

abstraction reactions (by H). This is reflected in the class analysis for phenoxy radical. The scenario for C_5H_6 and C_5H_5 changes even more substantially with respect to pyrolysis conditions: ADD_H is almost irrelevant, while H-atom abstraction by H occurs in the reverse direction; similar to the pyrolysis case, C_5H_6 and C_5H_5 also grow to naphthalene and indene. GROWTH-C5 class includes both $C_5 + C_5$ and A1 + C_5 reactions, where the latter set is relevant because of the large amount of benzene. Additionally, $CYC_5H_8 = C_5H_6 + H_2$ reaction (a decomposition) and $C_5H_6 + H = CYC_5H_7$ consume cyclopentadiene. As a result, hydrogenated C_5 species become relevant in the reactivity. Their decomposition leads to linear and cyclic alkanes/alkenes which either decompose or undergo H-atom additions. Many of these pathways eventually form C_2H_4 or CH_3 and therefore CH_4 , which well predicted by the model, in contrast with the pyrolysis case. Another important source of CH_3 are growth reactions of [A1-M][ADD_C5-M/RSR] classes, less relevant in pyrolysis conditions. On the other hand, C_2H_2 is only a minor product fraction, as it derives from direct C_5H_6 decomposition or H-atom addition to C_5H_6 . It is noted that the net small flux of ADD_H for C_5H_6 in the heat map derives from compensation effects of addition reactions consuming it (to CYC_5H_7 , LC_5H_7 , $C_2H_2 + C_3H_5$ -A), and producing it ($C_5H_5 + H$).

$C_{10}H_8$ simulated profile shows a peak that is not detected experimentally. In the kinetic mechanism, this is related to C_5H_5 concentration, which mostly governs its formation and also shows a peak at the same temperature. Consumption of naphthalene with various H additions, only estimated in the kinetic mechanism, may also contribute to this discrepancy. Experimental measurements also detect minor fractions of other aromatic products, such as $C_{14}H_{10}$, C_7H_8 , deriving from the growth of smaller species (often through [A1-M][ADD_C5-M/RSR] class). Overall, the predictions of the kinetic model for these species profiles is satisfactory, with maximum discrepancies of about a factor of 2.

Only two sets of experimental data are available for phenol oxidation, namely the PFR speciation data of Brezinsky et al. [125] and the RCM IDT measurements of Büttgen et al. [54]. Figure 6.61 compares the experimental and simulated species profiles for the PFR at 1173 K. Important products also detected in pyrolysis are also relevant in oxidation conditions, such as C_5H_6 , C_6H_6 , $C_{10}H_8$. However, the yields of smaller species such as CO, CO_2 , and C_2H_2 significantly increase with respect to pyrolysis conditions. Lean conditions accelerate the conversion and decrease naphthalene yield in favor of non-cyclic species at fuel-rich conditions. The model completely fails to predict phenol conversion: even shifting the data by -0.1 s does not allow us to reproduce the conversion satisfactorily. Hence, product profiles are reported as a function of conversion for comparison with experimental data. Early CO_2 formation might be related to unknown reaction pathways, as was also observed in anisole pyrolysis experiments, or it might be an effect of the experimental apparatus. The kinetic mechanism overpredicts the yields of cyclopentadiene and naphthalene at high conversion, while all the other products are underestimated, especially CO, CO_2 , and C_4H_6 .

The heat maps by class type and the flux analysis of Figure 6.62 guide the interpretation of the model. At fuel-rich conditions, the reactivity is analogous to pyrolysis, with slightly higher relevance of bimolecular reactions such as H-atom abstractions, ipso substitution, and ADD_H as a consequence of the larger radical pool. This effect is extremely enhanced at

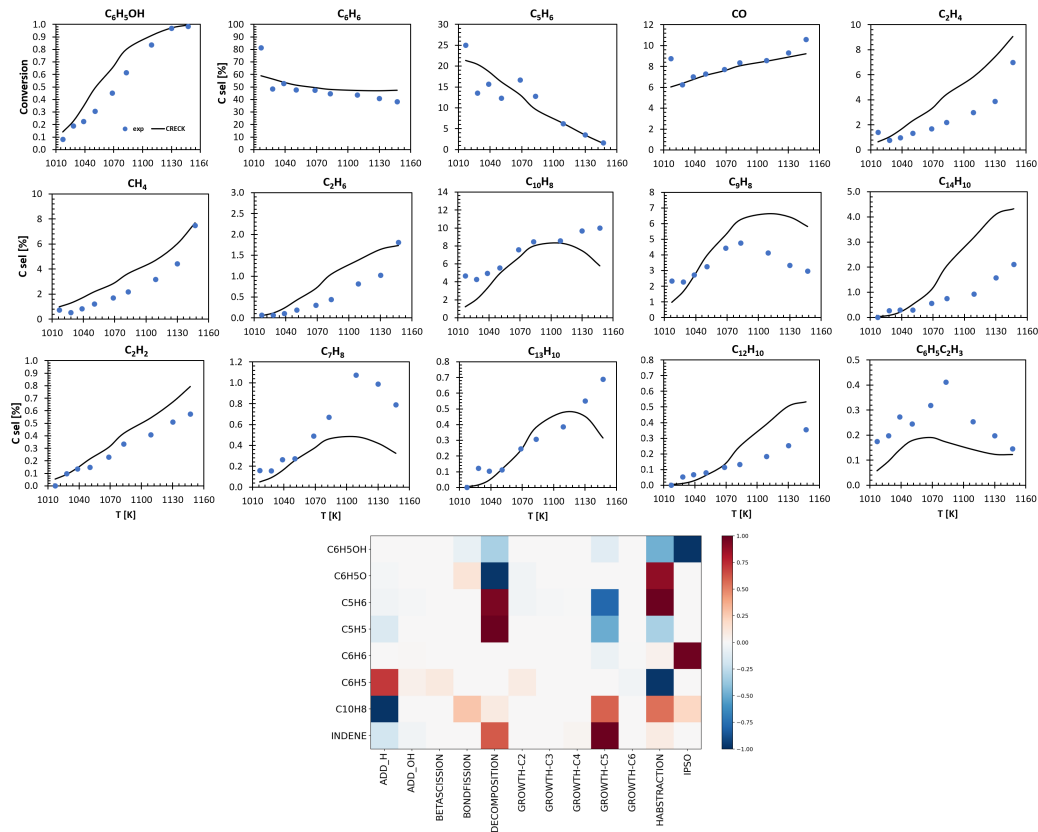


FIGURE 6.60: Experimental (dots) and simulated (lines) species profiles from phenol hydrogenolysis in the PFR of Manion and Louw [415] with class-type flux analysis for the relevant species at 1100 K (flux relative to the highest flux of each species, with a threshold of 1%).

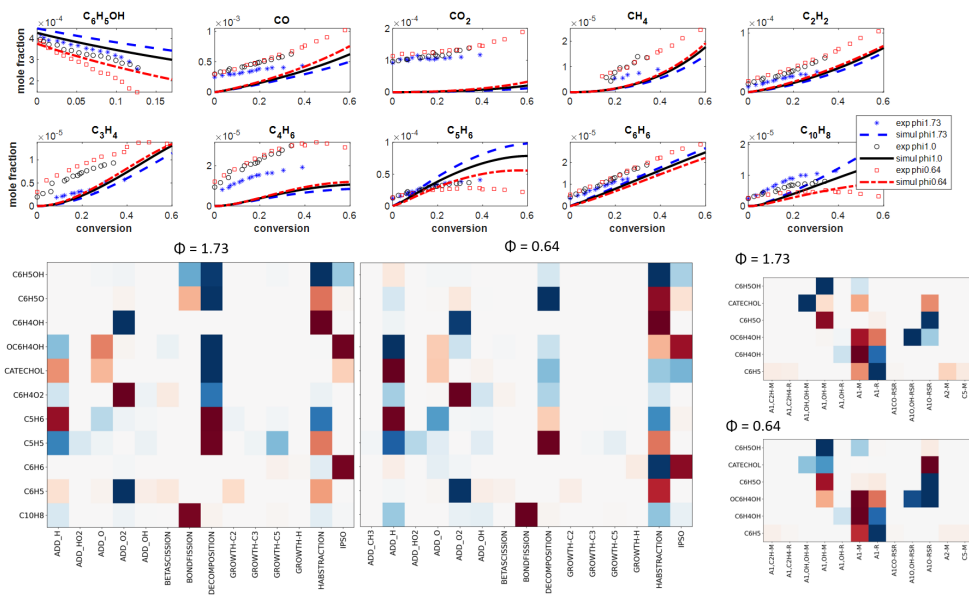


FIGURE 6.61: Experimental (dots) and simulated (lines) species profiles from phenol oxidation in the PFR of Brezinsky et al. [125] (1170 K, 1 atm) with class-type and species-type flux analysis for the relevant species at different equivalent ratios (flux relative to the highest flux of each species, with a threshold of 1%).

fuel-lean conditions, where decomposition reactions have a more marginal role. Figure 6.62 shows that the two main differences with respect to pyrolysis are oxidation reactions with O_2 and O , and the formation of C_6H_4OH from H-atom abstraction reactions from phenol ring, also inferred from the relevant role of A1-M species type in phenol consumption at $\Phi = 0.64$ (heat maps of Figure 6.61).

Relevant classes for C_6H_4OH and C_6H_5 are similar and involve consumption by ADD_O2. In fact, the reactivity of the former was derived from the latter. A1,OH-R also plays a role in C_6H_4OH consumption: the [A1,OH-R][REC_O2_EL_OH] reaction produces benzoquinone (Figure 6.62), which then decomposes to oxygenated C_5 species. On the other hand, the reactivity of OC_6H_4OH , mostly produced from the oxidation of hydroxyphenyl, is different from that of phenoxy radical: unimolecular decomposition plays a minor role with respect to [A1O,OH-RSR][REC_O2_EL_HO2], made possible by the presence of the two vicinal O and OH groups. At fuel-lean conditions, the A1O-RSR species type becomes more relevant because of the higher concentration of H atoms, which results in the production of catechol via [A1O-RSR][REC_H_WELL]. Finally, catechol has a very different reactivity from phenol, as it mostly decomposes via H transfer and subsequent ring opening, a reaction pathway of A1,OH,OH-M. At fuel-lean conditions instead, bimolecular consumption reactions typical of A1,OH-M types also contribute to the reactivity, (H-atom abstraction and ipso substitution reactions).

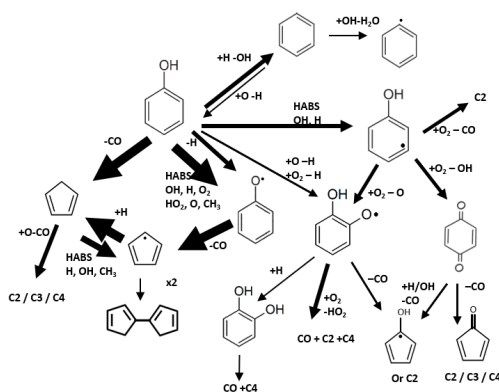


FIGURE 6.62: Global flux analysis for phenol oxidation at stoichiometric conditions in the PFR of Brezinsky et al. [125].

Figure 6.63 shows the sensitivity analysis run at stoichiometric conditions. Sensitive reactions for phenol, cyclopentadiene and benzene include unimolecular decompositions and bond-fissions, ipso substitution, and H-atom abstraction reactions, as well as $C_5H_5 + HO_2$, all of which were computed theoretically in this work, with the exception of $O + C_5H_6$ (estimated) and $FC_{10}H_{10}$ (lumped in Section 4.4.3). CO_2 , C_2H_2 and C_4H_6 are also sensitive to O_2 addition to C_6H_5O , C_6H_4OH , OC_6H_4OH , and C_6H_5OH . All of the small product species are increased by phenol bond-fission because of the H radical generation, similar to all other products, however they decrease due to the abstraction by OH from phenol forming phenoxy radical, which preferentially decomposes to C_5 species.

Overall, while it is unlikely that the model tuning would lead to significantly better

agreement with experimental data, especially for phenol conversion, the slow consumption of phenol also common to benzene oxidation and other systems (benzaldehyde, catechol, and anisole, as shown below) indeed highlights potentially significant shortcomings in the kinetic mechanism for phenol oxidation.

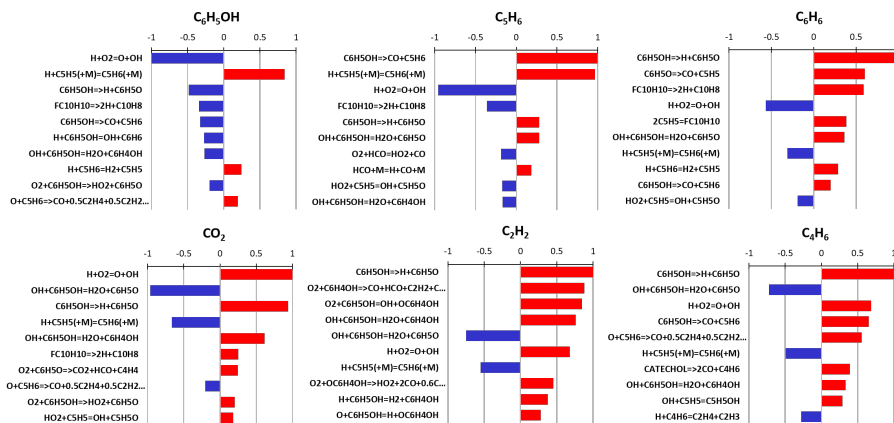


FIGURE 6.63: Global sensitivity analysis for the relevant species detected in phenol oxidation at stoichiometric conditions in the PFR of Brezinsky et al. [125].

Figure 6.64 shows the simulated IDT of phenol at stoichiometric and lean conditions in the RCM experiments of Büttgen et al. [54]. In this case, the model shows excellent predictions for the IDTs obtained with 20 bar experiments, while slight deviations are found at lower pressure. This trend certainly disagrees with the strong underestimation of the conversion in PFR oxidation. Heat map flux analysis shows that in this case fuel consumption occurs mostly via H-atom abstractions by OH and HO₂; on the other hand, abstraction by O₂ proceeds in the reverse direction, in contrast with the PFR case.

The larger concentration of radicals results in production of phenol via H recombination with phenoxy radical and the general high importance for ADD_H and IPSO classes. Additionally, the large amounts of C₆H₄OH and OC₆H₄OH are almost entirely consumed via ADD_O2, and also ADD_HO2 plays a role, while unimolecular decomposition reactions are less relevant. Large consumption of OC₆H₄OH via ADD_O2 is due to specific A1O,OH-RSR classes involving HO₂ and OH elimination. Rate constants for these classes were estimated, as well as those for [A1O-RSR][ADD_O2]. The rate constant for C₆H₅O + O₂ = C₆H₄O₂ + OH is more than one order of magnitude lower than the estimate of Narayanaswamy et al. [446], adopted in a previous version of the mechanism. Changing this rate constant would considerably change the consumption pathways for phenoxy radicals, and it would result in shorter IDTs by a factor of 2–5, as shown in Figure 6.64. Accelerating this rate however would not improve the agreement with the PFR data or other OAH oxidation experiments (i.e., benzaldehyde, catechol, and anisole). Indeed, the ADD_O2 and ADD_HO2 classes require more attention to understand their role in the reactivity at intermediate temperatures.

6.6.2.2 Catechol

The decomposition and oxidation of catechol was extensively studied in PFR experiments by the group of Wornat. Kinetic simulations of experiments on catechol co-pyrolysis with

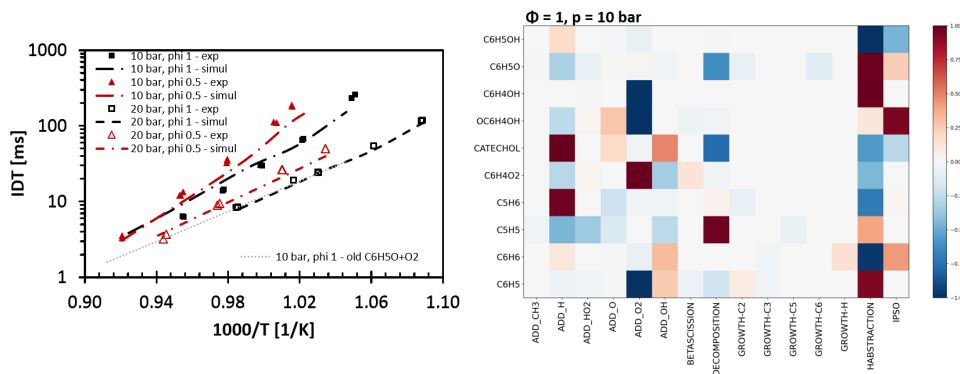


FIGURE 6.64: Experimental (dots) and simulated (lines) IDT of phenol oxidation in the RCM experiments of Büttgen et al. [54] with heat maps for the reaction class analysis at $\Phi = 1$, $p = 10$ bar, $T = 1200$ K (flux relative to the highest flux of each species, with a threshold of 1%).

other alkenes are not shown, as the results are very similar to the pyrolysis case.

Figure 6.65 shows species profiles for catechol pyrolysis in the PFR experiments of Thomas et al. [426], essentially identical to those of Figure 6.66 but also including measurements of 2-ring aromatic species. Catechol starts converting around 1000 K, and C_4H_6 and C_2H_2 have the highest yields, followed by C_4H_4 and C_2H_4 . Relevant cyclic products include C_5H_6 , C_6H_5OH , and C_6H_6 .

The kinetic simulations reproduce well the main product profiles, while C_6H_6 , C_6H_5OH and PAHs are underestimated. Additionally, CH_4 and C_3 yields do not follow the experimental trends, with changes in the slope around 1100 K.

The flux analysis depicted in Figure 6.65 and the heat maps depicted in Figure 6.66 show that the main conversion pathway for catechol is unimolecular decomposition to C_4H_6 and $2CO$ (rate constant from [134]). It is noted that this pathway is lumped as a single step, while in [442] CO elimination leads only to C_5H_5OH . Water elimination produces C_5H_4CO (as in [442]), which is assumed to partially decompose directly to C_2 – C_4 species to reproduce reasonably the experimental trends. Finally, decarbonylation –similar to phenol– forms C_5H_5OH , which then decomposes to C_4 species. Rate constants for this last pathway were adopted from phenol with no correction factors. Experimental C_4H_4 formation occurs at lower temperature than in the kinetic simulations: since C_4H_4 derives indirectly from the decomposition of C_5 species to C_4H_5 and particularly from C_5H_5OH , the correctness of the unimolecular decomposition for this system should be further assessed.

H-atom abstraction reactions from catechol (derived from phenol but with $E_A - 2$ kcal/mol, see Sections 6.4.4 and 6.5.2.4) produce OC_6H_4OH . The heat maps of Figure 6.66 show that compared to phenoxy radical, the unimolecular decomposition is considerably slower (as found in the theoretical calculations of this work, Section 6.3.3), in favor of the recombination with H atoms.

Phenol is formed from H ipso substitution on catechol, as studied in Section 6.5. Its decomposition produces C_5H_6 , as in phenol pyrolysis, while H-atom abstraction reaction by OH produces phenoxy radical. The ipso substitution on catechol can also form directly C_5H_6 due to the exothermicity of the reaction. The underprediction of phenol might be

explained by 1) overestimation of H-atom abstraction by OH and 2) overestimation of the reactivity of H in other reactions. For instance, $\text{OC}_6\text{H}_4\text{OH} + \text{H} \rightarrow \text{C}_6\text{H}_4(\text{OH})_2$ is the main source of H consumption; this rate constant was adopted from phenol system; however, it is probably slower, due to the higher stability of $\text{OC}_6\text{H}_4\text{OH}$. The formation of C_6H_6 and C_7H_8 mostly derives from the growth of smaller species. The underprediction of C_6H_6 is probably related to that of phenol, since H ipso substitution on phenol partially contributes to benzene formation.

Finally, the growth of $\text{C}_6\text{H}_5\text{C}_2\text{H}$, $\text{C}_6\text{H}_5\text{C}_2\text{H}_3$, C_9H_8 , and C_{10}H_8 occurs from oxygenated aromatic species (e.g., $\text{OC}_6\text{H}_4\text{OH}$ recombination). These reaction pathways are uncertain even in terms of product formation and their rate constants. They were all estimated in a previous version of the model, and were increased in the present work to better estimate experimental trends. The strong approximations result in relatively poor model predictions, such that future investigations are certainly encouraged.

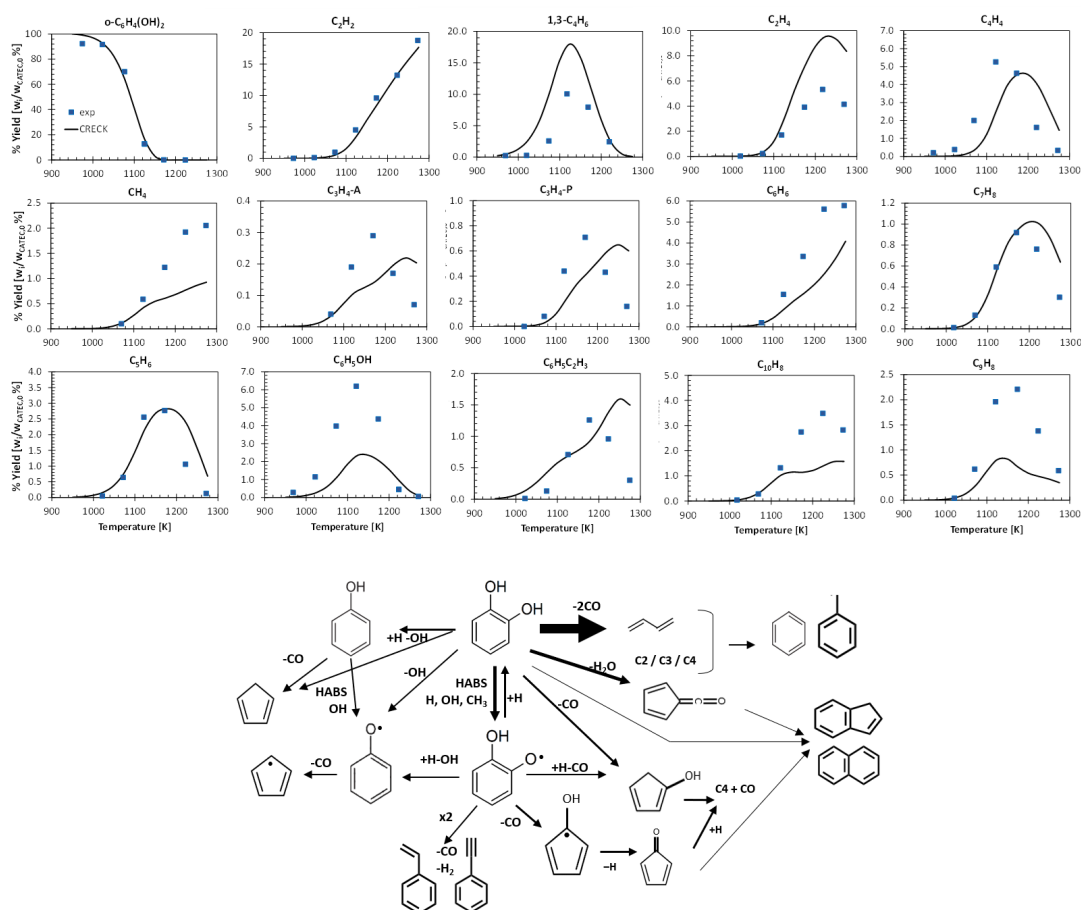


FIGURE 6.65: Experimental (dots) and simulated (lines) species profiles for catechol pyrolysis in the PFR of Thomas et al. [426] with flux analysis for the relevant species.

Figure 6.66 also reports the results for the kinetic simulations for catechol oxidation at different equivalence ratios. Indeed, the product distribution is not dramatically affected by the presence of oxygen, however a significantly larger amount of CO (and consequently CO_2 after complete conversion) is produced; the yields to C_2 – C_4 species –produced from direct

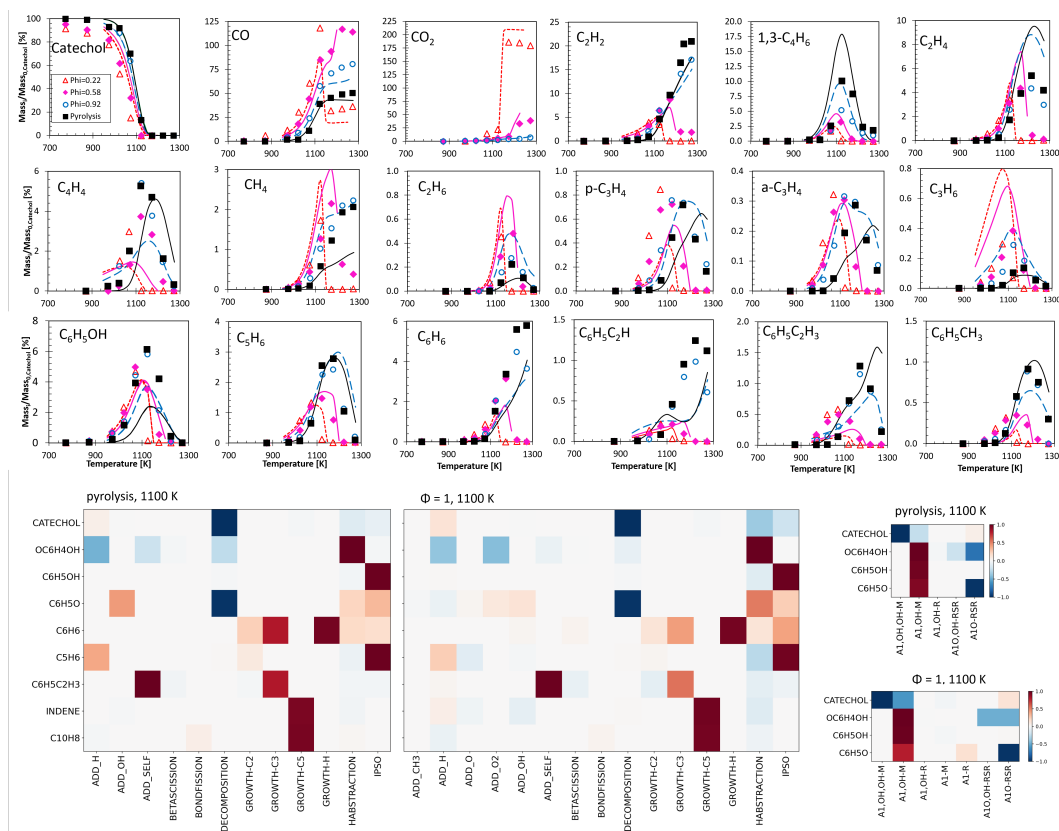


FIGURE 6.66: Experimental (dots) and simulated (lines) species profiles for catechol pyrolysis and oxidation in the PFR of Thomas et al. [424] with heat maps for class type and species type analysis for relevant species in pyrolysis and at stoichiometric conditions at 1100 K (flux relative to the highest flux of each species, with a threshold of 1%).

decomposition of catechol— and to cyclopentadiene, phenylacetylene, styrene and toluene decrease, while those to C_3 species, C_2H_6 and CH_4 increase. Overall, these trends are well reproduced by the model, which performs better in oxidation than in pyrolysis conditions. The main shortcomings of the model are early production of C_3H_6 and C_4H_4 .

The heat maps of Figure 6.66 show that compared to pyrolysis conditions, H-atom abstraction and ipso substitution reactions are more relevant due to the higher radical concentration, thus leading to higher concentrations of OC_6H_4OH and C_6H_5OH . The relative amounts of phenol and cyclopentadiene are well predicted, as well as the yields of other aromatic products. This better agreement suggests that unimolecular decomposition reactions of catechol, which largely determine predictions of pyrolysis experiments, need revision.

6.6.2.3 Anisole and guaiacol

This section presents the performance of the kinetic model for some relevant datasets of anisole and guaiacol pyrolysis and oxidation. The kinetic sub-mechanism for these species is extremely lumped according to a previous version of the mechanism [46], as also explained below. The main kinetic model updates performed in this work are H-atom abstraction and ipso substitution reactions.

Figure 6.67 shows experimental and simulated species profiles for relevant products for the anisole pyrolysis measured in Ghent's PFR [131]. Because of the low BDE of O-CH₃, anisole starts converting already at 800 K. The main aromatic products are C₆H₅OH, C₆H₆, HOC₆H₅CH₃ (cresol), C₆H₅CHO, and a small fraction of C₇H₈. A large amount of CO is also produced. Small products include CH₄ and C₂H₆. The model reproduces the main experimental trends, but overestimates all aromatic products besides phenol and benzofuran.

The flux analysis at 900 K of Figure 6.68 (derived for the JSR conditions presented later but also applicable to this case) guides the understanding of the formation of the main products according to the kinetic mechanism: anisole mostly dissociates via bond-fission to phenoxy radical and CH₃, or decomposes to C₅H₅CH₃ + CO, explaining the large amounts of CO, CH₄ and C₂H₆. Phenol can be formed from phenoxy or from H ipso substitution on anisole, while toluene mostly derives from CH₃ ring-enlargement from C₅H₅CH₃. Benzene and benzaldehyde are formed as lumped products of H-atom abstraction reactions from the methoxy group of anisole (C₆H₅OCH₂ radical is not included in the mechanism). Finally, cresol is formed via CH₃ recombination on the carbon sites of phenoxy radical.

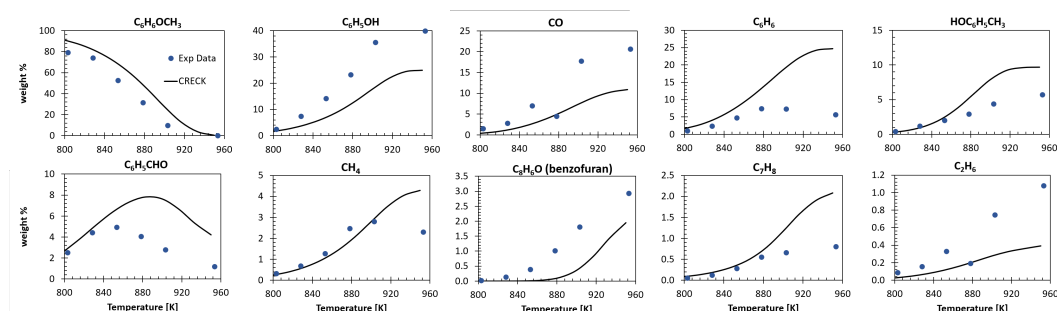


FIGURE 6.67: Experimental (dots) and simulated (lines) species profiles for anisole pyrolysis in the Ghent PFR [131].

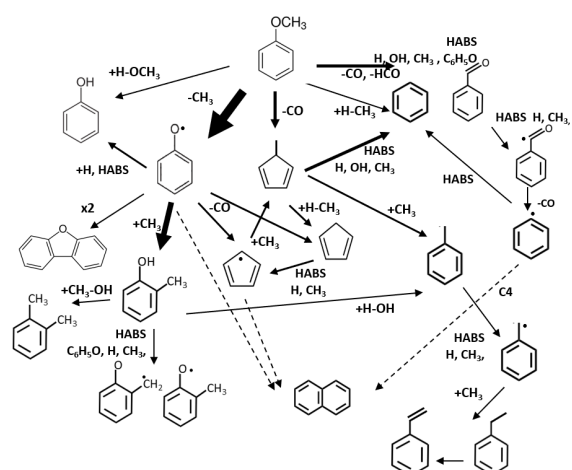


FIGURE 6.68: Flux analysis of anisole consumption in the JSR of Nowakowska et al. [51] at 900 K (~50% conversion).

Figure 6.69 presents the results for the JSR anisole pyrolysis experiments of Nowakowska et al. [51] (blue lines and symbols). The trends of the main product species are consistent

with the results for the PFR just presented, including the slight underestimation in the conversion of anisole. Experimental trends show an evident change in the reactive behavior corresponding to complete anisole conversion, i.e., ~ 1000 K, showing an inflection particularly evident in CO, CH₄, C₂ species, C₆H₅CHO, and C₆H₅C₂H₃. The kinetic mechanism (as well as other literature mechanisms [50], [51]) fails to reproduce this trend, resulting in a strong overestimation of CO, CH₄, C₄H₆, C₅H₆, and in the consumption of C₆H₆ and C₇H₈, which instead accumulate according to the experiments. Experimental profiles below 1000 K are better reproduced by the model, with general underprediction of small C₂–C₃ products.

This failure might be attributed to wrong or missing reactions describing the reactivity of the CH₃ radical. Its main production source is anisole bond-fission, however CH₃ is then involved in ipso substitutitons, H-atom abstraction, recombination and ring enlargement reactions. It is noted that the only simulated species profile which reproduces the experimental trend is C₆H₅C₂H₃. The flux analysis of Figure 6.68 shows that styrene derives from ethylbenzene, produced from C₇H₇ + CH₃.

The flux analysis of Figures 6.68 and 6.69 highlights the strong interconnection between anisole, phenol, phenoxy, benzene, benzaldehyde, toluene, cresol, and C₅ species. The CH₃ radical is key to the interconversion between species, and also leads to the formation of xylene. On the other hand, phenoxy radical leads to larger aromatics such as dibenzofuran and naphthalene via recombination reactions.

An important characteristic of the flux analysis not highlighted by the heat maps is that H-atom abstractions between aromatic species gain relevance, especially those by phenoxy-like radicals. The rate constants were all estimated with rate rules from the traditional approach of the CRECK modeling group.

The formation of C₂–C₄ products derives from different pathways. C₂ species mostly originate from methyl radicals, while C₃ species derive from decomposition pathways of C₅ rings such as C₅H₅CH₃; C₄ species are formed indirectly from addition and decomposition reactions of C₅ rings or aromatic species. In particular, C₄H₆ is formed from LC₅H₇ + CH₃, while C₄H₄ is formed from the decomposition of naphthalene; hence, their overestimation is directly linked to those of C₅H₆ and C₁₀H₈, respectively.

Overall, important model shortcomings which should be addressed in future investigations are:

- Primary reactions of anisole decomposition: in the mechanism, unimolecular decomposition and bond-fission pathways are estimated from other mechanisms and are pressure independent. Additionally, H-atom abstractions produce lumped products with fixed BFs between C₆H₆ and C₆H₅CHO, while experimental trends suggest that the onsets of benzaldehyde production is at lower temperature.
- C₅H₅CH₃ sub-mechanism (as highlighted in Section 6.6.1).
- HOC₆H₅CH₃ reactions: the sub-mechanism of cresol was entirely derived by analogy with phenol and toluene. The appropriateness of this choice should be better assessed, as the experiments suggest too early consumption of this species.

- Abstraction reactions between aromatic species: while some literature mechanisms do include such abstraction reactions, none of them were ever investigated theoretically.
- The impact of missing reactions of CH_3 with aromatic species (e.g., CH_3 recombination with the radicals of cresol) should be assessed.

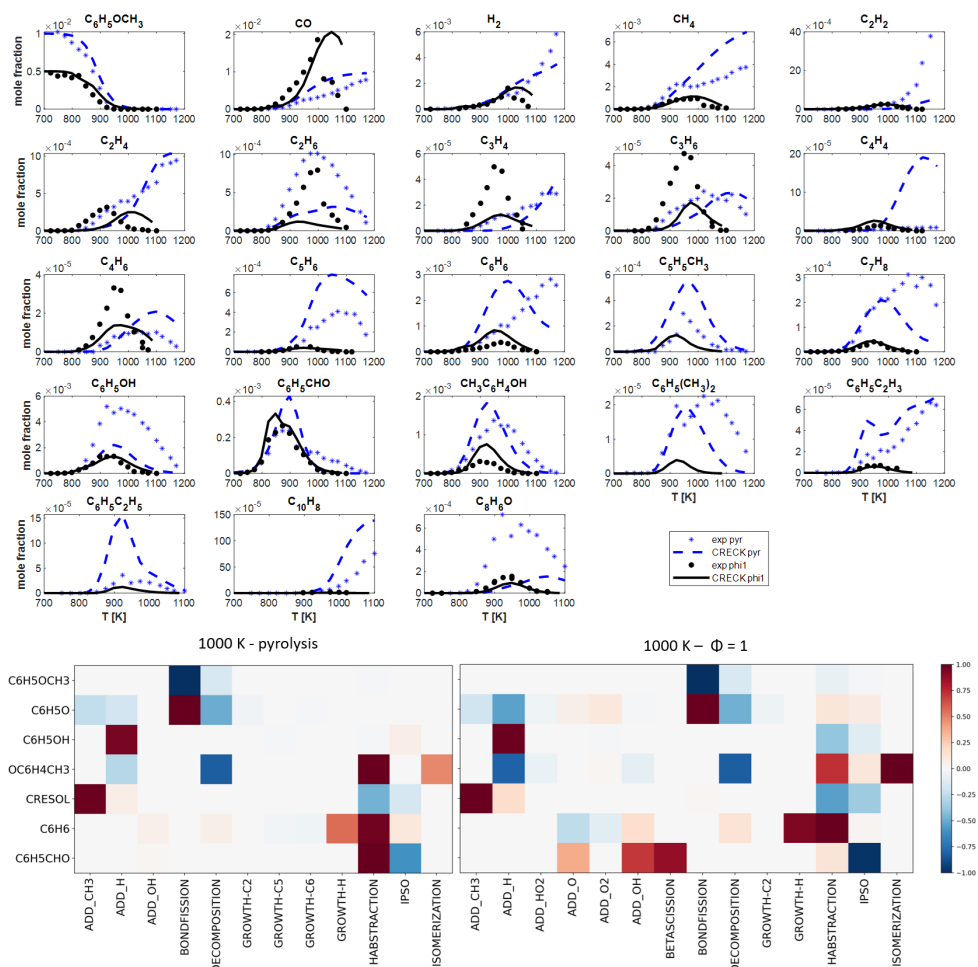


FIGURE 6.69: Experimental (dots) and simulated (lines) species profiles for anisole pyrolysis and oxidation ($\Phi = 1$) in the JSR experiments of Nowakowska et al. [51] with class type heat map analysis at 1000 K (flux relative to the highest flux of each species, with a threshold of 1%). Fluxes for pyrolysis are almost unchanged with respect to 900 K.

Figure 6.70 shows experimental and simulated species profiles for anisole oxidation at different equivalence ratios from the JSR experiments of Wagnon et al. [50]. The discussion also includes the stoichiometric oxidation experiments of Nowakowska et al. [51], which were performed at higher concentration of anisole (Figure 6.69).

The onset of anisole conversion in [50] is at around 900 K, which is a higher temperature than in the pyrolysis and oxidation data of Nowakowska et al. [51], as an effect of the more diluted conditions of the JSR of Wagnon et al. [50]. Anisole conversion as well as product profiles at incomplete conversion are barely affected by the equivalence ratio, and the main trends are the same as in pyrolysis conditions, including overprediction of C_6H_6 and C_{10} , of benzene consumption at high temperatures, and underprediction of C_3H_4 . On the other

hand, the kinetic model predicts very well C_2 and C_4 species profiles in the JSR of Wagnon et al. [50]. Overall, the kinetic model performance in [50] is better than in pyrolysis and in more concentrated oxidation conditions.

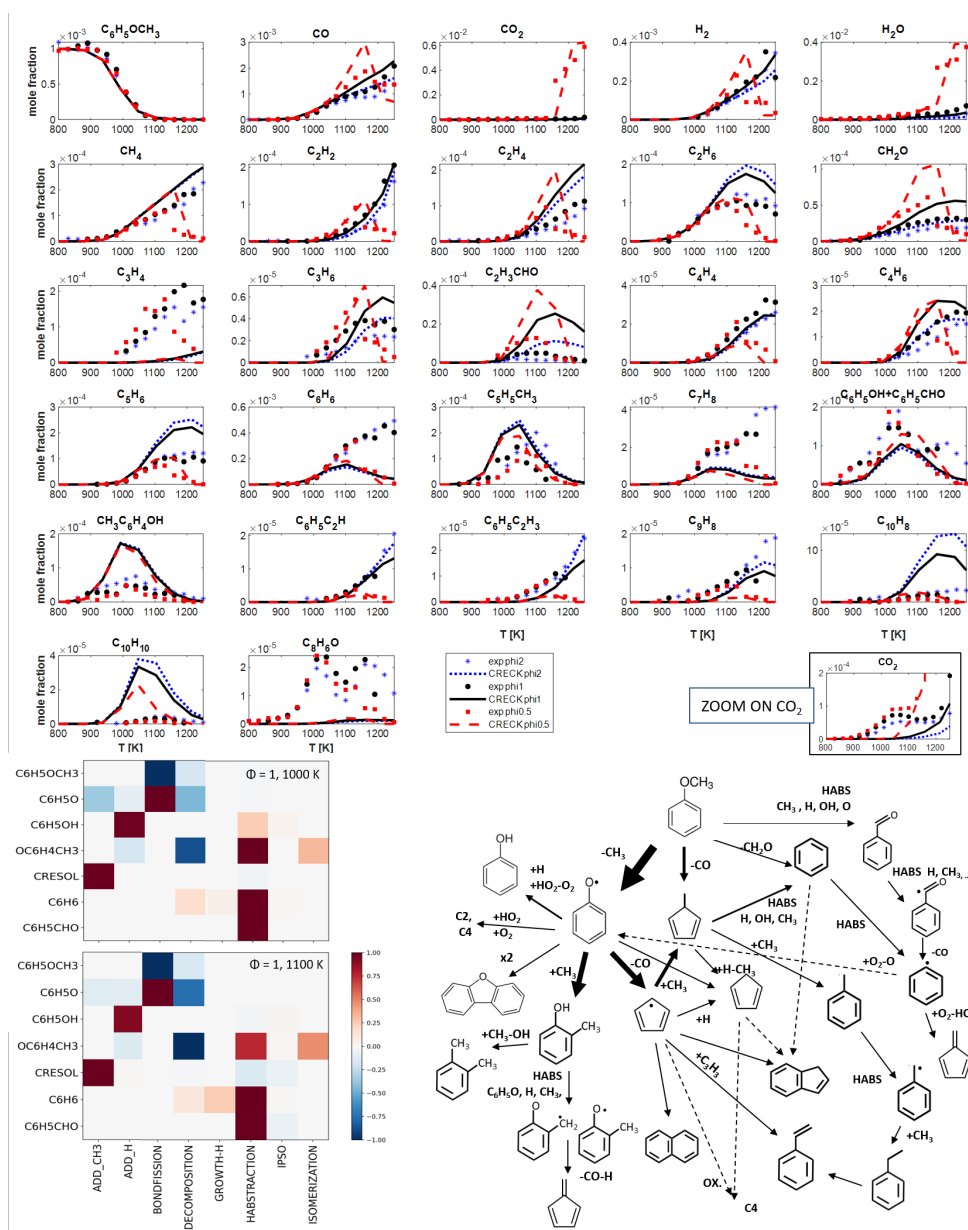


FIGURE 6.70: Experimental (dots) and simulated (lines) species profiles for anisole oxidation in the JSR experiments of Wagnon et al. [50] with class type heat map analysis at 1000 K and 1100 K at stoichiometric conditions (flux relative to the highest flux of each species, with a threshold of 1%) and schematic flux analysis at 1000 K.

The heat maps of Figure 6.70 and the schematic flux analysis show that ipso substitution reactions are definitely less relevant at more diluted conditions, as expected. H-atom abstraction reactions between aromatic species still appear in the flux analysis, as in the pyrolysis case, however they only have a minor contribution to the consumption of the phenoxy radical. Conversely, some unimolecular decomposition reactions, in particular those

of phenoxy and methylphenoxy radical (belonging to the same species type) are more important, especially at higher temperatures (and complete anisole conversion). It should be mentioned that CH_3 recombinations with $\text{HOC}_6\text{H}_4\text{CH}_2$ and $\text{OC}_6\text{H}_4\text{CH}_3$ might be relevant at these conditions (as it was the case for benzyl and phenoxy radicals), however it is not included in the mechanism because the corresponding product species are missing.

Because of the smaller importance of some bimolecular reaction classes, the formation pathways of small species and PAHs also change. In particular, C_2 and C_4 species are formed from C_5 and A1 oxidation reactions, especially from phenoxy radical oxidation with O_2 and HO_2 (estimated in the mechanism), and cyclopentadiene and cyclopentadienyl oxidation reactions (also estimated). The flux of Figure 6.70 also shows that phenyl radical can be oxidized with O_2 , and eventually form C_4H_5 . Also $\text{OC}_6\text{H}_4\text{OH}$ can be oxidized to C_4 species. Instead, C_3 species are mostly formed from $\text{C}_5\text{H}_5\text{CH}_3$ decomposition as in the pyrolysis case, and are in fact underestimated. Similarly to the findings of Wagnon et al. [50], early formation of CO_2 in oxidation conditions (zoomed at the bottom of Figure 6.70) is unexplained by the mechanism. Finally, the larger amount of C_5 species (mostly deriving from phenoxy radical decomposition) leads to substituted MAHs or PAH growth via GROWTH-C3 and GROWTH-C5 pathways.

The effect of the increase in the concentration can be inferred from the comparison of heat maps at stoichiometric conditions at 1100 K in Figure 6.70 and at 1000 K in Figure 6.69. While the main consumption pathways for anisole are essentially unchanged, at higher concentration ADD_OX classes appear in the flux analysis, unimolecular decomposition reactions decrease their relevance, while H-atom abstraction reactions and ipso substitutions consume accumulated molecular species. It must be noted that at 1000 K in the JSR of Wagnon et al. [50] (Figure 6.70) phenol is produced by H-atom abstraction reactions, and in particular by $\text{HO}_2 + \text{C}_6\text{H}_5\text{O}$; in the JSR of Nowakowska et al. [51] instead this reaction flux is compensated by the consumption of phenol by other abstraction reactions (with H, OH, and O_2).

Overall, kinetic model predictions in the oxidation experiments of Nowakowska et al. [51] are worse especially for small product profiles. Similar trends are obtained for the kinetic simulations of the JSR of Chen et al. [370], which occur at the most concentrated conditions (10^{-2} anisole mole fraction) and show extreme sensitivity to the $\text{HO}_2 + \text{C}_6\text{H}_5\text{O}$ (both abstraction and addition) reactions. Future model improvements should also focus on the formation of oxygenated PAHs: Chen et al. [572] were able to identify several oxygenated isomers, however only benzofuran and dibenzofuran are present in the kinetic mechanism.

Figure 6.71 shows kinetic simulations of the anisole IDT measured in the ST of Herzler et al. [431] and in the ST and RCM of Büttgen et al. [55]. Both datasets include IDTs at different pressures (10, 20, 40 bar) and stoichiometric conditions. Herzler et al. [431] also measured IDTs at $\Phi = 0.5$ (Figure 6.71b), however the effect of the equivalence ratio is almost negligible, consistent with the observations of JSR experiments [50].

The simulated IDTs are in very good agreement with experimental results, showing slightly slow reactivity for the ST experiments of Büttgen et al. [55]. Anisole reacts faster than both phenol (Figure 6.64) and benzene (Figure 6.56), consistent with its early onset of

conversion in both pyrolysis and oxidation conditions related to the low BDE of the methoxy lateral group.

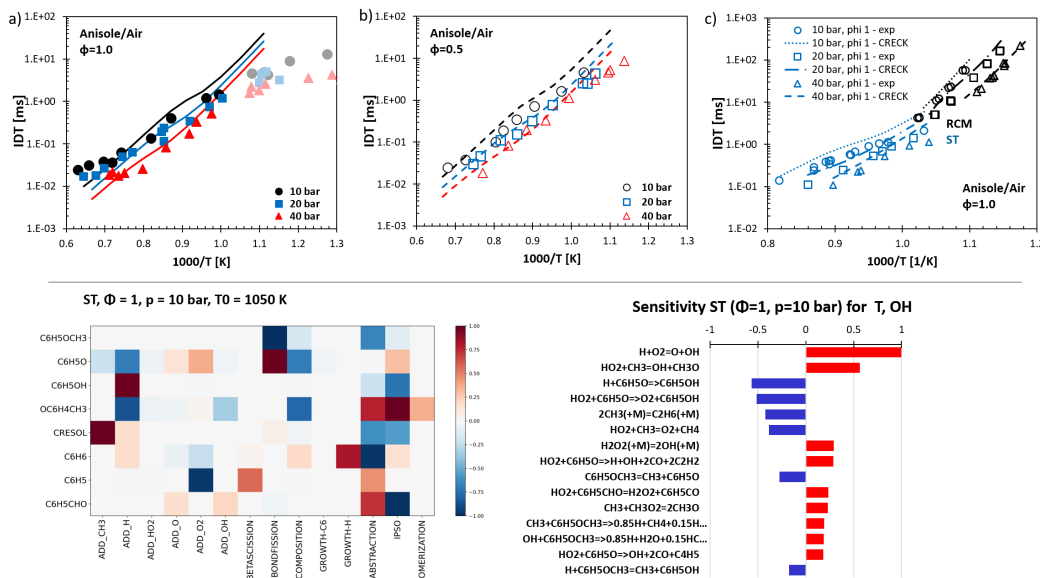


FIGURE 6.71: Experimental (dots) and simulated (lines) IDTs for anisole oxidation at a), c) stoichiometric and b) lean conditions at different pressures (10, 20, 40 bar) in the ST experiments of Herzler et al. [431] (a,b) and in the ST and RCM experiments of Büttgen et al. [55] (c). In a), shaded points correspond to low temperatures where ST measurements are unreliable. The bottom panel shows class-type heat map analysis for the ST of [55] and normalized sensitivity analysis for T and OH concentration ($T_0 = 1050$ K, $p = 10$ bar).

The heat map flux analysis at the bottom of Figure 6.71 shows that compared to the oxidation in JSR experiments [50], anisole is also largely consumed by H-atom abstraction reactions because of the higher radical concentration during the ignition. Overall, both H-atom abstractions and ipso substitutions are more relevant to species production and consumption. Consequently, benzene and benzaldehyde, and therefore phenyl radical, shape the reactivity of the system. In particular, benzene is consumed by H-atom abstraction reactions by H, OH, and O. The net flux for ipso substitutions produces benzene (from anisole and phenol), however IPISO_O on benzene is also a relevant formation pathway of phenoxy radical, as highlighted in the map. Phenoxy radical is also produced by ADD_O and ADD_O2, i.e., phenyl radical oxidation reactions. C_6H_5O is consumed by hydrogen bond-fission to phenol, unimolecular decomposition, and reverse H-atom abstraction by O_2 . While the net abstraction flux in the map is close to 0, this last reaction is extremely important for both phenoxy and overall radical termination. The key role of C_6H_5O is highlighted by the fact that $C_6H_5O + HO_2 / H$ are among the most sensitive reactions for the ignition of the system, as shown in Figure 6.71. The same reactions also control phenol ignition behavior, as discussed in Section 6.6.2.1 (Figure 6.64). Other sensitive reactions include anisole bond-fission and H-atom abstractions by CH_3 and OH from anisole.

Finally, Figure 6.72 shows the results for LFS measurements ($T_0 = 358$ K, $p = 1$ atm) of mixtures of anisole in air from the work of Wagnon et al. [50]. The present simulations strongly underestimate the experimental results ($\sim 3\text{--}6$ cm/s below the error bars). On

the other hand, kinetic simulations with the model of Wagnon et al. [50] are only slightly below the error bars. The heat map analysis in Figure 6.72 shows that anisole mostly converts via bond-fission and H-atom abstraction reactions. The higher relevance of ADD_H compared to IDT measurements is evident. It is noted that the phenoxy radical is almost entirely consumed by H recombination reactions to phenol. Therefore, in this case the net flux for H-atom abstraction reactions produces phenoxy, and $\text{HO}_2 + \text{C}_6\text{H}_5\text{O}$ is irrelevant. Similarly, benzene is produced from H-atom abstractions on anisole, and is entirely converted to phenyl radical via abstraction reactions, and then is produced back with ADD_H on phenyl. Phenyl radical converts to phenoxy and C_5 rings via ADD_O2. CH_3 recombination with the phenoxy radical to produce cresol is almost irrelevant in the flame.

The sensitivity analysis of Figure 6.72 shows that anisole LFS is controlled by reactions of cyclopentadienyl, phenoxy, phenyl, and only by one reaction involving anisole, i.e., the initial bond-fission. All fuel-specific reactions of the sensitivity analysis were updated in this work from theoretical calculations with the exception of $\text{C}_6\text{H}_5\text{OCH}_3 = \text{C}_6\text{H}_5\text{O} + \text{CH}_3$. These results suggest that the underestimation of the LFS for anisole is related to that of benzene (Figure 6.57). Figure 6.72 shows that the experimental results of Wagnon et al. 6.72 essentially match the benzene LFS measured at similar conditions by Ji et al. [373]. Similarly, kinetic simulations with the CRECK kinetic mechanism almost overlap at fuel-lean conditions.

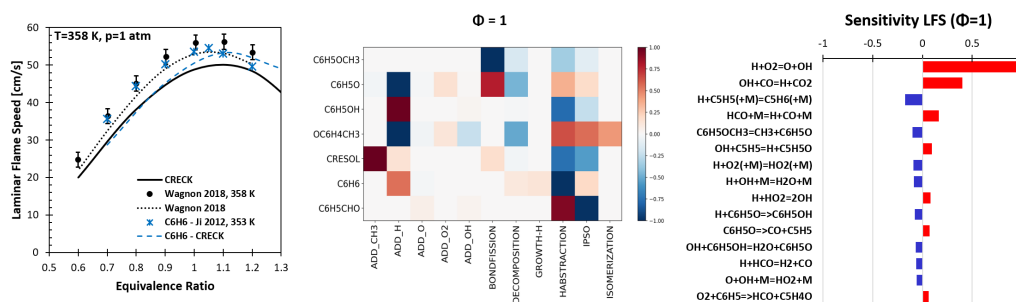


FIGURE 6.72: Experimental (dots) and simulated (lines) laminar flame speeds of anisole oxidation from the experiments of Wagnon et al. [50]. The dotted line reports simulations from [50], while blue stars and blue dashed lines refer to benzene LFS experiments at similar conditions (from Figure 6.57). A class type heat map analysis (flux relative to the highest flux of each species, with a threshold of 1%) and normalized sensitivity analysis for the mass flowrate at stoichiometric conditions are also reported.

To conclude, Figure 6.73 shows species profiles for guaiacol pyrolysis and oxidation in the JSR of Nowakowska et al. [45]. As anticipated in Section 6.1.2.4, the onset of guaiacol conversion is at temperatures as low as 700 K due to its low BDE. Catechol is the most abundant aromatic product, followed by salicylaldehyde ($\text{HOC}_6\text{H}_4\text{CHO}$), cresol, phenol, benzene, and benzaldehyde. Relevant small product species besides CO and H_2 are CH_4 and C_2 species, while C_3 and C_4 alkenes are less relevant. The addition of oxygen does not significantly affect the profiles of aromatic species, with the exception of catechol and salicylaldehyde, whose trends are inverted in pyrolysis and oxidation conditions. On the other hand, in oxidation conditions CO , H_2 , C_2H_4 , and C_3H_6 increase, as opposed to $\text{CH}_4/\text{C}_2\text{H}_6$, C_4H_4 , C_4H_6 , and C_5H_6 .

The kinetic mechanism performs pretty poorly in reproducing experimental trends. While guaiacol conversion and CO, CO₂, C₂H₆, and the main trends describing aromatic species are reasonably described, all other species highlight major model shortcomings, with some trends also common to kinetic simulations of catechol and anisole. This is not particularly surprising considering that the accuracy in the description of guaiacol decomposition kinetics is the lowest among all the aromatic species considered in this work, with all reactions (besides ipso substitution by H) estimated by analogy from other species or from the literature and potentially relevant tri-substituted intermediates are ignored.

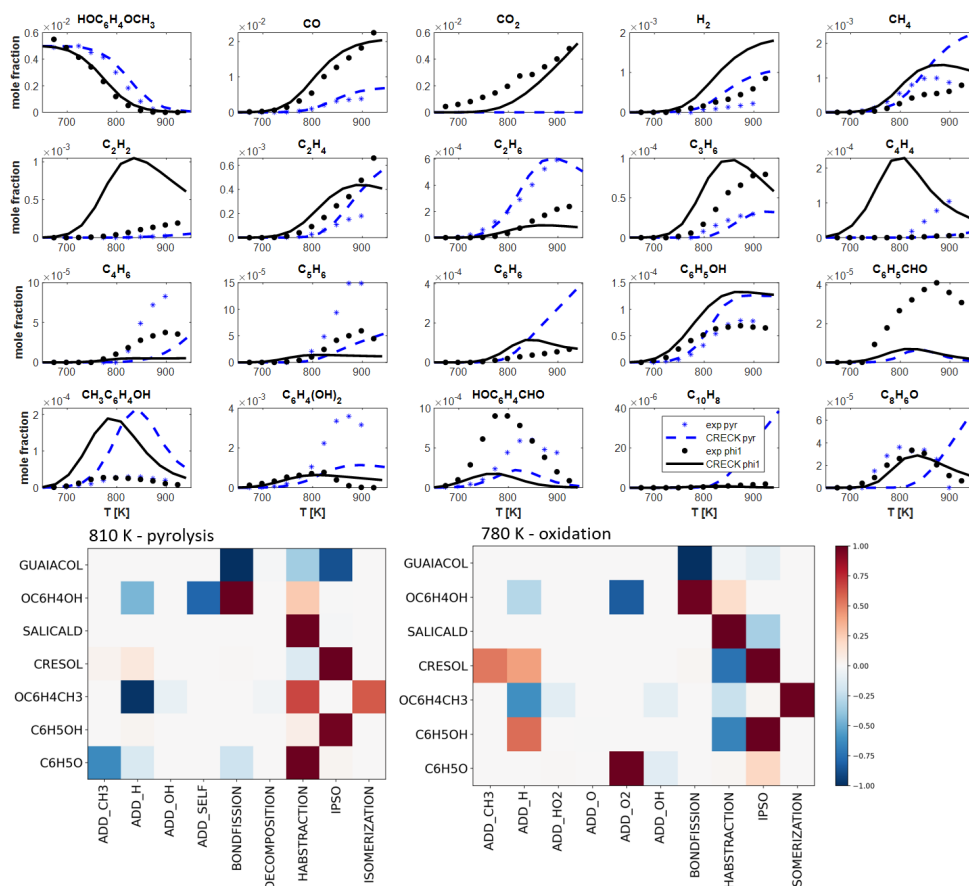


FIGURE 6.73: Experimental (dots) and simulated (lines) mole fraction profiles for guaiacol pyrolysis and oxidation at stoichiometric conditions in the JSR experiments of Nowkowska et al [45]. Class type heat map analyses (flux relative to the highest flux of each species, with a threshold of 1%) are also reported.

The heat maps of Figure 6.73 show that the reactivity is essentially dominated by abstractions, ipso additions, and a few recombination reactions with H and OH. The conversion of guaiacol is analogous to that of anisole, however in pyrolysis conditions H ipso substitutions to form cresol and phenol are almost as relevant as the bond-fission reaction. Hence, simultaneous production of OH and CH₃ radicals occur, such that the ADD_OH class also contributes to species consumption. In pyrolysis conditions, OC₆H₄OH converts to catechol, the most abundant aromatic product, via ADD_H, or to non-oxygenated aromatics via self-recombination (a heavily tuned reaction to match phenylacetylene and styrene product profiles in catechol pyrolysis). In the presence of oxygen, OC₆H₄OH reacts with O₂ (through

an estimated class of A1O,OH-RSR type) to lumped decomposition products, mostly C_4H_4 and C_2H_2 , which are clearly the reason for the overestimation of these species with respect to experimental data. Other di-substituted aromatics mostly convert via abstractions or ipso substitution reactions, finally decomposing to C_5 and smaller species.

Clarifying the kinetics of guaiacol decomposition and oxidation should shed light on relevant reactions of substituted resonance-stabilized aromatic radicals such as OC_6H_4OH , $OC_6H_4CH_3$, and $HOC_6H_4CH_2$. Prior to detailed kinetic mechanism development for these species, decisions on the actual level of detail for the model as well as the extent of product lumping should be made.

6.6.3 Summary

This section presented kinetic simulations of a wide range of experimental data for MAHs and OAH pyrolysis and oxidation, focusing on relevant reaction classes and potential directions for model improvement. Key aspects of the discussion are briefly summarized here.

Benzene pyrolysis starts at high temperatures, mostly via H-atom abstraction reactions by H. Phenyl then decomposes via ring-opening pathways to linear species and eventually C_2 and C_4 species. The growth of PAHs occurs via HACA pathways or aromatic ring additions. The model performance suggests that pressure effects, especially for the $C_6H_5 = LC_6H_5$ reaction, should be revised, as well as some of the rate constants for growth reactions ($A1 + C_3$, $A1 + A1$).

Benzene oxidation in flow reactors is controlled by HABS, IPSO_O, and ADD_O classes. Phenyl radical is mostly oxidized via ADD_O2, producing phenoxy radical. Phenoxy radical and phenol are also produced directly from benzene via ADD_O, and their interconversion is determined by ADD_H and HABS. In contrast, their decomposition produces C_5 species, which then decompose or oxidize to C_4/C_2 species. Growth pathways to naphthalene and indene mostly involve $C_5 + C_5$ and $C_5 + A1$ reactions, similar to cyclopentadiene oxidation. Most of the relevant reactions identified in the flux analysis were updated with theoretical calculations from this work. Overall, the model reproduces well experimental flow reactor oxidation data. C_5H_6 is slightly overestimated at fuel-rich conditions, while C_6H_5OH is overestimated especially at fuel-lean conditions. Higher concentrations of these species generally correspond to low C_2 – C_4 products. The better performances obtained at fuel-rich conditions suggest that imbalances in the radical pool may be due to reactions with $HO_2/O/O_2$. These limitations in the model also result in different trends with respect to experimental data as the initial concentration of benzene changes. Uncertain reactions never studied theoretically and therefore interesting for future investigations are

- $C_5H_6 + O$: often the main consumption reaction of cyclopentadiene, and an important source of C_2 – C_4 products in the oxidation of benzene and all OAHs.
- H-atom abstraction reactions from C_5H_4O and successive radical oxidation reactions: in the model, abstraction reactions were estimated and lead to decomposed products, contributing to the formation of C_2 – C_4 species.

- $C_6H_6 + O_2 = C_6H_5O + HO_2$, often present in kinetic mechanisms and relevant at high concentrations of benzene.
- Radical abstraction reactions between C5X-RSR (also highlighted in Section 5.4) and [C5X-RSR][ADD_O2], which are important at high concentrations and low temperatures.

At the higher temperatures and concentrations of premixed flame speciation experiments, H-atom abstraction reactions and ADD_H contribute the most to species consumption and interconversion. At lower pressures, unimolecular decomposition also plays an important role. In premixed flames, C_5H_6 and C_6H_5OH are slightly overestimated by the model, which is consistent with flow reactor data, however in flames the fraction of C_4 or C_2 species are often overestimated. Also in this case, these products derive from C_5 decomposition and oxidation reactions. Predictions for phenylacetylene often show inconsistent trends, i.e., overestimation or underestimation at similar experimental conditions. Among all PAH formation pathways, the HACA pathway included for phenylacetylene is the least lumped and strongly related to H equilibrium reactions. PAHs are generally well predicted.

The global reactivity of benzene in ST and LFS experiments shows a closer competition between H-atom abstraction reactions, ADD_H, ADD_O, ADD_O2, and IPSO. In ST experiments, the kinetic mechanism predicts too fast benzene ignition, especially at fuel-rich conditions. On the other hand, kinetic simulations significantly underpredict LFSs at fuel-lean conditions, while good agreement is obtained at fuel-rich conditions. This behavior was found to be strongly dependent on the sub-mechanism of C_5 oxidation: in LFS simulations, if $O + C_6H_5O$ were directly oxidized to $C_4H_5 + 2CO$ at a faster rate (as in an older version of the mechanism), excellent agreement would be reached with the experimental data. Since the present results predict that $O + C_6H_5O$ mostly produces $C_5H_4O + HCO$ with a relatively high exothermicity, the possibility of direct (prompt) dissociation of this product to $C_4H_4 + H + 2CO$, equivalent to the $C_4H_5 + 2CO$ channel mentioned above, will indeed be an interesting subject for future theoretical investigations.

Flux analysis highlighted the need for revision of similar reactions to those listed for flow reactor oxidation experiments. Other relevant reactions in need of further investigation are C_5H_6 unimolecular decomposition, competing with addition reactions, and recombination of O atom and OH radicals with C_6H_5 , forming phenol and phenoxy radicals.

Similar to the case of cyclopentadiene, besides more accurate estimates of the reactions listed, model optimization of relevant reactions (almost all computed theoretically) possibly including also microkinetic experiments (i.e., see Section 6.3.3), would probably help to solve some of the discrepancies.

The kinetic mechanism for OAH pyrolysis and oxidation is strongly connected with benzene and cyclopentadiene. Excellent model performances were obtained for phenol pyrolysis: the reactivity is entirely controlled by unimolecular decomposition, bond-fission, and H-atom abstraction by H, all computed theoretically in this work. Model performances are slightly worse when phenol decomposes in hydrogen: in this case, H ipso substitution on phenol is

the main decomposition pathway. The higher concentration of benzene largely contributes to A1 + C₅ growth class, which probably requires updating.

Phenol oxidation was not studied extensively. Phenol reactivity in RCM experiments in the 900–1100 K range is very well predicted by the model. The ignition is largely controlled by H-atom abstraction reactions by OH, HO₂, and O₂, with the latter proceeding in the reverse direction, similar to benzene. H-atom abstraction reactions or ADD_O and ADD_O2 reactions produce C₆H₄OH and OC₆H₄OH radicals: while their reactivity is partially derived from the corresponding A1-R and A1O-RSR species types, ADD_O2 or decomposition reaction classes controlling their consumption are specific to A1,OH-R and A1O,OH-RSR types, respectively. Products and rate constants for these species types as well as for [A1O-RSR][ADD_O], also relevant for decomposition to small products - were only estimated and require further investigation. Sensitivity analysis once again highlights the role of C₅H₆ + O reaction in the decomposition to small alkenes. Instead, the extremely slow conversion of phenol in PFR oxidation experiments, which seems related to the high phenol concentration in benzene oxidation experiments, highlighted potentially missing reaction pathways in phenol oxidation.

The kinetic mechanism of other substituted OAHs, i.e., catechol, anisole, and guaiacol, was less updated than the previous subsets and is less detailed. In all cases, the first decomposition steps are controlled by reactions characteristic of the lateral substituents: molecular decomposition in catechol, O–CH₃ bond-fission in anisole and guaiacol. Rate constants for the main consumption pathways of the fuels were estimated, while H-atom abstraction and ipso substitution reactions derive from theoretical calculations or analogy rules.

In catechol, unimolecular decomposition leads to C₄H₆ and CO. In the presence of oxygen and therefore larger amount of radicals, H ipso substitutions form large amounts of phenol. Both C₆H₅O and OC₆H₄OH are key to the reactivity, especially in oxidation conditions. The poorer predictions for pyrolysis conditions suggest the need to revise both unimolecular decomposition pathways and all growth reactions for OC₆H₄OH and oxygenated C₅ species, heavily approximated –and tuned– in the mechanism.

The analysis of the reactivity of anisole presents a great opportunity to investigate the sub-mechanism of decomposition and oxidation of C₆H₅O, formed very fast (and at low temperatures, i.e., ~800 K) from O–CH₃ bond-fission, as well as of OC₆H₄OH and OC₆H₄CH₃ resonance-stabilized radicals. Besides phenoxy radical and therefore phenol, anisole is directly connected to 1) benzene and benzaldehyde, produced from H-atom abstraction reactions, and 2) methylcyclopentadiene, formed from its molecular decomposition. Additionally, the large amounts of CH₃ radicals produced from the bond-fission also determine the relevance of the ADD_CH3 class, leading to cresol, toluene, and converting C₅H₅/C₅H₆ to C₅H₅CH₃. The abundance of CH₃ radical leads to CH₄ and C₂ species, while C₃/C₄ species derive from the decomposition of C₅ and aromatic species. In oxidation conditions, reactions of OAHs with O₂ also form C₂/C₄ species, which are better predicted by the model. Considering that anisole decomposition and oxidation kinetics depends on a large number of reactions including C₅ and many substituted MAHs and OAHs, the performance of the model is satisfactory. Highlights for future studies are:

- The model performance strongly depends on anisole concentration. This suggests shortcomings in bimolecular reactivity, particularly in relation to CH_3 addition to aromatics.
- Both $\text{C}_5\text{H}_5\text{CH}_3$ and cresol sub-mechanisms are approximate and needs revision. $\text{C}_5\text{H}_5\text{CH}_3$ decomposition leads to C_3 species, which are heavily underestimated.
- Flux analysis highlighted the relevance of abstraction reactions between aromatic species, which are sometimes suggested in the literature but never verified theoretically, and which not relevant in other OAHs decomposition experiments.
- Growth pathways to oxygenated PAHs should be added and revised.

As far as global reactivity is concerned, anisole ignites faster than both phenol and toluene, as expected from the low $\text{O}-\text{CH}_3$ BDE. Model predictions of IDTs are accurate. The ignition reactivity is almost entirely controlled by phenoxy radical interaction with HO_2 and phenyl oxidation. On the other hand, in LFS measurements phenoxy radical, still key to the reactivity, is produced from abstraction reactions and converts to phenol via H recombination. The simulated LFSs almost overlap with those obtained for benzene, and show the strong interconnection between the two systems, also in terms of the underprediction of the experimental results. Among all reactions from the LFS sensitivity analysis, only $\text{O}-\text{CH}_3$ bond-fission seems to have higher uncertainty, together with the $\text{C}_6\text{H}_5 + \text{O}_2$ reaction computed in Section 6.3.3.

Chapter 7

Conclusions and outlooks

For the past decades, fuel formulation and development have been driven by the kinetic modeling of simple compounds representative of complex fuel mixtures, allowing the characterization of combustion properties and pollutant formation. More recently, *ab initio* theoretical calculations to predict thermochemistry and kinetics became an essential tool for building kinetic mechanisms, thanks to increased computational power and the availability of automated codes for electronic structure calculations.

Recent theoretical and kinetic modeling efforts focused on the reactivity of monocyclic and polycyclic aromatic hydrocarbons (MAHs, PAHs). These compounds are precursors of soot, hence the understanding of their gas phase reactivity is essential to correctly predict soot emissions. While also produced from the incomplete combustion of conventional fuels, MAHs and in particular oxygenated MAHs (OAHs) are present in large amounts in biomass-derived biofuels, promising net-zero CO₂ high-energy density fuels for transportation.

Despite the interest in the kinetic modeling of the combustion of aromatic hydrocarbons, several challenges are still being tackled. In particular, *ab initio* theoretical calculations for aromatic systems are computationally expensive due to the large system size, and often involve complex and poorly automated aspects in the application of electronic structure methodologies. Recent theoretical calculations in the literature mostly focused on growth reactions to large PAHs rather than the underlying key MAHs kinetics and the competition with oxidation pathways. Besides the complexity of theoretical calculations, the multi-step reactivity of MAHs and PAHs generally involves large numbers of intermediate species, which is problematic for integration into global kinetic mechanisms aiming at relatively simple but possibly physical representation of the kinetics, and may even hinder their use for practical applications. Finally, also due to the lack of knowledge of relevant reactions in MAHs and PAHs pyrolysis and oxidation, no systematic model organization or classification was performed. Such organization proved essential to guide construction and performance improvement of kinetic mechanisms of more widely studied model compounds (e.g., alkanes).

In this context, this thesis presented a large number of theoretical calculations of relevant reaction classes for the pyrolysis and oxidation of aromatic hydrocarbons, critically assessing the validity of the theoretical methodologies adopted, and addressing the formulation of more or less complex rate rules for the extension of rate constants to similar compounds. The resulting rate constants were integrated into the CRECK kinetic mechanism mostly through a lumping approach specifically developed in this work to bridge detailed theoretical

calculations and global kinetic schemes. The kinetic model was also organized according to reaction classes for aromatic hydrocarbon pyrolysis and oxidation defined in the course of this work, focusing in particular on oxidation reaction pathways, guiding the understanding of model performances and highlighting directions of future improvements.

The main results are commented in the following sections, focusing on the future perspectives of the proposed approach and on the more general next challenges for theory-informed kinetic modeling.

7.1 Theoretical calculations and integration into global kinetic mechanisms

Sections 5.3, 6.3, 6.4, and 6.5 presented state-of-the-art theoretical calculations for relevant reactions of cyclopentadiene, indene, benzene, and substituted MAHs (phenol, toluene, anisole, benzaldehyde, ethylbenzene). An important contribution of this work is the critical evaluation of the sensitivity of the rate constants to the level of theory adopted. Relevant findings are listed below.

- T1 diagnostics was sometimes insufficient to determine the multireference character. In particular, unsuspected MR effects were found for the decarbonylation step in phenol decomposition (Section 6.3.2) and in the H-atom abstraction reaction by H from benzene (Section 6.4.3.1).
- Bimolecular reactions with torsional motions at the TS involving both fragments are extremely sensitive to the treatment of anharmonicities, resulting in large deviations for apparently simple reactions (H-atom abstraction reactions, see Section 6.4). In some cases, including anharmonic corrections to the zero point energy may impact the final barrier by 1 kcal/mol.
- The use of cartesian or internal coordinates for frequency calculation along the MEP may have a significant impact on the zero point energy and therefore the energy barrier of bimolecular reactions, especially when the transitional modes are low (e.g., H-atom abstractions by OH and O₂, see Section 6.4.3.10). The internal coordinate treatment seems more physically meaningful and therefore the more appropriate choice.
- VRC-TST calculations are often the only possible way to derive accurate theoretical rate constants for recombination reactions. Unfortunately, VRC-TST calculations are still poorly automated and results are significantly affected by the level of theory (Sections 5.3.2 and 6.3.3).
- The mystery of the reactivity of C₆H₅ + O₂ reaction, the most debated reaction of MAH oxidation in the literature, is partially still unsolved. Section 6.3.3 revealed the extreme sensitivity of the energy barrier for the insertion of oxygen in the aromatic ring, leading to very different results from recent literature calculations [353] performed at a similar level of theory. Computational power is probably still too low for a proper

theoretical treatment of this complex reaction. Hence, literature microkinetic ST experiments were used to aid in the derivation of the final rate constants.

The evaluation of the uncertainty of the theoretical methodologies applied in this work warns modelers with less experience in first-principle calculations against the misconception that a given level of theory always has the same degree of uncertainty, and that the strength of fundamentally-based kinetic mechanisms is their "internal consistency". In fact, the same theoretical methodology applied to different types of species and different reaction classes may indeed have a different degree of uncertainty, also considering various potential sources of error. This also applies to holistic theoretical approaches for kinetic mechanism generation, which therefore may have "imbalanced" uncertainties in the computed rate constants (and thermochemical properties).

The systematic theoretical investigations for H-atom abstraction reactions from benzene, phenol, toluene, anisole and ipso-substitution reactions on mono and di-substituted MAHs highlighted systematic trends within or between reaction classes, useful for rate-rule derivation. In particular:

- H-atom abstraction reactions (Section 6.4) from aromatic rings of benzene, substituted MAHs, and 2-ring PAHs are essentially identical. However, energy barrier corrections may be necessary for abstraction sites close to substituents able to form H-bonding like interactions with the abstractor, while entropy corrections should be applied in the presence of bulky substituents (OCH₃ or a second aromatic ring).
- Systematic analysis of H ipso-substitution reactions of OH, CH₃, HCO, OCH₃ and C₂H₅ groups (Section 6.5) revealed that the impact of a second lateral substituent has similar effects independently of the group being substituted, thus enabling inter-class rate rules derivation and possibly even extension to different class types (e.g., from ipso to H-abstractions).
- Energy barriers computed at higher (HL) and lower (L1) levels of theory (Section 6.4.4 and 6.5.3.1) for the same type of TS and species show systematic trends. The resulting scaling for energy barriers is very promising to obtain more accurate kinetic parameters for larger species (i.e., PAHs) when state-of-the-art ES methodologies are too computationally demanding.

The problem of including phenomenological but simplified description of the reactivity derived from complex multi-well potential energy surfaces into kinetic mechanisms was tackled with a new master equation-based lumping approach (Chapter 4). MEL treats the kinetics of single PESs, deriving lumped rate constants which group species with similar reactivity and skips unstable isomers. The effectiveness of this approach was shown with several successful examples. MEL was also extensively used for the updating of the CRECK kinetic mechanism with theoretical calculations from both this work and the literature.

An important future development of MEL is the automatic selection of pseudospecies, which will enable a simpler integrated workflow from theoretical calculations to kinetic mechanisms. MEL is also promising for chemical lumping of larger portions of a mechanism, rather

than single PESs. First example applications showed that the main challenge regards the interaction of lumped pseudospecies and the rest of the reactive mixture, which may change the composition of pseudospecies. From the perspective of automated kinetic mechanism generation, increasing model complexity, and the investigation of complex PAH chemistry, MEL will be an important step in integrated workflows for kinetic model development.

7.2 Reaction classes and rate rules for the reactivity of MAHs and PAHs

Considerable effort in this work was dedicated to the definition of reaction classes for the reactivity of C_5 and MAHs/OAHs (Sections 5.2 and 6.2), with particular focus on oxidation reactions. The sub-mechanism of C_5 , MAH/OAH and partially PAH pyrolysis and oxidation was classified hierarchically according to the type of chemical functionality controlling the reactivity. Several classes do not correspond to elementary steps –contrary to reaction classifications for e.g., alkanes– because of the complex multi-step reactivity and the lumped character of many reaction pathways. Reference kinetic parameters for each species and reaction type were assigned, and kinetic parameters within the same class were aligned according to analogy or rate rules formulated in this work. It is noted that in some cases the lumped nature of the CRECK mechanism prevented the extension of a reaction class to all species associated to a given type. For instance, H-atom abstractions from the aromatic ring [A1-M][HABS] of some OAHs (e.g., anisole, guaiacol) were not included due to the irrelevance of this class with respect to faster decomposition pathways and therefore to the absence of the corresponding radical in the kinetic mechanism.

The heat map class analysis implemented in this work proved to be a useful tool for the analysis of the performance of the kinetic mechanism, simplifying the understanding of the complex reaction network. In the course of this work, heat maps also helped to highlight missing pathways for analogous species.

While indeed useful for model construction, analysis, and consistency, the new classification presented is still partial and relatively model-specific, as often happens in the typical iterative approach of kinetic mechanism construction and refinement. However, it provides a solid basis for future mechanism development. Future improvement of the reaction classes formulated in this work include:

1. Refinement of the definition of classes, especially for growth reactions: the increasing availability of theoretical calculations for growth reaction pathways will also allow better identification of relevant elementary steps for global reaction classes, to be for instance integrated in automated reaction generators.
2. Application of analogy and rate rules: this work showed that it is often possible to formulate functional dependencies to describe rate constants within the same reaction class or for different reaction classes based on theoretical observations. Similar relations may be developed for instance to extend reference kinetic parameters from MAHs to

PAHs, an interesting but poorly assessed aspect. Rate rule approaches could also be tested for more complex class types involving multi-step reactivity.

3. Automated implementation of reaction classification and model alignment via analogy and rate rules: while the present model organization was performed manually, the logic behind it is relatively simple, and its automation would bring incredible advantages for kinetic mechanism development, organization, and update. A fully automated procedure should recognize the chemical functionality of a species (e.g., connecting species types to InChIs), build (or check for) all reaction classes typical of that species type (i.e., similarly to current automated mechanism generation procedures through reaction families), and scale reference parameters according to structural considerations as well as potentially more complex functional dependencies. Ideally, rate rules would also account for uncertainty propagation of the reference rate constant to the other reactions in the class according to the scaling relations adopted. This fully automated procedure could eventually lead to reaction class-based kinetic mechanism optimization.

7.3 First principles-based kinetic modeling: general comments and outlooks

The theoretical and kinetic modeling efforts of this work focused on the kinetic mechanism for C₅, MAHs, and OAHs pyrolysis and oxidation, setting solid grounds for future systematic model improvement. The performances of the updated kinetic model on ideal reactor data are overall reasonably good. However, several discrepancies with experimental data highlighted that many aspects in the kinetics of MAHs pyrolysis and oxidation are far from being understood and that the kinetic mechanism still needs updating and refinement. While detailed conclusive insights were provided in Sections 5.4.3 and 6.6.3, in the big picture, kinetic simulations showed that

- The complex kinetics of C₅, MAHs, OAHs, and PAHs, are all strictly interconnected. Therefore, model shortcomings in one subset inevitably generate failures in kinetic simulations of other subsets. Particular relevance was observed for the subset of C₅ oxidation reactions and all reactions involving phenoxy and substituted phenoxy radical species.
- Despite the strong interconnection between the sub-mechanism of each species, the first steps of fuel decomposition reactivity for instance in substituted OAHs are all fuel-specific. The first steps of OAH decomposition reactivity still seem to have relatively large uncertainty and will hopefully be the subject of future accurate investigations.
- Model shortcomings highlight that oxidation reactions of OAHs and of the corresponding resonantly-stabilized radicals are still unclear. Additional complexity derives from the early conversion of some OAHs, which might result in low-*T* pathways poorly

studied in combustion kinetics. Also the formation of PAHs and oxygenated PAHs is described very approximately in kinetic mechanisms.

These comments also lead to a more general discussion on the role of theoretical kinetics for kinetic modeling. Theoretical calculations performed in this work were validated, where possible, with microkinetic experimental data, and the resulting rate constants have relatively small uncertainties. The update of the kinetic mechanism with these parameters generally disrupted model performances, because of the resulting imbalance of error-compensation effects in the initial mechanism. Model performance analysis therefore iteratively led to new theoretical calculations or "tuning" of rate constants of more uncertain reactions.

Nevertheless, the kinetic model performance can fail even when all the sensitive reactions in the system are computed or carefully updated with theoretical calculations with a supposedly small uncertainty. For instance, the model predicted pretty poorly benzene LFSs (Section 6.6.1), despite the update of all relevant reaction pathways. Instead, replacing the more detailed phenyl oxidation subset with a lumped 2-step reaction forming directly C_4 and CO and therefore "skipping" C_5 reactivity and all the complex interplay of C_5 species with H/O atoms and OH radicals would lead to very good agreement with experimental data. This exemplifies what generally happens when introducing a greater level of detail (i.e., theoretical calculations) and therefore of complexity in a kinetic mechanism: adding more "nodes" (species) and the associated "connections" (reversible reactions) complicates the equilibrium controlling small radicals such as H and OH and therefore the global combustion/ignition behavior. In the present work, despite the extensive use of lumping techniques, some portions of the mechanism were described with a greater level of detail (e.g., oxidation with respect to growth) and probably generated some imbalances in the radical equilibrium of the system. More generally, a consequence of having a greater level of detail in a kinetic mechanism is the larger source of uncertainty (due to the larger number of parameters) and the higher sensitivity to experimental conditions, sometimes leading to less predictive models.

Overall, the approach presented in this thesis explored compromises between detailed theoretical descriptions and relatively human-understandable and manageable mechanisms, and therefore between complexity (holistic theoretical kinetic mechanisms) and oversimplified complexity (heavily lumped kinetic mechanisms). Despite the general success of this approach, future improvements are certainly encouraged. On the other hand, this work showed that many aspects of the reactivity of MAHs and PAHs are so poorly understood that full automation (generally relying on well-known milestones, at least as a starting point) is still too risky, also considering the partial failure of holistic theoretical approaches for more understood systems (i.e., alkanes). At present, a fully automated approach might lead to generating large amounts of erroneous data with no real fundamental understanding. At the same time, the complexity of the reactivity of aromatics encourages automated theoretical calculations for PES investigation. To this aim, this work contributes to a better understanding of the opportunities and limitations of the application of ES calculations for aromatic systems.

The final thoughts of this thesis are on the current general status of kinetic mechanism development. Scheme 7.1 shows an ideal fully-automated workflow for kinetic model generation, simplification, testing, and optimization, occurring in an iterative fashion. The steps of this workflow starts to be reliably implemented in the literature, mostly in open-source codes. For instance, MEL contributes to connecting computational chemistry with kinetic modeling as an "integration and simplification" step of Figure 7.1.

Essential steps for the future success of this increasingly complex workflow to produce kinetic mechanisms which are theory-informed, relatively simple, and most importantly predictive and useful for practical applications are: 1) the integration of all available tools into a smooth workflow; 2) database generation and management not only for reactor and microkinetic experimental data, but also for electronic structure and rate constant calculations, focusing on uncertainty quantification; 3) development of methodologies for reaction generation and classification able to compromise between the increasingly high level of detail of theoretical descriptions and the need to retain model generality, simplicity, and practical usefulness.

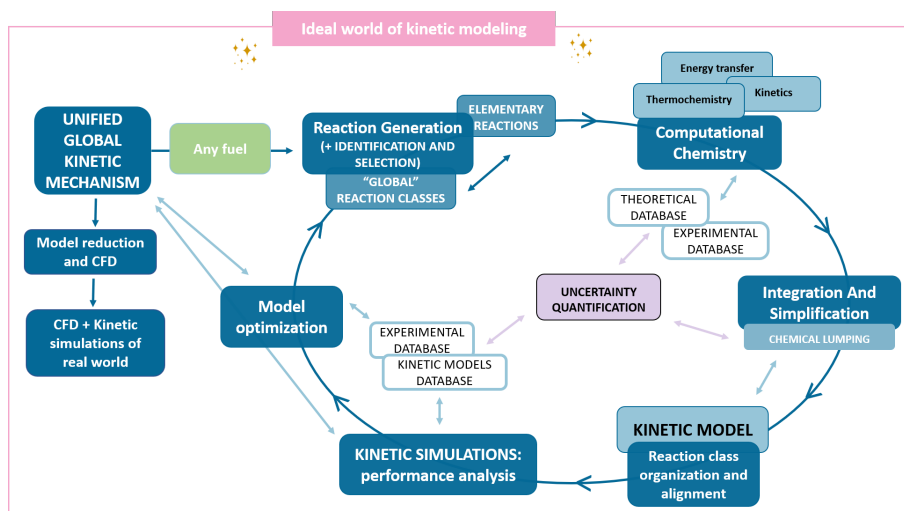


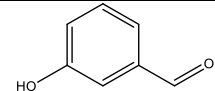
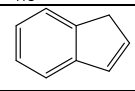
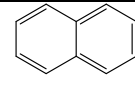
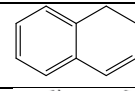
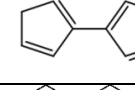
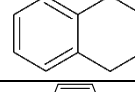
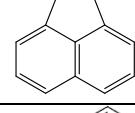
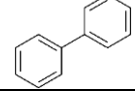
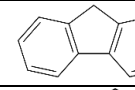
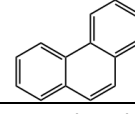
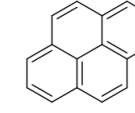
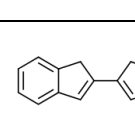
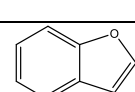
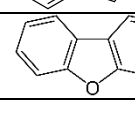

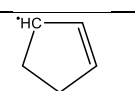
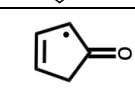
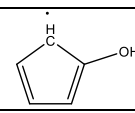
FIGURE 7.1: Scheme of an ideal interconnected and unified workflow for first principle-based kinetic modeling from mechanism generation to rate constant optimization via uncertainty quantification.

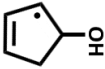
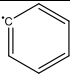
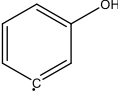
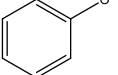
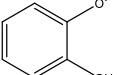
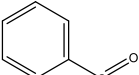
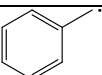
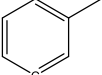
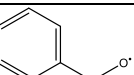
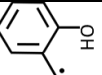
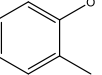
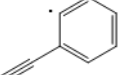
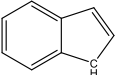
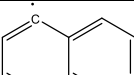
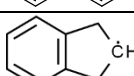
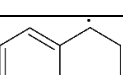
Appendix A

Species table

The species table presents the main species considered for reaction classification and model updates of this work. The species type according to the classification of Section 5.2 and 6.2 is also specified. * refers to lumped species. Species in bold highlight the species object of the main reaction classes updates. Species names are also those presented in the plots of the results in Section 5.4 and 6.6.

Name in CRECK (Alternative)	Species name	Structure	Standard InChI of selected structure	Species types
Molecules				
C5H6	Cyclopentadiene		InChI=1S/C5H6/c1-2-4-5-3-1/h1-4H,5H2	C5-M
CYC5H8	Cyclopentene		InChI=1S/C5H8/c1-2-4-5-3-1/h1-2H,3-5H2	C5,H2-M
C5H5CH3*	Methyl- cyclopentadiene		InChI=1S/C6H8/c1-6-4-2-3-5-6/h2-4H,5H2,1H3	C5-M C5,CH3-M
FULVENE (C5H4CH2)	Fulvene		InChI=1S/C6H6/c1-6-4-2-3-5-6/h2-5H,1H2	C5CH2-M
C5H5OH*	Cyclopentadienol		InChI=1S/C5H6O/c6-5-3-1-2-4-5/h1-3,6H,4H2	C5-M C5,OH-M
C5H4O	Cyclopentadienone		InChI=1S/C5H4O/c6-5-3-1-2-4-5/h1-4H	C5O-M
CYC6H4	Benzynes		InChI=1S/C6H4/c1-2-4-6-5-3-1/h1-4H	-
C6H6	Benzene		InChI=1S/C6H6/c1-2-4-6-5-3-1/h1-6H	A1-M
C7H8 (C6H5CH3)	Toluene		InChI=1S/C7H8/c1-7-5-3-2-4-6-7/h2-6H,1H3	A1-M A1,CH3-M
C6H5C2H	Phenylacetylene		InChI=1S/C8H6/c1-2-8-6-4-3-5-7-8/h1,3-7H	A1-M A1,C2H-M
C6H5C2H3	Styrene		InChI=1S/C8H8/c1-2-8-6-4-3-5-7-8/h2-7H,1H2	A1-M A1,C2H3-M
C6H5C2H5	Ethylbenzene		InChI=1S/C8H10/c1-2-8-6-4-3-5-7-8/h3-7H,2H2,1H3	A1-M A1,C2H5-M
C6H5(CH3)2* (o+m+p)	Xylene		InChI=1S/C8H10/c1-7-5-3-4-6-8(7)2/h3-6H,1-2H3	A1-M A1,CH3-M A1,CH3,CH3-M
C6H5OH	Phenol		InChI=1S/C6H6O/c7-6-4-2-1-3-5-6/h1-5,7H	A1-M A1,OH-M
C6H5CHO	Benzaldehyde		InChI=1S/C7H6O/c8-6-7-4-2-1-3-5-7/h1-6H	A1-M A1,CHO-M
C6H5OCH3	Anisole		InChI=1S/C7H8O/c1-8-7-5-3-2-4-6-7/h2-6H,1H3	A1-M A1,OCH3-M
C6H4O2 (para)	Benzoquinone		InChI=1S/C6H4O2/c7-5-3-1-2-4-6(5)8/h1-4H	A1,O2-M
OC6H4CH2*	Cyclohexadienone- methylene		InChI=1S/C7H6O/c1-6-4-2-3-5-7(6)8/h2-5H,1H2	A1,O,CH2-M
CATECHOL (HOC6H4OH)	Catechol		InChI=1S/C6H6O2/c7-5-3-1-2-4-6(5)8/h1-4,7-8H	A1-M A1,OH-M A1,OH,OH-M
HOC6H4CH3* (o+m+p)	Cresol		InChI=1S/C7H8O/c1-6-3-2-4-7(8)5-6/h2-5,8H,1H3	A1-M A1,CH3-M A1,OH-M

SALICALD* (HOC ₆ H ₄ CHO)	Salicylaldehyde		InChI=1S/C ₇ H ₆ O ₂ /c8-5-6-2-1-3-7(9)4-6/h1-5,9H	A1,CHO-M A1,OH-M
C₉H₈	Indene		InChI=1S/C ₉ H ₈ /c1-2-5-9-7-3-6-8(9)4-1/h1-6H,7H2	C5-M A1-M C5,A1-M
C₁₀H₈	Naphthalene		InChI=1S/C ₁₀ H ₈ /c1-2-6-10-8-4-3-7-9(10)5-1/h1-8H	A1-M A2-M
C ₁₀ H ₁₀ *	Dialin		InChI=1S/C ₁₀ H ₁₀ /c1-2-6-10-8-4-3-7-9(10)5-1/h1-3,5-7H,4,8H2	A1-M A1,H2,H2-M A2,H2,H2-M
FC ₁₀ H ₁₀ *	Fulvalene (Bicyclopentadienyl)		InChI=1S/C ₁₀ H ₁₀ /c1-2-6-9(5-1)10-7-3-4-8-10/h1,3,5-8H,2,4H2	C5-M C5,C5-M
C ₁₀ H ₁₂	Tetralin		InChI=1S/C ₁₀ H ₁₂ /c1-2-6-10-8-4-3-7-9(10)5-1/h1-2,5-6H,3-4,7-8H2	A1,H2,H2-M
C ₁₂ H ₈	Acenaphthylene		InChI=1S/C ₁₂ H ₈ /c1-3-9-4-2-6-11-8-7-10(5-1)12(9)11/h1-8H	A1-M A2-M
C ₁₂ H ₁₀	Biphenyl		InChI=1S/C ₁₂ H ₁₀ /c1-3-7-11(8-4-1)12-9-5-2-6-10-12/h1-10H	A1-M
C ₁₃ H ₁₀	Fluorene		InChI=1S/C ₁₃ H ₁₀ /c1-3-7-12-10(5-1)9-11-6-2-4-8-13(11)12/h1-8H,9H2	C5-M A1-M
C ₁₄ H ₁₀ *	Phenanthrene (Anthracene)		InChI=1S/C ₁₄ H ₁₀ /c1-3-7-13-11(5-1)9-10-12-6-2-4-8-14(12)13/h1-10H	A1-M A2-M
C ₁₆ H ₁₀ *	Pyrene		InChI=1S/C ₁₆ H ₁₀ /c1-3-11-7-9-13-5-2-6-14-10-8-12(4-1)15(11)16(13)14/h1-10H	A1-M A2-M
C ₁₈ H ₁₄ *	Bi-indene		InChI=1S/C ₁₈ H ₁₄ /c1-3-7-15-13(5-1)9-11-17(15)18-12-10-14-6-2-4-8-16(14)18/h1-12,17-18H	C5,A1-M
BZFUR (C ₈ H ₆ O)	Benzofuran		InChI=1S/C ₈ H ₆ O/c1-2-4-8-7(3-1)5-6-9-8/h1-6H	-
DIBZFUR (C ₁₂ H ₈ O)	Dibenzofuran		InChI=1S/C ₁₂ H ₈ O/c1-3-7-11-9(5-1)10-6-2-4-8-12(10)13-11/h1-8H	-
Radicals				
C₅H₅	Cyclopentadienyl		InChI=1S/C ₅ H ₅ /c1-2-4-5-3-1/h1-5H	C5-RSR
CYC₅H₇*	Cyclopentenyl		InChI=1S/C ₅ H ₇ /c1-2-4-5-3-1/h1-3H,4-5H2	C5H2-RSR (C3.D-RSR)
C₅H₅O*	-		InChI=1S/C ₅ H ₅ O/c6-5-3-1-2-4-5/h1-3H,4H2	C5O-RSR (C5-RSR)
C₅H₄OH	-		InChI=1S/C ₅ H ₅ O/c6-5-3-1-2-4-5/h1-4,6H	C5-RSR C5,OH-RSR

C5H6OH	-		InChI=1S/C5H7O/c6-5-3-1-2-4-5/h1-3,5-6H,4H2	C5OH-RSR C5H2-RSR
C6H5	Phenyl		InChI=1S/C6H5/c1-2-4-6-5-3-1/h1-5H	A1-R
C6H4OH* (meta + para)	Hydroxyphenyl		InChI=1S/C6H5O/c7-6-4-2-1-3-5-6/h1-2,4-5,7H	A1-R A1,OH-R
C6H5O* (phenoxy + o-C6H4OH)	Phenoxy		InChI=1S/C6H5O/c7-6-4-2-1-3-5-6/h1-5H	A1O-RSR
OC6H4OH (ortho)	Hydroxyphenoxy		InChI=1S/C6H5O2/c7-5-3-1-2-4-6(5)8/h1-4,7H	A1O-RSR A10,OH-RSR
C6H5CO	Benzoyl		InChI=1S/C7H5O/c8-6-7-4-2-1-3-5-7/h1-5H	A1CO-RSR
C7H7 (C6H5CH2)	Benzyl		InChI=1S/C7H7/c1-7-5-3-2-4-6-7/h2-6H,1H2	A1CH2-RSR
C6H4CH3 (o + m + p)	Methylphenyl		InChI=1S/C7H7/c1-7-5-3-2-4-6-7/h2-3,5-6H,1H3	A1-R A1,CH3-R
C6H5O2	Phenylperoxy		InChI=1S/C6H5O2/c7-8-6-4-2-1-3-5-6/h1-5H	-
HOC6H4CH2	hydroxybenzyl		InChI=1S/C7H7O/c1-6-4-2-3-5-7(6)8/h2-5,8H,1H2	A1CH2-RSR A1CH2,OH-RSSR
OC6H4CH3	Methylphenoxy		InChI=1S/C7H7O/c1-6-4-2-3-5-7(6)8/h2-5H,1H3	A1O-RSR A10,CH3-RSR
C6H4C2H*	Ethynylphenyl		InChI=1S/C8H5/c1-2-8-6-4-3-5-7-8/h1,3-6H	A1-R
C9H7*	Indenyl		InChI=1S/C9H7/c1-2-5-9-7-3-6-8(9)4-1/h1-7H	C5-RSR C5,A1-RSR
C10H7*	Naphthyl		InChI=1S/C10H7/c1-2-6-10-8-4-3-7-9(10)5-1/h1-7H	A1-R A2-R
C9H9*	Indanyl		InChI=1S/C9H9/c1-2-5-9-7-3-6-8(9)4-1/h1-6,9H,7H2	C5H2-RSR
RTETRALIN*	Tetralin radical		InChI=1S/C10H11/c1-2-6-10-8-4-3-7-9(10)5-1/h1-2,5-7H,3-4,8H2	A1,3H2-R

Bibliography

- [1] *Statistical Review of World Energy*, <https://www.bp.com/en/global/corporate/energy-economics/statistical-review-of-world-energy.html>.
- [2] *Energy Outlook | Energy economics | Home*, <https://www.bp.com/en/global/corporate/energy-economics/energy-outlook.html>.
- [3] A. Welch, D. Mumford, S. Munshi, *et al.*, “Challenges in Developing Hydrogen Direct Injection Technology for Internal Combustion Engines,” *SAE Technical Paper 2008-01-2379*, 2008. DOI: 10.4271/2008-01-2379.
- [4] M. Faizal, L. S. Chuah, C. Lee, A. Hameed, J. Lee, and M. Shankar, “review of hydrogen fuel for internal combustion engines,” *Journal of Mechanical Engineering Research and Development*, vol. 42, no. 3, pp. 35–46, 2019. DOI: 10.26480/jmerd.03.2019.35.46.
- [5] Q. Qiao, F. Zhao, Z. Liu, S. Jiang, and H. Hao, “Cradle-to-gate greenhouse gas emissions of battery electric and internal combustion engine vehicles in China,” *Applied Energy*, vol. 204, pp. 1399–1411, 2017. DOI: 10.1016/J.APENERGY.2017.05.041.
- [6] R. Kawamoto, H. Mochizuki, Y. Moriguchi, *et al.*, “Estimation of CO2 Emissions of Internal Combustion Engine Vehicle and Battery Electric Vehicle Using LCA,” *Sustainability 2019, Vol. 11, Page 2690*, vol. 11, no. 9, p. 2690, 2019. DOI: 10.3390/SU11092690.
- [7] P. K. Senecal and F. Leach, “Diversity in transportation: Why a mix of propulsion technologies is the way forward for the future fleet,” *Results in Engineering*, vol. 4, p. 100060, 2019. DOI: 10.1016/J.RINENG.2019.100060.
- [8] *Sources of Greenhouse Gas Emissions | US EPA*, <https://www.epa.gov/ghgemissions/sources-greenhouse-gas-emissions>.
- [9] A. S. Tomlin, “Air Quality and Climate Impacts of Biomass Use as an Energy Source: A Review,” *Energy & Fuels*, vol. 35, no. 18, pp. 14213–14240, 2021. DOI: 10.1021/ACS.ENERGYFUELS.1C01523.
- [10] P. C. Munasinghe and S. K. Khanal, “Biomass-derived syngas fermentation into biofuels: Opportunities and challenges,” *Bioresource Technology*, vol. 101, no. 13, pp. 5013–5022, 2010. DOI: 10.1016/J.BIORTECH.2009.12.098.
- [11] H. Lu, V. Yadav, M. Zhong, M. Bilal, M. J. Taherzadeh, and H. M. Iqbal, “Bio-engineered microbial platforms for biomass-derived biofuel production – A review,” *Chemosphere*, vol. 288, p. 132528, 2022. DOI: 10.1016/J.CHEMOSPHERE.2021.132528.

- [12] S. Van Den Bosch, W. Schutyser, R. Vanholme, *et al.*, “Reductive lignocellulose fractionation into soluble lignin-derived phenolic monomers and dimers and processable carbohydrate pulps,” *Energy & Environmental Science*, vol. 8, no. 6, pp. 1748–1763, 2015. DOI: 10.1039/c5ee00204d.
- [13] J. Lehto, A. Oasmaa, Y. Solantausta, M. Kytö, and D. Chiamonti, “Review of fuel oil quality and combustion of fast pyrolysis bio-oils from lignocellulosic biomass,” *Applied Energy*, vol. 116, pp. 178–190, 2014. DOI: 10.1016/J.APENERGY.2013.11.040.
- [14] M. S. Mettler, D. G. Vlachos, and P. J. Dauenhauer, “Top ten fundamental challenges of biomass pyrolysis for biofuels,” *Energy & Environmental Science*, vol. 5, no. 7, pp. 7797–7809, 2012. DOI: 10.1039/C2EE21679E.
- [15] R. C. Runnebaum, T. Nimmanwudipong, D. E. Block, and B. C. Gates, “Catalytic conversion of compounds representative of lignin-derived bio-oils: a reaction network for guaiacol, anisole, 4-methylanisole, and cyclohexanone conversion catalysed by Pt/g-Al₂O₃,” *Catalysis Science & Technology*, vol. 2, no. 1, pp. 113–118, 2012. DOI: 10.1039/c1cy00169h.
- [16] D. D. Laskar, M. P. Tucker, X. Chen, G. L. Helms, and B. Yang, “Noble-metal catalyzed hydrodeoxygenation of biomass-derived lignin to aromatic hydrocarbons,” *Green Chemistry*, vol. 16, no. 2, pp. 897–910, 2014. DOI: 10.1039/C3GC42041H.
- [17] P. Bi, J. Wang, Y. Zhang, *et al.*, “From lignin to cycloparaffins and aromatics: Directional synthesis of jet and diesel fuel range biofuels using biomass,” *Bioresource Technology*, vol. 183, pp. 10–17, 2015. DOI: 10.1016/J.BIORTECH.2015.02.023.
- [18] A. V. Bridgwater, “Review of fast pyrolysis of biomass and product upgrading,” *Biomass and Bioenergy*, vol. 38, pp. 68–94, 2012. DOI: 10.1016/J.BIOMBIOE.2011.01.048.
- [19] T. R. Carlson, G. A. Tompsett, W. C. Conner, and G. W. Huber, “Aromatic production from catalytic fast pyrolysis of biomass-derived feedstocks,” *Topics in Catalysis*, vol. 52, no. 3, pp. 241–252, 2009. DOI: 10.1007/S11244-008-9160-6/FIGURES/14.
- [20] T. Jin, H. Wang, J. Peng, *et al.*, “Catalytic pyrolysis of lignin with metal-modified HZSM-5 as catalysts for monocyclic aromatic hydrocarbons production,” *Fuel Processing Technology*, vol. 230, p. 107201, 2022. DOI: 10.1016/J.FUPROC.2022.107201.
- [21] J. Zhang, L. Lombardo, G. Gozaydin, P. J. Dyson, and N. Yan, “Single-step conversion of lignin monomers to phenol: Bridging the gap between lignin and high-value chemicals,” *Chinese Journal of Catalysis*, vol. 39, no. 9, pp. 1445–1452, 2018. DOI: 10.1016/S1872-2067(18)63132-8.
- [22] A. Maneffa, P. Priecel, and J. A. Lopez-Sanchez, “Biomass-Derived Renewable Aromatics: Selective Routes and Outlook for p-Xylene Commercialisation,” *ChemSusChem*, vol. 9, no. 19, pp. 2736–2748, 2016. DOI: 10.1002/CSSC.201600605.

- [23] E. Ranzi, P. E. A. Debiagi, and A. Frassoldati, “Mathematical Modeling of Fast Biomass Pyrolysis and Bio-Oil Formation. Note II: Secondary Gas-Phase Reactions and Bio-Oil Formation,” *ACS Sustainable Chemistry and Engineering*, vol. 5, no. 4, pp. 2882–2896, 2017. DOI: 10.1021/acssuschemeng.6b03098.
- [24] ———, “Mathematical Modeling of Fast Biomass Pyrolysis and Bio-Oil Formation. Note I: Kinetic Mechanism of Biomass Pyrolysis,” *ACS Sustainable Chemistry and Engineering*, vol. 5, no. 4, pp. 2867–2881, 2017. DOI: 10.1021/acssuschemeng.6b03096.
- [25] Y. Kim, A. E. Thomas, D. J. Robichaud, *et al.*, “A perspective on biomass-derived biofuels: From catalyst design principles to fuel properties,” *Journal of Hazardous Materials*, vol. 400, p. 123 198, 2020. DOI: 10.1016/J.JHAZMAT.2020.123198.
- [26] J. Quaas, “The soot factor,” *Nature*, vol. 471, no. 7339, pp. 456–457, 2011. DOI: 10.1038/471456a.
- [27] Y. Yao, J. Pan, Z. Liu, *et al.*, “Temporal association between particulate matter pollution and case fatality rate of COVID-19 in Wuhan,” *Environmental Research*, vol. 189, p. 109 941, 2020. DOI: 10.1016/J.ENVRES.2020.109941.
- [28] E. Bontempi, “First data analysis about possible COVID-19 virus airborne diffusion due to air particulate matter (PM): The case of Lombardy (Italy),” *Environmental Research*, vol. 186, p. 109 639, 2020. DOI: 10.1016/J.ENVRES.2020.109639.
- [29] *Sector contributions of emissions of primary particulate matter and secondary precursors (EEA member countries) — European Environment Agency*, <https://www.eea.europa.eu/data-and-maps/figures/sector-contributions-of-emissions-of-1>.
- [30] H. Shen, Y. Huang, R. Wang, *et al.*, “Global atmospheric emissions of polycyclic aromatic hydrocarbons from 1960 to 2008 and future predictions,” *Environmental Science and Technology*, vol. 47, no. 12, pp. 6415–6424, 2013. DOI: 10.1021/es400857z.
- [31] F. Karagulian, C. A. Belis, C. F. C. Dora, *et al.*, “Contributions to cities’ ambient particulate matter (PM): A systematic review of local source contributions at global level,” *Atmospheric Environment*, vol. 120, pp. 475–483, 2015. DOI: 10.1016/J.ATMOENV.2015.08.087.
- [32] B. Yang, W. Sun, K. Moshhammer, and N. Hansen, “Review of the Influence of Oxygenated Additives on the Combustion Chemistry of Hydrocarbons,” *Energy & Fuels*, vol. 35, no. 17, pp. 13 550–13 568, 2021. DOI: 10.1021/ACS.ENERGYFUELS.1C01841.
- [33] W. Leitner, J. Klankermayer, S. Pischinger, H. Pitsch, and K. Kohse-Höinghaus, “Advanced Biofuels and Beyond: Chemistry Solutions for Propulsion and Production,” *Angewandte Chemie - International Edition*, vol. 56, no. 20, pp. 5412–5452, 2017. DOI: 10.1002/anie.201607257.
- [34] C. Wang, H. Xu, J. M. Herreros, T. Lattimore, and S. Shuai, “Fuel Effect on Particulate Matter Composition and Soot Oxidation in a Direct-Injection Spark Ignition (DISI) Engine,” *Energy & Fuels*, vol. 28, no. 3, pp. 2003–2012, 2014. DOI: 10.1021/EF402234Z.

- [35] D. Saini, N. Gunture, J. Kaushik, R. Aggarwal, K. M. Tripathi, and S. K. Sonkar, "Carbon Nanomaterials Derived from Black Carbon Soot: A Review of Materials and Applications," *ACS Applied Nano Materials*, vol. 4, no. 12, pp. 12 825–12 844, 2021. DOI: 10.1021/ACSANM.1C02840.
- [36] S. Li, Y. Ren, P. Biswas, and S. D. Tse, "Flame aerosol synthesis of nanostructured materials and functional devices: Processing, modeling, and diagnostics," *Progress in Energy and Combustion Science*, vol. 55, pp. 1–59, 2016. DOI: 10.1016/J.PECS.2016.04.002.
- [37] T. Kathrotia, P. Oßwald, J. Zinsmeister, T. Methling, and M. Köhler, "Combustion kinetics of alternative jet fuels, Part-III: Fuel modeling and surrogate strategy," *Fuel*, p. 120 737, 2021. DOI: 10.1016/J.FUEL.2021.120737.
- [38] W. Charusiri and N. Numcharoenpinij, "Characterization of the optimal catalytic pyrolysis conditions for bio-oil production from brown salwood (*Acacia mangium* Willd) residues," *Biomass and Bioenergy*, vol. 106, pp. 127–136, 2017. DOI: 10.1016/J.BIOMBIOE.2017.08.030.
- [39] M. R. Djokic, T. Dijkmans, G. Yildiz, W. Prins, and K. M. Van Geem, "Quantitative analysis of crude and stabilized bio-oils by comprehensive two-dimensional gas-chromatography," *Journal of Chromatography A*, vol. 1257, pp. 131–140, 2012. DOI: 10.1016/J.CHROMA.2012.07.035.
- [40] S. Reale, A. Di Tullio, N. Spreti, and F. De Angelis, "Mass spectrometry in the biosynthetic and structural investigation of lignins," *Mass Spectrometry Reviews*, vol. 23, no. 2, pp. 87–126, 2004. DOI: 10.1002/mas.10072.
- [41] C. Mukarakate, A. M. Scheer, D. J. Robichaud, *et al.*, "Laser ablation with resonance-enhanced multiphoton ionization time-of-flight mass spectrometry for determining aromatic lignin volatilization products from biomass," *Review of Scientific Instruments*, vol. 82, no. 3, p. 033 104, 2011. DOI: 10.1063/1.3563704.
- [42] T. Faravelli, A. Frassoldati, G. Migliavacca, and E. Ranzi, "Detailed kinetic modeling of the thermal degradation of lignins," *Biomass and Bioenergy*, vol. 34, no. 3, pp. 290–301, 2010. DOI: 10.1016/J.BIOMBIOE.2009.10.018.
- [43] P. R. Patwardhan, R. C. Brown, and B. H. Shanks, "Understanding the Fast Pyrolysis of Lignin," *ChemSusChem*, vol. 4, no. 11, pp. 1629–1636, 2011. DOI: 10.1002/cssc.201100133.
- [44] K. Onarheim, Y. Solantausta, and J. Lehto, "Process Simulation Development of Fast Pyrolysis of Wood Using Aspen Plus," *Energy & Fuels*, vol. 29, pp. 205–217, 2015. DOI: 10.1021/ef502023y.
- [45] M. Nowakowska, O. Herbinet, A. Dufour, and P. A. Glaude, "Kinetic Study of the Pyrolysis and Oxidation of Guaiacol," *Journal of Physical Chemistry A*, vol. 122, pp. 7894–7909, 2018. DOI: 10.1021/acs.jpca.8b06301.

- [46] M. Pelucchi, C. Cavallotti, A. Cuoci, T. Faravelli, A. Frassoldati, and E. Ranzi, “Detailed kinetics of substituted phenolic species in pyrolysis bio-oils,” *Reaction Chemistry & Engineering*, vol. 4, pp. 490–506, 2019. DOI: 10.1039/c8re00198g.
- [47] L. Negahdar, A. Gonzalez-Quiroga, D. Otyuskaya, *et al.*, “Characterization and Comparison of Fast Pyrolysis Bio-oils from Pinewood, Rapeseed Cake, and Wheat Straw Using ^{13}C NMR and Comprehensive GC \times GC,” *ACS Sustainable Chemistry & Engineering*, vol. 4, 4974–4985, 2016. DOI: 10.1021/acssuschemeng.6b01329.
- [48] M. Bertero, G. de la Puente, and U. Sedran, “Fuels from bio-oils: Bio-oil production from different residual sources, characterization and thermal conditioning,” *Fuel*, vol. 95, pp. 263–271, 2012. DOI: 10.1016/J.FUEL.2011.08.041.
- [49] T. Zhang, C. Bhattarai, Y. Son, V. Samburova, A. Khlystov, and S. A. Varganov, “Reaction Mechanisms of Anisole Pyrolysis at Different Temperatures: Experimental and Theoretical Studies,” *Energy & Fuels*, vol. 35, no. 12, pp. 9994–10 008, 2021. DOI: 10.1021/acs.energyfuels.1c00858.
- [50] S. W. Wagnon, S. Thion, E. J. Nilsson, *et al.*, “Experimental and modeling studies of a biofuel surrogate compound: laminar burning velocities and jet-stirred reactor measurements of anisole,” *Combustion and Flame*, vol. 189, pp. 325–336, 2018. DOI: 10.1016/J.COMBUSTFLAME.2017.10.020.
- [51] M. Nowakowska, O. Herbinet, A. Dufour, and P.-A. Glaude, “Detailed kinetic study of anisole pyrolysis and oxidation to understand tar formation during biomass combustion and gasification,” *Combustion and Flame*, vol. 161, no. 6, pp. 1474–1488, 2014. DOI: 10.1016/J.COMBUSTFLAME.2013.11.024.
- [52] P. Zhang, N. W. Yee, S. V. Filip, C. E. Hetrick, B. Yang, and W. H. Green, “Modeling study of the anti-knock tendency of substituted phenols as additives: an application of the reaction mechanism generator (RMG),” *Physical Chemistry Chemical Physics*, vol. 20, no. 16, pp. 10 637–10 649, 2018. DOI: 10.1039/C7CP07058F.
- [53] R. L. McCormick, M. A. Ratcliff, E. Christensen, *et al.*, “Properties of Oxygenates Found in Upgraded Biomass Pyrolysis Oil as Components of Spark and Compression Ignition Engine Fuels,” *Energy & Fuels*, vol. 29, pp. 2453–2461, 2015. DOI: 10.1021/ef502893g.
- [54] R. D. Büttgen, L. Pratali Maffei, M. Pelucchi, T. Faravelli, A. Frassoldati, and K. A. Heufer, “Towards a better understanding of the combustion of oxygenated aromatic hydrocarbons . Comparing benzene , toluene , phenol and anisole with ignition delay times in a rapid compression machine,” in *9th European Combustion Meeting*, 2019.
- [55] R. Büttgen, M. Tian, Y. Fenard, H. Minwegen, M. Boot, and K. Heufer, “An experimental, theoretical and kinetic modelling study on the reactivity of a lignin model compound anisole under engine-relevant conditions,” *Fuel*, vol. 269, p. 117 190, 2020. DOI: 10.1016/j.fuel.2020.117190.

- [56] W. Pejpichestakul, E. Ranzi, M. Pelucchi, *et al.*, “Examination of a soot model in premixed laminar flames at fuel-rich conditions,” *Proceedings of the Combustion Institute*, vol. 37, pp. 1013–1021, 2019. DOI: 10.1016/j.proci.2018.06.104.
- [57] M. Commodo, K. Kaiser, G. De Falco, *et al.*, “On the early stages of soot formation: Molecular structure elucidation by high-resolution atomic force microscopy,” *Combustion and Flame*, vol. 205, pp. 154–164, 2019. DOI: 10.1016/j.combustflame.2019.03.042.
- [58] A. Nobili, L. Pratali Maffei, A. Baggioli, *et al.*, “On the radical behavior of large polycyclic aromatic hydrocarbons in soot formation and oxidation,” *Combustion and Flame*, vol. 235, p. 111692, 2021. DOI: 10.1016/J.COMBUSTFLAME.2021.111692.
- [59] A. Nobili, A. Cuoci, W. Pejpichestakul, M. Pelucchi, C. Cavallotti, and T. Faravelli, “Modeling soot particles as stable radicals: a chemical kinetic study on formation and oxidation. Part I. Soot formation in ethylene laminar premixed and counter-flow diffusion flames,” *Combustion and Flame*, p. 112073, 2022. DOI: 10.1016/J.COMBUSTFLAME.2022.112073.
- [60] A. Nobili, W. Pejpichestakul, M. Pelucchi, A. Cuoci, C. Cavallotti, and T. Faravelli, “Modeling soot particles as stable radicals: a chemical kinetic study on formation and oxidation. Part II. Soot oxidation in flow reactors and laminar flames,” *Combustion and Flame*, p. 112072, 2022. DOI: 10.1016/J.COMBUSTFLAME.2022.112072.
- [61] K. O. Johansson, M. P. Head-Gordon, P. E. Schrader, K. R. Wilson, and H. A. Michelsen, “Resonance-stabilized hydrocarbon-radical chain reactions may explain soot inception and growth,” *Science*, vol. 361, no. 6406, pp. 997–1000, 2018. DOI: 10.1126/science.aat3417.
- [62] H. Wang, “Formation of nascent soot and other condensed-phase materials in flames,” *Proceedings of the Combustion Institute*, vol. 33, no. 1, pp. 41–67, 2011. DOI: 10.1016/j.proci.2010.09.009.
- [63] E. Ranzi, M. Dente, A. Goldaniga, G. Bozzano, and T. Faravelli, “Lumping procedures in detailed kinetic modeling of gasification, pyrolysis, partial oxidation and combustion of hydrocarbon mixtures,” *Progress in Energy and Combustion Science*, vol. 27, no. 1, pp. 99–139, 2001. DOI: 10.1016/S0360-1285(00)00013-7.
- [64] E. Ranzi, T. Faravelli, P. Gaffuri, and A. Sogaro, “Low-temperature combustion: Automatic generation of primary oxidation reactions and lumping procedures,” *Combustion and Flame*, vol. 102, no. 1-2, pp. 179–192, 1995. DOI: 10.1016/0010-2180(94)00253-0.
- [65] E. Ranzi, A. Frassoldati, A. Stagni, M. Pelucchi, A. Cuoci, and T. Faravelli, “Reduced kinetic schemes of complex reaction systems: Fossil and biomass-derived transportation fuels,” *International Journal of Chemical Kinetics*, vol. 46, no. 9, pp. 512–542, 2014. DOI: 10.1002/kin.20867.

- [66] P. Pepiot, L. Cai, and H. Pitsch, "Model reduction and lumping procedures," in *Computer Aided Chemical Engineering*, vol. 45, 2019, pp. 799–827. DOI: 10.1016/B978-0-444-64087-1.00016-4.
- [67] S. Dong, S. W. Wagnon, L. Pratali Maffei, *et al.*, "A new detailed kinetic model for surrogate fuels: C3MechV3.3," *Applications in Energy and Combustion Science*, vol. 9, p. 100043, 2022. DOI: 10.1016/J.JAECS.2021.100043.
- [68] E. Ranzi, T. Faravelli, P. Gaffuri, E. Garavaglia, and A. Goldaniga, "Primary Pyrolysis and Oxidation Reactions of Linear and Branched Alkanes," *Industrial and Engineering Chemistry Research*, vol. 36, no. 8, pp. 3336–3344, 1997. DOI: 10.1021/IE960603C.
- [69] C. W. Gao, J. W. Allen, W. H. Green, and R. H. West, "Reaction Mechanism Generator: Automatic construction of chemical kinetic mechanisms," *Computer Physics Communications*, vol. 203, pp. 212–225, 2016. DOI: 10.1016/j.cpc.2016.02.013.
- [70] N. M. Vandewiele, K. M. Van Geem, M.-F. Reyniers, and G. B. Marin, "Genesys: Kinetic model construction using chemo-informatics," *Chemical Engineering Journal*, vol. 207–208, pp. 526–538, 2012. DOI: 10.1016/j.cej.2012.07.014.
- [71] E. Ranzi, M. Dente, T. Faravelli, and G. Pennati, "Prediction of Kinetic Parameters for Hydrogen Abstraction Reactions," *Combustion Science and Technology*, vol. 95, pp. 1–50, 1993. DOI: 10.1080/00102209408935325.
- [72] M. Frisch, G. Trucks, H. B. Schlegel, *et al.*, *Gaussian 09, revision D.01*, 2013.
- [73] H.-J. Werner, P. J. Knowles, G. Knizia, F. R. Manby, and M. Schütz, *Molpro: A General-Purpose Quantum Chemistry Program Package*, 2021.
- [74] S. J. Klippenstein, "From theoretical reaction dynamics to chemical modeling of combustion," *Proceedings of the Combustion Institute*, vol. 36, no. 1, pp. 77–111, 2017. DOI: 10.1016/j.proci.2016.07.100.
- [75] S. W. Benson, *Thermochemical kinetics : methods for the estimation of thermochemical data and rate parameters*. Wiley, 1976, p. 320.
- [76] S. W. Benson and J. H. Buss, "Additivity Rules for the Estimation of Molecular Properties. Thermodynamic Properties," *The Journal of Chemical Physics*, vol. 29, no. 3, p. 546, 1958. DOI: 10.1063/1.1744539.
- [77] E. Ranzi, M. Dente, S. Pierucci, and G. Biardi, "Initial Product Distributions from Pyrolysis of Normal and Branched Paraffins," *Industrial & Engineering Chemistry Fundamentals*, vol. 22, pp. 132–139, 1983. DOI: 10.1021/i100009a023.
- [78] J. Bugler, K. P. Somers, E. J. Silke, and H. J. Curran, "Revisiting the Kinetics and Thermodynamics of the Low-Temperature Oxidation Pathways of Alkanes: A Case Study of the Three Pentane Isomers," *Journal of Physical Chemistry A*, vol. 119, no. 28, pp. 7510–7527, 2015. DOI: 10.1021/acs.jpca.5b00837.
- [79] H. J. Curran, "Developing detailed chemical kinetic mechanisms for fuel combustion," *Proceedings of the Combustion Institute*, vol. 37, no. 1, pp. 57–81, 2019. DOI: 10.1016/j.proci.2018.06.054.

- [80] R. Kee, F. Rupley, E. Meeks, and J. Miller, "CHEMKIN-III: A FORTRAN chemical kinetics package for the analysis of gas-phase chemical and plasma kinetics," Sandia National Laboratories (SNL), Albuquerque, NM, and Livermore, CA (United States), Tech. Rep., 1996. DOI: 10.2172/481621.
- [81] G. D. Goodwin, H. K. Moffat, I. Schoegl, R. L. Speth, and B. W. Weber, *Cantera: An object-oriented software toolkit for chemical kinetics, thermodynamics, and transport processes, Version 2.5.1*, 2021. DOI: 10.5281/zenodo.6387882.
- [82] A. Cuoci, A. Frassoldati, T. Faravelli, and E. Ranzi, "OpenSMOKE++: An object-oriented framework for the numerical modeling of reactive systems with detailed kinetic mechanisms," *Computer Physics Communications*, vol. 192, pp. 237–264, 2015. DOI: 10.1016/j.cpc.2015.02.014.
- [83] M. S. Bernardi, M. Pelucchi, A. Stagni, *et al.*, "Curve matching, a generalized framework for models/experiments comparison: An application to n-heptane combustion kinetic mechanisms," *Combustion and Flame*, vol. 168, pp. 186–203, 2016. DOI: 10.1016/J.COMBUSTFLAME.2016.03.019.
- [84] A. S. Tomlin, "The role of sensitivity and uncertainty analysis in combustion modelling," *Proceedings of the Combustion Institute*, vol. 34, no. 1, pp. 159–176, 2013. DOI: 10.1016/J.PROCI.2012.07.043.
- [85] M. P. Burke, S. J. Klippenstein, and L. B. Harding, "A quantitative explanation for the apparent anomalous temperature dependence of $\text{OH} + \text{HO}_2 = \text{H}_2\text{O} + \text{O}_2$ through multi-scale modeling," *Proceedings of the Combustion Institute*, vol. 34, no. 1, pp. 547–555, 2013. DOI: 10.1016/J.PROCI.2012.05.041.
- [86] M. P. Burke, C. F. Goldsmith, S. J. Klippenstein, *et al.*, "Multiscale Informatics for Low-Temperature Propane Oxidation: Further Complexities in Studies of Complex Reactions," *Journal of Physical Chemistry A*, vol. 119, no. 28, pp. 7095–7115, 2015. DOI: 10.1021/acs.jpca.5b01003.
- [87] S. J. Klippenstein, "From theoretical reaction dynamics to chemical modeling of combustion," *Proceedings of the Combustion Institute*, vol. 36, pp. 77–111, 2017. DOI: 10.1016/j.proci.2016.07.100.
- [88] J. A. Miller, R. Sivaramakrishnan, Y. Tao, *et al.*, *Combustion Chemistry in the Twenty-First Century: Developing Theory-Informed Chemical Kinetics Models*, 2021. DOI: 10.1016/j.pecs.2020.100886.
- [89] N. M. O'Boyle, M. Banck, C. A. James, C. Morley, T. Vandermeersch, and G. R. Hutchison, "Open Babel: An Open chemical toolbox," *Journal of Cheminformatics*, vol. 3, no. 10, pp. 1–14, 2011. DOI: 10.1186/1758-2946-3-33.
- [90] F. Neese and J. Wiley, "The ORCA program system," *Wiley Interdisciplinary Reviews: Computational Molecular Science*, vol. 2, no. 1, pp. 73–78, 2012. DOI: 10.1002/WCMS.81.

- [91] F. Neese, “Software update: the ORCA program system, version 4.0,” *Wiley Interdisciplinary Reviews: Computational Molecular Science*, vol. 8, no. 1, e1327, 2018. DOI: 10.1002/WCMS.1327.
- [92] D. G. Smith, L. A. Burns, A. C. Simmonett, *et al.*, “PSI4 1.4: Open-source software for high-throughput quantum chemistry,” *Journal of Chemical Physics*, vol. 152, no. 18, p. 184108, 2020. DOI: 10.1063/5.0006002.
- [93] E. Epifanovsky, A. T. Gilbert, X. Feng, *et al.*, “Software for the frontiers of quantum chemistry: An overview of developments in the Q-Chem 5 package,” *Journal of Chemical Physics*, vol. 155, no. 8, p. 084801, 2021. DOI: 10.1063/5.0055522.
- [94] J. Zador and H. N. Najm, *KinBot 1.0: A code for automatic PES exploration*, <https://www.osti.gov/servlets/purl/1080032>, Sandia National Laboratories, Livermore, 2013.
- [95] R. Van De Vijver and J. Zádor, “KinBot: Automated stationary point search on potential energy surfaces,” *Computer Physics Communications*, vol. 248, p. 106947, 2020. DOI: 10.17632/hsh6dvv2zj.1.
- [96] P. L. Bhoorasingh, B. L. Slakman, F. Seyedzadeh Khanshan, J. Y. Cain, and R. H. West, “Automated Transition State Theory Calculations for High-Throughput Kinetics,” *Journal of Physical Chemistry A*, vol. 121, no. 37, pp. 6896–6904, 2017. DOI: 10.1021/acs.jpca.7b07361.
- [97] C. Cavallotti, M. Pelucchi, Y. Georgievskii, and S. J. Klippenstein, “ESTokTP: Electronic Structure to Temperature- and Pressure-Dependent Rate Constants—A Code for Automatically Predicting the Thermal Kinetics of Reactions,” *Journal of Chemical Theory and Computation*, vol. 15, no. 2, pp. 1122–1145, 2019. DOI: 10.1021/acs.jctc.8b00701.
- [98] S. N. Elliott, K. B. Moore, A. V. Copan, *et al.*, “Automated theoretical chemical kinetics: Predicting the kinetics for the initial stages of pyrolysis,” *Proceedings of the Combustion Institute*, vol. 38, no. 1, pp. 375–384, 2021. DOI: 10.1016/J.PROCI.2020.06.019.
- [99] A. W. Jasper, “Multidimensional Effects in Nonadiabatic Statistical Theories of Spin-Forbidden Kinetics: A Case Study of $3O + CO \rightarrow CO_2$,” *Journal of Physical Chemistry A*, vol. 119, no. 28, pp. 7339–7351, 2015. DOI: 10.1021/jp512942w.
- [100] J. Zheng, J. L. Bao, R. Meana-Pañeda, *et al.*, *Polyrate-version 2017-C*, <https://comp.chem.umn.edu/polyrate/>, University of Minnesota: Minneapolis, 2017.
- [101] S. Sharma, M. R. Harper, and W. H. Green, *CanTherm v1.0*, <https://sourceforge.net/projects/cantherm/>.
- [102] J. Kästner, “Theory and simulation of atom tunneling in chemical reactions,” *Wiley Interdisciplinary Reviews: Computational Molecular Science*, vol. 4, no. 2, pp. 158–168, 2014. DOI: 10.1002/wcms.1165.

- [103] L. B. Harding, Y. Georgievskii, and S. J. Klippenstein, "Predictive Theory for Hydrogen Atom-Hydrocarbon Radical Association Kinetics," *Journal of Physical Chemistry A*, vol. 109, pp. 4646–4656, 2005. DOI: 10.1021/jp0508608.
- [104] Y. Georgievskii, L. B. Harding, and S. J. Klippenstein, *VaReCoF : Variable Reaction Coordinate Flux*, <https://tcg.cse.anl.gov/papr/codes/varecof.html>, 2016.
- [105] J. Zheng, S. Zhang, and D. G. Truhlar, "Density functional study of methyl radical association kinetics," *Journal of Physical Chemistry A*, vol. 112, no. 46, pp. 11 509–11 513, 2008. DOI: 10.1021/JP806617M.
- [106] Y. Georgievskii, J. A. Miller, M. P. Burke, and S. J. Klippenstein, "Reformulation and Solution of the Master Equation for Multiple-Well Chemical Reactions," *Journal of Physical Chemistry A*, vol. 117, no. 46, pp. 12 146–12 154, 2013. DOI: 10.1021/jp4060704.
- [107] A. Barbato, C. Seghi, and C. Cavallotti, "An ab initio Rice-Ramsperger-Kassel-Marcus/master equation investigation of SiH₄ decomposition kinetics using a kinetic Monte Carlo approach," *Journal of Chemical Physics*, vol. 130, no. 7, p. 074 108, 2009. DOI: 10.1063/1.3077561.
- [108] D. R. Glowacki, C.-H. Liang, C. Morley, M. J. Pilling, and S. H. Robertson, "MESMER: An Open-Source Master Equation Solver for Multi-Energy Well Reactions," *Journal of Physical Chemistry A*, vol. 116, pp. 9545–9560, 2012. DOI: 10.1021/jp3051033.
- [109] J. R. Barker, "Multiple-Well, multiple-path unimolecular reaction systems. I. Multi-Well computer program suite," *International Journal of Chemical Kinetics*, vol. 33, no. 4, pp. 232–245, 2001. DOI: 10.1002/kin.1017.
- [110] A. W. Jasper and J. A. Miller, "Lennard-Jones parameters for combustion and chemical kinetics modeling from full-dimensional intermolecular potentials," *Combustion and Flame*, vol. 161, pp. 101–110, 2014. DOI: 10.1016/j.combustflame.2013.08.004.
- [111] A. W. Jasper, K. M. Pelzer, J. A. Miller, E. Kamarchik, L. B. Harding, and S. J. Klippenstein, "Predictive a priori pressure-dependent kinetics," *Science*, vol. 346, no. 6214, pp. 1212–1215, 2014. DOI: 10.1126/science.1260856.
- [112] A. W. Jasper and J. A. Miller, "Theoretical Unimolecular Kinetics for CH₄+M = CH₃+H+M in Eight Baths, M=He, Ne, Ar, Kr, H₂, N₂, CO, and CH₄," *Journal of Physical Chemistry A*, vol. 115, pp. 6438–6455, 2011. DOI: 10.1021/jp200048n.
- [113] ———, *OneDMin*, <https://tcg.cse.anl.gov/papr/codes/onedmin.html>, 2014.
- [114] A. W. Jasper, R. M. Zhang, and D. G. Truhlar, *DiNT, version 2.0*, <https://comp.chem.umn.edu/dint/>, 2020.

- [115] A. W. Jasper, ““Third-body” collision parameters for hydrocarbons, alcohols, and hydroperoxides and an effective internal rotor approach for estimating them,” *International Journal of Chemical Kinetics*, vol. 52, no. 6, pp. 387–402, 2020. DOI: 10.1002/KIN.21358.
- [116] M. Keçeli, S. N. Elliott, Y. P. Li, *et al.*, “Automated computational thermochemistry for butane oxidation: A prelude to predictive automated combustion kinetics,” *Proceedings of the Combustion Institute*, vol. 37, no. 1, pp. 363–371, 2019. DOI: 10.1016/J.PROCI.2018.07.113.
- [117] B. Ruscic and D. H. Bross, *Active Thermochemical Tables (ATcT) values based on ver. 1.122d of the Thermochemical Network Argonne National Laboratory (2018); available at ATcT.anl.gov.*
- [118] A. Miyoshi, “Systematic computational study on the unimolecular reactions of alkylperoxy (RO_2), hydroperoxyalkyl (QOOH), and hydroperoxyalkylperoxy (O_2QOOH) radicals,” *Journal of Physical Chemistry A*, vol. 115, no. 15, pp. 3301–3325, 2011. DOI: 10.1021/jp112152n.
- [119] S. M. Villano, H.-H. Carstensen, and A. M. Dean, “Rate Rules, Branching Ratios, and Pressure Dependence of the HO_2 + Olefin Addition Channels,” *Journal of Physical Chemistry A*, vol. 117, pp. 6458–6473, 2013. DOI: 10.1021/jp405262r.
- [120] L. Cai, H. Pitsch, S. Y. Mohamed, *et al.*, “Optimized reaction mechanism rate rules for ignition of normal alkanes,” *Combustion and Flame*, vol. 173, pp. 468–482, 2016. DOI: 10.1016/j.combustflame.2016.04.022.
- [121] S. M. Sarathy, A. Farooq, and G. T. Kalghatgi, “Recent progress in gasoline surrogate fuels,” *Progress in Energy and Combustion Science*, vol. 65, pp. 67–108, 2018. DOI: 10.1016/j.pecs.2017.09.004.
- [122] H. Curran, P. Gaffuri, W. Pitz, and C. Westbrook, “A Comprehensive Modeling Study of n-Heptane Oxidation,” *Combustion and Flame*, vol. 114, no. 1-2, pp. 149–177, 1998. DOI: 10.1016/S0010-2180(97)00282-4.
- [123] C. K. Westbrook, W. J. Pitz, O. Herbinet, H. J. Curran, and E. J. Silke, “A comprehensive detailed chemical kinetic reaction mechanism for combustion of n-alkane hydrocarbons from n-octane to n-hexadecane,” *Combustion and Flame*, vol. 156, pp. 181–199, 2009. DOI: 10.1016/j.combustflame.2008.07.014.
- [124] E. Ranzi, C. Cavallotti, A. Cuoci, A. Frassoldati, M. Pelucchi, and T. Faravelli, “New reaction classes in the kinetic modeling of low temperature oxidation of n-alkanes,” *Combustion and Flame*, vol. 162, no. 5, pp. 1679–1691, 2015. DOI: 10.1016/j.combustflame.2014.11.030.
- [125] K. Brezinsky, M. Pecullan, and I. Glassman, “Pyrolysis and Oxidation of Phenol,” *Journal of Physical Chemistry A*, vol. 102, pp. 8614–8619, 1998. DOI: 10.1021/jp982177.

- [126] A. B. Lovell, K. Brezinsky, and I. Glassman, "The gas phase pyrolysis of phenol," *International Journal of Chemical Kinetics*, vol. 21, pp. 547–560, 1989. DOI: 10.1002/kin.550210706.
- [127] C. Saggese, A. Frassoldati, A. Cuoci, T. Faravelli, and E. Ranzi, "A wide range kinetic modeling study of pyrolysis and oxidation of benzene," *Combustion and Flame*, vol. 160, pp. 1168–1190, 2013. DOI: 10.1016/j.combustflame.2013.02.013.
- [128] G. Vourliotakis, G. Skevis, and M. A. Founti, "A detailed kinetic modeling study of benzene oxidation and combustion in premixed flames and ideal reactors," *Energy & Fuels*, vol. 25, pp. 1950–1963, 2011. DOI: 10.1021/ef101712p.
- [129] M. Pelucchi, C. Cavallotti, T. Faravelli, and S. J. Klippenstein, "H-Abstraction reactions by OH, HO₂, O, O₂ and benzyl radical addition to O₂ and their implications for kinetic modelling of toluene oxidation," *Physical Chemistry Chemical Physics*, vol. 20, no. 16, pp. 10607–10627, 2018. DOI: 10.1039/c7cp07779c.
- [130] W. Sun, A. Hamadi, S. Abid, N. Chaumeix, and A. Comandini, "Probing PAH formation chemical kinetics from benzene and toluene pyrolysis in a single-pulse shock tube," *Proceedings of the Combustion Institute*, vol. 38, pp. 891–900, 2021. DOI: 10.1016/j.proci.2020.06.077.
- [131] M. Pelucchi, T. Faravelli, A. Frassoldati, *et al.*, "Experimental and Kinetic Modeling Study of Pyrolysis and Combustion of Anisole," *Chemical Engineering Transactions*, vol. 65, pp. 127–132, 2018. DOI: 10.3303/CET1865022.
- [132] C. Horn, K. Roy, P. Frank, and T. Just, "Shock-tube study on the high-temperature pyrolysis of phenol," *Symposium (International) on Combustion*, vol. 27, pp. 321–328, 1998. DOI: 10.1016/S0082-0784(98)80419-0.
- [133] Z. F. Xu and M. C. Lin, "Ab initio kinetics for the unimolecular reaction C₆H₅OH → CO + C₅H₆," *Journal of Physical Chemistry A*, vol. 110, pp. 1672–1677, 2006. DOI: 10.1021/jp055241d.
- [134] M. Altarawneh, B. Z. Dlugogorski, E. M. Kennedy, and J. C. Mackie, "Theoretical study of unimolecular decomposition of catechol," *Journal of Physical Chemistry A*, vol. 114, no. 2, pp. 1060–1067, 2010. DOI: 10.1021/jp909025s.
- [135] H. Yang, Y. Furutani, S. Kudo, J. i. Hayashi, and K. Norinaga, "Experimental investigation of thermal decomposition of dihydroxybenzene isomers: Catechol, hydroquinone, and resorcinol," *Journal of Analytical and Applied Pyrolysis*, 2016. DOI: 10.1016/j.jaap.2016.05.019.
- [136] Y. Furutani, S. Kudo, J.-i. Hayashi, and K. Norinaga, "Theoretical Study on Reaction Pathways Leading to CO and CO₂ in the Pyrolysis of Resorcinol," *Journal of Physical Chemistry A*, vol. 121, no. 3, pp. 631–637, 2017. DOI: 10.1021/acs.jpca.6b05168.
- [137] M. Frenklach and H. Wang, "Detailed modeling of soot particle nucleation and growth," *Symposium (International) on Combustion*, vol. 23, no. 1, pp. 1559–1566, 1991. DOI: 10.1016/S0082-0784(06)80426-1.

- [138] H. Wang and M. Frenklach, "Calculations of Rate Coefficients for the Chemically Activated Reactions of Acetylene with Vinylic and Aromatic Radicals," *Journal of Physical Chemistry*, vol. 98, pp. 11 465–11 489, 1994. DOI: 10.1021/j100095a033.
- [139] A. M. Mebel, Y. Georgievskii, A. W. Jasper, and S. J. Klippenstein, "Temperature- and pressure-dependent rate coefficients for the HACA pathways from benzene to naphthalene," *Proceedings of the Combustion Institute*, vol. 36, no. 1, pp. 919–926, 2017. DOI: 10.1016/J.PROCI.2016.07.013.
- [140] A. M. Mebel, A. Landera, and R. I. Kaiser, "Formation Mechanisms of Naphthalene and Indene: From the Interstellar Medium to Combustion Flames," *The Journal of Physical Chemistry A*, vol. 121, no. 5, pp. 901–926, 2017. DOI: 10.1021/acs.jpca.6b09735.
- [141] R. I. Kaiser and N. Hansen, "An Aromatic Universe—A Physical Chemistry Perspective," *Journal of Physical Chemistry A*, vol. 125, pp. 3826–3840, 2021. DOI: 10.1021/acs.jpca.1c00606.
- [142] J. W. Martin, L. Pascazio, A. Menon, *et al.*, " π -Diradical Aromatic Soot Precursors in Flames," *Journal of the American Chemical Society*, jacs.1c05030, 2021. DOI: 10.1021/JACS.1C05030.
- [143] S. Mohr, L. E. Ratcliff, L. Genovese, *et al.*, "Accurate and efficient linear scaling DFT calculations with universal applicability," *Physical Chemistry Chemical Physics*, vol. 17, no. 47, pp. 31 360–31 370, 2015. DOI: 10.1039/C5CP00437C.
- [144] C. Song and T. J. Martínez, "Reduced scaling CASPT2 using supporting subspaces and tensor hyper-contraction," *The Journal of Chemical Physics*, vol. 149, no. 4, p. 044 108, 2018. DOI: 10.1063/1.5037283.
- [145] M. Lesiuk, "Implementation of the Coupled-Cluster Method with Single, Double, and Triple Excitations using Tensor Decompositions," *Journal of Chemical Theory and Computation*, vol. 16, no. 1, pp. 453–467, 2020. DOI: 10.1021/acs.jctc.9b00985.
- [146] N. Mardirossian, J. D. McClain, and G. K. L. Chan, "Lowering of the complexity of quantum chemistry methods by choice of representation," *The Journal of Chemical Physics*, vol. 148, no. 4, p. 044 106, 2018. DOI: 10.1063/1.5007779.
- [147] Q. Ma and H. J. Werner, "Explicitly correlated local coupled-cluster methods using pair natural orbitals," *Wiley Interdisciplinary Reviews: Computational Molecular Science*, vol. 8, no. 6, pp. 1–32, 2018. DOI: 10.1002/wcms.1371.
- [148] N. J. Labbe, R. Sivaramakrishnan, C. F. Goldsmith, Y. Georgievskii, J. A. Miller, and S. J. Klippenstein, "Weakly Bound Free Radicals in Combustion: Prompt Dissociation of Formyl Radicals and Its Effect on Laminar Flame Speeds," *Journal of Physical Chemistry Letters*, vol. 7, no. 1, pp. 85–89, 2016. DOI: 10.1021/acs.jpcllett.5b02418.
- [149] J. Cho, Y. Tao, Y. Georgievskii, S. J. Klippenstein, A. W. Jasper, and R. Sivaramakrishnan, "The role of collisional energy transfer on the thermal and prompt dissociation of 1-methyl allyl," *Proceedings of the Combustion Institute* 39, vol. in press, 2022.

- [150] M. P. Burke, C. F. Goldsmith, Y. Georgievskii, and S. J. Klippenstein, "Towards a quantitative understanding of the role of non-Boltzmann reactant distributions in low temperature oxidation," *Proceedings of the Combustion Institute*, vol. 35, no. 1, pp. 205–213, 2015. DOI: 10.1016/J.PROCI.2014.05.118.
- [151] F. Lindemann, "Discussion on "the radiation theory of chemical action"," *Transactions of the Faraday Society*, vol. 17, pp. 598–606, 1922. DOI: 10.1039/TF9221700598.
- [152] J. Troe, "Fall-off Curves of Unimolecular Reactions," *Berichte der Bunsengesellschaft für physikalische Chemie*, vol. 78, no. 5, pp. 478–488, 1974. DOI: 10.1002/BBPC.19740780510.
- [153] —, "Theory of Thermal Unimolecular Reactions in the Fall-off Range. I. Strong Collision Rate Constants," *Berichte der Bunsengesellschaft für physikalische Chemie*, vol. 87, no. 2, pp. 161–169, 1983. DOI: 10.1002/BBPC.19830870217.
- [154] R. G. Gilbert, K. Luther, and J. Troe, "Theory of Thermal Unimolecular Reactions in the Fall-off Range. II. Weak Collision Rate Constants," *Berichte der Bunsengesellschaft für physikalische Chemie*, vol. 87, no. 2, pp. 169–177, 1983. DOI: 10.1002/BBPC.19830870218.
- [155] I. Glassman, R. A. Yetter, and N. G. Glumac, *Combustion Fifth Edition*. 2015. DOI: 10.1016/C2011-0-05402-9.
- [156] J. E. Lennard-Jones, "Cohesion," *Proceedings of the Physical Society*, vol. 43, no. 5, p. 461, 1931. DOI: 10.1088/0959-5309/43/5/301.
- [157] W. H. Stockmayer, "Second Virial Coefficients of Polar Gases," *Journal of Chemical Physics*, vol. 9, no. 5, p. 398, 2004. DOI: 10.1063/1.1750922.
- [158] N. J. Brown, L. A. Bastien, and P. N. Price, "Transport properties for combustion modeling," *Progress in Energy and Combustion Science*, vol. 37, no. 5, pp. 565–582, 2011. DOI: 10.1016/J.PECS.2010.12.001.
- [159] M. Ó Conaire, H. J. Curran, J. M. Simmie, W. J. Pitz, and C. K. Westbrook, "A comprehensive modeling study of hydrogen oxidation," *International Journal of Chemical Kinetics*, vol. 36, no. 11, pp. 603–622, 2004. DOI: 10.1002/KIN.20036.
- [160] J. Warnatz, "Hydrocarbon Oxidation at High Temperatures," *Berichte der Bunsengesellschaft für physikalische Chemie*, vol. 87, no. 11, pp. 1008–1022, 1983. DOI: 10.1002/BBPC.19830871111.
- [161] F. Battin-Leclerc, V. Warth, R. Bounaceur, B. Husson, O. Herbinet, and P. A. Glaude, "The oxidation of large alkylbenzenes: An experimental and modeling study," *Proceedings of the Combustion Institute*, vol. 35, no. 1, pp. 349–356, 2015. DOI: 10.1016/J.PROCI.2014.05.087.
- [162] M. Hartmann, I. Gushterova, M. Fikri, C. Schulz, R. Schießl, and U. Maas, "Auto-ignition of toluene-doped n-heptane and iso-octane/air mixtures: High-pressure shock-tube experiments and kinetics modeling," *Combustion and Flame*, vol. 158, no. 1, pp. 172–178, 2011. DOI: 10.1016/J.COMBUSTFLAME.2010.08.005.

- [163] M. Dente, E. Ranzi, and A. G. Goossens, "Detailed prediction of olefin yields from hydrocarbon pyrolysis through a fundamental simulation model (SPYRO)," *Computers & Chemical Engineering*, vol. 3, no. 1-4, pp. 61–75, 1979. DOI: 10.1016/0098-1354(79)80013-7.
- [164] S. M. Burke, U. Burke, R. Mc Donagh, *et al.*, "An experimental and modeling study of propene oxidation. Part 2: Ignition delay time and flame speed measurements," *Combustion and Flame*, vol. 162, no. 2, pp. 296–314, 2015. DOI: 10.1016/J.COMBUSTFLAME.2014.07.032.
- [165] H.-H. Carstensen and A. M. Dean, "Rate Constant Rules for the Automated Generation of Gas-Phase Reaction Mechanisms," *Journal of Physical Chemistry A*, vol. 113, pp. 367–380, 2009. DOI: 10.1021/jp804939v.
- [166] K. Wang and A. M. Dean, "Rate rules and reaction classes," in *Mathematical Modelling of gas-phase complex reaction systems: pyrolysis and combustion*, T. Faravelli, F. Manenti, and E. Ranzi, Eds., Elsevier B.V., 2019, ch. 4, pp. 203–257.
- [167] L. Cai and H. Pitsch, "Mechanism optimization based on reaction rate rules," *Combustion and Flame*, vol. 161, no. 2, pp. 405–415, 2014. DOI: 10.1016/j.combustflame.2013.08.024.
- [168] ———, "Optimized chemical mechanism for combustion of gasoline surrogate fuels," *Combustion and Flame*, vol. 162, no. 5, pp. 1623–1637, 2015. DOI: 10.1016/j.combustflame.2014.11.018.
- [169] M. Evans and M. Polanyi, "Some Applications of the Transition State Method To the Calculation of Reaction Velocities, Especially in Solution.," *Transactions of the Faraday Society*, vol. 31, pp. 875–894, 1935. DOI: 10.1039/TF9353100875.
- [170] A. Ratkiewicz, L. K. Huynh, T. N. Truong, H. Chi Minh City, and T. Chanh Hiep Ward, "Performance of First-Principles-Based Reaction Class Transition State Theory," *Journal of Physical Chemistry B*, vol. 120, pp. 1871–1884, 2016. DOI: 10.1021/acs.jpcc.5b09564.
- [171] H. H. Carstensen and A. M. Dean, "Development of detailed kinetic models for the thermal conversion of biomass via first principle methods and rate estimation rules," *ACS Symposium Series*, vol. 1052, pp. 201–243, 2010. DOI: 10.1021/bk-2010-1052.ch010.
- [172] L. P. Hammett, "The Effect of Structure upon the Reactions of Organic Compounds. Benzene Derivatives," *Journal of the American Chemical Society*, vol. 59, no. 1, pp. 96–103, 1937. DOI: 10.1021/ja01280a022.
- [173] J. Taft Robert W, "Linear free energy relationships from rates of esterification and hydrolysis of aliphatic and ortho-substituted benzoate esters," *Journal of the American Chemical Society*, vol. 74, no. 11, pp. 2729–2732, 1952.
- [174] T. N. Truong and T.-T. T. Truong, "A reaction class approach with the integrated molecular orbital+molecular orbital methodology," *Chemical Physics Letters*, vol. 314, no. 5-6, pp. 529–533, 1999. DOI: 10.1016/s0009-2614(99)01188-4.

- [175] J. F. Orrego, T. N. Truong, and F. Mondragón, “A Linear Energy Relationship between Activation Energy and Absolute Hardness: A Case Study with the O(³P) Atom-Addition Reactions to Polyaromatic Hydrocarbons,” *Journal of Physical Chemistry A*, vol. 112, no. 36, pp. 8205–8207, 2008. DOI: 10.1021/jp805012f.
- [176] R. Sumathi, H.-H. Carstensen, and W. H. Green, “Reaction Rate Prediction via Group Additivity Part 1: H Abstraction from Alkanes by H and CH₃,” *Journal of Physical Chemistry A*, vol. 105, pp. 6910–6925, 2001. DOI: 10.1021/jp010697q.
- [177] —, “Reaction Rate Prediction via Group Additivity, Part 2: H-Abstraction from Alkenes, Alkynes, Alcohols, Aldehydes, and Acids by H Atoms,” *Journal of Physical Chemistry A*, vol. 105, pp. 8969–8984, 2001. DOI: 10.1021/jp011827y.
- [178] R. Sumathi, H.-H. Carstensen, W. H. Green, and Y. Xch, “Reaction Rate Predictions Via Group Additivity. Part 3: Effect of Substituents with CH₂ as the Mediator,” *Journal of Physical Chemistry A*, vol. 106, pp. 5474–5489, 2002. DOI: 10.1021/jp013957c.
- [179] M. K. Sabbe, M. F. Reyniers, M. Waroquier, and G. B. Marin, “Hydrogen radical additions to unsaturated hydrocarbons and the reverse β -scission reactions: Modeling of activation energies and pre-exponential factors,” *ChemPhysChem*, vol. 11, no. 1, pp. 195–210, 2010. DOI: 10.1002/cphc.200900509.
- [180] A. Ince, H.-H. Carstensen, M.-F. Reyniers, and G. B. Marin, “First-principles based group additivity values for thermochemical properties of substituted aromatic compounds,” *AIChE Journal*, vol. 61, no. 11, pp. 3858–3870, 2015. DOI: 10.1002/aic.15008.
- [181] A. Ince, H.-H. Carstensen, M. Sabbe, M.-F. Reyniers, and G. B. Marin, “Group additive modeling of substituent effects in monocyclic aromatic hydrocarbon radicals,” *AIChE Journal*, vol. 63, no. 6, pp. 2089–2106, 2017. DOI: 10.1002/aic.15588.
- [182] —, “Modeling of thermodynamics of substituted toluene derivatives and benzylic radicals via group additivity,” *AIChE Journal*, vol. 64, no. 10, pp. 3649–3661, 2018. DOI: 10.1002/aic.16350.
- [183] M. Saeys, M.-F. Reyniers, V. Van Speybroeck, M. Waroquier, and G. B. Marin, “Ab Initio Group Contribution Method for Activation Energies of Hydrogen Abstraction Reactions,” *ChemPhysChem*, vol. 7, no. 1, pp. 188–199, 2006. DOI: 10.1002/cphc.200500206.
- [184] L. K. Huynh, S. Zhang, and T. N. Truong, “Kinetics of hydrogen abstraction O(³P) + alkane \rightarrow OH + alkyl reaction class: An application of the reaction class transition state theory,” *Combustion and Flame*, vol. 152, pp. 177–185, 2008. DOI: 10.1016/j.combustflame.2007.08.006.
- [185] S. Zhang and T. N. Truong, “Kinetics of Hydrogen Abstraction Reaction Class H + H-C(sp³): First-Principles Predictions Using the Reaction Class Transition State Theory,” *Journal of Physical Chemistry A*, vol. 107, pp. 1138–1147, 2003. DOI: 10.1021/jp021265y.

- [186] A. Ratkiewicz, J. Bieniewska, and T. N. Truong, “Kinetics of the Hydrogen Abstraction $R-OH + H \rightarrow$ Reaction Class Transition An Application of the $R-OH + H_2$ Reaction Class: State Theory,” *International Journal of Chemical Kinetics*, vol. 43, no. 3, pp. 154–160, 2011. DOI: 10.1002/kin.
- [187] P. A. Willems and G. F. Froment, “Kinetic Modeling of the Thermal Cracking of Hydrocarbons. 2. Calculation of Activation Energies,” *Industrial & Engineering Chemistry Research*, vol. 27, no. 11, pp. 1966–1971, 1988.
- [188] ———, “Kinetic Modeling of the Thermal Cracking of Hydrocarbons. 1. Calculation of Frequency Factors,” *Industrial & Engineering Chemistry Research*, vol. 27, no. 11, pp. 1959–1966, 1988.
- [189] A. Ratkiewicz and T. N. Truong, “Kinetics of the C-C Bond Beta Scission Reactions in Alkyl Radical Reaction Class,” *Journal of Physical Chemistry A*, vol. 116, pp. 6643–6654, 2012. DOI: 10.1021/jp3018265.
- [190] M. K. Sabbe, M. F. Reyniers, V. Van Speybroeck, M. Waroquier, and G. B. Marin, “Carbon-centered radical addition and β -scission reactions: Modeling of activation energies and pre-exponential factors,” *ChemPhysChem*, vol. 9, no. 1, pp. 124–140, 2008. DOI: 10.1002/cphc.200700469.
- [191] “Pressure-Dependent Rate Rules for Intramolecular H-Migration Reactions of Hydroperoxyalkylperoxy Radicals in Low Temperature,” *Journal of Physical Chemistry A*, vol. 121, no. 16, pp. 3001–3018, 2017. DOI: 10.1021/ACS.JPCA.6B10818.
- [192] “Pressure-dependent rate rules for intramolecular H-migration reactions of normal-alkyl cyclohexylperoxy radicals,” *Combustion and Flame*, vol. 204, pp. 176–188, 2019. DOI: 10.1016/J.COMBUSTFLAME.2019.03.011.
- [193] X. Sun, W. Zong, J. Wang, Z. Li, and X. Li, “Pressure-dependent rate rules for cycloaddition, intramolecular H-shift, and concerted elimination reactions of alkenyl peroxy radicals at low temperature,” *Physical Chemistry Chemical Physics*, vol. 21, no. 20, pp. 10 693–10 705, 2019. DOI: 10.1039/C9CP01207A.
- [194] J. D. Watts, J. Gauss, and R. J. Bartlett, “Coupled-cluster methods with noniterative triple excitations for restricted open-shell Hartree–Fock and other general single determinant reference functions. Energies and analytical gradients,” *Journal of Chemical Physics*, vol. 98, no. 11, p. 8718, 1993. DOI: 10.1063/1.464480.
- [195] G. Knizia, T. B. Adler, and H.-J. Werner, “Simplified CCSD(T)-F12 methods: Theory and benchmarks,” *Journal of Chemical Physics*, vol. 130, p. 054104, 2009. DOI: 10.1063/1.3054300.
- [196] T. J. Lee and P. R. Taylor, “A Diagnostic for Determining the Quality of Single-Reference Electron Correlation Methods,” *International Journal of Quantum Chemistry: Quantum Chemistry Symposium 23*, pp. 199–207, 1989.

- [197] D. Polino, S. J. Klippenstein, L. B. Harding, and Y. Georgievskii, "Predictive theory for the addition and insertion kinetics of $^1\text{CH}_2$ reacting with unsaturated hydrocarbons," *Journal of Physical Chemistry A*, vol. 117, no. 48, pp. 12 677–12 692, 2013. DOI: 10.1021/jp406246y.
- [198] C. F. Goldsmith, L. B. Harding, Y. Georgievskii, J. A. Miller, and S. J. Klippenstein, "Temperature and Pressure-Dependent Rate Coefficients for the Reaction of Vinyl Radical with Molecular Oxygen," *Journal of Physical Chemistry A*, vol. 119, no. 28, pp. 7766–7779, 2015. DOI: 10.1021/acs.jpca.5b01088.
- [199] H. J. Werner, "Third-order multireference perturbation theory The CASPT3 method," *Molecular Physics*, vol. 89, no. 2, pp. 645–661, 1996. DOI: 10.1080/002689796173967.
- [200] S. J. Klippenstein and C. Cavallotti, "Ab initio kinetics for pyrolysis and combustion systems," in *Mathematical Modelling of gas-phase complex reaction systems: pyrolysis and combustion*, T. Faravelli, F. Manenti, and F. Ranzi, Eds., Elsevier B.V., 2019, ch. 2, pp. 115–167.
- [201] C. P. Moradi, A. M. Morrison, S. J. Klippenstein, F. Goldsmith, and G. E. Douberly, "Propargyl + O_2 Reaction in Helium Droplets: Entrance Channel Barrier or Not?" *Journal of Physical Chemistry A*, vol. 117, pp. 13 626–13 635, 2013. DOI: 10.1021/jp407652f.
- [202] H.-J. Werner, P. J. Knowles, F. R. Manby, *et al.*, "The Molpro quantum chemistry package," *Journal of Chemical Physics*, vol. 152, p. 144 107, 2020. DOI: 10.1063/5.0005081.
- [203] B. O. Roos and K. Andersson, "Multiconfigurational perturbation theory with level shift - the Cr_2 potential revisited," *Chemical Physics Letters*, vol. 245, pp. 215–223, 1995.
- [204] G. Ghigo and O. Roos, "A modified definition of the zeroth-order Hamiltonian in multiconfigurational perturbation theory (CASPT2)," *Chemical Physics Letters*, vol. 396, pp. 142–149, 2004. DOI: 10.1016/j.cplett.2004.08.032.
- [205] R. G. Parr, "Density Functional Theory of Atoms and Molecules," in *Horizons of Quantum Chemistry*, Springer, Dordrecht, 1980, pp. 5–15. DOI: 10.1007/978-94-009-9027-2_2.
- [206] N. Mardirossian and M. Head-Gordon, "Thirty years of density functional theory in computational chemistry: An overview and extensive assessment of 200 density functionals," *Molecular Physics*, vol. 115, no. 19, pp. 2315–2372, 2017. DOI: 10.1080/00268976.2017.1333644.
- [207] J. P. Perdew, A. Ruzsinszky, J. Tao, V. N. Staroverov, G. E. Scuseria, and G. I. Csonka, "Prescription for the design and selection of density functional approximations: More constraint satisfaction with fewer fits," *Journal of Chemical Physics*, vol. 123, no. 6, p. 062 201, 2005. DOI: 10.1063/1.1904565.

- [208] Y. Zhao and D. G. Truhlar, "The M06 suite of density functionals for main group thermochemistry, thermochemical kinetics, noncovalent interactions, excited states, and transition elements: two new functionals and systematic testing of four M06-class functionals and 12 other function," *Theoretical Chemistry Accounts*, vol. 120, no. 1-3, pp. 215-241, 2008. DOI: 10.1007/s00214-007-0310-x.
- [209] J.-D. Chai and M. Head-Gordon, "Long-range corrected hybrid density functionals with damped atom-atom dispersion corrections," *Physical Chemistry Chemical Physics*, vol. 10, no. 44, p. 6615, 2008. DOI: 10.1039/b810189b.
- [210] S. Grimme, J. Antony, S. Ehrlich, and H. Krieg, "A consistent and accurate ab initio parametrization of density functional dispersion correction (DFT-D) for the 94 elements H-Pu," *The Journal of Chemical Physics*, vol. 132, no. 15, p. 154104, 2010. DOI: 10.1063/1.3382344.
- [211] A. L. East and L. Radom, "Ab initio statistical thermodynamical models for the computation of third-law entropies," *Journal of Chemical Physics*, vol. 106, no. 16, pp. 6655-6674, 1997. DOI: 10.1063/1.473958.
- [212] S. Sharma, S. Raman, and W. H. Green, "Intramolecular Hydrogen Migration in Alkylperoxy and Hydroperoxyalkylperoxy Radicals: Accurate Treatment of Hindered Rotors," *Journal of Physical Chemistry A*, vol. 114, no. 18, pp. 5689-5701, 2010. DOI: 10.1021/jp9098792.
- [213] J. Zheng, T. Yu, E. Papajak, I. M. Alecu, S. L. Mielke, and D. G. Truhlar, "Practical methods for including torsional anharmonicity in thermochemical calculations on complex molecules: The internal-coordinate multi-structural approximation," *Physical Chemistry Chemical Physics*, vol. 13, no. 23, pp. 10885-10907, 2011. DOI: 10.1039/C0CP02644A.
- [214] V. Barone, "Anharmonic vibrational properties by a fully automated second-order perturbative approach," *Journal of Chemical Physics*, vol. 122, p. 14108, 2005. DOI: 10.1063/1.1824881.
- [215] I. M. Alecu, J. Zheng, Y. Zhao, and D. G. Truhlar, "Computational Thermochemistry: Scale Factor Databases and Scale Factors for Vibrational Frequencies Obtained from Electronic Model Chemistries," *Journal of Chemical Theory and Computation*, vol. 6, no. 9, pp. 2872-2887, 2010. DOI: 10.1021/CT100326H.
- [216] L. G. Gao, J. Zheng, A. Fernández-Ramos, D. G. Truhlar, and X. Xu, "Kinetics of the Methanol Reaction with OH at Interstellar, Atmospheric, and Combustion Temperatures," *Journal of the American Chemical Society*, vol. 140, no. 8, pp. 2906-2918, 2018. DOI: 10.1021/JACS.7B12773.
- [217] R. M. Zhang, D. G. Truhlar, and X. Xu, "Kinetics of the Toluene Reaction with OH Radical," *Research*, pp. 1-19, 2019. DOI: 10.34133/2019/5373785.
- [218] A. Karton, "A computational chemist's guide to accurate thermochemistry for organic molecules," *Wiley Interdisciplinary Reviews: Computational Molecular Science*, vol. 6, no. 3, pp. 292-310, 2016. DOI: 10.1002/WCMS.1249.

- [219] A. Daniel Boese, M. Oren, O. Atasoylu, J. M. Martin, M. Kállay, and J. Gauss, "W3 theory: Robust computational thermochemistry in the kJ/mol accuracy range," *Journal of Chemical Physics*, vol. 120, no. 9, p. 4129, 2004. DOI: 10.1063/1.1638736.
- [220] M. E. Harding, J. Vázquez, B. Ruscic, A. K. Wilson, J. Gauss, and J. F. Stanton, "High-accuracy extrapolated ab initio thermochemistry. III. Additional improvements and overview," *Journal of Chemical Physics*, vol. 128, no. 11, p. 114111, 2008. DOI: 10.1063/1.2835612.
- [221] S. J. Klippenstein, L. B. Harding, and B. Ruscic, "Ab Initio Computations and Active Thermochemical Tables Hand in Hand: Heats of Formation of Core Combustion Species," *Journal of Physical Chemistry A*, vol. 121, no. 35, pp. 6580–6602, 2017. DOI: 10.1021/acs.jpca.7b05945.
- [222] L. C. Snyder, "Heats of Reaction from Hartree-Fock Energies of Closed-Shell Molecules," *The Journal of Chemical Physics*, vol. 46, no. 9, p. 3602, 1967. DOI: 10.1063/1.1841264.
- [223] A. Sengupta and K. Raghavachari, "Prediction of Accurate Thermochemistry of Medium and Large Sized Radicals Using Connectivity-Based Hierarchy (CBH)," *Journal of Chemical Theory and Computation*, vol. 10, pp. 4342–4350, 2014. DOI: 10.1021/ct500484f.
- [224] H. Eyring, "The Activated Complex in Chemical Reactions," *The Journal of Chemical Physics*, vol. 3, no. 2, pp. 107–115, 1935. DOI: 10.1063/1.1749604.
- [225] D. G. Truhlar, B. C. Garrett, and S. J. Klippenstein, "Current Status of Transition-State Theory," *Journal of Physical Chemistry*, vol. 100, no. 31, pp. 12771–12800, 1996. DOI: 10.1021/jp953748q.
- [226] D. G. Truhlar and B. C. Garrett, "Variational Transition-State Theory," *Accounts of Chemical Research*, vol. 13, no. 12, pp. 440–448, 1980. DOI: 10.1021/ar50156a002.
- [227] W. H. Miller, N. C. Handy, and J. E. Adams, "Reaction path Hamiltonian for polyatomic molecules," *The Journal of Chemical Physics*, vol. 72, no. 1, p. 99, 1980. DOI: 10.1063/1.438959.
- [228] R. A. Marcus and O. K. Rice, "The Kinetics of the Recombination of Methyl Radicals and Iodine Atoms," *Journal of Physical Chemistry*, vol. 55, pp. 894–908, 1951. DOI: 10.1021/j150489a013.
- [229] R. A. Marcus, "Unimolecular Dissociations and Free Radical Recombination Reactions," *Journal of Chemical Physics*, vol. 20, no. 3, p. 364, 1952. DOI: 10.1063/1.1700424.
- [230] O. K. Rice and H. C. Ramsperger, "Theories of unimolecular gas reactions at low pressures," *Journal of American Chemical Society*, vol. 49, no. 7, pp. 1618–1629, 1927. DOI: 10.1021/ja01406a001.
- [231] L. Stevenson Kassel, "Studies in homogeneous gas reactions I," *Journal of Physical Chemistry*, vol. 32, pp. 225–242, 1928. DOI: 10.1021/j150284a007.

- [232] ———, “Studies in homogeneous gas reactions II Introduction of quantum theory,” *Journal of Physical Chemistry*, vol. 32, pp. 1065–1079, 1928. DOI: 10.1021/j150289a011.
- [233] S. J. Klippenstein, “Variational optimizations in the Rice-Ramsperger-Kassel-Marcus theory calculations for unimolecular dissociations with no reverse barrier Variational optimizations in the Rice-Ramsperger-Kassel-Marcus theory calculations for unimolecular dissociations wit,” *Journal of Chemical Physics*, vol. 96, no. 1, pp. 367–371, 1992. DOI: 10.1063/1.462472.
- [234] Y. Georgievskii and S. J. Klippenstein, “Transition State Theory for Multichannel Addition Reactions: Multifaceted Dividing Surfaces,” *Journal of Physical Chemistry A*, vol. 107, pp. 9776–9781, 2003. DOI: 10.1021/jp034564b.
- [235] ———, “Variable reaction coordinate transition state theory: Analytic results and application to the $C_2H_3+H \rightarrow C_2H_4$ reaction,” *The Journal of Chemical Physics*, vol. 118, no. 12, pp. 5442–5455, 2003. DOI: 10.1063/1.1539035.
- [236] ———, “Long-range transition state theory,” *The Journal of Chemical Physics*, vol. 122, p. 194 103, 2005. DOI: 10.1063/1.1899603.
- [237] D. M. Wardlaw and R. A. Marcus, “RRKM reaction rate theory for transition states of any looseness,” *Chemical Physics Letters*, vol. 110, no. 3, pp. 230–234, 1984. DOI: 10.1016/0009-2614(84)85219-7.
- [238] ———, “Unimolecular reaction rate theory for transition states of partial looseness. II. Implementation and analysis with applications to NO_2 and C_2H_6 dissociations,” *The Journal of Chemical Physics*, vol. 83, no. 7, pp. 3462–3480, 1985. DOI: 10.1063/1.449151.
- [239] D. M. Wardlaw, R. A. Marcus, and A. Amos, “Unimolecular Reaction Rate Theory for Transition States of Any Looseness. 3. Application to Methyl Radical Recombination,” *J. Phys. Chem*, vol. 90, pp. 5383–5393, 1986. DOI: 10.1021/j100412a098.
- [240] S. J. Klippenstein, “Implementation of RRKM theory for highly flexible transition states with a bond length as the reaction coordinate,” *Chemical Physics Letters*, vol. 170, no. 1, pp. 71–77, 1990. DOI: 10.1016/0009-2614(90)87092-6.
- [241] F. Zhang, A. Nicolle, L. Xing, and S. J. Klippenstein, “Recombination of aromatic radicals with molecular oxygen,” *Proceedings of the Combustion Institute*, vol. 36, no. 1, pp. 169–177, 2017. DOI: 10.1016/J.PROCI.2016.06.021.
- [242] C. R. Mulvihill, A. D. Danilack, C. F. Goldsmith, *et al.*, “Non-Boltzmann Effects in Chain Branching and Pathway Branching for Diethyl Ether Oxidation,” *Energy & Fuels*, vol. 35, no. 21, pp. 17 890–17 908, 2021. DOI: 10.1021/ACS.ENERGYFUELS.1C02196.
- [243] S. J. Klippenstein and L. B. Harding, “Predictive theory for the combination kinetics of two alkyl radicals,” *Physical Chemistry Chemical Physics*, vol. 8, pp. 1133–1147, 2006. DOI: 10.1039/b515914h.

- [244] J. C. Light, "Phase-Space Theory of Chemical Kinetics," *The Journal of Chemical Physics*, vol. 40, pp. 3221–3229, 1964. DOI: 10.1063/1.1724989.
- [245] P. Pechukas and J. C. Light, "On Detailed Balancing and Statistical Theories of Chemical Kinetics," *The Journal of Chemical Physics*, vol. 42, no. 9, pp. 3281–3291, 1965. DOI: 10.1063/1.1696411.
- [246] D. G. Truhlar, "Intermediate Coupling Probability Matrix Approach to Chemical Reactions. Dependence of the Reaction Cross Section for $K + HCl = KCl + H$ on Initial Translational and Vibrational Energy," *Journal of the American Chemical Society*, vol. 97, no. 22, pp. 6310–6317, 1975. DOI: 10.1021/ja00855a004.
- [247] A. Fernández-Ramos, J. A. Miller, S. J. Klippenstein, and D. G. Truhlar, "Modeling the kinetics of bimolecular reactions," *Chemical Reviews*, vol. 106, no. 11, pp. 4518–4584, 2006. DOI: 10.1021/cr050205w.
- [248] B. C. Garrett and D. G. Truhlar, "Generalized Transition State Theory. Bond Energy-Bond Order Method for Canonical Variational Calculations with Application to Hydrogen Atom Transfer Reactions," *Journal of the American Chemical Society*, vol. 101, no. 16, pp. 4534–4548, 1979. DOI: 10.1021/ja00510a019.
- [249] R. Cvetanovic, "Evaluated chemical kinetic data for the reactions of atomic oxygen $O(^3P)$ with unsaturated hydrocarbons," *Journal of Physical Chemistry, Reference data*, vol. 16, no. 2, pp. 261–326, 1987. DOI: 10.1063/1.555783.
- [250] I. Gimondi, C. Cavallotti, G. Vanuzzo, N. Balucani, and P. Casavecchia, "Reaction Dynamics of $O(^3P) +$ Propyne: II. Primary Products, Branching Ratios, and Role of Intersystem Crossing from Ab Initio Coupled Triplet/Singlet Potential Energy Surfaces and Statistical Calculations," *Journal of Physical Chemistry A*, vol. 120, no. 27, pp. 4619–4633, 2016. DOI: 10.1021/acs.jpca.6b01564.
- [251] G. Vanuzzo, N. Balucani, F. Leonori, *et al.*, "Isomer-Specific Chemistry in the Propyne and Allene Reactions with Oxygen Atoms: $CH_3CH + CO$ versus $CH_2CH_2 + CO$ Products," *Journal of Physical Chemistry Letters*, vol. 7, no. 6, pp. 1010–1015, 2016. DOI: 10.1021/acs.jpcllett.6b00262.
- [252] Y. Bedjanian and J. Morin, "Reaction of $O(^3P)$ with C_3H_6 : Yield of the Reaction Products as a Function of Temperature," *Journal of Physical Chemistry A*, vol. 121, no. 8, pp. 1553–1562, 2017. DOI: 10.1021/acs.jpca.6b12739.
- [253] N. Balucani, F. Leonori, P. Casavecchia, B. Fu, and J. M. Bowman, "Crossed Molecular Beams and Quasiclassical Trajectory Surface Hopping Studies of the Multichannel Nonadiabatic $O(^3P) +$ Ethylene Reaction at High Collision Energy," *Journal of Physical Chemistry A*, vol. 119, no. 50, pp. 12498–12511, 2015. DOI: 10.1021/acs.jpca.5b07979.
- [254] L. Pratali Maffei, C. Cavallotti, A. Caracciolo, N. Balucani, and P. Casavecchia, "Rate rules for the reactions of oxygen atoms with terminal alkenes," *Fuel*, vol. 263, p. 116536, 2020. DOI: 10.1016/j.fuel.2019.116536.

- [255] C. Cavallotti, C. De Falco, L. Pratali Maffei, *et al.*, “Theoretical Study of the Extent of Intersystem Crossing in the $O(^3P) + C_6H_6$ Reaction with Experimental Validation,” *Journal of Physical Chemistry Letters*, vol. 11, no. 22, pp. 9621–9628, 2020. DOI: 10.1021/acs.jpcllett.0c02866.
- [256] J. N. Harvey, M. Aschi, H. Schwarz, and W. Koch, “The singlet and triplet states of phenyl cation. A hybrid approach for locating minimum energy crossing points between non-interacting potential energy surfaces,” *Theoretical Chemistry Accounts*, vol. 99, no. 2, pp. 95–99, 1998. DOI: 10.1007/s002140050309.
- [257] J. N. Harvey, “Understanding the kinetics of spin-forbidden chemical reactions,” *Physical Chemistry Chemical Physics*, vol. 9, pp. 331–343, 2007. DOI: 10.1039/b614390c.
- [258] C. Cavallotti, F. Leonori, N. Balucani, *et al.*, “Relevance of the channel leading to formaldehyde + triplet ethylidene in the $O(^3P) +$ propene reaction under combustion conditions,” *Journal of Physical Chemistry Letters*, vol. 5, no. 23, pp. 4213–4218, 2014. DOI: 10.1021/jz502236y.
- [259] X. Li, A. W. Jasper, J. Zádor, J. A. Miller, and S. J. Klippenstein, “Theoretical kinetics of $O + C_2H_4$,” *Proceedings of the Combustion Institute*, vol. 36, pp. 219–227, 2017. DOI: 10.1016/j.proci.2016.06.053.
- [260] W. Hu, G. Lendvay, B. Maiti, and G. C. Schatz, “Trajectory surface hopping study of the $O(^3P) +$ ethylene reaction dynamics,” *Journal of Physical Chemistry A*, vol. 112, no. 10, pp. 2093–2103, 2008. DOI: 10.1021/jp076716z.
- [261] C. Zener, “Non-Adiabatic Crossing of Energy Levels,” *Proceedings of the Royal Society A: Mathematical, Physical and Engineering Sciences*, vol. 137, no. 833, pp. 696–702, 1932. DOI: 10.1098/rspa.1932.0165.
- [262] J. N. Harvey, M. Aschi, H. Schwarz, and W. Koch, “The singlet and triplet states of phenyl cation. A hybrid approach for locating minimum energy crossing points between non-interacting potential energy surfaces,” *Theoretical Chemistry Accounts*, vol. 99, no. 2, pp. 95–99, 1998. DOI: 10.1007/s002140050309.
- [263] C. Eckart, “The penetration of a potential barrier by electrons,” *Physical Review*, vol. 35, no. 11, pp. 1303–1309, 1930. DOI: 10.1103/PhysRev.35.1303.
- [264] B. Widom, “Molecular transitions and chemical reaction rates,” *Science*, vol. 148, no. 3677, pp. 1555–1560, 1965. DOI: 10.1126/science.148.3677.1555.
- [265] J. A. Miller and S. J. Klippenstein, “Master Equation Methods in Gas Phase Chemical Kinetics,” *Journal of Physical Chemistry A*, vol. 110, pp. 10 528–10 544, 2006. DOI: 10.1021/jp062693x.
- [266] R. C. Reid, T. K. Sherwood, and R. E. Street, *The Properties of Gases and Liquids, Fifth edition*. 2001. DOI: 10.1063/1.3060771.
- [267] B. A. Finlayson, B. A. Finlayson, and C. Engineering, *Ullmann’s Encyclopedia of Industrial Chemistry*, October. 2007. DOI: 10.1002/14356007.b01.

- [268] A. W. Jasper, "Predicting third-body collision efficiencies for water and other polyatomic baths," *Faraday Discussions*, 2022. DOI: 10.1039/d2fd00038e.
- [269] J. T. Bartis and B. Widom, "Stochastic models of the interconversion of three or more chemical species," *Journal of Chemical Physics*, vol. 60, no. 9, pp. 3474–3482, 1974. DOI: 10.1063/1.1681562.
- [270] J. A. Miller and S. J. Klippenstein, "Determining phenomenological rate coefficients from a time-dependent, multiple-well master equation: "species reduction" at high temperatures," *Physical Chemistry Chemical Physics*, vol. 15, no. 13, pp. 4744–4753, 2013. DOI: 10.1039/c3cp44337j.
- [271] —, "The Recombination of Propargyl Radicals and Other Reactions on a C₆H₆ Potential," *Journal of Physical Chemistry A*, vol. 107, no. 39, pp. 7783–7799, 2003. DOI: 10.1021/jp030375h.
- [272] S. J. Klippenstein and J. A. Miller, "From the time-dependent, multiple-well master equation to phenomenological rate coefficients," *Journal of Physical Chemistry A*, vol. 106, pp. 9267–9277, 2002. DOI: 10.1021/jp021175t.
- [273] J. A. Miller and S. J. Klippenstein, "From the multiple-well master equation to phenomenological rate coefficients: Reactions on a C₃H₄ potential energy surface," *Journal of Physical Chemistry A*, vol. 107, pp. 2680–2692, 2003. DOI: 10.1021/jp0221082.
- [274] O. K. Rice, "On the relation between equilibrium constant and the nonequilibrium rate constants of direct and reverse reactions," *Journal of Physical Chemistry*, vol. 65, no. 11, pp. 1972–1976, 1961. DOI: 10.1021/j100828a014.
- [275] D. Polino, A. Barbato, and C. Cavallotti, "Theoretical investigation of germane and germylene decomposition kinetics," *Physical Chemistry Chemical Physics*, vol. 12, no. 35, pp. 10622–10632, 2010. DOI: 10.1039/c002221g.
- [276] M. Fürst, A. Bertolino, A. Cuoci, T. Faravelli, A. Frassoldati, and A. Parente, "OptiSMOKE++: A toolbox for optimization of chemical kinetic mechanisms," *Computer Physics Communications*, vol. 264, p. 107940, 2021. DOI: 10.1016/j.cpc.2021.107940.
- [277] A. Bertolino, M. Fürst, A. Stagni, *et al.*, "An evolutionary, data-driven approach for mechanism optimization: theory and application to ammonia combustion," *Combustion and Flame*, vol. 229, p. 111366, 2021. DOI: 10.1016/j.combustflame.2021.02.012.
- [278] Yuri Georgievskii, J. A. Miller, and S. J. Klippenstein, "Association rate constants for reactions between resonance-stabilized radicals: C₃H₃+C₃H₃, C₃H₃+C₃H₅, and C₃H₅+C₃H₅," *Physical Chemistry Chemical Physics*, vol. 9, no. 31, pp. 4259–4268, 2007. DOI: 10.1039/B703261G.
- [279] S. Wang, D. F. Davidson, and R. K. Hanson, "Shock tube techniques for kinetic target data to improve reaction models," in *Mathematical Modelling of Gas-Phase Complex Reaction Systems: Pyrolysis and Combustion*, T. Faravelli, F. Manenti, and E. Ranzi, Eds., Elsevier B.V., 2019, ch. 3, pp. 169–202.

- [280] N. Hansen, M. Schenk, K. Moshhammer, and K. Kohse-Höinghaus, “Investigating repetitive reaction pathways for the formation of polycyclic aromatic hydrocarbons in combustion processes,” *Combustion and Flame*, vol. 180, pp. 250–261, 2017. DOI: 10.1016/J.COMBUSTFLAME.2016.09.013.
- [281] A. M. Mebel, Y. Georgievskii, A. W. Jasper, and S. J. Klippenstein, “Pressure-dependent rate constants for PAH growth: formation of indene and its conversion to naphthalene,” *Faraday Discussions*, vol. 195, pp. 637–670, 2016. DOI: 10.1039/c6fd00111d.
- [282] A. Raj, M. J. Al Rashidi, S. Ho Chung, and S. Mani Sarathy, “PAH Growth Initiated by Propargyl Addition: Mechanism Development and Computational Kinetics,” *Journal of Physical Chemistry A*, vol. 118, pp. 2865–2885, 2014. DOI: 10.1021/jp410704b.
- [283] M. Chaos, A. Kazakov, Z. Zhao, and F. L. Dryer, “A High-Temperature Chemical Kinetic Model for Primary Reference Fuels,” *International Journal of Chemical Kinetics*, vol. 39, no. 7, pp. 399–414, 2007. DOI: 10.1002/kin.20532.
- [284] J. Wei and J. C. W Kuo, “A lumping analysis in monomolecular reaction systems - Analysis of Exactly Lumpable System,” *Industrial & Engineering Chemistry Fundamentals*, vol. 8, no. 1, pp. 114–123, 1969. DOI: 10.1021/i160029a019.
- [285] J. C. W Kuo and J. Wei, “A lumping analysis in monomolecular reaction systems - Analysis of Approximately Lumpable System,” *Industrial & Engineering Chemistry Fundamentals*, vol. 8, no. 1, pp. 124–133, 1969. DOI: 10.1021/i160029a020.
- [286] H. Huang, M. Fairweather, J. F. Griffiths, A. S. Tomlin, and R. B. Brad, “A systematic lumping approach for the reduction of comprehensive kinetic models,” *Proceedings of the Combustion Institute*, vol. 30, no. 1, pp. 1309–1316, 2005. DOI: 10.1016/j.proci.2004.08.001.
- [287] T. Nagy and T. Turányi, “Reduction of very large reaction mechanisms using methods based on simulation error minimization,” *Combustion and Flame*, vol. 156, no. 2, pp. 417–428, 2009. DOI: 10.1016/j.combustflame.2008.11.001.
- [288] P. Pepiot-Desjardins and H. Pitsch, “An automatic chemical lumping method for the reduction of large chemical kinetic mechanisms,” *Combustion Theory and Modelling*, vol. 12, no. 6, pp. 1089–1108, 2008. DOI: 10.1080/13647830802245177.
- [289] S. S. Ahmed, F. Mauß, G. Moreácz, and T. Zeuch, “A comprehensive and compact n-heptane oxidation model derived using chemical lumping,” *Physical Chemistry Chemical Physics*, vol. 9, pp. 1107–1126, 2006. DOI: 10.1039/b614712g.
- [290] C. Cavallotti, M. Pelucchi, and A. Frassoldati, “Analysis of acetic acid gas phase reactivity: Rate constant estimation and kinetic simulations,” *Proceedings of the Combustion Institute*, vol. 37, no. 1, pp. 539–546, 2019. DOI: 10.1016/j.proci.2018.06.137.
- [291] L. Pratali Maffei, M. Pelucchi, C. Cavallotti, A. Bertolino, and T. Faravelli, “Master equation lumping for multi-well potential energy surfaces: A bridge between ab initio based rate constant calculations and large kinetic mechanisms,” *Chemical Engineering Journal*, vol. 422, p. 129954, 2021. DOI: 10.1016/J.CEJ.2021.129954.

- [292] G. R. Galimova, V. N. Azyazov, and A. M. Mebel, "Reaction mechanism, rate constants, and product yields for the oxidation of Cyclopentadienyl and embedded five-member ring radicals with hydroxyl," *Combustion and Flame*, vol. 187, pp. 147–164, 2018. DOI: 10.1016/j.combustflame.2017.09.005.
- [293] A. R. Ghildina, A. D. Oleinikov, V. N. Azyazov, and A. M. Mebel, "Reaction mechanism, rate constants, and product yields for unimolecular and H-assisted decomposition of 2,4-cyclopentadienone and oxidation of cyclopentadienyl with atomic oxygen," *Combustion and Flame*, vol. 183, pp. 181–193, 2017. DOI: 10.1016/j.combustflame.2017.05.015.
- [294] A. D. Oleinikov, V. N. Azyazov, and A. M. Mebel, "Oxidation of cyclopentadienyl radical with molecular oxygen: A theoretical study," *Combustion and Flame*, vol. 191, pp. 309–319, 2018. DOI: 10.1016/j.combustflame.2018.01.010.
- [295] A. E. Long, S. S. Merchant, A. G. Vandeputte, *et al.*, "Pressure dependent kinetic analysis of pathways to naphthalene from cyclopentadienyl recombination," *Combustion and Flame*, vol. 187, pp. 247–256, 2018. DOI: 10.1016/j.combustflame.2017.09.008.
- [296] D. H. Kim, J. A. Mulholland, D. Wang, and A. Violi, "Pyrolytic Hydrocarbon Growth from Cyclopentadiene," *Journal of Physical Chemistry A*, vol. 114, no. 47, pp. 12411–12416, 2010. DOI: 10.1021/jp106749k.
- [297] M. R. Djokic, K. M. Van Geem, C. Cavallotti, A. Frassoldati, E. Ranzi, and G. B. Marin, "An experimental and kinetic modeling study of cyclopentadiene pyrolysis: First growth of polycyclic aromatic hydrocarbons," *Combustion and Flame*, vol. 161, no. 11, pp. 2739–2751, 2014. DOI: 10.1016/J.COMBUSTFLAME.2014.04.013.
- [298] A. J. Vervust, M. R. Djokic, S. S. Merchant, *et al.*, "Detailed Experimental and Kinetic Modeling Study of Cyclopentadiene Pyrolysis in the Presence of Ethene," *Energy & Fuels*, vol. 32, pp. 3920–3934, 2018. DOI: 10.1021/acs.energyfuels.7b03560.
- [299] J. Bugler, B. Marks, O. Mathieu, *et al.*, "An ignition delay time and chemical kinetic modeling study of the pentane isomers," *Combustion and Flame*, vol. 163, pp. 138–156, 2016. DOI: 10.1016/j.combustflame.2015.09.014.
- [300] A. Pegurri, T. Dinelli, A. Bertolino, *et al.*, "Coupling chemical lumping to data-driven optimization for the kinetic modeling of oxymethylene ethers (OME1-4) combustion," *In preparation*, 2022.
- [301] M. Szwarc, "The determination of bond dissociation energies by pyrolytic methods," *Chemical Reviews*, vol. 47, pp. 75–173, 1950. DOI: 10.1021/cr60146a002.
- [302] R. Spielmann and C. A. Cramers, "Cyclopentadienic compounds as intermediates in the thermal degradation of phenols. Kinetics of the thermal decomposition of cyclopentadiene," *Chromatographia*, vol. 5, no. 12, pp. 295–300, 1972. DOI: 10.1007/BF02310746.

- [303] P. Frank, J. Herzler, T. H. Just, and C. Wahl, "High-temperature reactions of phenyl oxidation," *Symposium (International) on Combustion*, vol. 25, no. 1, pp. 833–840, 1994. DOI: 10.1016/S0082-0784(06)80717-4.
- [304] A. B. Lovell, K. Brezinsky, and I. Glassman, "Benzene oxidation perturbed by NO₂ addition," *Symposium (International) on Combustion*, vol. 22, no. 1, pp. 1063–1074, 1989. DOI: 10.1016/S0082-0784(89)80116-X.
- [305] A. Burcat and M. Dvinyaninov, "Detailed kinetics of cyclopentadiene decomposition studied in a shock tube," *International Journal of Chemical Kinetics*, vol. 29, no. 7, pp. 505–514, 1997. DOI: 10.1002/(SICI)1097-4601(1997)29:7<505::AID-KIN4>3.0.CO;2-Y.
- [306] K. Roy, P. Frank, and T. Just, "Shock tube study of high-temperature reactions of cyclopentadiene," *Israel Journal of Chemistry*, vol. 36, pp. 275–278, 1996. DOI: 10.1002/ijch.199600038.
- [307] R. D. Kern, Q. Zhang, J. Yao, *et al.*, "Pyrolysis of cyclopentadiene: Rates for initial C-H bond fission and the decomposition of c-C₅H₅," *Symposium (International) on Combustion*, vol. 27, no. 1, pp. 143–150, 1998. DOI: 10.1016/S0082-0784(98)80399-8.
- [308] M. J. Bearpark, M. A. Robb, and N. Yamamoto, "A CASSCF study of the cyclopentadienyl radical: conical intersections and the Jahn–Teller effect," *Spectrochimica Acta Part A: Molecular and Biomolecular Spectroscopy*, vol. 55, no. 3, pp. 639–646, 1999. DOI: 10.1016/S1386-1425(98)00267-4.
- [309] J. H. Kiefer, R. S. Tranter, H. Wang, and A. F. Wagner, "Thermodynamic functions for the cyclopentadienyl radical: The effect of Jahn-Teller distortion," *International Journal of Chemical Kinetics*, vol. 33, no. 12, pp. 834–845, 2001. DOI: 10.1002/KIN.10006.
- [310] X. Zhong and J. W. Bozzelli, "Thermochemical and kinetic analysis on the addition reactions of H, O, OH, and HO₂ with 1,3 cyclopentadiene," *International Journal of Chemical Kinetics*, vol. 29, no. 12, pp. 893–913, 1997. DOI: 10.1002/(SICI)1097-4601(1997)29:12<893::AID-KIN2>3.0.CO;2-H.
- [311] ———, "Thermochemical and Kinetic Analysis of the H, OH, HO₂, O, and O₂ Association Reactions with Cyclopentadienyl Radical," *Journal of Physical Chemistry A*, vol. 102, no. 20, pp. 3537–3555, 1998. DOI: 10.1021/jp9804446.
- [312] L. V. Moskaleva, A. M. Mebel, and M. C. Lin, "The CH₃+C₅H₅ reaction: A potential source of benzene at high temperatures," *Symposium (International) on Combustion*, vol. 26, no. 1, pp. 521–526, 1996. DOI: 10.1016/S0082-0784(96)80255-4.
- [313] C. F. Melius, M. E. Colvin, N. M. Marinov, W. J. Pitt, and S. M. Senkan, "Reaction mechanisms in aromatic hydrocarbon formation involving the C₅H₅ cyclopentadienyl moiety," *Symposium (International) on Combustion*, vol. 26, no. 1, pp. 685–692, 1996. DOI: 10.1016/S0082-0784(96)80276-1.

- [314] N. M. Marinov, W. J. Pitz, C. K. Westbrook, *et al.*, “Aromatic and Polycyclic Aromatic Hydrocarbon Formation in a Laminar Premixed n-Butane Flame,” *Combustion and Flame*, vol. 114, no. 1-2, pp. 192–213, 1998. DOI: 10.1016/S0010-2180(97)00275-7.
- [315] M. J. Castaldi, N. M. Marinov, C. F. Melius, *et al.*, “Experimental and modeling investigation of aromatic and polycyclic aromatic hydrocarbon formation in a premixed ethylene flame,” *Symposium (International) on Combustion*, vol. 26, no. 1, pp. 693–702, 1996. DOI: 10.1016/S0082-0784(96)80277-3.
- [316] V. V. Kislov and A. M. Mebel, “Ab Initio G3-type/Statistical Theory Study of the Formation of Indene in Combustion Flames. I. Pathways Involving Benzene and Phenyl Radical,” *Journal of Physical Chemistry A*, vol. 111, pp. 3922–3931, 2007. DOI: 10.1021/jp067135x.
- [317] D. Wang, A. Violi, D. H. Kim, and J. A. Mullholland, “Formation of Naphthalene, Indene, and Benzene from Cyclopentadiene Pyrolysis: A DFT Study,” *Journal of Physical Chemistry A*, vol. 110, pp. 4719–4725, 2006. DOI: 10.1021/jp053628a.
- [318] C. Cavallotti, D. Polino, A. Frassoldati, and E. Ranzi, “Analysis of some reaction pathways active during cyclopentadiene pyrolysis,” *Journal of Physical Chemistry A*, vol. 116, no. 13, pp. 3313–3324, 2012. DOI: 10.1021/jp212151p.
- [319] C. Cavallotti, S. Mancarella, R. Rota, and S. Carrà, “Conversion of C5 into C6 Cyclic Species through the Formation of C7 Intermediates,” *Journal of Physical Chemistry A*, vol. 111, pp. 3959–3969, 2007. DOI: 10.1021/jp067117f.
- [320] S. Sharma, M. R. Harper, and W. H. Green, “Modeling of 1,3-hexadiene, 2,4-hexadiene and 1,4-hexadiene-doped methane flames: Flame modeling, benzene and styrene formation,” *Combustion and Flame*, vol. 157, no. 7, pp. 1331–1345, 2010. DOI: 10.1016/J.COMBUSTFLAME.2010.02.012.
- [321] M. Baroncelli, Q. Mao, S. Galle, N. Hansen, and H. Pitsch, “Role of ring-enlargement reactions in the formation of aromatic hydrocarbons,” *Physical Chemistry Chemical Physics*, vol. 22, pp. 4699–4714, 2020. DOI: 10.1039/c9cp05854k.
- [322] Q. Mao, L. Cai, R. Langer, and H. Pitsch, “The role of resonance-stabilized radical chain reactions in polycyclic aromatic hydrocarbon growth: Theoretical calculation and kinetic modeling,” *Proceedings of the Combustion Institute*, vol. 38, no. 1, pp. 1459–1466, 2021. DOI: 10.1016/J.PROCI.2020.07.117.
- [323] S. M. Xu, X. H. Sun, W. G. Zong, Z. R. Li, and X. Y. Li, “Kinetic Analysis for Reaction of Cyclopentadiene with Hydroperoxyl Radical under Low- And Medium-Temperature Combustion,” *Journal of Physical Chemistry A*, vol. 124, no. 40, pp. 8280–8291, 2020. DOI: 10.1021/acs.jpca.0c02882.
- [324] N. M. Vandewiele, G. R. Magoon, K. M. Van Geem, M. F. Reyniers, W. H. Green, and G. B. Marin, “Experimental and modeling study on the thermal decomposition of jet propellant-10,” *Energy & Fuels*, vol. 28, no. 8, pp. 4976–4985, 2014. DOI: 10.1021/ef500936m.

- [325] Y. Tao, R. Xu, K. Wang, *et al.*, “A Physics-based approach to modeling real-fuel combustion chemistry – III. Reaction kinetic model of JP10,” *Combustion and Flame*, vol. 198, pp. 466–476, 2018. DOI: 10.1016/J.COMBUSTFLAME.2018.08.022.
- [326] M. Djokic, H. H. Carstensen, K. M. Van Geem, and G. B. Marin, “The thermal decomposition of 2,5-dimethylfuran,” *Proceedings of the Combustion Institute*, vol. 34, no. 1, pp. 251–258, 2013. DOI: 10.1016/J.PROCI.2012.05.066.
- [327] H. A. Michelsen, M. B. Colket, E. Bengtsson, *et al.*, “A Review of Terminology Used to Describe Soot Formation and Evolution under Combustion and Pyrolytic Conditions,” *ACS Nano*, vol. 14, pp. 12 470–12 490, 2020. DOI: 10.1021/acsnano.0c06226.
- [328] K. Roy, C. Horn, P. Frank, V. G. Slutsky, and T. Just, “High-Temperature investigations on the pyrolysis of cyclopentadiene,” *Symposium (International) on Combustion*, vol. 27, pp. 329–336, 1998. DOI: 10.1016/S0082-0784(98)80420-7.
- [329] H. Jin, D. Liu, J. Zou, *et al.*, “Chemical kinetics of hydroxyl reactions with cyclopentadiene and indene,” *Combustion and Flame*, vol. 217, pp. 48–56, 2020. DOI: 10.1016/j.combustflame.2020.03.016.
- [330] L. Moskaleva and M. Lin, “Computational study of the kinetics and mechanisms for the reaction of H atoms with $c\text{-C}_5\text{H}_6$,” *Proceedings of the Combustion Institute*, vol. 29, no. 1, pp. 1319–1327, 2002. DOI: 10.1016/S1540-7489(02)80162-6.
- [331] L. B. Harding, S. J. Klippenstein, and Y. Georgievskii, “On the Combination Reactions of Hydrogen Atoms with Resonance-Stabilized Hydrocarbon Radicals,” *Journal of Physical Chemistry A*, vol. 111, pp. 3789–3801, 2007. DOI: 10.1021/jp0682309.
- [332] G. B. Bacskay and J. C. Mackie, “The pyrolysis of cyclopentadiene: quantum chemical and kinetic modelling studies of the acetylene plus propyne/allene decomposition channels,” *Physical Chemistry Chemical Physics*, vol. 3, no. 12, pp. 2467–2473, 2001. DOI: 10.1039/b101317n.
- [333] V. V. Kislov and A. M. Mebel, “The Formation of Naphthalene, Azulene, and Fulvalene from Cyclic C5 Species in Combustion: An Ab Initio/RRKM Study of 9-H-Fulvalenyl ($\text{C}_5\text{H}_5\text{-C}_5\text{H}_4$) Radical Rearrangements,” *Journal of Physical Chemistry A*, vol. 111, pp. 9532–9543, 2007. DOI: 10.1021/jp0732099.
- [334] Q. Mao, L. Cai, and H. Pitsch, “Theoretical analysis and kinetic modeling of hydrogen abstraction and addition of 1,3-cyclopentadiene and associated reactions on the C_5H_7 potential energy surface,” *Combustion and Flame*, vol. 222, pp. 423–433, 2020. DOI: 10.1016/j.combustflame.2020.09.004.
- [335] J. Orme, H. Curran, and J. Simmie, “Shock tube study of 5 membered cyclic hydrocarbon oxidation,” *Proceedings of the European Combustion Meeting*, 2005.
- [336] R. G. Butler and I. Glassman, “Cyclopentadiene combustion in a plug flow reactor near 1150 K,” *Proceedings of the Combustion Institute*, vol. 32, no. 1, pp. 395–402, 2009. DOI: 10.1016/j.proci.2008.05.010.

- [337] H. Jin, L. Xing, J. Hao, *et al.*, “A chemical kinetic modeling study of indene pyrolysis,” *Combustion and Flame*, vol. 206, pp. 1–20, 2019. DOI: 10.1016/j.combustflame.2019.04.040.
- [338] H. Wang, Z. Liu, S. Gong, *et al.*, “Experimental and kinetic modeling study on 1,3-cyclopentadiene oxidation and pyrolysis,” *Combustion and Flame*, vol. 212, pp. 189–204, 2020. DOI: 10.1016/j.combustflame.2019.10.032.
- [339] S. E. Johnson, D. F. Davidson, and R. K. Hanson, “Shock Tube/Laser Absorption Measurements of Cyclopentadiene Pyrolysis,” *The Journal of Physical Chemistry A*, vol. 126, no. 29, pp. 4818–4826, 2022. DOI: 10.1021/ACS.JPCA.2C04381.
- [340] V. D. Knyazev, V. S. Arutyunov, and V. I. Vedenev, “The mechanism of O(³P) atom reaction with ethylene and other simple olefins,” *International Journal of Chemical Kinetics*, vol. 24, no. 6, pp. 545–561, 1992. DOI: 10.1002/kin.550240605.
- [341] S. Sharma and W. H. Green, “Computed Rate Coefficients and Product Yields for c-C₅H₅+CH₃ Products,” *Journal of Physical Chemistry A*, vol. 113, pp. 8871–8882, 2009. DOI: 10.1021/jp900679t.
- [342] C. Cavallotti and D. Polino, “On the kinetics of the C₅H₅+C₅H₅ reaction,” *Proceedings of the Combustion Institute*, vol. 34, no. 1, pp. 557–564, 2013. DOI: 10.1016/j.proci.2012.05.097.
- [343] R. K. Robinson and R. P. Lindstedt, “On the chemical kinetics of cyclopentadiene oxidation,” *Combustion and Flame*, vol. 158, no. 4, pp. 666–686, 2011. DOI: 10.1016/J.COMBUSTFLAME.2010.12.001.
- [344] Q. Mao, C. Huang, M. Baroncelli, *et al.*, “Unimolecular reactions of the resonance-stabilized cyclopentadienyl radicals and their role in the polycyclic aromatic hydrocarbon formation,” *Proceedings of the Combustion Institute*, vol. 38, no. 1, pp. 729–737, 2021. DOI: 10.1016/j.proci.2020.08.009.
- [345] D. S. Parker, F. Zhang, R. I. Kaiser, V. V. Kislov, and A. M. Mebel, “Indene Formation under Single-Collision Conditions from the Reaction of Phenyl Radicals with Allene and Methylacetylene—A Crossed Molecular Beam and Ab Initio Study,” *Chemistry – An Asian Journal*, vol. 6, no. 11, pp. 3035–3047, 2011. DOI: 10.1002/ASIA.201100535.
- [346] D. S. Parker, R. I. Kaiser, O. Kostko, and M. Ahmed, “Selective Formation of Indene through the Reaction of Benzyl Radicals with Acetylene,” *ChemPhysChem*, vol. 16, no. 10, pp. 2091–2093, 2015. DOI: 10.1002/CPHC.201500313.
- [347] L. Zhao, R. I. Kaiser, W. Lu, *et al.*, “Molecular mass growth through ring expansion in polycyclic aromatic hydrocarbons via radical-radical reactions,” *Nature communications*, vol. 10, p. 3689, 2019. DOI: 10.1038/s41467-019-11652-5.
- [348] A. Laskin and A. Lifshitz, “Thermal decomposition of indene. Experimental results and kinetic modeling,” *Symposium (International) on Combustion*, vol. 27, pp. 313–320, 1998. DOI: 10.1021/jp0040392.

- [349] M. Lu and J. A. Mulholland, "Aromatic hydrocarbon growth from indene," *Chemosphere*, vol. 42, no. 5-7, pp. 625–633, 2001. DOI: 10.1016/S0045-6535(00)00236-8.
- [350] S. Fascella, C. Cavallotti, R. Rota, and S. Carrà, "Quantum Chemistry Investigation of Key Reactions Involved in the Formation of Naphthalene and Indene," *Journal of Physical Chemistry A*, vol. 108, no. 17, pp. 3829–3843, 2004. DOI: 10.1021/JP037518K.
- [351] J. A. Mulholland, M. Lu, and D. H. Kim, "Pyrolytic growth of polycyclic aromatic hydrocarbons by cyclopentadienyl moieties," *Proceedings of the Combustion Institute*, vol. 28, no. 2, pp. 2593–2599, 2000. DOI: 10.1016/S0082-0784(00)80677-3.
- [352] V. S. Krasnoukhov, M. V. Zagidullin, I. P. Zavershinskiy, and A. M. Mebel, "Formation of Phenanthrene via Recombination of Indenyl and Cyclopentadienyl Radicals: A Theoretical Study," *Journal of Physical Chemistry A*, vol. 124, no. 48, pp. 9933–9941, 2020. DOI: 10.1021/acs.jpca.0c09091.
- [353] A. N. Morozov, I. A. Medvedkov, V. N. Azyazov, and A. M. Mebel, "Theoretical Study of the Phenoxy Radical Recombination with the O(³P) Atom, Phenyl plus Molecular Oxygen Revisited," *Journal of Physical Chemistry A*, vol. 125, no. 18, pp. 3965–3977, 2021. DOI: 10.1021/acs.jpca.1c01545.
- [354] E. Ranzi, A. Frassoldati, R. Grana, *et al.*, "Hierarchical and comparative kinetic modeling of laminar flame speeds of hydrocarbon and oxygenated fuels," *Progress in Energy and Combustion Science*, vol. 38, no. 4, pp. 468–501, 2012. DOI: 10.1016/j.pecs.2012.03.004.
- [355] A. W. Jasper and N. Hansen, "Hydrogen-assisted isomerizations of fulvene to benzene and of larger cyclic aromatic hydrocarbons," *Proceedings of the Combustion Institute*, vol. 34, no. 1, pp. 279–287, 2013. DOI: 10.1016/J.PROCI.2012.06.165.
- [356] A. M. Dean, "Detailed Kinetic Modeling of Autocatalysis in Methane Pyrolysis," *Journal of Physical Chemistry*, vol. 94, pp. 1432–1439, 1990. DOI: 10.1021/j100367a043.
- [357] F. Carbone, K. Gleason, and A. Gomez, "Probing gas-to-particle transition in a moderately sooting atmospheric pressure ethylene/air laminar premixed flame. Part I: gas phase and soot ensemble characterization," *Combustion and Flame*, vol. 181, pp. 315–328, 2017. DOI: 10.1016/j.combustflame.2017.01.029.
- [358] M. Baroncelli, Q. Mao, H. Pitsch, and N. Hansen, "Effects of C1-C3 hydrocarbon blending on aromatics formation in 1-butene counterflow flames," *Combustion and Flame*, vol. 230, p. 111 427, 2021. DOI: 10.1016/J.COMBUSTFLAME.2021.111427.
- [359] A. Ristori, P. Dagaut, A. El Bakali, G. Pengloan, and M. Cathonnet, "Benzene oxidation: Experimental results in a JDR and comprehensive kinetic modeling in JSR, shock-tube and flame," *Combustion Science and Technology*, vol. 167, pp. 223–256, 2001. DOI: 10.1080/00102200108952183.
- [360] A. E. Bakali, M. Ribaucour, A. Saylam, G. Vanhove, E. Therssen, and J. F. Pauwels, "Benzene addition to a fuel-stoichiometric methane/O₂/N₂ flat flame and to n-heptane/air mixtures under rapid compression machine," *Fuel*, vol. 85, no. 7-8, pp. 881–895, 2006. DOI: 10.1016/j.fuel.2005.10.009.

- [361] M. Urban, J. Noga, S. J. Cole, and R. J. Bartlett, "Towards a full CCSDT model for electron correlation," *Journal of Chemical Physics*, vol. 83, no. 8, pp. 4041–4046, 1985. DOI: 10.1063/1.449067.
- [362] T. Dunning Jr., "Gaussian basis sets for use in correlated molecular calculations. I. The atoms boron through neon and hydrogen," *Journal of Chemical Physics*, vol. 90, no. 2, pp. 1007–1023, 1989. DOI: 10.1063/1.456153.
- [363] J. M. Martin, "Ab initio total atomization energies of small molecules — towards the basis set limit," *Chemical Physics Letters*, vol. 259, no. 5-6, pp. 669–678, 1996. DOI: 10.1016/0009-2614(96)00898-6.
- [364] E. E. Greenwald, S. W. North, Y. Georgievskii, and S. J. Klippenstein, "A Two Transition State Model for Radical-Molecule Reactions: A Case Study of the Addition of OH to C₂H₄," *Journal of Physical Chemistry A*, vol. 109, no. 27, pp. 6031–6044, 2005. DOI: 10.1021/JP058041A.
- [365] L. Pratali Maffei, M. Pelucchi, T. Faravelli, and C. Cavallotti, "Theoretical Kinetics of HO₂+C₅H₅: A Missing Piece in Cyclopentadienyl Radical Oxidation Reactions," *Proceedings of the Combustion Institute 39*, vol. in press, 2022.
- [366] G. Katzer and A. F. Sax, "Far-Infrared Spectra of Ring Compounds. VIII. The Effect of a Finite Central Barrier on Pseudorotation in Five-Membered Rings," *Journal of Chemical Physics*, vol. 117, p. 1434, 2002. DOI: 10.1063/1.1511723.
- [367] A. W. Jasper, S. J. Klippenstein, and L. B. Harding, "Theoretical rate coefficients for the reaction of methyl radical with hydroperoxyl radical and for methylhydroperoxide decomposition," *Proceedings of the Combustion Institute*, vol. 32 I, no. 1, pp. 279–286, 2009. DOI: 10.1016/j.proci.2008.05.036.
- [368] Y. Chai and L. D. Pfefferle, "An experimental study of benzene oxidation at fuel-lean and stoichiometric equivalence ratio conditions," *Fuel*, vol. 77, no. 4, pp. 313–320, 1998. DOI: 10.1016/S0016-2361(97)00192-0.
- [369] Z. Shi, Y. Jiang, J. Yu, *et al.*, "Develop the low-temperature oxidation mechanism of cyclopentane: an experimental and theoretical study," *Chemistry – A European Journal*, 2021. DOI: 10.1002/CHEM.202103546.
- [370] B. Chen, S. Kruse, R. Schmid, L. Cai, N. Hansen, and H. Pitsch, "Oxygenated PAH Formation Chemistry Investigation in Anisole Jet Stirred Reactor Oxidation by a Thermodynamic Approach," *Energy & Fuels*, vol. 35, no. 2, pp. 1535–1545, 2021. DOI: 10.1021/acs.energyfuels.0c03829.
- [371] Z. Zhao, M. Chaos, A. Kazakov, and F. L. Dryer, "Thermal decomposition reaction and a comprehensive kinetic model of dimethyl ether," *International Journal of Chemical Kinetics*, vol. 40, no. 1, pp. 1–18, 2008. DOI: 10.1002/KIN.20285.
- [372] C. Ji, R. Zhao, B. Li, and F. N. Egolfopoulos, "Propagation and extinction of cyclopentadiene flames," *Proceedings of the Combustion Institute*, vol. 34, no. 1, pp. 787–794, 2013. DOI: 10.1016/j.proci.2012.07.047.

- [373] C. Ji, E. Dames, H. Wang, and F. N. Egolfopoulos, "Propagation and extinction of benzene and alkylated benzene flames," *Combustion and Flame*, vol. 159, no. 3, pp. 1070–1081, 2012. DOI: 10.1016/j.combustflame.2011.10.017.
- [374] S. G. Davis and C. K. Law, "Determination of and Fuel Structure Effects on Laminar Flame Speeds of C1 to C8 Hydrocarbons," *Combustion Science and Technology*, vol. 140, pp. 427–449, 1998. DOI: 10.1080/00102209808915781.
- [375] R. J. Johnston and J. T. Farrell, "Laminar burning velocities and Markstein lengths of aromatics at elevated temperature and pressure," *Proceedings of the Combustion Institute*, vol. 30, no. 1, pp. 217–224, 2005. DOI: 10.1016/j.proci.2004.08.075.
- [376] D. M. Newitt and J. H. Burgoyne, "The oxidation of aromatic hydrocarbons at high pressures. I— Benzene. II— Toluene. III— Ethyl Benzene," *Proceedings of the Royal Society of London A*, vol. 153, no. 879, pp. 448–462, 1936. DOI: 10.1098/RSPA.1936.0014.
- [377] R. G. W. Norrish and G. W. Taylor, "The oxidation of benzene," *Proceedings of the Royal Society of London A*, vol. 234, no. 1197, pp. 160–177, 1956. DOI: 10.1098/RSPA.1956.0024.
- [378] J. A. Barnard and V. J. Ibberson, "The gaseous oxidation of toluene I—The general features of the reaction," *Combustion and Flame*, vol. 9, no. 1, pp. 81–87, 1965. DOI: 10.1016/0010-2180(65)90011-8.
- [379] —, "The gaseous oxidation of toluene II -The analytical results," *Combustion and Flame*, vol. 9, no. 2, pp. 149–157, 1965. DOI: 10.1016/0010-2180(65)90061-1.
- [380] R. J. Santoro and I. Glassman, "A Review of Oxidation of Aromatic Compounds," *Combustion Science and Technology*, vol. 19, no. 3-4, pp. 161–164, 1977. DOI: 10.1080/00102207908946877.
- [381] R. D. Kern and C. H. Wu, "Collaborative Shock Tube studies of benzene pyrolysis," *Symposium (International) on Combustion*, vol. 20, no. 2, pp. 789–797, 1984. DOI: 10.1016/S0082-0784(85)80569-5.
- [382] A. Laskin and A. Lifshitz, "Thermal decomposition of benzene. Single-pulse Shock-tube investigation," *Symposium (International) on Combustion*, vol. 26, pp. 669–675, 1996. DOI: 10.1016/S0082-0784(96)80274-8.
- [383] R. Sivaramakrishnan, K. Brezinsky, H. Vasudevan, and R. S. Tranter, "A shock-tube study of the high-pressure thermal decomposition of benzene," *Combustion Science and Technology*, vol. 178, no. 1-3, pp. 285–305, 2006. DOI: 10.1080/00102200500292340.
- [384] A. Comandini and K. Brezinsky, "Theoretical Study of the Formation of Naphthalene from the Radical/ π -Bond Addition between Single-Ring Aromatic Hydrocarbons," *Journal of Physical Chemistry A*, vol. 115, pp. 5547–5559, 2011. DOI: 10.1021/jp200201c.

- [385] A. Burcat, C. Snyder, and T. Brabbs, "Ignition Delay Times of Benzene and Toluene With Oxygen in Argon Mixtures," Tech. Rep., 1986.
- [386] I. Da Costa, R. Fournet, F. Billaud, and F. Battin-Leclerc, "Experimental and modeling study of the oxidation of benzene," *International Journal of Chemical Kinetics*, vol. 35, no. 10, pp. 503–524, 2003. DOI: 10.1002/kin.10148.
- [387] C. Venkat, K. Brezinsky, and I. Glassman, "High temperature oxidation of aromatic hydrocarbons," *Symposium (International) on Combustion*, vol. 19, no. 1, pp. 143–152, 1982. DOI: 10.1016/S0082-0784(82)80186-0.
- [388] K. Brezinsky, "The high-temperature oxidation of aromatic hydrocarbons," *Progress in Energy and Combustion Science*, vol. 12, no. 1, pp. 1–24, 1986. DOI: 10.1016/0360-1285(86)90011-0.
- [389] J. L. Emdee, K. Brezinsky, and I. Glassman, "A Kinetic Model for the Oxidation of Toluene near 1200 K," *Journal of Physical Chemistry*, vol. 96, no. 5, pp. 2151–2161, 1992. DOI: 10.1021/j100184a025.
- [390] J. M. Nicovich, C. A. Gump, and A. R. Ravlshankara, "Rates of Reactions of O(³P) with Benzene and Toluene," *Journal of Physical Chemistry*, vol. 86, pp. 1684–1690, 1982. DOI: 10.1021/j100206a040.
- [391] M. U. Alzueta, P. Glarborg, and K. Dam-Johansen, "Experimental and Kinetic Modeling Study of the Oxidation of Benzene," *International Journal of Chemical Kinetics*, vol. 32, no. 8, pp. 498–522, 2000. DOI: 10.1002/1097-4601(2000)32:8<498::AID-KIN8>3.0.CO;2-H.
- [392] A. Marchal, M. Cathonnet, P. Dagaut, *et al.*, in *Proceedings of the Joint Meeting of the French and German Sections of the Combustion Institute, Mulhouse*, 1995, pp. 11–13.
- [393] J. D. Bittner and J. B. Howard, "Composition profiles and reaction mechanisms in a near-sooting premixed benzene/oxygen/argon flame," *Symposium (International) on Combustion*, vol. 18, no. 1, pp. 1105–1116, 1981. DOI: 10.1016/S0082-0784(81)80115-4.
- [394] A. Tregrossi, A. Ciajolo, and R. Barbella, "The combustion of benzene in rich premixed flames at atmospheric pressure," *Combustion and Flame*, vol. 117, no. 3, pp. 553–561, 1999. DOI: 10.1016/S0010-2180(98)00157-6.
- [395] V. Detilleux and J. Vandooren, "Experimental study and kinetic modeling of benzene oxidation in one-dimensional laminar premixed low-pressure flames," *Combustion, Explosion and Shock Waves*, vol. 45, no. 4, pp. 392–403, 2009. DOI: 10.1007/s10573-009-0049-x.
- [396] F. Defoeux, V. Dias, C. Renard, P. J. Van Tiggelen, and J. Vandooren, "Experimental investigation of the structure of a sooting premixed benzene/oxygen/argon flame burning at low pressure," *Proceedings of the Combustion Institute*, vol. 30, no. 1, pp. 1407–1415, 2005. DOI: 10.1016/j.proci.2004.08.014.

- [397] C. Russo, F. Stanzione, A. Tregrossi, M. Alfè, and A. Ciajolo, “The effect of temperature on the condensed phases formed in fuel-rich premixed benzene flames,” *Combustion and Flame*, vol. 159, no. 7, pp. 2233–2242, 2012. DOI: 10.1016/j.combustflame.2012.02.014.
- [398] J. Yang, L. Zhao, W. Yuan, F. Qi, and Y. Li, “Experimental and kinetic modeling investigation on laminar premixed benzene flames with various equivalence ratios,” *Proceedings of the Combustion Institute*, vol. 35, no. 1, pp. 855–862, 2015. DOI: 10.1016/j.proci.2014.05.085.
- [399] A. N. Morozov and A. M. Mebel, “Theoretical study of the reaction mechanism and kinetics of the phenyl + propargyl association,” *Physical Chemistry Chemical Physics*, vol. 22, p. 6880, 2020. DOI: 10.1039/d0cp00306a.
- [400] B. Shukla, K. Tsuchiya, and M. Koshi, “Novel Products from C₆H₅ + C₆H₆/C₆H₅ Reactions,” *Journal of Physical Chemistry A*, vol. 115, pp. 5284–5293, 2011. DOI: 10.1021/jp201817n.
- [401] H. Jin, L. Ye, J. Yang, Y. Jiang, L. Zhao, and A. Farooq, “Inception of Carbonaceous Nanostructures via Hydrogen-Abstraction Phenylacetylene-Addition Mechanism,” *Journal of the American Chemical Society*, vol. 143, no. 49, pp. 20710–20716, 2021. DOI: 10.1021/JACS.1C0823.
- [402] A. Comandini, S. Abid, and N. Chaumeix, “Polycyclic Aromatic Hydrocarbon Growth by Diradical Cycloaddition/ Fragmentation,” *The Journal of Physical Chemistry A*, vol. 121, pp. 5921–5931, 2017. DOI: 10.1021/acs.jpca.7b05562.
- [403] A. S. Semenikhin, A. S. Savchenkova, I. V. Chechet, S. G. Matveev, M. Frenklach, and A. M. Mebel, “On the mechanism of soot nucleation. II. E-bridge formation at the PAH bay,” *Physical Chemistry Chemical Physics*, vol. 22, no. 30, pp. 17196–17204, 2020. DOI: 10.1039/D0CP02554B.
- [404] M. Frenklach, A. S. Semenikhin, and A. M. Mebel, “On the Mechanism of Soot Nucleation. III. The Fate and Facility of the E-Bridge,” *Journal of Physical Chemistry A*, vol. 125, no. 31, pp. 6789–6795, 2021. DOI: 10.1021/acs.jpca.1c04936.
- [405] R. I. Kaiser, L. Zhao, W. Lu, *et al.*, “Unconventional excited-state dynamics in the concerted benzyl (C₇H₇) radical self-reaction to anthracene (C₁₄H₁₀),” *Nature communications*, vol. 13, no. 1, pp. 1–8, 2022. DOI: 10.1038/s41467-022-28466-7.
- [406] K. Narayanaswamy, H. Pitsch, and P. Pepiot, “A chemical mechanism for low to high temperature oxidation of methylcyclohexane as a component of transportation fuel surrogates,” *Combustion and Flame*, vol. 162, no. 4, pp. 1193–1213, 2015. DOI: 10.1016/J.COMBUSTFLAME.2014.10.013.
- [407] M. Mehl, W. J. Pitz, C. K. Westbrook, and H. J. Curran, “Kinetic modeling of gasoline surrogate components and mixtures under engine conditions,” *Proceedings of the Combustion Institute*, vol. 33, no. 1, pp. 193–200, 2011. DOI: 10.1016/j.proci.2010.05.027.

- [408] Y. Zhang, K. P. Somers, M. Mehl, W. J. Pitz, R. F. Cracknell, and H. J. Curran, "Probing the antagonistic effect of toluene as a component in surrogate fuel models at low temperatures and high pressures. A case study of toluene/dimethyl ether mixtures," *Proceedings of the Combustion Institute*, vol. 36, no. 1, pp. 413–421, 2017. DOI: 10.1016/J.PROCI.2016.06.190.
- [409] G. Kukkadapu, D. Kang, S. W. Wagnon, *et al.*, "Kinetic modeling study of surrogate components for gasoline, jet and diesel fuels: C7-C11 methylated aromatics," *Proceedings of the Combustion Institute*, vol. 37, no. 1, pp. 521–529, 2019. DOI: 10.1016/J.PROCI.2018.08.016.
- [410] G. Issayev, K. Djebbi, G. Kukkadapu, *et al.*, "Experimental and kinetic modeling study of tetralin: A naphtheno-aromatic fuel for gasoline, jet and diesel surrogates," *Proceedings of the Combustion Institute*, vol. 38, no. 1, pp. 641–649, 2021. DOI: 10.1016/j.proci.2020.07.059.
- [411] P. Liu, B. Chen, Z. Li, *et al.*, "Experimental and theoretical evidence for the temperature-determined evolution of PAH functional groups," *Proceedings of the Combustion Institute*, vol. 38, no. 1, pp. 1467–1475, 2021. DOI: 10.1016/J.PROCI.2020.07.119.
- [412] W. Sun, A. Hamadi, S. Abid, N. Chaumeix, and A. Comandini, "An experimental and kinetic modeling study of phenylacetylene decomposition and the reactions with acetylene/ethylene under shock tube pyrolysis conditions," *Combustion and Flame*, vol. 220, pp. 257–271, 2020. DOI: 10.1016/j.combustflame.2020.06.044.
- [413] Y. Sun, K. Somers, Q. Wang, *et al.*, "Hindered Rotor Benchmarks for the Transition States of Free Radical Additions to Unsaturated Hydrocarbons," *Physical Chemistry Chemical Physics*, 2020. DOI: 10.1039/D0CP04194G.
- [414] M. Pelucchi, L. Cai, W. Pejpichestakul, *et al.*, "Computational Chemistry Consortium: Surrogate Fuel Mechanism Development, Pollutants Sub-Mechanisms and Components Library," in *SAE Technical Papers*, 2019. DOI: 10.4271/2019-24-0020.
- [415] J. A. Manion and R. Louw, "Rates, Products, and Mechanisms in the Gas-Phase Hydrogenolysis of Phenol between 922 and 1175 K," *Journal of Physical Chemistry*, vol. 93, no. 13, pp. 3563–3574, 1989. DOI: 10.1021/j100346a040.
- [416] J. C. Mackie, K. R. Doolan, and P. F. Nelson, "Kinetics of the thermal decomposition of methoxybenzene (anisole)," *Journal of physical chemistry*, vol. 93, no. 2, pp. 664–670, 1989. DOI: 10.1021/j100339a033.
- [417] I. W. C. E. Arends, R. Louw, and P. Mulder, "Kinetic Study of the Thermolysis of Anisole in a Hydrogen Atmosphere," *Journal of Physical Chemistry*, vol. 97, no. 30, pp. 7914–7925, 1993.
- [418] M. J. Wornat, E. B. Ledesma, and N. D. Marsh, "Polycyclic aromatic hydrocarbons from the pyrolysis of catechol (ortho-dihydroxybenzene), a model fuel representative of entities in tobacco, coal, and lignin," *Fuel*, vol. 80, no. 12, pp. 1711–1726, 2001. DOI: 10.1016/S0016-2361(01)00057-6.

- [419] M. Pecullan, K. Brezinsky, and I. Glassman, "Pyrolysis and Oxidation of Anisole near 1000 K," *Journal of Physical Chemistry A*, vol. 101, pp. 3305–3316, 1997.
- [420] E.-J. Shin, M. R. Nimlos, and R. J. Evans, "A study of the mechanisms of vanillin pyrolysis by mass spectrometry and multivariate analysis," *Fuel*, vol. 80, no. 12, pp. 1689–1696, 2001. DOI: 10.1016/S0016-2361(01)00055-2.
- [421] E. B. Ledesma, N. D. Marsh, A. K. Sandrowitz, and M. J. Wornat, "An experimental study on the thermal decomposition of catechol," *Proceedings of the Combustion Institute*, vol. 29, no. 2, pp. 2299–2306, 2002. DOI: 10.1016/S1540-7489(02)80280-2.
- [422] ———, "Global Kinetic Rate Parameters for the Formation of Polycyclic Aromatic Hydrocarbons from the Pyrolysis of Catechol, A Model Compound Representative of Solid Fuel Moieties," *Energy & Fuels*, vol. 16, no. 6, pp. 1331–1336, 2002. DOI: 10.1021/ef010261.
- [423] N. D. Marsh, E. B. Ledesma, A. K. Sandrowitz, and M. J. Wornat, "Yields of polycyclic aromatic hydrocarbons from the pyrolysis of catechol [ortho-dihydroxybenzene]: Temperature and residence time effects," *Energy and Fuels*, vol. 18, no. 1, pp. 209–217, 2004. DOI: 10.1021/ef010263u.
- [424] S. Thomas, E. B. Ledesma, and M. J. Wornat, "The effects of oxygen on the yields of the thermal decomposition products of catechol under pyrolysis and fuel-rich oxidation conditions," *Fuel*, vol. 86, no. 16, pp. 2581–2595, 2007. DOI: 10.1016/J.FUEL.2007.02.003.
- [425] L. Khachatryan, J. Adoukpe, and B. Dellinger, "Formation of Phenoxy and Cyclopentadienyl Radicals from the Gas-Phase Pyrolysis of Phenol," *Journal of Physical Chemistry A*, vol. 112, pp. 481–487, 2008. DOI: 10.1021/jp073999m.
- [426] S. Thomas and M. J. Wornat, "Effects of Acetylene Addition on Yields of the C₁-C₁₀ Hydrocarbon Products of Catechol Pyrolysis," *Energy & Fuels*, vol. 22, pp. 976–986, 2008. DOI: 10.1021/ef700535v.
- [427] ———, "Polycyclic aromatic hydrocarbons from the co-pyrolysis of catechol and 1,3-butadiene," *Proceedings of the Combustion Institute*, vol. 32, no. 1, pp. 615–622, 2009. DOI: 10.1016/j.proci.2008.05.043.
- [428] N. B. Poddar, S. Thomas, and M. J. Wornat, "Polycyclic aromatic hydrocarbons from the co-pyrolysis of catechol and propyne," *Proceedings of the Combustion Institute*, vol. 33, no. 1, pp. 541–548, 2011. DOI: 10.1016/j.proci.2010.06.072.
- [429] A. M. Scheer, C. Mukarakate, D. J. Robichaud, M. R. Nimlos, H.-H. Carstensen, and G. B. Ellison, "Unimolecular thermal decomposition of phenol and d 5-phenol: Direct observation of cyclopentadiene formation via cyclohexadienone," *Journal of Chemical Physics*, vol. 136, p. 44309, 2012. DOI: 10.1063/1.3675902.
- [430] B. Shu, J. Herzler, S. Peukert, M. Fikri, and C. Schulz, "A Shock Tube and Modeling Study about Anisole Pyrolysis Using Time-Resolved CO Absorption Measurements," *International Journal of Chemical Kinetics*, vol. 49, no. 9, pp. 656–667, 2017. DOI: 10.1002/kin.21105.

- [431] J. Herzler, M. Fikri, and C. Schulz, "Ignition Delay Time Study of Aromatic LIF Tracers in a Wide Temperature and Pressure Range," in *26th ICDERS, Boston MA, USA*, 2017.
- [432] T. Bierkandt, P. Hemberger, P. Oßwald, D. Krüger, M. Köhler, and T. Kasper, "Flame structure of laminar premixed anisole flames investigated by photoionization mass spectrometry and photoelectron spectroscopy," *Proceedings of the Combustion Institute*, vol. 37, no. 2, pp. 1579–1587, 2019. DOI: 10.1016/j.proci.2018.07.037.
- [433] A. Yerrayya, U. Natarajan, and R. Vinu, "Fast pyrolysis of guaiacol to simple phenols: Experiments, theory and kinetic model," *Chemical Engineering Science*, vol. 207, pp. 619–630, 2019. DOI: 10.1016/j.ces.2019.06.025.
- [434] S. Zare, S. Roy, A. El Maadi, and O. Askari, "An investigation on laminar burning speed and flame structure of anisole-air mixture," *Fuel*, vol. 244, pp. 120–131, 2019. DOI: 10.1016/j.fuel.2019.01.149.
- [435] W. Yuan, T. Li, Y. Li, *et al.*, "Experimental and kinetic modeling investigation on anisole pyrolysis: Implications on phenoxy and cyclopentadienyl chemistry," *Combustion and Flame*, vol. 201, pp. 187–199, 2019. DOI: 10.1016/j.combustflame.2018.12.028.
- [436] Y. He, W. Mallard, and W. Tsang, "Kinetics of Hydrogen and Hydroxyl Radical Attack on Phenol at high Temperatures," *Journal of Physical Chemistry*, vol. 92, pp. 2196–2201, 1988. DOI: 10.1021/j100319a023.
- [437] J. A. Manion and R. Louw, "Rates and mechanisms of gas-phase desubstitution of hexadeuteriobenzene and benzene derivatives C_6H_5X , $X = CH_3, CF_3, OH, Cl$, and F , by H atoms between 898 and 1039 K," *Journal of Physical Chemistry*, vol. 94, no. 10, pp. 4127–4134, 1990. DOI: 10.1021/j100373a046.
- [438] Q. Zhang, X. Qu, H. Wang, F. Xu, X. Shi, and W. Wang, "Mechanism and Thermal Rate Constants for the Complete Series Reactions of Chlorophenols with H ," *Environmental Science & Technology*, 2009. DOI: 10.1021/es9001778.
- [439] I. V. Tokmakov and M. C. Lin, "Kinetics and Mechanism of the $OH + C_6H_6$ Reaction: A Detailed Analysis with First-Principles Calculations," *Journal of Physical Chemistry A*, vol. 106, pp. 11 309–11 326, 2002. DOI: 10.1021/jp0211842.
- [440] M. B. Prendergast, B. B. Kirk, J. D. Savee, *et al.*, "Formation and stability of gas-phase o-benzoquinone from oxidation of ortho-hydroxyphenyl: a combined neutral and distonic radical study," *Physical Chemistry Chemical Physics*, vol. 18, no. 6, pp. 4320–4332, 2016. DOI: 10.1039/C5CP02953H.
- [441] P. Hemberger, G. da Silva, A. J. Trevitt, T. Gerber, and A. Bodi, "Are the three hydroxyphenyl radical isomers created equal? – The role of the phenoxy radical –," *Physical Chemistry Chemical Physics*, vol. 17, no. 44, pp. 30 076–30 083, 2015. DOI: 10.1039/C5CP05346C.

- [442] Y. Furutani, Y. Dohara, S. Kudo, J. I. Hayashi, and K. Norinaga, "Theoretical Study on the Kinetics of Thermal Decomposition of Guaiacol and Catechol," *Journal of Physical Chemistry A*, vol. 121, no. 44, pp. 8495–8503, 2017. DOI: 10.1021/acs.jpca.7b08112.
- [443] C. Y. Lin and M. C. Lin, "Thermal decomposition of methyl phenyl ether in shock waves: The kinetics of phenoxy radical reactions," *Journal of Physical Chemistry*, vol. 90, pp. 425–431, 1986. DOI: 10.1021/j100275a014.
- [444] M. Wang, C. Liu, X. Xu, and Q. Li, "Theoretical study of the pyrolysis of vanillin as a model of secondary lignin pyrolysis," *Chemical Physics Letters*, vol. 654, pp. 41–45, 2016. DOI: 10.1016/J.CPLETT.2016.03.058.
- [445] A. Mohan Verma and N. Kishore, "Molecular modelling approach to elucidate the thermal decomposition routes of vanillin," *New Journal of Chemistry*, vol. 41, p. 8845, 2017. DOI: 10.1039/c7nj02004j.
- [446] K. Narayanaswamy, G. Blanquart, and H. Pitsch, "A consistent chemical mechanism for oxidation of substituted aromatic species," *Combustion and Flame*, vol. 157, no. 10, pp. 1879–1898, 2010. DOI: 10.1016/j.combustflame.2010.07.009.
- [447] S. Yommee and J. W. Bozzelli, "Cyclopentadienone Oxidation Reaction Kinetics and Thermochemistry for the Alcohols, Hydroperoxides, and Vinylic, Alkoxy, and Alkylperoxy Radicals," *Journal of Physical Chemistry A*, vol. 120, no. 3, pp. 433–451, 2016. DOI: 10.1021/ACS.JPCA.5B09004/.
- [448] G. Da Silva, C.-C. Chen, and J. W. Bozzelli, "Toluene Combustion: Reaction Paths, Thermochemical Properties, and Kinetic Analysis for the Methylphenyl Radical + O₂ Reaction," *J. Phys. Chem. A*, vol. 111, pp. 8663–8676, 2007. DOI: 10.1021/jp068640x.
- [449] S. Namysl, M. Pelucchi, L. Pratali Maffei, *et al.*, "Experimental and modeling study of benzaldehyde oxidation," *Combustion and Flame*, vol. 211, pp. 124–132, 2020. DOI: 10.1016/J.COMBUSTFLAME.2019.09.024.
- [450] S. J. Klippenstein, L. B. Harding, and Y. Georgievskii, "On the formation and decomposition of C₇H₈," *Proceedings of the Combustion Institute*, vol. 31, no. 1, pp. 221–229, 2007. DOI: 10.1016/j.proci.2006.08.045.
- [451] M. A. Oehlschlaeger, D. F. Davidson, and R. K. Hanson, "Experimental Investigation of Toluene + H → Benzyl + H₂ at High Temperatures," *Journal of Physical Chemistry A*, vol. 110, pp. 9867–9873, 2006. DOI: 10.1021/jp062567t.
- [452] T. Seta, M. Nakajima, and A. Miyoshi, "High-temperature reactions of OH radicals with benzene and toluene," *Journal of Physical Chemistry A*, vol. 110, no. 15, pp. 5081–5090, 2006. DOI: 10.1021/jp0575456.
- [453] W. Yuan, Y. Li, P. Dagaut, J. Yang, and F. Qi, "Investigation on the pyrolysis and oxidation of toluene over a wide range conditions. I. Flow reactor pyrolysis and jet stirred reactor oxidation," *Combustion and Flame*, vol. 162, no. 1, pp. 3–21, 2015. DOI: 10.1016/j.combustflame.2014.07.009.

- [454] ———, “Investigation on the pyrolysis and oxidation of toluene over a wide range conditions. II. A comprehensive kinetic modeling study,” *Combustion and Flame*, vol. 162, no. 1, pp. 22–40, 2015. DOI: 10.1016/J.COMBUSTFLAME.2014.07.011.
- [455] E. Dames and H. Wang, “Isomerization kinetics of benzylic and methylphenyl type radicals in single-ring aromatics,” *Proceedings of the Combustion Institute*, vol. 34, pp. 307–314, 2013. DOI: 10.1016/J.PROCI.2012.05.014.
- [456] R. Bounaceur, I. D. Costa, R. Fournet, F. Billaud, and F. Battin-Leclerc, “Experimental and modeling study of the oxidation of toluene,” *International Journal of Chemical Kinetics*, vol. 37, no. 1, pp. 25–49, 2005. DOI: 10.1002/KIN.20047.
- [457] M. Derudi, D. Polino, and C. Cavallotti, “Toluene and benzyl decomposition mechanisms: elementary reactions and kinetic simulations,” *Physical Chemistry Chemical Physics*, vol. 13, no. 48, pp. 21 308–21 318, 2011. DOI: 10.1039/C1CP22601K.
- [458] G. da Silva, M. R. Hamdan, and J. W. Bozzelli, “Oxidation of the Benzyl Radical: Mechanism, Thermochemistry, and Kinetics for the Reactions of Benzyl Hydroperoxide,” *Journal of Chemical Theory and Computation*, vol. 5, no. 12, pp. 3185–3194, 2009. DOI: 10.1021/ct900352f.
- [459] G. Da Silva and J. W. Bozzelli, “Kinetic modeling of the benzyl + HO₂ reaction,” *Proceedings of the Combustion Institute*, vol. 32, pp. 287–294, 2009. DOI: 10.1016/j.proci.2008.05.040.
- [460] O. Herbinet, B. Husson, M. Ferrari, P. A. Glaude, and F. Battin-Leclerc, “Low temperature oxidation of benzene and toluene in mixture with n-decane,” *Proceedings of the Combustion Institute*, vol. 34, no. 1, pp. 297–305, 2013. DOI: 10.1016/J.PROCI.2012.06.005.
- [461] Q. Zhao, Y. Zhang, F. Zhang, and Z. Huang, “Pressure-dependent kinetics on benzoyl radical + O₂ and its implications for low temperature oxidation of benzaldehyde,” *Combustion and Flame*, vol. 214, pp. 139–151, 2020. DOI: 10.1016/j.combustflame.2019.12.039.
- [462] C. Chanmugathas and J. Heicklen, “Pyrolysis of acetylene-vinylacetylene mixtures between 400 and 500°C,” *International Journal of Chemical Kinetics*, vol. 18, no. 6, pp. 701–718, 1986. DOI: 10.1002/KIN.550180608.
- [463] J. A. Miller, S. J. Klippenstein, Y. Georgievskii, L. B. Harding, W. D. Allen, and A. C. Simmonett, “Reactions between resonance-stabilized radicals: Propargyl + allyl,” *Journal of Physical Chemistry A*, vol. 114, no. 14, pp. 4881–4890, 2010. DOI: 10.1021/jp910604b.
- [464] J. P. Senosiain and J. A. Miller, “The Reaction of n- and i-C₄H₅ Radicals with Acetylene,” *Journal of Physical Chemistry A*, vol. 111, pp. 3740–3747, 2007. DOI: 10.1021/jp0675126.

- [465] J. Aguilera-Iparraguirre and W. Klopper, "Density functional theory study of the formation of naphthalene and phenanthrene from reactions of phenyl with vinyl- and phenylacetylene," *Journal of Chemical Theory and Computation*, vol. 3, no. 1, pp. 139–145, 2007. DOI: 10.1021/ct600255u.
- [466] R. S. Tranter, S. J. Klippenstein, L. B. Harding, B. R. Giri, X. Yang, and J. H. Kiefer, "Experimental and Theoretical Investigation of the Self-Reaction of Phenyl Radicals," *Journal of Physical Chemistry A*, vol. 114, pp. 8240–8261, 2010. DOI: 10.1021/jp1031064.
- [467] M. Frenklach, Z. Liu, R. I. Singh, G. R. Galimova, V. N. Azyazov, and A. M. Mebel, "Detailed, sterically-resolved modeling of soot oxidation: Role of O atoms, interplay with particle nanostructure, and emergence of inner particle burning," *Combustion and Flame*, vol. 188, pp. 284–306, 2018. DOI: 10.1016/J.COMBUSTFLAME.2017.10.012.
- [468] C. A. Taatjes, D. L. Osborn, T. M. Selby, *et al.*, "Products of the benzene + O(³P) reaction," *Journal of Physical Chemistry A*, vol. 114, pp. 3355–3370, 2010. DOI: 10.1021/jp9114145.
- [469] T. L. Nguyen, J. Peeters, and L. Vereecken, "Theoretical Reinvestigation of the O(³P)+C₆H₆ Reaction: Quantum Chemical and Statistical Rate Calculations," *Journal of Physical Chemistry A*, vol. 111, no. 19, pp. 3836–3849, 2007. DOI: 10.1021/jp0660886.
- [470] L. Pratali Maffei, M. Pelucchi, T. Faravelli, and C. Cavallotti, "Theoretical study of sensitive reactions in phenol decomposition," *Reaction Chemistry & Engineering*, vol. 5, pp. 452–472, 2020. DOI: 10.1039/c9re00418a.
- [471] T. Ko, G. Y. Adusei, and A. Fontijn, "Kinetics of the O(³P) + C₆H₆ Reaction over a Wide Temperature Range," *Journal of Physical Chemistry*, vol. 95, no. 22, pp. 8745–8748, 1991. DOI: 10.1021/j100175a060.
- [472] S. J. Sibener, R. J. Buss, P. Casavecchia, T. Hirooka, and Y. T. Lee, "A crossed molecular beams investigation of the reactions O(³P)+ C₆H₆, C₆D₆," *Journal of Chemical Physics*, vol. 72, no. 8, p. 4341, 2008. DOI: 10.1063/1.439714.
- [473] G. Vanuzzo, A. Caracciolo, T. K. Minton, *et al.*, "Crossed-Beam and Theoretical Studies of the O(³P,¹D) + Benzene Reactions: Primary Products, Branching Fractions, and Role of Intersystem Crossing," *Journal of Physical Chemistry A*, vol. 125, no. 38, pp. 8434–8453, 2021. DOI: 10.1021/acs.jpca.1c06913.
- [474] A. Caracciolo, G. Vanuzzo, N. Balucani, *et al.*, "Combined Experimental and Theoretical Studies of the O(³P) + 1-Butene Reaction Dynamics: Primary Products, Branching Fractions, and Role of Intersystem Crossing," *Journal of Physical Chemistry A*, vol. 123, pp. 9934–9956, 2019. DOI: 10.1021/acs.jpca.9b07621.

- [475] F. Leonori, N. Balucani, V. Nevry, *et al.*, “Experimental and Theoretical Studies on the Dynamics of the $O(^3P) + \text{Propene}$ Reaction: Primary Products, Branching Ratios, and Role of Intersystem Crossing,” *Journal of Physical Chemistry C*, vol. 119, no. 26, pp. 14 632–14 652, 2015. DOI: 10.1021/jp512670y.
- [476] M. Tappe, V. Schliephake, and H. G. Wagner, “Reactions of Benzene, Toluene and Ethylbenzene with Atomic Oxygen ($O(^3P)$) in the Gas Phase,” *Zeitschrift für Physikalische Chemie*, vol. 162, no. 2, pp. 129–145, 1989. DOI: 10.1524/zpch.1989.162.Part_2.129.
- [477] B. Fu, Y.-C. Han, J. M. Bowman, *et al.*, “Experimental and theoretical studies of the $O(^3P) + C_2H_4$ reaction dynamics: Collision energy dependence of branching ratios and extent of intersystem crossing,” *Journal of Chemical Physics*, vol. 137, no. 22, 22A532, 2012. DOI: 10.1063/1.4746758.
- [478] P. Casavecchia, F. Leonori, and N. Balucani, “Reaction dynamics of oxygen atoms with unsaturated hydrocarbons from crossed molecular beam studies: primary products, branching ratios and role of intersystem crossing,” *International Reviews in Physical Chemistry*, vol. 34, no. 2, pp. 161–204, 2015. DOI: 10.1080/0144235X.2015.1039293.
- [479] H. Pan, K. Liu, A. Caracciolo, and P. Casavecchia, “Crossed beam polyatomic reaction dynamics: Recent advances and new insights,” *Chemical Society Reviews*, vol. 46, no. 24, pp. 7517–7547, 2017. DOI: 10.1039/c7cs00601b.
- [480] L. Zhu and J. W. Bozzelli, “Kinetics and Thermochemistry for the Gas-Phase Keto-Enol Tautomerism of Phenol To 2,4-Cyclohexadienone,” *Journal of Physical Chemistry A*, vol. 107, pp. 3696–3703, 2003. DOI: 10.1021/jp0212545.
- [481] S. Xu, R. S. Zhu, and M. C. Lin, “Ab initio study of the $OH + CH_2O$ reaction: The effect of the $OH \cdots OCH_2$ complex on the H-abstraction kinetics,” *International Journal of Chemical Kinetics*, vol. 38, no. 5, pp. 322–326, 2006. DOI: 10.1002/KIN.20166.
- [482] S. Olivella, A. Solé, and A. García-Raso, “Ab Initio Calculations of the Potential Surface for the Thermal Decomposition of the Phenoxy Radical,” *Journal of Physical Chemistry*, vol. 99, pp. 10 549–10 556, 1995. DOI: 10.1021/j100026a018.
- [483] R. Liu, K. Morokuma, A. M. Mebel, and M. C. Lin, “Ab Initio Study of the Mechanism for the Thermal Decomposition of the Phenoxy Radical,” *Journal of Physical Chemistry*, vol. 100, no. 22, pp. 9314–9322, 1996. DOI: 10.1021/jp953566w.
- [484] H.-H. Carstensen and A. M. Dean, “A Quantitative Kinetic Analysis of CO Elimination from Phenoxy Radicals,” *International Journal of Chemical Kinetics*, vol. 44, no. 1, pp. 75–89, 2012. DOI: 10.1002/kin.20622.
- [485] A. Karton, E. Rabinovich, J. M. L. Martin, and B. Ruscic, “W4 theory for computational thermochemistry: In pursuit of confident sub-kJ/mol predictions,” *The Journal of Chemical Physics*, vol. 125, p. 144 108, 2006. DOI: 10.1063/1.2348881.

- [486] O. Tishchenko, J. Zheng, and D. G. Truhlar, "Multireference Model Chemistries for Thermochemical Kinetics," *Journal of Chemical Theory and Computation*, vol. 4, pp. 1208–1219, 2008. DOI: 10.1021/ct800077r.
- [487] C. A. Grambow, A. Jamal, Y.-P. Li, *et al.*, "Unimolecular Reaction Pathways of a γ -Ketohydroperoxide from Combined Application of Automated Reaction Discovery Methods," *Journal of the American Chemical Society*, vol. 140, pp. 1035–1048, 2018. DOI: 10.1021/jacs.7b11009.
- [488] A. Jalan, I. M. Alecu, R. Meana-Pañeda, *et al.*, "New pathways for formation of acids and carbonyl products in low-temperature oxidation: The Korcek decomposition of γ -ketohydroperoxides," *Journal of the American Chemical Society*, vol. 135, no. 30, pp. 11 100–11 114, 2013. DOI: 10.1021/ja4034439.
- [489] N. E. Schultz, Y. Zhao, and D. G. Truhlar, "Density Functionals for Inorganometallic and Organometallic Chemistry," *Journal of Physical Chemistry A*, vol. 109, pp. 11 127–11 143, 2005. DOI: 10.1021/jp0539223.
- [490] S. G. Davis, H. Wang, K. Brezinsky, and C. K. Law, "Laminar Flame Speeds and Oxidation Kinetics of Benzene-Air and Toluene-Air Mixtures," in *Twenty-Sixth Symposium (International) on Combustion*, 1996, pp. 1025–1033. DOI: 10.1016/S0082-0784(96)80316-X.
- [491] J. M. Simmie and K. P. Somers, "Benchmarking Compound Methods (CBS-QB3, CBS-APNO, G3, G4, W1BD) against the Active Thermochemical Tables: A Litmus Test for Cost-Effective Molecular Formation Enthalpies," *Journal of Physical Chemistry A*, vol. 119, 7235–7246, 2015. DOI: 10.1021/jp511403a.
- [492] X. You, D. Y. Zubarev, W. A. Lester, and M. Frenklach, "Thermal Decomposition of Pentacene Oxyradicals," *Journal of Physical Chemistry A*, vol. 115, pp. 14 184–14 190, 2011. DOI: 10.1021/jp208974b.
- [493] P. Hemberger, M. Lang, B. Noller, *et al.*, "Photoionization of Propargyl and Bromopropargyl Radicals: A Threshold Photoelectron Spectroscopic Study," *J. Phys. Chem. A*, vol. 115, pp. 2225–2230, 2011. DOI: 10.1021/jp112110j.
- [494] G. Ghigo and G. Tonachini, "Benzene Oxidation in the Troposphere. Theoretical Investigation on the Possible Competition of Three Postulated Reaction Channels," *Journal of American Chemical Society*, vol. 120, pp. 6753–6757, 1998. DOI: 10.1021/ja973956r.
- [495] A. Mardyukov and W. Sander, "Matrix Isolation and Spectroscopic Characterization of the Phenylperoxy Radical and Its Rearranged Products," *Chemistry – A European Journal*, vol. 15, no. 6, pp. 1462–1467, 2009. DOI: 10.1002/CHEM.200801546.
- [496] B. B. Kirk, D. G. Harman, H. I. Kenttamaa, A. J. Trevitt, and S. J. Blanksby, "Isolation and characterization of charge-tagged phenylperoxyl radicals in the gas phase: direct evidence for products and pathways in low temperature benzene oxidation," *Physical Chemistry Chemical Physics*, vol. 14, pp. 16 719–16 730, 2012. DOI: 10.1039/c2cp43507a.

- [497] K. Tonokura, Y. Norikane, M. Koshi, *et al.*, “Cavity ring-down study of the visible absorption spectrum of the phenyl radical and kinetics of its reactions with Cl, Br, Cl₂, and O₂,” *Journal of Physical Chemistry A*, vol. 106, no. 24, pp. 5908–5917, 2002. DOI: 10.1021/jp025585t.
- [498] M. C. Lin and A. Mebel, “Ab Initio molecular orbital study of the O+C₆H₅O reaction,” *Journal of Physical Organic Chemistry*, vol. 8, pp. 407–420, 1995. DOI: 10.1002/poc.610080605.
- [499] M. J. Fadden and C. M. Hadad, “Unimolecular Decomposition of the 2-Oxepinoxy Radical: A Key Seven-Membered Ring Intermediate in the Thermal Oxidation of Benzene,” *Journal of Physical Chemistry A*, vol. 104, pp. 8121–8130, 2000. DOI: 10.1021/jp0017238.
- [500] I. V. Tokmakov, G.-S. Kim, V. V. Kislov, A. M. Mebel, and M. C. Lin, “The Reaction of Phenyl Radical with Molecular Oxygen: A G2M Study of the Potential Energy Surface,” *Journal of Physical Chemistry A*, vol. 109, no. 27, pp. 6114–6127, 2005. DOI: 10.1021/jp051712k.
- [501] T. Yu and M. C. Lin, “Kinetics of the C₆H₅ + O₂ Reaction at Low Temperatures,” *Journal of American Chemical Society*, vol. 116, pp. 9571–9576, 1994. DOI: 10.1021/ja00100a022.
- [502] K. Tanaka, M. Ando, Y. Sakamoto, and K. Tonokura, “Pressure Dependence of of Phenyl Radical with Formation in the Reaction Phenylperoxy Radical Molecular Oxygen,” *International Journal of Chemical Kinetics*, vol. 43, no. 3, pp. 42–49, 2011. DOI: 10.1002/kin.20532.
- [503] X. Gu, F. Zhang, and R. I. Kaiser, “Crossed beam reaction of the phenyl radical, (C₆H₅, X²A′) with molecular oxygen (O₂, X³Σ_g⁻): Observation of the phenoxy radical, (C₆H₅O, X²A′),” *Chemical Physics Letters*, vol. 448, no. 1-3, pp. 7–10, 2007. DOI: 10.1016/j.cplett.2007.09.022.
- [504] D. R. Albert and H. F. Davis, “Collision complex lifetimes in the reaction C₆H₅ + O₂ → C₆H₅O + O,” *Journal of Physical Chemistry Letters*, vol. 1, no. 7, pp. 1107–1111, 2010. DOI: 10.1021/jz100199z.
- [505] D. S. Parker, F. Zhang, and R. I. Kaiser, “Phenoxy radical (C₆H₅O) formation under single collision conditions from reaction of the phenyl radical (C₆H₅, X²A₁) with molecular oxygen (O₂, X³Σ_g⁻): The final chapter?” *Journal of Physical Chemistry A*, vol. 115, no. 42, pp. 11 515–11 518, 2011. DOI: 10.1021/jp206160q.
- [506] S. S. Kumaran and J. V. Michael, “Phenyl radical thermolysis and rate constants for phenyl + O₂,” in *21st International Symposium on Shock Waves*, 1997.
- [507] D. S. N. Parker, R. I. Kaiser, T. P. Troy, O. Kostko, M. Ahmed, and A. M. Mebel, “Toward the Oxidation of the Phenyl Radical and Prevention of PAH Formation in Combustion Systems,” *Journal of Physical Chemistry A*, vol. 119, pp. 7145–7154, 2015. DOI: 10.1021/jp509170x.

- [508] B. K. Carpenter, "Computational Prediction of New Mechanisms for the Reactions of Vinyl and Phenyl Radicals with Molecular Oxygen," *Journal of the American Chemical Society*, vol. 115, no. 21, pp. 9806–9807, 1993. DOI: 10.1021/ja00074a060.
- [509] A. M. Mebel and M. C. Lin, "Ab Initio Molecular Orbital Calculations of C₆H₅O₂ Isomers," *Journal of the American Chemical Society*, vol. 116, pp. 9577–9584, 1994. DOI: 10.1021/ja00100a023.
- [510] C. Barckholtz, M. J. Fadden, and C. M. Hadad, "Computational Study of the Mechanisms for the Reaction of O₂ (³Σ_g) with Aromatic Radicals," *Journal of Physical Chemistry A*, vol. 103, pp. 8108–8117, 1999. DOI: 10.1021/jp991692k.
- [511] M. J. Fadden, C. Barckholtz, and C. M. Hadad, "Computational study of the unimolecular decomposition pathways of phenylperoxy radical," *Journal of Physical Chemistry A*, vol. 104, no. 13, pp. 3004–3011, 2000. DOI: 10.1021/jp993990n.
- [512] N. Sebbar, J. W. Bozzelli, and H. Bockhorn, "The phenyl+ O₂ reaction: Thermodynamics and kinetics," in *Third European Combustion Meeting*, 2007.
- [513] N. Sebbar, H. Bockhorn, and J. Bozzelli, "Thermodynamic properties of the species resulting from the phenyl radical with O₂ reaction system," *International Journal of Chemical Kinetics*, vol. 40, no. 9, pp. 583–604, 2008. DOI: 10.1002/kin.20311.
- [514] V. V. Kislov, R. I. Singh, D. E. Edwards, A. M. Mebel, and M. Frenklach, "Rate coefficients and product branching ratios for the oxidation of phenyl and naphthyl radicals: A theoretical RRKM-ME study," *Proceedings of the Combustion Institute*, vol. 35, pp. 1861–1869, 2015. DOI: 10.1016/j.proci.2014.06.135.
- [515] G. Da Silva and J. W. Bozzelli, "Variational Analysis of the Phenyl + O₂ and Phenoxy + O Reactions," *Journal of Physical Chemistry A*, vol. 112, no. 16, pp. 3566–3575, 2008. DOI: 10.1021/jp7118845.
- [516] A. M. Mebel, E. W. Diau, M. C. Lin, and K. Morokuma, "Ab initio and RRKM calculations for multichannel rate constants of the C₂H₃ + O₂ reaction," *Journal of the American Chemical Society*, vol. 118, no. 40, pp. 9759–9771, 1996. DOI: 10.1021/ja961476e.
- [517] A. M. Mebel and V. V. Kislov, "The C₂H₃ + O₂ reaction revisited: Is multireference treatment of the wave function really critical?" *Journal of Physical Chemistry A*, vol. 109, no. 32, pp. 6993–6997, 2005. DOI: 10.1021/jp052772t.
- [518] X. Shi, Q. Wang, and A. Violi, "Chemical pathways for the formation of benzofuran and dibenzofuran in combustion," *Combustion and Flame*, vol. 212, pp. 216–233, 2020. DOI: 10.1016/J.COMBUSTFLAME.2019.10.008.
- [519] Q.-D. Wang, M.-M. Sun, and J. Liang, "Theoretical study of the hydrogen abstraction reactions from substituted phenolic species," *Computational and Theoretical Chemistry*, vol. 1196, p. 113120, 2021. DOI: 10.1016/j.comptc.2020.113120.

- [520] D. Hou and X. You, "Reaction kinetics of hydrogen abstraction from polycyclic aromatic hydrocarbons by H atoms," *Physical Chemistry Chemical Physics*, vol. 19, pp. 30 772–30 780, 2017. DOI: 10.1039/c7cp04964a.
- [521] L. Goerigk and S. Grimme, "Efficient and Accurate Double-Hybrid-Meta-GGA Density Functionals—Evaluation with the Extended GMTKN30 Database for General Main Group Thermochemistry, Kinetics, and Noncovalent Interactions," *Journal of Chemical Theory and Computation*, vol. 7, no. 2, pp. 291–309, 2010. DOI: 10.1021/CT100466K.
- [522] S. Grimme, "Semiempirical hybrid density functional with perturbative second-order correlation," *The Journal of Chemical Physics*, vol. 124, no. 3, p. 034 108, 2006. DOI: 10.1063/1.2148954.
- [523] S. Grimme, S. Ehrlich, and L. Goerigk, "Effect of the damping function in dispersion corrected density functional theory," *Journal of Computational Chemistry*, vol. 32, no. 7, pp. 1456–1465, 2011. DOI: 10.1002/JCC.21759.
- [524] E. Papajak, J. Zheng, X. Xu, H. R. Leverentz, and D. G. Truhlar, "Perspectives on Basis Sets Beautiful: Seasonal Plantings of Diffuse Basis Functions," *Journal of Chemical Theory and Computation*, vol. 7, no. 10, pp. 3027–3034, 2011. DOI: 10.1021/CT200106A.
- [525] Z. Tian, W. J. Pitz, R. Fournet, P. A. Glaude, and F. Battin-Leclerc, "A detailed kinetic modeling study of toluene oxidation in a premixed laminar flame," *Proceedings of the Combustion Institute*, vol. 33, no. 1, pp. 233–241, 2011. DOI: 10.1016/j.proci.2010.06.063.
- [526] S.-H. Li, J.-J. Guo, R. Li, F. Wang, and X.-Y. Li, "Theoretical Prediction of Rate Constants for Hydrogen Abstraction by OH, H, O, CH₃, and HO₂ Radicals from Toluene," *Journal of Physical Chemistry A*, vol. 120, pp. 3424–3432, 2016. DOI: 10.1021/acs.jpca.6b03049.
- [527] J. M. Nicovich and A. R. Ravishankara, "Reaction of hydrogen atom with benzene: Kinetics and mechanism," *Journal of Physical Chemistry*, vol. 88, no. 12, pp. 2534–2541, 1984. DOI: 10.1021/j150656a021.
- [528] B. R. Giri, T. Bentz, H. Hippler, and M. Olzmann, "Shock-tube study of the reactions of hydrogen atoms with benzene and phenyl radicals," *Zeitschrift fur Physikalische Chemie*, vol. 223, no. 4-5, pp. 539–549, 2009. DOI: 10.1524/zpch.2009.6036.
- [529] J. H. Kiefer, L. J. Mizerka, M. R. Patel, and H.-C. Wei, "A Shock Tube Investigation of Major Pathways in the High-Temperature Pyrolysis of Benzene," *The Journal of Physical Chemistry*, vol. 89, no. 10, pp. 2013–2019, 1985. DOI: 10.1021/j100256a043.
- [530] E. Heckmann, H. Hippler, and J. Troe, "High-temperature reactions and thermodynamic properties of phenyl radicals," *Symposium (International) on Combustion*, vol. 26, no. 1, pp. 543–550, 1996. DOI: 10.1016/S0082-0784(96)80258-X.

- [531] J. Park, I. V. Dyakov, and M. C. Lin, "FTIR and Mass-Spectrometric Measurements of the Rate Constant for the $C_6H_5 + H_2$ Reaction," *Journal of Physical Chemistry A*, vol. 101, pp. 8839–8843, 1997. DOI: 10.1021/jp972162w.
- [532] M. Krech and S. Price, "Hydrogen abstraction by methyl radicals from benzene and the pressure dependence of the recombination of methyl radicals," *Canadian Journal of Chemistry*, vol. 45, pp. 157–159, 1967. DOI: 10.1139/v67-031.
- [533] H.-X. Zhang, S. I. Ahonkhai, and M. H. Back, "Rate constants for abstraction of hydrogen from benzene, toluene, and cyclopentane by methyl and ethyl radicals over the temperature range 650–770 K," *Canadian Journal of Chemistry*, vol. 67, no. 10, pp. 1541–1549, 1989. DOI: 10.1139/v89-235.
- [534] T. V. Mai, A. Ratkiewicz, M. V. Duong, and L. K. Huynh, "Direct ab initio study of the $C_6H_6 + CH_3/C_2H_5 = C_6H_5 + CH_4/C_2H_6$ reactions," *Chemical Physics Letters*, vol. 646, pp. 102–109, 2016. DOI: 10.1016/j.cplett.2015.12.063.
- [535] I. V. Tokmakov, J. Park, S. Gheyas, and M. C. Lin, "Experimental and Theoretical Studies of the Reaction of the Phenyl Radical with Methane," *Journal of Physical Chemistry A*, vol. 102, pp. 3636–3645, 1999. DOI: 10.1021/jp983140s.
- [536] F. J. Duncan and A. F. Trotman-Dickenson, "The Reactions of Phenyl Radicals from the Photolysis of Acetophenone and the Strength of the C-H Bond in Benzene," *Journal of the Chemical Society*, pp. 4672–4676, 1962. DOI: 10.1039/JR9620004672.
- [537] F. P. Tully, A. R. Ravlshankara, R. L. Thompson, *et al.*, "Kinetics of the Reactions of Hydroxyl Radical with Benzene and Toluene," *Journal of Physical Chemistry*, vol. 85, no. 15, pp. 2262–2269, 1981. DOI: 10.1021/j150615a025.
- [538] S. Madronich and W. Felder, "Kinetics and Mechanism of the Reaction of OH with C_6H_6 over 790–1410 K," *Journal of Physical Chemistry*, vol. 89, no. 16, pp. 3556–3561, 1985. DOI: 10.1021/j100262a026.
- [539] W. Felder and S. Madronich, "High Temperature Photochemistry (HTP): Kinetics and Mechanism Studies of Elementary Combustion Reactions Over 300–1700 K," *Combustion Science and Technology*, vol. 50, no. 1-3, pp. 135–150, 1986. DOI: 10.1080/00102208608923929.
- [540] D. L. Baulch, C. J. Cobos, R. A. Cox, *et al.*, "Evaluated Kinetic Data for Combustion Modelling," *Journal of Physical and Chemical Reference Data*, vol. 21, no. 3, pp. 411–734, 1992. DOI: 10.1063/1.555908.
- [541] C. Ellis, M. S. Scott, and R. W. Walker, "Addition of toluene and ethylbenzene to mixtures of H_2 and O_2 at 772 K: Part 2: Formation of products and determination of kinetic data for $H+$ additive and for other elementary reactions involved," *Combustion and Flame*, vol. 132, no. 3, pp. 291–304, 2003. DOI: 10.1016/S0010-2180(02)00439-X.
- [542] H. Hippler, C. Reihs, and J. Troe, "Elementary steps in the pyrolysis of toluene and benzyl radicals," *Zeitschrift für Physikalische Chemie*, vol. 167, no. Part_1, pp. 1–16, 1990. DOI: 10.1524/zpch.1990.167.Part_1.001.

- [543] M. Braun-Unkhoff, P. Frank, and T. Just, "A shock tube study on the thermal decomposition of toluene and of the phenyl radical at high temperatures," *Symposium (International) on Combustion*, vol. 22, no. 1, pp. 1053–1061, 1989. DOI: 10.1016/S0082-0784(89)80115-8.
- [544] M. F. R. Mulcahy, B. G. Tucker, D. G. Williams, and J. R. Wilmshurst, "Reactions of Free Radicals with Aromatic Compounds in the Gaseous Phase. III. Kinetics of the Reaction of Methyl Radicals with Anisole (Methoxybenzene)," *Australian Journal of Chemistry*, vol. 20, no. 6, pp. 1155–1171, 1967. DOI: 10.1071/CH9671155.
- [545] S. Price and A. F. Trotman-Dickenson, "Kinetics of the reaction of methyl radicals with toluene," *Journal of the Chemical Society*, pp. 4205–4207, 1958.
- [546] M. F. Mulcahy, D. J. Williams, and J. R. Wilmshurst, "Reactions of free radicals with aromatic compounds in the gaseous phase. I. Kinetics of the reaction of methyl radicals with toluene," *Australian Journal of Chemistry*, vol. 17, no. 12, pp. 1329–1341, 1964. DOI: 10.1071/CH9641329.
- [547] M. Cher, C. S. Hollingsworth, and F. Sicilio, "The Vapor Phase Reaction of Methyl Radicals with Toluene at 100–300°," *Journal of Physical Chemistry*, vol. 70, no. 3, pp. 877–883, 1966. DOI: 10.1021/j100875a043.
- [548] A. N. Dunlop, R. J. Kominar, and S. J. W. Price, "Hydrogen abstraction from toluene by methyl radicals and the pressure dependence of the recombination of methyl radicals," *Canadian Journal of Chemistry*, vol. 48, no. 8, pp. 1269–1272, 1970. DOI: 10.1139/v70-208.
- [549] M. F. Mulcahy and D. J. Williams, "Reactions of Free Radicals with Aromatic Compounds in the Gaseous Phase. II. Kinetics of the Reaction of Methyl Radicals with Phenol," *Australian Journal of Chemistry*, vol. 18, no. 1, pp. 20–38, 1965. DOI: 10.1071/CH9650020.
- [550] R. Knispel, R. Koch, M. Siese, and C. Zetzsch, "Adduct Formation of Oh Radicals With Benzene, Toluene, and Phenol and Consecutive Reactions of the Adducts With NO_x and O₂," *Berichte Der Bunsen-Gesellschaft-Physical Chemistry Chemical Physics*, vol. 94, no. 11, pp. 1375–1379, 1990. DOI: 10.1002/bbpc.199000036.
- [551] V. Vasudevan, D. F. Davidson, and R. K. Hanson, "High-Temperature Measurements of the Reactions of OH with Toluene and Acetone," *Journal of Physical Chemistry A*, vol. 109, no. 15, pp. 3352–3359, 2005. DOI: 10.1021/JP0501143.
- [552] R. R. Baldwin, M. Scott, and R. W. Walker, "Addition of benzene and toluene to slowly reacting mixtures of hydrogen and oxygen at 773 K," *Symposium (International) on Combustion*, vol. 21, pp. 991–1000, 1986. DOI: 10.1016/S0082-0784(88)80330-8.
- [553] R. A. Perry, R. Atkinson, J. N. Pitts, *et al.*, "Kinetics and Mechanism of the Gas Phase Reaction of OH Radicals with Aromatic Hydrocarbons Over the Temperature Range 296–473 K," *The Journal of Physical Chemistry*, vol. 81, no. 4, pp. 296–304, 1977. DOI: 10.1021/j100519a004.

- [554] F. Xu, H. Wang, Q. Zhang, R. Zhang, X. Qu, and W. Wang, "Kinetic Properties for the Complete Series Reactions of Chlorophenols with OH Radicals Relevance for Dioxin Formation," *Environmental Science & Technology*, vol. 44, pp. 1399–1404, 2010. DOI: 10.1021/es9031776.
- [555] Y. Li, J. Cai, L. Zhang, J. Yang, Z. Wang, and F. Qi, "Experimental and modeling investigation on premixed ethylbenzene flames at low pressure," *Proceedings of the Combustion Institute*, vol. 33, no. 1, pp. 617–624, 2011. DOI: 10.1016/j.proci.2010.06.159.
- [556] Y. Li, J. Cai, L. Zhang, T. Yuan, K. Zhang, and F. Qi, "Investigation on chemical structures of premixed toluene flames at low pressure," *Proceedings of the Combustion Institute*, vol. 33, no. 1, pp. 593–600, 2011. DOI: 10.1016/j.proci.2010.05.033.
- [557] L. Zhao, Z. Cheng, L. Ye, *et al.*, "Experimental and kinetic modeling study of premixed o-xylene flames," *Proceedings of the Combustion Institute*, vol. 35, no. 2, pp. 1745–1752, 2015. DOI: 10.1016/j.proci.2014.06.006.
- [558] W. Yuan, Y. Li, G. Pengloan, C. Togbé, P. Dagaut, and F. Qi, "A comprehensive experimental and kinetic modeling study of ethylbenzene combustion," *Combustion and Flame*, vol. 166, pp. 255–265, 2016. DOI: 10.1016/j.combustflame.2016.01.026.
- [559] B. Husson, M. Ferrari, O. Herbinet, S. S. Ahmed, P. A. Glaude, and F. Battin-Leclerc, "New experimental evidence and modeling study of the ethylbenzene oxidation," *Proceedings of the Combustion Institute*, vol. 34, no. 1, pp. 325–333, 2013. DOI: 10.1016/j.proci.2012.06.002.
- [560] T. H. Lay, J. W. Bozzelli, and J. H. Seinfeld, "Atmospheric Photochemical Oxidation of Benzene: Benzene + OH and the Benzene-OH Adduct (Hydroxyl-2,4-cyclohexadienyl) + O₂," *Journal of Physical Chemistry*, vol. 100, pp. 6543–6554, 1996. DOI: 10.1021/jp951726y.
- [561] H. Uc, J. Raú L Alvarez-Idaboy, A. Galano, and A. Vivier-Bunge, "Theoretical Explanation of Nonexponential OH Decay in Reactions with Benzene and Toluene under Pseudo-First-Order Conditions," *Journal of Physical Chemistry A*, vol. 112, pp. 7608–7615, 2008. DOI: 10.1021/jp8026258.
- [562] D. Robaugh and W. Tsang, "Mechanism and Rate of Hydrogen Atom Attack on Toluene at High Temperatures," *Journal of Physical Chemistry*, vol. 90, pp. 4159–4163, 1986. DOI: 10.1021/j100408a064.
- [563] D. L. Baulch, C. T. Bowman, C. J. Cobos, *et al.*, "Evaluated Kinetic Data for Combustion Modeling: Supplement II," *Journal of Physical and Chemical Reference Data*, vol. 34, no. 3, pp. 757–1397, 2005. DOI: 10.1063/1.1748524.
- [564] L. Pratali Maffei, T. Faravelli, C. Cavallotti, and M. Pelucchi, "Electronic structure-based rate rules for : H ipso addition-elimination reactions on mono-aromatic hydrocarbons with single and double OH/CH₃/OCH₃/CHO/C₂H₅

- substituents: a systematic theoretical investigation,” *Physical Chemistry Chemical Physics*, vol. 22, pp. 20368–20387, 2020. DOI: 10.1039/d0cp03099f.
- [565] D. S. Hollman, A. C. Simmonett, and H. F. Schaefer, “The benzene+OH potential energy surface: Intermediates and transition states,” *Physical Chemistry Chemical Physics*, vol. 13, no. 6, pp. 2214–2221, 2011. DOI: 10.1039/c0cp01607a.
- [566] T. N. Truong, W. T. Duncan, and M. Tirtowidjojo, “A reaction class approach for modeling gas phase reaction rates,” *Physical Chemistry Chemical Physics*, vol. 1, pp. 1061–1065, 1999. DOI: 10.1039/A808438F.
- [567] T. N. Truong, “Reaction class transition state theory: Hydrogen abstraction reactions by hydrogen atoms as test cases,” *Journal of Chemical Physics*, vol. 113, no. 12, p. 4964, 2000. DOI: 10.1063/1.1287839.
- [568] H. Fischer and L. Radom, “Factors controlling the addition of carbon-centered radicals to alkenes,” *Angewandte Chemie International Edition*, vol. 40, pp. 1340–1371, 2001. DOI: 10.1002/1521-3900(200206)182:1<1::AID-MASY1>3.0.CO;2-S.
- [569] W. Sun, A. Hamadi, S. Abid, N. Chaumeix, and A. Comandini, “A comparative kinetic study of C8–C10 linear alkylbenzenes pyrolysis in a single-pulse shock tube,” *Combustion and Flame*, vol. 221, pp. 136–149, 2020. DOI: 10.1016/J.COMBUSTFLAME.2020.07.031.
- [570] ———, “Detailed experimental and kinetic modeling study of toluene/C2 pyrolysis in a single-pulse shock tube,” *Combustion and Flame*, vol. 226, pp. 129–142, 2021. DOI: 10.1016/J.COMBUSTFLAME.2020.11.044.
- [571] A. Hamadi, W. Sun, S. Abid, N. Chaumeix, and A. Comandini, “An experimental and kinetic modeling study of benzene pyrolysis with C2-C3 unsaturated hydrocarbons,” *Combustion and Flame*, vol. 237, p. 111858, 2022. DOI: 10.1016/J.COMBUSTFLAME.2021.111858.
- [572] J. T. Chen, Z. H. Jin, W. Li, *et al.*, “Experimental and kinetic modeling study of benzyl alcohol pyrolysis,” *Combustion and Flame*, vol. 231, p. 111477, 2021. DOI: 10.1016/J.COMBUSTFLAME.2021.111477.